Karlsruhe Institute of Technology

# Characterization and Minimization of Background Processes in the KATRIN Main Spectrometer

Zur Erlangung des akademischen Grades eines

Doktors der Naturwissenschaften

von der Fakultät für Physik
des Karlsruher Instituts für Technologie
genehmigte

Dissertation

von

**Dipl.-Phys. Fabian Thomas Harms**

aus Pfinztal

| | |
|---|---|
| Erstgutachter: | Prof. Dr. Guido Drexlin<br>Institut für Experimentelle Kernphysik, KIT |
| Zweitgutachter: | Prof. Dr. Ulrich Husemann<br>Institut für Experimentelle Kernphysik, KIT |

Tag der mündlichen Prüfung: 23. Oktober 2015

**Declaration of authorship**

I declare that I have developed and written the enclosed thesis in hand completely by myself, and have not used sources or means without any declaration in the text.

**Erklärung der Selbstständigkeit**

Hiermit versichere ich, die vorliegende Arbeit selbstständig angefertigt, alle dem Wortlaut oder Sinn nach entnommenen Inhalte anderer Werke an den entsprechenden Stellen unter Angabe der Quellen kenntlich gemacht und keine weiteren Hilfsmittel verwendet zu haben.

.....

**Fabian Thomas Harms**

**Pfinztal, den 07. Oktober 2015**

# Zusammenfassung

In dieser Arbeit wird über die Identifikation, Charakterisierung sowie die Minimierung verschiedener, teils zuvor unbekannter untergrunderzeugender Prozesse im Hauptspektrometer des Karlsruher Tritium Neutrino (KATRIN) Experiments berichtet. Die im Zuge einer umfangreichen Messkampagne gewonnenen Erkenntnisse sind für die Bestimmung der absoluten Neutrino-Massenskala mit einer bis dato unerreichten Sensitivität von $m_{\bar{\nu}_e} = 200\,\mathrm{meV}$ (90% C.L.) von entscheidender Bedeutung.

Das Standardmodell der Teilchenphysik kennt drei masselose, elektrisch neutrale Generationen von Neutrinos. Aufgrund ihrer schwachen Wechselwirkung mit Materie und der damit einhergehenden erschwerten Nachweisbarkeit stellt die detaillierte Untersuchung ihrer physikalischen Eigenschaften Forscher seit vielen Jahrzehnten vor große experimentelle Herausforderungen. Im Jahr 1998 konnte das bahnbrechende Super-Kamiokande-Experiment nachweisen, dass es zu einer Umwandlung zwischen den verschiedenen Neutrino-Generationen kommen kann. Die Beobachtung dieses Phänomens der sogenannten Neutrino-Oszillationen impliziert nichtverschwindende Neutrino-Ruhemassen und damit Physik jenseits des Standardmodells der Teilchenphysik. Da die wegweisenden Oszillations-Experimente nicht auf die absolute Massenskala der Neutrinos sensitiv sind, wurde in den letzten 20 Jahren eine Reihe experimenteller Ansätze verfolgt, um diese sowohl in der Teilchenphysik als auch in der Kosmologie enorm wichtige Größe zu bestimmen. Der auf Grund seiner Unabhängigkeit von theoretischen Modellen vielversprechendste Ansatz ist die hochpräzise Elektronenspektroskopie des Tritium $\beta$-Spektrums nahe des kinematischen Endpunktes von $E_0 = 18{,}6\,\mathrm{keV}$. In diesem Bereich manifestiert sich eine nichtverschwindende effektive Masse des Elektron-Antineutrinos $m_{\bar{\nu}_e}$ in einer geringfügigen Formänderung des Spektrums. Das KATRIN Experiment, welches derzeit von einer internationalen Kollaboration auf dem Gelände des Campus Nord des Karlsruher Instituts für Technologie (KIT) aufgebaut wird, stellt die neueste Generation solcher auf dem Tritium $\beta$-Zerfall basierender direkten Neutrinomassen-Messungen dar. Mit Hilfe des bekannten MAC-E Filterprinzips und durch die Verwendung einer hoch-luminösen, fensterlosen gasförmigen Tritiumquelle wird KATRIN die durch seine Vorgängerprojekte bestimmte und aktuell kleinste modellunabhängige Obergrenze für die Neutrinomasse $m_{\bar{\nu}_e} < 2{,}0\,\mathrm{eV}$ (90% C.L.) um eine Größenordnung verbessern. Um dieses hochgesteckte Ziel zu erreichen ist es jedoch unabdingbar, dass das Untergrundniveau in dem $1\,240\,\mathrm{m}^3$ fassenden Hauptspektrometer des Experiments auf einem Level von weniger als einem Ereignis pro Minute gehalten wird.

In einer ersten gemeinsamen Messphase des KATRIN Hauptspektrometers mit dem Detektorsystem des Experiments konnten im Jahr 2013 über einen Zeitraum von vier Monaten wichtige Erkenntnisse über das Untergrundverhalten innerhalb dieses komplexen Systems gewonnen werden. Gleichwohl war es zu diesem frühen Zeitpunkt aufgrund der anhaltenden technischen Herausforderungen bei der Inbetriebnahme der diversen Sub-Komponenten des Aufbaus noch nicht möglich, eindeutige und abschließende Aussagen über die relativen Beträge verschiedener untergrunderzeugender Prozesse zum absoluten Untergrundniveau innerhalb des Hauptspektrometers zu machen. Dies galt insbesondere für die Prozesse der Elektronenspeicherung im Volumen und der Emission von Sekun-

därelektronen von inneren Oberflächen des Spektrometers, welche für auf dem MAC-E Filterprinzip basierende Spektrometer typisch sind.

Ausgehend von den in der ersten gemeinsamen Messkampagne gewonnenen Erkenntnissen konnte anschließend die Leistung mehrerer Sub-Komponenten innerhalb des Spektrometer- und Detektorabschnitts entscheidend verbessert werden. Dies gilt insbesondere für die volle Funktionalität aller 148 Signalkanäle des segmentierten Silizium-PIN-Detektors sowie eine deutlich verbesserte Ausrichtung aller Sub-Komponenten entlang der Strahlachse des Experiments. Gerade diese beiden Punkte sind unabdingbar, um eine vollständige Abbildung des relevanten Volumens im Spektrometer auf den Detektor zu ermöglichen. Des Weiteren konnte erstmalig ein langfristiger, hochspannungsstabiler Betrieb des mit flüssigem Stickstoff gekühlten Kupfer-Baffle-Systems des Hauptspektrometers gewährleistet werden, das als passives Mittel zur Untergrundreduktion dient. Diese und weitere deutliche Verbesserungen der Hardware ermöglichten es, dass das Hauptspektrometer- und Detektorsystem im Verlauf einer elfmonatigen zweiten Messkampagne (SDS-II) von Oktober 2014 bis September 2015 zuverlässig und stabil betrieben werden konnten. Während dieser einzigartig langen Datennahme-Phase konnten zuvor unbekannte Untergrundquellen innerhalb des Spektrometers identifiziert, und bereits bekannte minimiert und im Detail charakterisiert werden.

## Identifikation von $^{210}$Pb innerhalb des Hauptspektrometers

Im KATRIN Experiment wird das Tritium $\beta$-Spektrum mittels eines integrierenden Spektrometers vermessen, das als Hoch-Energie-Pass für die Signalelektronen fungiert. Dadurch zählt der Detektor nur diejenigen Elektronen mit Energien in einem festgelegten Intervall (ROI), die das Retardierungspotential des Spektrometers überwunden haben. Während sich bisherige Untergrunduntersuchungen hauptsächlich auf die Vermessung der Ereignisrate in diesem Energieintervall fokussiert hatten, wurden im Zuge dieser Arbeit eine Reihe von Messungen durchgeführt die eine detaillierte Untersuchung des Spektrometeruntergrundes außerhalb des kleinen 5 keV breiten Energiefensters der ROI zum Ziel hatten. Dabei wurde eine bis dato unbekannte Signatur im Untergrundspektrum entdeckt, die zweifelsfrei K-Schalen Konversionselektronen aus dem Zerfall von $^{210}$Pb zugeordnet werden konnte. Für die vom Detektor beobachtete Rate dieser 30 keV Elektronen ergab sich $R = (2{,}2 \pm 0{,}2)$ mcps.

Im Folgenden wurde ein Scenario zur Deposition von $^{210}$Pb auf den inneren Oberflächen des Spektrometers entwickelt. Dieses Modell beruht auf dem Zerfall des natürlich vorkommenden Edelgases $^{222}$Rn im Spektrometertank während der fünfjährigen Einbauphase eines inneren Elektrodensystems. Die nächsten Zerfallsprodukte von $^{222}$Rn in der $^{238}$U-Zerfallskette sind kurzlebig und können sich auf Oberflächen absetzen, bevor das langlebige $^{210}$Pb als Folge des $\alpha$-Zerfalls von $^{214}$Po erzeugt wird. Aufgrund der hohen Kernrückstoßenergie von 146 keV in diesem Zerfall kann es zu einer Implantierung des Blei-Isotopes in Edelstahloberflächen im Spektrometer kommen. Dies können sowohl die Oberfläche des Tanks als auch Teile des inneren Elektrodensystems sein. Mittels Simulationen zur Implantationstiefe von $^{210}$Pb Ionen in Edelstahl sowie zu Energieverlusten von keV-Elektronen in entsprechend dünnen Edelstahlschichten konnte gezeigt werden, dass das entwickelte Implantationsmodell mit den experimentellen Beobachtungen im Einklang steht. Dies gilt insbesondere für eine leicht erhöhte Breite der Signatur durch die $^{210}$Pb Konversionselektronen im Untergrundspektrum.

Um die Wahrscheinlichkeit zu bestimmen, mit der ein auf den inneren Oberflächen des Spektrometers erzeugtes 30 keV Elektron den Detektor erreicht, wurden aufwändige Monte-Carlo-Simulationen durchgeführt. Diese zeigten, dass die Ankunftswahrscheinlichkeit sehr stark vom genauen Entstehungsort des Elektrons und damit vom genauen Depositionsprofil

von $^{210}$Pb im Hauptspektrometer abhängt. Ein Vergleich der experimentell beobachteten radialen Verteilung der Signale der Konversionselektronen auf dem Detektor mit den Simulationsergebnissen deutet darauf hin, dass die von $^{210}$Pb-Zerfällen herrührenden Elektronen ihren Ursprung hauptsächlich auf dem inneren Elektrodensystem haben. Unter der Annahme einer homogenen Deposition von $^{210}$Pb auf Letzterem konnte die absolute Aktivität des Blei-Isotopes im Spektrometer auf $(862 \pm 99)$ Bq abgeschätzt werden. Im Vergleich zu anderen oberflächenbezogenen Quellen hochenergetischer Elektronen stellt dies einen nicht zu vernachlässigenden Anteil dar.

Um abschätzen zu können, wie stark $^{210}$Pb induzierte niederenergetische Primärelektronen zum Untergrund in der Standard ROI des Experiments beitragen, wurden weitere Simulationen durchgeführt. Hierbei konnte bei kleinen Elektronenenergien eine deutlich verringerte Ankunftswahrscheinlichkeit der Elektronen auf dem Detektor festgestellt werden. Ein direkter Untergrundbeitrag durch $^{210}$Pb induzierte Elektronen in der ROI ist daher vernachlässigbar klein. Im Gegensatz dazu stellte sich jedoch heraus, dass hochenergetische Elektronen aus $^{210}$Pb Zerfällen, die kurzfristig in den äußeren Bereichen des Spektrometervolumens gespeichert werden, durch die Ionisation von Restgas-Molekülen indirekt zum Untergrund in der ROI beitragen können. Die radiale Verteilung der dabei entstehenden Sekundärelektronen reproduziert zudem die Charakteristika einer druckabhängigen Untergrundkomponente, die während der SDS-II Messungen beobachtet werden konnten.

Aufgrund der Vergleichbarkeit des $\beta$-Spektrums von $^{210}$Pb mit dem des Tritium-Zerfalls lassen die Charakteristika des $^{210}$Pb induzierten Untergrundes Rückschlüsse auf etwaige quellbedingte Untergrundbeiträge zu. Dies schließt insbesondere die im Falle einer nicht-idealen Tritium-Retention in der Transportsektion des Experiments auftretende Implantierung geringfügiger Mengen von Tritium-Ionen aus der Quelle in den Spektrometeroberflächen ein.

## Der Radon-induzierte Untergrund

In früheren Arbeiten konnten gespeicherte hochenergetische Elektronen in Folge von $\alpha$-Zerfällen der Radonisotope $^{219}$Rn und $^{220}$Rn im KATRIN Hauptspektrometer als großer Untergrundbeitrag identifiziert und charakterisiert werden. Aufgrund von technischen Limitierungen war es zu diesem Zeitpunkt jedoch nicht möglich, abschließende und eindeutige Aussagen über die Emanationsquellen dieser Radon-Isotope innerhalb des Tanks, über die Radon-Unterdrückungseffizienz des mit flüssigem Stickstoff gekühlten Baffle-Systems sowie über den exakten relativen Anteil der durch Radon induzierten Ereignisse am absoluten Untergrundniveau zu treffen. Dank der vollen Funktionalität aller Sub-Komponenten des Spektrometer- und Detektorsystems während SDS-II und der konsequenten Weiterentwicklung bereits existierender Analyse-Algorithmen zur Identifikation von Radon-Zerfallssignaturen in den Untergrunddaten, konnte der Radon-induzierte Untergrund im Zuge dieser Arbeit vollständig charakterisiert werden.

Die genaue Kenntnis der relativen Beträge verschiedener Radon-Emanationszentren im Hauptspektrometer zum absoluten Untergrundniveau ist essentiell, um mögliche Gegenmaßnahmen, wie z. B. das Baffle-System, sinnvoll und effizient einsetzen zu können. Um die erforderlichen Ultra-Hochvakuum-Bedingungen im Spektrometer zu gewährleisten, sind in jedem seiner drei Hauptpumpstutzen Getterstreifen (NEG) mit einer Gesamtlänge von je 1 km verbaut. Das NEG Material, welches hohe Pumpgeschwindigkeiten für Wasserstoff und Tritium garantiert, ist gleichzeitig aber auch eine bekannte Emanationsquelle von $^{219}$Rn. Zusammen mit anderen Radonquellen im Tank, wie z. B. den Edelstahloberflächen oder Vakuummessröhren, summiert sich die beobachtbare Gesamtaktivität von $^{219}$Rn und $^{220}$Rn im Spektrometer so auf $(196 \pm 4)$ mBq (Stand September 2013). Der Ausbau eines

Drittels des Gettermaterials ermöglichte es, die unterschiedlichen Radonbeträge im Zuge der SDS-II Messungen aufzulösen. So ergab sich ein Beitrag von $A_{\mathrm{NEG}} = (77 \pm 14)\,\mathrm{mBq}$ pro 1 km Getterstreifen und ein mit Null verträglicher Beitrag $A_{\mathrm{other}} = (-35 \pm 42)\,\mathrm{mBq}$ von anderen Radonquellen im Tank. Diese enorm wichtige Erkenntnis belegt eindeutig, dass das NEG-Material in den Pumpstutzen des Spektrometers die größte - wenn nicht sogar einzige - Quelle von Radon ist.

Die direkte Sichtlinie zwischen den Getterstreifen und dem sensitiven Volumen des Spektrometers wird durch drei mit flüssigem Stickstoff gekühlte Kupfer-Baffle-Systeme blockiert, die am spektrometerseitigen Ende des jeweiligen Pumpstutzens angebracht sind. Radonatome, die auf die kalten Kupferoberflächen auftreffen, werden dort für eine gewisse Zeitspanne haften bleiben und deshalb mit hoher Wahrscheinlichkeit auf der Baffleoberfläche und nicht im Spektrometervolumen zerfallen. Die erstmalige volle Einsatzfähigkeit des Bafflesystems während der SDS-II-Messphase ermöglichte es, die Effizienz dieses Systems in Bezug auf die Reduktion des Radon-induzierten Untergrundes detailliert zu untersuchen. Hierbei konnten die Radonzerfälle innerhalb des Spektrometervolumens bei einem kalten Betrieb aller drei Bafflesysteme um $(95{,}1 \pm 0{,}3)\%$ reduziert werden. Des Weiteren bekräftigte der Vergleich der experimentell bestimmten Reduktionseffizienzen mit den Ergebnissen aufwändiger Monte-Carlo-Simulationen die zuvor aufgestellte Hypothese, dass es sich bei den Getterstreifen um die hauptsächliche Emanationsquelle von Radon im Spektrometer handelt. Zusätzliche Messungen mit einer an verschiedenen Punkten des Spektrometers installierten künstlichen $^{220}$Rn-Quelle haben zudem signifikante Effizienzunterschiede zwischen den verschiedenen Bafflesystemen aufgezeigt, welche sich höchstwahrscheinlich auf eine unzureichende Temperaturregulierung einzelner Baffle zurückführen lassen.

Mittels eines detaillierten Vergleichs mehrerer Langzeit-Untergrundmessungen mit verschiedenen Kombinationen kalt-betriebener Baffle war es möglich, ein stringentes oberes Limit für die verbleibende Radon-induzierte Untergrundrate bei einem nominalen Betrieb des Spektrometers zu bestimmen. Im Falle von 3 km installierten Getterstreifen und dem kalten Betrieb aller Bafflesysteme ergab sich ein Limit von $R \leq 36^{+18}_{-15}\,\mathrm{mcps}$.

## Charakterisierung des nicht Radon-induzierten Untergrundes

Dank der erfolgreichen Reduzierung des Radon-induzierten Untergrundes mittels des Baffle-Systems war es während der SDS-II Messkampagne möglich, die nicht von Radonzerfällen herrührenden Untergrundereignisse im Spektrometer im Zuge dieser Arbeit detailliert zu charakterisieren. Im Nominalbetrieb des unausgeheizten Spektrometers zu Beginn von SDS-II wurde ein absolutes Untergrundlevel von $R = (691 \pm 1)\,\mathrm{mcps}$ im Spektrometer gemessen. Dieses konnte durch eine ausgiebige thermische Konditionierung der Spektrometer-Oberflächen um $(40{,}2 \pm 0{,}3)\%$ auf $(413 \pm 2)\,\mathrm{mcps}$ reduziert werden. Unter Inkaufnahme einer verschlechterten Energieauflösung des Experiments lässt sich der Untergrund durch eine Erhöhung des Magnetfeldes im Zentrum des Spektrometers und der damit einhergehenden Verringerung des beobachteten Volumens weiter in den Bereich von 100 mcps reduzieren. Selbst in diesem Extremfall wäre der Untergrund jedoch weiter zu hoch, um die angestrebte Sensitivität von KATRIN von 200 meV auf die effektive Masse des Elektron-Antineutrinos zu erreichen. Darum ist eine detaillierte Charakterisierung der Eigenschaften des verbleibenden Untergrundes unerlässlich.

Zu Beginn der SDS-II-Messphase wurde der Hauptteil des nicht Radon-induzierten Untergrundes auf die Emission von Myon-induzierten Sekundärelektronen von den inneren Oberflächen des Spektrometers zurückgeführt. Während SDS-II konnte im Zuge von Untersuchungen zur Sekundärelektronen-Emission eine Untergrenze für die Rate der von

der $690\,\mathrm{m}^2$ umfassenden Oberfläche des Spektrometertanks emittierten Elektronen von $R_{\mathrm{em}} \gtrsim 35 \times 10^3\,\mathrm{cps}$ bestimmt werden. Diese Rate konnte durch das Anlegen einer geringen Spannung von $-5\,\mathrm{V}$ auf dem inneren Elektrodensystem und die daraus resultierende elektrostatische Abschirmung der Tankoberfläche um bereits ca. 70% reduziert werden. Mittels einer Korrelationsanalyse der verbleibenden Untergrundrate mit dem Fluss kosmischer Myonen in der KATRIN-Spektrometerhalle konnte gezeigt werden, dass nur ein geringer Anteil der Sekundärelektronen von $(13{,}6 \pm 0{,}8)\%$ durch Myonen induziert wird. Diese Erkenntnis steht im krassen Widerspruch zu bisher gängigen, konventionellen Untergrundszenarien für ein auf dem MAC-E-Filterprinzip basierendes Spektrometer.

Aufgrund der nahezu perfekten Axialsymmetrie des magnetischen Feldes in einem MAC-E Filter wird die große Mehrheit der an den Oberflächen erzeugten Sekundärelektronen über die Zyklotronbewegung direkt an ihren Entstehungsort zurückgeführt. Nur ein sehr geringer Anteil aller an den Oberflächen erzeugten Elektronen schafft es, diese intrinsische magnetische Abschirmung des Filters zu überwinden und in den sensitiven Teil des Spektrometer-Volumens vorzudringen, wo er mittels der Ionisation von Restgas-Molekülen zum Untergrund beitragen kann. In einer ausgedehnten Untersuchung zur Abhängigkeit des Spektrometer-Untergrundes von verschiedenen Betriebsparametern des Experiments konnte gezeigt werden, dass die Effizienz der intrinsischen magnetischen Abschirmung die Erwartungen deutlich übertrifft. Deshalb konnte in SDS-II-Messungen keinerlei Korrelation zwischen dem Untergrundniveau im Spektrometer und dem Fluss kosmischer Myonen in der KATRIN-Experimentierhalle gefunden werden. Des Weiteren konnte gezeigt werden, dass die Untergrunddichte im Spektrometer vom absoluten Magnetfeld unabhängig ist; Eine Beobachtung, die ebenfalls in deutlichem Widerspruch zu den Erwartungen für herkömmliche Untergrundszenarien steht. Abschließend konnte zudem gezeigt werden, dass der Effekt, den eine elektrostatische Abschirmung der Spektrometer-Oberfläche mittels des inneren Elektrodensystems auf die Radialverteilung des Spektrometer-Untergrundes ausübt, nicht in Einklang mit einem hauptsächlich durch Sekundärelektronen induzierten Untergrund gebracht werden kann. Diese konventionelle Hypothese zur Entstehung des nicht durch Radonzerfälle hervorgerufenen Untergrundes im KATRIN-Hauptspektrometer konnte im Zuge dieser Arbeit somit widerlegt werden.

Eine weitere wichtige Beobachtung, die bei den SDS-II-Messungen gemacht werden konnte, ist die Unwirksamkeit aktiver Untergrund-Reduktionsmethoden, wie z. B. gepulsten oder statischen Dipolfeldern im Spektrometer. Diese Methoden sorgen normalerweise dafür, dass niederenergetische Elektronen, die im Volumen des Spektrometers gespeichert sind, aus diesem herausgedriftet werden und daher nicht länger durch die Ionisation von Restgas-Molekülen zum Untergrund beitragen können. Da dieser Effekt während SDS-II nicht beobachtet werden konnte, war es möglich, neben den bereits durch das Baffle-System minimierten Beiträgen durch Radon-induzierte hochenergetische gespeicherte Elektronen auch solche mit Energien im eV-Bereich als Ursache des Untergrundes auszuschließen. Diese Erkenntnis wurde weiter dadurch bekräftigt, dass eine Verstärkung des magnetischen Spiegeleffekts durch ein erhöhtes Magnetfeld auf der Detektorseite des Spektrometers nur zu einer geringen Untergrundreduktion führte. Diese Beobachtung verträgt sich ebenfalls nicht mit einem auf gespeicherten Elektronen basierenden Untergrundszenario.

Da im Zuge dieser Arbeit alle konventionellen untergrunderzeugenden Mechanismen in Spektrometern, die auf dem MAC-E-Filterprinzip basieren, als Ursache für das deutlich erhöhte Untergrundniveau im KATRIN-Hauptspektrometer ausgeschlossen werden konnten, muss ein komplett neuartiges Szenario entwickelt werden. Ein vielversprechendes Modell zur homogenen Erzeugung niederenergetischer Untergrundelektronen im gesamten Spektrometervolumen wurde hierbei vor Kurzem in der KATRIN-Kollaboration vorgestellt. Es beruht auf der Ionisation hochangeregter Wasserstoff-Rydbergatome durch die vom Spektrometertank bei einer Temperatur von $300\,\mathrm{K}$ emittierte Schwarzkörperstrahlung.

Dieses Untergrundszenario steht im Einklang mit allen während der SDS-II-Messphase beobachteten Charakteristiken des Spektrometer-Untergrundes. Es liefert dabei auf unkomplizierte Art und Weise unter anderem eine Erklärung für die Skalierbarkeit der Untergrundrate mit dem beobachteten Spektrometervolumen, für die radial unabhängige Wirkungsweise einer elektrostatischen Abschirmung der Tankoberflächen auf das Untergrundniveau und insbesondere, für die deutliche Reduktion des Untergrundes durch die thermische Konditionierung der inneren Oberflächen des Spektrometers im Zuge einer zweiwöchigen Ausheizphase des Spektrometers.

Abschließend lässt sich sagen, dass die in dieser Arbeit gewonnenen Erkenntnisse deutlich zum Verständnis der untergrunderzeugenden Prozesse in Spektrometern, die auf dem MAC-E Filterprinzip basieren beitragen, und einen Meilenstein auf dem Weg zu einer erfolgreichen Neutrino-Massenbestimmung mit KATRIN darstellen.

# Introduction and Objectives

The thesis in hand summarizes work performed in the context of the identification, characterization, and minimization of background sources in the large-scale main spectrometer of the Karlsruhe Tritium Neutrino (KATRIN) experiment. These works are of crucial importance to reach the nominal background level of 10 mcps ($10^{-3}$ counts per second) which is an essential prerequisite for KATRIN to assess the absolute mass scale of neutrinos with an unsurpassed sensitivity of 200 meV (90% C.L.).

When experiments like Super-Kamiokande or SNO found irrefutable evidence for the phenomenon of neutrino flavor oscillations more than a decade ago, they revolutionized the field of neutrino physics. Now that neutrinos are indisputably massive particles, their role in pointing to novel physics beyond the standard model of particle physics, has dramatically increased their key importance in this field of science. These observations have also motivated the development of a series of experiments to assess the absolute mass scale of neutrinos, a quantity not accessible by the pioneering oscillation experiments. There is a broad range of dedicated neutrino mass experiments, which range from cosmological surveys investigating the 'fingerprint' of primordial neutrinos on the evolution of the universe, to the search for rare processes like neutrinoless double $\beta$-decay. One very promising (and the only model-independent) approach sticks out: the direct determination of the effective mass of the electron antineutrino based on high-precision spectroscopy of electrons from tritium $\beta$-decays.

The KATRIN experiment represents the leading and most advanced next-generation project of such direct neutrino mass experiments, pushing this promising approach to the limits of technical feasibility. By combining an ultra-luminous windowless gaseous tritium source (WGTS) with a large-scale integrating spectrometer based on the well-established MAC-E filter technique, KATRIN is targeted to surpass the current upper sensitivity of $m_{\bar{\nu}_e} < 2.0\,\mathrm{eV}$ (95% C.L.), derived by its predecessor experiments, by one order of magnitude. With the recent arrival of the WGTS cryostat on site at the Campus North of the Karlsruhe Institute of Technology (KIT) on September $10^{\mathrm{th}}$, 2015, the 70-m long beam line of the experiment is completed and currently being prepared for the start of tritium data-taking in mid-2016.

As only a small fraction of the signal electrons features energies in the relevant endpoint region of the tritium $\beta$-spectrum close to 18.6 keV, where a non-zero neutrino rest mass will manifest in a change of the spectral shape, KATRIN relies on a background level in the few mcps regime in order to achieve its ambitious goals. With a total volume (surface) of about $1\,240\,\mathrm{m}^3$ ($690\,\mathrm{m}^2$), the 10-m diameter stainless steel vessel of the experiment's MAC-E filter spectrometer represents the major contribution to background processes. Therefore, a detailed characterization and minimization of spectrometer-related background mechanisms represents a key requirement for the success of KATRIN. This major task was accomplished in the course of this thesis in the context of an 11-months long commissioning measurement phase of the spectrometer and detector section (SDS) of the experiment.

The key objectives here were:

- The hardware preparation of the SDS setup for long-term operation to obtain full functionality of all of its subsystems, supplemented by an evaluation of the performance of all units over the course of several months of continuous operation.
- To perform an in-depth analysis of background levels and event signatures induced by $\alpha$-decays of radon atoms emanated into the spectrometer volume, to identify individual emanation sites of this isotope in the SDS setup, and to optimize the effectiveness of radon suppression by an array of liquid $N_2$-cooled copper baffles.
- To investigate spectrometer background processes producing events with energies outside of the KATRIN standard energy region-of-interest, in order to identify potential signatures from yet unaccounted-for sources of intrinsic radioactivity in the SDS setup.
- To fully characterize the remaining, non-radon-induced background in the nominal operation of the SDS setup and to study its dependence on key operating parameters of the system, so that a coherent model of background-generating processes in the KATRIN main spectrometer can be established.

**Outline**

In Chapter 1 of this thesis, a brief historical overview of the field of neutrino physics is given, which highlights experimental milestones such as the first discovery of neutrinos in the 1950s and the first observation of neutrino flavor oscillations in the 1990s. The impact of the latter investigations on the standard model of particle physics and more advanced theoretical methods to explain the massiveness of neutrinos are discussed. Finally, the different experimental approaches to assess the absolute $\nu$-mass scale with special emphasis on dedicated single $\beta$-decay experiments are presented.

The KATRIN experiment as the pre-eminent project of a variety of next-generation model-independent direct neutrino-mass measurements is introduced in Chapter 2. Its working principle based on the MAC-E filter technique for high-precision tritium $\beta$-spectroscopy is explained in detail. Furthermore, a brief overview of the main components of the setup is given, supplemented by an outline of the major challenges that have to be met to obtain the design sensitivity on the neutrino mass.

The focus of Chapter 3 lies on an in-depth description of the SDS part of the experiment as implemented prior to the 11-months long second commissioning measurement campaign (SDS-II). In this context, several major hardware improvements of the system are discussed and the performance of its main components during the long-term data-taking is presented in detail. This forms the basis for the subsequent discussion of background processes in the KATRIN main spectrometer.

Chapter 4 is targeted on the detailed investigation of a major background component: the electron-associated $\alpha$-decays of specific radon isotopes in the spectrometer volume. This was achieved by a consistent further development of preexisting analysis techniques and by applying them to high-quality data sets recorded in the context of this thesis. In this way conclusive statements can be made on the absolute level of radon-induced background, the sources of radon emanation in the SDS setup, and the effectiveness of the liquid $N_2$-cooled baffle system in terms of radon suppression.

Chapter 5 reports on the identification of a previously unknown background contribution by electrons generated via the decay of $^{210}$Pb on the main spectrometer surfaces. Based on the experience in other low-level experiments, a specific deposition model for this long-lived isotope in the spectrometer is derived, which allows to estimate its absolute activity

in the SDS setup. Furthermore, the impact of $^{210}$Pb decays and its progenies on the overall background level is discussed.

Based on the findings in the previous chapters, the non-radon-induced background is characterized in detail in Chapter 6. In this regard, the impact of several of the key operating parameters of the SDS apparatus on the background level is evaluated. In addition, electron emission processes from inner surfaces of the spectrometer are discussed, before a recently-proposed background model based on excited Rydberg states of hydrogen is investigated in detail.

The thesis in hand is completed by Chapter 7, where a detailed summary of the works performed and the main results is given. The chapter concludes with an outlook of the impact of this work on the KATRIN neutrino mass sensitivity.

# Contents

CHAPTER 1

# Neutrino Physics

*"Neutrino physics is largely an art of learning a great deal by observing nothing."*
Haim Harari, 1988 [Sch88]

The above quote nicely summarizes the long and strenuous quest in neutrino physics to first verify the existence and then to characterize the properties of these elusive particles. Due to their feeble interaction with matter, the experimental study of neutrinos has been a challenging enterprise from day one on. Accordingly, it took 30 years from their postulation by W. Pauli to their first detection in the famous 'Poltergeist' experiments. Driven by the groundbreaking discovery of neutrino flavor oscillations, neutrino physics provides a key path to physics beyond the standard model due to the solid evidence for massive neutrinos. The continuously growing field of neutrino physics, thus, has emerged as one of the most active parts of particle and astroparticle physics over the past twenty years. At the same time, the high number density of primordial neutrinos has left a 'fingerprint' in the evolution of the early universe, rendering the precise knowledge of their rest mass an important ingredient for cosmological studies. Unraveling the intrinsic properties of neutrinos is a world-wide effort pursued by dedicated experiments like the Karlsruhe Tritium Neutrino (KATRIN) experiment.

The objective of this Chapter is to put the KATRIN experiment into the context of many decades of experimental neutrino physics. Starting with a brief overview of the early history of the field in Section 1.1, the detection of the free neutrino in the famous 'Poltergeist' experiment is highlighted in Section 1.2. In the Standard Model (SM) of particle physics, neutrinos are treated as massless fermions (Section 1.3), an assumption that had to be discarded after the discovery of neutrino flavor oscillations 1998 (Section 1.4). The possibilities to incorporate non-zero neutrino rest masses into the SM are briefly discussed in Section 1.5, while Section 1.6 focuses on the dedicated approaches to assess the neutrino rest mass from an experimental point of view.

## 1.1 The Early History of Neutrino Physics

After the first discovery of the phenomenon of radioactivity by A. Becquerel in 1896, three different forms of radioactive decays were known by the beginning of the $20^{\text{th}}$ century [Bec01]: $\alpha$-, $\beta$- and $\gamma$-radiation [Rut03]. At that time it was common sense that the energy spectrum of the $\beta$-radiation should be of a characteristic discrete shape for each radioactive element, as it had already been observed in the case of $\alpha$-radiation. However, in 1914 J. Chadwick was able to proof the continuous nature of the $\beta$-decay spectrum during his work in the laboratories of H. Geiger in Berlin [Cha14]. To do so, he made use

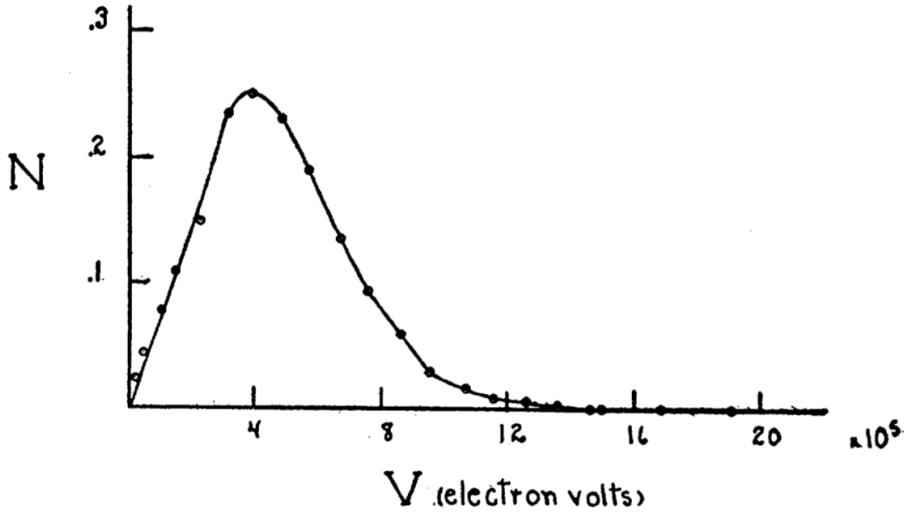


**Figure 1.1: The continuous $\beta$-spectrum of radium** measured with a Geiger-Mueller counter. From [Sco35].

of a detector, originally developed by Geiger (and later known as Geiger-Mueller counter), to study the energy spectrum of the $\beta$-decay of radium, as shown exemplary in Figure 1.1.

Up to this point the $\beta$-decay was assumed to be a two-body decay only, so that a continuous shape of the $\beta$-spectrum would imply a violation of the fundamental laws of energy and momentum conservation. This dilemma was not resolved until 1930 when W. Pauli wrote an open letter to L. Meitner and the "Radioactive Ladies and Gentlemen" of a meeting in Tübingen [Pau30]. In this famous letter he proposed a new, electrically neutral, spin-1/2 particle. This particle would be emitted from the nucleus during the $\beta$-decay together with the electron, making it a three body decay

$$ {}^{A}_{Z}\mathrm{X} \;\rightarrow\; {}^{A}_{Z+1}\mathrm{Y} + e^{-} + \overline{\nu}_{\mathrm{e}} \quad . \tag{1.1} $$

In this way, the electron would share the constant decay energy with the hypothetical particle, thus explaining the continuous $\beta$-spectrum. Pauli expected the mass of this new particle to be smaller than 0.01 proton masses [Pau30].

Two years later in 1932, J. Chadwick, then assistant director of research in the Cavandish Laboratory, Cambridge, discovered the neutron as part of the atomic nucleus when he investigated the properties of an unusual radiation emitted by a beryllium target bombarded by $\alpha$-radiation [Cha32]:

$$ \alpha + {}^{9}_{4}\mathrm{Be} \;\rightarrow\; {}^{12}_{6}\mathrm{C} + n \quad . \tag{1.2} $$

The findings of Chadwick encouraged the Italian physicist E. Fermi in 1934 to formulate a coherent theory for the three-body $\beta$-decay, describing it as a point-like weak interaction of the four involved fermions

$$ n \;\rightarrow\; p + e^{-} + \overline{\nu}_{\mathrm{e}} \quad . \tag{1.3} $$

Fermi in this context picked up Paulis idea of a third particle $\overline{\nu}_e$ produced in the $\beta$-decay and gave it its present name: Neutrino[1], meaning "the little neutral one" [Fer34]. In the same year H. Bethe and J. Peierls calculated the interaction cross section of an MeV-scale neutrino with a nucleus (inverse $\beta$-decay) to be $\sigma < 1 \times 10^{-44}\,\mathrm{cm}^2$. This corresponded

[1] To be precise, the particle involved in the $\beta$-decay reaction stated in Equation 1.3 is nowadays known as electron antineutrino.

to a penetration power of $10^{16}$ km in solid matter, causing them to conclude that it is "absolutely impossible to observe processes of this kind with the neutrinos created in nuclear transformations" [BP34]. For another two decades they were proven right as no experimental evidence for neutrinos was found so that they remained ghost-like particles.

## 1.2 The Experimental Discovery of Neutrinos

In 1951 C. L. Cowan, Jr., and F. Reines, at that time both working at Los Alamos, had the idea for "the first experiment in neutrino physics" [Rei97] which they named 'Project Poltergeist'. The nuclear fission reactors developed in the 1940s represented a new and potentially very strong source of neutrinos as a single fission reaction was theoretically expected to produce on average 6 antineutrinos with energies in the MeV-range. Cowan and Reines planned to use the high flux of antineutrinos from a reactor to observe the inverse $\beta$-decay reaction

$$\overline{\nu}_{\mathrm{e}} + p \;\rightarrow\; e^{+} + n \tag{1.4}$$

inside a target tank filled with water. The positron generated in the reaction annihilates with an electron, thereby generating characteristic $\gamma$-photons with energies of 511 keV each, which are emitted in opposite directions. Those photons are subsequently detected by liquid scintillators with photomultiplier readout surrounding the target tank. By dissolving cadmium chloride in the water, the neutrons generated in the reaction given in Equation 1.4 are absorbed by a cadmium nucleus after being thermalized in the water. The $\mathrm{Cd}^{*}$ nucleus de-excites to its ground state by emitting MeV $\gamma$-photons. By making use of a delayed coincidence measurement of the $\gamma$-photons from the positron annihilation and those from the subsequent $\mathrm{Cd}^{*}$ de-excitation, the crucial discrimination of background related to neutrons or $\gamma$-photons from the reactor was possible [Rei97] (see Fig. 1.2).

From 1955 on, the team of Cowen and Reines started its measurements at the Savannah River nuclear power plant in South Carolina, USA, using two target tanks filled with a total of 200 liters of a cadmium-chloride-water dissolution. The tanks were sandwiched in between three layers of scintillator detectors. While signals from inverse $\beta$-decay reactions in one of the target tanks appeared only in the two neighboring detector layers, background signals from cosmic muons would most likely appear in all three detectors in a random order. In this way, cosmic-muon induced backgrounds could be efficiently vetoed [Rei97]. In July 1956, after 1371 measurement hours the group of Cowan and Reines could claim the detection of the free electron antineutrino with a cross section for the inverse $\beta$-decay which was in good agreement with the theoretical expectations of $\sigma = 6.3 \times 10^{-44}\,\mathrm{cm}^2$ at that time[2] [Cow56].

In 1962, a second kind of neutrinos, the $\nu_{\mu}$, was found by a now famous experiment of M. Schwartz, L. M. Lederman, and J. Steinberger at Brookhaven National Laboratory (BNL). At BNL, high-energy protons from the particle accelerator AGS were used to bombard a beryllium target, thus generating pions which subsequently decayed in-flight via

$$\pi^{+} \;\rightarrow\; \mu^{+} + \nu_{\mu} \qquad \text{and} \qquad \pi^{-} \;\rightarrow\; \mu^{-} + \overline{\nu}_{\mu} \quad . \tag{1.5}$$

While muons as well as remaining pions or other particles such as neutrons were absorbed by a 13.5-m thick iron shielding, located at a distance of 21 m from the beryllium target, neutrinos were passing through the shield to reach a 10-ton aluminum spark chamber detector. Schwartz, Lederman, and Steinberger were able to show that only muons and no electrons were generated in reactions of the neutrinos inside the detector. This conclusively proved that $\nu_{\mu}$ and $\nu_{\mathrm{e}}$ are non-identical particles [Dan62].

[2] The theoretically and experimentally derived values for the cross-section doubled until 1960 as described in [Rei97].

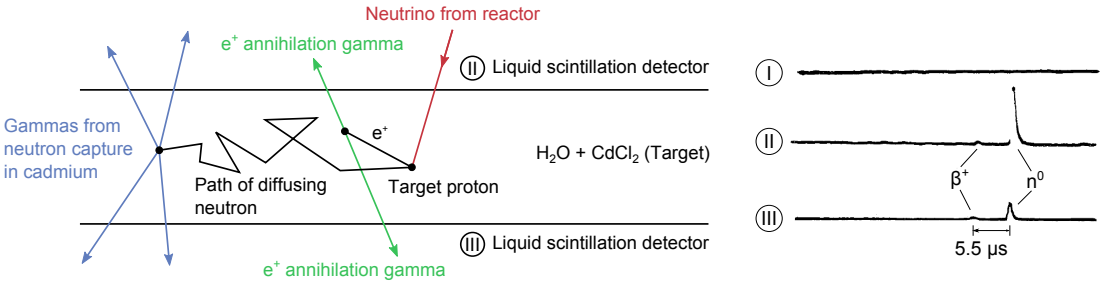


**Figure 1.2: The measurement principle of the 'Poltergeist' experiment. Left:** Schematic illustration of the inverse $\beta$-decay reaction of an incoming reactor neutrino (red) with a target proton. The generated positron annihilates promptly after its creation under the emission of two coincident $\gamma$-photons (green), whereas the neutron thermalizes in the $H_2O$ before being captured by a Cadmium nucleus. The exited Cd-nucleus decays to the ground state by the emission of several MeV $\gamma$-photons (blue). Figure inspired by [RC56]. **Right:** The characteristic scope record of an inverse $\beta$-decay reaction like the one shown on the left. The three traces correspond to three detectors. The prompt signal of the two $\gamma$-photons from the positron annihilation is followed by the delayed signal from the neutron capture. Signal amplification in this example was chosen to measure the pulse from the neutron capture. Figure adapted from [RC56].

With the discovery of the $\tau$ as the third leptonic particle besides the electron and the muon in 1975 [Per75], the existence of a third neutrino flavor state, the $\nu_\tau$, was already conceivable. Nevertheless, it took 25 years until the DONUT collaboration announced the experimental discovery of the $\nu_\tau$ in 2001. At Fermilab, the interactions of 800-GeV protons from the Tevatron accelerator impinging onto a tungsten beam dump were generating particle showers that contained unstable $D_S$ mesons. These subsequently decayed purely leptonically according to

$$D_S \rightarrow \tau + \overline{\nu}_\tau \quad , \tag{1.6}$$

to generate tau-neutrinos, both directly and via the following leptonic and hadronic decays of the $\tau$. Again, the neutrino beam was isolated from other generated particles via shielding by iron and lead wells. The target consisted of a series of stainless-steel sheets which were interleaved with emulsion plates. There, tauons from $\nu_\tau$-interactions were produced with a typical path length of the $\tau$ of about 2 mm. The characteristic decay kink in their trajectory was recorded by emulsion plates. This kink corresponds to a decay with large transverse momentum. In an ensemble of 203 identified neutrino induced reactions inside the emulsion plates, 4 tau-neutrino interactions were found with a contribution of background events estimated to 0.34 [DON01].

## 1.3 Neutrinos in the Standard Model of Particle Physics

The standard model (SM) of particle physics describes the three known, light generations of neutrinos ($\nu_e$, $\nu_\mu$, and $\nu_\tau$) together with their corresponding leptonic partners ($e^-$, $\mu^-$ and $\tau^-$) as three doublets transforming under the weak isospin SU(2) gauge symmetry[3]. Together with the U(1) symmetry of the hypercharge Y, the gauge group SU(2) $\otimes$ U(1) is formed, which unifies the electromagnetic and the weak interaction[4]. While the weak interaction is mediated by three massive gauge bosons ($W^\pm$ and $Z^0$), the electromagnetic interaction is mediated by the massless photon. The first attempts of an electroweak unification in the 1960s by S. Glashow [Gla61], A. Salam, and J. Ward [SW64] suffered from the fact that the introduction of mass terms into the SU(2) $\otimes$ U(1) Lagrangian broke the

[3] The same holds for the antineutrinos $\bar{\nu}_e$, $\bar{\nu}_\mu$, and $\bar{\nu}_\tau$.

[4] The SM is completed by introducing the $SU_c(3)$ symmetry for the strong interactions, thereby forming the $SU_c(3) \otimes SU(2) \otimes U(1)$ group.

gauge invariance of the theory. In 1967 S. Weinberg and A. Salam independently formulated a theory of leptons [Wei67, Sal68], where they used the so-called Higgs mechanism to give mass to the gauge bosons $W^{\pm}$ and $Z^0$. This then-new mechanism was formulated in 1964 by P. Higgs, F. Englert, and R. Brout when they extended the Goldstone theorem[5] [Gol61] to local U(1) gauge symmetries. By introducing a scalar Higgs field into the $SU(2) \otimes U(1)$ Lagrangian that couples with the gauge fields of U(1), mass is given to the gauge bosons $W^{\pm}$ and $Z^0$ via spontaneous symmetry breaking, with the photon remaining massless. Three unphysical massless Goldstone bosons were thus eliminated from the theory by the gauge freedom, while one massive boson remains [Hig64]. This theoretically predicted Higgs boson was finally discovered at the LHC in 2012 [ATL12, CMS12].

Already in 1956, C. S. Wu experimentally proved the important fact of maximal violation of parity conservation in weak interactions [Wu 57], which was suggested by T. D. Lee and C. D. Yang earlier in the same year [LY56]. As a result of these findings, a fundamental left-right asymmetry in weak interactions emerged, where only left-handed particles and right-handed antiparticles couple to the weak gauge bosons. The physical observable connected to the handedness of a particle, the helicity $h = \vec{s} \cdot \vec{p}$, denotes the projection of a particles spin $\vec{s}$ onto its momentum $\vec{p}$. As the helicity operator is not Lorentz-invariant one can always find a reference frame in which the momentum of a massive particle flips. Thus, massive particles can be detected with positive helicity (right-handed) even if they were generated in a weak interaction, while massless particles will have negative helicity (left-handed) only.[6] In 1958, M. Goldhaber and others investigated the electron capture of $^{152m}$Eu and the subsequent deexcitation of the daughter nucleus $^{152}$Sm$^*$ according to

$$\begin{aligned} e^- + {}^{152m}\mathrm{Eu} &\rightarrow {}^{152}\mathrm{Sm}^* + \nu_e + 950\,\mathrm{keV} \\ {}^{152}\mathrm{Sm}^* &\rightarrow {}^{152}\mathrm{Sm} + \gamma + 961\mathrm{keV} \quad . \end{aligned} \tag{1.7}$$

By measuring the polarization of photons and assuming conservation of momentum and angular momentum, they determined the helicity of neutrinos generated in the electron capture to $h_\nu = -1.0 \pm 0.3$ [GGS58]. Based on these key findings, neutrinos in the SM of particle physics are described as massless, left-handed particles, supplemented by their corresponding right-handed antiparticles $\overline{\nu}$.

In 1989, a full 12 years before the discovery of the $\nu_\tau$, the ALEPH experiment investigating the width of the $Z^0$ resonance at the LEP collider at CERN, found evidence for the existence of three light types of neutrinos participating in weak interactions. According to the electroweak theory, the $Z^0$ boson decays into all fermions that are kinematically allowed with comparable probabilities. Thus, the total decay width $\Gamma_{Z^0}$ increases with the number of light neutrino species $N_\nu$ according to:

$$\Gamma_{Z^0} = N_\nu \Gamma_\nu + 3\Gamma_{ee} + \Gamma_{\mathrm{had}} \quad . \tag{1.8}$$

The ALEPH finding of $N_\nu = 3.3 \pm 0.3$ was consistent with the SM expectation of three generations of light left-handed neutrinos[7] [DeC89]. More recent results from the combined analysis of LEP and SLC data gives $N_\nu = 2.9840 \pm 0.0082$ [Oli14].

[5] According to the Goldstone theorem a theory gains one massless boson for each continuous symmetry that is spontaneously broken.

[6] The probability to find a massive particle that is generated in a weak interaction with positive helicity is $P \propto (1 - \frac{v}{c})$.

[7] The ALEPH result does not exclude the existence of heavy neutrinos with $m_\nu > 0.5 \cdot m_{Z^0}$, nor of right-handed neutrinos which do not participate in weak interactions.

## 1.4 The Phenomenon of Neutrino Oscillations

At the end of the 1990s, a series of neutrino experiments found strong evidence for flavor transformations between the three neutrino generations. These findings indicated physics beyond the SM, implying that at least the masses of two neutrino generations are non-zero. Furthermore, oscillations between neutrino generations contradict the postulate of conservation of lepton flavor number. In the following, the important discovery of neutrino flavor oscillations is discussed from a historical, a theoretical, and an experimental point of view.

### 1.4.1 The Solar Neutrino Deficit

In 1964 R. Davis proposed an experiment to determine the flux of solar neutrinos based on an earlier idea of B. Pontecorvo from 1946 where he suggested to use the radio-chemical transformation of chloride into argon via an inverse $\beta$-decay to detect neutrinos [Dav64, Bet14b]

$$\nu_\mathrm{e} + {}^{37}\mathrm{Cl} \underset{\text{capture}}{\overset{\text{decay}}{\rightleftharpoons}} {}^{37}\mathrm{Ar} + e^- \quad . \tag{1.9}$$

The expected flux of neutrinos from fusion reactions in the sun had at that time already been calculated by J. Bahcall within the newly developed standard solar model (SSM) [Bah64a]. With the mean free path of photons emitted in the center of a sun-like star being by far smaller than the radius of the star, solar neutrinos with their small interaction cross sections with matter were seen as the only possible messenger particles from the core of the sun, to experimentally test the predictions of stellar models [Bah64b]. From 1970 on the so-called 'Davis experiment' started to take data. Located in the Homestake Mine in South Carolina, USA, the experiment used 615 tons of liquid $C_2Cl_4$ as target material for solar neutrinos [DEC79]. After a few weeks of exposure, the radioactive argon isotope $^{37}$Ar was created in small quantities based on the reaction given in Equation 1.9. Typically a handful of atoms was extracted by purging the $C_2Cl_4$ liquid with helium. Afterwards, the extracted $^{37}$Ar atoms were separated from the helium carrier via a cold trap. The 2.8-keV Auger electrons, emitted in the decay of $^{37}$Ar back to $^{37}$Cl via electron capture ($t_{1/2} = 35$ days), were registered in a small proportional counter [Dav64]. With an energy threshold of 814 keV (in the primary part of the reaction in Eq. 1.9), the experiment was sensitive to $^7$Be and $^8$B neutrinos, as can be seen in Figure 1.3.

From the first results in the early 1970s on, until the conclusion of the experiment in the 1990s, the observed flux of electron neutrinos was found to be significantly smaller than the one predicted from the SSM [BD76, DEC79]. The combined result of 108 extractions from the target volume was a production rate of $0.48 \pm 0.03\,(\text{stat.}) \pm 0.03\,(\text{syst.})$ $^{37}$Ar atoms per day [Dav94]. This result corresponds to a neutrino capture rate about 2/3 smaller than the one that was predicted from theory [BP95]. Thus, the famous 'solar neutrino deficit' was established. Several other experiments like GALLEX [GAL99], SAGE [AVV02], and GNO [GNO05], also based on radio-chemical transformations, now of $^{71}$Ga into $^{71}$Ge, confirmed the Homestake results in subsequent years. Importantly, with the Kamiokande experiment, an experiment providing real-time information, also confirmed the solar neutrino deficit with its water-based Cherenkov detector [Fuk96].

From the theoretical point of view, an explanation for this deficit is given by the theory of neutrino-flavor oscillations (Sec. 1.4.2), an idea already developed by B. Pontecorvo and others in the 1950s and 1960s [Pon57a, Pon57b, MNS62, Pon67]. In 1969, prior to the first published results from the Homestake experiment, B. Pontecorvo and V. Gribov applied this idea to the case of solar neutrinos: A fraction of the electron neutrinos generated via the fusion processes in the sun could change its flavor while traveling to the earth ($\nu_\mathrm{e} \rightarrow \nu_\mu$), such that they are no longer being detectable according to the reaction in

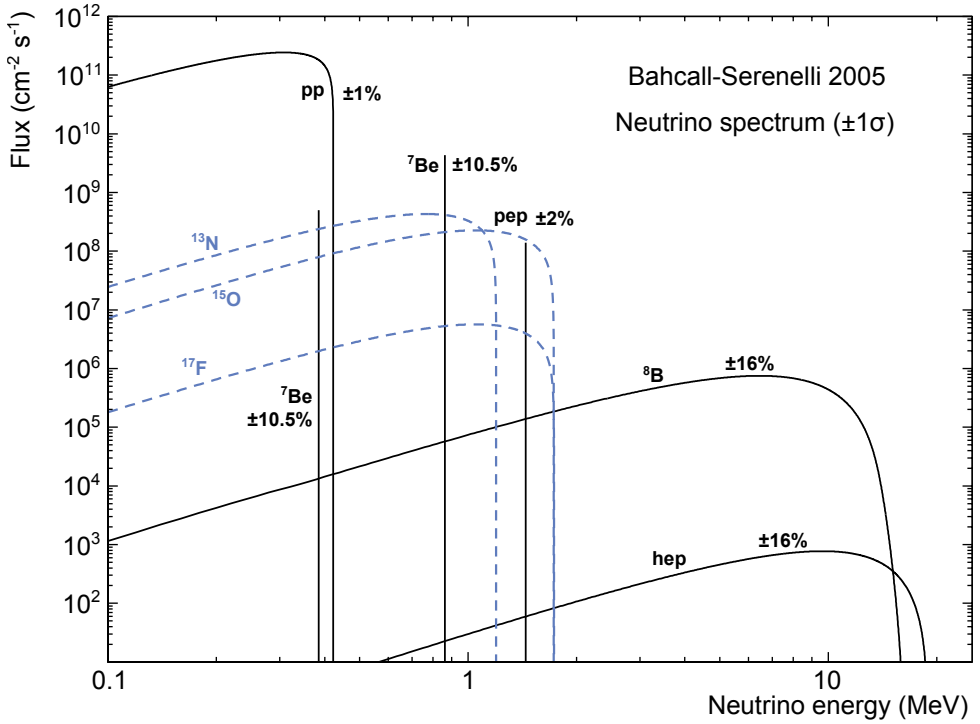


**Figure 1.3: The flux of solar neutrinos for different fusion processes in the sun** as predicted by the solar standard model. The stated numbers correspond to the theoretical uncertainties of the fluxes. Figure adapted from [Bah05].

Equation 1.9. Based on this idea, they predicted that a factor of 2 in a potential flux reduction of solar electron neutrinos should be measurable compared to the flux expected from the SSM [GP69]. While this prediction was consistent with the observations made in the radiochemical experiments, the latter could not definitively proof the existence of neutrino flavor oscillations, as they were only sensitive to $\nu_e$ but not to $\nu_\mu$.

The famous Sudbury Neutrino Observatory (SNO) experiment finally solved the problem of the solar neutrino deficit. Based on an imaging water Cherenkov detector, the experiment used 1 000 tons of heavy water ($D_2O$) contained in a 12-m diameter acrylic vessel, surrounded by 10 000 photomultiplier tubes, to detect Cherenkov light emitted by interactions of $^{8}$B-neutrinos with the $D_2O$ [SNO00]. In contrast to radiochemical experiments, being sensitive to charged-current (CC) reactions only, SNO could observe also neutral-current (NC), and elastic-scattering (ES) reactions according to

$$\nu_e + d \rightarrow p + p + e^- \quad \text{(CC)} \quad , \tag{1.10}$$

$$\nu_x + d \rightarrow \nu_x + p + n \quad \text{(NC)} \quad , \tag{1.11}$$

$$\nu_x + e^- \rightarrow \nu_x + e^- \quad \text{(ES)} \quad . \tag{1.12}$$

Here, the NC-reaction is 'flavor blind', whereas the forward-peaked ES reaction favors electron neutrinos, while still being sensitive to the other two flavors albeit with reduced cross-sections. A comparison between the CC-reactions and the NC- and ES-reactions observed with SNO allowed for a detection of neutrino oscillations independent from the SSM [Hel02]. Figure 1.4 shows the results of the salt-phase[8] of SNO. A non-zero flux of $\nu_\mu$ and $\nu_\tau$ neutrinos from the sun is found with high significance. As these neutrino flavors are not created in the sun, their appearance in the SNO detector confirmed the effect

[8] In this phase of the experiment a large amount of NaCl was dissolved in the $D_2O$ target to enhance the signal from the neutron capture in the NC-reaction.

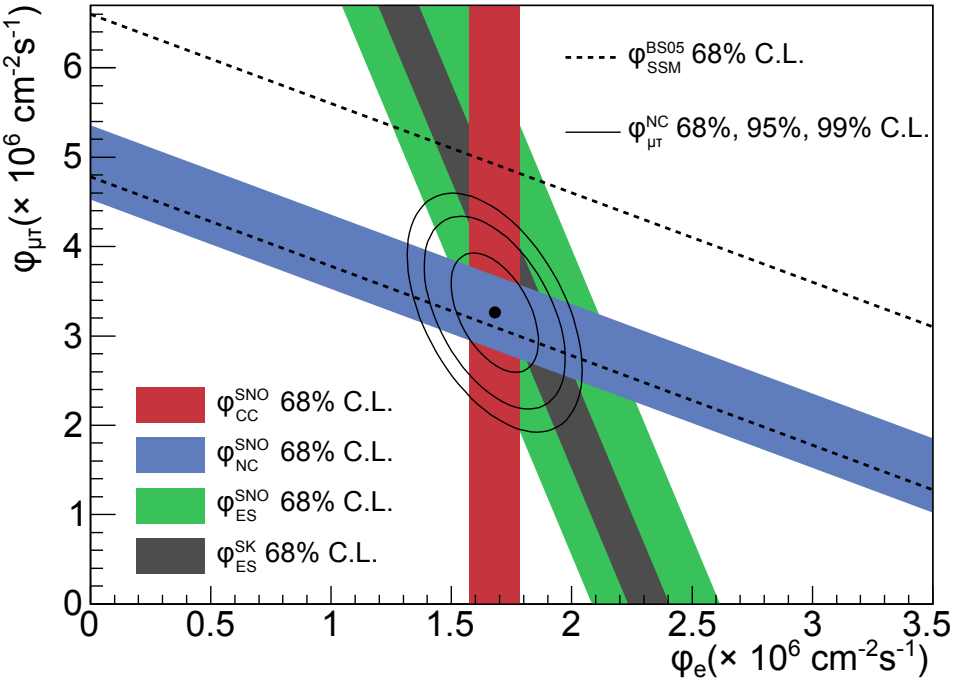


**Figure 1.4: The fluxes of $^8$B solar neutrinos $\varphi(\nu_\mu$ or $\nu_\tau)$ and $\varphi(\nu_e)$ deduced from the SNO salt phase.** The measured flux $\varphi_{\mu\tau}$ of $\mu$ and $\tau$ neutrinos versus the flux $\varphi_e$ of electron neutrinos gained from the CC-, NC-, and ES-reactions in the SNO detector is shown as red, blue, and green bands. The results from ES-reactions in the Super-Kamiokande (SK) detector [Fuk03, Fuk02] are shown as black band while the total flux of $^8$B neutrinos as predicted by the SSM is shown as black dashed lines [Bah05]. The intercept of the NC- and the CC-band is indicated by a black dot with the corresponding 68%, 95% and 99% confidence-level contours shown as black solid lines. Figure adapted from [Oli14] (Originally from [Aha05]).

of flavor oscillations for solar neutrinos and solved the problem with the 'solar neutrino deficit' [Aha05, Zub11].

### 1.4.2 The Theory of Neutrino Oscillations

The first theoretical description of neutrino oscillations was given by B. Pontecorvo as early as 1957 [Pon57a, Pon57b], at that time, however, in terms of neutrino-to-antineutrino oscillations. This initial idea was later on transferred to neutrino flavor oscillations by [MNS62, Pon67]. A full theoretical description of the phenomenon requires the use of quantum-field theory like it is for example done in [AS09]. In the following, a more simplified approach following [Zub11, Ams07] is used which still results in correct equations[9].

In the quark sector, the non-identical weak- and mass-eigenstates of quarks are connected by the well-known CKM matrix. In the case of a non-vanishing neutrino rest mass, the same effect can be thought of for leptons, where the $n$ flavor eigenstates $|\nu_\alpha\rangle$ ($|\bar{\nu}_\alpha\rangle$) and the $n$ mass eigenstates $|\nu_k\rangle$ ($|\bar{\nu}_k\rangle$) of a neutrino (antineutrino) are not identical but connected by a unitary $n \times n$ mixing matrix $U$ according to

$$|\nu_\alpha\rangle = \sum_k U_{\alpha k}|\nu_k\rangle \qquad \text{and} \qquad |\bar{\nu}_\alpha\rangle = \sum_k U^*_{\alpha k}|\bar{\nu}_k\rangle \quad . \tag{1.13}$$

The matrix $U$ can be parametrized with $n/2(n-1)$ weak mixing angles, $1/2(n-1)(n-2)$ CP-violating Dirac phases and $(n-1)$ additional CP-violating Majorana phases [Oli14].

[9] Throughout this thesis natural units with $c = \hbar = k_B = 1$ are used.

As neutrino-oscillation experiments are not sensitive to the latter, they are not taken into account in the following discussion[10].

With the mass states as stationary eigenstates of the free Hamiltonian H with eigenvalue E, their temporal propagation along a one-dimensional coordinate with momentum $p_k$ can be described by plane waves

$$|\nu_k(x,t)\rangle = e^{-i(E_k t - p_k x)}|\nu_k\rangle \quad . \tag{1.14}$$

After its creation in a weak interaction at time $t = 0$ and at location $x = 0$ in flavor state $|\nu_\alpha\rangle$, the neutrino state will develop in-flight according to

$$\begin{aligned} |\nu(x,t)\rangle &\overset{(1.13)}{=} \sum_k U_{\alpha k}|\nu_k(x,t)\rangle \\ &\overset{(1.14)}{=} \sum_k U_{\alpha k} e^{-i(E_k t - p_k x)}|\nu_k\rangle \\ &\overset{(1.13)}{=} \sum_{k,\beta} U_{\alpha k} U^*_{\beta k} e^{-i(E_k t - p_k x)}|\nu_\beta\rangle \quad . \end{aligned} \tag{1.15}$$

Thus, the spatial and time-dependent probability to detect the neutrino that was originally generated in flavor state $|\nu_\alpha\rangle$ at time $t$ and at location $x$ via a weak interaction (e.g. in a detector) in a different flavor state $|\nu_\beta\rangle$ is given by

$$P(\nu_\alpha \to \nu_\beta)(x,t) = |\langle\nu_\beta|\nu(x,t)\rangle|^2 = \sum_{k,l} U_{\alpha k} U^*_{\alpha l} U^*_{\beta k} U_{\beta l} e^{-i(E_k t - p_k x)} e^{i(E_l t - p_l x)} \quad . \tag{1.16}$$

Under the generic assumption of ultra-relativistic neutrinos, the relativistic energy and momentum relation can be simplified

$$E_k = \sqrt{p_k^2 + m_k^2} = p_k \cdot \sqrt{1 + \frac{m_k^2}{p_k^2}} \overset{(p_k \gg m_k)}{\simeq} p_k + \frac{m_k^2}{2p_k} \overset{(E \approx p_k)}{\simeq} E + \frac{m_k^2}{2E} \quad . \tag{1.17}$$

With $v \approx c = 1$ and the distance between the source of the neutrinos and their point of detection being given by the baseline length $L$, one derives that $x = L = v \cdot t \approx t$, such that Equation 1.16 can be simplified to

$$\begin{aligned} P(\nu_\alpha \to \nu_\beta)(x,t) = P(\nu_\alpha \to \nu_\beta)(L,E) &= \sum_{k,l} U_{\alpha k} U^*_{\alpha l} U^*_{\beta k} U_{\beta l} e^{-i\frac{\Delta m^2_{kl}}{2}\frac{L}{E}} \\ &= \sum_k |U_{\alpha k} U^*_{\beta k}|^2 + 2\mathrm{Re}\sum_{l>k} U_{\alpha k} U^*_{\alpha l} U^*_{\beta k} U_{\beta l} e^{-i\frac{\Delta m^2_{kl}}{2}\frac{L}{E}} \quad . \end{aligned} \tag{1.18}$$

Here, the important mass-related parameter $\Delta m^2_{kl} = m^2_k - m^2_l$ corresponds to the difference of the squared masses of the neutrino mass-eigenstates.

While the first term in Equation 1.18 corresponds to the average transition probability, the second one carries the time- and spatial-dependence and represents the quantum mechanical nature of the oscillations as an interference phenomenon. The parameter $\Delta m^2_{kl}$, together with the experimental variables $L$ and $E$ in this term, causes the oscillatory behavior of the transition probability. This, however, only holds as long as at least one mass eigenstate is non-zero (off-diagonal terms in $U$). As the transition probability in Equation 1.18 only depends on $\Delta m^2_{kl}$ and not on the absolute masses $m_k$ of the eigenstates,

[10] In Section 1.5, the Majorana phases will be of relevance again.

neutrino oscillation experiments are not sensitive to the absolute mass-scale, and neither to Majorana CP-violating phases (Sec. 1.5).

While Equation 1.18 gives the probability to detect a different flavor than the one generated in the source (appearance channel), the probability to find the original flavor (disappearance channel) is given by

$$P(\nu_\alpha \to \nu_\alpha) = 1 - \sum_{\alpha \neq \beta} P(\nu_\alpha \to \nu_\beta) \quad . \tag{1.19}$$

**Two-Neutrino Flavor Oscillations**

In the simplified case of two neutrino flavors, as was usually assumed in the early days [MNS62, Pon67], the $2 \times 2$ mixing matrix $U$ can be parametrized by a single mixing angle $\theta$ and without CP-violating Dirac phase. Similar to the Cabbibo matrix in the quark sector, the mixing can be written as

$$\begin{pmatrix} \nu_\alpha \\ \nu_\beta \end{pmatrix} = \begin{pmatrix} \cos(\theta) & \sin(\theta) \\ -\sin(\theta) & \cos(\theta) \end{pmatrix} \cdot \begin{pmatrix} \nu_1 \\ \nu_2 \end{pmatrix} \quad . \tag{1.20}$$

From Equation 1.18, it follows

$$\begin{aligned} P(\nu_\alpha \to \nu_\beta) &= |U_{11}U_{21}|^2 + |U_{12}U_{22}|^2 + 2 \cdot \left[ U_{11}U_{12}U_{21}U_{22} \cdot \mathrm{Re}\left( e^{-i\frac{\Delta m^2_{12}}{4}\frac{L}{E}} \right) \right] \\ &= 2 \cdot \sin^2(\theta)\cos^2(\theta) \cdot \left[ 1 - \mathrm{Re}\left( e^{-i\frac{\Delta m^2_{12}}{2}\frac{L}{E}} \right) \right] \\ &= \frac{1}{2}\sin^2(2\theta) \cdot \left[ 1 - \cos\left( \frac{\Delta m^2_{12}}{2}\frac{L}{E} \right) \right] \\ &= \sin^2(2\theta) \cdot \sin^2\left( \frac{\Delta m^2_{12}}{4}\frac{L}{E} \right) = 1 - P(\nu_\alpha \to \nu_\alpha) \quad . \end{aligned} \tag{1.21}$$

This result shows that the mixing angle $\theta$ defines the amplitude of the neutrino oscillations, while the difference in the squared masses $\Delta m^2_{12} = m^2_1 - m^2_2$ between $\nu_1$ and $\nu_2$ relates to the frequency of the oscillations. If either of the two parameters is zero, no oscillation will occur.

The energy $E$ of the observed neutrinos and the baseline length $L$ are the experiment-specific parameters. In order to classify experiments with regards to their sensitivity to an oscillation signal, it is reasonable to introduce the characteristic oscillation length

$$L_0 = \frac{4\pi E}{\Delta m^2} = 2.48 \frac{E\,[\mathrm{MeV}]}{\Delta m^2[\mathrm{eV}^2]}\,\mathrm{m} \quad , \tag{1.22}$$

which describes the period of one full oscillation cycle. Now, three cases can be considered:

- $L \ll L_0$: No observation of an oscillation. Due to the short distance of the detector relative to the source for a given neutrino energy $E$, the oscillation does not has the time to develop.
- $L \approx L_0$: Maximal sensitivity to the oscillation signal.
- $L \gg L_0$: Now, one is only sensitive to the average transition probability. Several oscillation cycles have happened already and the detector cannot identify individual cycles due to its finite energy resolution ($\delta E$) and/or the non-zero extension of the neutrino source ($\delta L$).

The two-oscillation case is still frequently used in the data analysis of neutrino-oscillation experiments due to the difference in the $\Delta m^2_{kl}$ values.

**Three-Neutrino Flavor Oscillations**

High-precision neutrino oscillation experiments of the latest generation must, however, consider mixing between all three flavor ($\nu_\mathrm{e}$, $\nu_\mu$, $\nu_\tau$) and mass eigenstates ($\nu_1$, $\nu_2$, $\nu_3$) in their analysis. For $n = 3$, the $3 \times 3$ mixing matrix $U$, known as the Pontecorvo-Maki-Nakagawa-Sakata (PMNS) matrix, can be parametrized (similar to the CKM matrix) by three mixing angles ($\theta_{12}$, $\theta_{23}$, $\theta_{13}$) and one CP-violating Dirac phase $\delta$ according to

$$U = \begin{pmatrix} c_{12}c_{13} & s_{12}c_{13} & s_{13}e^{-i\delta} \\ -s_{12}c_{23} - c_{12}s_{23}s_{13}e^{i\delta} & c_{12}c_{23} - s_{12}s_{23}s_{13}e^{i\delta} & s_{23}c_{13} \\ s_{12}s_{23} - c_{12}c_{23}s_{13}e^{i\delta} & -c_{12}s_{23} - s_{12}c_{23}s_{13}e^{i\delta} & c_{23}c_{13} \end{pmatrix} , \tag{1.23}$$

with $c_{kl} = \cos(\theta_{kl})$ and $s_{kl} = \sin(\theta_{kl})$. The Dirac phase $\delta$ can in principle be accessed via dedicated oscillation experiments, so that leptonic CP violation is measurable via $P(\nu_\alpha \rightarrow \nu_\beta) \neq P(\bar{\nu}_\alpha \rightarrow \bar{\nu}_\beta)$, in principle [Oli14].

The general formula for the transition probability $P(\nu_\alpha \rightarrow \nu_\beta)$ in the three-flavor case is rather complex. It depends on the three mixing angles and the differences in squared masses $\Delta m^2_{13}$, $\Delta m^2_{12}$, and $\Delta m^2_{32} = \Delta m^2_{13} - \Delta m^2_{12}$, which enter in magnitude and sign. The latter effect can be due to interactions in matter by the so-called MSW effect [Wol78, MS86] or a possible CP violating Dirac phase $\delta$. To derive simplified expressions for the transition probabilities in the three-flavor case, assumptions on the specific neutrino mass hierarchy have to be made (Fig. 1.7) [Zub11].

### 1.4.3 Neutrino-Oscillation Experiments

To experimentally derive the three neutrino mixing angles $\theta_{kl}$ and the two independent differences in squared masses $\Delta m^2_{12}$ and $\Delta m^2_{32}$, a variety of neutrino-oscillation experiments has been carried out over the last decades. In principle one differentiates between experiments searching for a disappearance of a specific neutrino flavor (disappearance channel), and those searching for an appearance (appearance channel). However, as the sensitivity of an experiment on the above mentioned parameters is related to its specific baseline length $L$ and energy $E$ of the neutrino beam, a large variety of experiments with different neutrino sources has to be conducted.

**Solar Neutrinos**

The energy of solar neutrinos originating from different fusion processes in the sun range up to about 15 MeV (Fig. 1.3). As only electron neutrinos are generated in these processes, solar neutrino oscillation experiments focus on the disappearance of $\nu_\mathrm{e}$ due to a transformation into $\nu_\mu$ and $\nu_\tau$ on their $L = 15 \times 10^7$-km long path from the solar interior to Earth. From Equation 1.22 and with $L \approx L_0$ it follows that the solar neutrino experiments are most sensitive to very small values of $\Delta m^2_{12} \approx 10^{-11}\,\mathrm{eV}^2$. However, if their energy is larger than $E^\nu_\mathrm{crit} \approx 1.9\,\mathrm{MeV}$, neutrinos can undergo matter-enhanced oscillations in the sun due to the MSW effect [Hax13]. The value of $E^\nu_\mathrm{crit}$ conveniently is located in the central region of the solar-neutrino energy spectrum. Accordingly, $\nu_\mathrm{e}$ from $^8$B reactions are strongly influenced by MSW effects while e.g. neutrinos from pp-reactions are not.

The previously mentioned SNO experiment not only gives an explanation for the solar neutrino deficit in terms of flavor transitions of $\nu_\mathrm{e}$ into $\nu_\mu$, the combination of three measurement phases, together with other constraints also allowed to specify the values for $\theta_{12}$ and $\Delta m^2_{12}$ [Aha13]

$$\begin{aligned} \tan^2(\theta_{12}) &= 0.427^{+0.033}_{-0.029} \\ \Delta m^2_{12} &= 5.6^{+1.9}_{-1.4} \times 10^{-5}\,\mathrm{eV}^2 \quad . \end{aligned} \tag{1.24}$$

Together with other Cherenkov-based experiments as for example Super-Kamiokande, SNO has a rather large energy CC-threshold of $E_{\text{thres}} \geq 3.5\,\text{MeV}$ [Aha10] and therefore is sensitive only to the high-energy part of $^8$B neutrinos[11], which are subject to the MSW effect. The Borexino experiment, on the other hand, is based on an ultra-pure 278-ton organic scintillator target to carry out solar $\nu$-spectroscopy down to energies below 2 MeV [Ali09]. In its first data-taking phase from 2007 to 2010, the experiment was able to detect $^7$Be, pep, and pp solar neutrinos in 'real-time' for the first time [Bel14a, Bel14b]. These low-energy neutrinos importantly are not affected by the MSW effect. In line with this, a combined analysis of Borexino, SNO, and Super-Kamiokande data allowed to confirm experimentally the transition of the survival probability of high-energy electron neutrinos due to the MSW effect to the purely vacuum-oscillation dominated probability at lower energies [Bel14a].

**Atmospheric Neutrinos**

Charged primary cosmic rays that strike the upper atmosphere of the earth are mainly composed of GeV-scale protons and $\alpha$-particles. When these nuclei interact with molecules in the air a cascade of secondary particles is produced. In the case of the protons mainly pions (and to a lesser extent kaons) are produced. Charged pions, in turn, preferably decay purely leptonically according to

$$\begin{aligned} \pi^+ &\to \mu^+ + \nu_\mu \qquad & \mu^+ &\to e^+ + \nu_\text{e} + \overline{\nu}_\mu \\ \pi^- &\to \mu^- + \overline{\nu}_\mu \qquad & \mu^- &\to e^- + \overline{\nu}_\text{e} + \nu_\mu \end{aligned} \tag{1.25}$$

The resulting atmospheric neutrinos generated in these decays, thus, feature a flavor ratio of $\varphi(\nu_\mu+\bar{\nu}_\mu)/\varphi(\nu_\text{e}+\bar{\nu}_\text{e}) \approx 2$ for energies[12] of $E_\nu \approx 1\,\text{GeV}$. Furthermore, for $\nu$-energies up to the TeV-scale, the earth remains transparent for neutrino propagation. Consequently, interactions with matter due to the MSW effect do not have to be taken into account in the following brief discussion.

An important feature of atmospheric neutrinos is the up-down symmetry of their flux for energies[13] above a few GeV. In 1988, the Kamiokande experiment reported a deficit of $\nu_\mu$-induced events in the 1 000-t fiducial volume of their water-Cherenkov detector[14], while the flux of $\nu_\text{e}$ followed the expectation from Monte-Carlo (MC) simulations [Hir88b]. This observation was later confirmed by other projects like the IMB experiment [Bec92] or Soudan-2 [All97], such that the 'atmospheric neutrino anomaly' was established. While not being the favored scenario at that time[15], neutrino flavor oscillations of $\nu_\mu$ ($\bar{\nu}_\mu$) into $\nu_\tau$ ($\bar{\nu}_\tau$) on the path from their point of creation in the atmosphere to the detector, represented a reasonable explanation for the deficit of $\nu_\mu$ ($\bar{\nu}_\mu$) with the flux of electron (anti)neutrinos remaining unaffected. Due to the large range of baselines $10 \leq L \leq 10\,000\,\text{km}$, such oscillations introduce a top-bottom asymmetry. With their very good sensitivity to the direction of the final-state leptons, water-Cherenkov detectors are ideal to resolve this asymmetry. In 1994, the Kamiokande experiment reported a final asymmetry in $\varphi(\nu_\mu + \bar{\nu}_\mu)$ with regards to the zenith angle of $2.8\sigma$ [Fuk94]. Four years later, the 20 times larger Super-Kamiokande detector [Fuk03] confirmed the top-bottom asymmetry with a significance

[11] Neutrinos from the hep-process in the sun are neglected at this point due to their significantly reduced flux.

[12] At higher energies, the probability of muons to reach the earth before they decay increases, such that the ratio of muonic neutrinos to electron neutrinos increases accordingly.

[13] Below these energies, the geomagnetic field significantly bends primary cosmic rays, thereby inducing a distinct up-down asymmetry of the neutrino flux.

[14] Note that water-Cherenkov detectors are not sensitive on the charge of the final-state leptons such that they cannot differentiate between neutrinos and antineutrinos.

[15] Similarly to the quark sector, the mixing angles between neutrino flavors where expected to be small, if at all present. The explanation of the atmospheric neutrino deficit by flavor oscillations, however, required large mixing angles and was therefore disfavored.

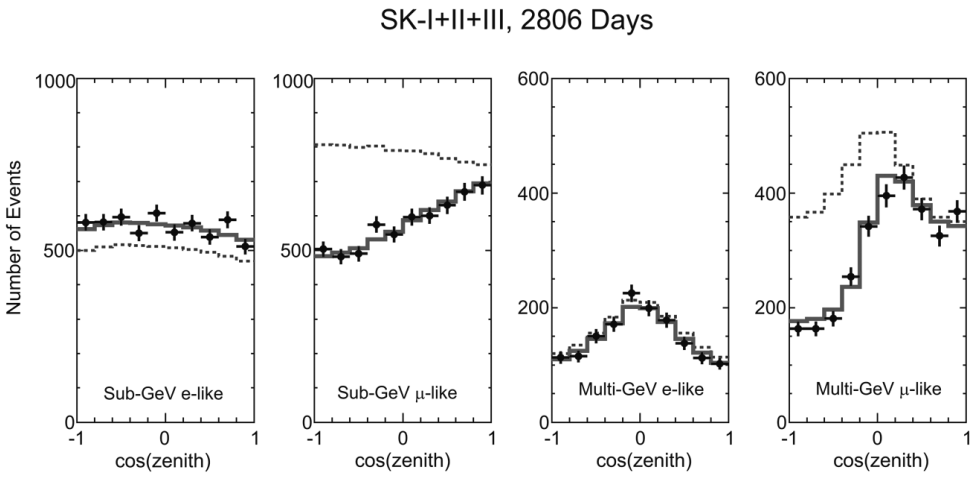


**Figure 1.5: Zenith angle distributions of $\nu_\mu$ and $\nu_e$ in 2 806 days of detector exposure in Super-Kamiokande phases I + II + III.** Sub-GeV (Multi-GeV) events are defined to have visible energies below (above) $E_\nu = 1.33\,\text{GeV}$. The dotted histograms represent MC results for no $\nu_\mu \rightarrow \nu_\tau$ oscillations, while the best-fit of the data with oscillations included is shown as solid histograms. Figure adapted from [Kaj10].

of $6\sigma$ [Kaj98, Fuk98], a result later corroborated by the experiments MACRO [Amb98] and Soudan-2 [All99]. Figure 1.5 shows the corresponding zenith angle distributions for the flux of electron and muon neutrinos in a combined analysis of 2 806 days of detector exposure in the phases I, II, and III of the Super-Kamiokande experiment.

In 2013, with the disappearance of atmospheric $\nu_\mu$ being firmly established, the Super-Kamiokande collaboration announced $3.8\sigma$ evidence for $\nu_\tau$ appearance [Abe13]. More recently the IceCube experiment, originally designed to study high-energy neutrinos from cosmic sources [GH14], reported results of atmospheric $\nu$-studies targeted on the mixing angle $\theta_{23}$ and the difference in squared masses $\Delta m^2_{32}$ which are comparable to those of dedicated oscillation experiments [Aar15]

$$\begin{aligned} \sin^2(\theta_{23}) &= 0.53^{+0.09}_{-0.12} \\ \Delta m^2_{32} &= 2.72^{+0.19}_{-0.20} \times 10^{-3}\,\text{eV}^2 \quad , \end{aligned} \tag{1.26}$$

for a normal mass ordering (see Fig. 1.7).

### Accelerator Neutrinos

Apart from atmospheric sources of $\nu_\mu$, also man-made sources like accelerators are used to study $\nu_\mu \rightarrow \nu_\tau$ oscillations via the disappearance of $\nu_\mu$. A GeV-scale $\nu_\mu$-beam is typically generated by irradiating a fixed target with a beam of high-energy protons from a storage ring. A fraction of the resulting mesons, predominantly kaons and pions, subsequently decay inside a decay tunnel (see Eq. 1.25), generating a beam of $\nu_\mu$ or $\bar{\nu}_\mu$. In notable contrast to atmospheric neutrino sources, accelerators allow to select either $\nu_\mu$ or $\bar{\nu}_\mu$ by beam optical devices, such as magnetic horns. At the end of the decay tunnel, a large muon shield is used to stop all particle species except of neutrinos. The primary undistorted energy spectrum as well as the radial profile of the neutrino beam is usually measured in a near detector, located close behind the muon shield, while the main detector is typically placed at distances of up to several hundreds of kilometers [Zub11].

Compared to atmospheric neutrino oscillation searches, accelerator-based ones have the disadvantage that the baseline is fixed, so that the energy of neutrinos has to be tuned (typically to sub-GeV energies) to achieve the highest sensitivity on the neutrino oscillation parameters. For example, in the case of the T2K experiment [Abe11], which is the successor

to the pioneering K2K experiment [Ahn06], the baseline from the J-PARC facility where the neutrino beam is produced to the Super-Kamiokande detector, where it is detected, amounts to only 295 km. For a mass splitting of $\Delta m^2_{32} \approx 2.5 \times 10^{-3}\,\mathrm{eV}^2$, as expected from the results of the atmospheric neutrino oscillation searches, Equation 1.22 gives an ideal neutrino energy of $E_\nu \approx 300\,\mathrm{MeV}$ to obtain maximum sensitivity on the disappearance of $\nu_\mu$ ($\bar{\nu}_\mu$). In its latest publication, the T2K collaboration reported values of

$$\begin{aligned} \sin^2(\theta_{23}) &= 0.514^{+0.055}_{-0.056} \\ \Delta m^2_{32} &= (2.51 \pm 0.10) \times 10^{-3}\,\mathrm{eV}^2 \quad , \end{aligned} \tag{1.27}$$

at 68% C.L. for the normal mass ordering [Abe15]. This result is in good agreement with the results from atmospheric oscillation searches (see Eq. 1.26) and those of other accelerator based experiments like MINOS [Ada13] or OPERA. The latter uses the CNGS $\nu_\mu$-beam from CERN to observe $\nu_\mu \rightarrow \nu_\tau$ oscillations in appearance mode with a present significance of $5.1\sigma$ [Aga15].

Apart from $\theta_{23}$ and $\Delta m^2_{32}$, a typical accelerator experiment is in principle also sensitive to other neutrino oscillation parameters, in particular when looking for $\nu_\mathrm{e}$-appearance in a $\nu_\mu$-beam and by taking into account three-flavor oscillations and interactions with matter. This more advanced analysis typically has to include the mixing angle $\theta_{13}$, the CP-violating phase $\delta$, and the absolute mass hierarchy (i.e. the sign of $\Delta m^2_{13}$). However, due to the large number of parameters, it is difficult to disentangle all of them. The latest results from T2K are given in [Abe15], where a parameter regime $\delta = [0.15, 0.83]\pi$ ($\delta = [-0.08, 1.09]\pi$) is excluded with 90% C.L. in case of the normal mass hierarchy (inverted mass hierarchy) by using rector data to constrain $\theta_{13}$ (see next paragraph). A promising new accelerator-based oscillation experiment is the NOvA experiment [Fel07], which features a very long baseline of about 810 km. The aim here is to potentially resolve not only $\theta_{13}$ and $\delta$, but also the mass hierarchy of neutrinos. This experiment has recently presented first oscillation results, however, with limited statistics [Mes15].

**Reactor Neutrinos**

Of all man-made (anti)neutrino sources, the $\beta$-decays of neutron-rich fission products in a nuclear reactor constitute the strongest one. In a standard 3-GW electric-power reactor about $10^{21}$ $\bar{\nu}_\mathrm{e}$ are generated per second with energies in the few MeV-range. As this energy is far below the threshold for creating $\mu$- or $\tau$-leptons, reactor-based neutrino oscillation experiments exclusively look for the disappearance of $\bar{\nu}_\mathrm{e}$. The detection of $\bar{\nu}_\mathrm{e}$ is still based on the inverse $\beta$-decay reaction, given in Equation 1.4. Typically, a large-volume organic liquid scintillator detector is used, similar to the pioneering 'Poltergeist' experiment in 1956 (Sec. 1.2) [Zub11].

An important reactor-based experiment searching for neutrino oscillations was KamLAND, located at the Kamioka Observatory. At the time of measurements it was being surrounded by 53 Japanese commercial nuclear reactors with an average flux-weighted distance of about 180 km. This allowed to precisely measure the oscillation parameters

$$\begin{aligned} \tan^2(\theta_{12}) &= 0.56^{+0.10}_{-0.07} \\ \Delta m^2_{12} &= 7.58^{+0.14}_{-0.13}(\mathrm{stat.})^{+0.15}_{-0.15}(\mathrm{syst.}) \times 10^{-5}\,\mathrm{eV}^2 \quad , \end{aligned} \tag{1.28}$$

in a two-flavor oscillation analysis with $\theta_{13}$ set to zero [Abe08]. These results are slightly larger than the SNO results given earlier in Equation 1.24.

In March 2012, the Daya Bay experiment announced the discovery of $\bar{\nu}_\mathrm{e}$ disappearance at a medium baseline of about 1.7 km with $5.2\sigma$ significance [An 12]. This observation allowed to fix the third mixing angle $\theta_{13}$. Similar results were obtained by the RENO [Ahn12]

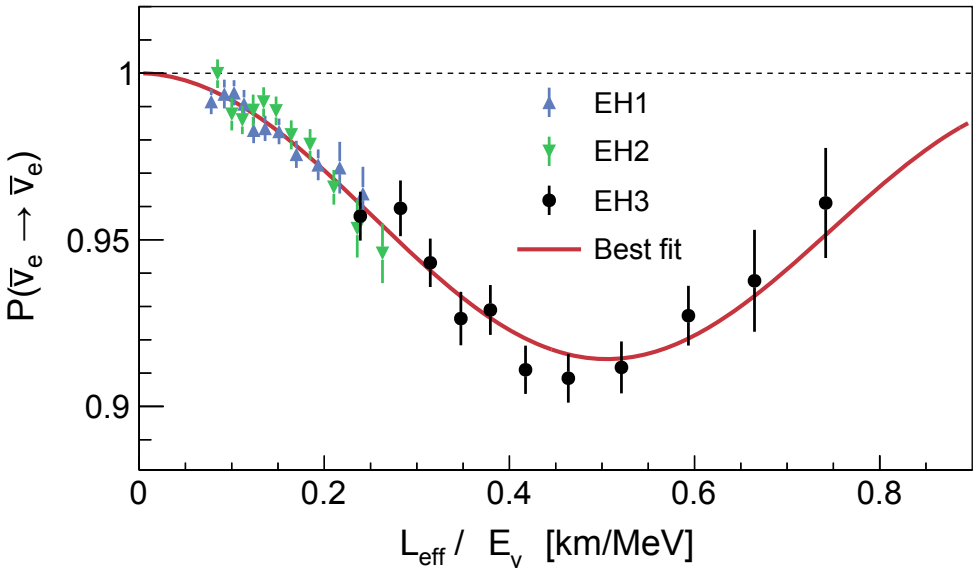


**Figure 1.6: Survival probability of $\bar{\nu}_e$ in the latest Daya-Bay data** as function of the effective propagation distance $L_{\text{eff}}$, divided by the average antineutrino energy $E_\nu$. The data points correspond to the ratios of the observed antineutrino spectra to the ones expected for no oscillation, as measured by large-volume detectors in three different experimental halls EH1, EH2, and EH3. With the best estimates of $\sin^2(2\theta_{13}) = 0.084$ and $|\Delta m^2_{\text{ee}}| = 2.42 \times 10^{-3}\,\text{eV}^2$, the red solid line is obtained. A common mass-splitting scale $\Delta m^2_{\text{ee}} \approx \Delta m^2_{31} \approx \Delta m^2_{32}$ is used in reactor experiments, as they are not sensitive to the small mass splitting $\Delta m^2_{12}$. Figure adapted from [An 15].

and DoubleChooz experiments [Abe12]. All of these three modern reactor-neutrino experiments are specifically designed for high sensitivity on $\theta_{13}$, by using two detectors, one located close to the reactor with $L \approx 0.4\,\text{km}$, and one far detector with $L = 1\text{-}2\,\text{km}$. This configuration allows a direct prediction of the $\bar{\nu}_e$-rate in the far detector based on the data from the near detector, thereby significantly reducing systematic uncertainties from reactor-related effects [Dwy15].

The Daya Bay collaboration has just recently published their latest result

$$\sin^2(2\theta_{13}) = 0.084 \pm 0.005 \quad , \tag{1.29}$$

based on a total exposure of $6.9 \times 10^5$-GW ton days [An 15]. Figure 1.6 shows the survival probability $P(\bar{\nu}_e \rightarrow \bar{\nu}_e)$ as function of the effective propagation distance $L_{\text{eff}}$, divided by the average energy of the antineutrinos $E_\nu$. The sinusoidal characteristic of $P(\bar{\nu}_e \rightarrow \bar{\nu}_e)$ can nicely be seen.

**Summary**

Table 1.1 gives a comprehensive overview of recent results for key neutrino oscillation parameters. While the oscillation experiments allow to derive differences in squared masses $\Delta m^2_{kl}$ of the three neutrino mass eigenstates with high precision over the last two decades, these experiments are not sensitive to the absolute mass scale of neutrinos. Furthermore, the sign of $\Delta m^2_{13}$ is still unknown, even if experiments of the latest generation like for example NOvA are expected to be sensitive to it.

Based on the current knowledge, three generic mass scenarios are possible: a quasi-degenerate case where $m_1 \approx m_2 \approx m_3 \gg 10^{-3}\,\text{eV}^2$, the so so-called normal mass hierarchy with $m_1 < m_2 \ll m_3$, and an inverted mass hierarchy with $m_3 \ll m_1 < m_2$. Figure 1.7 illustrates the latter two cases with the flavor contents of each mass eigenstate shown in addition. In order to gain information on the absolute mass scale, approaches other

**Table 1.1: Recent experimental results on neutrino oscillation parameters.** All stated results assume a normal mass hierarchy. Results for the CP-violating phase $\delta$ are not listed.

| Parameter | Result | Experiment |
|---|---|---|
| $\sin^2(2\theta_{12})$ | $0.846^{+0.021}_{-0.021}$ | KamLAND + solar + accelerator [Gan11] |
| $\Delta m^2_{12}$ | $(7.53 \pm 0.18) \times 10^{-5}\,\mathrm{eV}^2$ | KamLAND + solar + accelerator [Gan11] |
| $\sin^2(2\theta_{23})$ | $0.999^{+0.001}_{-0.018}$ | T2K [Abe14, Oli14] |
| $\lvert\Delta m^2_{32}\rvert$ | $(2.44 \pm 0.06) \times 10^{-3}\,\mathrm{eV}^2$ | T2K [Oli14] |
| $\sin^2(2\theta_{13})$ | $0.084 \pm 0.005$ | Daya Bay [An 15] |

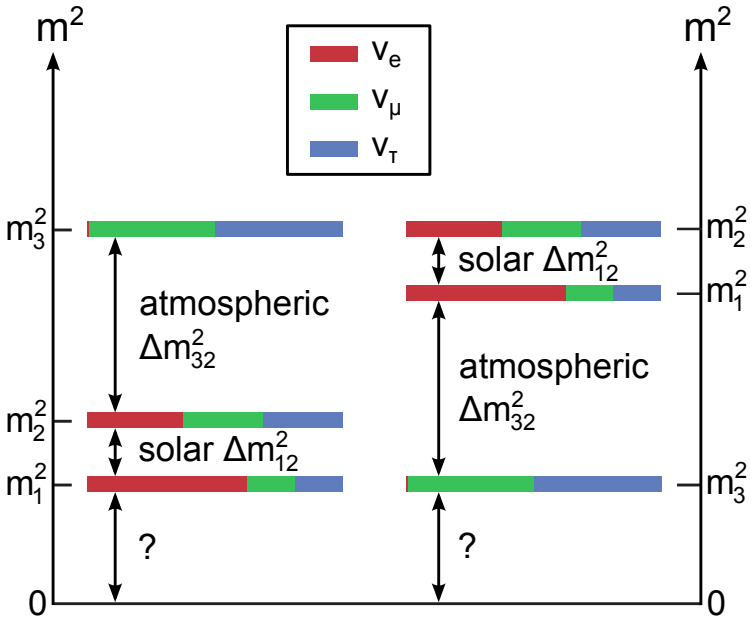


**Figure 1.7: Neutrino mass hierarchy in the normal and the inverted case.** For each mass eigenstate the relative contributions of the three flavor eigenstates are indicated. Figure adapted from [KL13].

than neutrino oscillation experiments are needed. These experiments will be discussed in Section 1.6.

## 1.5 Theory of Neutrino-Mass Generation

In the SM of particle physics, neutrinos (antineutrinos) are assumed to be massless left-handed (right-handed) fermions. The large number of neutrino oscillation experiments described in the last section, however, has shown that at least two of the three neutrino mass-eigenstates must be massive. The inclusion of neutrino masses into the SM can be done in two ways: Firstly, by including a right-handed (left-handed) neutrino (antineutrino) singlet into the theory like for all other fermions, which allows to formulate a Dirac neutrino-mass term with a Yukawa coupling to the Higgs field. The large difference between the masses of the charged leptons and the light neutrinos must then be explained by a correspondingly smaller Yukawa coupling. In a second approach, additional fermions need not to be added to the theory, when neutrinos are assumed to be Majorana particles with $\nu_\alpha = \bar{\nu}_\alpha$ [Maj37]. Different to charged fermions, this scenario is possible for neutral particles such as neutrinos. However, this concept implies a violation of lepton number conservation. In the following this second approach is briefly described, based on [Zub11].

In special relativity, the mass terms for a four-component Dirac spinor field $\psi$ in a Lagrangian $\mathcal{L}$ must be Lorentz-invariant and Hermitian. In the most general case, four terms fulfill this requirement with

$$2\mathcal{L} = m_{\mathrm{D}} \left[\bar{\psi}_{\mathrm{L}}\psi_{\mathrm{R}} + \bar{\psi}^{\mathrm{c}}_{\mathrm{L}}\psi^{\mathrm{c}}_{\mathrm{R}}\right] + m_{\mathrm{L}}\bar{\psi}_{\mathrm{L}}\psi^{\mathrm{c}}_{\mathrm{R}} + m_{\mathrm{R}}\bar{\psi}^{\mathrm{c}}_{\mathrm{L}}\psi_{\mathrm{R}} + \mathrm{h.c.} \quad , \tag{1.30}$$

where $\psi_{\mathrm{L,R}}$ correspond to the chiral representation of the Dirac field $\psi$ as Weyl spinors and $\psi^{\mathrm{c}}$ corresponds to the charge conjugate of $\psi$. In a more compact representation, Equation 1.30 can be written as

$$2\mathcal{L} = (\bar{\psi}_{\mathrm{L}}, \psi^{\mathrm{c}}_{\mathrm{L}}) \cdot \underbrace{\begin{pmatrix} m_{\mathrm{L}} & m_{\mathrm{D}} \\ m_{\mathrm{D}} & m_{\mathrm{R}} \end{pmatrix}}_{M} \cdot \begin{pmatrix} \psi^{\mathrm{c}}_{\mathrm{R}} \\ \psi_{\mathrm{R}} \end{pmatrix} + \mathrm{h.c.} \quad . \tag{1.31}$$

At this point it is reasonable to introduce a mixing angle $\theta$ according to

$$\tan(2\theta) = \frac{2m_{\mathrm{D}}}{m_{\mathrm{R}} - m_{\mathrm{L}}} \quad , \tag{1.32}$$

and thereby two independent Majorana fields

$$\begin{aligned} \phi_1 &= \cos\theta \cdot (\psi_{\mathrm{L}} + \epsilon_1\psi^{\mathrm{c}}_{\mathrm{R}}) - \sin\theta \cdot (\psi^{\mathrm{c}}_{\mathrm{L}} + \epsilon_1\psi_{\mathrm{R}}) \\ \phi_2 &= \sin\theta \cdot (\psi_{\mathrm{L}} + \epsilon_2\psi^{\mathrm{c}}_{\mathrm{R}}) + \cos\theta \cdot (\psi^{\mathrm{c}}_{\mathrm{L}} + \epsilon_2\psi_{\mathrm{R}}) \quad . \end{aligned} \tag{1.33}$$

Here, $\epsilon_k = \pm 1$ corresponds to the CP-eigenvalue of the Majorana field $\phi_k$ with

$$\phi^{\mathrm{c}}_k = \epsilon_k\phi_k \quad . \tag{1.34}$$

By diagonalizing the matrix $M$ and with the use of Equations 1.32, 1.33, and 1.34, one obtains

$$2\mathcal{L} = m_1\bar{\phi}_1\phi_1 + m_2\bar{\phi}_2\phi_2 \quad . \tag{1.35}$$

The positive masses $m_1$ and $m_2$ here are related to the mass eigenvalues $\tilde{m}_{1,2}$ of the matrix $M$ according to

$$\epsilon_{1,2} \cdot m_{1,2} = \tilde{m}_{1,2} = \frac{1}{2}\left[(m_{\mathrm{L}} + m_{\mathrm{R}}) \pm \sqrt{(m_{\mathrm{L}} - m_{\mathrm{R}})^2 + 4m^2_{\mathrm{D}}}\right] \quad , \tag{1.36}$$

where the parameters $\epsilon_k$ are chosen such that $m_k \geq 0$ at all times [Kla88].

Based on the general mass terms in the Lagrangian in Equation 1.35 three special cases will be discussed in the following:

- **Pure Dirac Case:** For $m_{\mathrm{L}} = m_{\mathrm{R}} = 0$, it follows that $m_{1,2} = m_{\mathrm{D}}$. Thus, one can construct a Dirac field $\psi$ such that Equation 1.35 reduces to a pure Dirac mass-term

  $$\mathcal{L} = m_{\mathrm{D}}\bar{\psi}\psi \quad . \tag{1.37}$$

  Correspondingly, the case of Dirac neutrinos in the SM of particle physics can be seen as a special case of the more general one given in Equation 1.35.

- **Pure Majorana Case:** For $m_{\mathrm{D}} = 0$ one obtains $m_{1,2} = m_{\mathrm{L,R}}$ such that neutrinos have pure Majorana character.

- **See-Saw Case:** For $m_{\mathrm{L}} = 0$ and $m_{\mathrm{R}} \gg m_{\mathrm{D}}$, Equation 1.36 gives

  $$m_1 \approx \frac{m^2_{\mathrm{D}}}{m_{\mathrm{R}}} \quad \text{and} \quad m_2 \approx m_{\mathrm{R}} \quad . \tag{1.38}$$

In this way, a very light mass $m_1$ and a heavy mass $m_2$ are obtained together with a mixing angle of $\theta \approx 0°$. By using the latter result, Equation 1.33 becomes

$$\begin{aligned} \phi_1 &\approx \psi_\mathrm{L} + \epsilon_1 \psi_\mathrm{R}^\mathrm{c} \\ \phi_2 &\approx \psi_\mathrm{L}^\mathrm{c} + \epsilon_2 \psi_\mathrm{R} \quad . \end{aligned} \tag{1.39}$$

By interpreting $\phi_1$ as the mass eigenstate of the light active neutrino with $\psi_\mathrm{L}$ and $\psi_\mathrm{R}^\mathrm{c}$ participating in weak interactions, and with $\phi_2$ as a heavy sterile neutrino not interacting with the gauge bosons of the SM, this so-called See-Saw mechanism (type I) [MS80, Moh81] nicely explains the large differences in mass scales between charged and neutral leptons[16].

## 1.6 Experimental Approaches to Measure the Neutrino Mass

As oscillation experiments (Sec. 1.4.3) are sensitive only to the differences in squared masses of neutrino mass-eigenstates, but not to the absolute mass scale (Fig. 1.7), other experimental methods are required to determine this parameter. In the following, the most prominent approaches are discussed. Those can be divided into direct methods that purely rely on the kinematics of a $\beta$-decay and, thus, do not depend on any underlying model (Sec. 1.6.4) and indirect methods that do rely on specific theoretical assumptions, which introduces model-dependent uncertainties on the derived neutrino mass (limit).

### 1.6.1 Cosmology

The evolution of the universe from the initial Big Bang to the present day, where it is dominated by dark energy ($\Lambda$) and cold dark matter (CDM), can be described rather successfully within the (standard) $\Lambda$CDM cosmological model (see e.g. [Lid03, BG06]). This model predicts the existence of a cosmic neutrino background (C$\nu$B) and a cosmic microwave background (CMB). The former emerged after the decoupling of neutrinos from the primordial plasma at about $t = 0.1\,\mathrm{s}$ after the Big Bang, when the weak-interaction rate dropped below the Hubble expansion rate of the universe. The latter radiation, the CMB, originates from the decoupling of photons from matter at about $t = 380\,000\,\mathrm{years}$, when the universe had further cooled down by its Hubble expansion, such that the energy of photons dropped to values too low for photo-disintegration of deuterium nuclei. At the present time, the effective mean temperature of the CMB is found to be $(2.7255 \pm 0.0006)\,\mathrm{K}$ [Fix09].

Due to their low energy and associated tiny interaction cross-sections with matter, the relic neutrinos from the C$\nu$B have not yet been detected. However, from the $\Lambda$CDM model their temperature is expected to be $T_\nu = 1.95\,\mathrm{K}$, with a large number density of $336\,\mathrm{cm}^{-3}$ [Zub11]. This makes them the most abundant fermionic matter particles in the universe. In the $\Lambda$CDM model, only the sum of the neutrino masses is of relevance as it is directly linked to the contribution $\Omega_\nu$ of relic neutrinos to the total energy density ($\Omega_\mathrm{tot}$) of the universe

$$\sum_k m_k = 93\,\Omega_\nu h^2\,\mathrm{eV} \quad , \tag{1.40}$$

where $h$ is the dimensionless Hubble parameter. With the latest result from the Planck surveyor of $h = 0.678 \pm 0.009$ [Ade15], and assuming a neutrino-dominated, flat universe ($\Omega_\mathrm{tot} = \Omega_\nu = 1$), an upper limit on the sum of all neutrino masses of

$$\sum_k m_k \lesssim 42.75 \pm 0.01\,\mathrm{eV} \tag{1.41}$$

[16] In addition to the type-I See-Saw mechanism, also a type-II exists which assumes $m_\mathrm{L} > 0$ [Laz81].

can be derived.

Owing to their large free-streaming length[17], primordial neutrinos have played an important role in the structure formation of the early universe by washing-out small-scale structures while not affecting large-scale ones. In this way, information on the sum of the neutrino masses enters large-scale structures as well as the power spectrum of the CMB radiation temperature anisotropy. The latter has been extensively surveyed over the past 25 years with the COBE [Fix96] (1989 - 1993), WMAP [Hin13] (2001 - 2010), and finally the Planck [Ade15] (2009 - today) satellite.

In its latest 2015 results, the Planck collaboration states a model-dependent upper limit for $\sum_k m_k$ of

$$\sum_k m_k \leq 0.23\,\text{eV} \quad (95\,\%\ \text{C.L.}) \quad . \tag{1.42}$$

To derive this rather stringent limit, Planck data was supplemented by external data from baryonic acoustic oscillation measurements [Beu11], a joint light-curve analysis from SNLS and SDSS supernovae surveys, plus several samples from low redshift supernovae [Bet14a].

In order to extract the information on $\sum_k m_k$ from these diverse data sets, a large number of input parameters needs to be fitted to several different cosmological data sets, some of which are strongly correlated. This fact makes the neutrino-mass limits obtained from cosmology not only strongly model-dependent, but also shows that these measurements cannot substitute a determination of neutrino masses under controlled conditions in a laboratory-based experiment. Taking this argument vice versa, a determination of the neutrino mass from a laboratory experiment would allow to fix one input parameter to the ΛCDM model which would reduce the large parameter space governing it.

### 1.6.2 Time-of-Flight of Supernova Neutrinos

If the core of a heavy star ($R > 8R_\odot$) cannot further generate energy via fusion processes, it will collapse under its own gravitational force (supernovae type II, Ib, or Ic). As a result, a large amount of MeV-neutrinos will carry away 99% of the gravitational energy within about 10 seconds. By measuring the time $T$ that the ultra-relativistic neutrinos need to propagate from the supernovae at distance $L$ to a detector on earth, one can gain information on their mass by detecting an energy-dependent clustering of arrival times:

$$T = \frac{L}{v} \approx L \cdot \left(1 + \frac{m_\nu^2}{2E_\nu^2}\right) \quad . \tag{1.43}$$

Apart from the observable, the mass $m_\nu$, the neutrino time-of-flight, thus, depends on the energy $E_\nu$ of a neutrino. Two neutrinos emitted from the supernovae at times $t_{01}$ and $t_{02}$ with different energies $E_{\nu,1} > E_{\nu,2}$ will therefore arrive at the detector over a time span

$$\Delta t = t_2 - t_1 = \Delta t_0 + \frac{L m_\nu^2}{2} \cdot \left(\frac{1}{E_{\nu,2}^2} - \frac{1}{E_{\nu,1}^2}\right) \quad . \tag{1.44}$$

While the detector on earth can measure the parameters $\Delta t$, $E_{\nu,1}$ and $E_{\nu,2}$, the distance $L$ can be derived from astrophysical observations. Thus, only the difference in emission times of the neutrinos $\Delta t_0 = t_{02} - t_{01}$ and their mass $m_\nu$ remain unknown. By constraining $\Delta t_0$ to a specific model for neutrino emission in a core-collapse supernovae, one can derive an upper limit on the neutrino mass, however with the drawback of a model-dependence due to the modelings of $\Delta t_0$ [Zub11].

[17] The free-streaming length $\lambda_{\text{FS}}$ of neutrinos characterizes the scale on which they become non-relativistic. On smaller scales, $\lambda < \lambda_{\text{FS}}$ they can therefore hardly be confined.

The famous supernovae SN1987A that occurred in February 1987, was observed by the underground detectors Kamiokande II [Hir87, Hir88a], IMB [Bio87, Bra88], and possibly also the Baksan Neutrino Observatory [Ale87, Ale88]. A total of 25 neutrino events in all three detectors was used in [LL02] to derive upper limits for the mass of the electron antineutrino of

$$\begin{array}{rcll} m_{\bar{\nu}_\mathrm{e}} & \leq & 8.9\,\mathrm{eV} & \\ m_{\bar{\nu}_\mathrm{e}} & \leq & 5.7\,\mathrm{eV} & (95\%\ \mathrm{C.L.}) \quad , \end{array} \tag{1.45}$$

depending on the underlying model for supernovae emission profiles.

### 1.6.3 Neutrinoless Double Beta-Decay

In nuclear physics, the binding energies of nucleons in nuclei can be described by the semi-empirical Bethe-Weizsäcker equation [vW35]. For isobars with a fixed nucleon number $A$, this equation simplifies to a parabola. In the case of $A$ being even, the spin coupling between the constituents in the nucleus causes this so-called mass parabola to split up into one lower-lying one for nuclei with an even-even configuration of $N$ and $Z$ (ee-nuclei) and one with higher binding energies for those with an odd-odd configuration (oo-nuclei). This splitting can lead to the case of a single $\beta$-decay of an ee-nucleus being forbidden by energy conservation as both neighboring oo-nuclei possess higher binding energies. In this case, a double $\beta$-decay can occur, where the initial ee-nucleus directly decays into the next lower-lying ee-nucleus according to

$$\begin{array}{lll} {}^{A}_{Z}\mathrm{X} \;\rightarrow\; {}^{A}_{Z+2}\mathrm{Y} + e^- + e^- + \bar{\nu}_\mathrm{e} + \bar{\nu}_\mathrm{e} & \left(2\nu\beta^-\beta^-\right) & \\ {}^{A}_{Z}\mathrm{X} \;\rightarrow\; {}^{A}_{Z-2}\mathrm{Y} + e^+ + e^+ + \nu_\mathrm{e} + \nu_\mathrm{e} & \left(2\nu\beta^+\beta^+\right) & . \end{array} \tag{1.46}$$

Similar to the single $\beta$-decay this can either happen by a transformation of two neutrons into two protons ($2\nu\beta^-\beta^-$-decay) or vice versa ($2\nu\beta^+\beta^+$-decay). As double $\beta$-decays represent second-order processes of the weak interaction, they have long half-lives in the order of $\approx 10^{20}$ years [Zub11]. While double $\beta$-decay was already postulated in 1935 [Goe35], it took several decades before it was observed for the first time in 1969 in a geochemical experiment by the $2\nu\beta^-\beta^-$-decay of $^{82}$Se into $^{82}$Kr with a half life of $1.4 \times 10^{20}$ years (error of 20%) [KM69]. To the present day, the double $\beta$-decay of 10 further isotopes has been observed via geochemical or laboratory experiments [Zub11].

Shortly after E. Majorana postulated that neutrinos could be their own antiparticle [Maj37] (see Sec. 1.5), an alternative process through which a double $\beta$-decay could occur was proposed by G. Racah in 1937 [Rac37] and W. Furry in 1939 [Fur39]. Their novel scenario involved the exchange of a virtual Majorana-like neutrino, so that two neutrons can transform into protons or vice versa according to

$$\begin{array}{lll} {}^{A}_{Z}\mathrm{X} \;\rightarrow\; {}^{A}_{Z+2}\mathrm{Y} + e^- + e^- & \left(0\nu\beta^-\beta^-\right) & \\ {}^{A}_{Z}\mathrm{X} \;\rightarrow\; {}^{A}_{Z-2}\mathrm{Y} + e^+ + e^+ & \left(0\nu\beta^+\beta^+\right) & . \end{array} \tag{1.47}$$

The left side of Figure 1.8 illustrates the process schematically, where the Majorana neutrino $\nu_\mathrm{m}$ is emitted and absorbed within the nucleus. The two charged leptons that can be detected share the full Q-value of the decay. As a result, their total energy appears as a peak at the endpoint of the $2\nu\beta\beta$-spectrum, shown on the right side of Figure 1.8. Such a process is forbidden in the SM of particle physics as it violates lepton number conservation ($L_\mathrm{initial} \neq L_\mathrm{final}$). Hence, an observation of this so-called neutrinoless double $\beta$-decay ($0\nu\beta\beta$) mode would indicate physics beyond the SM.

For the most simple case of purely left-handed V-A weak currents and light massive Majorana neutrinos, the half-life of the neutrinoless double $\beta$-decay is given by

$$(t^{0\nu}_{1/2})^{-1} = G^{0\nu}(E_0, Z) \cdot \left| M^{0\nu}_\mathrm{GT} - \frac{g_\mathrm{V}^2}{g_\mathrm{A}^2} M^{0\nu}_\mathrm{F} \right|^2 \cdot \langle m_{\beta\beta} \rangle^2 \quad , \tag{1.48}$$

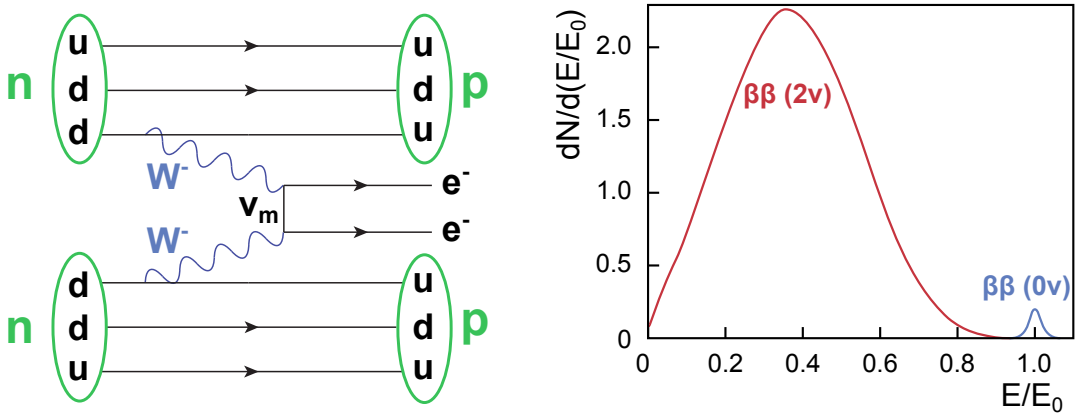


**Figure 1.8: The double $\beta$-decay. Left: Schematic overview of the neutrinoless double $\beta^-$-decay.** By the exchange of a virtual Majorana-like neutrino, two neutrons are transformed into protons, thereby emitting two electrons. Figure adapted from [Sch14c]. **Right: Electron energy spectrum for the neutrino-afflicted and the neutrinoless double $\beta$-decay.** The spectrum of the $2\nu\beta\beta$-decay is scaled to 1, while the $0\nu\beta\beta$-spectrum is scaled to 0.2. The energy resolution at the endpoint is taken as 5%. Figure adapted from [Sch13a, EV02].

where $G^{0\nu}(E_0, Z)$ corresponds to the exactly calculable phase-space integral, $M^{0\nu}_{\mathrm{GT}}$ and $M^{0\nu}_{\mathrm{F}}$ are the Gamov-Teller and Fermi nuclear matrix elements, $g_{\mathrm{V}}$ ($g_{\mathrm{A}}$) is the vector (axial-vector) coupling constant of the electroweak interaction, and $\langle m_{\beta\beta}\rangle$ corresponds to the effective neutrino mass [EV02]. The latter is given by the coherent sum of the neutrino mass eigenstates

$$\langle m_{\beta\beta}\rangle^2 = \left|\sum_{k=1}^{3} U_{\mathrm{e}k}^2 m_k\right|^2 = \left|\sum_{k=1}^{3} |U_{\mathrm{e}k}|^2 e^{\alpha_{k1}} m_k\right|^2 \quad , \tag{1.49}$$

where the $\alpha_{k1}$ correspond to the CP-violating Majorana phases shortly mentioned in Section 1.4.2. Those can lead to cancellations in the coherent sum, such that $\langle m_{\beta\beta}\rangle < m_k$.

If the half-life of a $0\nu\beta\beta$-decay is experimentally derived and the nuclear matrix elements are known, the corresponding effective neutrino mass can be derived from Equation 1.48. Up to the present day, however, no such decay has yet been observed[18], so that only lower (upper) limits can be given for its half-life (the effective neutrino mass).

The $0\nu\beta\beta$-decay is currently being investigated by several experiments like COBRA [Ebe13], EXO-200 [Alb14], KamLAND-Zen [Asa15], GERDA [Ack13], and others, which use different known $2\nu\beta\beta$-decay isotopes as source/detector.

The GERDA experiment, which serves as a a good example of a state-of-the-art neutrinoless double $\beta$-decay experiment, investigates the potential $0\nu\beta\beta$-decay mode of $^{76}$Ge according to

$$^{76}\mathrm{Ge} \;\rightarrow\; ^{76}\mathrm{Se} + 2e^- \quad , \tag{1.50}$$

with a Q-value of 2 039 keV. The experiment is located underground in the Laboratori Nazionali del Gran Sasso (LNGS) and uses high-purity enriched $^{76}$Ge-diodes as both source and detector. Based on data from the first phase of the experiment with a total exposure of 21.6 kg · y and a background of about 0.01 cts/(keV · kg · y), a lower limit for the half-life of the $0\nu\beta\beta$-decay of $^{76}$Ge could be derived [Ago13]

$$t^{0\nu}_{1/2} > 2.1 \times 10^{25}\,\mathrm{y} \quad (90\,\%\ \mathrm{C.L.}) \quad . \tag{1.51}$$

[18] Evidence for an observation of $0\nu\beta\beta$-decays in the Heidelberg-Moscow experiment that was claimed by a subgroup of the collaboration [Kla01] was not confirmed by recent experiments like GERDA, EXO, or KamLAND-Zen.

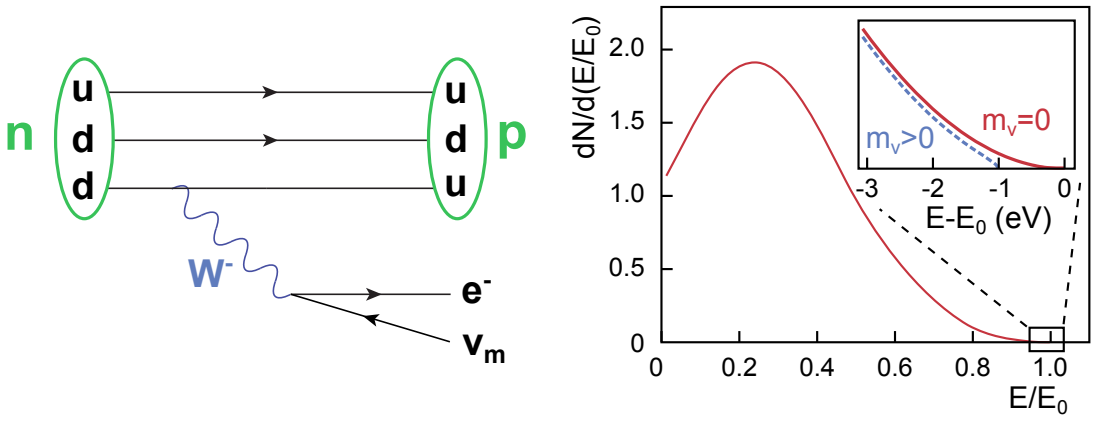


**Figure 1.9: The single $\beta$-decay. Left: Schematic illustration of the single $\beta^-$-decay process.** A neutron transforms into a proton by emitting an electron and an electron antineutrino. Figure adapted from [Sch14c]. **Right: Electron energy spectrum of the single $\beta$-decay.** The $x$-axis is scaled to the endpoint energy $E_0$, while the $y$-axis is given in arbitrary units. The inset shows the relevant endpoint region of the spectrum in a magnified view. The shape of the spectrum is shown for a vanishing neutrino mass (red solid line) and for an arbitrary non-zero neutrino mass of $m_{\overline{\nu}_e} = 1\,\text{eV}$ (blue dashed line). Figure adapted from [Sch13a].

Depending on the theoretical nuclear model used for calculating the nuclear matrix elements in Equation 1.48, this value corresponds to an upper limit of the effective mass of Majorana-like neutrinos of

$$m_{\beta\beta} < (0.2 - 0.4)\,\text{eV} \quad . \tag{1.52}$$

This sensitivity is in the same range as results obtained by other experiments like EXO or KamLAND-Zen [Oli14].

In difference to single $\beta$-decay experiments, which will be discussed in the next section, the results for the effective neutrino mass derived via $0\nu\beta\beta$-decay experiments rely on detailed models not only in terms of the Majorana character of neutrinos but also for the calculation of the nuclear matrix elements.

### 1.6.4 Kinematics of the Single Beta-Decay

The most straightforward method to directly access the absolute mass scale of neutrinos in a model-independent way is the investigation of the single $\beta^-$-decay by kinematic means. The left side of Figure 1.9 shows a schematic illustration of the three-body decay reaction

$$n \;\rightarrow\; p + e^- + \overline{\nu}_e \quad . \tag{1.53}$$

The $\beta$-decay spectrum of the outgoing electron, which is shown on the right side of Figure 1.9, carries information on the rest mass of the electron antineutrino due to the basic principles of energy and momentum conservation. By precise spectroscopy of the kinetic energy of electrons, the effective mass of the electron antineutrino can therefore be derived, relying only on the relativistic energy-momentum equation $E^2 = m^2 + p^2$. This relation directly reveals the experimental challenge, as the uncertainty on the neutrino mass $\delta m_\nu$ relates to the energy uncertainty $\delta E_\nu$ of the experiment according to

$$\delta m_\nu = \frac{E_\nu}{m_\nu} \cdot \delta E_\nu = \gamma \cdot \delta E_\nu \quad . \tag{1.54}$$

Thus, the uncertainty on the neutrino rest mass scales with the Lorentz factor $\gamma$ such that a relativistic neutrino hides away its rest mass. It is for this reason why experiments are

forced to focus on the low-statistics endpoint region on the far right part of the $\beta$-spectrum in Figure 1.9, as only these neutrinos are non-relativistic.

The theoretical description of the $\beta$-decay reaction in Equation 1.53 is given by Fermi's golden rule

$$\Gamma_{i\to f} = 2\pi \cdot |M_{fi}|^2 \rho(E_f) \quad , \tag{1.55}$$

where $\Gamma_{i\to f}$ describes the transition rate from the initial state $|i\rangle$ to the final state $|f\rangle$, $M_{fi}$ corresponds to the transition matrix element between the two states, and $\rho(E_f)$ gives the density of final states for an energy $E_f$. Making use of the relativistic energy-momentum relation and focusing on the special case of super-allowed nuclear transitions, the $\beta$-decay rate as function of the electron energy can be obtained by integrating over all possible discrete and continuous final states [Ang05, Ott10, Dre13]

$$\frac{\mathrm{d}N^2}{\mathrm{d}E\mathrm{d}t} = \frac{G_\mathrm{F}^2 \cdot \cos^2(\theta_\mathrm{C})}{2\pi^3} \cdot |M|^2 \cdot F(Z+1,E) \cdot p \cdot (E+m_\mathrm{e}) \times \\ \times (E_0 - E) \cdot \sqrt{(E_0-E)^2 - m_{\bar{\nu}_\mathrm{e}}^2} \cdot \Theta(E_0 - E - m_{\bar{\nu}_\mathrm{e}}) \quad . \tag{1.56}$$

Here, $G_\mathrm{F}$ is the Fermi coupling constant, $\theta_\mathrm{C}$ is the Cabbibo angle, $M$ corresponds to the energy-independent nuclear matrix element of the super-allowed transition, and $F(Z+1,E)$ denotes the Fermi function which accounts for the Coulomb interaction of the outgoing electron with the daughter nucleus and the shell electrons. The Heaviside step function $\Theta$ ensures conservation of energy in such a way that a neutrino can only be created if the available energy in the decay is greater than its rest mass $m_\nu$. The endpoint energy $E_0$ corresponds to the maximum kinetic energy that an emitted electron can possess. When disregarding the recoil of the daughter nucleus, this parameter corresponds to the Q-value of the decay.

From Equation 1.56 it follows that the experimental observable in single $\beta$-decay experiments is the squared mass $m_{\bar{\nu}_\mathrm{e}}^2$ of the flavor eigenstate of an electron antineutrino. This quantity is given by the weighted average of the masses $m_k$ of the neutrino mass eigenstates

$$m_{\bar{\nu}_\mathrm{e}}^2 = \sum_{k=1}^{3} |U_{ek}|^2 m_k^2 \ , \tag{1.57}$$

which in contrast to the effective Majorana neutrino mass (Eq. 1.49) only depends on the probabilities $U_{ek}$ to generate one of the three mass eigenstates $\nu_k$ in the weak $\beta$-decay reaction, but not on the CP-violating Majorana phases $\alpha_{k1}$. In principle, this incoherent sum given in Equation 1.57 will lead to a fine structure close to the endpoint of the $\beta$-spectrum, where the splitting of the spectral features relates to the differences in squared masses of the neutrino mass eigenstates $\Delta m_{kl}^2$, which are well known from the oscillation experiments. However, due to the smallness of the parameters $\Delta m_{kl}^2 \lesssim 10^{-3}\,\mathrm{eV}^2$, the energy resolution of the state-of-the-art single $\beta$-decay experiments is still too coarse to resolve these tiny structures.

In general, three properties have to be maximized in single $\beta$-decay based neutrino-mass experiments to achieve the best possible sensitivity on $m_{\bar{\nu}_\mathrm{e}}^2$. These are

- the accepted solid angle $\Omega$ of the emitted electrons in order to increase the statistics in the relevant endpoint region of the $\beta$-spectrum,
- the energy resolution of the experiment in order to resolve the small change in the shape of the $\beta$-spectrum close to the endpoint that a non-zero $m_{\bar{\nu}_\mathrm{e}}^2$ causes,
- and the signal-to-background ratio close to the endpoint.

### Rhenium and Holmium Experiments

The signal rate of $\beta$-electrons with energies close to the kinematic endpoint scales with $E_0^{-3}$. Thus, $\beta$-emitters with low endpoint energies would be favorable in terms of increased statistics in the relevant energy window[19]. The lowest endpoint energy of all $\beta$-radiators is measured for $^{187}$Re with $E_0 = 2\,465.3 \pm 0.5\,(\text{stat.}) \pm 1.6\,(\text{syst.})\,\text{eV}$ [Sis04]. $^{187}$Re decays according to

$$^{187}\text{Re} \;\rightarrow\; ^{187}\text{Os}^{+} + e^{-} + \overline{\nu}_\text{e} \quad . \tag{1.58}$$

Even in this favorite case, only a tiny fraction of $6 \times 10^{-11}$ of all decays will result in the emission of an electron whose energy is within 1 eV below the endpoint. However, the $^{187}$Re half-life of $t_{1/2} = [43.2 \pm 0.2\,(\text{stat.}) \pm 0.1(\text{syst.})] \times 10^9$ years [Sis04] is exceedingly long, so that a large amount of this isotope is required in order to achieve a reasonable activity [Dre13]. The long half-life is due to the fact that the decay given in Equation 1.58 corresponds to a first unique forbidden transition, such that Equation 1.56 does not hold. Furthermore, $^{187}$Re has a rather complicated electron shell and a precise calculation of the final states of the daughter nucleus $^{187}$Os appears difficult. Therefore, experiments that try to derive $m_{\overline{\nu}_\text{e}}$ from the $\beta$-decay of $^{187}$Re use a 'source-equals-detector' arrangement, similar to $0\nu\beta\beta$ experiments like GERDA. While the latter makes use of the semiconductor behavior of germanium, the $^{187}$Re-based single $\beta$-decay experiments have to use low temperature microcalorimeters where a sensitive thermometer has to translate the temperature increase in a rhenium-based absorber into an electrical signal. The advantage of this detection technique is that all of the energy that is released in the $\beta$-decay, apart from the neutrino energy, is deposited in the detector and automatically summed-up. In this way, systematic uncertainties due to unconsidered energy contributions in the decay can be kept relatively small.

The great challenge of microcalorimeter-based experiments, however, is given by the fact that only a small fraction of all $\beta$-decays will occur with neutrinos being emitted non-relativistically (see Eq. 1.54). By being forced to measure the entire $\beta$-spectrum, great care has to be taken to avoid large pile-up effects in the intrinsically slow thermal detectors. This can be achieved by subdividing the microcalorimeters into arrays to limit the activity per detector. The technical realization of large-scale microcalorimeter arrays currently represents the limiting factor of these type of $\beta$-decay experiments [Sis04, And07, Dre13].

The best upper limit on $m_{\overline{\nu}_\text{e}}$ that could yet be derived from the investigations of $^{187}$Re $\beta$-decays was published by the Milano experiment [Nuc02] in 2004 with [Sis04]

$$m_{\overline{\nu}_\text{e}} < 15\,\text{eV} \quad (90\%\ \text{C.L.}) \quad . \tag{1.59}$$

The now abandoned successor project MARE was planning to improve the sensitivity further to the sub-eV scale [Nuc12]. Due to solid-state effects in $^{187}$Re-based microcalorimeters, a lot of attention is recently paid to another isotope that is suitable for a direct neutrino-mass measurement, namely $^{163}$Ho. In contrast to $^{187}$Re, it decays via electron capture with a Q-value of $[2\,833 \pm 30\,(\text{stat.}) \pm 15\,(\text{syst.})]\,\text{eV}$ [Eli15]. The ECHo experiment, as well as others, is thus planning to utilize $^{163}$Ho to reach a sub-eV sensitivity on $m_{\overline{\nu}_\text{e}}$ [Gas14].

### Tritium Experiments

Of all $\beta$-decaying isotopes, tritium is considered as the most feasible one to derive $m_{\overline{\nu}_\text{e}}$ in means of pure kinematics from the single $\beta$-decay

$$^{3}\text{H} \;\rightarrow\; ^{3}\text{He}^{+} + e^{-} + \overline{\nu}_\text{e} \quad . \tag{1.60}$$

[19] This often used statement neglects the fact that the $\beta$-decay rate scales as $\propto E_0^5$, which counteracts the $E_0^{-3}$ scaling.

Over the last decades several high-sensitivity experiments based on various spectroscopic techniques have made full use of the ideal characteristics of $^3$H in terms of

- **low endpoint energy:** With $E_0 \approx 18.6\,\text{keV}$, tritium has the second lowest endpoint energy after $^{187}$Re (not counting $^{163}$Ho). Besides the rather high event rate close to $E_0$, this fact makes it technically feasible to use the well-established concept of MAC-E (magnetic adiabatic collimation combined with an electrostatic) filter based spectrometers [BPT80, KR83] to scan the endpoint region of the $\beta$-spectrum with sub-eV precision (see Chapter 2).
- **short half-life:** With a half-life of $t_{1/2} = (12.32 \pm 0.02)\,\text{years}$ [LU00], tritium features a very high specific activity, guaranteeing a high luminosity of the source even when using only small amounts of source material. In this way, inelastic scattering processes of the $\beta$-electrons in the source can be minimized.
- **the decay being super-allowed:** Due to the fact that $^3$H and $^3$He are mirror nuclei, the nuclear matrix element of the transition is energy-independent so that the $\beta$-spectrum is fully determined by the available phase space (Eq. 1.56). The nuclear matrix element of $|M|^2 = 5.55$ [RK88] is rather large, close to that of the free neutron $\beta$-decay [Dre13].
- **a simple atomic-shell structure:** Due to the low nuclear charge $Z = 1$ ($Z = 2$) of the mother (daughter) nucleus, both systems have a rather simple atomic-shell structure, which minimizes the effects from inelastic scattering processes of $\beta$-electrons in the source and allows for a reliable calculation of the Fermi function $F(Z = 2, E)$.
- **its gaseous phase:** The fact that tritium remains in the gaseous phase even at cryogenic temperatures of 30 K has the distinct advantage that solid-state effects such as cluster formation do not have to be considered when using a windowless gaseous tritium source in this temperature regime (see Chapter 2).

The best model-independent limits on the effective mass of the electron antineutrino come from the MAC-E filter based tritium $\beta$-decay experiments in Mainz [Ott94] and Troitsk [Lob85]. The former used a solid quench-condensed tritium source and reported a final limit of

$$m_{\bar{\nu}_e} < 2.3\,\text{eV}\ (95\,\%\ \text{C.L.}) \quad , \tag{1.61}$$

based on data from phase II of the experiment [Kra05].

In contrast to the Mainz experiment, the Troitsk setup made use of a windowless source of molecular tritium to derive an upper limit of [Ase11]

$$m_{\bar{\nu}_e} < 2.05\,\text{eV}\ (95\,\%\ \text{C.L.}) \quad . \tag{1.62}$$

Finally, a combined analysis of both results yields

$$m_{\bar{\nu}_e} < 2.0\,\text{eV}\ (95\,\%\ \text{C.L.}) \quad , \tag{1.63}$$

as quoted by the Particle Data Group [Oli14]. This value is the currently most sensitive model-independent upper limit for the effective mass of the electron antineutrino.

While providing impressive limits, the experiments in Mainz and Troisk were limited by systematic uncertainties and restricted source statistics. Thus, in order to access the important sub-eV scale of neutrino masses, a new generation of single $\beta$-decay experiments is needed. The KATRIN experiment that is currently being constructed at the KIT Campus North site is the most advanced and forerunner of these experiments. Based on the concept of a windowless gaseous tritium source that was successfully used at the Troitsk experiment, and the well-established MAC-E filter principle, the KATRIN experiment is targeted to surpass the sensitivity of its predecessor experiments by a factor of 10 [Ang05].

CHAPTER 2

# The KATRIN Experiment

The KATRIN experiment represents the next generation of tritium $\beta$-decay based measurements of the effective electron neutrino mass by kinematic means. With a final sensitivity of $m_{\bar{\nu}_e} \leq 200\,\text{meV}$ (90% C.L.) and a discovery potential of $m_{\bar{\nu}_e} = 350\,\text{meV}$ at $5\sigma$ after five years of operation, it is targeted to exceed the sensitivity of previous direct neutrino-mass experiments by a factor of 10. To achieve this ambitious goal, the experiment must resolve the tiny spectral distortions that a non-vanishing neutrino rest mass causes close to the kinematic endpoint at $E_0 \approx 18.6\,\text{keV}$ with a high signal-to-background ratio.

The underlying MAC-E filter principle that is used by KATRIN in high-precision tritium energy spectroscopy combines excellent energy resolution with a large angular acceptance for $\beta$-decay electrons from the tritium source. The characteristic of such a filter as well as potential background processes are described in Section 2.1. With a total length of about 70 m and its key element, the 10-m diameter main spectrometer, the experimental setup of KATRIN is almost 10 times larger than former tritium $\beta$-decay experiments. Section 2.2 gives an overview of the major components of the KATRIN beamline before the essential design parameters of the experiment and its analysis principle are outlined in Section 2.3.

## 2.1 The Measurement Principle

To scan the endpoint region of the tritium $\beta$-decay spectrum with high precision, the KATRIN experiment makes use of the MAC-E filter concept. In the following, the working principle of such a filter as well as characteristic background processes related to it are outlined.

### 2.1.1 The Working Principle of MAC-E Filter Spectrometers

The MAC-E filter principle for high-precision electron-energy analysis was initially proposed and described in [BPT80] and [KR83], and later adapted to neutrino-mass measurements by the Troitsk [Lob85] and Mainz [Pic90] experiments. The key feature of MAC-E filters is to combine high energy resolution with very large angular acceptance, making them ideally suited to resolve the tiny distortions in the tritium $\beta$-spectrum that a non-vanishing neutrino rest mass causes, while at the same time using most of the source luminosity. Figure 2.1 illustrates the working principle of such a MAC-E filter.

#### Magnetic Guidance

In a MAC-E filter, strong magnetic fields provided by superconducting solenoids are used to adiabatically transport a large number of tritium $\beta$-electrons which are emitted isotropically in a source with magnetic field $B_S$, through a spectrometer section and onto a

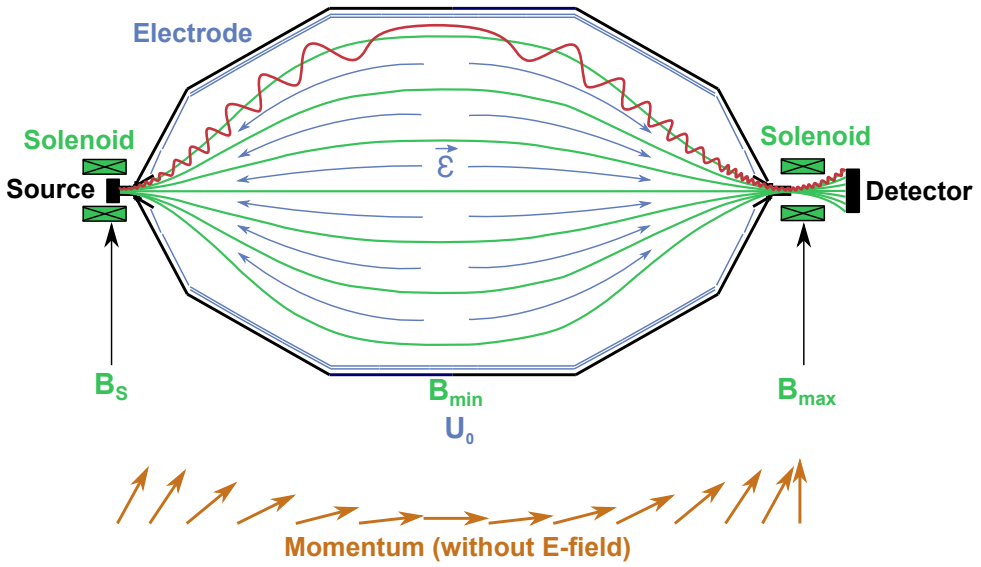


**Figure 2.1: Illustration of the MAC-E filter principle.** Two superconducting solenoids, one on each side of the spectrometer, provide the guiding magnetic field so that electrons, emitted isotropically in the source, move on cyclotron trajectories (red, shown exaggerated in size) along the magnetic field lines (green) into the spectrometer. A slow drop of the magnetic field towards the center of the spectrometer causes an adiabatic transformation of the electron's momentum (orange), such that nearly all of its kinetic energy is stored in the longitudinal energy component $E_{\parallel}$ when it reaches the minimum magnetic field $B_{min}$ in the so-called analyzing plane. Here, the electric potential reaches its maximum $qU_0$ and the electric field $\vec{\mathcal{E}}$ (blue arrows), which acts on the longitudinal energy component only, filters out those electrons with $E_{\parallel} < |qU_0|$. Electrons that overcome this high-pass filter leave the spectrometer on the opposite side and are counted by an electron detector. Adapted from [Wan13a].

detector. The momentum $p$ of an electron, which is emitted in the source under a polar angle $\theta$ relative to the magnetic field lines, can be split into a longitudinal component, parallel to the magnetic field line $p_{\parallel} = \cos\theta \cdot |\vec{p}|$, and a transverse component $p_{\perp} = \sin\theta \cdot |\vec{p}|$ perpendicular to it. The corresponding kinetic energies are given by

$$E_{\text{kin}} = \frac{|\vec{p}|^2}{2m} = E_{\parallel} + E_{\perp} \quad . \tag{2.1}$$

While the transverse component of the electron momentum is responsible for the cyclotron motion around the magnetic field line due to the Lorentz force, the longitudinal component causes the electron to propagate along the magnetic field line through the experiment.

### Electrostatic Filtering

An essential part of a MAC-E filter is the electrostatic filtering of the signal electrons with respect to their kinetic energy. To do so, the spectrometer vessel (or an inner electrode system) is elevated to a negative potential $U_0$ such that an electric field $\vec{\mathcal{E}}$, parallel to the magnetic field lines, prohibits electrons with insufficient longitudinal kinetic energies $E_{\parallel} < |qU_0|$ to overcome the potential barrier $|qU_0|$ in the central, so called analyzing plane of the spectrometer. In contrast, those electrons with sufficient longitudinal kinetic energy $E_{\parallel} > |qU_0|$ are transmitted and are counted by a detector. By varying the retarding potential $U_0$ the energy spectrum of the $\beta$-decay electrons can be scanned in an integral way. However, as $\beta$-electrons are emitted isotropically in the source, they typically have non-negligible parts of their kinetic energy stored in the transverse component $E_{\perp}$, which is not analyzed by the retarding potential. Hence, an adiabatic collimation of their mo-

mentum $p$ into longitudinal direction is necessary to guarantee a high-precision analysis of their total kinetic energy.

**Magnetic-Adiabatic Collimation**

In non-relativistic approximation the first adiabatic invariant of an 18.6-keV electron ($\gamma = 1.04$) propagating in an inhomogeneous magnetic field is given by its magnetic moment

$$\mu = \frac{E_\perp}{B} = \text{const.} \quad . \tag{2.2}$$

Thus, a decrease of the magnetic field from the source to the analyzing plane of the spectrometer ($B_\mathrm{S} \rightarrow B_\mathrm{min}$) causes the transverse kinetic energy of the electron to decrease accordingly. If the gradient of the magnetic field is kept sufficiently small at all times, the adiabacity of this process is guaranteed and the transverse kinetic energy will pass over into longitudinal kinetic energy ($E_\perp \rightarrow E_\parallel$), i.e. the momentum of the electron is collimated into longitudinal direction when it approaches the analyzing plane. Accordingly, a sufficiently large drop of the magnetic field will guarantee that nearly all of the kinetic energy of the electron is analyzed by the retarding potential $qU_0$ of the filter. The important prerequisite of maintaining sufficiently small gradients of the magnetic field, in combination with the ratio of $B_\mathrm{min}$ to $B_\mathrm{max}$, defines the minimum length of a MAC-E filter based spectrometer.

**Conservation of the Magnetic Flux**

Besides the invariant magnetic moment of the electrons, the magnetic flux $\Phi$ remains constant at all times

$$\Phi = \int_\mathrm{A} \vec{B} \cdot \mathrm{d}\vec{A} = \text{const.} \quad . \tag{2.3}$$

Thus, a decrease of the magnetic field will result in an increase of the diameter of the magnetic flux tube, which is initially defined by the source magnetic field $B_\mathrm{S}$ and its diameter $d_\mathrm{S}$. The maximum diameter is reached in the analyzing plane of the spectrometer with

$$d_\mathrm{AP} = d_\mathrm{S} \cdot \sqrt{\frac{B_\mathrm{S}}{B_\mathrm{min}}} \quad , \tag{2.4}$$

defining the radial extension of a MAC-E filter spectrometer.

**The Magnetic-Mirror Effect**

The opposite effect of the previously described magnetic-adiabatic collimation of the electrons momentum is the well-known magnetic-mirror effect, where electrons are magnetically reflected when traveling from a weak into a strong magnetic field. As the maximum magnetic field strength in some MAC-E filters (like the KATRIN main spectrometer) is not given in the source, but downstream of the spectrometer with $B_\mathrm{S} < B_\mathrm{max}$, some fraction of the signal electrons will be reflected in this high field region. With $|\vec{p}_{\mathrm{S},\perp}| = \sin\theta \cdot |\vec{p}|$ in the source, and making use of the condition that at the point of $B_\mathrm{max}$ all of the kinetic energy of a particle which is just transmitted is stored in its transverse energy component $E_{\mathrm{max},\perp} = E_\mathrm{kin}$, one can derive the maximum polar emission angle $\theta_\mathrm{max}$ of an electron emitted in the source magnetic field $B_\mathrm{S}$ to not be reflected in the maximum field $B_\mathrm{max}$ from Equations 2.1 and 2.2 to

$$\theta_\mathrm{max} = \arcsin\left(\sqrt{\frac{B_\mathrm{S}}{B_\mathrm{max}}}\right) \quad . \tag{2.5}$$

A reflection of signal electrons with large polar emission angles in a MAC-E filter is somehow favorable, as the trajectories of these electrons through the experiment are rather

long, increasing the probability for undesired energy losses due to scattering processes or via the continuous emission of synchrotron radiation in the high-B-field beamline.

**The Energy Resolution**

As the minimum magnetic field in the analyzing plane of the spectrometer necessarily is larger than zero ($B_{\mathrm{min}} > 0$), a very small fraction of the kinetic energy of an electron will always remain stored in the transverse component $E_{\perp}$ and will not be analyzed by the MAC-E filter. This remaining transverse component maximizes for an electron which has only transverse energy $E_{\mathrm{max},\perp} = E_{\mathrm{kin}}$ at the point of the maximum magnetic field $B_{\mathrm{max}}$. This corresponds to the energy resolution, or more precisely the filtering width of the MAC-E filter. It can be calculated from Equation 2.2 to

$$\Delta E = \frac{B_{\mathrm{min}}}{B_{\mathrm{max}}} \cdot E_{\mathrm{kin}} \quad . \tag{2.6}$$

**The Transmission Function**

As a MAC-E filter based spectrometer scans the endpoint region of the tritium $\beta$-spectrum in an integral way by acting as a high-pass filter, the count rate on the detector for a specific retardation potential $qU_0$ is given by

$$\frac{\mathrm{d}N(qU_0)}{\mathrm{d}t} \propto \int_{qU_0}^{E_0} \frac{\mathrm{d}^2 N}{\mathrm{d}E\mathrm{d}t}(E_0, m_{\bar{\nu}_{\mathrm{e}}}^2) \cdot T(E, qU_0)\ \mathrm{d}E \quad . \tag{2.7}$$

Here, $\frac{\mathrm{d}^2 N}{\mathrm{d}E\mathrm{d}t}(E_0, m_{\bar{\nu}_{\mathrm{e}}}^2)$ corresponds to the differential tritium $\beta$-decay spectrum according to Equation 1.56, while the transmission probability for an electron is given by the transmission function of the MAC-E filter $T(E,\ qU_0)$. The exact shape of this function depends on the angular distribution of the electrons at the entrance of the filter. In case of tritium $\beta$-decays, where the electrons are emitted isotropically, an analytical expression for the transmission function can be derived to

$$T(E,\ qU_0) = \begin{cases} 0 & \text{if } E < |qU_0| \\ \dfrac{1-\sqrt{1-\frac{E-qU_0}{E}\cdot\frac{B_{\mathrm{S}}}{B_{\mathrm{min}}}}}{1-\sqrt{1-\frac{B_{\mathrm{S}}}{B_{\mathrm{max}}}}} & \text{if } |qU_0| \leq E \leq |qU_0| + \Delta E \\ 1 & \text{if } E > |qU_0| + \Delta E \end{cases} \tag{2.8}$$

While this transmission function only describes the spectroscopic features of a MAC-E filter, the overall response function of the experiment $R(E, qU_0)$ has to be derived by a convolution of the transmission function with the energy-loss distribution of the signal electrons in the source.

A more detailed discussion of the MAC-E filter properties and an in-depth modeling of the response function can be found in [Gro15], while a rather clear mathematical derivation of the magnetic-mirror effect and the adiabatic invariance is given in [Gal13].

### 2.1.2 Background Processes in a MAC-E Filter

With their superior energy resolution and high angular acceptance MAC-E filters are perfectly suited for high-precision tritium $\beta$-spectroscopy. Nevertheless, as the distortion in the endpoint region of the $\beta$-spectrum, caused by a non-vanishing neutrino rest mass, is rather small, a low background level is essential to achieve a sufficient signal-to-background ratio. In the following, the four most prominent sources of background in MAC-E filter spectrometers are discussed.

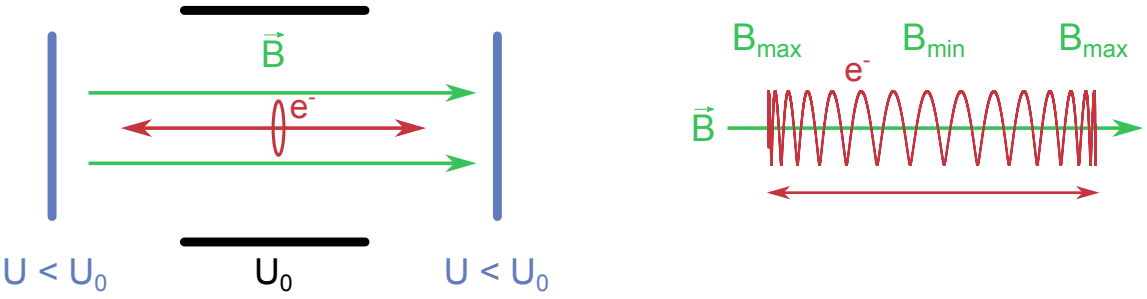


**Figure 2.2: Illustration of particle-trapping processes in a MAC-E filter. Left: Penning traps** are formed by the interplay of electric and magnetic fields. An electron that is generated in a region with electric potential $U_0$ (black) is trapped between two potential barriers with $U < U_0$ (blue) while moving on a cyclotron trajectory (red) along the magnetic field lines (green). **Right: Magnetic-bottle traps** are based on two magnetic mirrors, where electrons generated in a weak field $B_{\text{min}}$ are reflected by a turn-over of their momentum vector in the strong magnetic field $B_{\text{max}}$. Figure adapted from [Gro10].

### Penning Traps

A Penning trap is a localized volume where the specific configuration of electric and magnetic fields results in a storage of charged particles. Due to the interplay of the electromagnetic fields, they represent a notorious source of background in MAC-E filter spectrometers. A typical Penning trap configuration is shown on the left-hand side of Figure 2.2. A low-energy electron that is generated in an electric potential $U_0$ is trapped between two cathodes with $U < U_0$ in axial direction, while the Lorentz force that is induced by the magnetic field $\vec{B}$ prevents a radial movement. Instead, the electron propagates on a cyclotron trajectory, bouncing back and forth between the two cathodes. An electron that is stored in such a trap will sooner or later ionize residual gas thereby generating further, secondary electrons as well as positive ions and photons. While the secondary electrons are also stored in the trap, the positively charged ions and the photons will leave the trap to generate backgrounds by additional ionizations in the sensitive flux volume of the MAC-E filter, or will hit one of the cathodes. In the latter case, tertiary electrons, which further fill the trap, will be generated. In extreme cases, where large Penning traps are filled with a large number of low-energy electrons, an unstable plasma can be generated that can lead to a vacuum breakdown in the MAC-E filter, a so called Penning discharge [Pen36, Pic92, Byr05].

As Penning traps can cause large backgrounds in MAC-E filter experiments [Fra10] and potential Penning discharges pose a considerable risk of damage to the experimental apparatus, a careful design of all electromagnetic components of a MAC-E filter is mandatory [FGV14].

### Magnetically Stored Particles

As described in the previous section, electrons that are generated in a weak magnetic field $B_{\text{min}}$ can be reflected by the magnetic-mirror effect when traveling to a region with strong magnetic field $B_{\text{max}}$, equivalent to a turn-over of their momentum vector. The right-hand side of Figure 2.2 shows the combination of two such magnetic mirrors, representing a so-called magnetic bottle. According to Equation 2.5, a low-energy electron which is generated in the weak magnetic field $B_{\text{min}}$ with polar angle $\theta < \theta_{\text{max}}$ will be reflected by the strong magnetic fields on both sides of the bottle while again being restricted in radial direction due to its cyclotron motion around the magnetic field line. With its characteristic magnetic field configuration, a MAC-E filter spectrometer can act as a magnetic bottle for a large fraction of electrons generated in its center. Such electrons can be emitted in

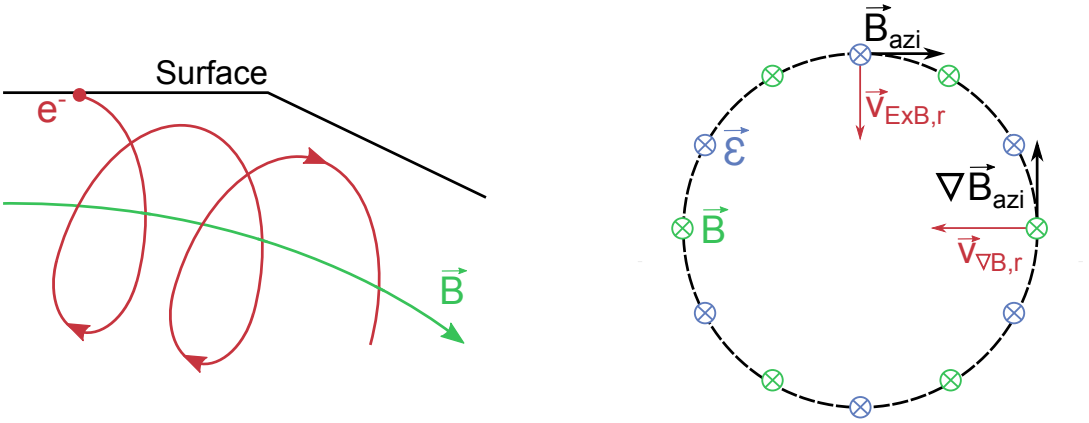


**Figure 2.3: Illustration of electron-drift processes into the sensitive volume of a MAC-E filter. Left:** If the magnetic field lines proceed not fully parallel to the inner surfaces of the spectrometer, electrons generated at a surface are not necessarily guided back to it by the Lorentz force. **Right:** In the presence of non-axially symmetric magnetic fields, the non-vanishing azimuthal component of the magnetic field $\vec{B}_{\text{azi}}$ causes two radial drift processes of the electrons, the $\vec{E} \times \vec{B}$- and the $\nabla \vec{B} \times \vec{B}$-drift. Both processes can cause the stored electrons to move into the sensitive flux volume of the MAC-E filter. The right illustration is adapted from [Wan13a].

various processes such as nuclear decays of either tritium or other radioactive isotopes, the atomic relaxation of highly exited atoms, or the ionization of residual gas by positive ions originating from e.g. a Penning trap.

As will be discussed in detail in Chapter 4 in the context of radon $\alpha$-decays in the main spectrometer, magnetically stored electrons in a MAC-E filter can cause characteristic time-correlated backgrounds by the ionization of residual gas, which significantly worsen the sensitivity on the neutrino mass.

**Electron Emission from Inner Surfaces**

Due to the dimensions of the retarding spectrometer, the large inner surface area can be a source of background where electrons can be generated by different processes:

- Secondary electron emission: Cosmic rays or high-energy $\gamma$-photons from environmental radioactivity can penetrate the spectrometer vessel and generate low-energy secondary electrons at the inner surface [Lei14]. Furthermore, radioactive decays of isotopes that have previously been adsorbed on the inner surface of the spectrometer, or even been implanted into sub-surface layers, will lead to the emission of electrons of various energies, as will be discussed in detail in Chapter 5.
- Field electron emission: Even if extreme care is taken in the electromagnetic design of MAC-E filters to avoid e.g. Penning traps, any remaining sharp edge on an inner surface exposed to an electric field can cause a very high local electric-field strength. This in turn can lead to field electron emission [For12], where electrons leave the bulk material by the tunnel effect. More details on the field electron emission in MAC-E filters are given in [Sch14c].

However, based on the characteristic axially-symmetric shape of the flux tube, a MAC-E filter usually provides an excellent intrinsic magnetic shielding against electrons emitted from inner surfaces. Due to the Lorentz force, the radial momentum of an emitted electron does not allow propagation into the sensitive flux volume. The electron is forced onto a cyclotron motion around a magnetic field line and is guided back to its point of creation

at the surface after one gyration. Nevertheless, this is only the case if the magnetic field lines are aligned parallel to the surface geometry. The left side of Figure 2.3 shows an example where this is not the case and an electron that is emitted from the surface can propagate along the field line without being immediately terminated on a surface again. Instead, this electron can for example be stored in the outer flux tube regions by the previously described magnetic-bottle effect. In this case, non-axial contributions to the magnetic field, which can be induced by e.g. magnetic materials in the surrounding of the spectrometer, will cause a radial drift of the stored electron towards the center and into the sensitive flux tube of the MAC-E filter, as illustrated on the right-hand side of Figure 2.3. In this way, a small fraction of the electrons that are emitted from inner surfaces of the spectrometer can enter the sensitive flux volume on time-scales of a few milliseconds and generate secondary background electrons via scattering off residual gas [Lei14]. Nevertheless, a careful minimization of non-axial fields will allow to achieve a shielding factor of about $10^5$ from the intrinsic magnetic shielding alone, thus, strongly suppressing backgrounds due to electron emission from inner surfaces [Wan13a].

**Intrinsic Detector Background**

In addition to the processes in a MAC-E filter described previously, all intrinsic background signals at, or in the vicinity of, the detector must be kept at a reasonably small level as well. These backgrounds are mostly induced by cosmic rays and the natural radioactivity of the structural materials around the detector. An overview of the detector related background contributions in the KATRIN experiment is given in Chapter 3 of this thesis, while a more detailed discussion of the topic can be found in [Sch14c].

## 2.2 The Experimental Setup of KATRIN

The 70-m long experimental setup of KATRIN is currently being assembled on site at the KIT Campus North. There, the Tritium Laboratory Karlsruhe (TLK) provides the extensive infrastructure and expertise which is required to process the large throughput of gaseous molecular tritium for the KATRIN source. Figure 2.4 gives an overview of the different subsystems of the experiment.

### 2.2.1 Windowless Gaseous Tritium Source

In order to restrict energy losses of the tritium $\beta$-electrons in the source only to scattering processes off tritium gas, the KATRIN experiment makes use of a windowless gaseous tritium source (WGTS), which combines high luminosity with great stability of all operating parameters. Figure 2.5 shows a CAD drawing of the source cryostat together with a schematic overview of its internal structures. The 16-m long cryostat was assembled at *ri GmbH* at Bergisch Gladbach and installed at TLK on September $10^{\text{th}}$, 2015. Since then it is being prepared for the tritium operation, which is expected to start in mid 2016.

In the center of the 10-m long stainless steel beam tube with a diameter of 90 mm, gaseous molecular tritium is injected through a set of capillaries with an inlet pressure of about $10^{-3}$ mbar. The molecules propagate along the beam tube and are pumped out at both ends by the differential pumping systems DPS1-R and DPS1-F. These initial pumping stages reduce the tritium flow into the adjacent systems by about a factor of 100. Each of the 3-m long systems houses a total of six turbo-molecular pumps (TMPs) that collect the tritium gas and feed it into the closed inner-loop system [Stu10]. Here, the gas is processed by a permeator and its isotopic composition is monitored by Laser-Raman spectroscopy via the so-called LARA-setup [Sch13b, Sch13a] in real time. A small part of the tritium is processed ensuring a tritium purity of $\epsilon_{\text{T}} > 95\%$ of the gas that is re-injected into the WGTS beam tube. In this way, a throughput of tens of grams of molecular tritium is

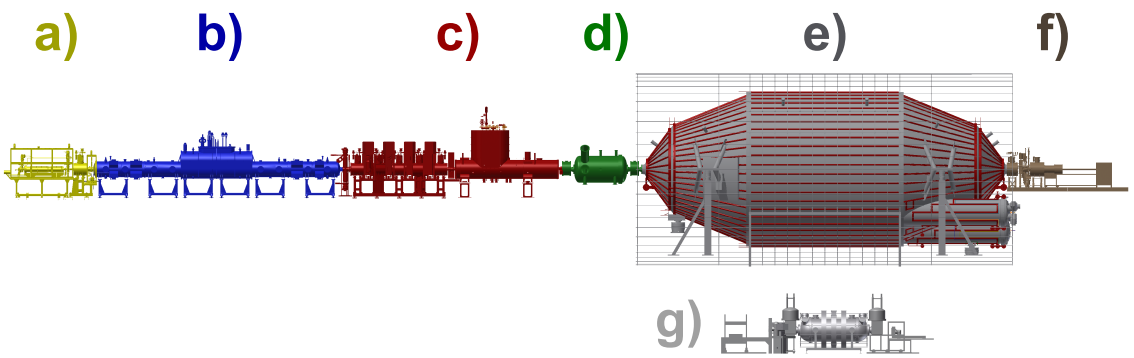


**Figure 2.4: Overview of the 70-m long KATRIN experimental setup.** The experiment consists of seven main components: **(a)** The rear section, which monitors the source parameters and is used for regular calibration purposes. **(b)** The windowless source where the molecular tritium is injected with high precision. **(c)** The transport section through which the signal electrons from the source are guided magnetic-adiabatically, while the tritium gas is extracted via differential and cryogenic pumping. **(d)** The pre-spectrometer where low-energy $\beta$-electrons can be pre-filtered. **(e)** The MAC-E filter based main spectrometer for high-resolution tritium $\beta$-spectroscopy. **(f)** The focal-plane detector system where the $\beta$-electrons that passed the retarding potential of the main spectrometer are counted with high efficiency. **(g)** The monitor spectrometer that is used to monitor the stability of the main spectrometer retarding potential.

cycled through the WGTS per day to retain a stable column density in the beam tube of $\rho d = 5 \times 10^{17}\,\mathrm{molecules/cm^2}$. This corresponds to a total $\beta$-decay activity of $A \approx 10^{11}\,\mathrm{Bq}$ [Ang05].

To minimize distortions of the signal-electron energies due to thermal Doppler-broadening and to reduce the tritium throughput, the WGTS beam tube is kept at a stable operating temperature of $T = 30\,\mathrm{K}$ [Bod11, Gro11]. The beam tube cooling system uses a novel two-phase neon cooling concept to keep the temperature stable to better than $10^{-3}$. Test measurements with the WGTS demonstrator assembly in 2009/10 have shown peak-to-peak temperature fluctuations of the beam tube of 3 mK within 4 hours, which is a factor 10 better than required to stabilize the column density to a $10^{-3}$ level [Hoe12, Gro13].

The guiding magnetic field of $B_\mathrm{S} = 3.6\,\mathrm{T}$ for the isotropically emitted tritium $\beta$-decay electrons is provided by three superconducting solenoids. In order to compensate possible misalignments of the whole experimental apparatus and to suppress plasma-related surface phenomena close to the beam tube walls [Kuc16], only the inner part ($d_\mathrm{S} = 8.2\,\mathrm{cm}$) of the 9-cm beam-tube diameter in the source is used for the neutrino-mass analysis, corresponding to a 'transported' source cross-section of $A_\mathrm{S} \approx 53\,\mathrm{cm^2}$. This results in a magnetic flux of $\Phi = B_\mathrm{S} \cdot A_\mathrm{S} = 191\,\mathrm{Tcm^2}$ that must be transported undisturbed through the entire experiment. Furthermore, an increased magnetic field of 5.6 T in the DPS1-F section prevents signal electrons with large polar emission angles to be guided out of the source and into the adjacent transport section. These electrons are reflected (see Sec. 2.1.1) and contribute to keeping the source in a quasi-neutral state.

More information concerning the WGTS can be found in [Gro11, Bab12, Gro13].

### The Rear Section

At the upstream end of the source, behind the DPS1-R, the Rear Section is located. This multi-purpose control- and monitor-unit is used to

- monitor the source activity by $\beta$-induced X-ray spectroscopy (BIXS) [RP13, Roe15],
- define the electric potential of the tritium plasma in the source [Bab12, Bab14],

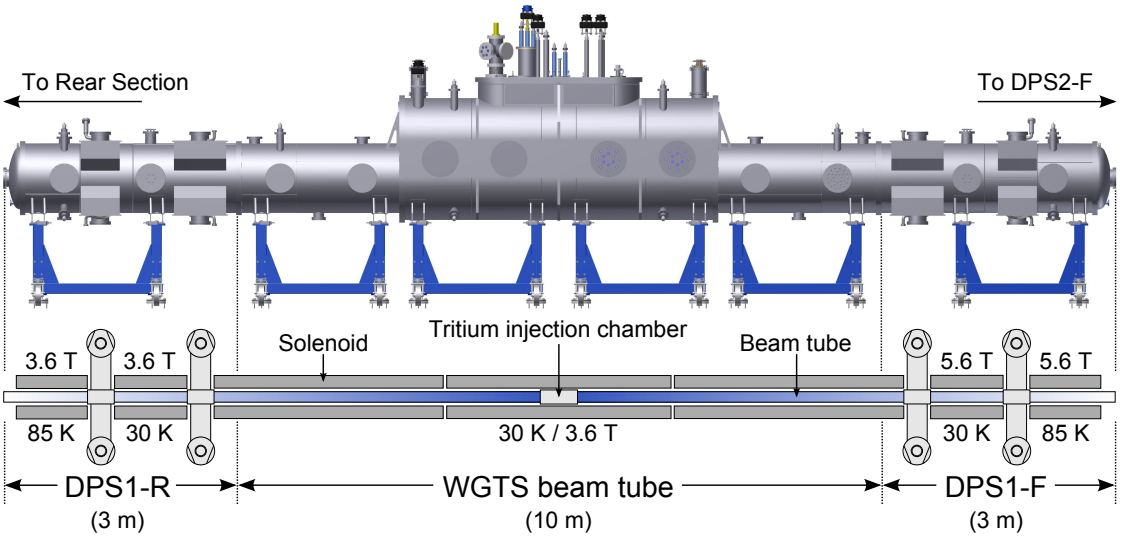


**Figure 2.5: Illustration of the windowless gaseous tritium source (WGTS)** consisting of the 10-m long central beam tube which is temperature-stabilized to 30 K. In its center, high-purity molecular tritium is injected via a set of capillaries. Two 3-m long differential pumping systems (DPS1-R and DPS1-F) pump-out the injected tritium molecules together with all other gas species at both ends of the beam tube. The $\beta$-decay electrons are guided via superconducting solenoids to the transport section on the right or to the Rear Section on the left. Figure inspired by [Kos12].

- measure the source column density in regular intervals via the inelastic scattering of electrons in the source by the use of an angular-resolved electron gun [Bab14].

This electron gun will also be used during the start-up campaign of the KATRIN neutrino-mass measurement to measure the energy-loss function and the inelastic scattering cross sections of 18.6-keV electrons with tritium molecules in the WGTS [Gro15].

The final assembly of the Rear Section currently takes place in the TLK and is expected to be finished in 2016 [MP15]. More details about this system can be found in [Bab14].

### 2.2.2 Transport Section

The KATRIN transport section connects the high-luminosity tritium source, where gaseous $T_2$ molecules are injected at a rate of $1.853\,\mathrm{mbar}\cdot\ell/\mathrm{s}$ [Ang05], with the ultra-high vacuum (UHV) spectrometer section. The maximal tritium inflow into the spectrometer must be smaller than $\approx 10^{-14}\,\mathrm{mbar}\cdot\ell/\mathrm{s}$ in order to keep the background below the KATRIN design limits [Mer12a]. Thus, the tritium flow from the source needs to be reduced by 14 orders of magnitude within the transport section, while an undisturbed magnetic-adiabatic guidance of signal electrons to the spectrometer section must be guaranteed at the same time. For this purpose, two different pumping systems, schematically shown in Figure 2.6, are used, namely the differential pumping section DPS2-F, and the cryogenic pumping section CPS.

#### The Differential Pumping Section (DPS2-F)

While the DPS1-F, located at the downstream end of the WGTS cryostat will already reduce the tritium flow into the transport section by two orders of magnitude, the main differential pumping is performed by the DPS2-F unit, which is schematically shown on the left-hand side of Figure 2.6. A total of four large TMPs installed along two 20°-chicanes in the beamline, plus additional TMPs at the entry of the DPS2-F reduce the tritium flow by up to five orders of magnitude. The chicanes will suppress the molecular beaming effect

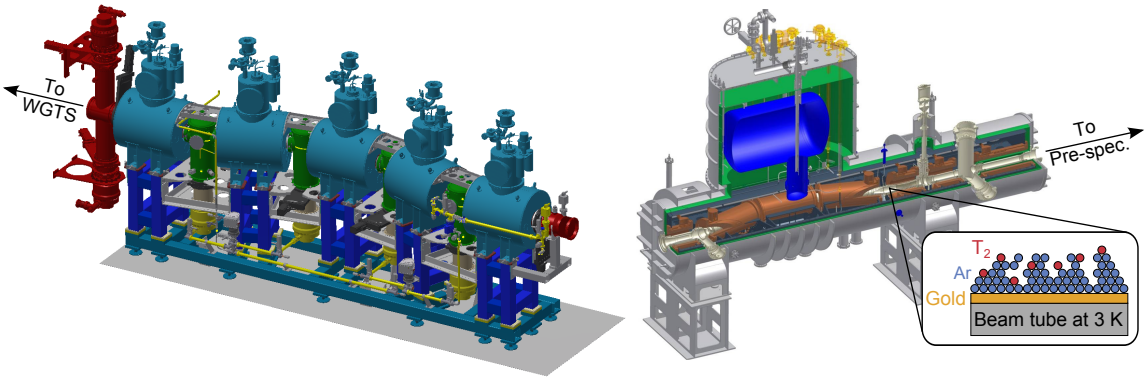


**Figure 2.6: Illustration of the KATRIN transport section. Left: The differential pumping section DPS2-F** consists of five superconducting solenoids (dark cyan) which guide the signal electrons magnetic-adiabatically through two chicanes in the beam tube (red). In the corners of the chicanes, four turbo-molecular pumps (yellow) reduce the tritium gas flow from the source by four to five orders of magnitude. Figure adapted from [Jan15]. **Right: The cryogenic pumping section CPS** uses seven superconducting coils to guide the $\beta$-electrons through another two chicanes in its 3-K cold, gold-plated beam tube that is covered by an argon frost. Tritium molecules which passed the DPS2-F adsorb on the large effective cold surface and the tritium flux is reduced by another seven orders of magnitude. Figure adapted from [Wan13a].

such that tritium pumping speeds of 2 400 $\ell$/s per TMP are achieved [Luo06, Jan15]. Along the 7-m long beamline of the DPS2-F, five superconducting solenoids generate a magnetic guiding field of 5.6 T to transport the signal electrons adiabatically through the beamline chicanes. Positive ions from the large number of $\beta$-decays in the WGTS are not influenced by the differential pumping and are guided by the magnetic field towards the spectrometer section. As these ions would cause large backgrounds when entering the spectrometers, three different subsystems are installed to the beamline of the DPS2-F in order to identify the ion species and to extract them from the active flux volume:

- A so-called FT-ICR diagnostic unit is used to identify the ion species via a Fourier-transformation of their cyclotron resonance signal inside a Penning trap during specific measurements [Ubi09, Ubi11].
- A ring-shaped blocking electrode at the end of the DPS2-F prevents positive ions from entering the spectrometer section via a blocking potential of +100 V.
- Three dipole electrodes that are installed inside the DPS2-F deflect the ions via an $\vec{E} \times \vec{B}$ drift onto the walls of the beam tubes, thereby preventing the build-up of a positive space charge along the beamline [Rei09, Win11, Hac15].

The DPS2-F unit is currently being assembled at TLK and is expected to be fully operational by the end of 2015. Additional information concerning the DPS2-F can be found in [Luk12, Jan15, Hac15].

### The Cryogenic Pumping Section (CPS)

The cryogenic pumping section CPS is located downstream of the DPS2-F and uses the principle of cryosorption to reduce the remaining tritium flow by another seven orders of magnitude. For this purpose a part of the beam tube elements of the CPS is cooled to cryogenic temperatures of 3 K and covered by a thin argon frost layer. In this way, the trapping efficiency for $T_2$-molecules is increased by the very large effective cold surface (see right side of Figure 2.6). Two 15°-chicanes in the beamline ensure that the propagating tritiated molecules undergo a collision with the cold surface. A proof-of-principle for this kind of cryogenic pump was given by the TRAP experiment, which achieved a tritium

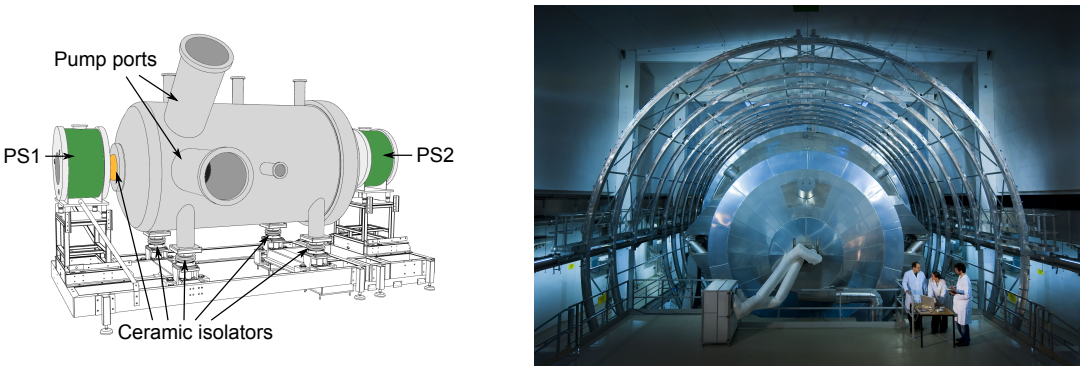


**Figure 2.7: The KATRIN spectrometer section. Left: Illustration of the pre-spectrometer** with the two superconducting solenoids PS1 on the upstream (left) side, and PS2 on the downstream (right) side. The spectrometer is electrically isolated from its support structure by ceramic insulators and can be operated at $-18.3\,\mathrm{kV}$ in order to filter-out low-energy $\beta$-electrons. Two major pump ports house vacuum gauges as well as cascaded turbo pumps and a NEG pump in order to achieve UHV conditions of $10^{-11}\,\mathrm{mbar}$ in its volume of $8.5\,\mathrm{m}^3$. Figure adapted from [Fra10]. **Right: Photography of the main spectrometer** prior to the installation of the pre-spectrometer, looking from the source side. The 23.3-m long vessel with a diameter of 10 m is surrounded by a system of air coils to fine-shape the magnetic field inside the spectrometer. Like the pre-spectrometer it is operated at UHV conditions. Photo: KIT, 2009.

flow-rate reduction factor of $3 \times 10^7$ [Eic08]. After 3 months of continuous operation, it is expected that a tritium activity of 37 GBq has been accumulated on the argon frost layer so that a regeneration of the CPS beam tube surface is required. For this purpose, the beam tube is warmed-up to 100 K and is flushed with warm gaseous helium. Afterwards the system is cooled-down again and a new argon frost layer is prepared [Gil10, Jan15].

Seven superconducting solenoids along the CPS beamline transport the 191-Tcm$^2$ flux tube to the pre-spectrometer, while a forward beam monitoring detector measures the activity in the WGTS by counting $\beta$-electrons in the outer flux tube regions in real time [Bes10, Bab11]. Furthermore, the CPS will house a condensed krypton source that can be moved in and out of the flux tube to be used for regular calibration procedures of the main spectrometer [Bot12, Bau13a]. After the recent delivery of the CPS cryostat on site to TLK in July 2015 the unit is currently being commissioned and implemented into the KATRIN beamline. It is expected to be fully operational in mid-2016.

### 2.2.3 Spectrometer System

The high-resolution $\beta$-spectroscopy of electrons close to the endpoint $E_0$ is achieved via a tandem setup of two electrostatic retardation spectrometers, both based on the MAC-E filter principle (Sec. 2.1.1). Due to the efficient reduction of the tritium flow from the source by 14 orders of magnitude in the previously described transport section, the partial pressure of tritiated molecules in both spectrometers is sufficiently low so that $\beta$-decays of those gas species do not generate a significant background level. At the same time, both spectrometers are operated at UHV conditions of about $10^{-11}\,\mathrm{mbar}$ to keep the scattering probabilities of signal $\beta$-electrons with residual gas small. Only by combining both methods (stringent UHV and tritium pumping) the high-luminosity WGTS can be coupled to the spectrometers.

#### The Pre-Spectrometer

The pre-spectrometer is the first component in the KATRIN beamline which is basically free of tritium and is, thus, located outside of the radiation-monitored TLK area. The

left side of Figure 2.7 shows the two superconducting solenoids PS1 and PS2 placed on both sides of the 3.4-m long spectrometer vessel. In the standard tritium scanning mode of KATRIN both solenoids are operated at nominal magnetic field of 4.5 T. This results in an energy resolution of this MAC-E filter of $\Delta E \approx 70\,\mathrm{eV}$ at 18.6 keV.

The pre-spectrometer can be operated at $-18.3\,\mathrm{kV}$ in order to act as a pre-filter for low-energy electrons that do not contribute to the relevant endpoint region of the $\beta$-spectrum. This would reduce the flux of signal electrons into the main spectrometer by about 7 orders of magnitude, so that contributions by the scattering of $\beta$-electrons off residual gas can be neglected in background considerations. However, an operation of the pre-spectrometer at high potential will result in a strong Penning trap between pre- and main spectrometer so that sophisticated countermeasures will be required to assure no background contributions from this trap [PRG12].

From 2006 to 2011, the pre-spectrometer was intensively used as a stand-alone test facility to investigate the electron transport and the background characteristics in a MAC-E filter [Hab09, Fra10, Mer12a, Wan13a, Goe14]. The experience gained there has significantly influenced the design process of the main spectrometer.

**The Main Spectrometer**

With its length of 23 m and diameter of 10 m resulting in a total volume of $1\,240\,\mathrm{m}^3$, the KATRIN main spectrometer represents the final step in the size of MAC-E filter type spectrometers. Two superconducting solenoids, the PS2 magnet, that is shared with the pre-spectrometer on its entrance side, and the 6-T pinch magnet of the detector system on its exit side provide the guiding magnetic field. With a minimum field of 3.0 G in its analyzing plane, this MAC-E filter achieves (according to Equation 2.6) an energy resolution of $\Delta E = 0.93\,\mathrm{eV}$ at 18.6 keV, thus, allowing for high-precision tritium $\beta$-spectroscopy [Ang05]. Due to the large dimensions of the spectrometer, a dedicated low field coil system (LFCS), consisting of 15 normal-conductive coils that surround the vessel (see right-hand side of Figure 2.7), is needed to fine-shape the magnetic flux tube in the center of the spectrometer. Another 16 vertical and 10 horizontal cosine coils of the earth magnetic field compensation system (EMCS) are used to compensate the non-axially symmetric earth magnetic field [Glu13]. In the standard measurement mode, the whole spectrometer vessel is kept at high negative potential. At the inside, the electric potential is fine-shaped by a nearly massless two-layer wire electrode system. In addition, this electrode system provides electrostatic shielding of low-energy background electrons that originate from the inner surfaces of the spectrometer in addition to the dominant magnetic shielding [Val06, Hug08, Val09, Zac09, Val10]. During neutrino-mass measurements, the retarding potential $qU_0$ of the main spectrometer is varied in a rather narrow range of $E_0 - 30\,\mathrm{eV} \leq qU_0 \leq E_0 + 5\,\mathrm{eV}$ to scan the endpoint region of the tritium $\beta$-spectrum [Kle14].

In 2013, the main spectrometer was operated for the first time together with the detector system in a 3-month commissioning measurement phase (SDS-I) [Bar14, Sch14c, Lei14, Gro15]. The experience gained during these measurements was used to improve the design of various of its sub-components [Ban14, Mue15b]. An essential part of this thesis is based on the subsequent second campaign of commissioning measurements (SDS-II) that took place in 2014 and 2015. The hardware improvements implemented before the SDS-II campaign were used to further characterize the background processes in this complex apparatus. An in-depth description of the experimental setup and the performance of the KATRIN spectrometer and detector section (SDS), consisting of the main spectrometer and the focal-plane detector (FPD) system during SDS-II, is given in Chapter 3 of this thesis.

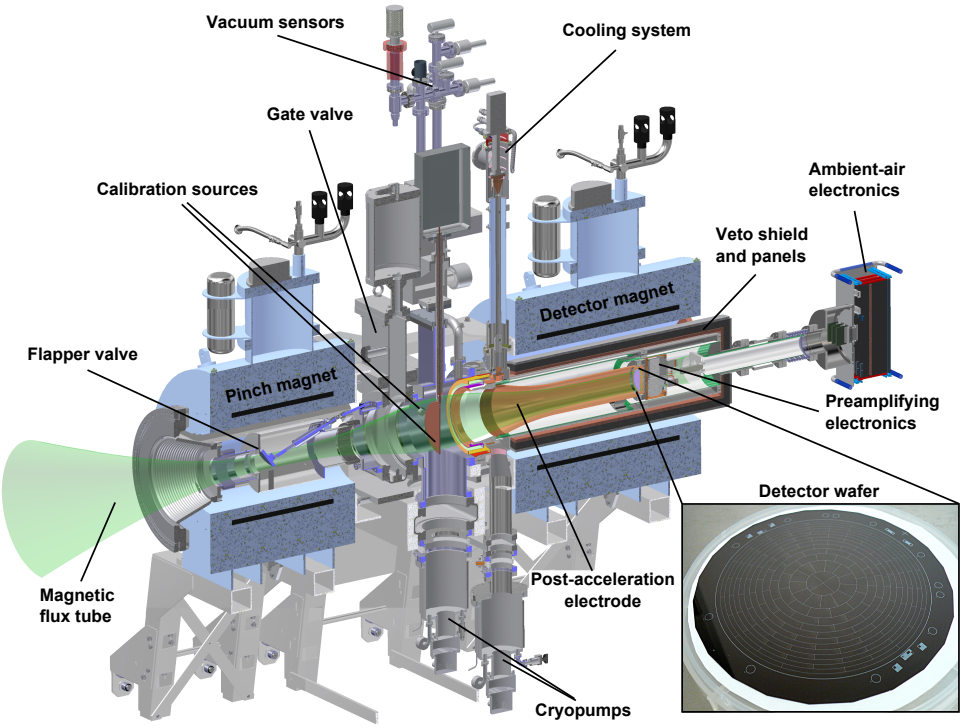


**Figure 2.8: Overview of the KATRIN focal-plane detector system.** The signal electrons that pass the main spectrometer retarding potential are guided by the pinch magnet (6 T) and the detector magnet (3.6 T) onto the segmented silicon PIN-diode detector wafer. A post-acceleration electrode allows to boost the kinetic energies of signal electrons to an energy region where a large signal-to-background ratio is expected. More details on this setup can be found in Chapter 3. Figure adapted from [Ams15].

### The Monitor Spectrometer

In parallel to the main KATRIN beamline a second, smaller beamline that includes the former Mainz spectrometer has been set up between 2010 and 2012 on-site [Gou10, Sch11, Erh12]. This so called monitor spectrometer has a length of 4 m, a diameter of 1 m and achieves, based on its 6-T superconducting solenoids on each side, the same energy resolution as the main spectrometer. Unlike for the operation of the pre- and the main spectrometer, the vessel of the monitor spectrometer is kept at ground potential while the retardation potential is applied to a system of solid electrodes on the inside. In KATRIN neutrino-mass measurements, the monitor spectrometer is set to the same retarding potential as the main spectrometer. A solid-state $^{83m}$Kr source, elevated to about $-800$ V and located at the entrance side provides a mono-energetic electron source via K-32 conversion electrons with an energy of 17.8 keV. A silicon PIN-diode detector on the exit side counts electrons which passed the retarding potential. In this way, subtle drifts of the main spectrometer retardation voltage on the ppm-level can be detected via on-line monitoring of the position and width of the K-32 conversion line [Sle11, Zbo11, Sle13]. Further information concerning this spectrometer can be found in [Erh14].

## 2.2.4 Focal-Plane Detector System

In the main KATRIN beamline, the signal electrons that have passed the retardation potential of the main spectrometer are guided by two superconducting solenoids, the pinch magnet at 6 T and the detector magnet at 3.6 T, through the FPD system (shown in Figure 2.8). There, electrons are counted by a silicon PIN-diode array with high efficiency and nearly free of background. The 90-mm diameter sensitive area of the 500-µm thick detector

wafer is segmented into 148 pixels of equal area to allow to spatially resolve the observed 210 Tcm$^2$ flux tube. A post-acceleration electrode (PAE) located upstream of the detector wafer allows to boost the energy of $\beta$-electrons to an energy regime where low intrinsic detector backgrounds are expected. In addition, low-activity lead and copper shields as well as veto scintillation panels are used as passive and active background countermeasures. A custom-made flapper valve and a full-metal gate valve at the entrance side allow to separate the detector system from the main spectrometer. Several built-in calibration sources such as an $^{241}$Am $\gamma$-source can be used for a regular calibration of the detector [Ams15].

The FPD-system was developed by the University of Washington in Seattle and shipped to KIT in 2011. It has been commissioned at the KATRIN experimental hall from 2011 to 2013 [Har12] before it was operated for the first time together with the main spectrometer during the SDS-I measurement phase in 2013 [Bar14, Sch14c]. Being an essential part of the SDS beamline, its subsystems as well as their performance during the SDS-II measurement phase are described in detail in Chapter 3 of this thesis.

## 2.3 Neutrino-Mass Measurements with KATRIN

This section focuses on the essential design parameters that the experiment needs to fulfill, in order to achieve its design sensitivity of $m_{\bar{\nu}_e} \leq 200\,\text{meV}$ (90% C.L.). Furthermore, the underlying principles of the neutrino-mass analysis used in KATRIN is explained briefly.

### 2.3.1 The KATRIN Design Parameters

As the next generation tritium $\beta$-decay experiment KATRIN is targeted to improve the neutrino-mass sensitivity of the former experiments in Troitsk [Ase11] and Mainz [Kra05] by a factor of 10 to the sub-eV scale (this is equivalent to an improvement by two orders of magnitude for the observable $m^2_{\bar{\nu}_e}$). To achieve this ambitious goal, a large signal-to-background ratio, a sufficiently good energy resolution, as well as small systematic uncertainties are required.

- **Luminosity of the source:** The luminosity of the gaseous tritium source is directly related to the signal strength close to the endpoint $E_0$. It depends on the tritium column density $\rho d$ and the tritium purity $\epsilon_T$ in the source as well as on the accepted forward solid angle $\Omega = \frac{2\pi}{1-\cos\theta_{max}}$ of the MAC-E filter. As an increase of the column density also results in an increase of the inelastic scattering probability of signal electrons off tritium molecules in the source, as well as in an increase of systematic uncertainties, an optimum column density of $\rho d = 5 \times 10^{17}\,\text{molecules}/\text{cm}^2$ has been chosen for KATRIN. This corresponds to an increase by a factor 2 (3) compared to the Mainz (Troitsk) experiments. Based on the technological expertise of TLK a long-term tritium purity of $\epsilon_T > 95\%$ can be expected which is significantly better than in the former tritium $\beta$-decay experiments. The choice of a source magnetic field $B_S = 3.6\,\text{T}$ and of a maximum magnetic field $B_{max} = 6.0\,\text{T}$ limits the maximally accepted polar angle to $\theta_{max} = 51°$. Nevertheless, the effective source area has still been increased by a factor of 40 (20) to $A_S^{eff} = A_S \cdot B_S/B_{max} = 31.8\,\text{cm}^2$ compared to the former experiments in Mainz (Troitsk).
- **Energy resolution of the spectrometer:** The source cross section $A_S$ and the source magnetic field $B_S$ define the KATRIN sensitive flux tube to $\Phi = 191\,\text{Tcm}^2$. This flux tube must be kept free of collisions with beam tube elements while being transported through the entire experiment. In KATRIN, an improvement of the energy resolution by a factor of 5 (4) compared to the former experiments in Mainz (Troitsk) to a value of $\Delta E = 0.93\,\text{eV}$ at 18.6 keV, requires a minimum magnetic field

of $B_{\mathrm{min}} = 3.0\,\mathrm{G}$ in the analyzing plane. This design criterion results in an increased effective diameter of the flux tube by a factor 10 (8) in the center of the spectrometer of 9 m. This corresponds to an analyzing plane of $63.6\,\mathrm{m}^2$ area. However, due to the sophisticated inner-electrode system installed in the main spectrometer, as well as the requirement of safety margins of the flux tube relative to internal structures, the spectrometer has a total inner diameter of almost 10 m, which is at the limit of the technical feasibility.

- **Overall background rate:** In order to reach sufficiently large signal-to-background ratios, the KATRIN experiment is designed to achieve a 100 times larger signal in the endpoint region than the former experiments in Mainz and Troitsk. At the same time, it aims for a total background rate of $R_{\mathrm{bg}} \leq 0.01\,\mathrm{cps}$, similar to the previous experiments. Here, a 10% contribution to the overall background rate is conceded for additional systems like the detector system, while the main background contribution is expected from the large-volume spectrometer. This is a most challenging design goal for the spectrometer, and corresponds to an effective background reduction by a factor $\approx 50$ ($\approx 400$) if the increase of the surface area (volume) compared to the Mainz spectrometer is taken into account [Ang05].
- **Systematic uncertainties:** According to [Ang05], unaccounted-for systematic effects at KATRIN have to be limited to an overall systematic uncertainty budget of $\sigma_{\mathrm{syst,tot}} \leq 0.017\,\mathrm{eV}^2$. This again corresponds to a factor of 100 reduction compared to the previous experiments in Mainz and Troitsk.

Based on these design parameters of the experiment, the analysis principle of KATRIN is outlined in the next section. It is then used to obtain the expected statistical uncertainty and overall neutrino-mass sensitivity of the experiment.

### 2.3.2 The Sensitivity on the Neutrino Mass

As already outlined in Section 2.1.1, a MAC-E filter measures the integral tritium $\beta$-decay spectrum, where the total count rate of the detector depends on the applied retarding potential $U_0$, the constant background rate $R_{\mathrm{bg}}$, the tritium endpoint $E_0$, and the experimental observable, the squared neutrino mass $m^2_{\bar{\nu}_e}$. If the background rate is assumed to be Poisson-distributed, the expected count rate of the detector at a given retarding potential $U_i$ can be derived from Equation 2.7

$$R_{\mathrm{exp}}(U_i, C, R_{\mathrm{bg}}, E_0, m^2_{\bar{\nu}_e}) = R_{\mathrm{sign}}(U_i, C, E_0, m^2_{\bar{\nu}_e}) + R_{\mathrm{bg}} \quad . \tag{2.9}$$

Here, the signal count rate $R_{\mathrm{sign}}$ is given by

$$R_{\mathrm{sign}}(U_i, C, E_0, m^2_{\bar{\nu}_e}) = C \cdot N_T \cdot \epsilon_{\mathrm{det}} \cdot \frac{\Omega}{4\pi} \int_{qU_i}^{E_0} \frac{\mathrm{d}^2 N}{\mathrm{d}E\mathrm{d}t}(E_0, m^2_{\bar{\nu}_e}) \cdot R(E, qU_i)\ \mathrm{d}E \quad , \tag{2.10}$$

where $N_T = A_S \cdot \rho d \cdot 2 \cdot \epsilon_T$ corresponds to the number of tritium nuclei in the source, $\epsilon_{\mathrm{det}}$ gives the detector efficiency, $R(E, qU_i)$ is the response function of the MAC-E filter, and $C$ is a proportionality constant. The top part of Figure 2.9 shows the expected count rate $R_{\mathrm{exp}}$ as a function of the retarding energy $qU_i - E_0$ for a vanishing neutrino mass (black curve) and for a 2-eV neutrino mass (blue curve). The background here is assumed to be the nominal value $R_{\mathrm{bg}} = 0.01\,\mathrm{cps}$. In addition to the two integrated spectra, toy measurement points for a neutrino mass of 1 eV and an effective measurement time of 3 years have been calculated via a Monte-Carlo (MC) simulation and are shown as red dots. The influence of changes of the parameters $C$, $E_0$, $R_{\mathrm{bg}}$, and $m^2_{\bar{\nu}_e}$ on the spectral shape is indicated by arrows. The background rate $R_{\mathrm{bg}}$ acts as a constant offset to the

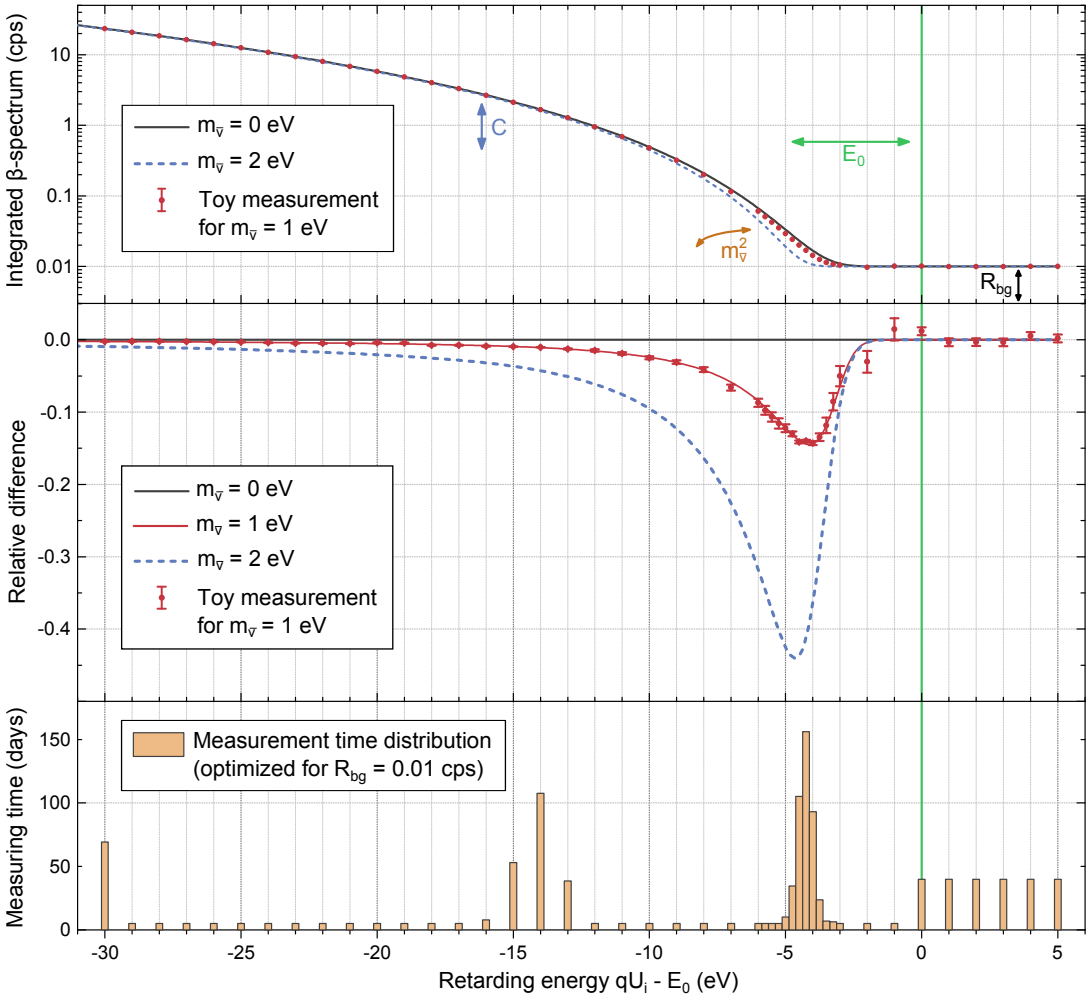


**Figure 2.9: The integral tritium $\beta$-spectrum and the measurement-time distribution. Top:** The shape of the expected integral tritium $\beta$-spectrum $R_{\mathrm{exp}}(U_{\mathrm{i}}, C, R_{\mathrm{bg}}, E_0, m^2_{\bar{\nu}_{\mathrm{e}}})$ for a vanishing neutrino mass (black solid line) and a neutrino mass of 2-eV (blue dashed line) are shown. Additionally, Monte-Carlo (MC) toy measurement points for a neutrino mass of $m_{\bar{\nu}_{\mathrm{e}}} = 1\,\mathrm{eV}$ and a net KATRIN run time of 3 years are shown in red. The parameters $C$, $R_{\mathrm{bg}}$, $E_0$, and $m^2_{\bar{\nu}_{\mathrm{e}}}$ of the theoretical model are varied to fit the measurement data best. **Middle:** The direct comparison of the theoretical spectrum for a 1-eV / 2-eV neutrino mass and of the toy measurement points to the theoretical spectrum for a vanishing neutrino mass reveals the retarding potentials at which the spectral shape is most sensitive to the neutrino mass. The statistical fluctuations of the toy measurement points depend on the measurement time spent at a specific retarding potential $U_{\mathrm{i}}$. **Bottom:** Measurement time distribution optimized for the best possible exclusion of a zero neutrino mass with a KATRIN design background of $R_{\mathrm{bg}} = 0.01\,\mathrm{cps}$ and an effective measurement time of 3 calendar years. More details are given in the text. Figure kindly provided by M. Kleesiek.

$\beta$-spectrum, the exact value of the endpoint position $E_0$ shifts the spectrum to the left and the right, while the constant parameter $C$ varies the amplitude of the spectrum. The effect of a non-vanishing neutrino rest mass can be seen as a distinct change of the spectral shape in a narrow range of a few eV below the endpoint.

In the final KATRIN neutrino-mass analysis, the measured count rate $R_{\mathrm{meas}}(U_{\mathrm{i}})$ for each retarding potential $U_{\mathrm{i}}$ is compared to the expected spectrum $R_{\mathrm{exp}}(U_{\mathrm{i}}, C, R_{\mathrm{bg}}, E_0, m^2_{\bar{\nu}_{\mathrm{e}}})$, where the free parameters $C$, $R_{\mathrm{bg}}$, $E_0$ and $m^2_{\bar{\nu}_{\mathrm{e}}}$ are varied such that

$$\chi^2(C, R_{\mathrm{bg}}, E_0, m^2_{\bar{\nu}_{\mathrm{e}}}) = \sum_i \left( \frac{R_{\mathrm{meas}}(U_{\mathrm{i}}) - R_{\mathrm{exp}}(U_{\mathrm{i}}, C, R_{\mathrm{bg}}, E_0, m^2_{\bar{\nu}_{\mathrm{e}}})}{\frac{1}{t(U_{\mathrm{i}})} \cdot \sigma_{\mathrm{exp}}(U_{\mathrm{i}}, C, R_{\mathrm{bg}}, E_0, m^2_{\bar{\nu}_{\mathrm{e}}})} \right)^2 \tag{2.11}$$

is minimized. Here, $\sigma_{\mathrm{exp}}(U_{\mathrm{i}}) = \sqrt{t(U_{\mathrm{i}}) \cdot R_{\mathrm{exp}}(U_{\mathrm{i}}, C, R_{\mathrm{bg}}, E_0, m^2_{\bar{\nu}})}$ corresponds to the expected statistical uncertainties at each retarding potential. These strongly depend on the chosen measurement time distribution, i.e. the measurement time $t(U_{\mathrm{i}})$ spent at a particular retarding potential $U_{\mathrm{i}}$. A measurement time distribution which is optimized for an exclusion of the zero neutrino-mass hypothesis is shown in the lower part of Figure 2.9. Here, four structures are of interest:

1. A rather long measuring time is spent at the low-energy end of the $\beta$-spectrum, as this part gives the best sensitivity on the parameter $C$.
2. The spectrum above the endpoint is used to fix the background rate $R_{\mathrm{bg}}$. A splitting of the measurement time on six different retarding voltages allows to investigate any energy dependence of the background.
3. About 4 eV below the endpoint, the spectral shape is most sensitive on the neutrino mass so that most of the measurement time is spent here. In order to derive the shape of the spectrum in this region with high precision, smaller bin widths are chosen here.
4. The second longest measurement period is located at retarding energies about 14 eV below the endpoint. The data gathered there allows to break the correlation between the relative amplitude parameter $C$ and the endpoint energy $E_0$.

The middle part of Figure 2.9 shows the difference of a toy measurement and a 2-eV neutrino-mass theoretical spectrum relative to the standard model ($m_{\bar{\nu}_{\mathrm{e}}} = 0\,\mathrm{eV}$) case. In addition, the theoretically expected spectrum for a 1-eV neutrino mass is shown with respect to the zero-hypothesis (red line). The influence of the measurement time distribution on the statistical fluctuation of the toy measurement points can be seen nicely. By applying Equation 2.11 to such MC-toy measurement points, the statistical sensitivity of KATRIN for the squared neutrino mass in an effective measurement time of $t_{\mathrm{eff}} = 3\,\mathrm{years}$ can be derived to

$$\sigma_{\mathrm{stat}} = 0.018\,\mathrm{eV}^2 \quad . \tag{2.12}$$

Here, $t_{\mathrm{eff}}$ is chosen such that the statistical uncertainty is in the same range as the expected systematic uncertainties of the experiment. Due to maintenance and calibration phases the total run time of KATRIN will amount to 5 calendar years. When adding the systematic and statistical uncertainties quadratically one obtains a total error budget of

$$\sigma_{\mathrm{tot}} = 0.025\,\mathrm{eV}^2 \quad . \tag{2.13}$$

In the case of a vanishing neutrino-mass signal this corresponds to a sensitivity of the KATRIN experiment of

$$m_{\bar{\nu}_{\mathrm{e}}} \leq \sqrt{1.64 \cdot \sigma_{\mathrm{tot}}(m^2_{\bar{\nu}_{\mathrm{e}}})} = 200\,\mathrm{meV}\ (90\%\ \mathrm{C.L.}) \quad , \tag{2.14}$$

which is one order of magnitude better than the corresponding values reached by the former experiments in Mainz and Troitsk [Gro15, Kle14].

CHAPTER 3

# The Spectrometer and Detector Section

After the first commissioning measurement phase SDS-I in 2013, several hardware sub-systems of the KATRIN spectrometer and detector section (SDS) were revised and upgraded in order to allow for a more detailed and optimized characterization of the electron transport and background generating mechanisms in the SDS-apparatus. Based on these improvements, a second extended commissioning measurement phase was carried out in the time period from October 2014 to September 2015. This campaign was split into a first phase (SDS-IIA) lasting until March 2015, and a second part (SDS-IIB) from June 2015 on, after a complete vacuum bake-out of the main spectrometer. As most of the measurements that are of relevance for this thesis were carried out during the SDS-IIA phase, the discussion of the performance parameters of the SDS sub-systems in this chapter mainly focuses on the first part of the measurement campaign. However, selected aspects of the system performance during SDS-IIB with specific relevance for the analyses in this thesis are discussed as well.

Figure 3.1 gives an overview of the SDS-IIA experimental setup including the magnet system (Sec. 3.1), the main-spectrometer and detector vacuum system (Sec. 3.2), the high-voltage system with the inner wire electrode and the post-acceleration electrode (Sec. 3.3), the read-out and data-acquisition chains of the FPD (Sec. 3.4), the active muon-detection system (Sec. 3.5), and the slow-control and data-management systems (Sec. 3.6). The calibration sources of the FPD and the stability of the detector calibration over the course of SDS-IIA are presented in Section 3.7, while the intrinsic detector background is discussed in Section 3.8. At last, the alignment of the detector wafer and magnets to the beamline is investigated in detail in Section 3.9. An angular-selective electron gun that was installed at the upstream side of the spectrometer during SDS-IIA and used to characterize the transmission properties of the MAC-E filter has, similar to the monitor spectrometer, no direct relevance for this thesis and is, thus, not discussed further at this point. More details on the electron gun and its performance during SDS-II can be found in [Erh15, Kra15a, Beh15].

## 3.1 The Magnet System

In the spectrometer and detector section, a total of four superconducting solenoids and an array of normally conductive air coils are used to transport electrons through the spectrometer towards the detector system and to fine shape the magnetic fields inside the MAC-E filter. Magnetic field sensor systems installed at various parts of the SDS apparatus allow to monitor the magnetic fields in near real-time and at high accuracy.

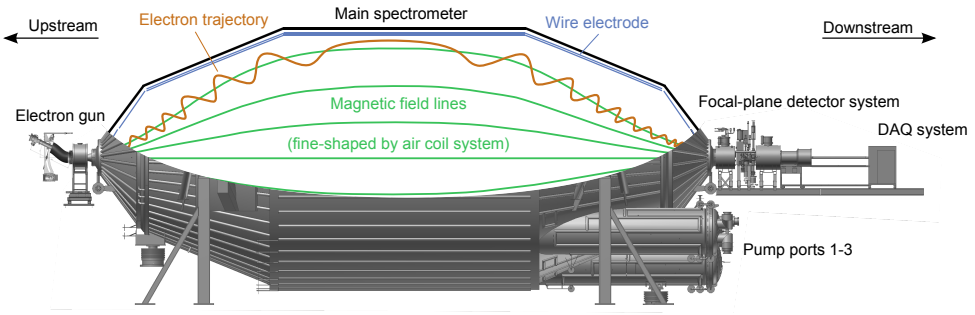


**Figure 3.1: Overview of the SDS-IIA experimental setup** including the electron gun on the upstream side of the spectrometer and the focal-plane detector system on the downstream side. The system of air coils which axially and azimuthally surrounds the spectrometer and the PS1 magnet on the upstream side are not shown.

### The Pre-Spectrometer Magnets

At the upstream side of the main spectrometer, two stand-alone 400-mm diameter warm-bore, cryogen-free magnet systems manufactured by *Cryogen Ltd.*, the PS1 and PS2 magnets, provide maximal fields of 4.5 T at an operating current of 157 A. The 320-mm long coil of each magnet with an inner radius of 227.5 mm is operated at temperatures of $< 4.2$ K by a two-stage *Sumitomo SRDK-415D* cryo-cooler supplied by a *Sumitomo CSW-71D* compressor unit. A two-layer thermal shield installed in an insulating vacuum chamber with an operating pressure of $\approx 10^{-4}$ mbar reduces incident heat radiation from the atmosphere. Several RhFe and Cernox temperature sensors are used throughout the system to monitor the coil and shield temperatures. Both magnets are continuously operated in driven mode[1] by two *FuG NTS 800.5* power supplies of high stability with current fluctuations of $< 5 \times 10^{-5}$ A at 157 A. Due to a missing communication interface of the power supplies, the currents through the magnet coils are monitored via digital direct current transformers of type *LEM - IT 200-S Ultrastab* [Cry03, Goe14].

During the SDS-II campaign, the coil center of the PS2 magnet was installed at a distance of 12.1 m to the analyzing plane and operated at its nominal field of 4.5 T (157 A). The PS1 magnet was positioned further upstream. During SDS-IIA, its coil center was located 3.4 m upstream from the center of the PS2 magnet and being operated at 3.0 T (104 A) to allow for ideal transport properties of electrons from the angular-selective electron gun mounted between the two magnets. As this electron gun was not used in SDS-IIB, the PS1 magnet was moved close to its final position in the KATRIN beamline with a distance of 16.5 m between its coil center and the main-spectrometer analyzing plane. In addition, it was now operated at its nominal field of 4.5 T (157 A), identical to the PS2 magnet.

### The Magnets of the FPD System

At the downstream side of the main spectrometer, the two warm-bore superconducting solenoids of the FPD system, shown in Figure 3.2, provide the magnetic guiding field for the transmitted electrons. Here, the pinch magnet (PCH) provides the maximum field $B_{\mathrm{max}}$ along the KATRIN beamline. Thus, according to Equation 2.6, it directly defines the energy resolution of the MAC-E filter. The center of its coil is located 12.2 m downstream of the analyzing plane and constrains the magnetic flux tube at the exit side of the main spectrometer. In contrast, the detector magnet (DET), located about 1.6 m further downstream, maps incident electrons onto the detector wafer that is located another $\approx 14$ cm downstream of its coil center inside the warm bore.

[1] In driven mode, the current through a superconducting coil is permanently given by the connected power supply unit.

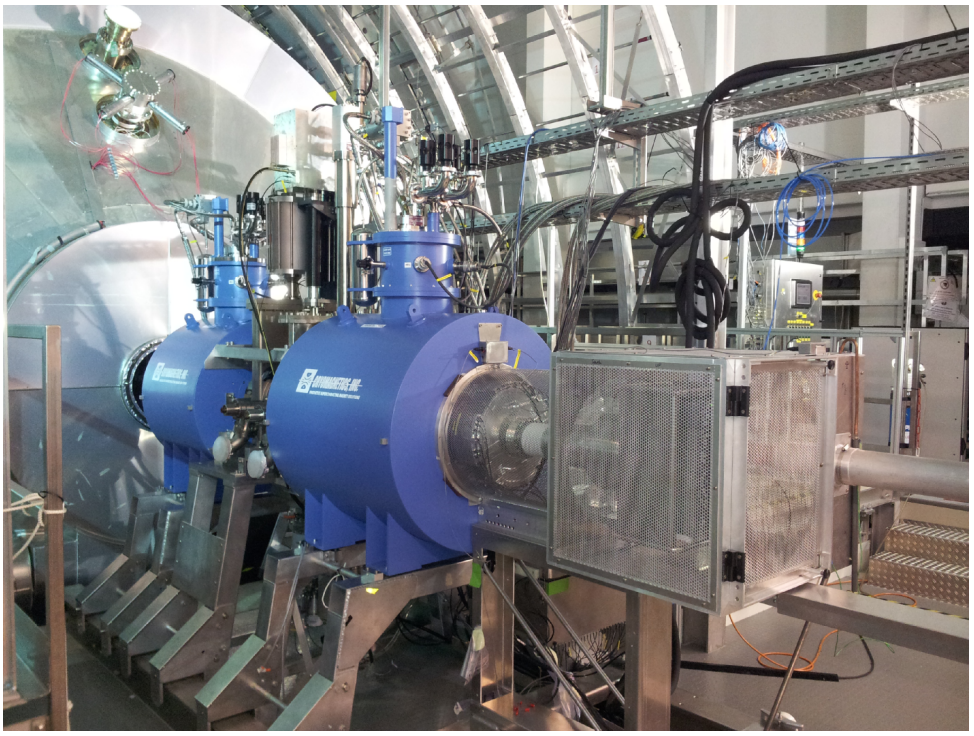

**Figure 3.2: Picture of the pinch and the detector magnet of the FPD system.** The pinch magnet is operated close to the main spectrometer (shown in the back). Picture adapted from [Har12].

Both magnets are manufactured by the US-supplier *Cryomagnetics, Inc.* from Oak Rigde (TN) and provide a maximum field of 6 T at 87.15 A (pinch magnet) and 93.59 A (detector magnet). With the KATRIN nominal fields of $B_{\mathrm{PCH}} = 6\,\mathrm{T}$ and $B_{\mathrm{DET}} = 3.6\,\mathrm{T}$ the magnetic field at the location of the detector wafer is $B_{\mathrm{FPD}} \approx 3.3\,\mathrm{T}$ and defines the observed flux tube of $\Phi = 210\,\mathrm{Tcm}^2$. Due to an attractive force of 54 kN at full field, the cryostats of the two magnets are separated by four aluminum spreader bars. In the outer insulating vacuum chamber (0.1 mbar) of each cryostat multiple layers of thermal shields surround the inner liquid-helium vessel with a filling capacity of 65 $\ell$ (75 $\ell$) in the case of the pinch (detector) magnet. Inside the liquid-helium bath, the superconducting coil of the pinch (detector) magnet with a length of 500 mm (700 mm) and an inner diameter of 454 mm (540 mm) is held at a temperature of $< 4.2\,\mathrm{K}$. The coils are made of twisted multi-filamentary NbTi/Cu wire with a bare NbTi persistent current switch to turn the magnets into persistent mode[2]. The magnetic field stability of the FPD magnets in persistent mode of $^{\Delta B}/_{B} = 3.5 \times 10^{-8}$ is measured to be a factor of 100 better than in driven mode, where the coils are continuously connected to the *Cryomagnetics 4G* power supplies [Fis12]. A nuclear-magnetic resonance probe (NMR probe) temporarily installed in the bore of the pinch magnet which was operated at nominal field in persistent mode revealed an upper limit for drifts of its magnetic field strength of less than 20 ppm over 30 days [Sch14c]. At the top of the magnet cryostats, boiled-off helium is re-condensed by a two-stage *Cryomech PT40* pulse-tube cryo cooler connected to a *Cryomech CP2800* compressor package. The pressure inside the helium vessel is regulated to 1 041 mbar via an electric heater element. Several Pt-100 and $RuO_2$ sensors monitor the temperature of the coils and the thermal shields of the magnets [CB11, Ams15, Sch14c].

[2] After charging a superconducting solenoid via a power supply, the coil can be short-circuited to isolate it from the external source. Due to the absence of noticeable ohmic resistance, the current confined in the coil essentially remains constant over time in this so-called persistent mode.

During the early commissioning phase in 2013, four unexplainable quenches[3] of the pinch magnet occurred in joint operation with the detector magnet at nominal fields [Doe13, Sch14c]. This limited the operation of the two FPD magnets to a non-nominal configuration with $B_{\mathrm{PCH}}^{\mathrm{SDS\text{-}I}} = 5\,\mathrm{T}$ and $B_{\mathrm{DET}}^{\mathrm{SDS\text{-}I}} = 3.5\,\mathrm{T}$ during SDS-I [Bar14]. The resulting change of the ratio $B_{\mathrm{PCH}}/B_{\mathrm{DET}}$ from the nominal value of $5/3$ to $10/7$ caused significant blocking effects of the observed magnetic flux tube by parts of the FPD-system vacuum chamber (Sec. 3.9). In order to prevent these effects, the FPD magnets were operated at $B_{\mathrm{PCH}}^{\mathrm{SDS\text{-}IIA}} = 5\,\mathrm{T}$ and $B_{\mathrm{DET}}^{\mathrm{SDS\text{-}IIA}} = 3\,\mathrm{T}$ during the SDS-IIA phase, restoring the nominal ratio of the two magnetic fields. This resulted in a reduced magnetic field strength at the location of the detector wafer of $B_{\mathrm{FPD}}^{\mathrm{SDS\text{-}IIA}} \approx 2.7\,\mathrm{T}$, which corresponds to an observed magnetic flux of $\Phi = 172\,\mathrm{Tcm}^2$.

During the maintenance break between the first and the second part of SDS-II, the outdated pinch magnet was replaced by a new one [Cry15], likewise manufactured by *Cryomagnetics, Inc.* In difference to the old one, the coil of the new magnet is reduced by 10 mm in length, but is equipped with an additional compensation coil on each side, similar to the design of the magnets of the differential pumping section [Hac15]. The new pinch magnet has allowed for joint operation together with the detector magnet at nominal fields of $B_{\mathrm{PCH}}^{\mathrm{SDS\text{-}IIB}} = 6\,\mathrm{T}$ (86.98 A) and $B_{\mathrm{DET}}^{\mathrm{SDS\text{-}IIB}} = 3.6\,\mathrm{T}$ (56.15 A) during SDS-IIB.

**The Air-Coil System**

In order to fine-shape the magnetic fields inside the main spectrometer two large-scale air-coil systems are used, the LFCS and the EMCS [Wan09, Glu13]. The earth magnetic field in the KATRIN experimental hall is homogeneous with a vertical (horizontal) contribution of $B_{\mathrm{vert}} = 43.6\,\mu\mathrm{T}$ ($B_{\mathrm{hor}} = 5\,\mu\mathrm{T}$) relative to the beamline [Glu13]. In order to compensate these fields, a dedicated system of cosine coils, the EMCS, surrounds the spectrometer. It is based on 16 current loops in horizontal planes that compensate $B_{\mathrm{vert}}$, and 10 loops with vertical planes to balance out $B_{\mathrm{hor}}$. The currents for these compensation coils are generated by two *Delta Elektronika SM3000* power supplies. The currents of the EMCS usually are not varied during the standard SDS operation and are held at their nominal values of 50 A (9 A) for the vertical (horizontal) compensation.

Based on fourteen 12.6-m diameter coils arranged coaxially to the spectrometer tank, the second air coil system, the LFCS, allows to regulate the magnetic field strength in the analyzing plane in a range of $0.33\,\mathrm{mT} \leq B_{\mathrm{min}} \leq 1\,\mathrm{mT}$ by individually adjusting the currents in each coil via *Delta Elektronika SM3000* power supplies. Here, the fields in the analyzing plane are limited by the dimensions of the 210-$\mathrm{Tcm}^2$ flux tube in the spectrometer (lower limit) and by the maximum current of 100 A provided by some of the power supplies (upper limit). In addition, the LFCS is used to compensate the field asymmetry in the main spectrometer which is caused by the imbalance of the stray fields of the PS2 and the pinch magnet on each side. For this purpose, the LFCS coil next to the pinch magnet (LFCS coil 14) is used as a counter coil. While all other coaxially arranged coils as well as the superconducting solenoids are polarized such that the magnetic field lines in the SDS apparatus point upstream, the polarity of LFCS coil 14 is flipped to reduce the strong stray field of the pinch magnet.

The currents through the air coils are monitored via digital direct current transformers of type *LEM - IT 200-S Ultrastab*. Additionally, the 14 LFCS coils as well as the 2 EMCS cosine-coil systems are equipped with custom-made hardware switches based on H-bridge circuits, the so-called flip boxes. These can be controlled by the operator to change the polarity of an individual air coil on a ms time scale without ramping the corresponding power supply [Beh14a]. This allows e.g. for an active background reduction by short magnetic pulses during long-term measurements [Beh14b].

[3] The sudden loss of the superconductive state in a part of a magnet coil is referred to as a quench.

### The Magnetic-Field Sensor System

In order to monitor the magnetic-field strength in the main spectrometer in near real-time, three magnetic-field sensor systems are used:

1. Directly on the outer surface of the main spectrometer vessel a total of 24 magneto-resistive sensors from *Philips* (*KMZ10B* and *KMZ20M*) measure the magnetic field in axial, radial, and tangential direction relative to the beam axis. These sensors are arranged in rings of eight at $z = \pm 3.6\,\mathrm{m}$ and $z = 0.0\,\mathrm{m}$ relative to the analyzing plane of the spectrometer with an angular spacing between the sensors of 45° [Wue07, Ada15].

2. Due to long-term drifts of the *Philips* sensors, 14 additional *Mag-03MSB100* sensors from *Bartington Instruments* were installed at the spectrometer hull prior to SDS-II [Ada15]. Those are arranged in two rings of four at $z = -4.5\,\mathrm{m}$ and $z = +4.3\,\mathrm{m}$ relative to the analyzing plane and a ring of six directly at the analyzing plane. These sensors offer a 50-nT precision and a 0.1°-resolution of the axial, radial, and tangential fields.

3. Two of the 14 LFCS coils are equipped with so-called Mobile Sensor Units (MobSU). As the only non-stationary magnetic-field sensors these units circle the main spectrometer vessel on a radius of 5.87 m along the LFCS coils 6 and 12. Every 10°, a *FLC3-70* (or alternatively a *FL3-500*) flux-gate magnetometer by *Stefan Mayer Instruments* measures the magnetic field in axial, radial, and tangential direction [Osi12, Ada15].

More details on the magnetic-field sensor systems and the magnetic-field monitoring during SDS-II can be found in [Erh15].

### Relevant Magnet-Field Settings during SDS-IIA

During the SDS-IIA measurements several different magnetic-field settings along the spectrometer were used to investigate the electron transmission and background characteristics of the MAC-E filter in detail. Table 3.1 lists all implemented field settings of relevance in the context of this thesis, together with the corresponding current set points for the superconducting solenoids and the air coils. These settings can be divided into two types: those with 'symmetric' magnetic fields, where the flux tube which is observed by the detector passes through the spectrometer, as in the standard KATRIN operation, and those with 'asymmetric' magnetic fields, where (most of) the flux tube maps inner structures of the spectrometer onto the detector. In the latter case, either the pre-spectrometer magnets are turned off (setting A1), or the flip-box devices are used to invert the polarity of some of the LFCS coils (setting A2). An example of the field lines along the spectrometer for setting A1 is given in Figure 3.24. In case of the symmetric magnetic-field settings, the currents of the LFCS are optimized via the KATRIN simulation framework KASSIOPEIA [FG15] to fulfill the transmission condition for electrons that pass through the spectrometer and to adjust the magnetic-field strength in the analyzing plane to a desired value between 0.33 mT and 1 mT [Sta13, Erh15]. Additionally, the air-coil currents can be adjusted to generate a one-minimum or a two-minima solution of the magnetic fields in the spectrometer. In the latter case, the magnetic field along the outer, off-axis field lines features two local minima (at $z < 0\,\mathrm{m}$ and $z > 0\,\mathrm{m}$) and a local maximum in the analyzing plane [Glu13]. Such two-minima solutions are expected to offer a better magnetic shielding due to the parallelism of the field lines to the inner structures of the spectrometer (Sec. 2.1.2) compared to the one-minimum solutions with a single global minimum of the magnetic field in the analyzing plane. The currents of the FPD solenoids and the EMCS were kept at their nominal SDS-IIA values in all measurements used throughout this thesis.

**Table 3.1: Magnetic-field configurations commonly used during SDS-IIA** and in the context of this thesis. In the 3.8-G, the 4.3-G, the 5-G, and the 9-G setting all field lines from the detector pass through the spectrometer and the transmission conditions for signal electrons are fulfilled. In contrast, in the 'asymmetric' field settings A1 and A2 the field lines connect to the inner structures of the spectrometer and map those onto the detector wafer. In the case of A1 this is accomplished by setting the PS1 and PS2 magnet to zero field while in A2 the flip-box systems are used to change the polarity of some of the LFCS coils. The symmetric settings are either optimized for a one-minimum solution (*one*), or for a two-minima solution (*two*) of the magnetic field in the spectrometer. More details are given in the text. The listed current set points are given in A.

| Magnet | 3.8 G *(two)* | 4.3 G *(one)* | 5 G *(two)* | 9 G *(two)* | A1 | A2 |
|---|---|---|---|---|---|---|
| PS1 | 104.0 | 104.0 | 104.0 | 104.0 | 0.0 | 104.0 |
| PS2 | 156.0 | 156.0 | 156.0 | 156.0 | 0.0 | 156.0 |
| LFCS coil 1 | 21.14 | 30.35 | 52.94 | 84.63 | 0.0 | −100.0 |
| LFCS coil 2 | 25.66 | 35.25 | 15.17 | 99.97 | 0.0 | −100.0 |
| LFCS coil 3 | 20.30 | 20.66 | 33.73 | 55.99 | 0.0 | −50.0 |
| LFCS coil 4 | 28.36 | 31.92 | 34.47 | 99.54 | 50.0 | 20.0 |
| LFCS coil 5 | 38.82 | 25.92 | 61.83 | 99.68 | 100.0 | 20.0 |
| LFCS coil 6 | 27.52 | 35.75 | 75.65 | 80.45 | 100.0 | 50.0 |
| LFCS coil 7 | 34.37 | 20.51 | 27.05 | 95.40 | 100.0 | 60.0 |
| LFCS coil 8 | 50.68 | 23.25 | 49.49 | 98.10 | 100.0 | 60.0 |
| LFCS coil 9 | 10.37 | 28.77 | 64.38 | 84.01 | 100.0 | 40.0 |
| LFCS coil 10 | 44.44 | 29.28 | 46.64 | 89.12 | 100.0 | 30.0 |
| LFCS coil 11 | 37.19 | 42.52 | 52.53 | 68.80 | 100.0 | 0.0 |
| LFCS coil 12 | 20.96 | 28.16 | 29.78 | 99.15 | 100.0 | 0.0 |
| LFCS coil 13 | 43.32 | 23.20 | 52.21 | 93.43 | 100.0 | 0.0 |
| LFCS coil 14 | −50.35 | −31.06 | −47.82 | −28.08 | 0.0 | 0.0 |
| vert. EMCS | 50.0 | 50.0 | 50.0 | 50.0 | 50.0 | 50.0 |
| horiz. EMCS | 9.0 | 9.0 | 9.0 | 9.0 | 9.0 | 9.0 |
| Pinch | 72.625 | 72.625 | 72.625 | 72.625 | 72.625 | 72.625 |
| Detector | 46.795 | 46.795 | 46.795 | 46.795 | 46.795 | 46.795 |

For each of the magnetic-field settings the dimension of the observed flux tube inside the spectrometer is changed. Figure 3.3 shows the extension of the flux tube in the spectrometer for four symmetric settings with 3.8 G, 4.3 G, 5 G, and 9 G magnetic-field strength in the analyzing plane, respectively. The flux-tube dimension also defines the volume that is magnetically mapped on the individual detector rings. In the context of studying the various possible mechanisms through which background electrons are generated in the volume of the spectrometer (see Chapters 4 and 6), these changes in the observed volume are of major relevance. Thus, KASSIOPEIA [FG15] was used to calculate the observed volume per detector ring under the assumption of axial symmetry for the different symmetric magnetic-field settings listed above. The results are given in Table 3.2. Note that the one-minumum setting with 4.3 G magnetic field in the analyzing plane corresponds to nearly the same observed volume than the 5-G two-minima setting. Due to the different position and field of the PS1 magnet during SDS-IIB, air-coil currents different than those listed in Table 3.1 were required to achieve comparable magnetic-field strengths in the analyzing plane. These settings are given in Table C.4 in Appendix C, while the corresponding observed volumes are given in Table C.5.

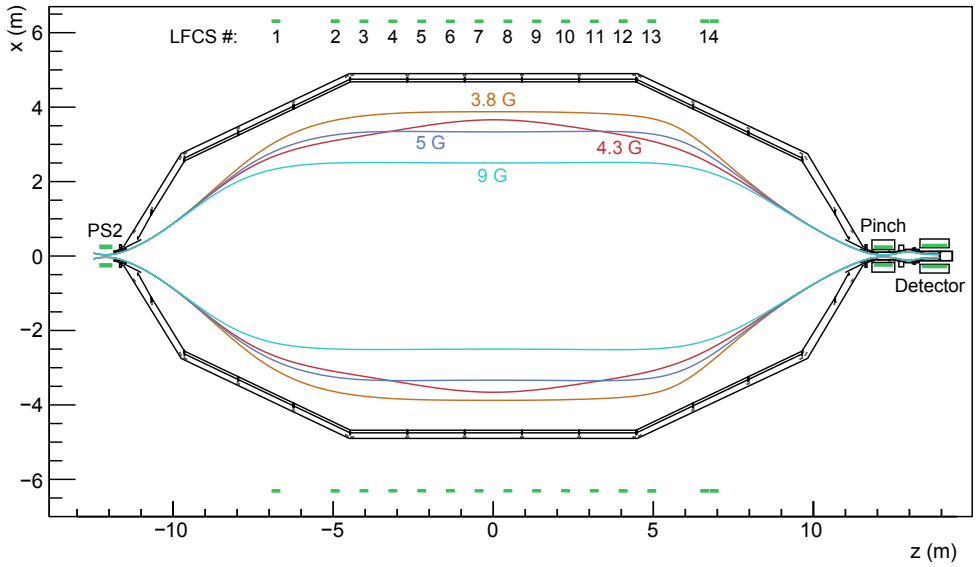


**Figure 3.3: Prominent magnetic flux tube configurations during SDS-IIA.** The dimension of the observed flux tube for the most prominent symmetric magnetic-field configurations listed in Table 3.1 are simulated with KASSIOPEIA. While the 3.8-G (orange), 5-G (blue), and 9-G (cyan) settings feature two local minima in the magnetic field, the 4.3-G (red) setting has only one minimum directly in the analyzing plane. The coils of the PS2, pinch, and detector magnet, as well as the LFCS system are shown in green. The PS1 magnet on the upstream side is not shown. More details are given in the text.

## 3.2 The Vacuum Setup

The KATRIN main spectrometer and detector vacuum system is designed to achieve pressures in the few $10^{-11}$-mbar regime within the 1240-m$^3$ volume [Wol15a] of the 23.2-m long spectrometer vessel manufactured by *MAN DWE GmbH*. With a total inner surface[4] of about 1240 m$^2$, the outgassing of hydrogen from the *316N* stainless steel in the spectrometer represents the major gas load in the system. After electro-polishing, cleaning, and vacuum-baking at up to 300 °C, the hydrogen out-gassing rate was estimated to be $(1.4\text{-}2.5)\times10^{-12}$ mbar $\cdot\,\ell/s$ during SDS-I [Wol15b]. Three 1.7-m diameter pump ports on the detector side of the spectrometer vessel, each with a length of about 3 m, accommodate an array of vacuum pumps, gauges, and liquid-nitrogen ($LN_2$) cooled baffle systems for passive background suppression purposes (Chapter 4). On the upper half of the spectrometer vessel eleven additional 50-cm long DN200 ports, equipped with 6-way crosses on top, house electrical feedthroughs into the UHV, an additional vacuum gauge, a 500-mbar burst disc and a remotely controlled gas-inlet system. On both sides of the spectrometer, DN200 flanges connect the vessel volume to the other beamline elements. In the SDS-IIA configuration these were the angular-selective electron gun on the upstream and the FPD system on the downstream side. The latter is usually connected to the spectrometer via a custom-made in-line flapper valve with a *Kalrez* O-ring sealing. This valve is located inside the warm bore of the pinch magnet and allows, together with a *VAT* DN250 all-metal gate valve of the detector system, to mechanically separate the two units without breaking the vacuum. The detector system consists of two vacuum chambers: the UHV chamber, which houses the detector wafer on its downstream end, and the high-vacuum (HVac) chamber with the first amplification stage of the detector electronics (Sec. 3.4) that is usually operated at a vacuum in the $10^{-6}$-mbar regime.

Prior to SDS-II, a leak in the actuation mechanism of the in-line flapper valve was identified

[4] This includes the inner surface of the spectrometer vessel of about 690 m$^2$ as well as all internal structures like for example the inner electrode system.

**Table 3.2: Observed flux-tube volumes per detector ring for the standard magnetic-field configurations during SDS-IIA.** The volumes were calculated for $|z| \leq 12\,\mathrm{m}$ with the KATRIN simulation framework KASSIOPEIA [FG15]. Note that the innermost detector ring (bullseye) has only 4 segments compared to the other rings with 12 pixels. Thus, the volume that is observed by ring 0 is reduced by a factor of about 3. All volumes listed are given in $\mathrm{m}^3$.

| Detector ring | 3.8 G *(two)* | 4.3 G *(one)* | 5 G *(two)* | 9 G *(two)* |
|---|---|---|---|---|
| 0 | 16.8 | 13.7 | 13.5 | 8.5 |
| 1 | 51.0 | 41.5 | 40.9 | 25.5 |
| 2 | 52.1 | 42.2 | 41.5 | 25.8 |
| 3 | 53.2 | 42.8 | 42.2 | 26.0 |
| 4 | 54.3 | 43.5 | 42.9 | 26.3 |
| 5 | 55.4 | 44.1 | 43.6 | 26.5 |
| 6 | 56.6 | 44.8 | 44.3 | 26.8 |
| 7 | 57.9 | 45.5 | 45.0 | 27.0 |
| 8 | 59.2 | 46.2 | 45.8 | 27.3 |
| 9 | 60.5 | 46.9 | 46.6 | 27.5 |
| 10 | 62.0 | 47.7 | 47.4 | 27.8 |
| 11 | 63.5 | 48.4 | 48.3 | 28.1 |
| 12 | 65.1 | 49.2 | 49.2 | 28.4 |
| Total | 707.4 | 556.5 | 551.1 | 331.4 |

so that the entire beam tube had to be replaced by a simple beam pipe consisting of three stainless-steel tubes connected by two bellows [Ban14]. Due to the missing flapper valve, a proper bake-out procedure of the spectrometer could not be realized. For this reason the SDS-II measurements were divided into two parts: first, during the initial SDS-IIA phase an unbaked spectrometer was operated, whereas in the second SDS-IIB phase with the repaired in-line flapper valve installed, a properly baked-out spectrometer was used. A schematic overview of the entire main spectrometer and detector vacuum system during SDS-IIA is given in Figure 3.4.

### The Vacuum Pumps

For the initial pump-down of the spectrometer volume a *Leybold SP630* screw pump with a pumping speed of $630\,\mathrm{m}^3/\mathrm{h}$ is temporarily installed to pump port 2. After this first pump-down, three different kinds of vacuum pumps are used in the SDS configuration to achieve and maintain the stringent UHV conditions:

- Six *Leybold MAG-W-200* TMPs, installed in groups of three to the two outer pump ports of the spectrometer, provide an effective pumping speed of $10^4\,\ell/\mathrm{s}$ for hydrogen in the spectrometer volume [Wol15b]. Each set of three TMPs is backed by an additional 300-$\ell/\mathrm{s}$ TMP in series with a scroll pump. With this cascaded setup, the required hydrogen compression ratios are achieved. In standard operation, the main purpose of the TMPs is to pump non-getterable gases, like noble gases and methane.
- Due to the large stray magnetic fields of the pinch and detector magnet, TMPs cannot be used to ensure the vacuum quality in the detector chambers during normal operation. Instead, two *Marathon CP-8* cryogenic pumps from *Sumitomo* are used, each serving one of the two FPD vacuum chambers. Over the course of SDS-IIA the operation of both cryo pumps had to be stopped due to instabilities in their performance. The reason for this was most probably a failure of expendable parts in the cold heads, the cryo panels, or the charcoal absorbers of the pumps. The cold

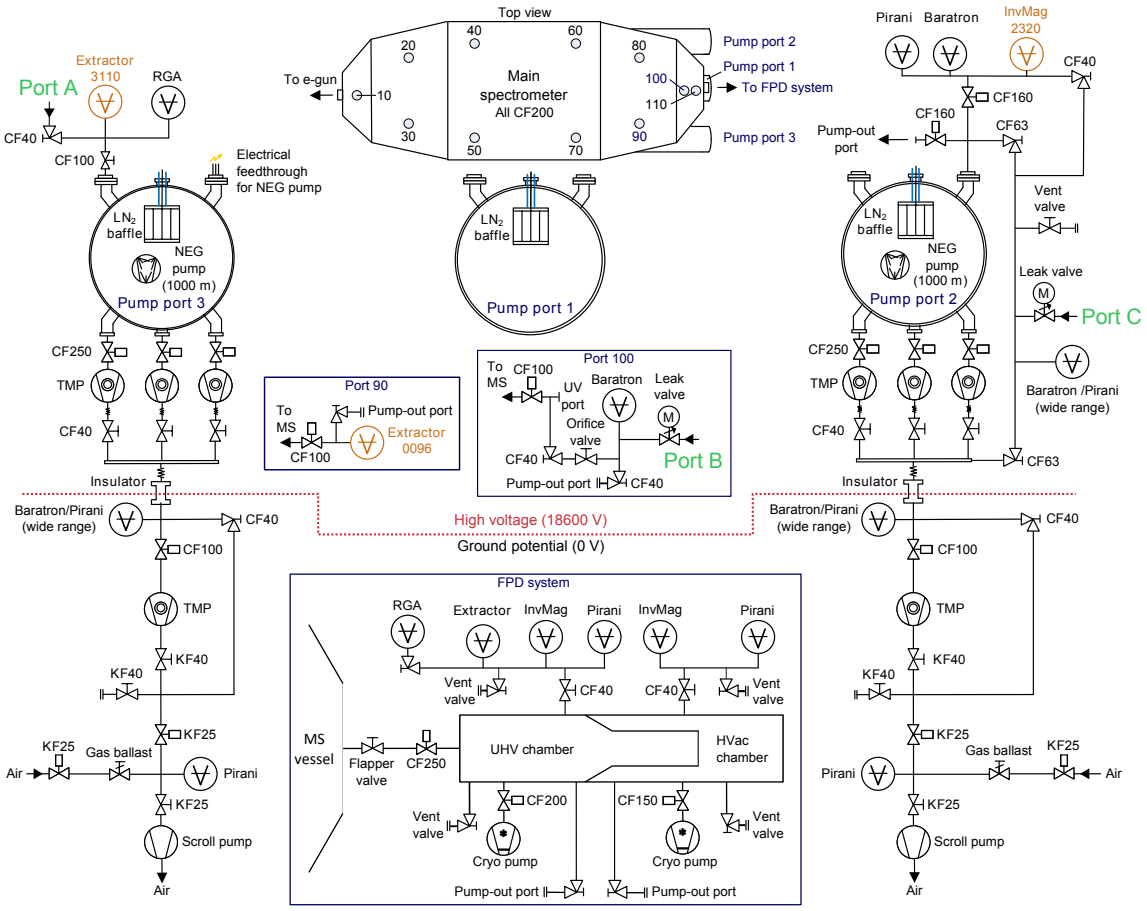


**Figure 3.4: Schematic overview of the SDS-IIA main spectrometer and detector vacuum system.** An overview of all ports of the main spectrometer is given at the top. The pump ports 2 and 3 which house most of the vacuum equipment are shown on the right and left side, while an overview of the detector vacuum system is given at the bottom. Furthermore, two small diagrams in the center show the vacuum equipment installed at ports 90 and 100 of the apparatus. The three main vacuum gauges of the spectrometer are marked in orange. The ports A, B, and C (marked in green) were used during SDS-II to install auxiliary equipment such as an artificial radon source or an alternative gas-inlet system to the spectrometer. Details on the different components are given in the text. Figure adapted from [Wol15b].

heads are operated by a single *HC-8E4* helium compressor from *Sumitomo*. While the UHV chamber of the detector system was pumped by the main-spectrometer vacuum pumps only in the following, a temporary pump-out system was installed to provide the HVac in the electronics chamber. This system consisted of a *TMU 971 TurboDrag* pump from *Pfeiffer* backed by a *XDS 10* dry scroll pump from *BOC Edwards*, both placed outside the 3-mT area of the FPD magnets and connected to the HVac chamber via an about 2.5-m long DN63 pipe.

- In the standard configuration each of the three main pump ports of the spectrometer is foreseen to be equipped with 1 000 1-m long *SAES St707* non-evaporable getter (NEG) strips[5]. After thermal activation these NEG pumps provide a combined pumping speed of $10^6$ $\ell/s$ for hydrogen in the spectrometer volume [Wol15b]. During SDS-I all three NEG pumps were partly activated by the thermal radiation emitted from the 300-°C walls during the spectrometer vacuum bake-out. However, due to thermal deformations of the CuBe rods feeding the inner electrode system that

[5]The final configuration of *SAES St707* getter strips is currently under discussion due to the results obtained in this thesis.

were observed during this bake-out (Sec. 3.3), the maximum temperature of the spectrometer vessel was from then on limited to a maximum value of 200 °C. Thus, the NEG pump in port 3 was modified for electrical heating at up to 400 °C before the start of SDS-II. In this way a NEG activation was possible without a spectrometer bake-out in SDS-IIA.

The NEG pumps of the KATRIN main spectrometer are indispensable to reach the required pressure levels of $< 10^{-10}$ mbar. However, their material is also a known emanation source of specific radon isotopes that can undergo $\alpha$-decays in the spectrometer volume and thus generate background electrons. For this reason, prior to SDS-II the NEG pump in port 1 was completely removed from the system. The dismounted NEG material allowed to investigate the radon activity in the spectrometer during SDS-II in detail (see Chapter 4).

**The $LN_2$-Cooled Baffle System**

In order to prevent single radon atoms that emanate from the NEG material to enter the MAC-E filter, a $LN_2$-cooled baffle system is installed between each of the three main pump ports and the spectrometer volume. This system uses cryosorption to trap radon onto its cold surfaces so that it can decay there, well outside of the sensitive flux tube. For this purpose, each baffle consists of 22 V-shaped blades made of oxygen-free copper that are cooled to $LN_2$ temperature. The left side of Figure 3.5 shows a photography of the copper blades taken from inside of the spectrometer. The $LN_2$ cooling is technically realized by an array of vertical stainless-steel pipes that are attached to the copper blades. These pipes are framed by a ring pipe which surrounds the baffle. This system is flooded with $LN_2$ from the bottom while vaporized nitrogen gas can escape through a return pipe at its top. As the copper blades prevent a direct line of sight between the NEG pump and the observed flux tube, radon migration is prohibited by enforcing at least one hit of the cold copper surface. In return, the baffle geometry reduces the total effective pumping speed of the NEG pumps to $3.75 \times 10^5$ $\ell/s$ [Wol15b]. The CAD drawing on the right side of Figure 3.5 shows an overview of the NEG pump and the baffle system, both installed in pump port 3. The temperature of the baffles is monitored by three sensors on the top, middle, and bottom of the central copper blade, plus a single sensor on an outer blade. Due to an elevated pressure of 1.5 bar in the nitrogen supply lines, limited thermal couplings, and the radiative heat load from the spectrometer vessel, the temperature of the baffle system of about 86 K is somewhat higher than the 77-K boiling temperature of nitrogen.

The $LN_2$ circuit that supplies the baffle systems consists of three major components:

- A vacuum insulated $LN_2$ storage tank manufactured by *Messer GmbH* with a capacity of 51 550 $\ell$ which is installed outside of the KATRIN experimental hall to ensure a permanent supply of the baffle system.
- Vacuum insulated *Cryoflex* transfer lines connect the supply tank to a valve box from *Nexans* which allows to regulate the $LN_2$-flow rate into the three baffles individually.
- The transfer lines from the valve box to the baffle contain high voltage separators which are installed at the backside of the three pump ports to enable a long-term stable HV operation of the spectrometer while the baffles are permanently supplied with liquid nitrogen[6].

While the supply tank and the valve box were already installed during SDS-I, the high-voltage separators were not, so that a combined operation of the main spectrometer at elevated potential and the baffle system at $LN_2$ temperatures was strongly limited in time [Goe14]. At the begin of the SDS-II phase, major research and development efforts

[6] The relative permittivity of $LN_2$ is $\epsilon_r = 1.46$.

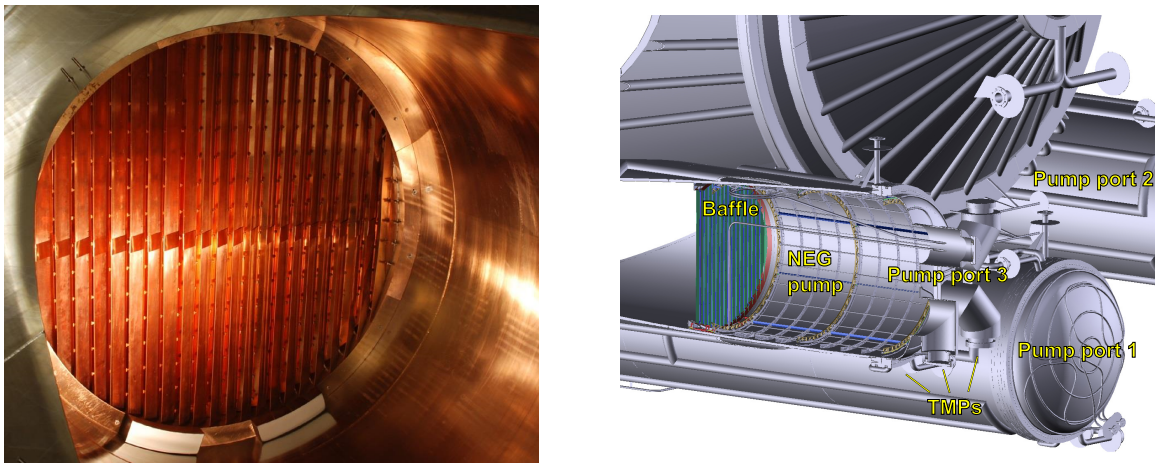


**Figure 3.5: Overview of the $LN_2$-cooled baffle system and the NEG pumps. Left:** Photography of the V-shaped copper blades of the baffle in pump port 3. The picture, which is adapted from [Goe14], is taken from the inside of the main spectrometer. **Right:** A CAD drawing of pump port 3 shows the NEG pump and the baffle system. The drawing is adapted from [Kle14].

concerning the design of the HV separators were made [Mue15b]. In this context, a HV insulator design from *Babcock-Noell* was found as being the most reliable one in dielectric strength with a break-down free operation of up to 35 kV. Other designs, based on ceramic insulators from *Allectra*, were prone to HV instabilities at voltages higher than 20 kV. During SDS-IIA, the $LN_2$-cooled baffle system was fully functional and a first long-term high-voltage operation period with cold baffles was possible. For this purpose, the baffles in pump ports 2 and 3 were equipped with *Allectra* ceramic insulators while *Babcock-Noell* insulators were installed to pump port 1. During the measurement phase, the insulators of pump port 3 had to be replaced by *Babcock-Noell* ones, due to a HV break-down. Based on the known instabilities of the *Allectra* ceramic insulators, also pump port 2 was equipped with *Babcock-Noell* insulators after SDS-IIA and prior to SDS-IIB.

As the main spectrometer could not be surface conditioned by a bake-out prior to SDS-II, the residual-gas composition was strongly dominated by water during SDS-IIA. With their $LN_2$-cold surfaces, the baffles were however acting as cryogenic traps for $H_2O$ molecules in the spectrometer volume. Correspondingly, temperature variations of individual baffles due to short-term cool-down or warm-up phases influenced the pressure level in the spectrometer volume significantly during SDS-IIA. This effect resulted in considerable changes of the pressure, ranging from the medium $10^{-9}$-mbar regime in the beginning of the measurement phase, to about $3 \times 10^{-10}$ mbar at the end of SDS-IIA.

While the concept of the $LN_2$-cooled baffle system and its supply circuitry has already been described in detail in [Goe14], the characterization of its high-voltage separators is discussed in [Mue15b]. The efficiency of the baffle system in terms of a reduction of radon-induced backgrounds in the main spectrometer is investigated in Chapter 4 of this work.

### The Vacuum Gauges

Within the SDS vacuum scheme shown in Figure 3.4, more than 15 different vacuum gauges are used to monitor and control the UHV and the fore-vacuum conditions. However, in the context of the measurements presented in this work, three vacuum gauges were of particular relevance:

- An *Ionivac IE514* extractor ion gauge from *Leybold* (Extractor 0096, calibration factor: 0.841) is installed to port 90 to monitor the pressure in the vessel. However,

in the standard measurement configuration this gauge had to be turned off as it produced background electrons in the spectrometer volume.

- A second extractor ion gauge of the same type (Extractor 3110, calibration factor: 0.779) is installed at the end of pump port 3. As it is located behind the baffle and the (activated) NEG pump, its pressure reading is usually slightly lower than that of gauge 0096. However, as it has no direct line-of-sight into the sensitive flux volume this gauge can be operated during measurements and was used as main pressure monitor during SDS-IIA.
- At the end of pump port 2, also behind the baffle and the (unactivated) NEG pump, an *HPS 421* inverted magnetron gauge from *MKS* (InvMag 2320, calibration factor: 1.056) is installed. During specific measurements of SDS-II, where the Extractor gauge 3110 could not be used due to an artificial radon source being installed to port A right next to it (see App. A), this less reliable magnetron gauge was used as main monitor of the pressure in the spectrometer.

In addition to the vacuum gauges, an *MKS Mikrovision II* quadrupole mass spectrometer (RGA) being installed next to the extractor gauge 3110 in port 3 was used to monitor the residual-gas composition in the main spectrometer.

**The Gas-Inlet System**

In order to calibrate the vacuum gauges for different gas species and to allow for measurements at elevated pressure, a gas-inlet system is installed to port 100. A remotely controlled *UHV ND3* leak valve from *nenion*, a Baratron gauge, and an orifice valve are used to set the flow rate from a gas source, connected to port B, into the spectrometer to a desired level [WH14]. During some of the SDS-IIA measurements an artificial radon source was installed to port B and the gas injection was controlled via a second leak valve of the same kind at port C.

**The Main Spectrometer Bake-Out**

After the end of SDS-IIA and the installation of the repaired in-line flapper valve, the spectrometer was baked-out at 200 °C for eight consecutive days. A thermal oil temperature unit from *HTT energy systems GmbH* controls the flow of 9 $m^3$ of *Marlotherm LH* heat-transfer fluid through two thermal circuits that surround the spectrometer vessel and its pump-ports. In this way, the temperature of the spectrometer can be regulated at the 1°C level. With a total heating power of the *HTT* unit of 440 kW a maximal baking temperature of 350 °C can be achieved. In the standard operation, the spectrometer temperature is regulated to 20 °C, while 60 kW of cooling power allow a minimum operating temperature of 10 °C. In addition to the thermal circuits, more than 50 electrical heating tapes are used to bake-out small components like valves. During the bake-out procedure, more than 350 Pt-100 and Pt-1000 sensors monitor the temperature of the vessel and the inner electrode system.

As a consequence of the bake-out sequence between SDS-IIA and SDS-IIB, the residual-gas composition in the spectrometer changed. While it was dominated by water vapor during the earlier SDS-IIA phase, the bake-out removed the thin $H_2O$ layer from the stainless-steel surfaces such that the water-vapor pressure in SDS-IIB was reduced by more than two orders of magnitude. The absolute pressure in the spectrometer, as measured by the $N_2$-calibrated extractor gauge 3110, was improved from a minimum value of about $3 \times 10^{-10}$ mbar during SDS-IIA to a minimum pressure of about $6 \times 10^{-11}$ mbar in SDS-IIB. The rather good pressure in the unbaked SDS-IIA system can be explained by the $LN_2$-cooled baffle surfaces that did act as additional cryogenic pumps for water vapor.

A detailed description of the vacuum system and the bake-out procedure of the main spectrometer is given in [Wol15b] while the detector vacuum system is described in [Ams15].

## 3.3 The High-Voltage Concept

The retarding potential of the main spectrometer is provided by elevating the entire vessel to negative high voltage. For this purpose, the whole apparatus rests on six large-scale insulators, while ceramic cones on each side insulate it against the grounded beamline to the pre-spectrometer and the FPD system. In this way, the spectrometer can be operated at up to −35 kV. However, due to the welding process of the large-scale stainless-steel vessel, its inner surface exhibits small deformations from an ideal cylinder up to the cm-scale [Cor14]. For this reason and in particular to fine-shape the potential in the analyzing plane an inner electrode system was installed to the spectrometer.

**The Inner Electrode System**

The whole inner surface of the main spectrometer is covered by 248 wire-electrode modules with a total of more than 23 000 quasi-massless wires which are arranged along 15 coaxial rings. In the central and flat-cone parts of the spectrometer, the modules feature a double-layer concept with an inner layer of 200-µm diameter wires and an outer layer with wires of 300-µm diameter. The modules in the steep cones contain only a single layer of wires. In the high electric-field regions at the upstream and downstream end of the spectrometer, a titanium-made anti-Penning electrode and a full-metal ground electrode, made of high-purity aluminum, are used to prevent Penning traps (Sec. 2.1.2). Furthermore, the central and flat-cones part of the electrode system are divided into two half shells which can be operated at a maximum voltage difference of 1 kV. In this way, a pulsed or static dipole mode can be used to actively reduce backgrounds from stored electrons [Wan13a]. Ten high-voltage feedthrough ports at the top of the spectrometer are used to apply individual voltages to the inner electrode rings, wire layers, and dipole halfs in the UHV (see Fig. 3.7). The alignment of the whole electrode system relative to the main spectrometer axis was determined via laser tracker measurements [Jur09] and is known to $\leq$ 1 mm accuracy [Pra11]. With this setup, deviations of the vessel surface from ideal roundness are largely compensated and the axial symmetry of the electric field in the spectrometer is improved.

Besides the fine-shaping of the electrostatic fields, the wire-electrode system serves a further task. As described in Section 2.1.2, low-energy secondary electrons which are generated at the inner surface of the spectrometer by cosmic rays, intrinsic or environmental radiation, or via field electron emission are a potential source of background for KATRIN. Prior to the SDS-II measurement campaign it was expected that the excellent intrinsic magnetic-shielding properties of the MAC-E filter might not be sufficient so that these electrons could contribute to the spectrometer background. By operating the wire electrodes at a slightly more negative potential than the vessel, an additional electrostatic shielding of such low-energy electrons with a shielding factor of 100 was achieved in a specific configuration [Sch14c]. The maximum potential difference between the vessel and the wire electrodes is limited to 1 kV. Figure 3.6 shows two photographies of a wire module of the central spectrometer part with the inner (outer) wire layer indicated by green (blue) dashed lines. In the lower right part of the figure, the electrostatic-shielding principle is explained. The innermost wire layer is held at the retarding potential $U_{\text{inner}} = U_0$, whereas the 7-cm distant outer layer and the vessel are held at more positive potentials: $U_{\text{vessel}} > U_{\text{outer}} > U_{\text{inner}}$. In this way, low-energy electrons from the vessel are shielded by the 15-cm distant outer wire layer while the inner layer also shields electrons which are emitted from the comb-shaped support structures of the electrode system. In all cases, however, the dominant shielding is achieved by the axially-symmetric magnetic field.

During the 300°C bake-out of the spectrometer prior to SDS-I, thermal deformations of the CuBe-based high-voltage distribution lines of the electrode system inside the vessel caused several short-circuits not only between the inner and the outer wire layers but also

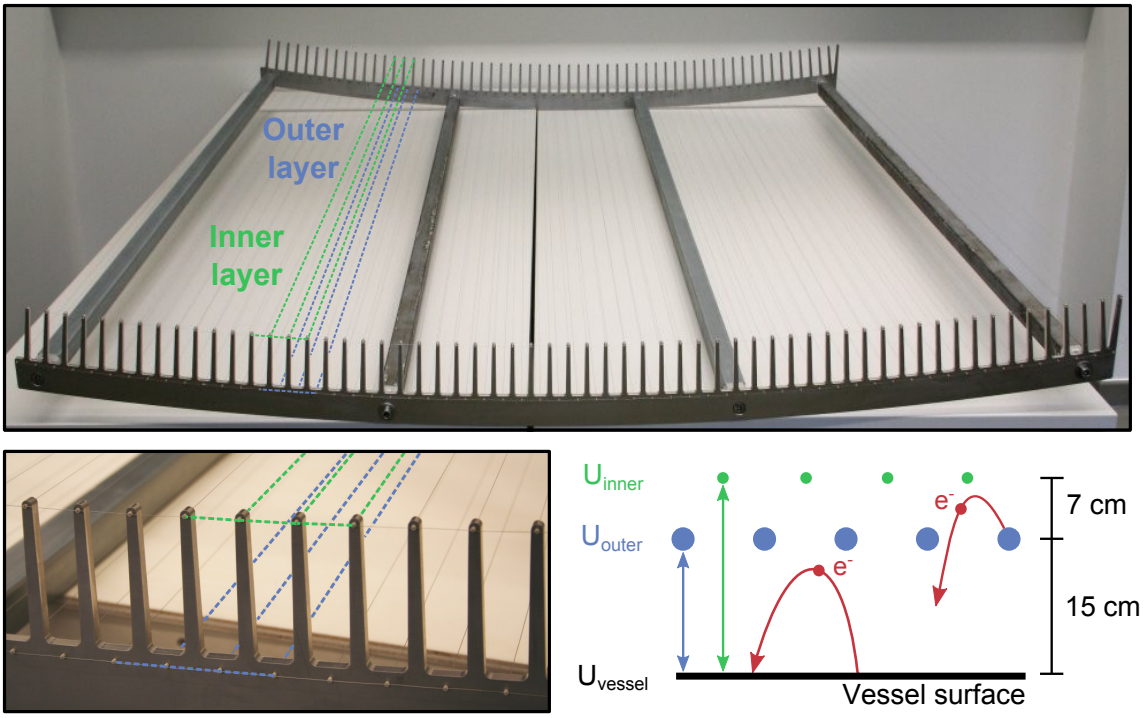


**Figure 3.6: Illustration of the electrostatic-shielding principle by a wire-electrode module. Top:** Photograph of a double-layer wire-electrode module from the cylindrical part of the spectrometer. The inner (green) and outer (blue) wire layers are marked by dashed lines. **Bottom left:** Magnified view of the electrode wire module. The photographs are taken from [Han07]. **Bottom right:** Illustration of the electrostatic-shielding principle. Low-energy electrons starting from the inner surface of the spectrometer vessel or the outer wire layer are electrostatically repelled by the applied negative potentials $U_{\text{inner}} < U_{\text{outer}} < U_{\text{vessel}}$. The wires of the innermost layer have a diameter of 200 µm, making them nearly massless.

between neighboring electrode rings. As nearly all of the electrode rings were affected, a double-layer operation of the electrode system was not possible during SDS-I so that the massive support structures of the inner electrode system had to be kept electrostatically unshielded [Han13, Beh13]. After the end of SDS-I strong efforts were made to resolve the short circuits by accessing the corresponding distribution lines through the HV feedthrough ports of the spectrometer. In this way, six of fourteen short-circuits could be resolved prior to SDS-II [Dyb14]. Nevertheless, the remaining short-circuits, marked in Figure 3.7, prevented a reasonable long-term double-layer operation during SDS-II and all measurements presented in this work are taken in a 'single wire-layer mode' ($U_{\text{inner}} = U_{\text{outer}}$) if not stated differently. Note that two additional short-circuits appeared during the bake-out between SDS-IIA and SDS-IIB even as the spectrometer temperature at this time was limited to 200 °C.

### The High-Voltage Distribution

With a total of 44 electrically-isolated electrode segments, consisting of individual rings, wire layers, and dipole halfs, the main-spectrometer high-voltage system is rather complex and the potential of an individual wire-electrode segment is supplied by a chain of power supplies that lean on each other. Figure 3.8 shows an overview of the HV distribution concept that was used during the SDS-II measurements.

The common potential of the main-spectrometer vessel of up to $U_{\text{vessel}} = -35\,\text{kV}$ is provided by a *FuG-70M-35000* high-precision power supply. Besides the spectrometer vessel also equipment in a HV cabinet, located at the basement of the KATRIN experimental hall, is elevated to $U_{\text{vessel}}$. This cabinet contains all further power supplies which lean with

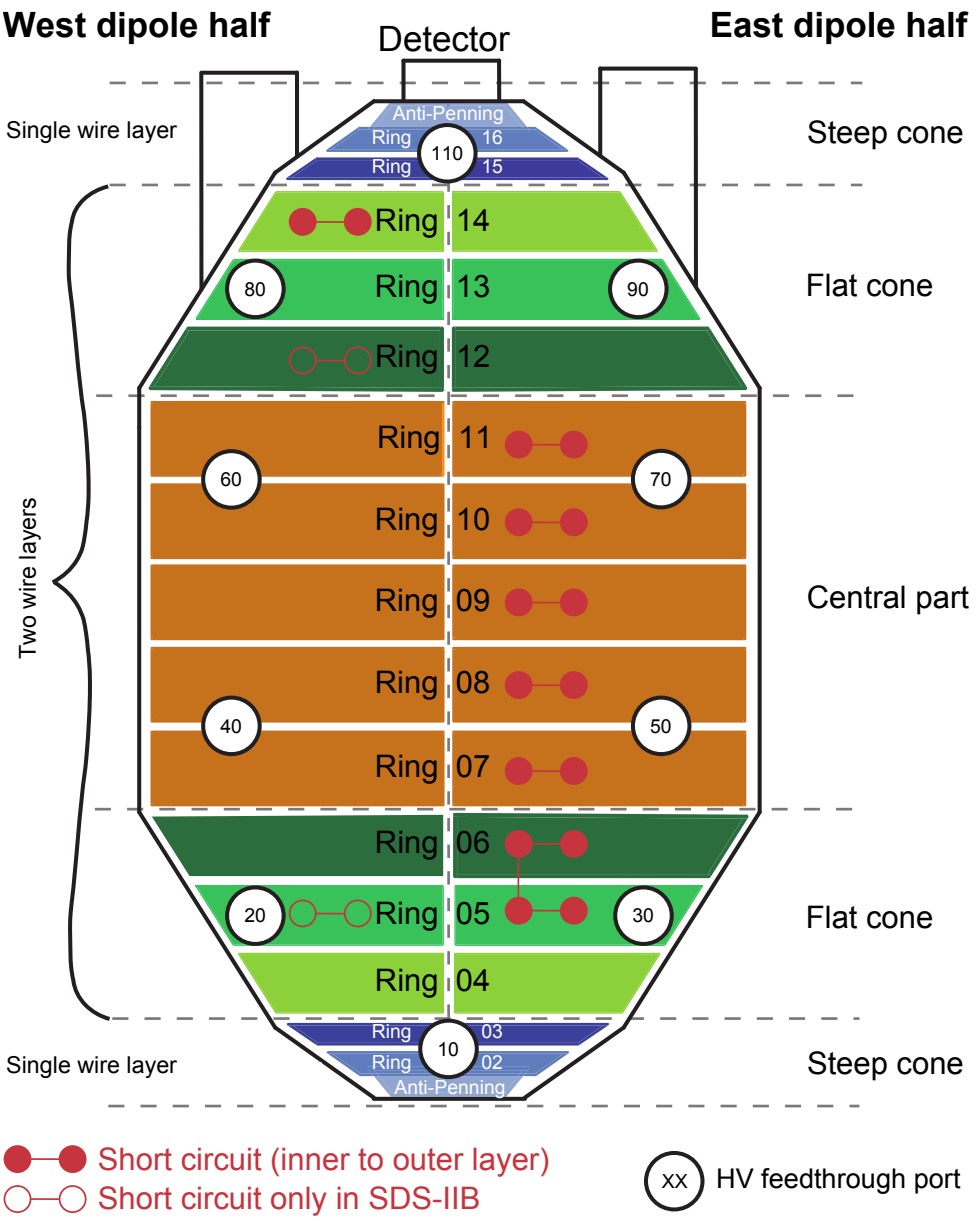


**Figure 3.7: Overview of the inner-electrode system installed inside the KATRIN main spectrometer.** The system consists of 15 wire-module rings plus an additional solid anti-Penning electrode on each end. While the wire modules in the central part and the flat cones are double layered and separated into a west and an east dipole half, the steep-cone modules only feature a single wire layer and are not divided into west and east. The different potentials of the rings and wire layers are fed through ten HV feedthrough ports into the spectrometer vessel. During SDS-II, some of the wire modules showed short-circuits between the inner and the outer wire layer and between neighboring rings. These are marked by red circles. Figure adapted from [Han13].

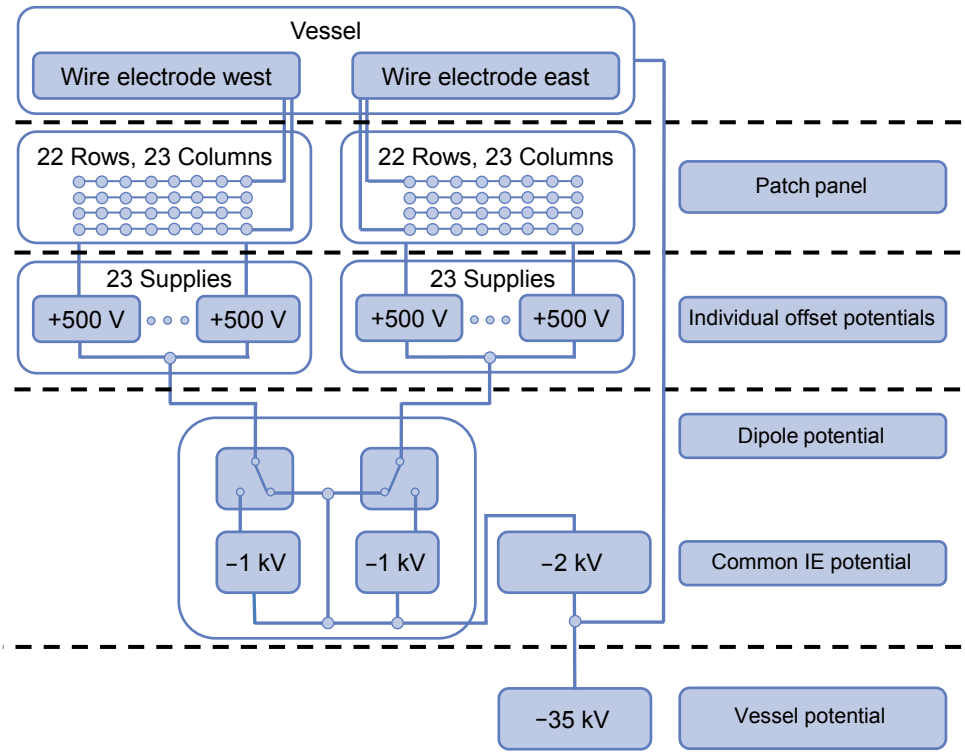


**Figure 3.8: Overview of the KATRIN high-voltage concept during the SDS-II measurement phase.** A −35-kV power supply is used to provide the vessel potential. Leaning on the vessel potential, a −2-kV supply allows to elevate the whole inner electrode system to a negative offset potential for electrostatic-shielding purposes. Furthermore, a −1-kV dipole power supply can be used to generate an electric dipole field inside the spectrometer. In a last stage, six 8-channel offset power supplies can be used to set single wire layers or rings to individual positive offset potentials of up to +500 V via a custom-made patch panel. Figure adapted from [Kra15a].

their ground onto the vessel potential. One of these is an *ISEG NHQ 122m* power supply which is used to set the potential on all 15 rings of the inner electrode system commonly up to $U_{\mathrm{IE,common}} = -2\,\mathrm{kV}$ more negative than the vessel potential for electrostatic-shielding purposes. At its output, an additional *FuG HCV 2M-1000* dipole power supply allows to apply voltages of up to $-1\,\mathrm{kV}$ to one of the dipole halfs in order to actively remove stored particles from the spectrometer volume. Six *ISEG EHS 8 205p-K* 8-channel power supplies are used to apply individual positive offset potentials of up to $U_{\mathrm{offset,i}} = +500\,\mathrm{V}$ to a single segment i of the electrode system. To achieve maximum flexibility, a patch panel is used with which the output of a specific offset power-supply channel can be distributed to a desired electrode segment. In contrast to the ring elements of the inner electrode, the two full-metal anti-Penning electrodes of the spectrometer are usually held at the desired vessel potential. However, an *ISEG NHQ 122m* power supply that leans on the vessel potential is used in some of the measurements presented in Chapter 5 of this thesis, to set the anti-Penning electrode on the detector side to a negative offset potential of $U_{\mathrm{APE}} = -200\,\mathrm{V}$.

As the stability of the retarding potential $U_0$ in the analyzing plane of the spectrometer is directly related to the sensitivity of the KATRIN neutrino-mass measurements, the main spectrometer HV system features a series of high-precision monitoring and voltage regulation devices. This includes two custom-made high-voltage dividers [Thu09, Bau13b], a post-regulation system that has been tested for the first time during SDS-II [Wac15, Kra15a], and the monitor spectrometer [Erh14]. However, in the measurements presented

**Figure 3.9: The post-acceleration electrode of the FPD system.** The picture is adapted from [Har12] and shows the electrode prior to its installation into the FPD system.

throughout this work, the stability of the potential in the analyzing plane is of minor importance and only needs to be known to an accuracy of a few V.

For this purpose the read-back values of the corresponding power supplies are accurate enough and used to define the retarding potential according to

$$U_0 = U_{\text{vessel}} + U_{\text{IE,common}} + U^{\text{Inner}}_{\text{offset,09}} \quad . \tag{3.1}$$

Here, $U^{\text{Inner}}_{\text{offset,09}}$ corresponds to the offset potential applied to the inner wire layer of the central electrode ring 9.

### The Post-Acceleration Electrode

Inside the FPD system a trumpet-shaped 3-mm thick copper electrode (see Fig. 3.9), manufactured by *Beverly Microwave Division of Communications and Power Industries*, allows to post-accelerate signal electrons from the main spectrometer by up to 30 keV [Ams15]. This post-acceleration electrode (PAE) comes with several advantages. First, it allows to boost the longitudinal energy of the signal electrons into regions where lower detector backgrounds from intrinsic $\gamma$-radiation are expected [Ams15]. Second, the probability of signal electrons for backscattering from the detector wafer is reduced when their incident angle is decreased [Ren11]. In the context of the background measurements presented in this thesis, the post-acceleration electrode provides another, more practical advantage: It allows to boost the energy of background electrons above the detector noise threshold even if the spectrometer is operated at zero potential (see Chapter 5).

Inside of the FPD system, the PAE forms the physical boundary between the UHV and the HVac chamber with the wafer and the front-end electronics mounted onto its downstream side, respectively. Like the electrode, these components are elevated to the post-acceleration potential by a *Spellman TOF3000* high-voltage power supply. On its upstream side, the PAE is connected to the grounded vacuum chamber via an insulating ceramic. Inside the HVac chamber, the PAE and the detector electronics are surrounded by a series

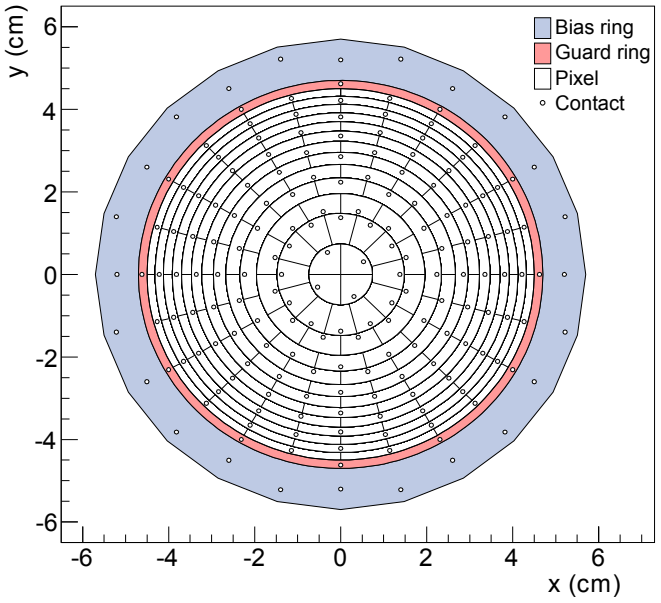


**Figure 3.10: Segmentation pattern of the focal-plane detector** on the backside of the wafer. The 148 detector pixels are surrounded by a guard ring (red) and a bias ring (blue). The electric contacts are marked as black circles. Figure adapted from [Ams15].

of cylindrical quartz tubes with stainless-steel foils covering their inner and outer surfaces. In this way, the inner surface can be set to the PAE potential while the outer surface is connected to the grounded vacuum chamber, confining the electric field into the insulator. This design has been chosen to allow for a breakdown-free operation of the PAE up to +30 kV. However, in SDS-I and SDS-II the PAE could not be operated at potentials of more than +11 kV due to the occurrence of severe breakdowns. In the context of the design of the HV separators for the $LN_2$-cooled baffle system (Sec. 3.2), high electric fields at so-called triple points where an insulator (quartz tube) and a conductor (foil electrode) are connected in a vacuum, were identified as possible sources of these breakdowns [Mue15b, Mue14b]. Based on these findings, a maintenance phase of several months after the end of SDS-IIB will be used to modify the high-voltage concept of the PAE to allow for breakdown-free operation at potentials higher than +11 kV. During SDS-II, however, the nominal PAE potential was set to $U_{\mathrm{PAE}} = +10\,\mathrm{kV}$.

## 3.4 Detector Read-Out Chain and Data Acquisition

To count the signal electrons that overcome the retarding potential of the main spectrometer with high efficiency, a segmented PIN diode array is used. It is housed on a 503-µm thick monolithic silicon wafer with a total diameter of 125 mm which was manufactured by *Canberra Industries Inc*. The unsegmented, shallowly ion implanted, $n^{++}$-ohmic entrance side of the wafer includes the 90-mm diameter uncoated sensitive area. In contrast, the p-type backside of the wafer is fully coated with non-oxidizing TiN and provides electrical connections for the signal read-out and the bias voltage supply. This segmented backside is divided into 148 pixels of equal area ($A = 44.1\,\mathrm{mm}^2$) which are arranged in twelve concentric rings of twelve pixels each, plus a four-pixel bullseye in the center. This design allows spatially resolve the magnetic flux tube which is mapped onto the detector. An overview of the detector segmentation pattern is given in Figure 3.10. The pixel segments of 8.2-pF capacitance are separated by 50-µm thick boundary layers of 1-GΩ resistance, while a 2-mm thick guard ring protects the outermost pixel rings against field distortions by the 15.5-mm thick bias ring that surrounds it. This bias ring wraps around the edges

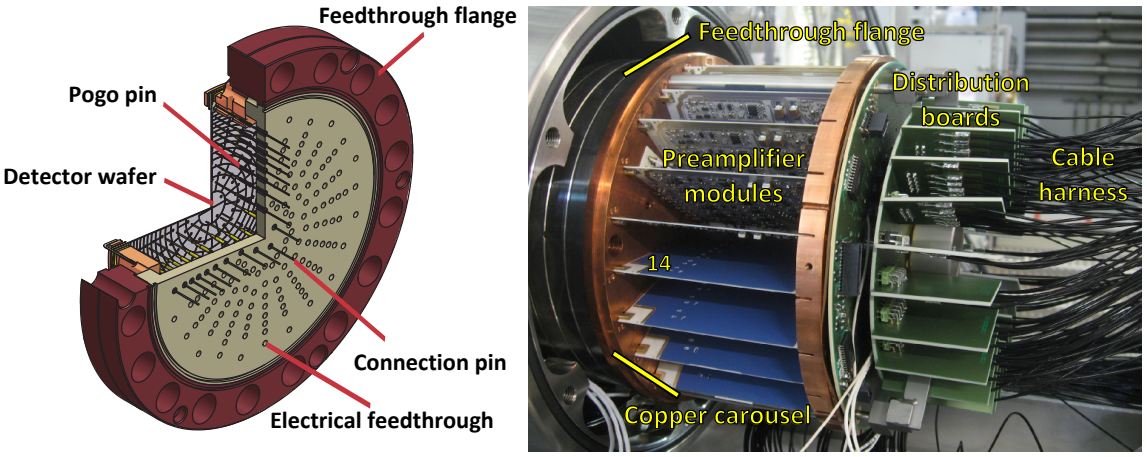


**Figure 3.11: The detector feedthrough flange and the read-out electronics. Left:** CAD drawing of the detector feedthrough flange. Figure adapted from [Ams15]. **Right:** Photography of the detector read-out electronics located in the HVac chamber, including the feedthrough flange, the 24 preamplifier modules, the distribution boards, and the cable harness. The preamplifier card 14, which is explicitly marked in the picture, showed instabilities in performance during SDS-II. Photography taken from [Sch14c].

of the wafer connecting the insensitive outer areas of the entrance side to the bias voltage of +120 V, applied from the segmented backside. At room temperature leakage currents of well below 1 nA per pixel of the PIN diode have been found [Van12, Ams15]. The specified insensitive dead layer of the wafer of 100 nm has been confirmed by energy-loss measurements with hydrogen anions $H^-$ in [Sch14c].

In a semiconductor diode detector, the number of electron-hole pairs produced via ionization and scattering of an incident keV-electron is proportional to its kinetic energy as long as the electron is fully stopped. With a mean ionization energy of silicon of 3.62 eV, more than 5 000 electron-hole pairs are generated by an 18.6-keV electron incident on the wafer. Due to the applied bias voltage this generated charge is efficiently collected at the backside of the wafer from where it needs to be fed out of the UHV chamber and into the amplifying electronics in the HVac chamber [Kno10]. For this purpose, the detector wafer is mounted on a custom-made feedthrough flange manufactured by *Amtek Hermetic Seal Corp.* shown on the left side of Figure 3.11. This feedthrough flange is directly mounted to the downstream end of the PAE and separates the two vacuum chambers of the FPD system. It houses 184 electrical feedthrough pins sealed in type-L21 borosilicate glass to feed 148 signal read-outs, 12 guard-ring, and 24 bias contacts from one chamber to the other. Spring-loaded pogo pins manufactured by *Interconnect Devices Inc.* press with a total force of 50 N onto the segmented backside of the wafer to establish the electrical connection between the wafer contacts and the feedthrough pins. The force causes the center of the wafer to deform by 0.24 mm. According to [Van12] this causes no performance loss of the PIN diode. On the backside of the feedthrough flange 24 charge-sensitive preamplifier modules, shown in the picture on the right side of Figure 3.11, directly connect to the feedthrough pins. Each of these modules features the first amplification stage for the signals of either six or seven pixel read-out channels. Such a channel consists of an N-channel junction field-effect transistor (JFET) of type *NXP/Philips BF862* and a low-noise operational amplifier (*Analog Devices AD829JR*). The heat generated by the power dissipation of 0.6 to 1.0 W per module is conducted via copper mounting plates and pins to the feedthrough flange and the adjacent PAE. A custom-built heat-pipe cooling system is connected to the PAE and provides 60 W of cooling power by boiling liquid nitrogen, while the mean temperature of the entire in-vacuum electronics can be monitored by a Pt-100 temperature sensor ($T_{\text{carousel}}$) on the so-called carousel, a copper plate located be-

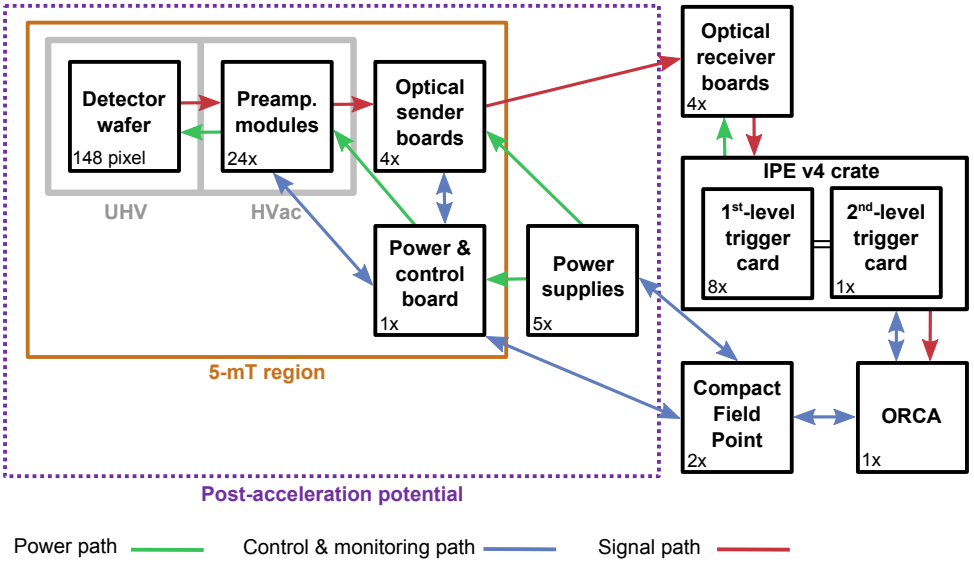


**Figure 3.12: Schematic overview of the detector signal read-out and control architecture.** Figure adapted from [Sch14c].

tween the feedthrough flange and the amplifier modules. The in-vacuum electronics are completed by two circular distribution boards and a cable harness, which lead the signals to a custom-made feedthrough flange at the end of the HVac chamber. Here, they are fed to the ambient-air electronics via six 50-pin vacuum-tight sub-D type feedthroughs manufactured by *Amtek Hermetic Seal Corp.*

On the ambient-air side, the signals are processed by four optical sender boards that house variable gain stages (*Analog Devices AD5426YRM*) to electronically calibrate the detector pixel-by-pixel, the second amplification stage by dual operational amplifiers (*Texas Instruments LMH6628MA*), and fiber-optical transmitters (*Avago Technologies HFBR-1527*) which convert the analog signals into optical before they are transmitted via optical fiber links to the data acquisition (DAQ). This transformation is essential as the whole detector read-out chain up to this point floats on the post-acceleration potential, while the DAQ is grounded. In the analog backplane of the DAQ rack, fiber optical receivers (*Avago Technologies HFBR-2526*) on eight optical receiver boards convert the signals again into analog before they are fed into the digitizers of the DAQ system.

A single power-and-control board represents the control and monitoring interface to the in-vacuum electronics and the optical sender boards. At the same time, it provides the filtered power regulation of the in-vacuum electronics and houses over-voltage protection circuits, the temperature read-out of the preamplifier modules, and the control of the variable gain stages of the optical sender boards. The ambient-air as well as the in-vacuum electronics are driven by five *Amrel* power supplies that are located in a rack outside of the 5-mT magnetic-field area. This rack floats on the PAE potential and is connected to the 230-V AC mains voltage by an isolation transformer [Wue11, Ams15, Sch14c]. A schematic overview of the entire signal read-out and control chain including the DAQ system is given in Figure 3.12.

### The DAQ System

The data-acquisition hardware of the KATRIN focal-plane detector follows the concept of the Pierre-Auger Cosmic-Ray Observatory and is provided by the Institute for Data Processing and Electronics (IPE), KIT. It consists of 8 first-level trigger (FLT) cards and one second-level trigger (SLT) card, all housed in a single *IPE v4* crate. Additional FLT cards can be used to read out the active veto of the detector system, external pulsers, or synchro-

nization signals from other subcomponents of KATRIN. On each FLT card, the analog inputs of up to 24 detector channels are digitized via serial ADCs with 12-bit precision and a sampling rate of 20 MHz. Three (slave) field programmable gate arrays (FPGAs) of type *Altera Cyclone II EP2C35* per FLT card, each serving eight detector channels, determine the event-energy and event-time information based on a two-stage trapezoidal filter. This filter is defined by a shaping length[7] L and a gap length[8] G, both adjustable by the operator [JK94, Ams15]. If the determined energy exceeds a programmable threshold, the corresponding 2048-sample (102.4-µs long) waveform is written into an ADC circular buffer with 64 pages. The paging of this auxiliary memory allows to acquire data in a specific page while the data in all other pages is read out by an additional (master) FPGA on the FLT card, that also performs the time synchronization of the slave FPGAs.

All FLT cards installed in the DAQ crate are initialized and coordinated by a single-board computer running Linux, which is housed on the SLT card. The clock of the SLT card is synchronized with a high-precision 10-MHz clock of an external global synchronization unit ensuring that all FLT cards in the KATRIN network receive exactly the same clock phase. The communication between the SLT card and the DAQ computer at the end of the data-acquisition chain is provided by a Gbit-Ethernet interface [Kop08, Phi10, Ber12].

On the DAQ computer, the object-oriented real-time control and acquisition software package ORCA provides access to the FLT and SLT cards [How04, How14]. It allows the operator to start and stop measurements of adjustable runtime and to change the filter parameters of the trapezoidal filter on the FLT cards as well as the energy thresholds via the ORCA user interface. During a measurement, several low-level analysis tools allow the operator to monitor the recorded data in real-time via dynamic ADC histograms or a pixel-by-pixel representation of the rates on the detector. As it is fully scriptable, the operator can automate measurements via ORCA. A communication link to the data-management and Slow-Control systems (Sec. 3.6) allows to control hardware parameters like the spectrometer voltage.

In order to handle the vastly different data rates ranging from a few mcps during background measurements up to high rates of several hundreds of kcps during calibration runs, the operator can choose between different measurement modes via ORCA. In the context of this thesis, all relevant measurements have been taken in the so-called 'energy mode', where ORCA stores the energy, channel, and time information of each recorded event on the hard-disk drive of the local DAQ computer. After completion of a run, the data is automatically transferred to the KATRIN data server (Sec. 3.6) in form of ROOT-based files [BR96, BR97, How09]. Besides the detector system, the main-spectrometer muon-detection system (Sec. 3.5) uses ORCA as well.

**Performance during SDS-II**

The first main spectrometer commissioning measurements in 2013 were suffering from shorts between adjacent pixels on the detector wafer (#96724) [Sch14c]. As a result, a set of five new wafers was ordered from *Canberra Industries Inc.* after the end of SDS-I. Subsequently, all of these new wafers were checked via a custom-made test board [Mar14] and a wafer without any electric shorts (#115878) was installed into the FPD system prior to the SDS-II measurement phase [Sch14a]. In this way, full functionality of all 148 detector channels has been achieved for the first time. Nevertheless, during the course of SDS-II, temperature fluctuations of the detector electronics caused a significant shift of the noise shoulder of some signal channels to higher energies. These channels are located

[7] The shaping length L corresponds to an integration time and is mainly used to average out noise in the data.

[8] The gap length G ensures that the 200-ns pulse rise time is excluded, when averaging out noise via the shaping length L.

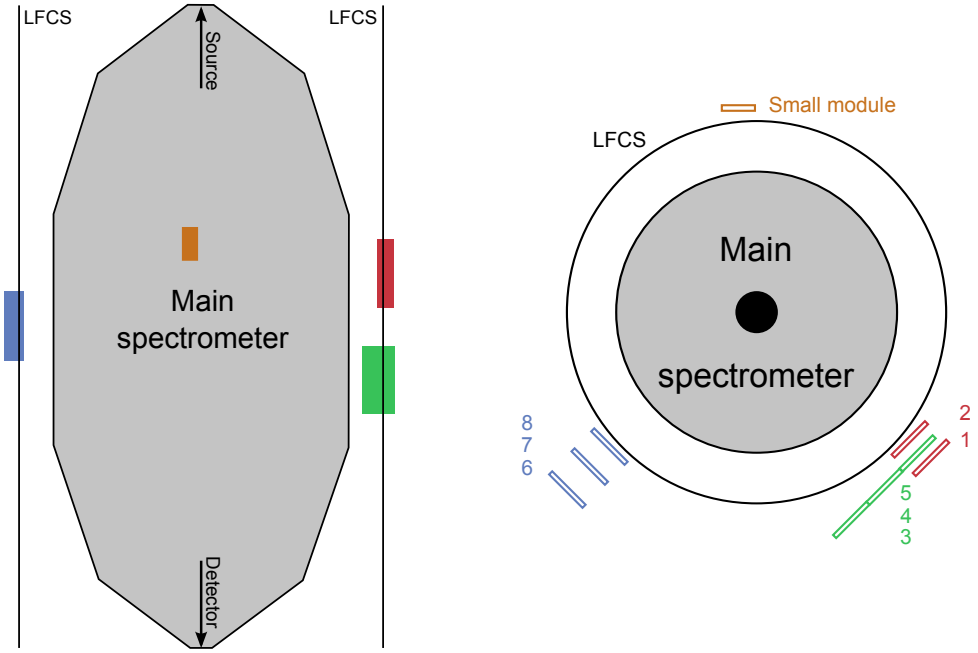


**Figure 3.13: Sketches of the positions of the main-spectrometer muon-detection panels in the KATRIN experimental hall.** The main spectrometer, the LFCS coils, and the nine muon panels are shown in a top view (left) and a front view (right). The sketches are adapted from [Lin15].

on a newly installed preamplifier module[9] in slot 14 marked in Figure 3.11. Thus, the detector pixels 10, 34, 58, 82, 106 and 130, which are served by this module, had to be excluded in some of the analyses presented in this work. Furthermore, all measurements discussed in this thesis have been taken with a shaping length of $L = 1.6\,\mu s$ and a gap length of $G = 200\,ns$ of the trapezoidal filter, if not stated differently.

## 3.5 The Main-Spectrometer Muon-Detection System

With its above ground location and large inner surface of about $690\,m^2$ the KATRIN main spectrometer vessel is exposed to a cosmic muon flux of more than $10^5\,{}^1/_s$ [Lei14]. As minimum-ionizing particles these muons pass easily through the spectrometer walls where they deposit some of their energy via the ionization and excitation of atoms in the lattice of the stainless steel. This leads to the emission of low-energy secondary electrons from the inner surface into the volume of the spectrometer. Even with the excellent intrinsic magnetic shielding of a MAC-E filter and the electrostatic shielding by the advanced inner electrode system, a noticeable contribution of muon-induced secondary electrons to the overall spectrometer background was expected prior to the SDS-II phase. In order to study variations of the muon flux in the KATRIN experimental hall and its correlation to the spectrometer background level, a muon-detection system was installed in the hall [Rov13]. It consists of eight large scintillator panels with a sensitive area of $2.05\,m^2$ each and a single small panel ($0.3\,m^2$), positioned around the main spectrometer according to the sketches in Figure 3.13. The panels are made of *Bicron BC-412* organic plastic scintillators and provide an absolute photon yield of about $7.1\,{}^{photons}/_{keV}$ [Rei98]. On both ends of the large (small) modules four (two) *VALVO XP 2262* photomultiplier tubes (PMTs) from *Philips* record the light pulses that through-going muons produce in the scintillator. If an event is recorded by the PMTs on both sides of a module, the summed signal of the

[9] The original (SDS-I) preamplifier module in this slot was found to be faulty prior to SDS-II and was replaced by one of a different batch.

four (two) PMTs is recorded by a DAQ system which is similar to the one of the FPD system. Instead of two trapezoidal filters in series, the muon DAQ uses a box-car filter in a first and a trapezoidal filter in a second stage to determine the time of an event. A high precision clock is used to synchronize the muon DAQ system with the detector one. As the PMTs operate close to the LFCS coils, they are magnetically shielded by several layers of permalloy foil. However, in the analysis of the correlation between the muon flux and the high-energy FPD-events (the spectrometer background rate) presented in Chapter 5 (Chapter 6), the modules 1 and 2 had to be excluded due to disturbances in their signals by the magnetic fields.

## 3.6 The Slow-Control and Data-Management System

Besides the data acquisition system handling the focal-plane detector and the muon-detection system via ORCA, several thousands of sensors and control systems installed along the SDS beamline [Kle14], like pressure or temperature sensors, heaters or valve status indicators, must be read out and controlled. This task is fulfilled by two different Slow-Control systems, the *Simatic PCS-7* system from *Siemens* [Sie14] and a series of *compact Field Point* (*cFP*) devices from *National Instruments*. In the SDS-part of KATRIN, *PCS-7* systems cover the main-spectrometer vacuum, temperature, and heater monitor and control systems as well as the cryogenic circulatory system of the baffles. The detector system, the air coils, and the magnetic-field sensors are covered by *cFP* devices. The control and sensor read-out of the high-voltage system is handled by an interplay of both systems. Each of the two Slow-Control systems provides user interfaces through which the operator can control valves, heaters, vacuum gauges, and further devices while monitoring the read-back values in real time. Additionally, all sensor read-back values are written into a series of SQL-based databases as shown in the schematic overview in Figure 3.14.

The advanced data-extraction infrastructure (ADEI) [Chi10] is used at KATRIN to provide access to the Slow-Control data. To do so, ADEI utilizes a highly modular architecture where a PHP-based back-end system organizes access to the databases and preprocessing of the data, while a web-based front-end provides navigation through the data, low-level analysis, as well as export possibilities for the user. An additional control subsystem in ADEI allows for communication in the opposite direction, such that set points of Slow-Control systems can be changed via ADEI. Together with a control link between the ORCA systems and ADEI this enables the automation of measurements via ORCA scripts.

The direct user access to both, the Slow-Control data as well as the data acquired by the ORCA systems, is realized by two program packages based on C++. On the server side, the data is preprocessed by the KDBServer software package that handles the calibration tables of sensors or detector channels. On the client computer side, the KATRIN library (KaLi) software package allows the user to retrieve the recorded ORCA data as well as sensor data from the database for further analyses. In addition, the user can update the calibration tables on the server side via KaLi, e.g. after new calibration measurements with the detector have been performed [Kle14].

## 3.7 Detector Calibration Sources

In order to allow for a stand-alone operation independent from the main spectrometer and a regular calibration of the detector ADC spectrum, the FPD system is equipped with several calibration sources such as the injection of test pulses into the vacuum electronics or a photo-electron disc to study the detector response on mono-energetic electrons [Sch14c, Ams15]. However, only one of these calibration sources was actively used during SDS-II,

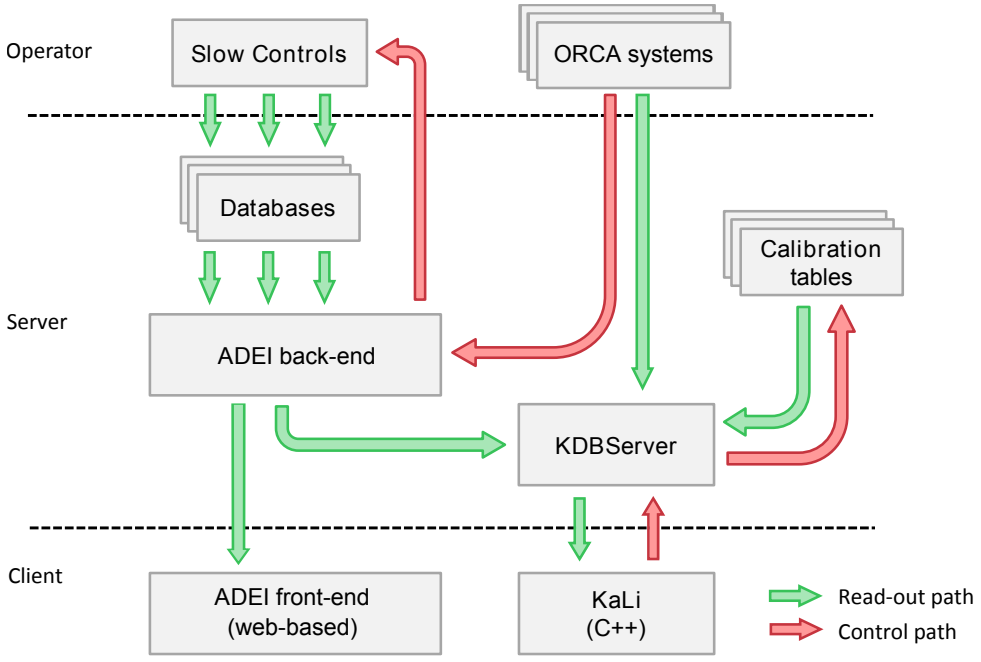


**Figure 3.14: Simplified schematic overview of the SDS Slow-Control and data-management structure.** While the Slow-Control and ORCA systems are controlled by the operator of a measurement, the acquired data is automatically stored, processed, and calibrated on a server and can be accessed by a client via the web-based ADEI front-end or via the KaLi C++ library for a further analysis. In addition, the server-sided ADEI back-end provides a communication link between the ORCA and the Slow-Control systems and, therefore, allows for an automation of measurements.

namely an 18.5-MBq $^{241}$Am source which allows to measure the detector response for mono-energetic $\gamma$-photons, to calibrate the detector ADC spectra in the keV-energy range. Via a system of bellows and air-driven motors this source can be moved in and out of the FPD beamline without breaking the UHV. Figure 3.15 shows the global $^{241}$Am energy spectrum in the range from 4 keV to 65 keV, as measured by 146 detector pixels with specific filter settings of $L = 6.4\,\mu$s and $G = 200$ ns. Besides several fluorescence lines that originate from the copper post-acceleration electrode as well as X-ray lines from excited levels of the daughter nucleus $^{237}$Np, the spectrum features two characteristic mono-energetic $^{241}$Am $\gamma$-lines at 26.34 keV and 59.54 keV. The positions of these lines in the ADC spectrum are used together with the zero point to derive the detector calibration pixel-wise via a linear fit according to $E = m \cdot \mathrm{ADC} + c$ [Sch14c].

In the following, the detector performance concerning its response to the $\gamma$-photons from the $^{241}$Am-source during SDS-IIA is discussed. For SDS-IIB comparable results are expected.

### Energy Resolution

The left side of Figure 3.16 shows the measured energy resolutions of each detector pixel for a cooled-down detector system ($T_{\mathrm{carousel}} \approx -34°$C) right at the beginning of the SDS-II measurement phase (Runs #20001 - #20006). The resolution displayed here corresponds to the full width at half maximum (FWHM) of the 59.54-keV peak in the $^{241}$Am spectrum, as measured by the corresponding detector pixel. A gradual increase of the energy resolution towards outer detector rings is observed while the mean resolution of all pixels is about 2.2 keV (see right side of Figure 3.16). This is about 0.8 keV larger than the mean resolution obtained during the SDS-I measurements, as reported in [Sch14c]. At that time no radial dependence of the detector energy resolution has been observed. An

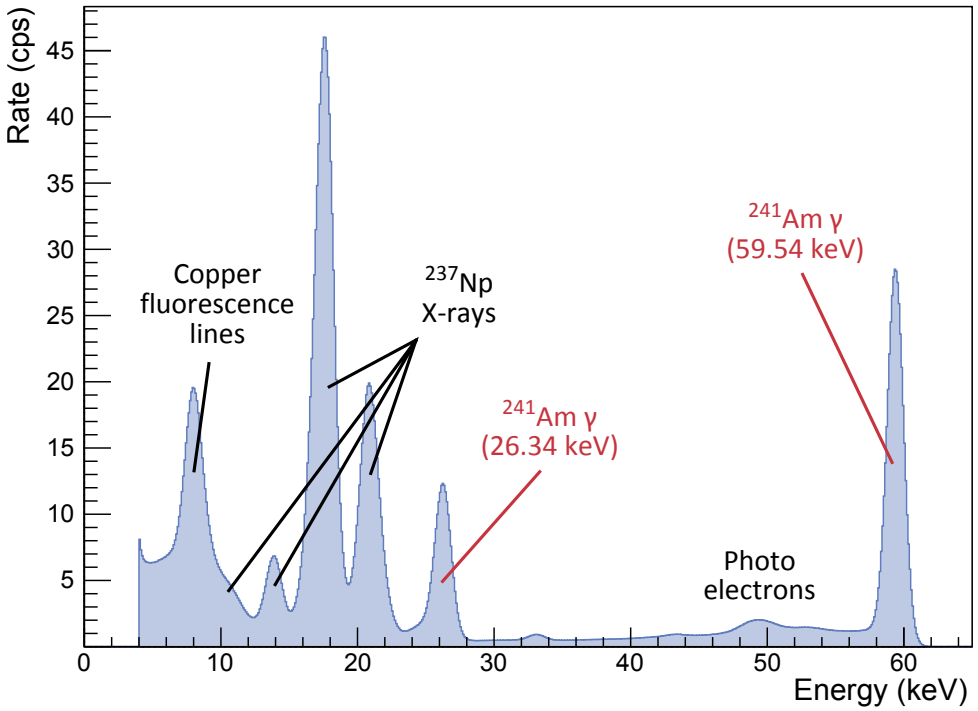


**Figure 3.15: The energy spectrum of the $^{241}$Am detector calibration source** between 4 keV and 65 keV. Besides several fluorescence and X-ray lines, the spectrum features two prominent mono-energetic $\gamma$-photon lines at 26.34 keV and 59.54 keV. The positions of these lines in the ADC spectrum are used to calibrate the detector. More details on the calibration procedure are given in the text. Figure adapted from [Sch14c].

investigation of the SDS-II detector noise spectrum in [Sch14a] shows a strong contribution of flicker noise[10], which points towards the detector wafer as source of the additional noise, i.e. the higher energy resolution. This seems reasonable, as a new wafer (#115878) from a different production batch was installed into the FPD system prior to the SDS-II measurements. Nevertheless, due to the immense technical risks of a wafer replacement procedure, which includes a complete disassembly of the detector HVac-chamber, the inferior energy resolution during the SDS-II phase was accepted in view of the advantage of operating with 100% working detector channels.

### Long-Term Stability

Over the course of the SDS-IIA measurement phase, a total of 19 detector calibration measurements listed in Table 3.3 was performed with the $^{241}$Am source. During about 150 days of nearly continuous detector operation, the suite of regular calibrations was only interrupted by the 2.5-weeks Christmas break. Figure 3.17 gives an overview of the calibration stability over the course of SDS-IIA by displaying a pixel-wise comparison of the relative change of the position of the 59.54-keV $\gamma$-line between consecutive calibration runs. In the lower part of Figure 3.17, the detector temperature in terms of $T_{\text{carousel}}$ is shown over the course of SDS-IIA. Several features in Figure 3.17 are of interest:

- The majority of the detector channels shows only small variations of the peak position of less than 1% between consecutive calibrations, while some individual channels show fluctuations of up to more than 3%.
- After the 2.5-weeks Christmas break, where long-term background measurements but no regular calibration run was performed, no significant changes in the line positions

[10] Flicker noise is a type of electronic noise where the power spectral density in the frequency spectrum is inversely proportional to the frequency of the signal. It is characteristic for semiconductor devices.

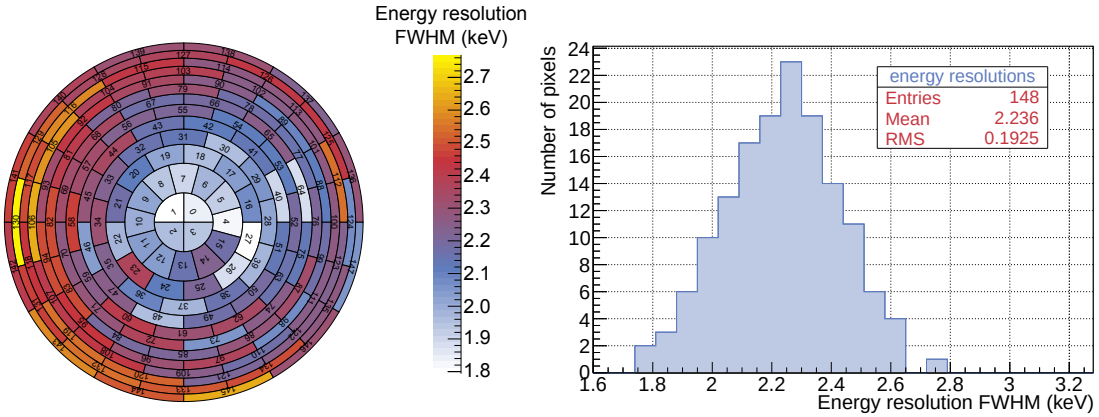


**Figure 3.16: Energy resolution of the individual detector pixels at the beginning of SDS-II. Left:** The energy resolution (FWHM) for the individual detector channels is determined via a Gaussian fit of the 59.54-keV $\gamma$-line in the $^{241}$Am energy spectrum. The resolutions are not randomly distributed across the wafer but show an increase to outer pixel rings. **Right:** The distribution of the energy resolutions of all 148 detector channels for 59.54-keV $\gamma$-photons is centered around 2.2 keV (FWHM) with a root-mean-square error (RMS) of 0.2 keV.

were observed.

- A temporary warm-up of the detector system from $-30$ to $-10\,^{\circ}$C around day 80, as well as a cool-down of the system from room-temperature to $-30\,^{\circ}$C around day 90, caused slight line shifts of all detector channels. The same effect was observed between day 120 and day 150 where a steady increase of the detector temperature resulted in a continuous shift of all line positions to higher ADC values with time, i.e. the center of the relative line position distributions is greater than zero for four consecutive calibration runs.
- Around day 114, several additional synchronization channels were installed at the backside of the detector DAQ rack. The calibration that was performed immediately afterwards shows a large shift of the line position of one channel of more than 5%.

From these observations it can be concluded that a 10-days interval of detector calibrations is sufficient to guarantee a stability on the 1%-level for the majority of the detector channels. Furthermore, mechanical works on the backside of the detector DAQ rack directly influence the line positions and require an immediate calibration afterwards. This fits to similar observations documented in [Ams15]. In addition, a drift of the detector operating temperature causes the line positions to shift, as described in detail in [Sch14c]. Nevertheless, the drifts between subsequent calibration runs observed during SDS-IIA are small enough to be neglected in the upcoming analyses in this thesis.

Figure 3.18 shows the same analysis as Figure 3.17 but this time focusing on the relative changes of the width of the 59.54-keV line, i.e. on the pixel-wise changes in energy resolution over the course of SDS-IIA. As in the case of the peak position, the resolution of the majority of the detector channels does not change significantly between consecutive calibration runs (<10%). Nevertheless, some channels show significant fluctuations of up to 70%. A fraction of these rather large relative changes can be attributed to an inaccuracy in the Gaussian fits of the 59.54-keV line at this point. Still, the detector region of interest (ROI) must be set sufficiently large, in order to reduce a systematic effect through such changes in resolution.

**Table 3.3: Summary of the detector calibration measurements during SDS-IIA.** A total of 19 calibration runs was performed over the course of about 150 days in regular intervals with a gap of 2.5 weeks during the 2014/2015-Christmas break. Additional calibrations were performed after hardware changes on the detector system (see additional notes).

| Date (dd.mm.yyyy) | Runs | Additional notes |
|---|---|---|
| 22.10.2014 | #20001 - #20006 | |
| 28.10.2014 | #20114 - #20117 | |
| 07.11.2014 | #20288 - #20291 | |
| 18.11.2014 | #20552 - #20555 | |
| 25.11.2014 | #20823 - #20826 | |
| 01.12.2014 | #20966 - #20971 | |
| 10.12.2014 | #21141 - #21144 | |
| 18.12.2014 | #21293 - #21296 | |
| 07.01.2015 | #21765 - #21768 | |
| 12.01.2015 | #21903 - #21906 | After a partial warm-up of the detector system. |
| 20.01.2015 | #21978 - #21985 | After the subsequent cool-down of the detector system. |
| 26.01.2015 | #22130 - #22137 | |
| 02.02.2015 | #22265 - #22268 | |
| 09.02.2015 | #22390 - #22393 | |
| 16.02.2015 | #22652 - #22653<br>#22673 - #22674 | After the installation of additional synchronization channels. |
| 24.02.2015 | #23082 - #23085 | Calibration with FPD magnets off. |
| 05.03.2015 | #23653 - #23654<br>#23656 - #23657 | |
| 16.03.2015 | #24098 - #24099<br>#24101 - #24102 | |
| 23.03.2015 | #24314 - #24315<br>#24317 - #24318 | |

### Detector Region of Interest

The detector ROI represents the accepted energy interval for signal electrons by the detector. Its central position is defined by the calculated incident energy $E_{\mathrm{inc}}$ of signal electrons on the detector. Its extension to lower and higher energies has to take into account the following issues: On the one hand, the measured energy resolution of the detector and energy-losses of electrons in its dead layer call for a sufficiently broad interval. On the other hand, a broad ROI will increase the contribution of the weakly energy-dependent intrinsic detector background (Sec. 3.8). To guarantee compatibility with the results of SDS-I, the same ROI has been chosen for the SDS-II measurements presented in this thesis. This ROI ranges from 3 keV below the $E_{\mathrm{inc}}$-peak to 2 keV above it. The position of the $E_{\mathrm{inc}}$-peak in the detector energy spectrum is given by

$$E_{\mathrm{inc}} = -e \cdot (U_0 - U_{\mathrm{PAE}} - U_{\mathrm{bias}}) \quad . \tag{3.2}$$

Here, $U_0$ is the (negative) retarding potential in the analyzing plane of the spectrometer (Sec. 3.1), $U_{\mathrm{PAE}}$ gives the (positive) post-acceleration potential, and $U_{\mathrm{bias}} = +120\,\mathrm{V}$ corresponds to the detector bias voltage. With the nominal SDS-II retarding potential of $U_0 = -18.6\,\mathrm{kV}$ and $U_{\mathrm{PAE}} = +10\,\mathrm{kV}$, the $E_{\mathrm{inc}}$ peak is located at 28.72 keV and the detector

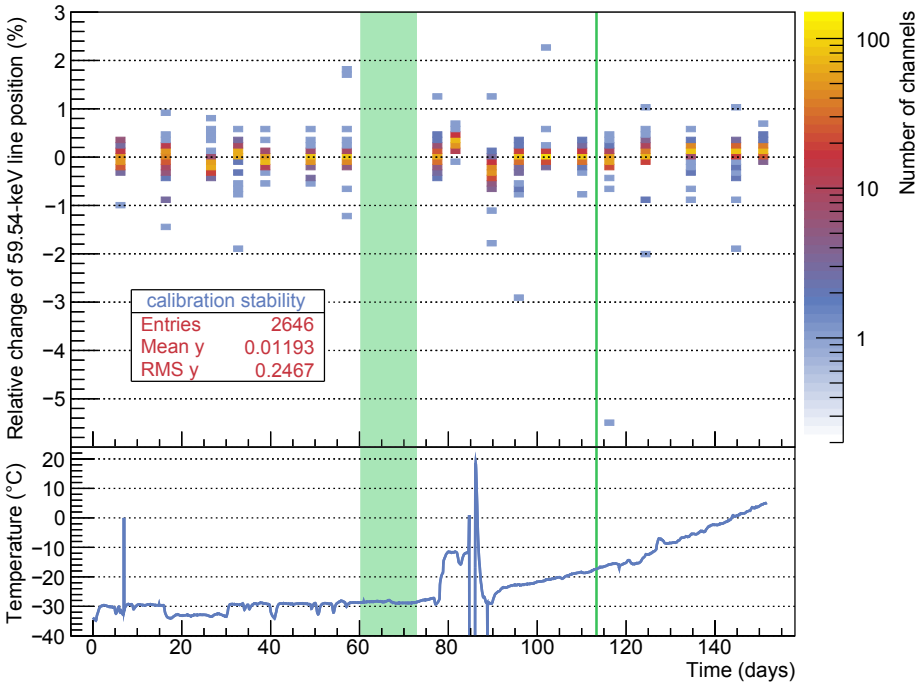


**Figure 3.17: Stability of the detector calibration over the course of SDS-IIA.** The relative deviations of the positions of the 59.54-keV $^{241}$Am $\gamma$-line in the ADC-spectrum of the detector is shown for all calibrated channels and for 18 of the 19 calibration measurements performed over the course of SDS-IIA. The first calibration is excluded as no relative changes can be stated here. The green box marks the two-weeks Christmas break during which no calibration was performed. The green line marks the installation of several additional synchronization channels to the detector DAQ rack. The lower graph shows the temperature of the detector electronics ($T_{\mathrm{carousel}}$) over the course of SDS-IIA. After a temporary warm-up of the detector around day 80 and the subsequent cool-down, $T_{\mathrm{carousel}}$ continuously increased.

ROI ranges from 25.72-30.72 keV. However, several key measurements presented in the context of this thesis were taken at non-standard potential configurations. To ensure an equivalent shift of the detector ROI in the analysis of such measurements, an automated readout of the relevant potentials via the Slow Control database is used in most of the cases. According to [Sch15b], the large spread of energy resolutions per detector pixel, ranging from about 1.8 keV in the wafer center to about 2.8 keV for some pixel on the outer detector rings, results in a spread of the ratio of events in the ROI to the total event rate per pixel of less than 6%. This small systematic effect was not taken into account in the analyses presented later in this thesis. In the final neutrino-mass measurements with KATRIN, however, the ROI must be defined on a pixel-by-pixel basis in order to prevent such systematic effects. Moreover, it is strongly recommended to exchange the currently installed detector wafer after the end of SDS-IIB with one that provides 100% functional channels and an energy resolution comparable to that of the SDS-I campaign.

## 3.8 Intrinsic Detector Background

The KATRIN focal-plane detector system is designed for high efficiency in electron-counting, whilst at the same time providing a low intrinsic background contribution of less than 1 mcps in the ROI of the final neutrino-mass measurements. To achieve this ambitious goal, all materials that are used in the setup of the FPD were pre-selected with respect to low intrinsic radioactivity. Furthermore, the detector wafer is surrounded by low-activity copper and lead shielding against environmental radiation. Both passive elements are installed inside the warm bore of the detector magnet. An additional muon-veto system,

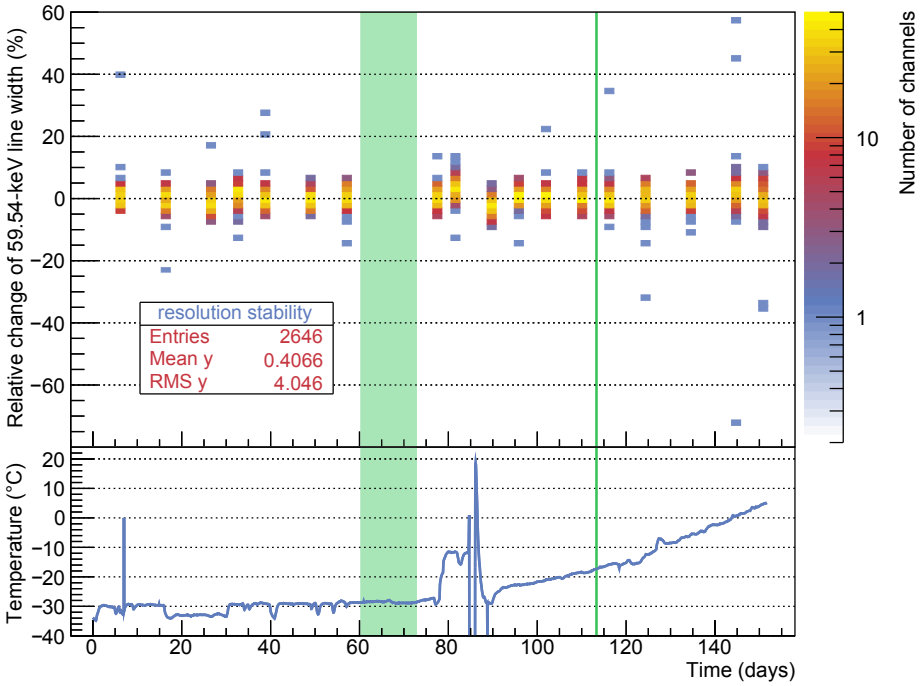


**Figure 3.18: Stability of the detector energy resolution over the course of SDS-IIA.** The relative deviations of the widths of the 59.54-keV $^{241}$Am $\gamma$-line in the ADC-spectrum of the detector is shown for all calibrated channels and for 18 of the 19 calibration measurements performed over the course of SDS-IIA. The first calibration is excluded as no relative changes can be stated here. The green box marks the two-weeks Christmas break during which no calibration was performed. The green line marks the installation of several additional synchronization channels to the detector DAQ rack. The lower graph shows the temperature of the detector electronics ($T_{\text{carousel}}$) over the course of SDS-IIA. After a temporary warm-up of the detector around day 80 and the subsequent cool-down, $T_{\text{carousel}}$ continuously increased.

based on scintillator panels that surround the passive shields, allows to actively tag events which are induced by cosmic muons passing through the system [Ams15].

Compared to the spectrometer-related backgrounds which are discussed in detail in the following chapters of this thesis, the contribution of the intrinsic background from the FPD to the total background rate in the ROI is relatively small. Figure 3.19 shows the global energy spectrum of the background measured with 148 pixels over the course of 222.5 hours (Runs #20292 - #20451 and #20556 - #20619) at the beginning of SDS-II. These measurements were carried out with the gate valve to the main spectrometer closed, to mechanically separate the two systems. As the detector wafer in this case directly 'looks' onto the metal surface of the closed valve, a non-zero post-acceleration potential will accelerate low-energy electrons emitted from the metal surface onto the detector. According to [Sch14c], this results in an additional background contribution in terms of peaks at multiples of $e \cdot U_{\text{PAE}}$ in the energy spectrum. In order to prevent these artifacts, the measurements of the intrinsic detector background were carried out with zero post-acceleration potential. In the relevant energy range from 10-120 keV, the background energy spectrum of the detector is anyways dominated by fluorescence light emitted from materials that surround the wafer. It is, thus, in first approximation independent of the potential that is applied to the PAE.

The emission of the fluorescence light is induced by environmental and intrinsic radiation as well as cosmic-rays [Leb10]. Below 10 keV, the detector background spectrum features three prominent fluorescence lines from decays in the copper PAE. These lines appear as single broad peak in the measured spectrum due to the limited energy resolution of

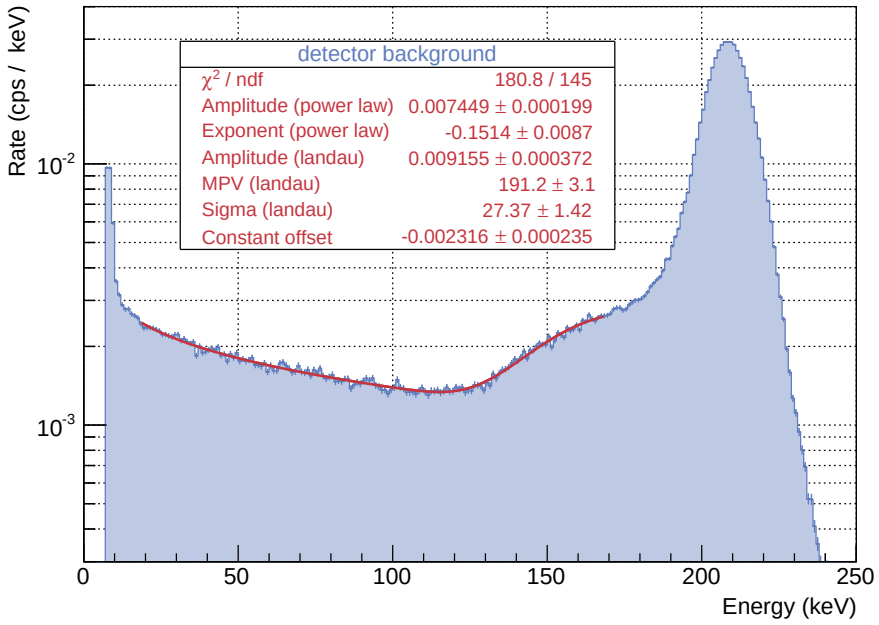


**Figure 3.19: Energy spectrum of the detector background** in the energy range between 7 keV and 250 keV. The electronic noise shoulder below 7 keV is cut off. Apart from a single peak around 8 keV, induced by fluorescence lines of copper, the spectrum follows a power-law like distribution in the relevant energy range up to 120 keV. The high-energy part of the spectrum above 120 keV is dominated by the Landau distribution of the energy-loss fluctuations of ionizing charged particles that pass directly through the thin detector wafer. The most energetic ones of these events end up in the overflow bin of the detector DAQ which, due to baseline fluctuations, appears as a broad peak around 210 keV. More details are given in the text.

the detector. Above 120 keV, the detector background is no longer dominated by X-ray photons but by energy losses of minimum-ionizing muons from cosmic-rays that directly pass through the detector wafer. Here the energy spectrum follows the characteristic Landau distribution for energy-loss fluctuations of ionizing charged particles in a thin layer of matter [Lan44]. Around about 210 keV the overflow events that exceed the upper accepted signal height of the detector DAQ appear as a Gaussian peak due to baseline fluctuations from channel to channel [Sch14c]. Within the standard SDS-II ROI the intrinsic detector background contribution is about 2 $^{\text{mcps}}/_{\text{keV}}$. Due to hardware issues, the muon veto of the FPD system, which allows to actively remove background events that are identified as cosmic-ray induced, was not used during SDS-II. Furthermore, a so-called multi-pixel cut, where events that appear with interarrival times of less than 2 µs on the detector are identified as false signals due to charge-sharing and cross-talk effects, is not used in the analyses presented in this thesis. These two additional background cuts allow to further reduce the FPD intrinsic background in the ROI by about 50% to the 1-$^{\text{mcps}}/_{\text{keV}}$ regime, as described in detail in [Sch14c]. During SDS-II the corresponding total detector background rate in the standard ROI between 25.72 keV and 30.72 keV is derived to

$$B_{\text{FPD}} = 11.0 \pm 0.1\,\text{mcps} \quad . \tag{3.3}$$

This is still small compared to the main spectrometer background contributions presented later. Figure 3.20 shows the pixel-wise intrinsic detector background rate on the left and the background rate per detector ring on the right side, both limited to events within the standard ROI. As all detector pixels have the same sensitive area, the innermost detector ring with only four segments (bullseye) sees a rate which is smaller by a factor of about 3

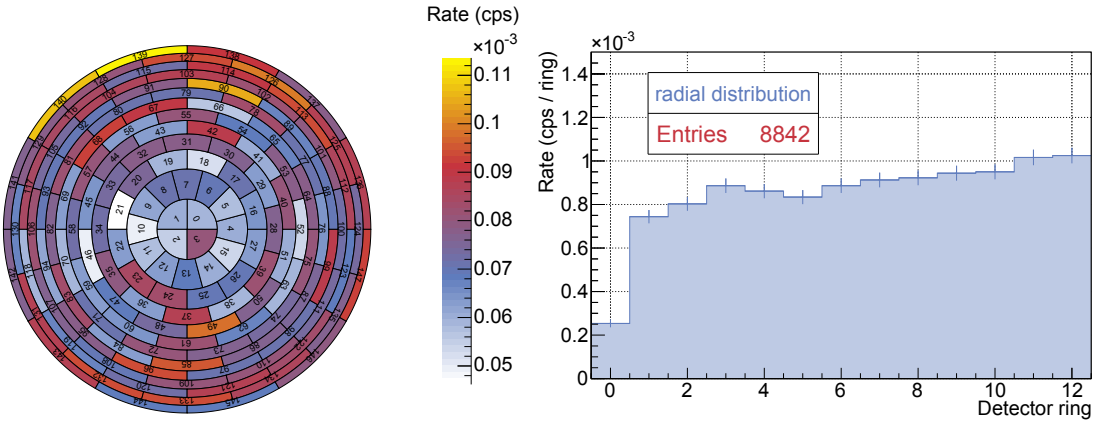


**Figure 3.20: Event pattern of the detector background in the SDS-II region of interest. Left:** The background rates in the standard SDS-II ROI between 25.72 keV and 30.72 keV are shown per pixel. **Right:** The background rate per detector ring shows a slight increase to outer rings. Note that ring 0 has only four segments and therefore observes a reduced rate.

compared to the other rings with 12 segments each. Additionally, a small increase of the FPD background to outer rings is observed which can either be explained by background entering the flux tube volume from the outside or by the slightly larger flux tube volumes inside the FPD system that are observed by the outer detector rings. More details about the intrinsic detector background can be found in [Ams15, Sch14c], while detailed MC-simulations concerning this topic are presented in [Leb10].

## 3.9 The Beamline Alignment

The spatial resolution of the FPD was severely impacted during the SDS-I campaign, where 22 detector channels could not be used in the analysis due to shadowing effects. This shadowing, where mechanical parts along the SDS beamline like the main spectrometer ground electrode, the flapper valve, or the upstream part of the PAE blocked parts of the sensitive flux tube, was caused by non-negligible misalignments along the SDS beam tube. These occurred during the complex mechanical connection procedure of the FPD system to the main spectrometer. In particular, the limited mechanical flexibility of the beamline between the two systems, that houses the in-line flapper valve, was identified as main cause of the misalignments [Sch14c]. Furthermore, the reduced magnetic field strength of the pinch magnet during SDS-I of $B_{\mathrm{PCH}}^{\mathrm{SDS\text{-}I}} = 5\,\mathrm{T}$ compared to the field of the detector magnet of $B_{\mathrm{DET}}^{\mathrm{SDS\text{-}I}} = 3.5\,\mathrm{T}$ resulted in an increase of the dimensions of the observed flux tube within the FPD system and increased the shadowing.

In preparation for the second commissioning phase SDS-II, several measures were carried out in the context of this thesis in order to guarantee a sufficient alignment along the SDS beamline as well as the usability of all 148 detector channels in the analysis. In the following, the most critical measures are listed:

- The beamline between the main spectrometer and the FPD system which houses the in-line flapper valve has been equipped with a second bellow in order to increase its flexibility during the connection process of the two systems. Nevertheless, as discussed in Section 3.2, the flapper valve could only be used in the second part of the commissioning measurements (SDS-IIB), whereas a replacement beam pipe, likewise equipped with two bellows, was used during SDS-IIA.
- During SDS-IIA, the pinch magnet could still only be operated at a reduced field strength of $B_{\mathrm{PCH}}^{\mathrm{SDS\text{-}IIA}} = 5\,\mathrm{T}$. In order to keep the ratio $B_{\mathrm{PCH}}/B_{\mathrm{DET}}$ and, thus, the

**Table 3.4: Deviation of the sub-components of the FPD system from their design positions during SDS-IIA.** The tilts of the components are given in Euler angles ($x$-convention) where the third Euler angle is given by $\gamma = -\alpha$ due to the axial symmetry of the components. For the PAE the same tilt as in [Sch14c] has been assumed while an axial shift of the pinch-magnet coil against its cryostat of 3.6 mm, found in [Mue14a], is taken into account as well.

| Component | $\Delta x$ (mm) | $\Delta y$ (mm) | $\Delta z$ (mm) | $\alpha$ (°) | $\beta$ (°) |
|---|---|---|---|---|---|
| Pinch magnet cryostat | 0.1 | −0.1 | −1.4 | −13.99 | −0.04 |
| Pinch magnet coil | 0.0 | 0.0 | 3.6 | 0.0 | 0.0 |
| Detector magnet cryostat | 0.0 | −0.5 | 1.6 | −51.35 | 0.06 |
| Vacuum chamber | −0.6 | 0.3 | 8.5 | −88.35 | 0.04 |
| Post-acceleration electrode | 0.0 | 0.0 | 0.0 | −86.82 | −0.115 |

dimensions of the observed flux tube in the FPD system similar to the design value of 5/3, the detector magnet was operated at a reduced field of $B_{\mathrm{DET}}^{\mathrm{SDS\text{-}IIA}} = 3\,\mathrm{T}$ during SDS-IIA.

- To further strengthen the mechanical stability of the FPD system against the vacuum forces of the main spectrometer, additional bracing hardware has been designed and installed to the system prior to the main spectrometer pump-out.
- The alignment and connection procedure of the FPD system to the main spectrometer has been refined and, where possible, simplified in order to make the process of connecting the two systems less challenging.
- The geometries of the detector system, the revised in-line flapper valve, as well as the replacement beam pipe have been implemented in detail into KASSIOPEIA [FG15] in order to allow for precise alignment simulations of the whole SDS apparatus.

**Alignment of the FPD Sub-Components during SDS-IIA**

With the connection of the detector system to the main spectrometer established, a *FaroArm*[11] [Far14] system was used to measure the positions and tilts of the pinch and detector magnet cryostats as well as of the FPD vacuum chamber relative to the main spectrometer axis in a similar approach as in [Sch14c]. The resulting deviations relative to the design positions are given in Table 3.4 and are visualized in Figure 3.21. An intrinsic misalignment of the PAE that was found in [Sch14c], and a shift of the pinch-magnet coil against its cryostat, identified in [Mue14a], are taken into account. All alignment results are given in the KATRIN coordinate system where the $z$-axis corresponds to the spectrometer axis looking downstream (north), the $y$-axis points towards the top, and the positive $x$-axis points to the west.

Of all sub-components, the vacuum chamber shows the largest deviation from the spectrometer axis in the $z$-$x$-plane of more than 1 mm on its downstream side. However, this misalignment is intended in order to compensate an intrinsic tilt of the PAE and to position the detector wafer close to the spectrometer axis. All other components show radial deviations of less than 1 mm, which is more than sufficient and at the limit of the achievable accuracy. In axial direction the sub-components show large deviations from their design positions of up to 8.5 mm in the case of the detector vacuum chamber, or 3.6 mm for the pinch magnet cryostat. In difference to the radial displacements, these axial misalignments are not of major concern. In the case of the pinch magnet, the shift of the magnets coil against the cryostat partly compensates the shift of the latter against its design position.

[11] A portable coordinate measuring machine.

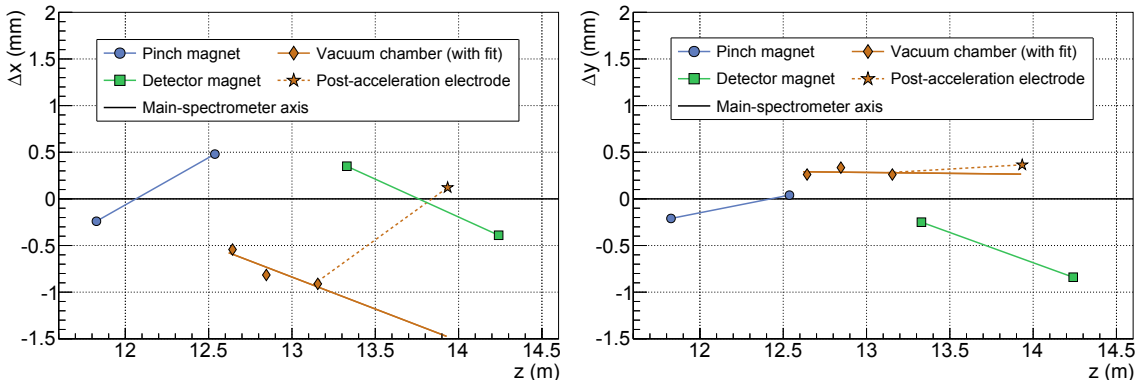


**Figure 3.21: Measured displacement of the detector subcomponents previous to SDS-IIA.** The displacements of the pinch magnet (blue dots), the detector magnet (green squares), and the detector vacuum system (orange rhombs) against the main-spectrometer axis (black line) are shown in the $z$-$x$-plane (left) and the $z$-$y$-plane (right). An intrinsic tilt of the PAE against the detector vacuum chamber is taken into account (orange dashed line) and the wafer position is indicated by an orange star. Figure inspired by [Sch14c].

Furthermore, the large shift of the vacuum chamber in downstream direction is required by the increased length of the replacement beam pipe compared to the standard beam tube with the flapper valve. As the magnetic field inside the warm bore of the detector magnet is relatively constant, a shift of the detector wafer by a few mm does not significantly change the magnetic-field strength at the wafer position, i.e. the dimensions of the observed flux tube.

The deviations of the positions of the FPD sub-components that are listed in Table 3.4 are implemented into the revised detector geometries in KASSIOPEIA and are used to simulate the observed magnetic flux tube inside the detector system and the replacement beam pipe. The results are displayed in Figure 3.22 for the $z$-$x$- and the $z$-$y$-plane. The outermost field lines (orange) form the envelope of the total flux tube that is observed by the detector and must be transported undisturbed through the beamline. In both, the $z$-$x$- and the $z$-$y$-plane, two bottlenecks for the flux tube are found: firstly, the ground electrode of the main spectrometer at $z \approx 11.8\,\mathrm{m}$ and secondly the upstream end of the PAE at $z \approx 13.2\,\mathrm{m}$, where the flux tube at positive $x$- and $y$-coordinates barely fits through the detector geometry. Nevertheless, based on the alignment-measurement results listed in Table 3.4 and the corresponding field-line simulations it can be concluded that, in difference to the SDS-I measurement phase, none of the 148 detector pixels is affected by a shadowing effect in SDS-IIA. During the course of the SDS-IIA data-taking no contrary observations were made.

### Alignment of the FPD Sub-Components during SDS-IIB

Prior to the second part of the SDS-II measurement phase, three significant hardware changes concerning the overall system alignment were made:

- The old pinch magnet that had to be operated at a reduced magnetic-field strength of 5 T during SDS-I and SDS-IIA was replaced by a new magnet (Sec. 3.1). This allows for an operation of the two magnets at their nominal fields of 6 T and 3.6 T.
- The detector system was mechanically decoupled from the main spectrometer and the replacement beam pipe was exchanged with the original beamline including the in-line flapper valve.
- The PS1 magnet was moved to its design position, about 1 m further upstream than during SDS-IIA.

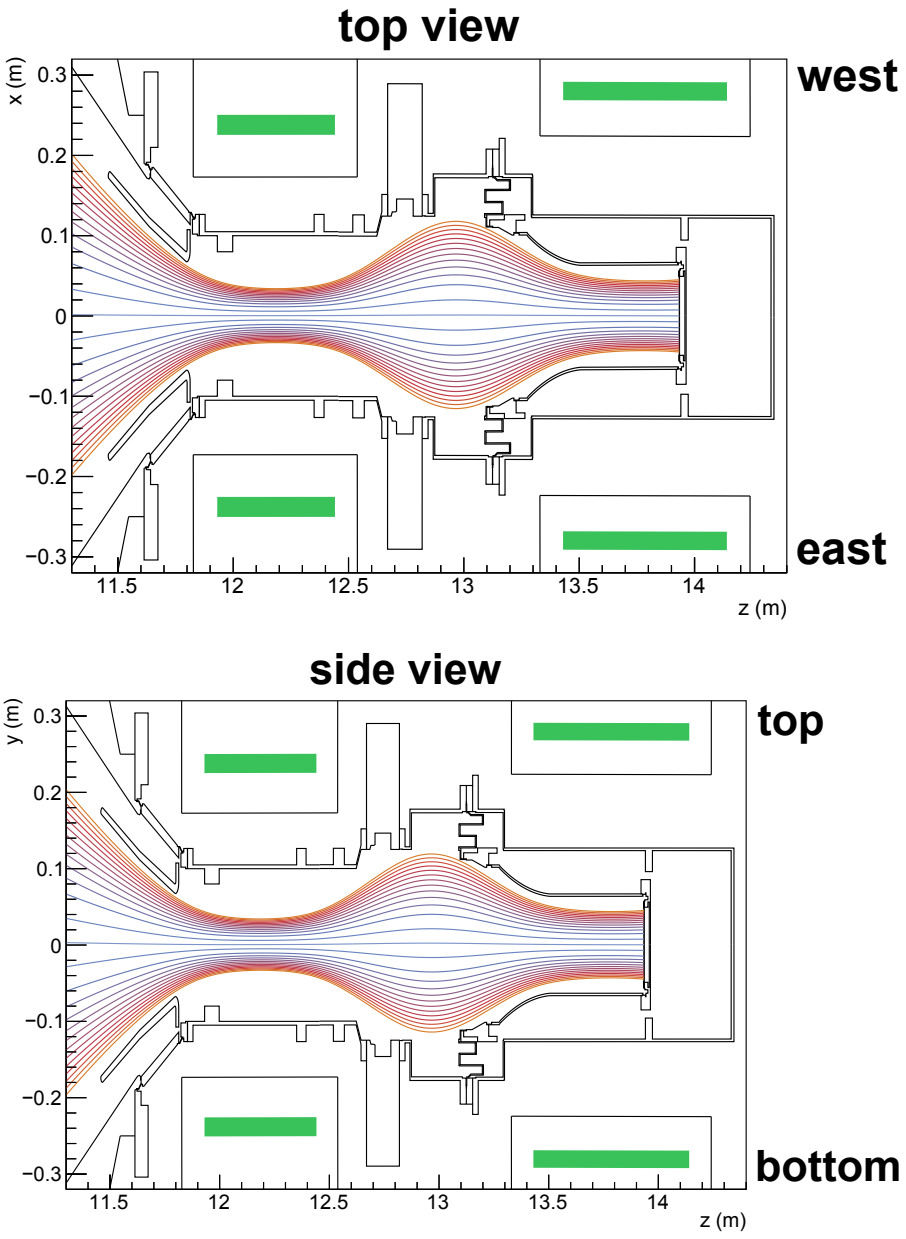


**Figure 3.22: Simulation of the magnetic field lines inside the FPD system including the replacement beam pipe during SDS-IIA** with the use of the KASSIOPEIA simulation framework [FG15]. The pinch magnet (detector magnet) is set to 5 T (3 T). The measured misalignments of the detector sub-components, as stated in Table 3.4, are taken into account. Each magnetic field line corresponds to a ring boundary on the detector wafer, located at $z \approx 13.9\,\mathrm{m}$, i.e. the innermost field line (blue) ends on the center of the detector wafer while the outermost (orange) field lines correspond to the outer ends of the sensitive wafer area at $r = 0.045\,\mathrm{m}$. The coils of the superconducting pinch magnet (left) and detector magnet (right) are shown as green bars.

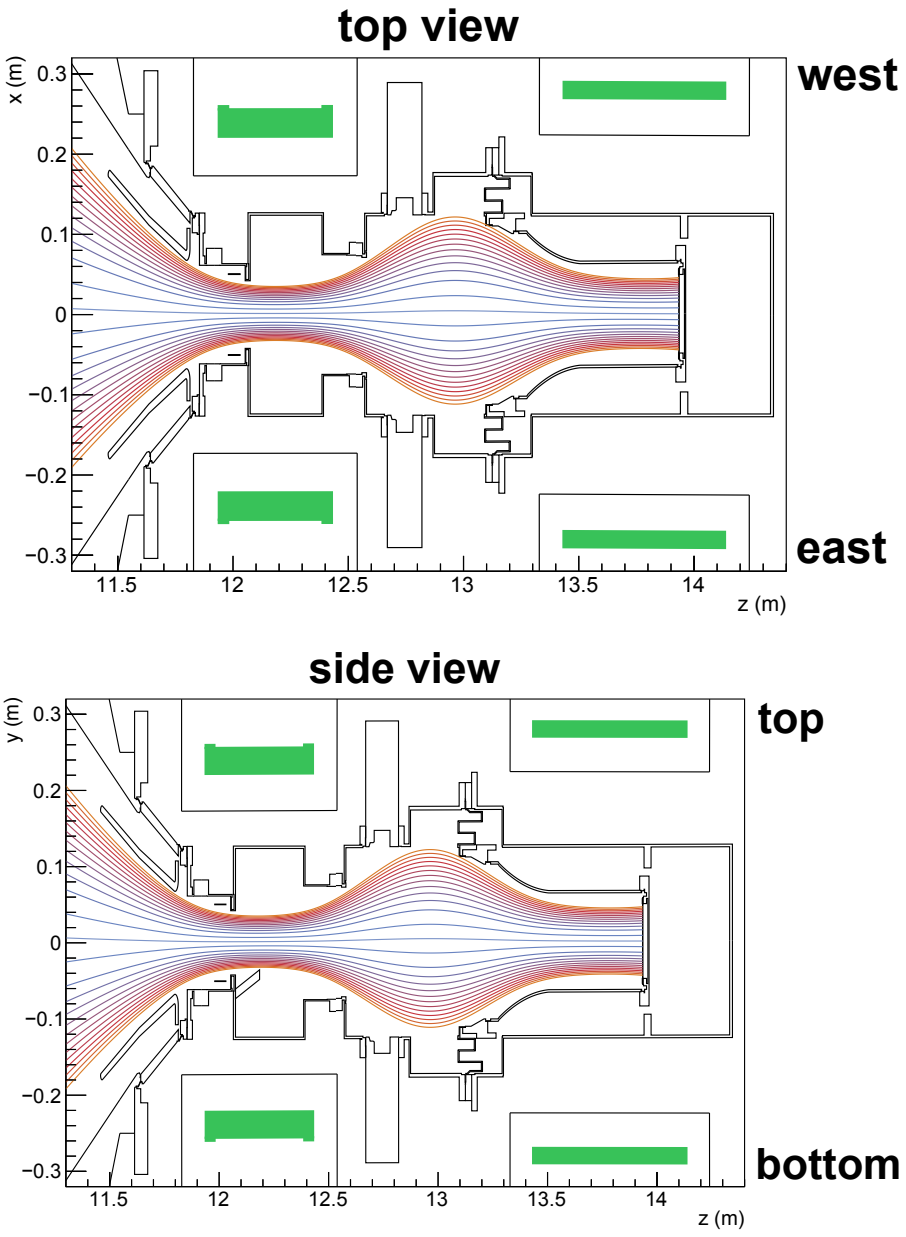


**Figure 3.23: Simulation of the magnetic field lines inside the FPD system including the in-line flapper valve during SDS-IIB** with the use of the KASSIOPEIA simulation framework [FG15]. The pinch magnet (detector magnet) is set to 6 T (3.6 T). The measured misalignments of the detector sub-components during SDS-IIB, as stated in Table 3.5, are taken into account. Each magnetic field line corresponds to a ring boundary on the detector wafer that is located at $z \approx 13.9\,\mathrm{m}$, i.e. the innermost field line (blue) ends on the center of the detector wafer while the outermost (orange) field lines correspond to the outer ends of the sensitive wafer area at $r = 0.045\,\mathrm{m}$. The coils of the superconducting pinch (left) and detector magnet (right) are shown as green bars.

**Table 3.5: Deviation of the sub-components of the FPD system from their design positions during SDS-IIB.** The tilts of the components are given in Euler angles ($x$-convention) where the third Euler angle is given by $\gamma = -\alpha$ due to the axial symmetry of the components. For the PAE the same tilt as in [Sch14c] has been assumed.

| Component | $\Delta x$ (mm) | $\Delta y$ (mm) | $\Delta z$ (mm) | $\alpha$ (°) | $\beta$ (°) |
|---|---|---|---|---|---|
| Pinch magnet cryostat | 0.0 | 0.3 | 0.4 | −11.78 | −0.08 |
| Detector magnet cryostat | −0.5 | 0.6 | 1.1 | −74.94 | 0.08 |
| Vacuum chamber | −0.6 | 1.2 | 8.6 | 0.07 | −0.05 |
| Post-acceleration electrode | 0.0 | 0.0 | 0.0 | −86.82 | −0.115 |

While the first two changes significantly influence the flux tube clearances in the FPD system, the latter is of minor importance here.

Figure 3.23 shows a similar simulation as the one in Figure 3.22, this time for the SDS-IIB hardware configuration with the in-line flapper valve installed, the pinch and detector magnets at nominal fields of 6 T and 3.6 T, and the new pinch magnet geometry implemented into KASSIOPEIA. Furthermore, the deviations of the detector sub-components from their design positions during SDS-IIB, that were measured with the *FaroArm* and are listed in Table 3.5, are taken into account. Besides the two bottlenecks for the flux tube that were already present during SDS-IIA, the in-line flapper valve, located at $z \approx 12.2\,\mathrm{m}$, represents a third shortage for the flux tube. However, in contrast to SDS-I, where this valve caused a severe shadowing of pixels [Sch14c], there is just enough clearance during SDS-IIB for the observed flux tube to fit through. Still, due to the slightly changed mechanical orientations of the FPD sub-components compared to the SDS-IIA case, the field lines from the outermost detector ring now barely touch the upstream part of the PAE at positive $x$- and $y$-coordinates. This can cause background electrons, generated e.g. by cosmic muons, to be guided by the magnetic field lines from this inner surface to the outer rings of the detector wafer. However, as these electrons originate from the detector system, they are not accelerated by the retarding potential of the spectrometer and have therefore energies well outside the standard ROI.

**Alignment Measurements at 'Asymmetric' Magnetic-Field Configurations**

Besides a mechanical blocking inside the FPD vacuum chamber, also the alignment of the observed flux tube relative to the main spectrometer geometry is of key interest for the studies in this work. In [Sch14c] it has been shown that low-energy electrons emitted from the inner electrode comb structures can be used to map these structures onto the detector wafer. Thus, a similar measurement approach has been used at the beginning of SDS-IIA to investigate the alignment between the magnetic flux tube that is observed by the detector and the inner electrode system of the spectrometer. In difference to the main spectrometer vessel, that shows deviations in radius of more than 1 cm due to thermal expansions during the welding process [Jur08, Cor14], the alignment of the individual wire modules of the inner electrode system to the spectrometer beamline was verified via laser tracker measurements to $\leq 1\,\mathrm{mm}$ accuracy [Jur09, Hil11].

The mapping of the comb structures on the detector is realized by an 'asymmetric' magnetic field configuration in the main spectrometer with the currents of the superconducting solenoids and air coils set according to configuration A1 in Table 3.1. The corresponding (simulated) field lines in the main spectrometer are given in the top part of Figure 3.24 with the relevant comb structures marked by black dashed circles. In a second simulation, electrons are started uniformly on these comb structures and are tracked to the detector. The mean of the endpoints of all simulated tracks on the detector is calculated to $\Delta x_{\mathrm{sim}} = -0.34\,\mathrm{mm}$ and $\Delta y_{\mathrm{sim}} = -0.84\,\mathrm{mm}$.

At the right bottom of Figure 3.24, the results of a two-hour data set (runs #20102 - #20103) with the main spectrometer vessel grounded ($U_{\text{vessel}} = 0\,\text{V}$), an inner electrode offset potential of $U_{\text{IE,common}} = -300\,\text{V}$, and the same magnetic-field setting as used in the previous simulations (setting A1) is shown. Here, the PAE potential was set to $U_{\text{PAE}} = +10\,\text{kV}$ in order to lift the electrons that come from the spectrometer energetically above the detector noise threshold. Two ring-shaped patterns are found in the data within the ROI from 7.42 keV to 12.42 keV. With the use of a ring-fit algorithm, provided by the KATRIN analysis framework BEANS, the offsets of the ring centers compared to the wafer center are determined to

$$\Delta x_{\text{inner}} = 2.125\,\text{mm} \quad \Delta y_{\text{inner}} = -2.625\,\text{mm} \tag{3.4}$$

$$\Delta x_{\text{outer}} = 1.375\,\text{mm} \quad \Delta y_{\text{outer}} = -1.625\,\text{mm} \quad , \tag{3.5}$$

and are marked by two black dots. Compared to the simulation result (green dot), both ring offsets are slightly shifted to the lower right corner. Nevertheless, with the uncertainty of the ring-fit algorithm of about 1 mm and the uncertainties of the alignment measurements with the *FaroArm*, the measurement and the simulation are in good agreement. Furthermore, a detailed study of the EMCS currents that are needed to fully compensate the earth magnetic field inside the main spectrometer, which was carried out in [Erh15], has shown that the standard EMCS currents of 50 A (vertical) and 9 A (horizontal) cause a small distortion of the magnetic flux tube in the main spectrometer. This distortion can explain parts of the misalignments given in Equations 3.4 and 3.5. In the same work, the alignment of the pre-spectrometer magnets and the angular-selective electron gun on the upstream side of the spectrometer is discussed in detail. However, the small misalignments of these components are of no significance for the analyses presented in the context of this thesis.

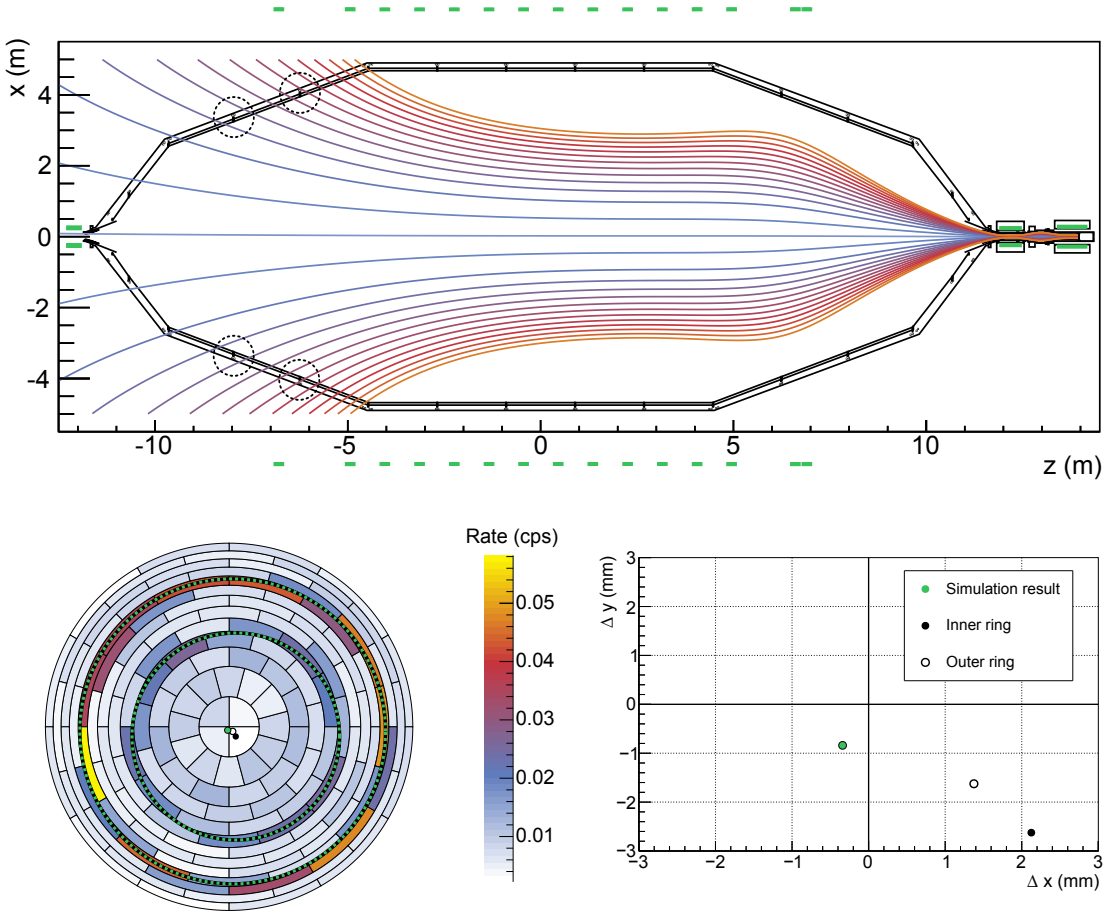


**Figure 3.24: Imaging of inner-electrode comb structures onto the detector during measurements at 'asymmetric' magnetic-field settings. Top:** Simulation of the magnetic field lines inside the spectrometer with KASSIOPEIA [FG15] for the magnetic field setting A1 listed in Table 3.1. The misalignments of the detector sub-components listed in Table 3.4 are taken into account and the comb structures of the inner electrode, from where electrons are emitted, are marked by dashed black circles. **Bottom left:** The results of the measurements that were performed during SDS-IIA at the magnetic-field configuration A1. The center point of the fit of the inner (outer) ring structure is marked by a solid black dot (black circle). In addition, the mean position of the endpoints of simulated tracks of electrons that are started at the comb structures and tracked onto the detector is marked with a green dot. **Bottom Right:** The same results as in the plot on the left-hand side, this time in a zoomed-in representation and with mm-scales shown.

CHAPTER 4

# Radon-Induced Background

Extensive background measurements at the KATRIN pre-spectrometer in 2009 and 2010 have revealed a previously unknown background contribution due to electrons originating from radioactive decays of specific radon isotopes inside the spectrometer volume. These electrons with energies from the few eV up to the multi-keV scale are stored due to the specific characteristics of a MAC-E filter, generating background events by ionizing residual gas [Fra10, Goe10, Fra11, Mer12a, Wan13a, Wan13b, Mer13]. During the first main spectrometer commissioning phase SDS-I in 2013, great efforts were made in order to investigate the contribution of this radon-induced events to the overall spectrometer background. In this context, various measurement and analysis techniques have been developed and refined, demonstrating that radon-induced backgrounds can be identified with high efficiency [Sch14c], as well as the feasibility of passive countermeasures employing $LN_2$-cooled copper baffles inside the main spectrometer [Goe14]. Due to hardware limitations at that time, conclusive statements concerning the radon-induced background level at standard measurement configurations as well as the sources of radon emanation inside the spectrometer, could not be made in the course of the SDS-I measurements.

Based on the recent hardware improvements of the SDS apparatus, described in Chapter 3, a series of radon background measurements was carried out during the second main spectrometer commissioning phase SDS-IIA in the context of this thesis. Based on the detailed model of the radon-induced background at KATRIN (Sec. 4.1), the existing measurement and analysis techniques have been further refined and significantly improved (Sec. 4.2) to conclusively determine the contribution of radon-induced events to the total spectrometer background (Sec. 4.3). Furthermore, comparisons of the SDS-I and SDS-IIA results as well as MC-based vacuum simulations of the effectiveness of the baffle system are used to establish a concise model of the radon sources inside the main spectrometer (Sec. 4.4), before final conclusions and recommendations are given (Sec. 4.5).

## 4.1 Radon in the KATRIN Main Spectrometer

As part of the primordial decay chains of $^{235}$U, $^{232}$Th, and $^{238}$U, the naturally occurring radon isotopes $^{219}$Rn,$^{220}$Rn, and $^{222}$Rn are one of the largest contributers to the worldwide background-radiation dose. In astroparticle physics, the isotope $^{222}$Rn represent a major background source in low-background experiments, such as GERDA [Sim06] or BOREXINO [Sim03]. At the KATRIN main spectrometer two radon isotopes and emanation sources are of concern. Firstly, radon atoms can emanate from the large stainless-steel surface of the vessel ($690\,\mathrm{m}^2$), the inner electrode, and auxiliary equipment installed in the system. Secondly, the NEG material, which has been installed in large quantities (60 kg) inside the spectrometer to achieve the UHV conditions of $p \leq 10^{-11}$ mbar, is a known source

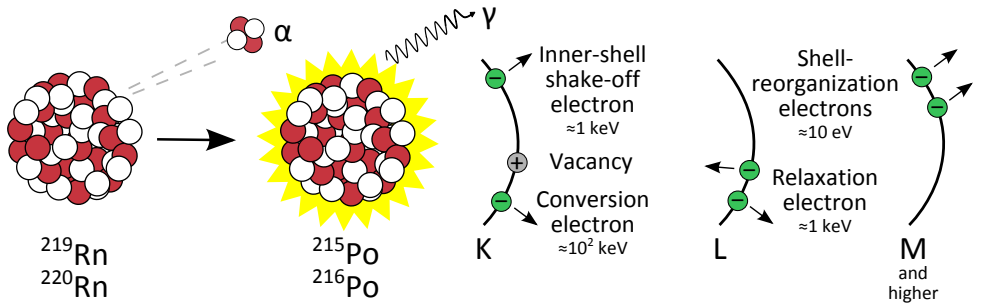


**Figure 4.1: Illustration of the electron-emission processes following radon α-decays.** Non-equilibrium decay chains of $^{235}$U and $^{232}$Th lead to the emanation of the short-lived radon isotopes $^{219}$Rn and $^{220}$Rn inside the KATRIN main spectrometer. The $\alpha$-decay into an excited state of $^{215}$Po$^*$ or $^{216}$Po$^*$ is accompanied by the emission of up to 20 electrons due to shake-off, internal conversion (mainly $^{219}$Rn), and subsequent shell relaxation processes. The stated electron energies are approximated-average values. Sketch adapted from [Sch14c].

of radon emanation. As low-level $\gamma$-measurements have shown, the $^{220}$Rn contribution from the NEG material is at least two orders of magnitude smaller than the contribution from $^{219}$Rn so that this isotope can be neglected there [Fra10]. The propagation of neutral noble gases such as radon isotopes in a UHV environment is not influenced by the electromagnetic fields, so they will enter the active flux volume of the spectrometer undisturbed. As a result, the short-lived isotopes $^{219}$Rn ($t_{1/2} = 3.96\,\mathrm{s}$) and $^{220}$Rn ($t_{1/2} = 55.6\,\mathrm{s}$) will decay homogeneously distributed in the spectrometer via $\alpha$-decays into $^{215}$Po and $^{216}$Po. In contrast, the probability for the long-lived isotope $^{222}$Rn ($t_{1/2} = 3.82\,\mathrm{d}$) to decay inside the spectrometer volume is rather small as it will efficiently be pumped-out with an average pump-out time of $t_{\mathrm{MS}} \approx 360\,\mathrm{s}$ well before it can decay. The decay of $^{222}$Rn can therefore be neglected at this point. Interestingly, it still affects the background level of KATRIN indirectly as it will be shown in Chapter 5.

### 4.1.1 Electron-Emission Accompanying Radon α-Decays

Neither the heavy $\alpha$-particles nor possible fluorescence photons generated in the radon decays are of concern for the background studies with the main spectrometer, as both particle types do not follow the magnetic-field lines to the detector but instead will hit the inner surfaces of the spectrometer rather than generating background. However, disturbances of the atomic shell during the $\alpha$-decay in an UHV environment can cause the emission of up to 20 electrons with energies in the eV to keV range through several atomic processes (see Fig. 4.1):

- **Internal Conversion:** In the case of $^{219}$Rn, 20.6% of the $\alpha$-decays leave the daughter nucleus in an excited state $^{215}$Po*. The subsequent transition of the excited level to the ground state can either take place via radiative processes or by the emission of an internal-conversion electron. In the latter case, the excited nucleus interacts electromagnetically with an inner-shell electron which in the specific case of $^{215}$Po* subsequently leaves the atom with energies in the range from 40 - 500 keV. The total probability for internal-conversion processes, following the $\alpha$-decay of $^{219}$Rn, sum up to 3.3%, whereas the probability for an internal conversion of the daughter nucleus of $^{220}$Rn is insignificantly small.

- **Inner-shell Shake-off:** The outgoing $\alpha$-particle can interact with an inner-shell electron via the Coulomb field, sharing some of its decay energy to eject the electron into the continuum (shake-off) or to lift it into a higher shell (shake-up). The typical energies of shake-off electrons are in the same range as the binding energy of the

electrons in the atomic shell, resulting in a continuous energy spectrum with an endpoint at some tens of keV.

- **Atomic Relaxation:** The emission of a conversion or shake-off electron will leave a vacancy in one of the inner shells of the atom and, therefore, causes a series of radiative (fluorescence) and non-radiative transitions. In the latter case, electrons from higher (sub-)shells will fill the vacancy, thereby transferring the released binding energy to a second shell electron that is subsequently emitted. These transitions can be split into two classes. If the vacancy is filled by an electron from a higher shell, a so-called Auger-electron [Mei22, Aug23] is emitted, while the process is called Coster-Kronig transition [CK35] if the vacancy is filled by an electron from a different sub-shell of the same shell. Radiative transitions will simply transfer the initial vacancy to a higher shell. In contrast, non-radiative transitions will double the number of vacancies in the atomic shell. Thus, a cascade of relaxation processes (Auger explosion) will propagate up to the outermost shell of the atom, resulting in the emission of several electrons with typical energies up to some tens of keV.
- **Atomic-shell Reorganization:** The probability for inner conversion or shake-off processes is rather small. However, the change of the nuclear charge $(Z-2)$ due to the $\alpha$-decay also initiates a reorganization of the atomic-shell electrons. The outer-shell electrons will rearrange to the orbitals of the final state in a non-adiabatic manner. The energy released in this process is shared statistically by two electrons from outer atomic shells, which typically are emitted into the continuum with energies in the eV-range.

More information on the electron-emission processes following $^{219}$Rn and $^{220}$Rn $\alpha$-decays as well as detailed discussions on the energy spectrum of the emitted electrons can be found in [Wan13b].

### 4.1.2 Characteristics of Stored-Particle Induced Backgrounds

As already mentioned, an $\alpha$-decay of a single radon atom inside the main spectrometer is followed by the isotropic emission of up to 20 primary electrons into the sensitive flux volume. As outlined above, MAC-E-filter based spectrometers inherently act as magnetic bottle for those kinds of electrons, where the latter are reflected back and forth by the magnetic-mirror effect (see Chapter 2). An electron, emitted during the $\alpha$-decay of a radon atom with an initial kinetic energy $E_{\mathrm{kin}}(\vec{x_{\mathrm{s}}})$ at position $\vec{x_{\mathrm{s}}}$, is trapped if its polar starting angle $\theta$ to the magnetic-field lines fulfills the following condition:

$$\theta > \theta_{\mathrm{max}} = \arcsin\left(\sqrt{\frac{qU(\vec{x_{\mathrm{s}}})}{E_{\mathrm{kin}}(\vec{x_{\mathrm{s}}})} \cdot \frac{B(\vec{x_{\mathrm{s}}})}{B_{\mathrm{max}}}}\right) \quad . \tag{4.1}$$

Here, $U(\vec{x_{\mathrm{s}}})$ and $B(\vec{x_{\mathrm{s}}})$ denote the electrostatic potential and the magnetic field at $\vec{x_{\mathrm{s}}}$, whereas $B_{\mathrm{max}}$ is the maximal magnetic field along the flight path of the electron. With an initial magnetic field of 0.5 mT in the analyzing plane, a potential of $U_0 = -18.6\,\mathrm{kV}$ and a maximal magnetic field of 5 T, the initial polar angle of a shell-reorganization electron with a kinetic energy of 10 eV must be below $\theta_{\mathrm{max}} = 25.5°$ to leave the trap. In contrast, a K-shell conversion electron, emitted during the deexcitation of the 5/2+ to the 7/2+ state of $^{215}$Po* with an energy of 37.5 keV, is trapped as long as its initial polar angle is larger than $\theta_{\mathrm{max}} = 0.4°$. However, two further effects can cause electrons, in particular those with high energies ($E_{\mathrm{kin}} > 10\,\mathrm{keV}$), to leave the trap. Firstly, the cyclotron radius of high-energy electrons can exceed the dimensions of the main spectrometer. In this case, the electrons will hit the vessel walls or the inner electrode structures. Secondly, electrons can leave the trap due to non-adiabatic effects for which the orbital magnetic moment

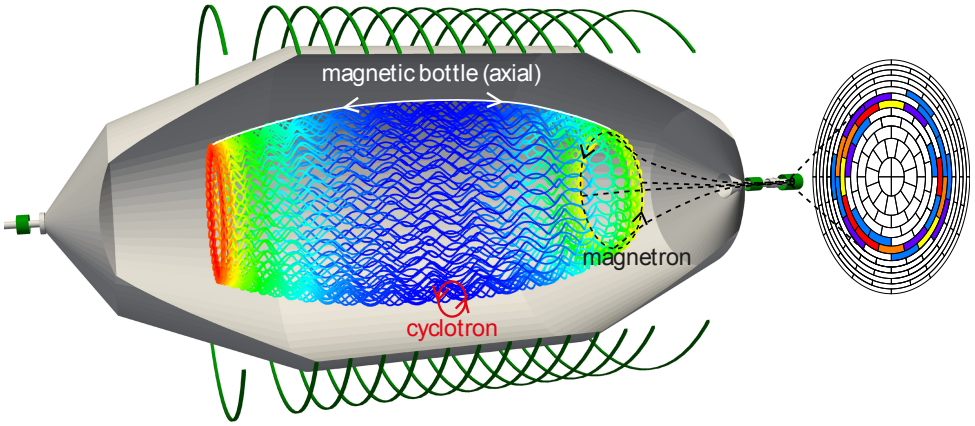


**Figure 4.2: Visualization of the trajectory of a magnetically-stored electron inside the main spectrometer.** While being reflected in the high magnetic field regions at both ends of the spectrometer, the electron performs a slow magnetron drift around the spectrometer axis which is superimposed by the fast cyclotron motion. Along its flight path, the primary electron cools-down via scattering off residual-gas molecules. Secondary electrons that are generated in inelastic scatterings will share the same magnetron radius as the primary electron. When breaking the storage conditions, these electrons generate a ring-like event pattern on the detector which is characteristic for backgrounds that are induced by magnetically-stored particles. Adapted from [Bar14].

$\mu = {}^{E_\perp}/_{B}$ is no longer conserved. This can happen in particular in the low magnetic field regions close to the analyzing plane and for large electron surplus energies.

Figure 4.2 visualizes the trajectory of a magnetically-trapped electron in the main spectrometer: While moving back and forth on its fast cyclotron path between the two magnetic mirrors at each end of the spectrometer, the electron performs an additional slow drift around the axis of the spectrometer, the so-called magnetron drift. The stored electron can loose energy via two different processes. According to [Wan13a], the energy loss by synchrotron radiation can be approximated by ${}^{\Delta E_\perp}/_{\Delta t} \approx 0.4 \cdot B^2 \cdot E_\perp$ and dominates for electrons with large transverse energies $E_\perp > 10\,\mathrm{keV}$. At lower energies, the cross section for inelastic (and elastic) scattering with residual-gas molecules strongly increases, making those processes the dominant cool-down mechanism.

A stored electron will continuously lose energy until it breaks the storage condition described by Equation 4.1. At the same time, secondary electrons are continuously generated via the ionization of residual-gas molecules in inelastic scatterings. These secondaries will share the same magnetron radius as the primary electron and will, depending on their initial angle and energy, be stored as well. As a result, they can, for their part, generate further, tertiary electrons. In this way, one high-energy primary electron can generate up to several hundreds of low-energy electrons. With the UHV conditions in the spectrometer it can take hours until a keV-electron is cooled-down far enough to leave the trap. Consequently, the correlated secondary electrons with energies in the eV-range will leave the spectrometer towards the detector over the course of hours. As these electrons are accelerated by the retarding potential and are guided adiabatically to the detector, they cannot be differentiated from signal electrons. The non-Poisson nature of this correlated background events potentially has a huge impact on the neutrino-mass sensitivity of KATRIN in case of no countermeasures [Mer13].

As all secondary electrons share the magnetron radius of the primary electron, they are observed as a ring-shaped event pattern on the detector (see right side of Fig. 4.2). Nevertheless, due to the long time periods, over which these correlated electrons appear on

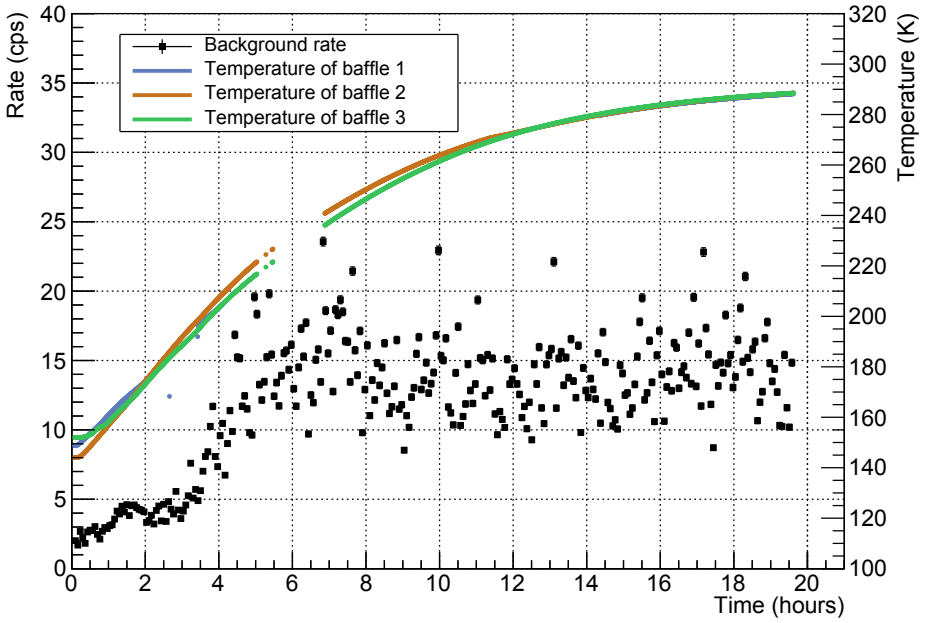


**Figure 4.3: Influence of the warm-up of all three baffles on the spectrometer-background rate during SDS-I measurements.** A special electromagnetic setting, described in [Goe14], has been used to artificially increase the radon-induced background rate. During the parallel warm-up of all three baffles, a rate increase of about 500% was observed. Note that the Pt-1000 sensors, that were used for the temperature monitoring during SDS-I, were located at the exhaust lines of the baffles. Their readings have been found to be unreliable concerning the absolute value (see [Goe14]).

the detector, the ring-shaped patterns of different decays, as well as the event pattern of the non-radon-induced background, do overlap in measurements at standard spectrometer configurations. In this case, an identification of the radon background via the detector event pattern is only possible in a statistical way (see [Sch14c]).

### 4.1.3 Radon Reduction by a $LN_2$-Cooled Baffle System

In order to minimize the background contribution from radon-induced stored electrons, several passive and active countermeasures have been developed [Wan13a, Mer12a, Goe14]. In the context of this thesis, the effectiveness of the passive background reduction mechanism by the $LN_2$-cooled baffle system (Sec. 3.2) is investigated. The copper baffles block the direct line-of-sight between the NEG pumps and the sensitive flux volume of the spectrometer. In this way, radon atoms emanating from the getter strips and propagating with thermal velocities towards the spectrometer volume have to pass the baffle system. There they stick to the $LN_2$-cooled copper surfaces for a prolongated time period and, thus, decay well outside of the observed flux tube volume. Based on measurements at the pre-spectrometer and on vacuum simulations, the baffles are designed as a trade-off between the cryogenic adsorption of radon and the pumping speed of the NEG pumps for hydrogen and tritium inside the spectrometer volume. First measurements concerning the efficiency of the baffle system were already performed during SDS-I and are discussed in [Goe14] and [Sch14c].

Figure 4.3 shows the effect that a warm-up of all three baffles to room temperature had on the background rate during SDS-I. Note that a special electromagnetic field configuration with the spectrometer at zero potential was used in these measurements to artificially increase the number of secondary electrons that are generated per stored particle. In this

**Table 4.1: Baffle configurations used during the SDS-IIA radon-background measurements.** Five different baffle configurations were used over the course of SDS-IIA in order to study the radon-induced background with a retarding potential of $U_0 = -18.6\,\mathrm{V}$. All measurements were performed with a magnetic field of 0.5 mT in the analyzing plane, an offset voltage of the full inner electrode of $U_{\mathrm{IE,common}} = -100\,\mathrm{V}$, and a pressure of about $1 \times 10^{-8}$ mbar (measured by extractor gauge 3110). Note that pump ports 2 and 3 were equipped with $^{219}$Rn-emanating NEG pumps, while pump port 1 was kept empty during SDS-II. Furthermore, the six detector channels served by preamplifier module 14 showed high noise levels during the course of data set E (see Sec. 3.4 for details). In the analyses that include setting E, the corresponding channels are excluded. An overview of the three main spectrometer pump ports is given in Figure 3.5.

| Data set | Baffle 1 | Baffle 2 | Baffle 3 | Run time (h) | Runs |
|---|---|---|---|---|---|
| A | warm | warm | warm | 18.5 | #20972 - #20990 |
| B | warm | cold | warm | 23.0 | #21113 - #21135 |
| C | warm | cold | cold | 44.2 | #20921 - #20965 |
| D | cold | cold | cold | 61.9 | #22064 - #22125 |
| E | cold | cold | warm | 43.5 | #24039 - #24082 |

way, a rate increase by a factor of five has been observed during the parallel warm-up of all three baffles, demonstrating their functionality as a passive radon countermeasure. Unfortunately, due to hardware limitations of the $LN_2$-supply system during the SDS-I campaign (Sec. 3.2), a continuous $LN_2$-operation with the spectrometer at its standard configuration ($U_0 = -18.6\,\mathrm{kV}$) was not possible.

With its $LN_2$-circulation system and high-voltage insulation fully functional, the baffle system was operated together with the main spectrometer in its standard configuration over several months during the SDS-II phase. For the first time it was thus possible to investigate the efficiency of the $LN_2$-cooled baffles in a systematic way and under comparable conditions. In the context of this thesis, five long-term background-measurement sets, listed in Table 4.1, have been taken over the course of SDS-IIA to investigate the effect of a baffle cool-down on the radon-induced background in detail. Furthermore, an artificial $^{220}$Rn-source was installed to different positions in the spectrometer vacuum system in order to study the efficiency of the baffles for different sources of radon in the spectrometer, and for different operating temperatures of the baffles. The corresponding analyses are presented in Appendix A.

## 4.2 The Experimental Approach to Study Radon-Induced Backgrounds

All radon-related measurements have been carried out using special spectrometer configurations, in particular at elevated pressure, in order to allow for a separation of the radon-induced backgrounds from other, uncorrelated backgrounds. In this section, the experimental approach to perform this separation is described in detail.

### 4.2.1 Measurements at Artificially-Elevated Pressure

As already mentioned in Section 4.1.2, UHV conditions with $p \approx 10^{-10}$ mbar inside the spectrometer imply exceedingly long storage times of primary electrons, which make it difficult to relate a single detector event to one specific radon decay. When artificially increasing the pressure, the cool-down speed of the primary electron will be fastened considerably. The analytical expression of the average time between two scatterings has

been derived in [Wan13a] to

$$t_{\mathrm{scat}}(p) = \sqrt{\frac{T^2 \cdot m_{\mathrm{e}}}{2 \cdot \sigma_{\mathrm{tot}}^2(E_{\mathrm{kin}}) \cdot E_{\mathrm{kin}}}} \cdot \frac{1}{p} \quad . \tag{4.2}$$

As $t_{\mathrm{scat}}$ is inversely proportional to the pressure $p$, an increase of the spectrometer pressure by a factor $10^3$ up to $p = 1 \times 10^{-8}$ mbar will decrease the average time between two scatterings to the sub-second scale. Thus, the total cool-down time of the primary keV-scale electron will be reduced to seconds, so that the detection times of secondary electrons fall into a narrow time window. As a consequence, single radon decays in the spectrometer volume appear as short bursts of elevated background rate during high-pressure measurements. Figure 4.4 shows the background rate over the course of 1 000 s in an SDS-I measurement at elevated pressure (runs #8531 - #8533), as compared to run #8289 at a standard pressure of $1 \times 10^{-10}$ mbar. The peaks in the high-pressure measurement correspond to individual radon $\alpha$-decays. In the low-pressure measurement, the primary electrons cool down slowly and the appearance of the secondary electrons is smeared out over long time-scales. Thus, single radon decays cannot be resolved. The difference in the total number of entries in the two measurements is due to a pressure dependence of both, the remaining non-radon-induced background (see Chapter 6), and the number of secondaries per radon-induced stored primary electron [Sch13c]. The latter can be explained by the increased scattering probability of the primary electrons compared to energy losses via synchrotron radiation in the case of high-pressure measurements. Thus, the number of secondary electrons per primary electron increases and only the number of radon decays can be assumed as being pressure independent. In this thesis, the spike-like structures observed in high-pressure measurements are termed 'clusters', whereas events within those clusters are denoted as 'cluster events'.

In order to achieve the desired elevated-pressure level, the gas inlet system described in Section 3.2 was used to inject dry helium gas of purity 6.0 (99.9999%) into the main spectrometer at constant flow rate. All measurements stated in Table 4.1 were taken at a pressure reading of the Extractor ion gauge 3110 of about $1 \times 10^{-8}$ mbar. Due to the influence that the cool-down of the baffles had on the vacuum conditions during SDS-IIA, different helium injection rates were necessary for each of the cold-baffle configurations. Accordingly the exact gas composition in the spectrometer differed from measurement to measurement. In general, specific correction factors for the different gas species have to be taken into account at this point in order to deduce the correct pressure from the reading of the Extractor gauge [Oer07]. These correction factors represent the variations of electron-impact ionization cross sections for the different gas species. The average time $t_{\mathrm{scat}}$ between two scattering events of a radon-induced primary electron, however, depends on the same cross section. Thus, as long as the cross sections of two gas compositions X and Y are proportional according to

$$\frac{\sigma_{\mathrm{tot}}(X, E_{\mathrm{kin}})}{\sigma_{\mathrm{tot}}(Y, E_{\mathrm{kin}})} \approx \text{const.} \quad , \tag{4.3}$$

the correction factors can be neglected to first order. Even a direct comparison to SDS-I measurements, where argon instead of helium was injected into the spectrometer, is possible as the ionization cross sections of these two noble gases fulfill the condition in Equation 4.3. It should be noted that the effect of double-ionization in the case of argon is not taken into account at this point.

**Spatial Distribution of Cluster Events**

The left-hand side of Figure 4.5 displays the typical event pattern of a stored high-energy electron from radon decays: a total of 44 events over a time scale of less than 2 seconds

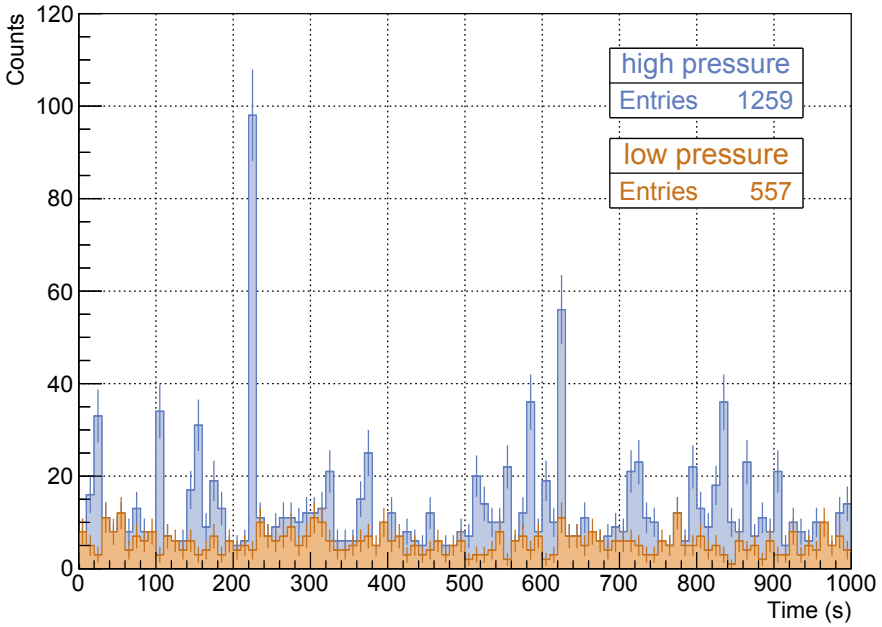


**Figure 4.4: Comparison of the background rate as a function of time for high- and low-pressure measurements.** Both measurements have been performed during the SDS-I phase for comparable electromagnetic configurations in the spectrometer. A total of 122 detector channels has been used in the analysis. The high-pressure measurement with $p \approx 1 \times 10^{-8}$ mbar (blue) shows spike-like structures in the background time distribution, each originating from a single radon decay in the sensitive flux volume. At low pressures of $p \approx 1 \times 10^{-10}$ mbar (orange), the spike structures are smeared out and cannot be separated from the uncorrelated background.

generate a ring-shaped pattern on the detector. An unweighted ring fit of all detector pixels with at least one hit has been applied to the pattern in order to determine the center point of the ring. An unweighted fit ensures that those (late time) parts of the magnetron drift trajectory where the primary electron energy is small and consequently the ionization cross section is large, do not get overbalanced in the ring fit.

As already described in [Sch14c], the center of such a ring fit contains information about the alignment of the detector wafer relative to the magnetic flux tube inside the main spectrometer. In contrast to the alignment measurements described in Section 3.9, this approach is independent of the relative alignment of internal mechanical structures and only focuses on the magnetic alignment. Over the course of the high-pressure background data set A, a total of 8 312 clusters, each including at least 10 cluster events, was identified as spikes in the background time-distribution. The plot on the right-hand side of Figure 4.5 shows the distribution of the ring centers for the 4 518 clusters with ring radii larger than 30 mm on the detector wafer. The center of the distribution is shifted by $\Delta x = (0.51 \pm 0.03)$ mm in $x$-direction and $\Delta y = (-0.37 \pm 0.03)$ mm in $y$-direction. The rather large standard deviations of the distribution can be explained by the cyclotron-smearing of the magnetron-drift trajectory.

Table 4.2 lists the results of the fits of the radon ring patterns and the alignment results obtained in Section 3.9. When comparing the numbers, several things have to be considered. First of all, the uncertainty on the results of the '*Faro* arm measurements' is expected to be in the range of about 0.5 mm. These results are related to the mechanical misalignments of the detector vacuum chamber and the PAE relative to the axis of the main spectrometer only. Besides these numbers, also the measured misalignments of the

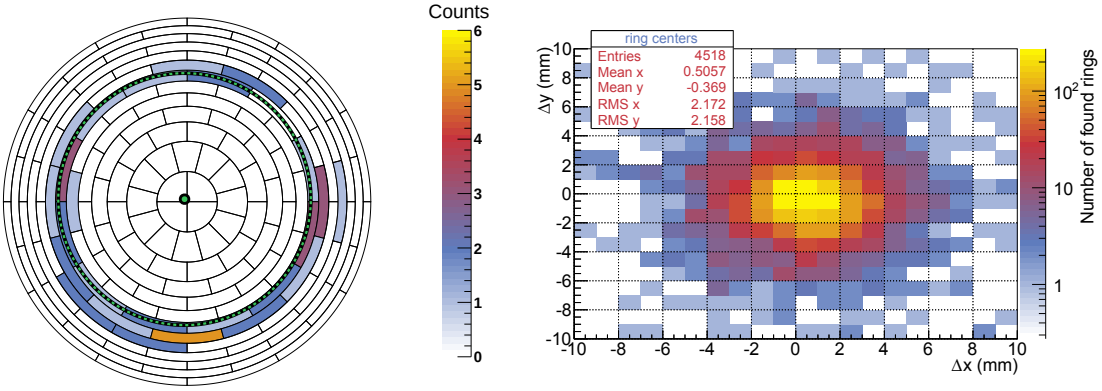


**Figure 4.5: Characteristic radon-induced ring-patterns at elevated spectrometer pressure. Left: A radon-induced event cluster forms a ring-like pattern on the detector.** The observed ring in this particular case consists of 44 events over a time period of less than 1 second with the ring center located $\Delta x = -0.625\,\text{mm}$ / $\Delta y = 0.625\,\text{mm}$ (obtained by a ring fit) away from the center of the detector wafer. **Right: Distribution of ring centers obtained by ring fits of a total of 4 518 ring patterns.** A minimum of 10 events per pattern was enforced in the analysis. The center of the distribution is shifted $\Delta x = 0.51 \pm 0.03\,\text{mm}$ / $\Delta y = -0.37 \pm 0.03\,\text{mm}$ away from the center of the detector wafer.

**Table 4.2: Results for the detector wafer alignment** relative to the axis of the magnetic flux tube ('Radon ring pattern'), the axis of the spectrometer (' *Faro* arm measurement' and 'Alignment simulation'), and relative to the inner electrode system ('Alignment measurements'). Apart from the radon ring pattern, the listed results are obtained in Section 3.9. Note that the ring-fit algorithm that is used to derive last three results has an uncertainty of about 1 mm [Sch14c], whereas for the *Faro* arm results an uncertainty of about 0.5 mm is expected. The latter are used in the 'Alignment simulation' together with the misalignment results for the FPD magnets (which suffer from similar uncertainties).

| | $\Delta x\,(\text{mm})$ | $\Delta y\,(\text{mm})$ |
|---|---|---|
| Radon ring pattern | $0.51 \pm 0.03$ | $-0.37 \pm 0.03$ |
| *Faro* arm measurement | 0.12 | 0.37 |
| Alignment simulation | $-0.34$ | $-0.84$ |
| Alignment measurement (outer ring) | 1.375 | $-1.625$ |
| Alignment measurement (inner ring) | 2.125 | $-1.625$ |

two FPD magnet cryostats enter the 'alignment simulation' with KASSIOPEIA. Thus, the uncertainty on the simulation results is expected to be $\geq 0.5\,\text{mm}$. In the 'alignment measurements', ring-like comb-structures of the inner electrode system where magnetically imaged onto the FPD. The ring-fit was applied to resulting event-patterns on the detector. In difference to the radon ring patterns, where thousands of fits where applied to obtain a distribution of results (see Fig. 4.5), only two single ring fits were applied here. Thus, the uncertainty of the results of these single fits is large and is approximated to 1 mm in [Sch14c].

Apart from the radon ring patterns, all alignment results suffer from large uncertainties such that differences in the alignment of the detector against the mechanical axis of the spectrometer and the axis of the magnetic flux tube cannot be resolved at this point.

### Interarrival-Time Distribution

While the ring-shaped pattern on the detector is a distinct topological feature, the spatial correlation of the radon-induced events over an extended period of time is not useful

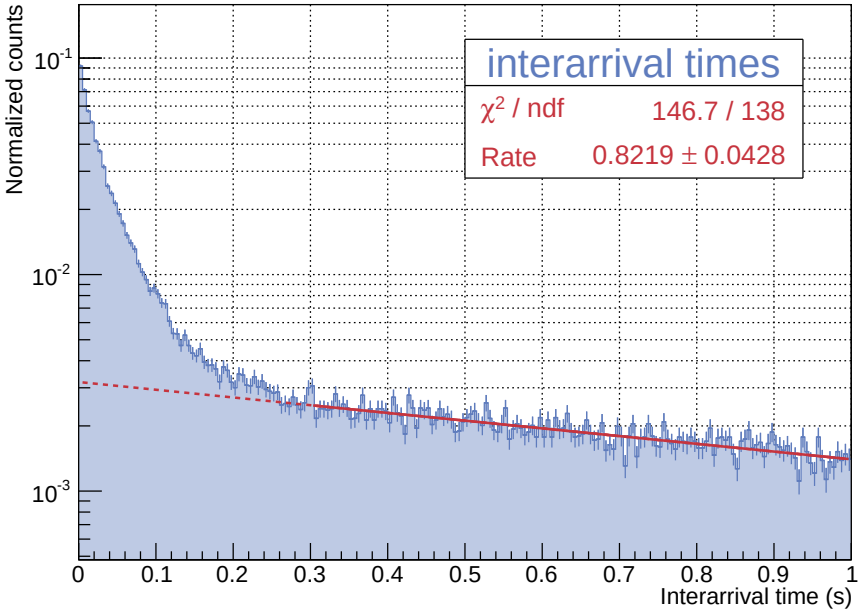


**Figure 4.6: Time differences between subsequent detector events during measurements at elevated pressure.** For interarrival times larger than 0.2 s, the distribution shows an exponential slope, corresponding to uncorrelated background events. At times $< 0.2$ s, the distribution is dominated by the correlated events within radon-induced clusters. An exponential fit of the distribution for interarrival times larger than 0.3 s gives a rate of $R_{\mathrm{fit}} = (822 \pm 42)$ mcps.

for an effective event-by-event differentiation between radon-induced events and other background contributions. Here, the correlation of the arrival times of the events on the detector is more auspicious. In the following discussion, the rate of single, not radon-induced events will be denoted by $R_{\mathrm{S}}$, while the rate of radon-induced events, i.e. events within clusters, will be denoted by $R_{\mathrm{CE}}$. The latter should not be confused with the rate of the clusters itself $R_{\mathrm{C}}$, which is equivalent to the rate of observed radon decays.

Figure 4.6 gives an overview of the distribution of interarrival times between subsequent detector events in data set A. Below about 0.2 s the interarrival-time distribution gets dominated by correlated events from radon-induced clusters that appear due to electron cooling within short timescales. The exponential slope of the distribution at large interarrival times corresponds to Poisson-distributed background processes that sum up to a rate of $R_{\mathrm{fit}} = (822 \pm 42)$ mcps. In a first-order approximation, the interarrival times that contribute to the distribution can be grouped into three categories:

1. A first uncorrelated fraction, where two non-radon-induced background events follow each other.

2. A correlated fraction, where two radon-induced events within the same cluster are measured.

3. A second uncorrelated fraction, where the last event in a radon cluster is followed by a subsequent event, which can either be a non-radon-induced background event or the first event of the next radon cluster.

Due to the third-category contribution to the interarrival times, the rate determined by the exponential fit in Figure 4.6 does not correspond to the true value of $R_{\mathrm{S}}$ but to the sum of $R_{\mathrm{S}}$ and $R_{\mathrm{C}}$. This shows that an effective differentiation between the radon-induced

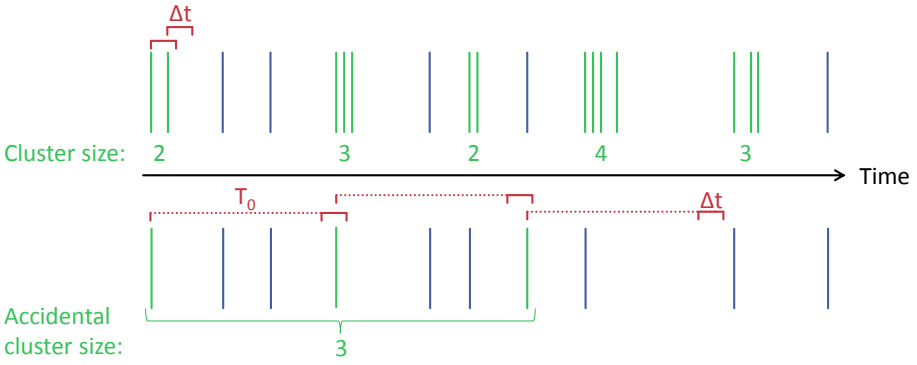


**Figure 4.7: Schematic illustration of the algorithm that is used to identify event clusters and to estimate the contribution by accidentals. Top: Cluster identification.** For each event $i$, the algorithm checks whether $t(i+1) - t(i) \leq \Delta t$, with a specified time-window length $\Delta t$. If the condition is fulfilled, the algorithm continues and checks for the time difference between events $i$+1 and $i$+2, and so on. As soon as $\Delta t < t(i+j+1) - t(i+j)$, the events $i$ to $i$+$j$ are stored as cluster of size $j$+1 and the algorithm starts over again, beginning with event $i$+$j$+1. **Bottom: Accidental correction.** A second algorithm uses the result of the cluster identification and merges each of the clusters found to a single event with the time stamp from the first event of the cluster. The resulting event list is checked for accidental clusters by the usage of the same algorithm as the cluster search, but including a large arbitrary time offset $T_0$. For each event $i$ it searches for another event $k$ in a time window $T_0$ to $T_0 + \Delta t$. If the event $k$ lies within the window, the search is repeated from event $k$ on. The events $i$, $k$, etc. are stored as accidental cluster events and are deleted from the event list before the algorithm starts over with the next event that might lie between the former accidental events $i$ and $k$.

events and those originating from other background processes has to be performed on an event-by-event basis rather than by analyzing the distribution that is shown in Figure 4.6.

### 4.2.2 The Event-Cluster Identification Algorithm

The top part of Figure 4.7 illustrates the procedure that was already used for the SDS-I data in order to identify event clusters [Sch14c, Goe14, Oer14]. A time-window length $\Delta t$ is defined and the events $i$, $i$+1 and $i$+2 are identified as cluster of size $N = 3$ if $t_{i+1} - t_i \leq \Delta t$ and $t_{i+2} - t_{i+1} \leq \Delta t < t_{i+3} - t_{i+2}$. This procedure allows for an event-by-event identification of clusters and the corresponding cluster events. Nevertheless, several higher-order effects will affect the efficiency of this cluster search. For example, uncorrelated background events can appear within the time interval of a cluster, and can thus be misinterpreted as one of the cluster events. Furthermore, uncorrelated events may have, by coincidence, interarrival times of less than 0.2 s to form a so called accidental cluster which then is falsely identified as being radon-induced. In particular for cold baffle measurements, where the rate of radon-induced clusters is small compared to the uncorrelated event rate, this effect will lead to a significant overestimation of clusters. In order to preserve the purity of the radon-induced clusters in the SDS-I analysis, conservative and rather large cluster-size thresholds $N_0$ have been used, where only clusters of size $N \geq N_0$ were assumed as radon-induced.

In the context of this thesis, the cluster-identification algorithm has been extended in order to take into account the above mentioned effect of accidentals. For this purpose, an off-time coincidence technique is used to estimate the contribution of accidental clusters to the total number of clusters found. While a true radon cluster is formed by correlated events, the occurrence of an accidental cluster is a purely statistical process. Thus, the introduction of a large (arbitrary) time offset $T_0$ into the cluster-identification algorithm

will break the correlation of real clusters, while the number of accidental clusters will remain the same. The working principle of the accidental cluster estimation is illustrated in the lower part of Figure 4.7. Once the total number of clusters is identified in a first scan through the data with a specified time-window length $\Delta t$, all cluster events except the first one of each cluster are sorted out. In a subsequent second scan of the data, the same time-window length $\Delta t$ is used in combination with the above mentioned time offset $T_0$ to estimate the contribution of accidental clusters.

**Efficiency of the Cluster-Identification Algorithm**

Figure 4.8 shows the number of identified clusters in the radon data-set A as a function of the search parameters $\Delta t$, $T_0$ and the cluster-size threshold $N_0$. While the number of clusters found is independent of the time offset $T_0$ as long as $T_0 \gg \Delta t$, this quantity strongly depends on the chosen window length $\Delta t$. For the important minimum case $N_0 = 2$, two different effects are observed. First, for low values of $\Delta t$, the search algorithm wrongly splits-up large-size clusters into several smaller ones. The overestimation of the number of clusters results in the peak-like structure at $\Delta t < 0.05\,\mathrm{s}$. Secondly, the number of clusters found increases steadily for larger $\Delta t$, which is due to the increasing contamination by accidental clusters. The accidental-correction algorithm significantly influences both, the absolute value as well as the shape of the number of clusters found as a function of $\Delta t$. The algorithm reduces the number of clusters for $N_0 = 2$ by a factor of about two in the relevant range $0.15 < \Delta t < 0.25\,\mathrm{s}$, independent of $\Delta t$. For the more restrictive case of $N_0 = 4$, the contamination by accidental clusters is quite small from the start and the correction mechanism thus has no significant influence.

In order to get a better understanding of the detection efficiency for a true radon-induced cluster, a MC-generator was used to reproduce the interarrival times for the data sets A and D. Based on the measured cluster-size (Fig. 4.10) and interarrival-time distributions of cluster events in the respective data set, for each of a given number of clusters $N_C$ the generator randomly samples the number of events within the cluster as well as time differences between those events. The start times of the clusters themselves are assumed as Poisson-distributed. In a next step, the simulated, correlated events are overlapped by $N_\mathrm{S} = N_\mathrm{total} - N_\mathrm{CE}$ additional events with Poisson-distributed time differences, representing the remaining, uncorrelated background. Here, $N_\mathrm{total}$ is the total number of events in the corresponding data set and $N_\mathrm{CE}$ is the number of events within the previously simulated clusters. In Figure 4.9, the effectiveness of the cluster-search algorithm for data-set A (warm baffles) and set D (cold baffles) is compared for events that were simulated with the MC generator. In the case of data-set A, where the correlated events make up a large part of the total background, the number of clusters found shows a plateau in the range of $0.15 < \Delta t < 0.25$ which is in agreement with the simulated number of 4 026 clusters. In contrast, the algorithm underestimates the number of accidental clusters in the case of the cold-baffle data set D, where the correlated events from the radon clusters only make up a small part of the overall background rate. The number of clusters found in this case is overestimated by a factor of 1.5 to 2.5 s within the range of $0.15 < \Delta t < 0.25\,\mathrm{s}$. This is assumed to be due to higher-order effects that are not taken into account in the accidental search and become relevant if the number of real radon-induced cluster events is very small compared to other background contributions.

**The Distribution of Cluster Sizes**

Figure 4.10 compares the cluster-size distributions for data set A (all baffles warm) and data set D (all baffles cold). The strong contribution of accidentals for small cluster sizes $N < 5$ significantly changes the shape of the distribution. For the cold-baffle measurements, the two bins at $N = 2$ and $N = 3$ show an excess, even after applying the

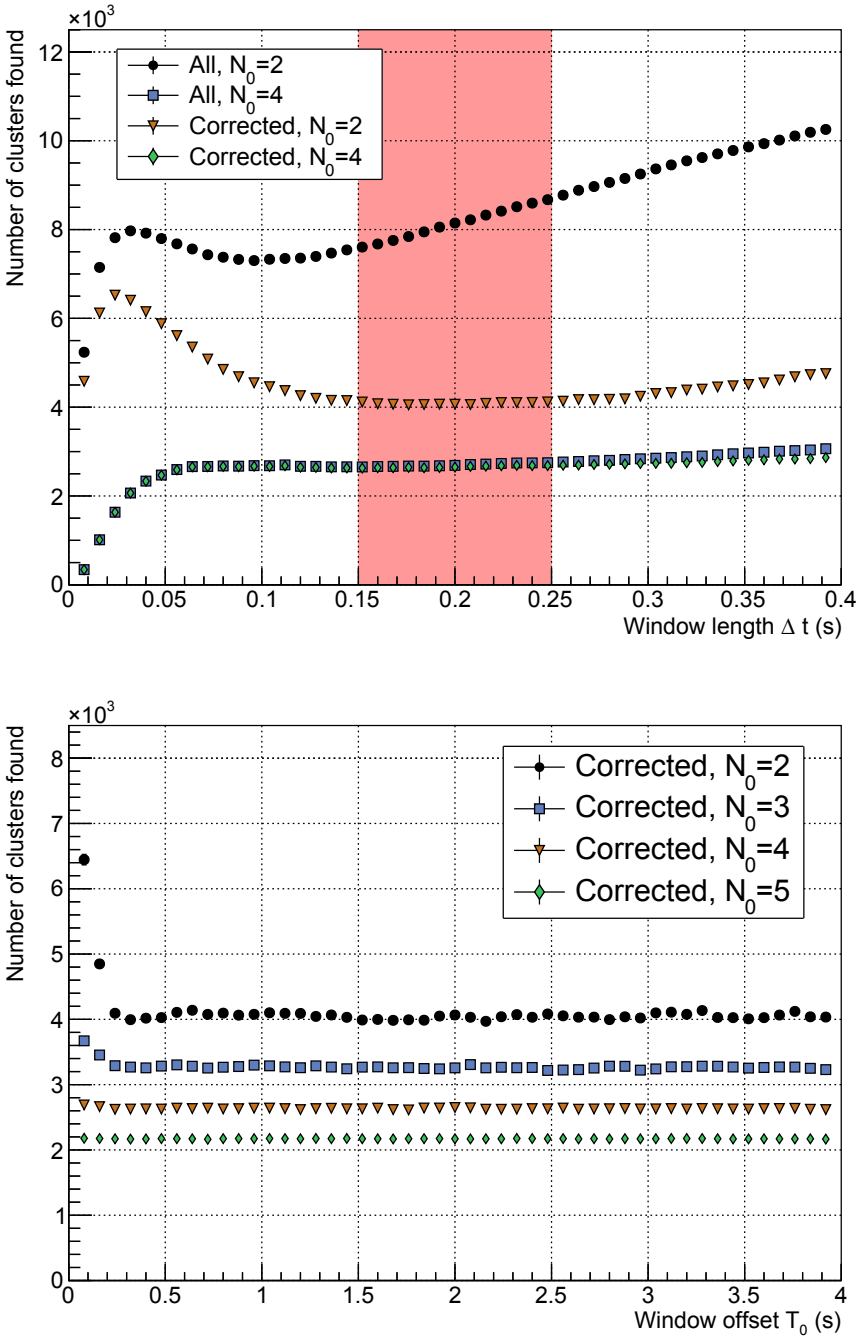


**Figure 4.8: Top: Number of identified clusters as a function of the specified time-window length $\Delta t$ and cluster-size threshold $N_0$** both with and without an accidental correction applied. The shaded area marks the relevant range of $\Delta t$ between 0.15 s and 0.25 s. **Bottom: Number of identified clusters as a function of the specified time offset $T_0$ and the cluster-size threshold $N_0$** with $\Delta t$ fixed to 0.2 s. The results are independent of $T_0$ as long as $T_0 \gg \Delta t$. Both plots are based on the radon data set A, listed in Table 4.1.

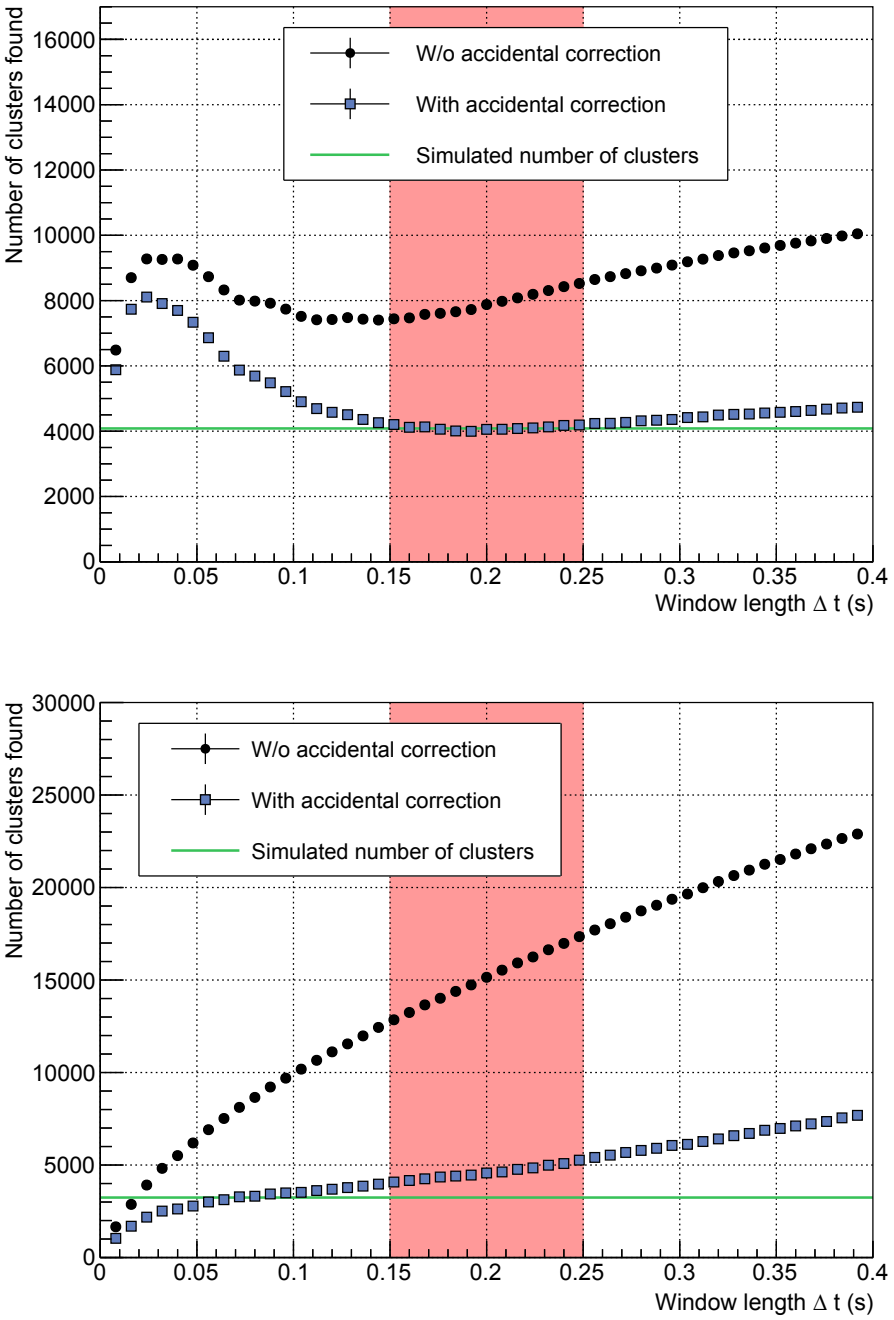


**Figure 4.9: Efficiency of the accidental-corrected cluster-identification algorithm.** A Monte-Carlo event time generator is used to simulate background rates for different cluster to non-cluster event ratios. The principle of the simulation is outlined in the text. The simulated events are used as an input for the cluster-identification algorithm. **Top:** Simulation of 4 084 clusters using radon data set A as input. **Bottom:** Simulation of 3 242 clusters using radon data set D as input. Both data sets are introduced in Table 4.1.

accidental correction. This can be traced back to the above mentioned ineffectiveness of the accidental-search algorithm for cold-baffle measurements.

Even if the cluster-size distribution and, therefore, the number of secondaries that are produced per radon decay, is somehow related to the energy of the primary electron, it is challenging to extract information concerning the energy distribution of the primary electrons out of it. On the one hand, the energy loss of the primary high-energy electron is not only due to ionization but also occurs via synchrotron radiation, for example. On the other hand, some primaries will leave the spectrometer at an early stage of their cool-down phase due to non-adiabatic effects or as a result of their large cyclotron radii. Furthermore, the secondary electrons that are created can leave the spectrometer towards the pre-spectrometer, without being detected. The latter effect will be discussed in more detail in Section 4.4.2.

**The Radial Distribution of the Radon Clusters**

As radon atoms are expected to decay homogeneously distributed over the entire sensitive flux volume of the main spectrometer, radon-induced clusters mapped onto the detector should be independent of the radial position, once the different observed volumes per detector ring are taken into account. Figure 4.11 shows the volume-normalized rate of clusters with $N \geq N_0 = 2$ as a function of the radius $r_{\mathrm{AP}}$ in the analyzing plane of the spectrometer for the two data sets A and D. The location of the first event of a cluster on the detector is taken as the cluster's origin. Each bin corresponds to one detector ring, where the radius of each ring $r_{\mathrm{D}}$ is scaled to the corresponding radius in the analyzing plane according to $r_{\mathrm{AP}} = r_{\mathrm{D}} \cdot B_{\mathrm{AP}}/B_{\mathrm{D}}$ with a magnetic field of $B_{\mathrm{AP}} = 0.5\,\mathrm{mT}$ in the analyzing plane, and of $B_{\mathrm{D}} = 2.7\,\mathrm{T}$ at the location of the detector wafer. The radial distributions of both data sets show an increase of the total cluster rate to large radii. In case of data set A this increase can be traced back to accidental clusters so that the corrected distribution is flat, showing no dependence on the radius as expected for radon decays. In data set D, the corrected distribution still shows a small excess of clusters at large radii, in agreement with the expectation due to the larger impurity of the event ensemble here.

**Conclusion**

The extended cluster-search algorithm, including the correction for accidental clusters, gives reliable estimates of the number of clusters even for a small $N_0$, as long as the number of cluster events is of the same order of magnitude as the uncorrelated events. This is the case for measurements with warm baffles. However, for cold-baffle measurements, for which the background is dominated by uncorrelated events, the number of clusters is overestimated by a factor of up to about two, due to higher order effects from accidentals. In this case, it is challenging to obtain accurate results for (low statistics) observables that require the usage of small cluster-size thresholds $N_0$. One possible mitigating approach is to take into account the radial distribution of cluster events, i.e. to restrict the analysis to the innermost detector rings only.

All radon-specific analyses presented in this thesis are performed with a time-window length of $\Delta t = 0.2\,\mathrm{s}$, a cluster-size threshold of $N_0 = 2$ and an accidental correction with a time offset $T_0 = 2.0\,\mathrm{s}$, if not stated otherwise.

## 4.3 Contribution of Radon-Induced Events to the Total Spectrometer Background

Based on the findings of the previous section, the contribution of radon-induced events to the total spectrometer background is derived in the following analysis. Here, two quantities are of particular interest: first, the level of the remaining radon-induced background when

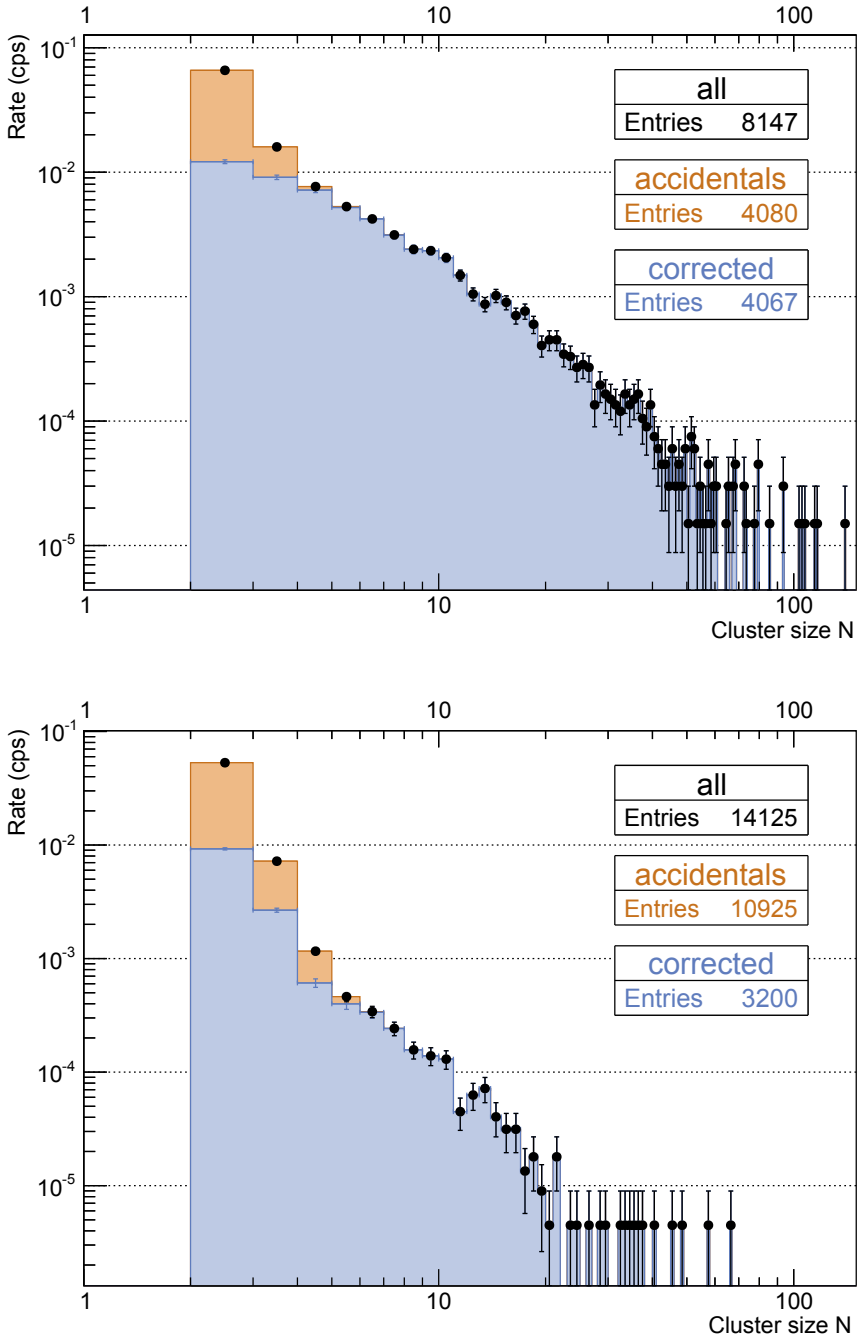


**Figure 4.10: Cluster-size distributions for different baffle configurations.** The distribution of all identified clusters is given by black dots. After the algorithm to obtain the distribution of the accidental clusters (orange) is applied, the corrected distribution (blue) is obtained. A time-window length of $\Delta t = 0.2\,\mathrm{s}$ and a time offset of $T_0 = 2\,\mathrm{s}$ were used to identify the clusters. **Top: Measurement configuration A - All baffles warm.** Approximately half of the identified clusters are accidentals, largely at small cluster sizes. **Bottom: Measurement configuration D - All baffles cold.** More than 75% of all clusters found are accidental ones. The corrected cluster-size distribution shows an excess of events in the first two bins when compared it to the distribution obtained with data set A.

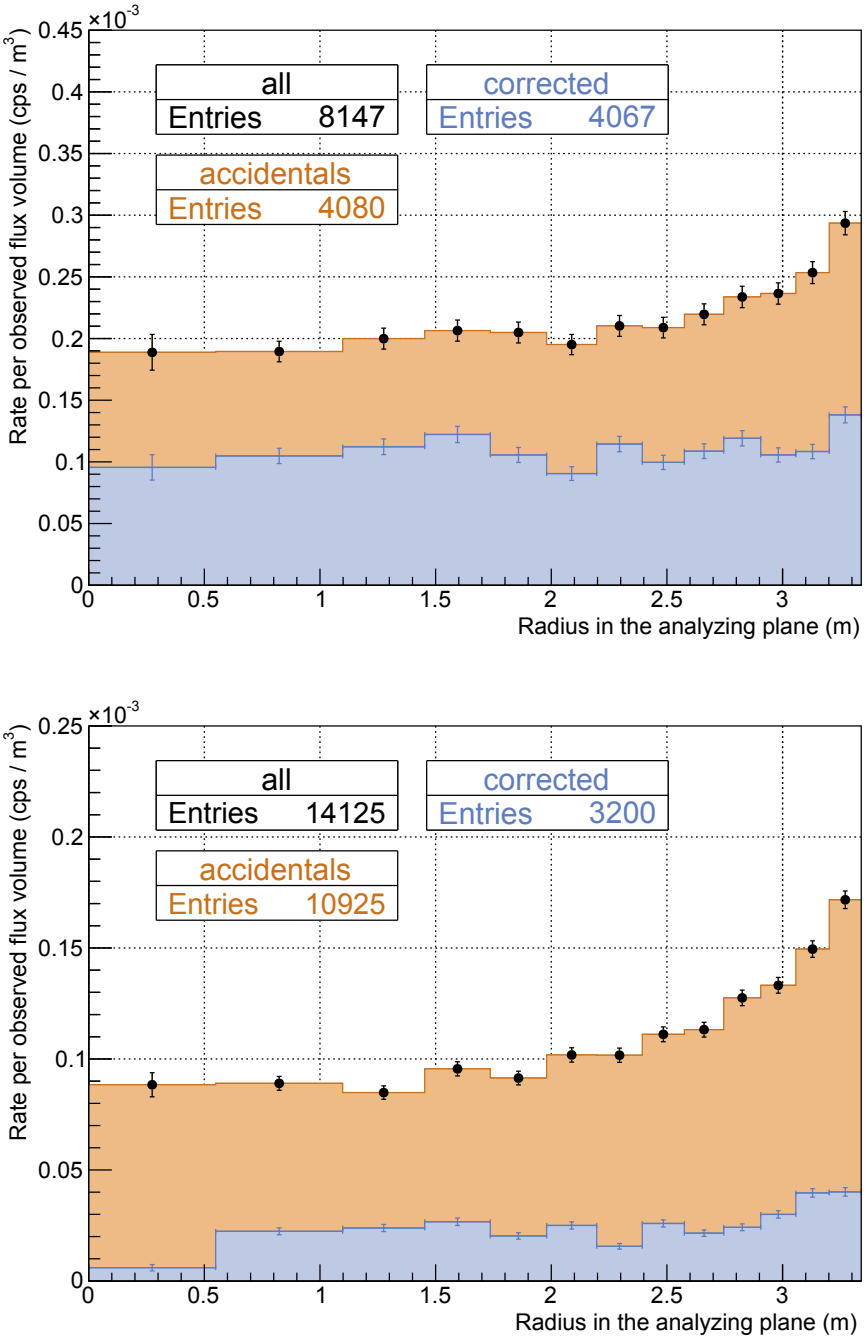


**Figure 4.11: Radial distribution of clusters for different baffle configurations.** The measured rates per detector ring are normalized by the observed flux-tube volumes (see Tab. 3.2). The $x$-axis indicates the radius that the observed flux tube of each detector ring has in the analyzing plane. The distribution of all identified clusters is indicated by black dots. If it is corrected by the accidental clusters (orange), the corrected radial distribution (blue) is obtained. A time-window length of $\Delta t = 0.2\,\mathrm{s}$ and a time offset of $T_0 = 2\,\mathrm{s}$ have been used in the cluster identification. **Top: Measurement configuration A - All baffles warm.** The radial distribution of all found clusters shows an increase to large radii which originates from the accidental clusters. This is in agreement with the radial distribution of the uncorrelated non-radon-induced backgrounds. The distribution corrected for accidentals appears flat, corresponding (as expected) to a uniform distribution of radon decays in the flux tube volume. **Bottom: Measurement configuration D - All baffles cold.** With all baffles cold, the corrected distribution of clusters shows a slight increase to large radii.

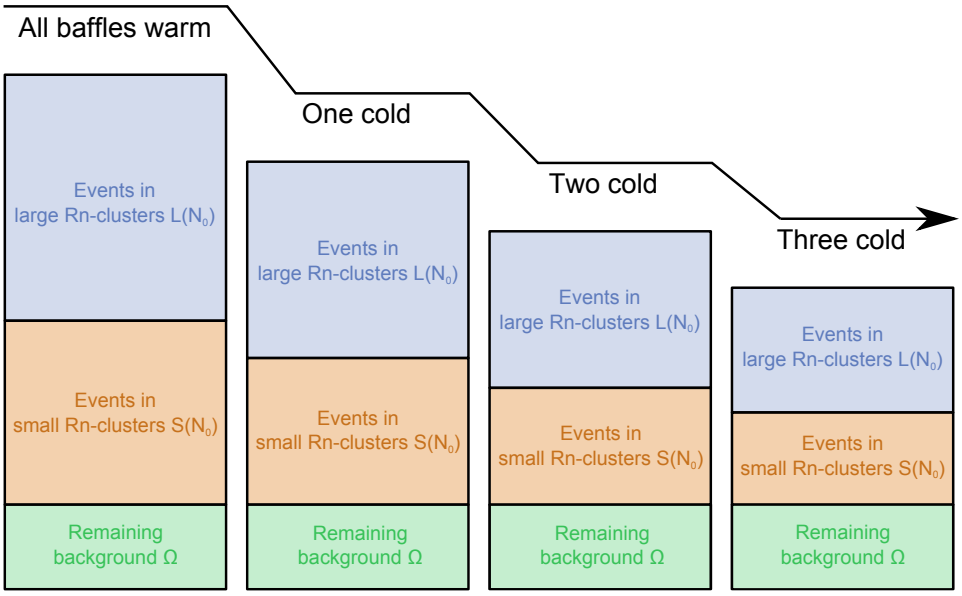


**Figure 4.12: Illustration of the background composition at different cold-baffle configurations.** The non-radon-induced background (green) remains unaffected by the baffle cool-down. By contrast, the total radon-induced background decreases with the number of cold baffles, while the ratio $\alpha_{N_0}$ between events in radon-induced clusters of small size $S(N_0)$ (orange) and those in large-size clusters $L(N_0)$ (blue) should remain constant.

all three baffles are cold and secondly, the rate of radon-induced 'single events'. The latter event class corresponds to the observed number of radon decays per unit time which appear as clusters of size $N = 1$ on the detector. While the radon investigations during the SDS-I phase were quite successful, definite statements about either of these quantities were not possible at that time, largely due to the restricted hardware status of the $LN_2$-cooled baffle system [Sch14c].

In the following, the SDS-II radon background data sets listed in Table 4.1 are used to derive conclusive results on the remaining radon-induced background with cold baffles as well as on the ratio of radon-induced single events to the clustered events.

To do so, two assumptions have to be made:

1. The remaining, non-radon-induced background rate $\Omega$ is assumed to be independent of the number of cold baffles.
2. The shape of the cluster-size distribution is expected to be independent of the number of cold baffles. In particular, the ratio $\alpha_{N_0}$ between events in small clusters $S(N_0)$ with size $N < N_0$ and events in large clusters $L(N_0)$ with $N \geq N_0$ is assumed to be independent of the baffle temperature (warm or cold).

The first assumption is rather intuitive as long as the cool-down of the baffles does not change the pressure in the spectrometer, while the second assumption can be justified based on the following arguments:

- The cool-down of the baffles will reduce only the total number of radon atoms which decay inside the sensitive flux volume and will not influence the cool-down characteristics of a stored primary electron. As the cluster-size distribution only depends on the latter process, its shape should be independent of a baffle cool-down[1].

[1] This statement does not hold strictly, as the cold baffles will reduce the $H_2O$ partial pressure in the vessel. Due to the large cross section of electrons with $H_2O$ molecules a large $H_2O$ partial pressure will in general speed up electron cool-down times. However, this effect is here assumed to be small, as such cross-section related effects are in parts compensated by the used measurement technique (see Eq. 4.3)

- Most of the high-energy conversion electrons of $^{219}$Rn that were observed in the pre-spectrometer measurements will not be stored in the main spectrometer due to the much smaller magnetic field in the analyzing plane of the latter and their cyclotron radius thereby increased. Thus, most of these electrons are not observed in measurements with the main spectrometer. Apart from the conversion lines, the energy spectra of the electrons emitted in the decays of $^{219}$Rn and $^{220}$Rn are quite similar. Thus, a change in the $^{219}$Rn to $^{220}$Rn ratio inside the main spectrometer, e.g. by blocking $^{219}$Rn from the NEG pumps with cold baffles, should not significantly change the energy spectrum of stored primaries, and therefore the cluster-size distribution.
- The cluster rate in the radon background data sets A to E is rather small. Thus, differences in the cluster-size distributions due to overlapping radon clusters at large rates can be excluded at this point.

Figure 4.12 illustrates the influence of a baffle cool-down on the different background contributions under the above mentioned assumptions. The total background rate $B_{\mathrm{tot}}$ is then given by

$$B_{\mathrm{tot}} = S(N_0) + L(N_0) + \Omega \quad . \tag{4.4}$$

From the second assumption it follows that $S(N_0) = \alpha_{\mathrm{N}_0} \cdot L(N_0)$ so that $B_{\mathrm{tot}}$ can be written as

$$B_{\mathrm{tot}} = (1 + \alpha_{\mathrm{N}_0}) \cdot L(N_0) + \Omega \quad . \tag{4.5}$$

Thus, the total measured background rate $B_{\mathrm{tot}}$ is expected to increase linearly as a function of the observed rate of events in large clusters $L(N_0)$.

In the following, the five data sets A to E are used to test this hypothesis. Figure 4.13 shows the total background rate $B_{\mathrm{tot}}$, as measured by 142 detector channels, as a function of the rate of (accidental-corrected) events in clusters of size $N \geq N_0 = 2$. Each data set has been divided into one hour segments in order to visualize the spread that is induced by the random (Poisson) behavior of the radon decays. The uncertainties of each one-hour segment arises from the cluster-size distribution of the corresponding data set.

The data points in Figure 4.13 indeed follow the expected linear slope, so that a linear fit is applied to the mean values of the rates of the five data sets. With Equation 4.5, the $y$-intercept corresponds to the remaining, non-radon-induced background rate $\Omega$, while the slope corresponds to $(1 + \alpha_{\mathrm{N}_0})$. As indicated in Figure 4.13, the slope of the fit increases for larger thresholds $N_0$, due to the changed ratio of events in small and in large clusters. In the shown case of $N_0 = 2$, the parameter $\alpha_2$ directly corresponds to the ratio of radon-induced single events to clustered radon events and is derived from the fit as

$$\alpha_2 = 0.14 \pm 0.04 \quad . \tag{4.6}$$

Thus, a fraction of 14% of the radon-induced background is due to single events, making such clusters of size $N = 1$ the most prominent background contribution from radon decays.

The $y$-intercept of the linear fits[2], which corresponds to the remaining, non-radon-induced background rate $\Omega$, should be independent of the applied cluster-size threshold $N_0$. Figure 4.14 shows $\Omega$ as a function of $N_0$ both with and without a correction for accidentals. For large thresholds $N_0 \geq 6$, $\Omega$ becomes independent of $N_0$, as expected. Nevertheless, at low thresholds of $N_0 < 6$ the non-radon-induced background is underestimated by up to 5% (for $N_0 = 2$). This effect can be traced back to an insufficient accidental-correction for the cold baffle data sets. In these data sets, even with the correction for accidentals being

[2]Note that the slope and the intercept of the fits are anti-correlated.

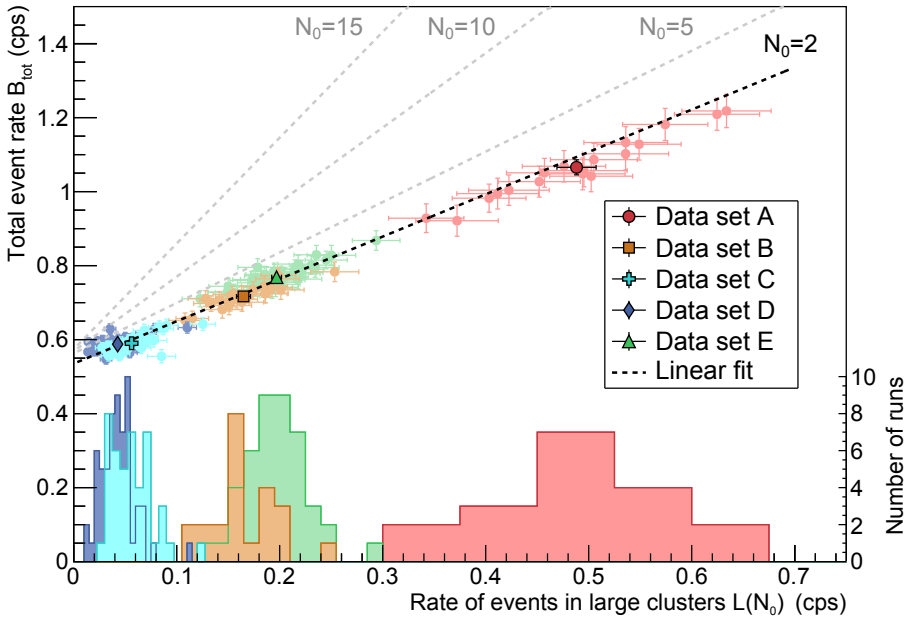


**Figure 4.13: Contribution of radon-induced cluster events to the overall spectrometer background rate.** The five data sets A to E detailed in Table 4.1 were split into one-hour run segments each (brighter colors), to visualize the spread due to the underlying Poisson statistics of radon decays. The error bars of each single one-hour segment correspond to the standard deviation that originates from the accidental-corrected cluster-size distribution (Fig. 4.10). The dark-colored points correspond to the mean rates of each data set and the corresponding uncertainty of the mean value. In this particular case a cluster-size threshold $N_0 = 2$ has been used to identify the events $L(2)$ in radon clusters of size $N \geq N_0 = 2$. A linear fit (black-dashed line), according to Equation 4.5, has been applied, where the slope of the linear fit corresponds to $(1+\alpha_2)$. The $y$-intercept gives the remaining, non-radon-induced background rate $\Omega$. The fit results for larger cluster-size thresholds $N_0$ (5, 10, 15) are shown as gray-dashed lines.

applied, some of the non-radon-induced events are falsely identified as being radon-induced ones, as discussed in Section 4.2.2. Therefore, only the data points with $N_0 \geq 6$ in Figure 4.14 are used to determine the remaining, non-radon-induced background rate, measured by 142 detector pixels. A constant fit gives the important result

$$\Omega = 565^{+8}_{-9}\,\text{mcps} \quad . \tag{4.7}$$

The conservative uncertainties stated here are given by the maximal deviation of the correlated data points (+uncertainty) from the fit result along the fit range.

The results for $\Omega$ and $\alpha_2$ are used in Figure 4.15 to calculate the different radon contributions to the observed background rates in the data sets A to E. With the absolute background rate for three cold baffles (data set D) of $B_{\text{tot}}(D) = (588 \pm 2)\,\text{mcps}$, the remaining background contribution from radon $R(D)$ with three cold baffles and for 148 detector pixels, during SDS-IIA, can be calculated as

$$R(D) = \frac{148}{142} \cdot [B_{\text{tot}}(D) - \Omega] = \frac{148}{142} \cdot 23^{+11}_{-10}\,\text{mcps} = 24^{+12}_{-10}\,\text{mcps} \quad \text{(2 NEG pumps)}. \tag{4.8}$$

Here, the uncertainty is given by the maximum error propagation of $B_{\text{tot}}(D)$ and $\Omega$. As already mentioned before, the number of events per radon cluster N increases with increasing pressure. The remaining radon rate with cold baffles $R(D)$ can, therefore, be interpreted as an upper limit. Furthermore, the remaining, non-radon-induced background $\Omega$ is somewhat pressure dependent, too, as will be discussed in Chapter 6.

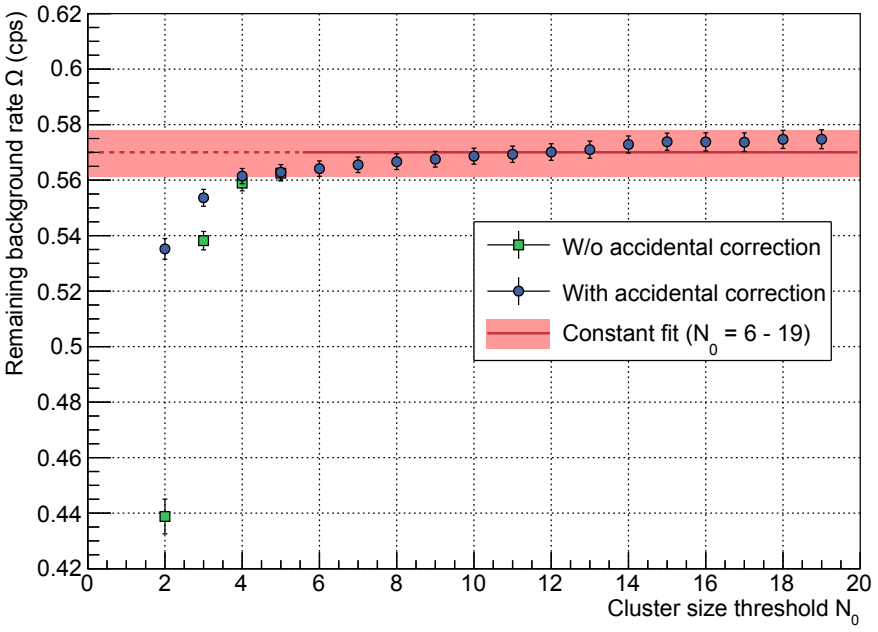


**Figure 4.14: Remaining non-radon-induced background rate Ω as a function of the cluster-size threshold $N_0$.** For $N_0 \geq 6$, the accidental correction no longer shows an effect. The error bars represent the uncertainty of the linear fits that are used to determine Ω (see Fig. 4.13). Due to the integral character of $N_0$, the data points are highly correlated. A constant fit of the data for $N_0 \geq 6$ (red line) gives $\Omega = 565^{+8}_{-9}$ mcps, where the errors are given by the absolute spread of the correlated data points (+error) along the fit range (red shaded area).

## 4.4 Sources of Radon in the KATRIN Main Spectrometer

The nominal background level for the KATRIN experiment is 10 mcps [Ang05]. In comparison, the upper limit for the remaining radon-induced background rate $R(D)$ with all baffles cold exceeds this specification by about a factor of two. Furthermore, an additional NEG pump is foreseen to be installed in pump port 1 in the final KATRIN setup, which will further increase the radon-induced background. Thus, detailed knowledge of the sources of radon inside the spectrometer and the efficiency of the baffle system to trap radon atoms emanating from these sources is of great importance for the success of KATRIN.

In the following, a model of the radon sources in the main spectrometer is established. At first, previous results on this subject are discussed in Section 4.4.1.

In contrast to earlier attempts, the SDS-II measurement phase provided two unique opportunities to study the origin of radon sources in the main spectrometer in the context of this thesis:

1. In SDS-II only two out of three main spectrometer pump ports were equipped with NEG material. Thus, a reduction of the radon activity from the NEG material to approximately two thirds of the activity during the SDS-I phase is expected. Based on this, the contributions of the different radon sources to the total activity in the spectrometer are estimated in Section 4.4.2.

2. The full long-term functionality of the $LN_2$-cooled baffle system (Sec. 3.2) allowed for detailed background measurements with different cold-baffle configurations and at elevated pressure. Thus, the radon background data sets A to E are used in Section 4.4.3 to derive the radon-reduction efficiencies for different cold-baffle configurations.

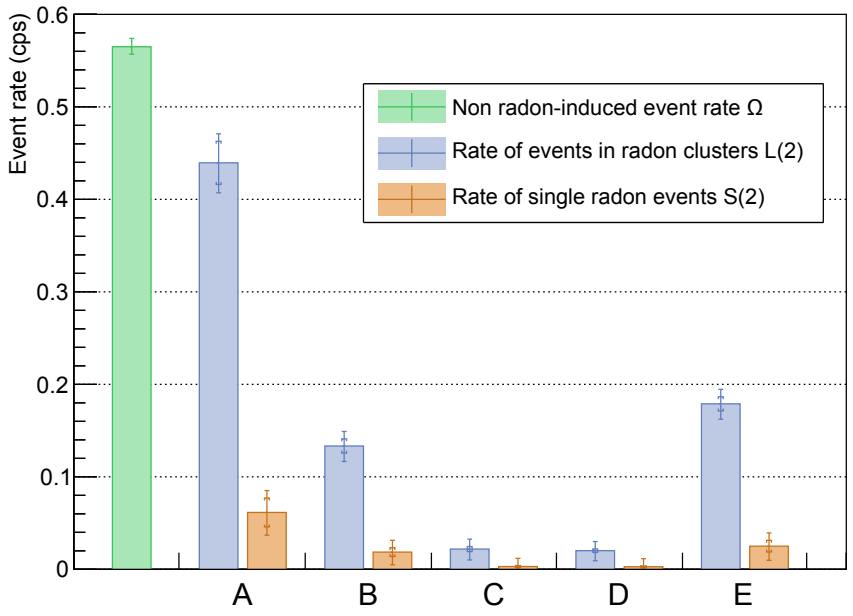


**Figure 4.15: Contribution of radon-induced events to the spectrometer background for different cold-baffle configurations.** The results for Ω (green) and $\alpha_2$ are used to calculate the background rates of radon-induced cluster events $L(2)$ (blue) and single events $S(2)$ (orange) in the data sets A to E (see Tab. 4.1). The symmetric uncertainty that originates from $\alpha_2$ is shown by brackets while the total error bars take the asymmetric error of Ω into account, as well. The shown rates correspond to the results for 142 out of 148 detector channels.

These efficiencies are then used to derive the radon-emanation rates from the NEG pumps and from other sources in the spectrometer, based on a similar analysis approach as already used in [Goe14] for the SDS-I measurements. In Section 4.4.4, this analysis is repeated, this time using a novel approach with advanced MC-based vacuum simulations which take into account adsorption and desorption processes as well as the baffle geometries. Finally, the results are compared to the findings in Section 4.4.2.

### 4.4.1 Previous Results on the Subject

In 2009 and 2010 dedicated measurements were performed at the KATRIN pre-spectrometer which targeted the radon-induced background in MAC-E filters [Fra10, Goe10, Fra11]. The findings of these measurements were used to extrapolate to the expected radon activities in the main spectrometer [Mer13]. In these studies, the total radon activity $A^{\mathrm{Rn}}_{\mathrm{total}}$ is connected to the emanation rates $E^{\mathrm{Rn}}_i$ of the different radon sources $i$ in the main spectrometer according to

$$A^{\mathrm{Rn}}_{\mathrm{total}} = \sum_i A^{\mathrm{Rn}}_i = \sum_i E^{\mathrm{Rn}}_i \cdot P_i \quad , \tag{4.9}$$

where $P_i$ corresponds to the probability for radon atoms emanating from source $i$ to decay inside the spectrometer volume. In case of the extrapolations performed in [Mer13] it was assumed that radon atoms, when hitting a cold baffle surface, will stick to it with a sticking probability of $c = 0.8$ and remain on the cold surface until they decay. Furthermore, a 100% blocking efficiency of a cold baffle for radon that emanates from the NEG pump in the corresponding pump port was assumed. Under these assumptions, an analytic expression

**Table 4.3: Expected radon activities and emanation rates in the main spectrometer** based on the results of measurements at the pre-spectrometer. The expected activities $A_i^{\mathrm{Rn}}$ for radon inside the main spectrometer are calculated from the emanation rates $E_i^{\mathrm{Rn}}$ stated in [Mer13], via Equations 4.9 and 4.10, by using the average pumping speed $S_{\mathrm{TMP}}$ of the spectrometer TMPs for both radon isotopes [Mer13] and the pumping speed $S_{\mathrm{baffle}}$ of three cold baffles for radon from the spectrometer volume [Goe14]. The emanation of $^{219}$Rn from the NEG pump is set to zero in the case of cold baffles, i.e. a 100% blocking efficiency of the baffles for radon from the NEG pumps is assumed.

| | Warm baffles | Cold baffles |
|---|---|---|
| $E^{\mathrm{Rn}}_{219,\mathrm{NEG}}$ ($^1/_{\mathrm{s}}$) | $0.12 \pm 0.03$ | 0.0 |
| $E^{\mathrm{Rn}}_{219,\mathrm{walls}}$ ($^1/_{\mathrm{s}}$) | $0.03 \pm 0.03$ | $0.03 \pm 0.03$ |
| $E^{\mathrm{Rn}}_{220,\mathrm{walls}}$ ($^1/_{\mathrm{s}}$) | $0.08 \pm 0.06$ | $0.08 \pm 0.06$ |
| $S_{\mathrm{TMP}}$ ($^{\ell}/_{\mathrm{s}}$) | 3 505 | 3 505 |
| $S_{\mathrm{baffle}}$ ($^{\ell}/_{\mathrm{s}}$) | 0.0 | 180 000 |
| $A^{\mathrm{Rn}}_{219,\mathrm{NEG}}$ (mBq) | $118 \pm 30$ | 0.0 |
| $A^{\mathrm{Rn}}_{219,\mathrm{walls}}$ (mBq) | $30 \pm 30$ | $16 \pm 16$ |
| $A^{\mathrm{Rn}}_{220,\mathrm{walls}}$ (mBq) | $65 \pm 49$ | $6 \pm 5$ |

for the probability $P_i$ can be derived to

$$P_i = \left(1 + \frac{S_{\mathrm{eff}}}{V_{\mathrm{MS}} \cdot \lambda_i^{\mathrm{Rn}}}\right)^{-1} \quad . \tag{4.10}$$

Here, $V_{\mathrm{MS}} = 1\,240\,\mathrm{m}^3$ is the volume of the main spectrometer, $\lambda_i^{\mathrm{Rn}} = {}^1/_{\tau_i^{\mathrm{Rn}}}$ are the decay constants of the two radon isotopes $^{219}$Rn and $^{220}$Rn, and $S_{\mathrm{eff}} = S_{\mathrm{TMP}} + S_{\mathrm{baffle}}$ is the effective combined pumping speed of the TMPs and the baffles for radon. The extrapolated emanation rates, the effective pumping speeds, and the calculated expectations on the radon activities in the main spectrometer for warm and for cold baffles are listed in Table 4.3. The pumping speed of the cold baffles for radon in the spectrometer volume are based on

$$S_{\mathrm{baffle}} = c \cdot \frac{\overline{v}}{4} \cdot A \quad , \tag{4.11}$$

where $A$ is the cold surface area of the baffle system, and $\overline{v}$ is the average velocity of the radon gas [Mer12a]. The expected activities in the main spectrometer stated in Table 4.3 suffer from large uncertainties, which are due to the rather low statistics of the pre-spectrometer measurements.

In 2013, during the initial SDS-I phase, low-pressure measurements with different configurations of cold baffles were performed in order to identify the different radon sources inside the spectrometer due to differences in the total observed background rate [Goe14]. These measurements were strongly limited in time as the $LN_2$-circulation system and the HV-insulation of the baffle system were not fully functional at that point. In contrast to the earlier pre-spectrometer measurements, it was also not possible to change the amount of getter material in the pump ports within the measurement phase. Furthermore, electromagnetic-tracking simulations with KASSIOPEIA [FG15] were needed in order to translate the expected activities into expected background rates, as the measurements were carried-out with low spectrometer pressures, where single radon decays cannot be identified in the data.

In a second approach, warm-baffle measurements at a 5-G 'symmetric' magnetic field setting were carried out during SDS-I at an elevated pressure of $p = 1 \times 10^{-8}$ mbar (detector runs #8531 - #8533). They were used to extrapolate to the total detectable activity of radon inside the main spectrometer of $A_{\text{tot}} = (196 \pm 10)$ mBq [Sch14c]. This result is in reasonable agreement with the expectations based on the pre-spectrometer measurements. However, the different contributions of radon, which emanates from the NEG or the vessel walls could not be disentangled, as all elevated pressure measurements during this campaign were performed with warm baffles and with the same amount of getter material installed in the system.

### 4.4.2 Comparison of the Measured Activities with the SDS-I Results

In the following, the radon activities measured during SDS-I, for which all three pump ports were equipped with NEG material, are compared to the corresponding SDS-II data, where pump port 1 was not equipped with getter material. The same analysis principle that was successfully applied in [Sch14c] is utilized to extrapolate the measured activities in the observed flux tube volume per detector ring to the total activity in the entire spectrometer volume $V_{\text{MS}} = 1\,240\,\text{m}^3$. In this context it is assumed that radon clusters do not overlap in time so that each observed cluster corresponds to only one radon decay in the volume. This assumption is justified in [Sch14c], where the probability of two radon clusters to overlap in a 5-G high-pressure measurement is derived to $P \approx 1.4\%$. In the SDS-I analysis in [Sch14c] a conservative cluster-size threshold of $N_0 \geq 3$ had to be used in order to prevent a too large contamination from accidental clusters. By contrast, the accidental-correction algorithm, introduced in Section 4.2.2, is used in this work for $N_0 \geq 2$ to take into account even small clusters with $N = 2$ to calculate the observed activities. As radon is distributed homogeneously inside the main spectrometer, the observed activity is expected to increases linearly with the observed volume.

Figure 4.16 shows a comparison of the observed activities for a SDS-I measurement at a 5-G magnetic field in the analyzing plane (detector runs #8531 $-$ #8533) and the results for the SDS-II data set A. Both measurements were carried out under similar experimental conditions, such as a spectrometer pressure of $1 \times 10^{-8}$ mbar, an inner electrode offset of $-100$ V, and a post-acceleration potential of $+10$ kV. During the SDS-I phase, 26 out of 148 detector pixels could not be used for the data analysis, mostly due to shadowing effects along the beam line (Sec. 3.9). This limitation is taken into account by subtracting the non-mapped volumes of the corresponding detector rings. A linear extrapolation of the SDS-I data shown in Figure 4.16 yields an observed radon activity of $A^*_{\text{SDS-I}} = (200 \pm 3)$ mBq in good agreement with $A_{\text{tot}}$ derived in [Sch14c]. In order to estimate the effect of the missing 26 detector channels in the SDS-I analysis, the SDS-II data set A is analyzed in two ways. In the first approach, the same 26 pixels as for the SDS-I data are excluded from the analysis, resulting in an activity of $A^*_{\text{SDS-II}} = (139 \pm 1)$ mBq. In a second analysis step all 148 detector channels of SDS-II are used, giving

$$A_{\text{SDS-II}} = (136 \pm 1)\,\text{mBq} \quad . \tag{4.12}$$

Thus, the observed activity is overestimated by $(2 \pm 1)\%$ due to the missing 26 detector channels. With this correction applied, the SDS-I activity becomes

$$A_{\text{SDS-I}} = (196 \pm 4)\,\text{mBq} \quad . \tag{4.13}$$

As outlined earlier, the SDS-I measurements were performed with NEG pumps installed in all three pump ports of the main spectrometer, whereas during the SDS-II measurements pump port 1 remained empty. Thus, a comparison of the radon activities measured in

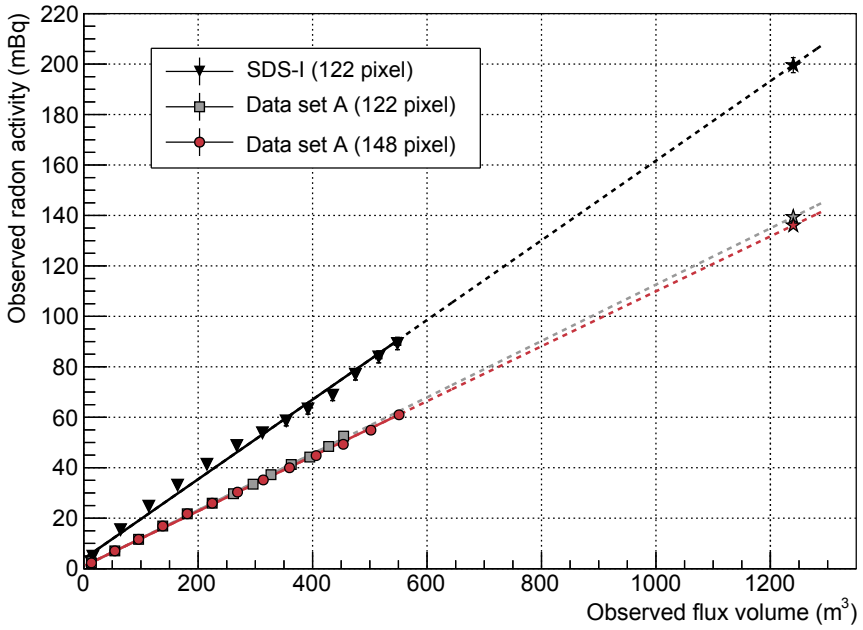


**Figure 4.16: Comparison of the observed radon activities in the SDS-I and SDS-II elevated-pressure measurements with warm baffles.** The observed radon activity is determined by repeating the cluster-search algorithm (with accidental correction), using detector rings 1 to $i$, where $i$ is increased from 1 to 13. The smallest volume corresponds to the bullseye only, while the largest is obtained by using all 13 detector rings for the analysis. The SDS-I results are given by black triangles. Here, the observed volumes are corrected for the 26 detector pixels which could not be used for mapping during SDS-I. The SDS-II data set A is analyzed in two ways: first, with the same volume correction as applied to the SDS-I data (gray squares), and secondly by using all 148 detector pixels (red dots) for the analysis. Linear fits (solid lines) are used to extrapolate (dashed lines) to the overall activity in the entire spectrometer volume (marked by stars). Note that the integral character of the applied analysis results in a correlation of the data points, which is not taken into account by the invisibly small statistical error bars.

SDS-I and those observed in data set A of SDS-II allows to disentangle the radon contribution from a single NEG pump $A_{\mathrm{NEG}}$ and those from other sources like the spectrometer walls and auxiliary equipment $A_{\mathrm{other}}$ according to:

$$\begin{aligned} A_{\text{SDS-I}} &= 3 \cdot A_{\mathrm{NEG}} + A_{\mathrm{other}} \\ A_{\text{SDS-II}} &= 2\,(1+\beta) \cdot A_{\mathrm{NEG}} + A_{\mathrm{other}} \end{aligned} \tag{4.14}$$

Here, the factor $\beta$ takes into account the relative increase of the radon activity of the NEG pumps over time. This increase originates from the non-secular character of the decay chain of $^{235}$U in the getter material, due to an excess of $^{231}$Pa. This isotope causes a steady increase of the activity of the subsequent decay products like $^{219}$Rn. In 2008, the activities of $^{231}$Pa and its daughter nucleus $^{231}$Ac were measured for several samples of the getter material (*St 707*) used in the main spectrometer NEG pumps via $\gamma$-spectroscopy. Based on the measured values of $A_{\text{Pa-231}} = (8\,427 \pm 561)\,^{\mathrm{mBq}}/_{\mathrm{kg}}$ and $A_{\text{Ac-227}} = (995 \pm 79)\,^{\mathrm{mBq}}/_{\mathrm{kg}}$ [For08], the relative increase of the $^{219}$Rn activity in the NEG material in the time interval ($t = 439$ days) between the SDS-I and the SDS-II measurements can be calculated to $\beta = 0.11 \pm 0.08$.

Solving the Equations in 4.14 for this value of $\beta$ gives

$$\begin{aligned} A_{\mathrm{NEG}} &= (77 \pm 14)\,\mathrm{mBq} \\ A_{\mathrm{other}} &= (-35 \pm 42)\,\mathrm{mBq} \quad . \end{aligned} \tag{4.15}$$

In contrast to the results for the total detectable activity in SDS-I, these results for the radon activity per NEG pump ($A_{\mathrm{NEG}}$) and from other sources ($A_{\mathrm{other}}$) do not confirm the extrapolations from the pre-spectrometer measurements stated in Table 4.3. While these expectations attributed only half of the radon activity to the getter material, the results derived in this work are consistent with the getter material being the major (or even only) source of radon in the spectrometer. However, it should be noted that the values stated in Table 4.3 suffer from the uncertainties of the low statistics of the pre-spectrometer measurements.

**The Total Activities of Radon in the Main Spectrometer**

The activities stated in the previous paragraph do not correspond to the total radon activities in the main spectrometer, as only clusters with $N \geq 2$, observed by the detector, are used to derive them. In order to obtain the total radon activity from the observed activities in Equations 4.15, two effects have to be taken into account:

1. In Section 4.3 it was found that a significant number of radon decays (shell reorganization) are only detected as a single event on the detector. These clusters of size $N = 1$ have to be taken into account when deriving the total activities.

2. A certain fraction of electrons that are generated by a radon decay in the volume will leave the main spectrometer on its upstream side so that it is not recorded by the detector. In the hypothetical case that all electrons from a radon decay would leave the spectrometer in this direction, the decay would not be detected at all, resulting in an underestimation of the radon activity by a factor $1/\kappa$ (see Eq. 4.18).

While the first effect can easily be corrected for by taking into account the ratio of radon-induced single events to clustered events $\alpha_2 = 0.14 \pm 0.04$, a correction of the second effect is more challenging. The ratio of electrons that leave the spectrometer on its upstream side depends on the absolute magnetic field of the PS2 magnet compared to the pinch magnet field. The probability $p = 0.6$ of an electron to escape towards the pre-spectrometer side, given in [Mer12a] has been derived under the assumption of a nominal pinch magnet field of 6 T versus a PS2 magnet field of 4.5 T. As the pinch magnet has been used during both SDS-I as well as SDS-IIA at a reduced field strength of 5 T, a probability of $p = 0.5$ has been assumed here. To determine the exact value, a detailed calculation of the radon-induced background in the main spectrometer is required, which is unavailable at the present time.

With a total number of $N$ electrons that is generated via to a single radon $\alpha$-decay in the spectrometer, the probability to only observe k of these electrons with the detector is given by the binomial distribution

$$B(k \mid p, N) = \binom{N}{k} p^{\mathrm{k}} \, (1-p)^{\mathrm{n\text{-}k}} \quad . \tag{4.16}$$

The mean difference $\Delta_{\mathrm{tot}}$ between the total number of observed clusters $\Gamma_{\mathrm{tot}}$ and the real number of radon decays $\Theta_{\mathrm{tot}}$ in the spectrometer is therefore given by

$$\Delta_{\mathrm{tot}} = \sum_{N=0}^{\infty} \Delta(N) = \sum_{N=0}^{\infty} B(0 \mid p, N) \cdot \Theta(N) \quad , \tag{4.17}$$

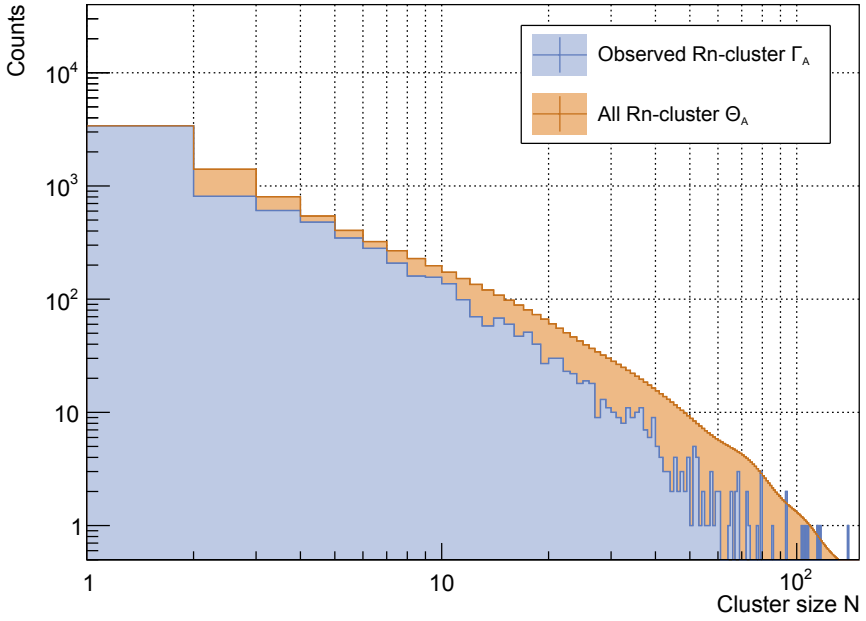


**Figure 4.17: The cluster-size distribution including 'invisible' radon clusters.** Equation 4.20 has been used to correct the measured cluster-size distribution of data set A (blue) for 'invisible' cluster events, i.e. events leaving the spectrometer on its upstream side. The rate of radon clusters with size 1 has been estimated from the factor $\alpha_2 = 0.14$, determined via the fit in Figure 4.13, multiplied by the rate of events found in clusters of size $N \geq 2$. The probability for a single electron to leave the spectrometer on its upstream side has been approximated to $p = 0.5$. The corrected distribution (orange) is shifted to higher cluster sizes, while the total cluster rate is increased by a factor $\kappa = 1.34 \pm 0.04$.

where $\Theta(N)$ represents the number of counts in the $\mathrm{N}^{\mathrm{th}}$ bin of the original cluster-size distribution, or in other words the distribution of the number of electrons which are actually created inside the spectrometer subsequent to a radon $\alpha$-decay, including secondary electrons. From Equation 4.17 the desired correction factor $\kappa$ can be derived according to

$$\kappa = \frac{\Gamma_{\mathrm{tot}} - \Delta_{\mathrm{tot}}}{\Gamma_{\mathrm{tot}}} \quad . \tag{4.18}$$

To determine $\Delta_{\mathrm{tot}}$, the original cluster-size distribution $\Theta$ needs to be known. Unfortunately, due to the statistical nature of the binomial process, there are infinitely many different possible original distributions for a given measured distribution and the 'real' one can not be reconstructed from the data. However, the most probable of all of these distributions can be calculated by using the negative binomial probability distribution

$$B(N \mid p, k) = \binom{N-1}{k-1} p^{\mathrm{k}} \, (1-p)^{\mathrm{n\text{-}k}} \quad . \tag{4.19}$$

Here, $B(N \mid p, k)$ is defined as the probability that $N$ trials are needed in order to achieve $k$ (fixed) successes in a Bernoulli-process, where the probability of a success in a single trial is given by the probability $p$.

Figure 4.17 shows the observed cluster-size distribution $\Gamma_{\mathrm{A}}$ of data set A in blue, where the height of the first bin $\Gamma_{\mathrm{A}}(1)$ corresponds to the number of radon-induced single events $S(2) = \alpha_2 \cdot L(2)$. The most probable of all possible original cluster-size distributions $\Theta_{\mathrm{A}}$

is shown in orange, where the number of entries $\Theta_{\mathrm{A}}(N)$ in the $\mathrm{N}^{\mathrm{th}}$ bin is given by

$$\Theta_{\mathrm{A}}(N) = \left[\sum_{k=1}^{N} B(N \mid p,k)\cdot\Gamma_{\mathrm{A}}(k)\right]\cdot\frac{1}{1-B(0\mid p,N)} \quad . \tag{4.20}$$

Note that the fraction at the end takes those clusters into account which were not observed by the detector at all ($k=0$). It has been derived from Equation 4.17 under the assumption of an emission of at least one electron per radon decay ($\Theta(0)=0$), which is justified from the atomic physics point-of-view.

By comparing the number of entries in $\Theta_{\mathrm{A}}$ to those in the measured distribution $\Gamma_{\mathrm{A}}$, the correction factor can be approximated to $\kappa = 1.34 \pm 0.04$. The factor $\kappa$, and the fact that radon clusters of size $N=1$ are not taken into account in the activity determination, can be combined in a total correction factor $\eta = 2.9 \pm 0.5$. With this factor the total radon activities can be calculated from the observed activities given in Equation 4.15 to

$$\begin{aligned} A^{\mathrm{tot}}_{\mathrm{NEG}} &= (223 \pm 56)\,\mathrm{mBq} \\ A^{\mathrm{tot}}_{\mathrm{other}} &= (-101 \pm 123)\,\mathrm{mBq} \quad . \end{aligned} \tag{4.21}$$

Note that the result for $A^{\mathrm{tot}}_{\mathrm{NEG}}$ represents a 'snapshot' of the activity per NEG pump in September 2013. Due to the steady increase of the radon activity in the getter material, this contribution will further increase with time. The total activity of radon in the main spectrometer during SDS-II (December 2014) can be derived from the result stated in Equation 4.12 to

$$A^{\mathrm{tot}}_{\text{SDS-II}} = A_{\text{SDS-II}}\cdot\eta = (394 \pm 68)\,\mathrm{mBq} \quad . \tag{4.22}$$

### 4.4.3 Radon-Reduction Efficiency of the Baffle System

Due to the long time span of 439 days between the SDS-I and the SDS-II measurement phases which was accompanied by major hardware works on the main-spectrometer vacuum system, a second approach is used in this section to disentangle the sources of radon in the spectrometer, this time based on SDS-II data only.

#### The Cluster-Rate Reduction Efficiencies

With the radon background data set A (warm baffles) serving as a reference, the cluster-reduction efficiencies *Eff*$(X)$ in the cold baffle data sets B to E can be calculated according to

$$\textit{Eff}(X) = 100\%\cdot\left(1-\frac{R_X}{R_A}\right) \quad . \tag{4.23}$$

Here, $R_A$ corresponds to the cluster rate with warm baffles and $R_X$ is the corresponding cluster rate in one of the data sets B to E. However, in Section 4.2.2 it has been shown that the rate of observed clusters in cold-baffle measurements is dominated by accidental clusters. Even the accidental-correction algorithm, as developed in the context of this work, has been found to be inaccurate for the very low radon decay rates in the cold-baffle measurements. Thus, a simple calculation of the baffle efficiency according to Equation 4.23 would significantly underestimate the efficiency of the baffle system when using the standard cluster-size threshold of $N_0 = 2$ to determine $R_A$ and $R_X$. However, if one assumes that (similar as in Section 4.3) the shape of the cluster-size distribution does not change by a cool-down of the baffles, the cluster-reduction efficiencies *Eff*$(X)$ can be calculated by using a larger threshold $N_0 > 2$. Unfortunately, it is not possible to use an arbitrarily high value of $N_0$, as the statistics of the different data sets vary significantly and the reference data set A, with warm baffles, has by far larger statistics than the others. Due to the integral character of the threshold $N_0$, the contribution of empty bins in the cluster-size

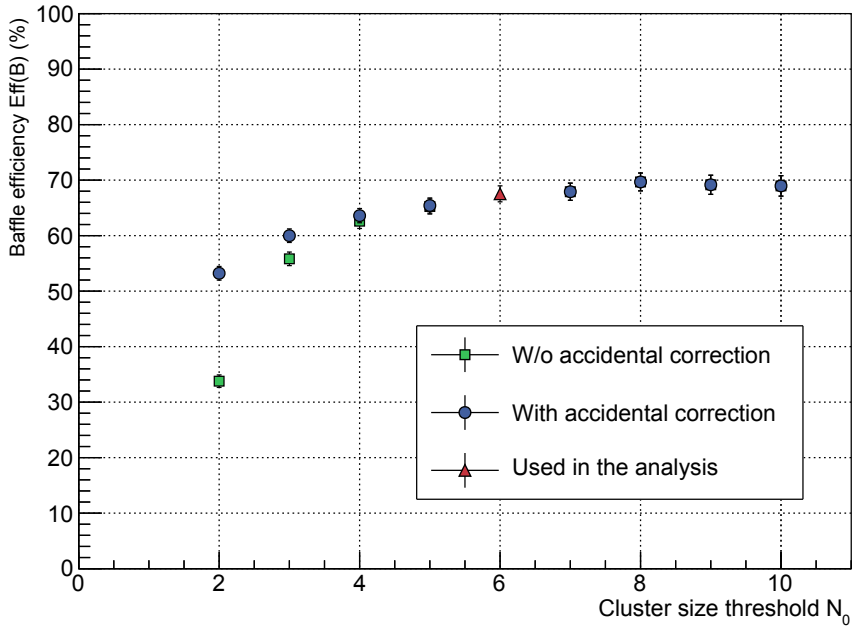


**Figure 4.18: Efficiency of the radon background suppression by a single baffle cool-down.** The relative reduction of the observed rate of radon clusters between data sets A and B (see Table 4.1) is determined according to Equation 4.23 for different cluster-size thresholds $N_0$. The assumption of Gaussian errors per data point is verified via MC-simulations. Nevertheless, the correlation between the data points, which originates from the integral character of the threshold $N_0$, is not taken into account by the error bars. An underestimation of the efficiency at low $N_0 < 6$ is partly compensated by the accidental correction. The efficiencies for $N_0 \geq 6$ are not affected by the accidental correction anymore. The reduction efficiency at $N_0 = 6$ (red triangle) is therefore used in the analyses.

distribution of the cold-baffle data sets increases with increasing $N_0$. Thus, the efficiency $Eff(X)$ increases for large $N_0$ due to the low statistics in the cold baffle data sets.

An example of the dependency of the baffle efficiencies on the cluster-size threshold can be found in Figure 4.18, where the cluster-reduction efficiency $Eff(B)$ for the cool-down of baffle 2 is shown as a function of $N_0$. In the interval $N_0 < 6$, the efficiency is significantly underestimated due to accidental clusters in data set B, which are falsely identified as radon-induced. An accidental-cluster correction in this case shows a significant influence, even if it does not allow to fully compensate the underestimation of the baffle efficiency. For $N_0 \geq 6$ the accidental correction no longer has a significant effect on the result and the deduced baffle efficiencies are independent of $N_0$ up to $N_0 = 10$. Therefore, a cluster-size threshold of $N_0 = 6$ is used to determine the cluster reduction efficiencies stated in Table 4.4.

The background reduction efficiency $Eff(B)$ of a cool-down of the baffle in the getter-equipped pump port 2 is found to be significantly larger than 50%. This shows that the cold baffle not only blocks radon that emanates from the NEG material behind it, but also pumps radon that emanates from elsewhere inside the spectrometer. This can either be radon from the walls and auxiliary equipment, or $^{219}$Rn emanating from the second getter-equipped pump port 3. If the baffle in pump port 3 is additionally cooled-down (data set C), the cluster-reduction efficiency $Eff(C)$ increases to more than 90%. Thus, a cool-down of the baffles in front of both getter-equipped pump ports already eliminates nearly all radon-induced clusters, so that the cool-down of the last baffle in the getter-free pump port 1 is less prominent [see $Eff(D)$]. This result is compatible with the results stated

**Table 4.4: Cluster-reduction efficiencies for the different cold-baffle configurations** listed in Table 4.1. The efficiencies listed here are calculated according to Equation 4.23 relative to the large-statistics data set A with warm baffles and for a cluster-size threshold of $N_0 = 6$.

| Baffle configuration | Efficiency *Eff* (%) |
|---|---|
| B | $67.5 \pm 1.4$ |
| C | $92.0 \pm 0.5$ |
| D | $95.1 \pm 0.3$ |
| E | $61.0 \pm 1.3$ |

in Equation 4.21, where the NEG material in the pump ports is identified as major source of radon. However, a large contribution of radon from the walls and auxiliary equipment cannot be ruled out at this point, if one assumes a large pumping efficiency of the baffles for radon originating from the spectrometers main volume.

A conclusive answer to this issue can be given by measurement E, where the two baffles in the getter-equipped pump port 2 and the getter-free pump port 1 were cold. The comparison of *Eff*$(E)$ and *Eff*$(C)$ shows that the observed cluster-reduction efficiency is significantly larger if two cold baffles block the two getter-equipped pump ports. This can only be explained by $^{219}$Rn from the NEG pumps being the dominant source of radon inside the main spectrometer as long as similar pumping efficiencies of the three baffles for radon in the volume are assumed. Nevertheless, a comparison of the results of the data sets B and E, both with one of the NEG pumps blocked by a cold baffle, shows that *Eff*$(E)$ is slightly smaller than *Eff*$(B)$. This is somewhat inconsistent, as the additional cold baffle in pump port 1 in measurement E should reduce or at least keep the radon cluster rate at the same level, rather than increasing it. One possible explanation for this inconsistency is that data set E was taken directly after measurements with an artificial $^{220}$Rn source installed to pump port 3 (see Appendix A). Here, a small contamination from the artificial source inside pump port 3 or a small leak in the valve to this source could explain the slightly too large radon cluster rate.

**Radon Activity with Cold Baffles**

The same analysis principle that has already been used in Section 4.4.2 to derive the observed radon activity in data set A can also be used to determine the activity in the cold-baffle data sets B to E. Figure 4.19 shows the extrapolations to the observed radon activities in the full spectrometer volume for the data sets at cold baffles. While the data points of set A are in good agreement with a linear slope, in particular the data of sets C and D significantly deviate from a linear slope for large observed volumes (outer detector rings). This can be explained by the large contribution of uncorrected accidental clusters in the cold-baffle measurements. In Section 4.2.2 it was found that the contribution of these accidentals increases to larger radii due to the spacial distribution of the non-radon-induced background. Thus, in the case of the cold baffle data sets B to E, only the innermost 7 detector rings are used to scale up to the activities in the full spectrometer volume. The results of the extrapolation for all five data sets are listed in the first column of Table 4.5.

However, even at small radii, the uncorrected accidentals will cause a significant overestimation of the radon activities. Thus, a second approach has been pursued by using the baffle efficiencies that are stated in Table 4.4 to calculate the activities for the cold-baffle data sets B to E out of the observed activity of data set A, at warm baffles. As the

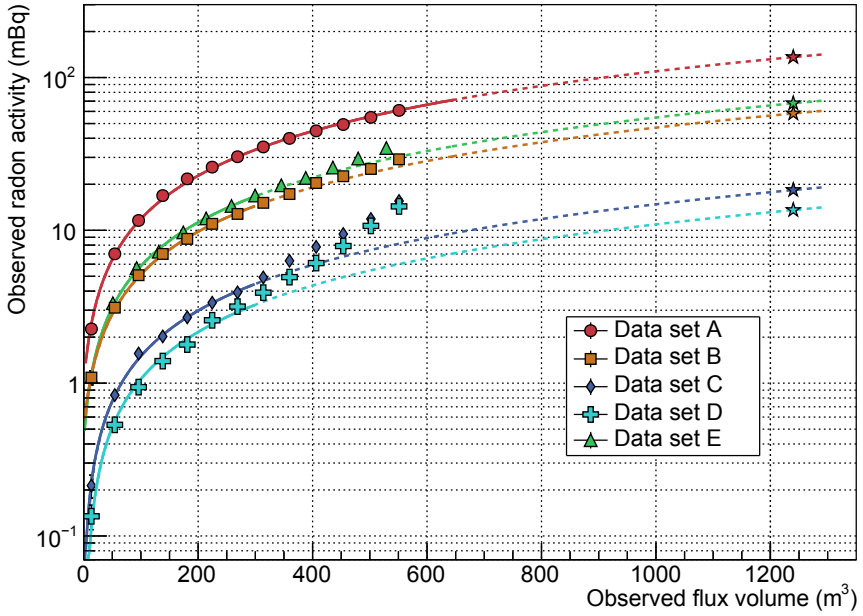


**Figure 4.19: Measured radon activity as a function of the observed flux volume for the different baffle configurations during SDS-II** (see Table 4.1). A logarithmic scale for the observed radon activity has been used in order to visualize the small differences between the measurements. For data set A, with all baffles warm, the measured activity shows a linear dependence on the observed volume. In the case of cold baffles (B to E), the slope increases for volumes of $> 300\,\mathrm{m}^3$. Here, only the innermost 7 data points are used for the extrapolation to the full spectrometer volume (marked by stars). The resulting activities are given in the first column of Table 4.5. Note that the 6 missing pixels in data set E cause a shift in the corresponding data points to lower observed volumes.

accidental-correction algorithm successfully works in the case of warm-baffle measurements (Fig. 4.9) and the baffle efficiencies are calculated using a large $N_0 = 6$, this approach is expected to give more reliable results. The activities derived in this way are stated in the second column of Table 4.5.

### Determination of the Radon Emanation Rates

In order to determine the contributions of $^{219}$Rn originating from the NEG pumps and $^{220}$Rn emanating from other regions of the spectrometer, a similar approach as in [Goe14] is utilized. Equations 4.9 and 4.10 are used to find the best fit for the emanation rates $E_{\mathrm{NEG}}$ and $E_{\mathrm{other}}$ to reproduce activities, equivalent to those stated in Table 4.5. In contrast to the SDS-I analysis in [Goe14], however, simulation input is not needed at this point to deduce activities from background rates, due to the fact that the SDS-II cold-baffle measurements were performed at elevated pressure. Note that similar to the SDS-I analysis, radon emanation sites other than the NEG pumps are assumed to produce $^{220}$Rn only. The pumping speed of a single cold baffle for radon in the spectrometer volume, $S_{\mathrm{baffle}}$, as well as the emanation rates $E_{\mathrm{NEG}}$, and $E_{\mathrm{other}}$ are free fit parameters. The minimization is performed by using the ROOT package MINUIT [BR96], [BR97] and the results are listed in Table 4.6.

Figure 4.20 shows the corresponding $\chi^2$/ndf distribution for a fixed pumping speed of $S_{\mathrm{baffle}} = 35\,000\,\ell/\mathrm{s}$ and different emanation rates $E_{\mathrm{NEG}}$ and $E_{\mathrm{other}}$. The rather large uncertainties on all three parameters result from the small number of data points. As opposed to the results obtained in Section 4.4.2, now a significant contribution by $^{220}$Rn from sources

**Table 4.5: Observed radon activity in the spectrometer for the different SDS-II radon-background measurements** listed in Table 4.1. The total activities in the spectrometer are determined via the linear extrapolations shown in Figure 4.19. In the second column, the cluster reduction efficiencies stated in Table 4.4 are used to determine the activities for data sets B to E out of the extrapolation result of data set A.

| Baffle configuration | Extrapolated activity (mBq) | Calculated activity (mBq) |
|---|---|---|
| A | $136 \pm 1$ | $136 \pm 1$ |
| B | $58 \pm 1$ | $44 \pm 2$ |
| C | $18 \pm 1$ | $11 \pm 1$ |
| D | $13.6 \pm 0.4$ | $6.7 \pm 0.4$ |
| E | $67 \pm 1$ | $53 \pm 2$ |

**Table 4.6: Minimization results of the SDS-I analysis method** for the radon emanation rates from the NEG pumps $E_{\mathrm{NEG}}$, from other sources in the spectrometer $E_{\mathrm{other}}$, and the effective pumping speed $S_{\mathrm{baffle}}$ of a single cold baffle for radon.

| Free parameter | Result |
|---|---|
| $E_{\mathrm{NEG}}$ | $0.04 \pm 0.01\ ^{1}/_{\mathrm{s}}$ |
| $E_{\mathrm{other}}$ | $0.06 \pm 0.03\ ^{1}/_{\mathrm{s}}$ |
| $S_{\mathrm{baffle}}$ | $35\,000^{+20\,000}_{-18\,000}\ ^{\ell}/_{\mathrm{s}}$ |

other than the NEG pumps is found. This is in good agreement with the results obtained in [Goe14], where a similar kind of minimization was performed. However, the analysis presented here is based on the simplifying assumption that a radon atom, once impinging on a cold baffle surface, will stick there for a prolonged time period to decay there. In a more generalized approach, time-dependent adsorption and desorption processes of radon atoms have to be taken into account, in particular the fact that radon atoms can desorb from the baffle surface after a mean desorption time $\tau_{\mathrm{des}}$. This effect is of particular relevance here as the main spectrometer was not baked-out prior to SDS-II. Accordingly, a water-allocation on the baffle surfaces is expected. This will significantly decrease $\tau_{\mathrm{des}}$ [Eic00a] and therefore increase the desorption probability of radon from the cold baffles. For rather short desorption times which are of the same order of magnitude as $\tau_{219}^{\mathrm{Rn}}$, the earlier assumption of a 100% blocking efficiency of a baffle for radon emanating from the NEG pump behind it cannot be maintained further.

In order to obtain more reliable results for the different radon contributions in the main spectrometer, time-dependent adsorption and desorption processes have to be taken into account. Therefore, the results listed in Table 4.6 have to be used with caution and are only meant to show the comparability of the SDS-I measurement results given in [Goe14] with the SDS-II measurements presented in this work.

### 4.4.4 Comparison with Molflow+ Simulations

Based on the findings in the SDS-I campaign [Goe14, Sch14c], considerable efforts were made to simulate radon adsorption and desorption processes for a simplified main spectrometer geometry that includes all ports, the baffles, the NEG pumps, and the TMPs [Kra15b]. This geometry is used as an input for the test-particle MC-simulation program MolFlow+ [AK14]. The freely available MolFlow+ code is originally designed for vacuum

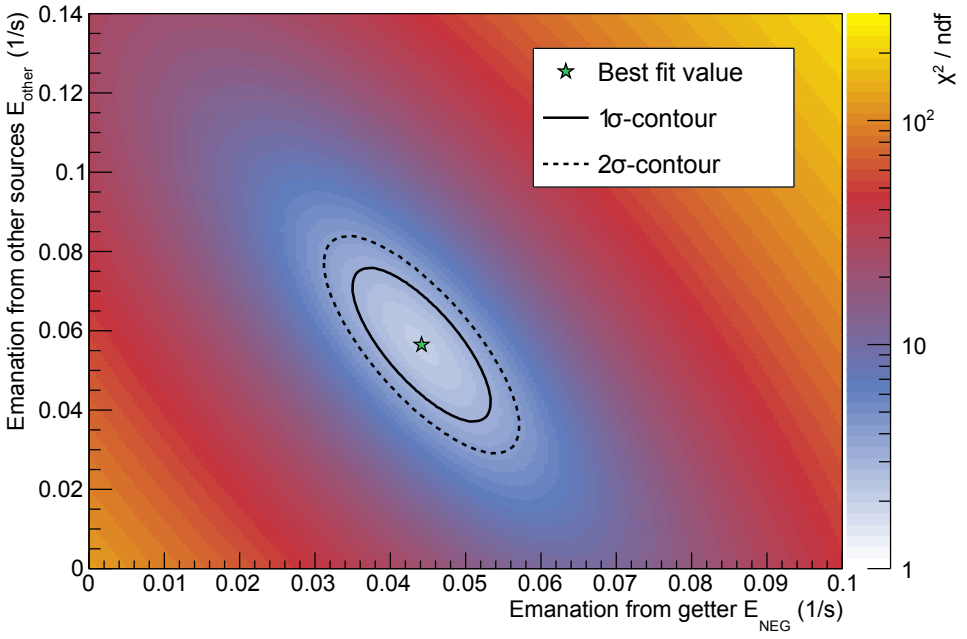


**Figure 4.20: $\chi^2$/ndf distribution for different radon emanation rates from the NEG material and from other sources.** The effective pumping speed is fixed at its best-fit value of $S^{\text{Baffle}} = 35\,000\,\ell/\text{s}$ and the optimal composition of $E_{\text{NEG}}$ and $E_{\text{other}}$ with $\chi^2/\text{ndf} = 2.15$ is indicated by a green star. In addition, the $1\sigma$ ($2\sigma$) contour is shown as solid (dashed) line. The corresponding results are listed in Table 4.6.

simulations in the free-molecular flow regime and was extended in [Kra15b] to account for the decay of short-lived (radioactive) particles and in particular multiple sorption processes of particles from surfaces. This allows to simulate the interactions of radon atoms with the cold baffle surfaces for which a mean desorption time $\tau_{\text{des}}$ defines the time period that a radon atom will stick to the surface after its adsorption. The mean desorption time is given by

$$\tau_{\text{des}} = \tau_0 \cdot \exp\left(-\frac{H_{\text{des}}}{R \cdot T}\right) \quad , \tag{4.24}$$

where $\tau_0$ corresponds to the period of vibration of the bond between the adsorbate and the adsorbent, $H_{\text{des}}$ defines the desorption enthalpy, $R = 8.3145\,\text{J}/\text{mol}\cdot\text{K}$ is the gas constant, and $T$ denotes the surface temperature of the baffle. The two parameters $H_{\text{des}}$ and $\tau_0$ depend on the material and particularly its surface conditions, as will be discussed in detail in Appendix A. The mean desorption time $\tau_{\text{des}}$ can be related to an effective sticking coefficient, $c_{\text{eff}}$, according to

$$c_{\text{eff}} = c_0 \cdot \left(1 - \frac{1}{1 + \frac{\tau_{Des}}{\ln(2) \cdot t_{1/2}}}\right) \quad , \tag{4.25}$$

where $t_{1/2}$ represents the half-life of the corresponding radon isotope [Wol15a].

In the context of this thesis, vacuum simulations with MolFlow+ were carried out for three different sources of radon in the spectrometer: for $^{219}$Rn emanating from the two NEG pumps in ports 2 and 3, and for $^{220}$Rn and $^{219}$Rn which emanate from the stainless steel surfaces inside the spectrometer vessel. For each of the three radon sources, simulations were carried out for measurement configurations A to E. While the sticking coefficient of the baffles was set to $c_0 = 1.0$, within each simulation set $\tau_{\text{des}}$ was varied between $0.01 \cdot t_{1/2}$ and $10.0 \cdot t_{1/2}$ with $t_{1/2}$ corresponding to the half-life of the corresponding radon isotope.

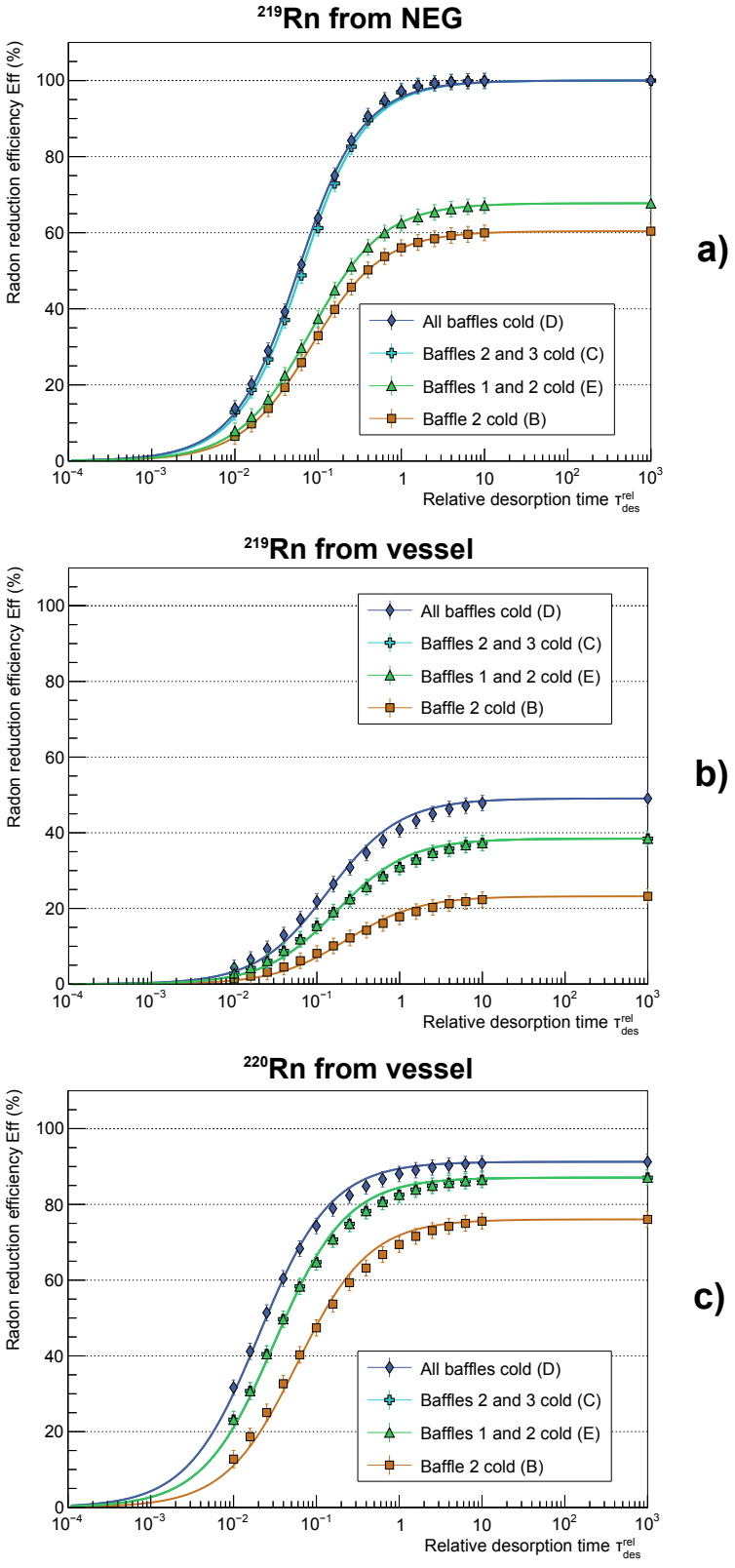


**Figure 4.21: Radon-reduction efficiencies for different cold-baffle configurations, simulated with MolFlow+** in dependence of the (relative) mean desorption time $\tau_{\mathrm{des}}^{\mathrm{rel}}$. The obtained efficiencies $Eff\,(\tau_{\mathrm{des}}^{\mathrm{rel}})_{\mathrm{sim}}$ are given relative to a simulation for which all baffles are in a warm state. The efficiency results $Eff\,(\infty)_{\mathrm{sim}}$ of simulations with an infinite mean desorption time are indicated by markers on the right border of the graphs. Note that in the case of $^{219}$Rn emanating from the NEG-pumps, no simulation for infinite desorption times has been performed for configurations C and D. The efficiency is here limited to 100% for $\tau_{\mathrm{des}}^{\mathrm{rel}} \to \infty$. For each measurement configuration, an arctangent-function according to Equation 4.27 is fitted to the simulated data points.

Figure 4.21 shows the efficiencies $Eff_{\mathrm{sim}}$ of radon suppression obtained from the MolFlow+ simulations as a function of $\tau_{\mathrm{des}}$ for all three relevant radon sources in the spectrometer. Similar to the values for configurations B to E in Table 4.1, the reduction efficiencies are given with respect to a configuration in which all baffles are warm (like data set A, see Eq. 4.23)[3]. Due to a small inaccuracy in the geometry input data used for the main spectrometer, an additional uncertainty of 2% for each simulated efficiency is assumed (see [Mue15b]).

As described in [Mue15b], the functional relation of the efficiency *Eff* and the desorption time $\tau_{\mathrm{des}}^{\mathrm{rel}}$ can be approximated by an arctangent

$$Eff\,(\tau_{\mathrm{des}}^{\mathrm{rel}})_{\mathrm{sim}} = p_0 \cdot \arctan\left(p_1 \cdot \tau_{\mathrm{des}}^{\mathrm{rel}} + p_2\right) + p_3 \quad \text{with} \quad \tau_{\mathrm{des}}^{\mathrm{rel}} = \frac{\tau_{\mathrm{des}}}{t_{1/2}} \quad . \tag{4.26}$$

In order to obtain the limit $\tau_{\mathrm{des}}^{\mathrm{rel}} \to \infty$ of the baffle efficiencies, an additional simulation with an infinite mean desorption time was performed for each configuration and for each radon source. The results on $Eff\,(\infty)_{\mathrm{sim}}$ and the boundary condition $Eff\,(\tau_{\mathrm{des}}^{\mathrm{rel}} \to 0)_{\mathrm{sim}} = 0$ are used to eliminate two out of the four free parameters in Equation 4.26, which then becomes

$$Eff\,(\tau_{\mathrm{des}}^{\mathrm{rel}})_{\mathrm{sim}} = Eff\,(\infty)_{\mathrm{sim}} - \frac{Eff\,(\infty)_{\mathrm{sim}}}{\frac{\pi}{2} - \arctan(p_2)} \left[\frac{\pi}{2} - \arctan(p_1 \cdot \tau_{\mathrm{des}}^{\mathrm{rel}} + p_2)\right] \quad . \tag{4.27}$$

The fits according to Equation 4.27 are shown in Figure 4.21 together with the simulated data points.

For the important case of $^{219}$Rn emanating only from the two NEG pumps in ports 2 and 3, and for large desorption times $\tau_{\mathrm{des}}^{\mathrm{rel}} > 1\,\mathrm{s}$, a reduction efficiency of almost 100% is achieved, for all configurations where the baffles in front of both NEG-equipped pump ports are held cold (cyan and blue curve). Nevertheless, for smaller values of $\tau_{\mathrm{des}}^{\mathrm{rel}}$, the reduction efficiency decreases in both cases so that the assumption of a 100% blocking of radon from the NEG pumps is no longer justified. If only one of the two NEG-equipped pump ports is blocked by a cold baffle (orange curve), the reduction efficiency is still larger than 50%, as the remaining cold baffle not only blocks radon from its own pump port, but also pumps radon that emanates from the NEG strips located in the other pump port. As expected, an additional cool-down of the baffle in the empty pump port 1 has only a minor effect on the reduction efficiency (green curve).

For the case of $^{219}$Rn and $^{220}$Rn emanating exclusively from the spectrometer walls, the different roles of baffles 1 and 3 vanish, so that the cyan and green curves are identical for Fig. 4.21 b) and c). In the case of $^{220}$Rn, a configuration with one cold baffle (orange curve) already significantly reduces the number of radon decays in the spectrometer volume and with all three baffles cold, a maximal reduction efficiency of about 90% can be achieved (blue curve). For the isotope $^{219}$Rn directly emanated into the spectrometer volume the situation is different, as its specific half-life is relatively short. Thus, in a close to optimum configuration with all baffles cold and even in case of large $\tau_{\mathrm{des}}^{\mathrm{rel}}$, the probability for $^{219}$Rn to decay before being adsorbed onto the cold baffle surfaces is large, and a maximal reduction efficiency of only about 50% can be achieved.

In the following analysis, the results of the arctangent-fits[4] shown in Figure 4.21 are used to find the ratio $Q_{\mathrm{NEG}}$ of $^{219}$Rn emanating from the NEG pumps to the $^{219}$Rn/$^{220}$Rn emanation from the stainless-steel walls of the spectrometer which reproduces best the

[3] By normalizing the efficiencies to the warm baffle case, the pumping efficiency of the TMPs for radon cancels out.

[4] Note that a linear interpolation between the simulated data points instead of the arctangent fits gives compatible results in the analysis.

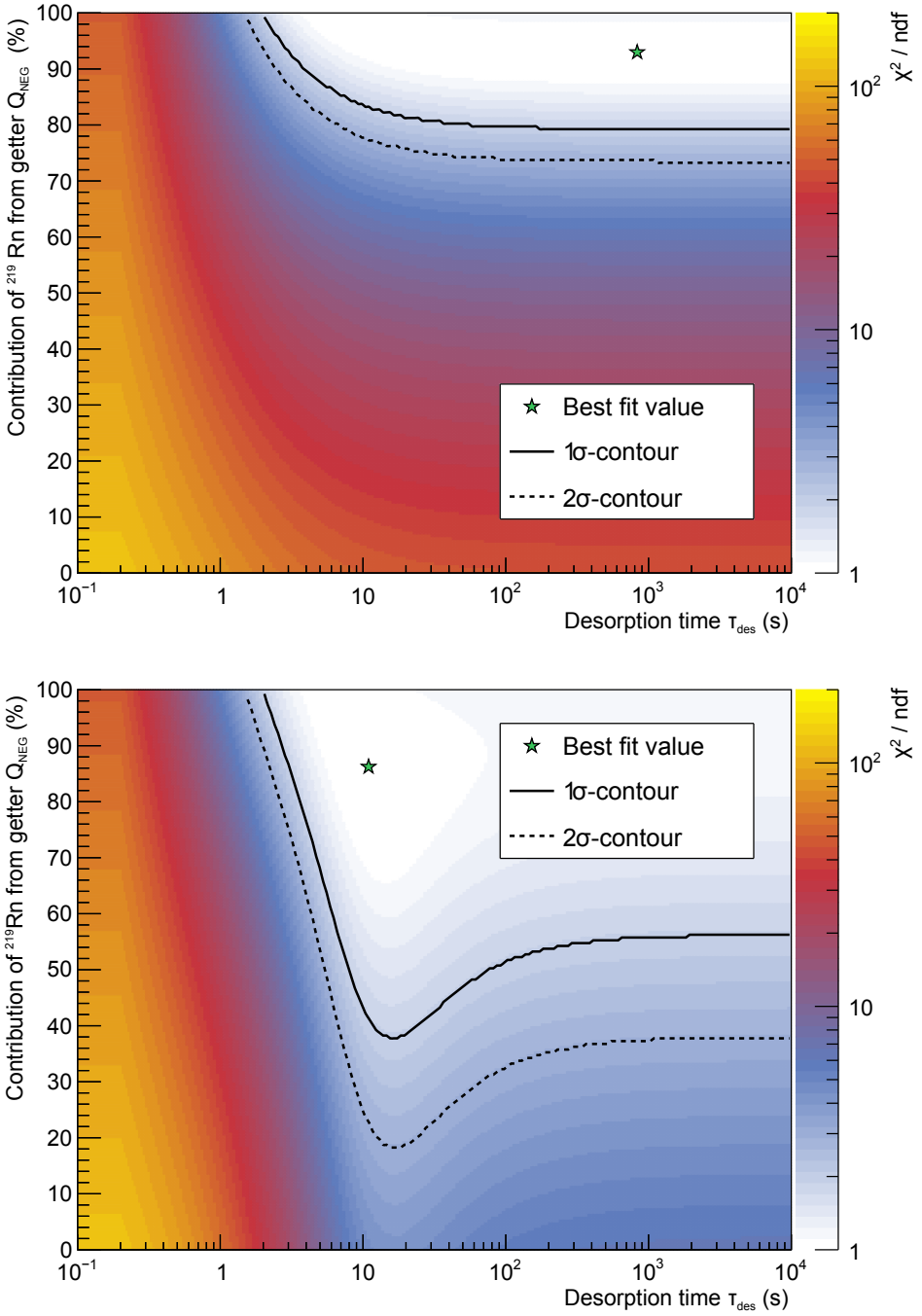


**Figure 4.22: $\chi^2$/ndf distributions for different contributions of $^{219}$Rn from the NEG pumps and different mean desorption times $\tau_{\mathrm{des}}$. Top: Distribution for the case of additional $^{219}$Rn emanation from the spectrometer walls.** The minimum $\chi^2/\mathrm{ndf} = 0.96$, marked by a green star, is achieved for a large contribution of $^{219}$Rn from the NEG pumps of $Q_{\mathrm{NEG}} \approx 93\%$ and a desorption time of $\tau_{\mathrm{des}} \approx 460\,\mathrm{s}$. The $1\sigma$- (solid line) and $2\sigma$-contour (dashed line) indicate the uncertainty of these results. **Bottom: Distribution for the alternative case of $^{220}$Rn emanating from the spectrometer walls.** The best fit value for the ratio of $^{219}$Rn from the NEG pumps of $Q_{\mathrm{NEG}} \approx 86\%$ and $\tau_{\mathrm{des}} \approx 11\,\mathrm{s}$ with $\chi^2/\mathrm{ndf} = 0.94$ is marked by a green star. The uncertainties of these results are likewise indicated by the $1\sigma$- (solid line) and $2\sigma$-contour (dashed line).

measured reduction efficiencies stated in Table 4.4. Besides $Q_{\mathrm{NEG}}$, the mean desorption time $\tau_{\mathrm{des}}$ appears as a second free parameter in the minimization which is performed with MINUIT. In order to prevent a third free parameter, the minimization is once performed for only $^{220}$Rn emanating from the spectrometer walls and once for only $^{219}$Rn. The $\chi^2$/ndf-distributions of these two minimizations are shown in Figure 4.22.

In the case of $^{219}$Rn emanation only, the best fit value is found for the major radon contribution coming from the NEG pumps ($Q_{\mathrm{NEG}} \approx 93\%$) together with a rather large mean desorption time of $\tau_{\mathrm{des}} \approx 460\,\mathrm{s}$. However, as the $1\sigma$- and $2\sigma$-contours indicate, the uncertainties on both parameters are rather large, such that only lower limits of $\tau_{\mathrm{des}} \geq 2\,\mathrm{s}$ (68% C.L.) and $Q_{\mathrm{NEG}} \geq 79.25\%$ (68% C.L.) are given here.

If only $^{220}$Rn is expected to emanate from the spectrometer walls, the best fit results again in a dominant contribution $Q_{\mathrm{NEG}} \approx 86\%$, albeit at a shorter $\tau_{\mathrm{des}} \approx 11\,\mathrm{s}$. However, as in the previous case, the uncertainties of both paramteres are large and again only lower limits of $\tau_{\mathrm{des}} \geq 2\,\mathrm{s}$ (68% C.L.) and $Q_{\mathrm{NEG}} \geq 37.75\%$ (68% C.L.) can be given.

The large uncertainties obtained for $Q_{\mathrm{NEG}}$ and $\tau_{\mathrm{des}}$ can be related to the fact that the number of data sets is small, and to the highly correlated nature of the two parameters. In addition, the simulation results in Figure 4.21 already indicate that the radon-reduction efficiency only very weakly depends on $\tau_{\mathrm{des}}$ for large mean desorption times. However, the results on $Q_{\mathrm{NEG}}$ obtained here are consistent with the ones obtained in Section 4.4.2, where the emanation of $^{219}$Rn from the NEG pumps was identified as main source of radon inside the main spectrometer. Furthermore, the lower limit on the desorption time $\tau_{\mathrm{des}} \geq 2\,\mathrm{s}$ is consistent with the results that are obtained in Appendix A, where measurements with an artificial radon source are used to derive the radon reduction efficiency for different sources of radon in the spectrometer and different operating temperatures of the baffles.

## 4.5 Conclusion

In this chapter, a large variety of long-term background measurements during the SDS-II measurement campaign were analyzed in order to determine the absolute pumping efficiency of the $LN_2$-cooled baffle system for radon. The two key findings are a radon suppression efficiency of $(95.1 \pm 0.3)\%$, and the fact that the NEG pumps could be identified as the major source of radon inside the KATRIN main spectrometer. In this context, the well-known algorithm that is used to identify radon-induced clusters in the data of the background measurements at elevated pressure was extended to correct for accidental cluster events via an off-time coincidence technique. In this way, the radon background contribution in measurements with warm-baffles can be determined with high accuracy. Furthermore, it was demonstrated that the first-order accidental correction algorithm significantly overestimates the radon-induced background for small accidental clusters of size $N < 6$ in cold-baffle measurements.

By comparing several elevated-pressure measurements with different combinations of baffles cooled to $LN_2$-temperatures, the radon-induced background rate with three cold baffles is determined to $R = 24^{+12}_{-10}\,\mathrm{mcps}$ during SDS-II. Furthermore, a comparison of the radon activity with warm baffles in SDS-I and the results obtained during SDS-II is used to derive the contribution of a single getter pump to the total radon activity in the SDS-setup to $A_{\mathrm{NEG}} = (223 \pm 56)\,\mathrm{mBq}$ (as in September 2013). At the same time, the contribution from other radon sources, like the inner surfaces of the spectrometer, is found to be consistent with zero: $A_{\mathrm{other}} = (-101 \pm 123)\,\mathrm{mBq}$. To cross-check these results, a second analysis approach is used, where the measured reduction efficiencies for radon at different cold-baffle configurations during SDS-II are compared to the results of test-particle MC-vacuum simulations. These simulations take into account the main spectrometer geometry,

the adsorption and desorption processes of radon on the cold baffle surfaces, as well as the decays of radon inside the spectrometer volume. In this way, a radon emanation fraction from the NEG pumps of $Q_{\mathrm{NEG}} \approx 93\%$ ($Q_{\mathrm{NEG}} \approx 86\%$) compared to the total $^{219}$Rn ($^{220}$Rn) emanation is found. While the uncertainties on these results are substantial, they are in good agreement with the activities derived when comparing the SDS-I to the SDS-II data set. It can thus be concluded that the large majority of the radon that is observed in the main spectrometer stems from the NEG pumps. Based on this finding, an upper limit for the remaining radon-induced background rate with three installed NEG pumps and all baffles cold can be calculated to

$$R_{\mathrm{tot}} = \frac{3}{2} \cdot R = \left(36^{+18}_{-15}\right) \text{ mcps} \quad (3 \text{ NEG pumps}).$$

This background contribution still significantly exceeds the KATRIN design goal of a background level of $< 10$ mcps, implying that additional active or passive countermeasures are required to further lower the radon-induced background. With the NEG pumps identified as the major source, a further improvement of the pumping efficiency of each baffle for radon appears to be the most promising solution. In Appendix A it is shown that the pumping speed of the baffle in pump port 3 is significantly better than that of baffle 2. This can be explained by an improvement of the temperature monitoring of baffle 3 prior to the SDS-II phase that allows for a more precise temperature regulation of this baffle. A similar improvement for the baffles in pump ports 1 and 2 after the end of SDS-IIB is highly recommended at this point. Furthermore, a better understanding of the effectiveness of active radon-reduction methods like the electric dipole [Wan13a], the magnetic pulse [Beh14a], or the electron-cyclotron resonance technique [Mer12b] is needed. Finally, a possible reduction of the number of getter pumps in the spectrometer, as suggested here, which would come at the expense of an increased final pressure and a reduced tritium pumping speed has to be reevaluated, based on the findings in this work.

For the following discussion of the non-radon-induced backgrounds in Chapter 5 and 6 of this thesis, the remaining radon contribution with both NEG-equipped pump ports shielded by cold baffles is, however, small enough to investigate these further background sources without large systematic uncertainties.

CHAPTER 5

# $^{210}$Pb in the KATRIN Spectrometer

In the last chapter, radioactive decays of specific radon isotopes inside the volume of the main spectrometer and the resultant consequences for the background level in the KATRIN ROI were discussed in detail. This chapter focuses on background sources and processes which contribute to events with visible energies that lie outside of the ROI defined for signal events (i.e. electrons with small surplus energies on the few eV-scale). The results obtained here have helped to identify a novel background class originating from radioactive decays located at the inner surfaces of the spectrometer. This background cannot be related to radon and is unaffected by an operation of the $LN_2$-cooled baffle system. The corresponding specific measurements were carried out with the spectrometer being operated at zero potential as well as for standard HV operation during the SDS-IIA phase. The goal was to identify electrons from $\beta$-decays of $^{210}$Pb as the source of this background component (Sec. 5.1). Based on previous experiences from low-level experiments like BOREXINO or GERDA for this lead isotope, a detailed model of the mechanism of the deposition of $^{210}$Pb on the spectrometer surfaces is derived (Sec. 5.2). Furthermore, MC simulations are utilized to calculate the activity of $^{210}$Pb inside the main spectrometer and to estimate the impact of $^{210}$Pb and its progenies on the background level in the ROI (Sec. 5.3), before final conclusions are drawn (Sec. 5.4).

## 5.1 Identification of the $^{210}$Pb Background

Most of the background measurements and analyses that were carried out during the SDS-I phase were focused on background events with measured energies in the detector ROI (cosmic- or radon-induced low-energy electrons with very low surplus energies $E < 0.2\,\mathrm{keV}$) [Lei14, Sch14c, Goe14], or in a specific region a few keV below the ROI ($H^-$-anion signal) [Sch14c]. In the context of this thesis, the energy spectrum of the background was investigated over a wider range of visible energies on the FPD ($0.2 < E < 260\,\mathrm{keV}$). To do so, several long-term measurements with the spectrometer at zero potential and in normal HV-configuration were carried out. The identification of the novel $^{210}$Pb background source, in the data sets listed in Table 5.1 is described in the following.

### 5.1.1 Measurements with the Spectrometer at Zero Potential

Most of the background electrons leaving the main spectrometer exhibit small surplus energies of a few eV only, relative to $U_0$. Consequently they appear in the energy spectrum within the so-called $E_{\mathrm{inc}}$-peak, which is defined according to Equation 3.2. In case of the standard spectrometer configuration with $U_0 = -18.6\,\mathrm{kV}$ and $U_{\mathrm{PAE}} = +10\,\mathrm{kV}$,

**Table 5.1: Summary of background measurements targeting the $^{210}$Pb identification.** The listed measurements have been carried out at a magnetic-field strength of 3.8 G in the analyzing plane. $U_{\text{vessel}}$ corresponds to the potential on the spectrometer vessel, $U_{\text{PAE}}$ gives the PAE potential, and $U_{\text{APE}}$ states the blocking potential that is applied to the detector-side anti-Penning electrode. In the SDS-IIA data sets F-J, the six detector channels of pre-amplifier card 14 are excluded from the analyses if not stated differently, whereas 22 unusable detector channels are removed from the SDS-I data set K. Furthermore, data set K represents a composition of various runs at different inner-electrode offset potentials with $-40 \leq U_{\text{IE,common}} \leq 0$ V. All listed voltages are given in kV.

| Set | $U_0$ | $U_{\text{PAE}}$ | $U_{\text{APE}}$ | Runs | Additional notes |
|---|---|---|---|---|---|
| F | 0 | +10 | −0.2 | #20118 - #20120<br>#20133 - #20137<br>#20161 - #20179<br>#20247 - #20260 | |
| G | 0 | +10 | −0.2 | #20622 - #20634<br>#20642 - #20655 | Baffle in pump port 3 cold |
| H | 0 | +10 | 0 | #20710 - #20720<br>#21181 - #21185 | |
| I | 0 | 0 | −0.2 | #20180 - #20195 | |
| J | −18.6 (and −18.5) | +4 | 0 | #21427 + $i \cdot 3$ and #21428 + $i \cdot 3$ ending with #21749 (excluding runs #21521 and #21670) | Series of measurements over the 2014 Christmas break with inner-electrode offset potentials of −5 V and −100 V |
| K | 0 | +10 | 0 | #5006 - #5034<br>#5044 - #5045<br>#5047 - #5051<br>#5057 - #5064<br>#5099 - #5106<br>#5112 - #5156 | SDS-I measurements with different inner-electrode offset potentials and 22 unusable detector channels. |

the $E_{\text{inc}}$-peak is located close to 28.6 keV. However, due to the rather coarse energy resolution of the detector of about 2.3 keV (FWHM) given in Section 3.7, electrons with moderate starting energies of $0.2 \lesssim E \lesssim 2.0$ keV cannot be distinguished from eV-scale electrons when the spectrometer is operated in its normal HV-mode. Therefore, specific runs in a non-standard configuration were performed for $U_0 = 0$ V, where the anti-Penning electrode (APE) on the detector side was operated at a negative blocking potential of $U_{\text{APE}} = -0.2$ kV to prevent low-energy background electrons from leaving the main spectrometer. In this way, the $E_{\text{inc}}$-peak could be suppressed in data sets F and G, allowing moderate-energy electrons to be analyzed. A positive PAE potential of $U_{\text{PAE}} = +10$ kV ensured that even electrons with small starting energies were energetically boosted above the detector noise threshold in measurements F, G, H, and K.

Figure 5.1 shows the energy spectrum of the background in the range from 7 to 120 keV, where data sets F and G were combined in order to increase statistics for the analysis. With the low-energy background electrons with $E < 0.2$ keV being electrostatically blocked by the APE, the background spectrum is now dominated by intrinsic detector background as visualized in Figure 3.19. If the latter is subtracted from the measured spectrum, two significant structures remain: a range with elevated count rates at energies up to 20 keV

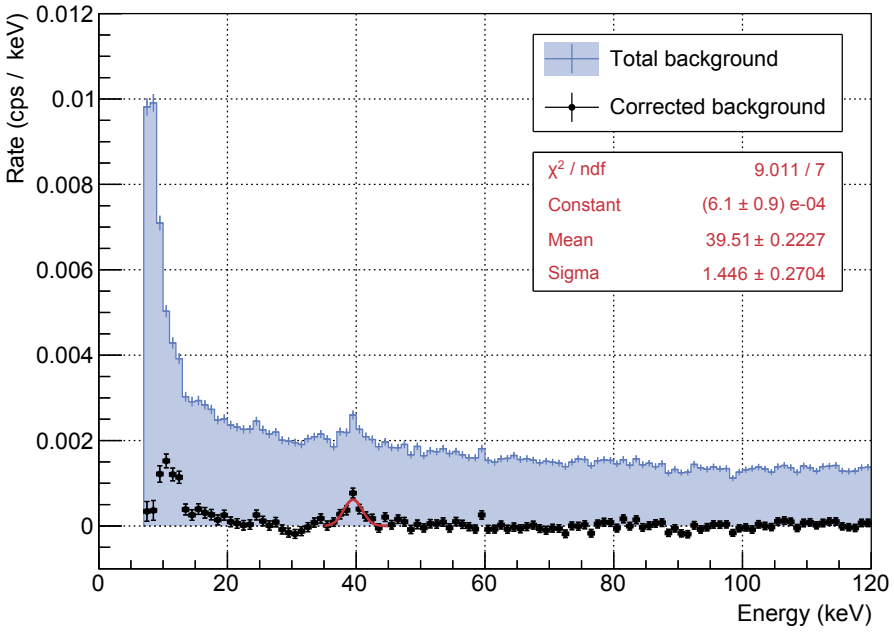


**Figure 5.1: Energy spectrum of the spectrometer background at zero vessel potential.** The background spectrum of the combined data sets F and G is shown over a range from 7-120 keV (blue). After correcting for the intrinsic detector background (see Fig. 3.19), two significant structures remain (black dots). A continuous part is visible below 20 keV and a peak-like structure manifests at 40 keV. A Gaussian-fit of the latter ranging from 35-45 keV (red) gives a line position of $(39.5 \pm 0.2)$ keV and a peak width of $3.4 \pm 0.6$ keV (FWHM).

and a rather unexpected peak-like structure around 40 keV. A Gaussian-fit of the latter gives a line position of $(39.5 \pm 0.2)$ keV with a width of $(3.4 \pm 0.6)$ keV (FWHM), a value which is slightly larger than the expected energy resolution of the detector at this energy. The observed line structure at this point could either be due to $\gamma$-photons of about 40-keV, or due to mono-energetic 30-keV electrons originating from the main spectrometer boosted to the final energy by the PAE.

To clarify the source of the observed structures, data set I was used as it was taken with a PAE potential of $U_{\mathrm{PAE}} = 0$ kV. Thus, electrons should appear with about 10 keV less energy on the detector, in contrast to $\gamma$-photons which are not affected by the PAE potential. Figure 5.2 shows the corresponding background spectrum: the above mentioned patterns are no longer noticeable. This points towards electrons as the source of both structures, particularly as now a region of elevated rate around 30 keV is observed. However, due to the rather low statistics of this data set, a peak cannot be identified clearly. The complete disappearance of the continuous low-energy structure can be explained by the missing PAE boost of electrons above the detector noise threshold.

### Comparison to SDS-I Data

At this point it is important to check whether the above described background signatures did appear only recently or were present in earlier measurements as well. For this purpose several SDS-I runs at zero vessel potential but with different inner-electrode offset potentials ($-40 \leq U_{\mathrm{IE,common}} \leq 0$ V) are combined to data set K to obtain sufficient statistics. Figure 5.3 shows the corresponding energy spectrum. Again, a peak-like structure centered at $(39.5 \pm 0.2)$ keV is found. Due to the better energy resolution of the detector during SDS-I, the width of the peak of $(2.7 \pm 0.4)$ keV (FWHM) is smaller than during the SDS-IIA phase. In contrast to data sets F and G, data set K was recorded without

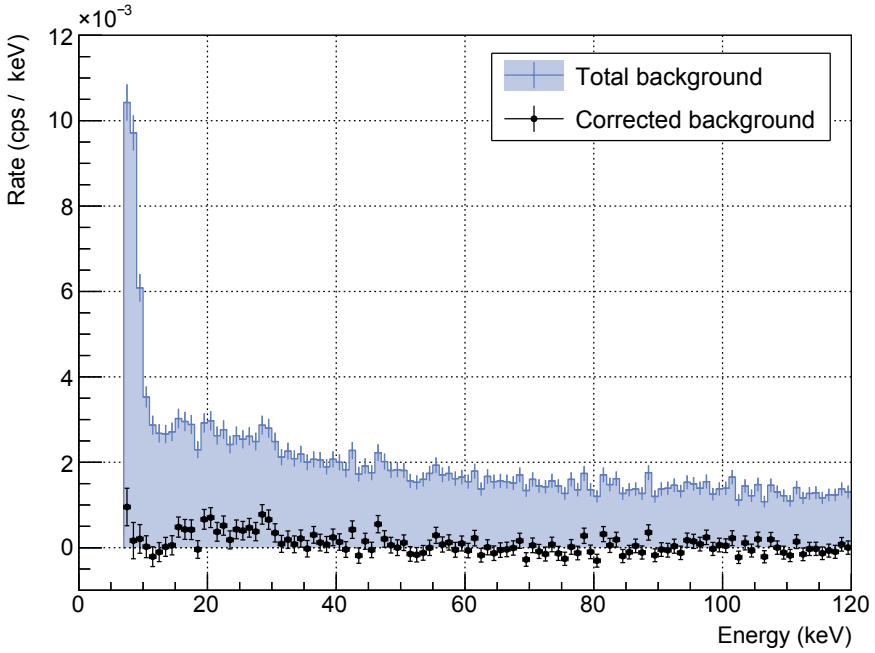


**Figure 5.2: Energy spectrum of background events when no post-acceleration is applied.** Even after the correction by the intrinsic detector background (black dots) none of the two structures that were found in the energy spectrum of the data sets F and G are observed. However, a region of elevated rate around 30 keV in this low-statistics data set I is most probably be due to mono-energetic 30-keV electrons. More details are given in the text.

applying a blocking potential to the APE on the detector side. Thus, for energies smaller than about 13 keV the spectrum is dominated by low-energy electrons from the $E_{\mathrm{inc}}$-peak. Still, a part of the continuous structure is observed as well.

### Contribution from Radon

Based on the above findings it can be stated that electrons with a continuous energy distribution between 0.2 and 10 keV as well as mono-energetic 30-keV electrons generate significant structures in the main spectrometer background spectrum. These electrons definitely originate from inside of the spectrometer vessel since they are not noticeable in the intrinsic detector background (see Sec. 3.8). Previously, the only known source of keV-scale electrons in the active flux tube of the main spectrometer is given by the decay of $^{219}$Rn (and potentially $^{220}$Rn) that was investigated in detail in Chapter 4. At first view, mono-energetic conversion electrons of the $^{219}$Rn-decay with line positions of some tens of keV seem to be ideal candidates to cause the observed peak structure. However, in this context only the 37.5-keV K-shell conversion line would be a candidate to explain the 30-keV peak. Nevertheless, despite the moderate detector energy resolution this conversion line is out of question to explain the observed peak, accordingly radon decays can be excluded as its source.

For the background component with continuous energies between 0.2 and 10 keV the situation is different. Here, shake-off, relaxation, and shell reorganization electrons emitted during a radon $\alpha$-decay will contribute to a continuous energy spectrum up to 20 keV and could therefore explain the observed structure. As shown in Chapter 4, the number of radon decays within the sensitive flux tube volume is significantly reduced by the cool-down of a single baffle. In this context, figure 5.4 shows a comparison of data sets F (all baffles warm) and G (baffle 3 cold), which where previously analyzed in a combined way. The two energy spectra only differ in the energy region between 10 and 15 keV (corre-

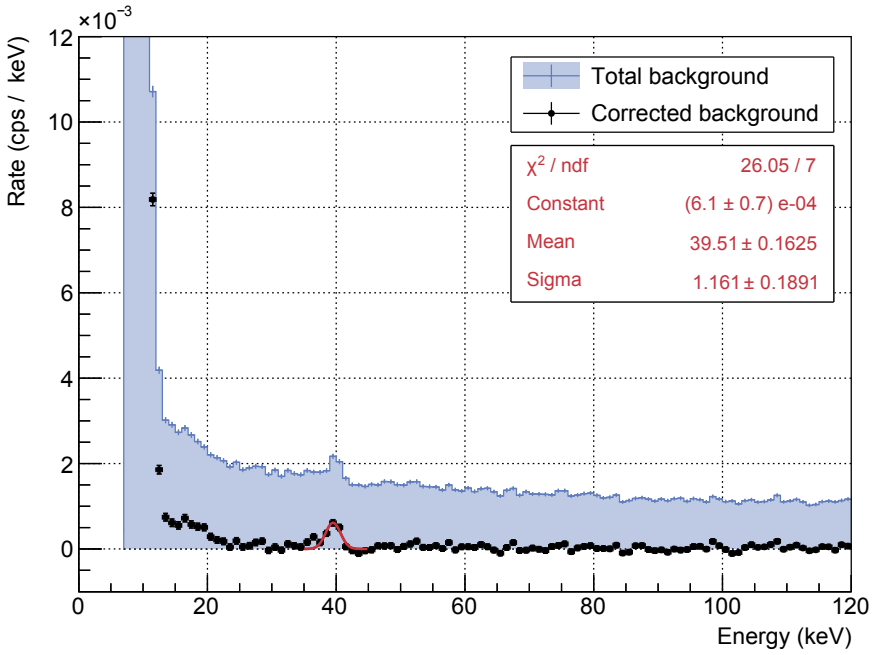


**Figure 5.3: Energy spectrum of the spectrometer background in SDS-I measurements.** In the detector background corrected energy spectrum of data set K (black dots) the same peak that was already found in the SDS-IIA data is identified in the energy spectrum at $39.5 \pm 0.2$ keV with a peak width of $2.7 \pm 0.4$ keV (FWHM). Due to the missing blocking potential on the anti-Penning electrode in these SDS-I measurements, the low-energy part of the spectrum is dominated by events from the $E_{\mathrm{inc}}$-peak. More details are given in the text.

sponding to electrons with starting energies of $0.2 < E < 5.0$ keV in the spectrometer), where the background rate is noticeably reduced if baffle 3 is cold. This observation points strongly to radon decays as major source of these low-energy electrons. As expected, the peak at 40 keV is not affected by the baffle cool-down, corroborating the hypothesis that this feature is not radon associated.

No other known background processes such as cosmic muons, field electron emission, Penning discharges, etc., are suitable sources to generate mono-energetic 30-keV electrons. Thus, a completely new contribution to the main-spectrometer background has been observed for the first time. It will be further characterized in the following parts of this chapter.

### 5.1.2 The Energy Spectrum of the $^{210}$Pb $\beta$-Decay

A survey of all naturally occurring radioactive isotopes reveals the isotope $^{210}$Pb from the primordial $^{238}$U-decay chain to be the best candidate to explain the observed peak in the main-spectrometer background spectrum. This isotope with a rather long half-life of $t_{1/2} = 22.2$ years emits, inter alia, conversion electrons with an energy of 30.15 keV during its $\beta$-decay into $^{210}$Bi. In astroparticle physics, $^{210}$Pb is known as prominent background source in low-background experiments like GERDA or BOREXINO [WZ13a] as will be discussed in more detail in Section 5.2.

Figure 5.5 illustrates the decay scheme of $^{210}$Pb and the corresponding electron energy spectrum. The most prominent electron-emission processes are listed in Table 5.2. The energy spectrum features two continuous $\beta$-spectra with endpoints at 17.0 and 63.5 keV. Superimposed are two conversion lines at 30.15 and 42.54 keV as well as distinct structures from Auger and shell reorganization processes. Besides the protruding L-shell conversion line,

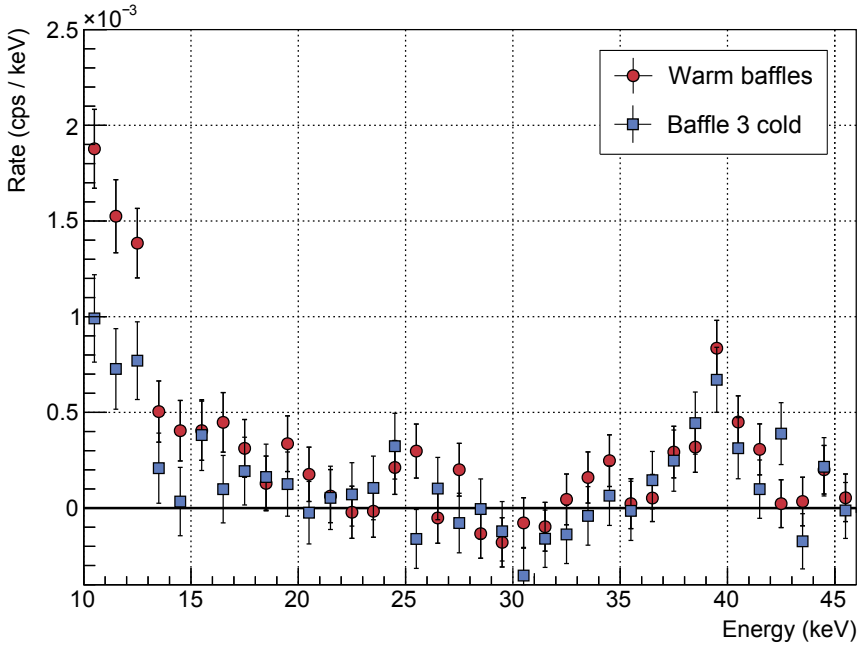


**Figure 5.4: Influence of a baffle cool-down on the energy spectrum of the spectrometer background** at zero vessel potential. A separate analysis of data sets F (warm baffles, red dots) and G (baffle 3 cold, blue squares) was performed. Both spectra are corrected for the intrinsic detector background. The peak-like structure around 40 keV remains unaffected by the baffle cool-down, while the low-energy background below 15 keV is reduced by about 50%.

also the low-energy part of the $^{210}$Pb spectrum below 15 keV fits well to the observed region of elevated count rate that is found in the background spectrum above $E_{\mathrm{inc}}$. Nevertheless, in the last section it was shown that a cool-down of a single baffle significantly reduces this contribution, which points towards radon as major source of it. However, a direct comparison of the theoretical energy spectrum $(\mathrm{d}N/\mathrm{d}E)_{\mathrm{theo}}$ of the $^{210}$Pb decay to the measured background spectrum $(\mathrm{d}N/\mathrm{d}E)_{\mathrm{meas}}$ is not possible, as the probability $P(E_{\mathrm{initial}}, \vec{x}_{\mathrm{initial}})$ for an electron being generated in the spectrometer volume to reach the detector strongly depends on the point of its creation $\vec{x}_{\mathrm{initial}}$ and its initial energy $E_{\mathrm{initial}}$. Thus, low-energy Auger-, $\beta$- and shell-reorganization electrons that are emitted in the decay of $^{210}$Pb each have a different probability to reach the detector in comparison of high-energy conversion electrons. This fact can significantly alter the measured background spectrum compared to the theoretical one according to

$$\left(\frac{\mathrm{d}N(E_{\mathrm{initial}})}{\mathrm{d}E}\right)_{\mathrm{meas}} = P(E_{\mathrm{initial}}, \vec{x}_{\mathrm{initial}}) \cdot \left(\frac{\mathrm{d}N(E_{\mathrm{initial}})}{\mathrm{d}E}\right)_{\mathrm{theo}} \quad . \tag{5.1}$$

Accordingly, detailed MC-tracking simulations of electrons propagating in the electro- and magnetostatic fields of the spectrometer are required to obtain the probability function $P(E_{\mathrm{initial}}, \vec{x}_{\mathrm{initial}})$ of detection, for comparison of the two spectra (see Sec. 5.3).

To conclusively identify $^{210}$Pb decays inside the main spectrometer (without relying on MC simulations), an observation of the second, M-shell conversion line in the background spectrum is required. However, this is not possible at the present moment due to the limited measurement time allocated to a zero-potential configuration in SDS-IIA.

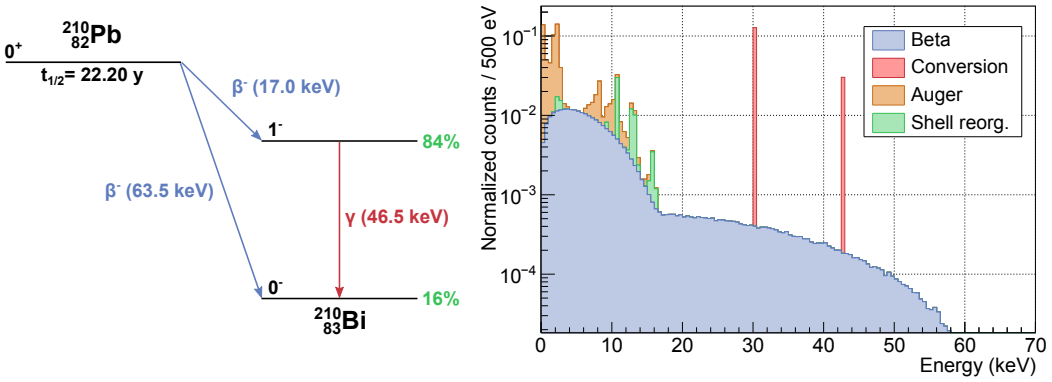


**Figure 5.5: The decay-scheme of $^{210}$Pb and the corresponding electron-energy spectrum. Left:** The decay scheme of $^{210}$Pb. The endpoint energies of the two $\beta^-$-decays are given in blue brackets while the probabilities of the transitions are stated in green [Nat15]. **Right:** The energy spectrum of electrons generated in the $^{210}$Pb decay including $\beta$- (blue), internal conversion (red), Auger (orange), and shell-reorganization electrons (green) [LT14].

**Table 5.2: Prominent electron-emission processes in the $^{210}$Pb decay.** The energy stated for the $\beta^-$-decays correspond to the mean energy of the transition, whereas the other processes generate mono-energetic electrons. Only processes with intensities of more than 10% are given here [Nat15].

| Process | Energy (keV) | Intensity (%) |
|---|---|---|
| $\beta^-$ | $4.2 \pm 0.1$ | $84 \pm 3$ |
| $\beta^-$ | $16.2 \pm 0.1$ | $16 \pm 3$ |
| Auger (L-shell) | 8.15 | $35 \pm 1$ |
| Conversion (L-shell) | $30.152 \pm 0.001$ | $58 \pm 1$ |
| Conversion (M-shell) | $42.540 \pm 0.001$ | $13.6 \pm 0.2$ |

### 5.1.3 Measurements with the Spectrometer at High Potential

While the measurement time at zero vessel potential was quite limited during the SDS-I and SDS-II phases, several long-term background measurements in the standard mode with the spectrometer at high potential were performed during both measurement campaigns. With a retarding potential of $U_0 = -18.6\,\text{kV}$, a PAE potential of $U_\text{PAE} = +10\,\text{kV}$, and a detector bias voltage of $U_\text{bias} = +0.12\,\text{kV}$, the L-shell (M-shell) conversion electrons from the $^{210}$Pb decay are expected to appear at about 58.87 keV (71.26 keV) in the measured background spectrum. Unfortunately, nearly all high-potential measurements that were carried out during SDS-I suffered from a dominant two-electron peak with an energy of $2 \cdot E_\text{inc}$. This peak originates from two electrons that appear on the same detector pixel with interarrival times smaller than the detectors timing resolution. In the standard HV mode of the spectrometer stated above, the $E_\text{inc}$-peak is located at about 28.72 keV. Thus, the two-electron peak appears at 57.44 keV in the spectrum and, thus, dominates the energy region where the signal of $^{210}$Pb L-shell conversion electrons is expected. This is one of the major reasons why $^{210}$Pb was not identified during the SDS-I phase.

Following the initial observation of a 30-keV electron signal in the zero-potential measurements at the begin of SDS-IIA (Sec. 5.1.1), a long-term (296 hours) data-taking phase targeted at background investigations was carried out from December 2014 to January 2015 with reduced PAE potential of $U_\text{PAE} = +4\,\text{keV}$ (data set J). In this way, the two-electron

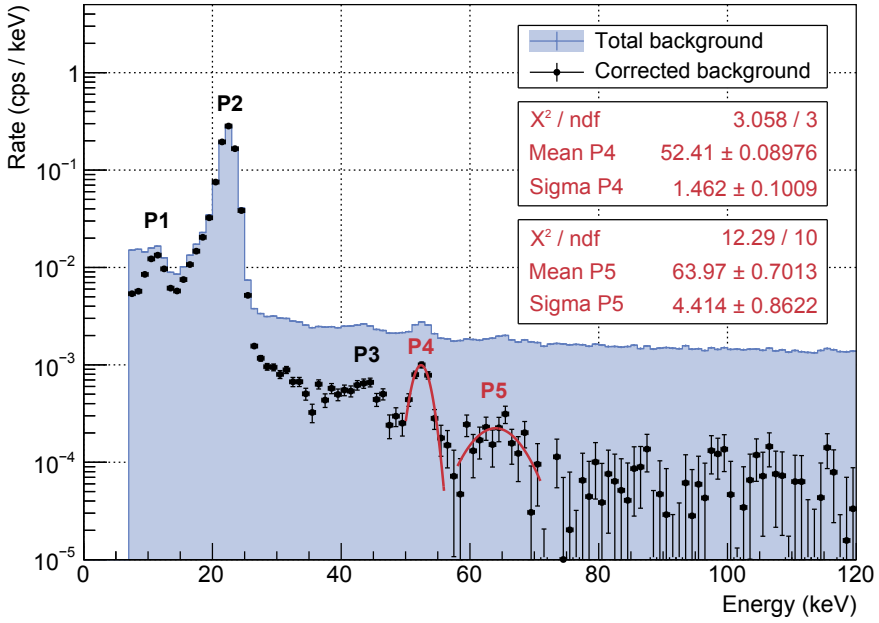


**Figure 5.6: Background spectrum with the main spectrometer operated at high potential.** The raw energy spectrum (blue) is measured with all 148 detector pixels at a retarding potential of $U_0 = -18.6\,\mathrm{kV}$. The PAE was set to a reduced potential of $U_{\mathrm{PAE}} = +4\,\mathrm{kV}$. Note that two measurement sets with different inner-electrode offset potentials ($-5\,\mathrm{V}$ and $-100\,\mathrm{V}$) have been combined to form data set J to obtain better statistics. When corrected by the intrinsic detector background, several peak-like structures remain (black dots). Peaks P1 and P2 correspond to $H^-$- and $E_{\mathrm{inc}}$-events, respectively. Peak P3 is located at $2 \cdot E_{\mathrm{inc}}$ and can be explained by two $E_{\mathrm{inc}}$-electrons that arrive at the same detector pixel with interarrival times smaller than the detector timing resolution. The two remaining peak structures P4 and P5 are fitted by two Gaussian functions (red line) and are attributed to the L- and M-shell conversion lines of $^{210}$Pb, respectively.

peak at 45.44 keV does not overlap with the expected line position of L-shell (M-shell) conversion electrons from $^{210}$Pb at about 52.87 keV (65.26 keV).

Figure 5.6 shows the corresponding energy spectrum of data set J which features several peak structures:

- **P1** corresponds to $H^-$-anions that are generated on the surface of the spectrometer and then guided to the detector by the magnetic fields. Their incident energy $E_{\mathrm{inc}}$ on the detector is the same as for low-energy electrons. However, due to the large energy losses that these anions experience in the detector dead layer, their signal appears at a reduced energy of about 11 keV in the measured background spectrum. More details on the $H^-$-signal can be found in [Sch14c].
- **P2** marks the $E_{\mathrm{inc}}$-peak of low-energy background electrons that are created in the spectrometer volume and, thus, appear within the standard ROI on the detector. These background events are studied in detail in Chapters 4 and 6.
- **P3** represents the two-electron peak that was explained previously. Compared to P2 this peak shows a more pronounced low-energy tail. This is due to the effect of tail pile-up [Kno10] and the fact that the energy losses of both electrons in the detector dead layer sum up.
- **P4** is located at $(52.4 \pm 0.1)\,\mathrm{keV}$ which is in agreement with the $^{210}$Pb L-shell conversion line which is theoretically expected at 52.87 keV. The width of the peak of

$(3.5 \pm 0.2)$ keV (FWHM) is slightly larger than the energy resolution of the detector for $\gamma$-photons, derived in Section 3.7.

- **P5** features rather low statistics, so it is not really identified as a peak but more as a broader region of elevated rate. A Gaussian fit of the structure with a mean of $(64.0 \pm 0.7)$ keV is quite close to the expected energy of the $^{210}$Pb M-shell conversion line at 65.26 keV. The large width of the peak of $(10.4 \pm 2.1)$ keV (FWHM) is attributed to the limited statistics and to high-energy 'continuum' events extending beyond 100 keV.

With the observation of distinct conversion-electron signatures in the background spectrum, $^{210}$Pb is successfully identified as novel background source in the KATRIN main spectrometer. However, up to this point it has not been specified how $^{210}$Pb is being deposited in the system and how it contributes to the background level in the standard ROI of the experiment. These questions are investigated in the following sections.

## 5.2 The Deposition Mechanism of $^{210}$Pb

Low-level experiments in astroparticle physics have revealed that exposure of large-area surfaces to ambient air over prolongated periods of time can cause surface-related background due to the radon content in the air. In case of the spectrometer, the large inner surface was exposed to filtered air over several years, which contains the radon isotopes $^{219}$Rn, $^{220}$Rn, and $^{222}$Rn.

In particular the vessel itself, the inner electrode as well as its support structures, all of which are made of stainless steel, make up most of the surfaces inside the spectrometer with 1 240 m$^2$ out of 1 451 m$^2$ [Wol15a]. Other large surface contributors are e.g. the copper baffle system, the NEG strips or the ceramic insulators on each side of the spectrometer. Nevertheless, these sub-systems are located either relatively far away from the observed flux tube or in regions with large magnetic fields, so that 30-keV electrons from $^{210}$Pb decays cannot enter the observed flux-tube volume due to their small cyclotron radius. Thus, the most plausible sources of $^{210}$Pb inside the spectrometer are the stainless-steel surfaces of the vessel and the inner electrode system. Particularly the central part and the flat cones of the spectrometer, where the magnetic field strengths are small and the observed flux tube reaches close to the internal structures, are favorable candidates in this context.

During the design process of the spectrometer vessel and the inner electrode system, particular care was devoted to a high radio purity of all materials. According to [Val05, Han08, PSW14] a contamination by $^{210}$Pb during the production process of these components to an extent that would be of significance here can therefore be excluded. Furthermore, the inner surface of the spectrometer vessel as well as the support structures of the inner electrode system were electropolished after their production. According to [WZ13b, Sch14b], $^{210}$Pb contaminations on stainless-steel surfaces are very effectively reduced by electropolishing, with a reduction factor of up to 400. Thus, it is reasonable to assume that the $^{210}$Pb deposition took place after the process of electropolishing.

Figure 5.7 shows the primordial decay series of $^{238}$U that leads to $^{210}$Pb. The decay of the eponymous $^{238}$U is followed by several $\alpha$- and $\beta$-decays before $^{222}$Rn is generated in an $\alpha$-decay of $^{226}$Ra. Due to its high mobility as noble gas $^{222}$Rn atoms can easily diffuse to the surface of bulk materials from where they emanate into the ambient air. The indoor $^{222}$Rn concentrations in the air can vary over several orders of magnitude depending on the specific location. According to [Uni15], the average outdoor radon activity is about 15 $^{\mathrm{Bq}}/_{\mathrm{m}^3}$, whereas the indoor radon activity is about 50 $^{\mathrm{Bq}}/_{\mathrm{m}^3}$, though activities of up to thousands of $^{\mathrm{Bq}}/_{\mathrm{m}^3}$ have also been measured e.g. in mines and caves [Leu06].

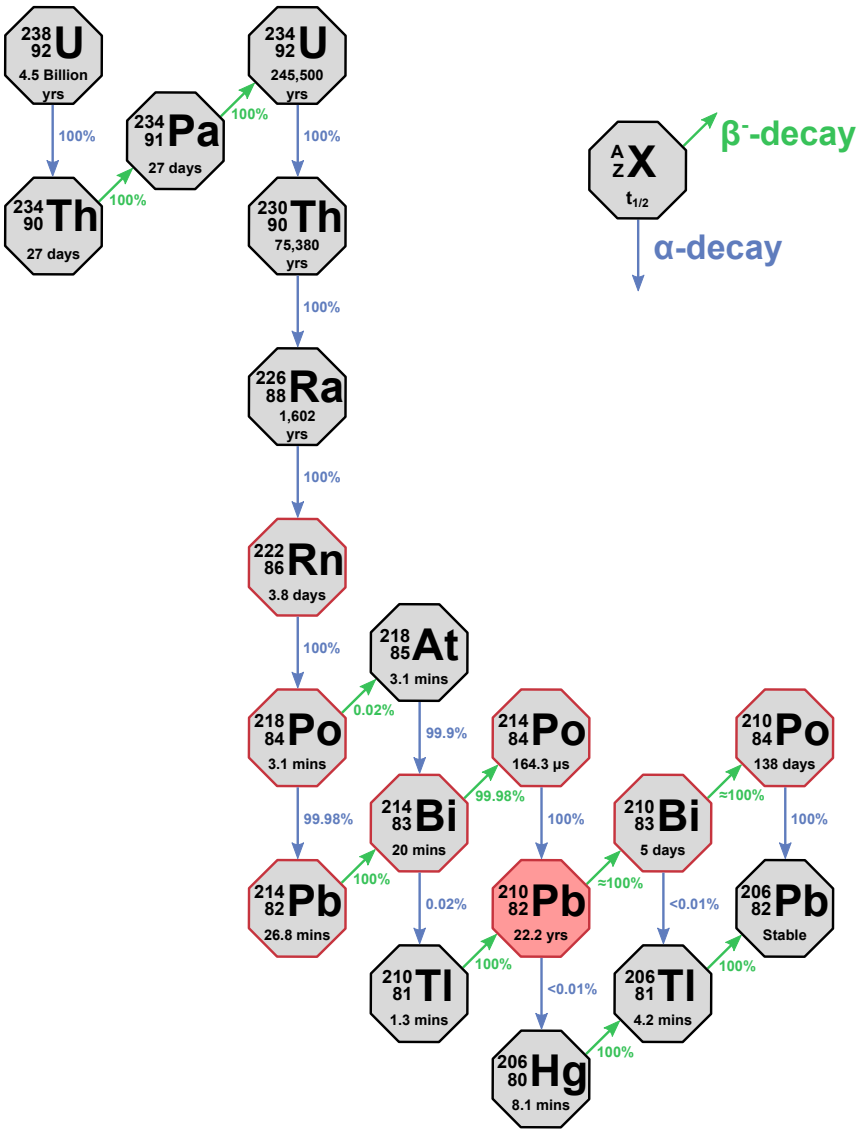


**Figure 5.7: Illustration of the uranium decay series** including $^{210}$Pb (marked in red). The isotopes which are relevant for the discussion in this chapter are marked by a red contour. The illustration is inspired by [Wik15].

Several low-background experiments like BOREXINO or GERDA faced major challenges due to $^{222}$Rn in the ambient air. Since the $\alpha$-decay of $^{222}$Rn is followed by several short-lived isotopes in the uranium decay chain ($^{218}$Po, $^{214}$Pb, $^{214}$Bi, and $^{214}$Po), the long-lived $^{210}$Pb typically emerges within one hour after the initial decay of $^{222}$Rn in the air [Gui10, WZ13a]. In this way, $^{210}$Pb is plated out on surfaces of detector components that are exposed to ambient air. Furthermore, the 146 keV of recoil energy of the $^{210}$Pb nucleus as a result of the $\alpha$-decay of $^{214}$Po can even cause its implantation into sub-layers of the surfaces [WZ13b]. With its long half-life of 22.2 years, $^{210}$Pb and its progenies $^{210}$Bi and $^{210}$Po are of major concern for low-background experiments as they will contribute to the background even a long time after exposure of surfaces to air [Leu06].

During data-taking the KATRIN main spectrometer is operated under stringent UHV conditions. Thus, any $^{222}$Rn atom emanating e.g. from the vessel walls or the NEG material is pumped out with an average pumping time of $t_{\mathrm{MS}} \approx 360\,\mathrm{s}$. This is much faster than the half-life of $^{222}$Rn of $t_{1/2} = 3.8\,\mathrm{days}$ and is why only the short-lived radon isotopes $^{219}$Rn and $^{220}$Rn pose a direct source of background for KATRIN (see Chapter 4). Nevertheless, significant amounts of $^{222}$Rn are expected to have entered the spectrometer during the

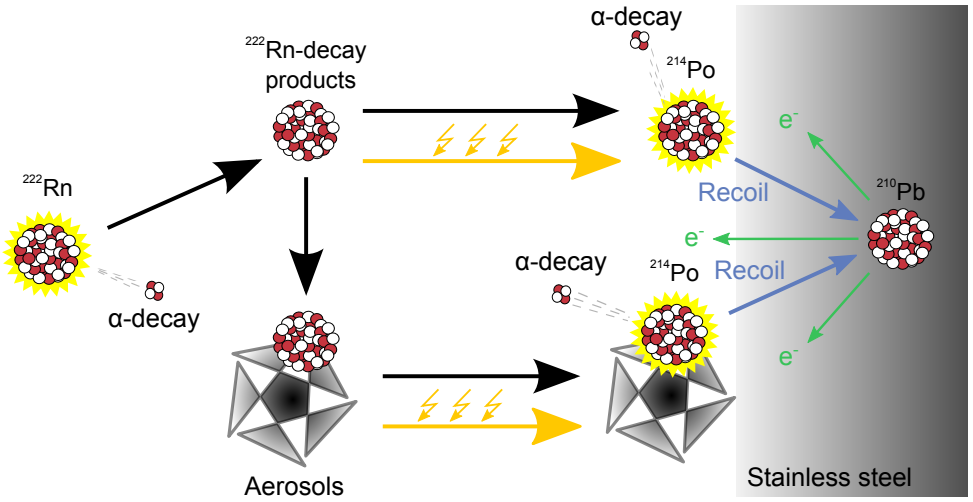


**Figure 5.8: Illustration of the deposition mechanism of $^{210}$Pb in the spectrometer.** The short-lived progenies of $^{222}$Rn can be transported in three different ways to the inner surfaces of the spectrometer: directly via diffusion (upper path), indirectly via aerosol attachment (lower path), or via electric forces (indicated by orange arrows). $^{210}$Pb is implanted into sub-surface layers of the stainless steel via the recoil of the $^{214}$Po $\alpha$-decay on, or close to the surface (blue arrows). Electrons generated in the decay of $^{210}$Pb have to pass through several nm of stainless steel before entering the main spectrometer volume (green arrows).

construction and maintenance phases where the vessel was vented to atmosphere. Here, the time period from the first pump-down test in 2007 to the pump-down for the SDS-I phase in 2012 represents by far the longest exposure. During this time period the vessel could be accessed via a clean room connected to its three pump ports in order to install the sophisticated inner electrode system as well as the $LN_2$-cooled baffles and the NEG pumps (see Chapter 3). A ventilation system equipped with HEPA filters provided a constant exchange of air inside the clean room and the spectrometer with 3-4 full exchanges per hour. In this way, a constant flow of $^{222}$Rn from ambient air has entered the spectrometer volume via the ventilation system, albeit in small quantities of 50 $^{\mathrm{Bq}}/_{\mathrm{m}^3}$. In the vented 1 240-m$^3$ spectrometer volume this corresponds to a total radon activity of 62.5 kBq. Over the course of the construction and maintenance phase (5 calendar years) this corresponds to more than $N_{222}^{\mathrm{Rn}} \approx 10^{13}$ decays in the spectrometer. If all of these decays would have resulted in a deposition of $^{210}$Pb on the stainless-steel surfaces, an upper limit for the activity of $^{210}$Pb in the spectrometer volume can be approximated to

$$A_{210}^{\mathrm{Pb}} \approx \lambda_{210}^{\mathrm{Pb}} \cdot N_{222}^{\mathrm{Rn}} \approx 10\,\mathrm{kBq} \quad . \tag{5.2}$$

However, this result only represents a very rough approximation, as the fraction of $^{222}$Rn decays to actually cause a deposition or even implantation of $^{210}$Pb on inner surfaces needs to be taken into account.

In the context of the BOREXINO experiment, a very detailed discussion of possible transport and deposition mechanisms of the radon progeny onto surfaces is given in [Leu06]. Three different transport processes are evaluated, all of which are illustrated in Figure 5.8:

- **Direct transport to the surfaces via diffusion:** In contrast to the noble gas $^{222}$Rn, its progenies easily adsorb onto and desorb from surfaces. Thus, the surface concentration can be calculated as the integrated flux of all radon progeny atoms to the surfaces $J_i(\vec{x}, t)$ over an exposure time $\tau$, where $i$ represents one of the four short-lived isotopes $^{218}$Po, $^{214}$Pb, $^{214}$Bi, and $^{214}$Po. In equilibrium, where the concentration of the $^{222}$Rn atoms in the air is constant over time and space so that $C_i(\vec{x}, t) = C_i$, the flux $J_i$ can be taken as the product of the concentration $C_i$ and the deposition

velocity $v_d$, which is related to the diffusion constant $D$. The surface concentration $\sigma$ of all radon progenies can now be written as:

$$\sigma = \sum_{i=1}^{4} C_i v_d \tau \quad . \tag{5.3}$$

In the case of KATRIN, radon progenies were deposited on the spectrometer surfaces over the course of several years. On these time-scales, $\sigma$ directly corresponds to the concentration of $^{210}$Pb on the surface. According to [Sch84], the deposition velocity of radon progenies in ambient air typically amounts to $4 \times 10^{-3}$ m/s. However, the exact value strongly depends on the local air circulation and the particle concentration in the air.

- **Indirect transport via aerosols:** Instead of a direct adsorption mechanism of a radon progeny on the surface, it can stick to aerosols in the air. Depending on their size these will attach to surfaces either through diffusion or via gravitational forces. The attachment to aerosols lowers the deposition velocity by a factor of 10.

  In the case of KATRIN, the concentration of large aerosols inside the spectrometer was small due to the good clean-room conditions provided by the HEPA filters. The attachment rate of radioactive atoms on aerosols (according to [LR60]) is proportional to $e^{-t/\tau}$ where $\tau$ scales with the radius of the aerosols $R$

  $$\tau = \frac{1 + h \cdot R}{\pi R^2 N \bar{v}} \quad . \tag{5.4}$$

  Here, $N$ denotes the aerosol concentration in the air, $\bar{v}$ the average velocity of the diffusing radon progeny atoms, and $h$ is a constant. Thus, the sticking probability of the radon progeny to the aerosols of small radius, which even remain in a clean-room environment, is expected to be small.

- **Transport triggered by electrostatic charges:** When electrostatic charges are present, they dominate the deposition mechanism. The radon daughter $^{218}$Po as well as $^{214}$Pb are both formed via an $\alpha$-decay and, thus, are usually emitted as ions. These isotopes will either react chemically with the environment, attach to aerosols, or get neutralized by an interaction with other ions or free electrons in the air. For a typical negative-ion concentration of $2 \times 10^8$ $^1/_{m^3}$, the half-life for neutralization is $t_{1/2} = 20$ mins [Raa69]. During this prolonged time period the radon progeny can be attracted by parts of structural materials that carry electrostatic charges which speed up the deposition mechanism.

  In the context of KATRIN, a deposition via electrostatic forces is of high relevance as the contamination by $^{210}$Pb most probably took place during the installation of the inner electrode system. As its two wire layers are isolated against the vessel potential, it is reasonable to assume that stainless-steel parts of the inner electrodes were floating during the installation process. This would have mainly supported the deposition of the radon progenies on the corresponding floating surfaces.

Irrespective of the exact transport mechanism of the radon progenies to the surfaces in the spectrometer, the deposition mechanism ends with the $\alpha$-decay of $^{214}$Po into $^{210}$Pb. With 146 keV of recoil energy, the daughter nucleus can be implanted into sub-surface layers of the stainless steel of the spectrometer or the inner electrode system [WZ13b].

Figure 5.9 shows the distribution of implantation depths for 146-keV $^{210}$Pb-ions that impact isotropically onto a stainless-steel surface, as simulated with the SRIM program package [Zie04, Zie13]. A mean implantation depth of $(12.35 \pm 0.02)$ nm is found, while some

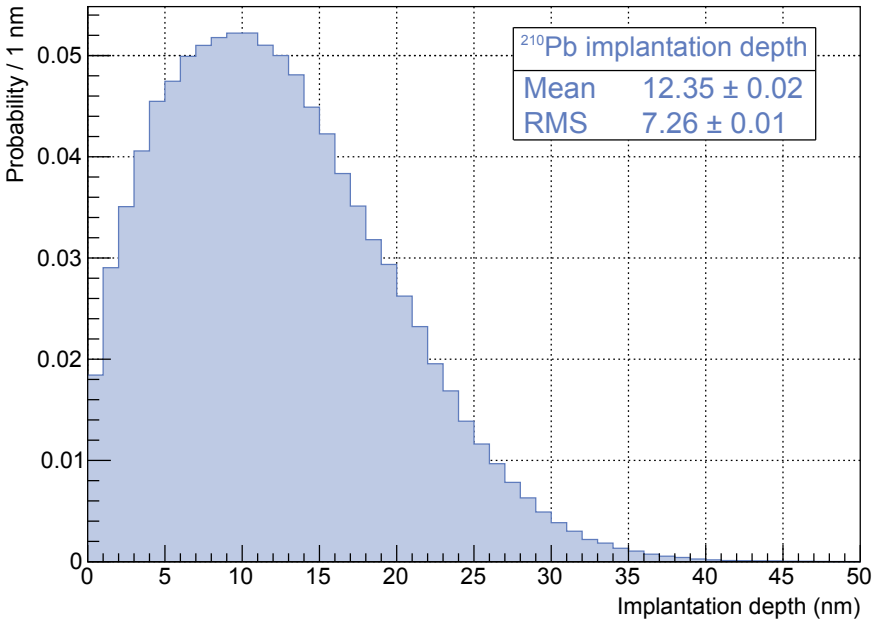


**Figure 5.9: Simulation of the implantation depths of $^{210}$Pb ions in bulk stainless steel.** The simulations were performed with the SRIM program package [Zie04, Zie13]. Here, the trajectories of 146-keV $^{210}$Pb ions impinging onto stainless steel with 19 different polar angles of incidence between 0° and 90° were simulated. The results were then combined and weighted by a sinusoidal distribution in order to model an isotropic impact.

of the trajectories reach as far as 40 nm into the bulk material. When a $^{210}$Pb atom has been implanted, the electrons emitted during its $\alpha$-decay have to pass through several nm of stainless steel before entering the vacuum of the main spectrometer. In this way they will lose some of their initial kinetic energy via scattering in the bulk, which distorts the theoretical electron-emission spectrum shown in Figure 5.5. The corresponding energy loss of transmitted electrons was simulated with the PENELOPE 2008 program package [Bar95]. In this context, initial electron energies were calculated from the theoretical $^{210}$Pb-decay electron spectrum (Fig. 5.5) and the initial position was diced from the implantation-depth distribution (Fig. 5.9). The resulting electron energy distribution is given in Figure 5.10. Compared to the theoretical spectrum, most of the low-energy structures now are smeared-out, while the two conversion lines remain. Owing to small energy losses in the bulk, both conversion peaks show sizable low-energy tails. This fact naturally explains why the measured peak width of both lines is slightly wider as expected from the detector energy resolution. Depending on the real implantation profile of $^{210}$Pb in the stainless-steel bulk, these effects are more or less pronounced and can lead to an additional small shift of the peak positions to lower energies. A similar effect on signal electrons is well-known from the dead layer of the detector wafer [Wal14].

Based on the simulations with SRIM and PENELOPE 2008 it can be concluded that a shallow implantation of $^{210}$Pb into sub-layers of the stainless-steel surfaces of the spectrometer is in agreement with the observed background spectrum shown in Figure 5.1. The implantation processes can also explain the relatively broad peak widths as well as the small shifts of the peak positions to lower energies. Together with the deposition model of radon progenies on the inner surfaces of the spectrometer, discussed earlier in this section, this scenario provides a reasonable explanation for the observed $^{210}$Pb background contribution. However, the actual activity of $^{210}$Pb inside the spectrometer still has to be determined.

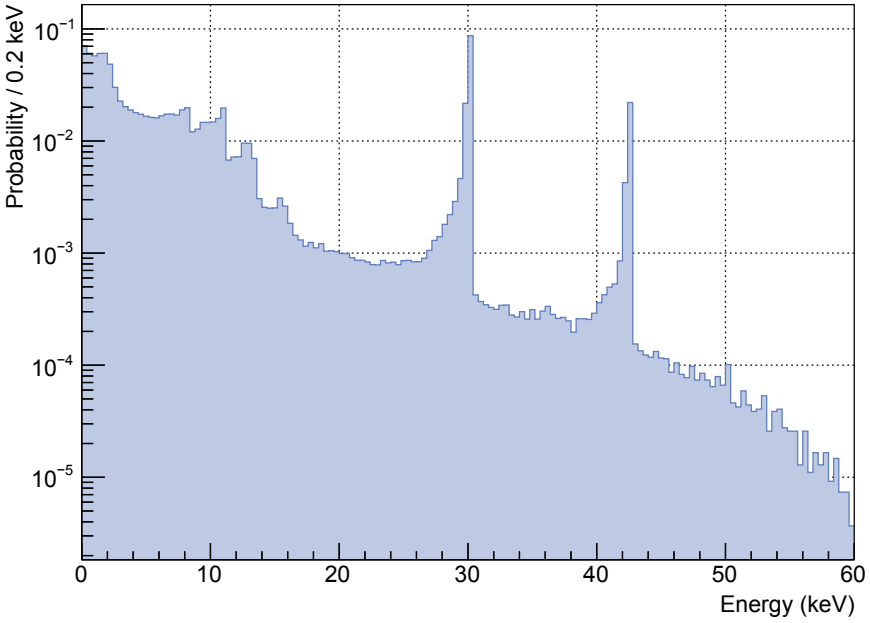


**Figure 5.10: Simulation of the energy spectrum of transmitted $^{210}$Pb electrons through a thin layer of stainless steel.** The simulations were performed with the PENELOPE 2008 program package [Bar95]. The initial electron energies were diced from the $^{210}$Pb decay spectrum in Figure 5.5 while the initial electron positions in the stainless-steel layer were diced from the implantation profile in Figure 5.9.

## 5.3 Consequences of the $^{210}$Pb Background for the KATRIN Experiment

In this section, advanced MC-tracking simulations are used to estimate the activity of $^{210}$Pb in the KATRIN main spectrometer. Furthermore, the consequences of the surface deposition of $^{210}$Pb and its progenies for the background level in the standard ROI of KATRIN are discussed.

### 5.3.1 The $^{210}$Pb Activity in the Main Spectrometer

In order to investigate the characteristics of $^{210}$Pb decays in the spectrometer in more detail, it is reasonable to define a 'lead ROI' around the observed peak of the 30-keV conversion electrons (see Fig. 5.1 and 5.6). Similar to the standard ROI which has been defined in Section 3.7, this new ROI extends from 3 keV below to 2 keV above the expected incident energy. This is required in order to take into account scattering effects in the stainless-steel bulk and detector dead layer. In the case of the zero-potential data sets F, G, and H, this 'lead ROI' extends from 37.27 to 42.27 keV, while in the HV data set J it reaches from 49.87 to 54.87 keV.

The left-hand side of Figure 5.11 shows the rate in the lead ROI per pixel and with the intrinsic detector background (Fig. 3.20) subtracted. Even in the high-statistics data set J the statistical uncertainties from pixel-to-pixel are considerable, making the identification of specific structures in the pixel pattern rather difficult. However, the rate on the inner-most three detector rings appears to be significantly reduced compared to the outer parts of the wafer. This effect is more clearly visible on the right-hand side of Figure 5.11, where the measured rates per detector ring are shown (scaled to the radius of the observed flux tube in the analyzing plane). In this case, the statistics are sufficient to identify a rate

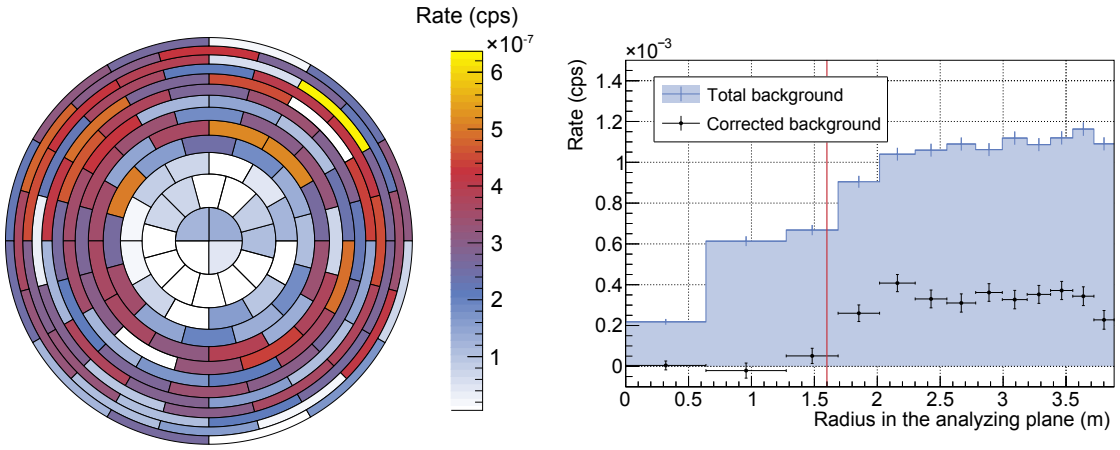


**Figure 5.11: Detector event pattern of the 30-keV conversion electrons from $^{210}$Pb decays. Left:** The event rate within a lead ROI between 49.87 and 54.87 keV is shown for data set J with the spectrometer operated at HV. Due to the low statistics, the rates per pixel suffer from large uncertainties. **Right:** The rate in the lead ROI per detector ring for data set J (blue) is corrected by the detector background (black markers). In the ring-wise representation the statistics are sufficient to see an increase of the rate at about a radius of 1.5-2 m in the analyzing plane. The minimum radius up to which 30-keV electrons from the inner electrode system can gyrate is marked by a red solid line.

drop for inner radii smaller than 2 m. With 30 keV of kinetic energy, the cyclotron radius of $^{210}$Pb L-shell conversion electrons in the 3.8-G magnetic-field is about 1.56 m. At the cylindrical part of the spectrometer, the inner electrode system is located at a radius of 4.68 m and the inner vessel surface at 4.9 m. Thus, conversion electrons that are emitted from these internal structures can only gyrate up to a minimum radius of $1.6 - 1.8$ m in the analyzing plane. This fits well the observed radial distribution.

In order to estimate the true activity of $^{210}$Pb in the spectrometer, the mapping probability $P(30\,\text{keV}, \vec{x}_{\text{initial}})$ of the 30-keV electrons, starting from the surface, onto the detector needs to be found (see Eq. 5.1). This task can only be accomplished by advanced electromagnetic tracking simulations with KASSIOPEIA [FG15]. However, as the exact deposition pattern of $^{210}$Pb onto the different spectrometer surfaces (vessel, inner electrode) is not known a priori, the simulations are restricted to simplified cases such as a homogeneous distribution of $^{210}$Pb on the inner vessel surface or on the electrode system. As the electric-field calculations in the complex main-spectrometer geometry are rather time-consuming and in view of the large number of electrons to be tracked, the simulations were carried out only for a grounded main spectrometer configuration so that the results can be compared to the zero-potential data sets F, G, and H. The magnetic fields in the simulations were chosen similar to the 3.8-G magnetic-field setting and scattering processes of conversion electrons off residual hydrogen gas with a partial pressure of $p = 1 \times 10^{-9}$ mbar were taken into account, as well. The latter processes are of particular relevance if conversion electrons are stored over longer time scales in the spectrometer (see Chapter 4). In order to ensure a reasonable computation time, stored electrons were terminated once they had lost more than 3 keV of their initial energy due to scattering processes and, therefore, would not have appeared in the lead ROI anymore.

In a first simulation $5 \times 10^7$ electrons were started homogeneously distributed on the vessel surface, while the inner electrode system was not taken into account. Out of this ensemble, a total of only 190 electrons left the spectrometer on the detector side to appear on the wafer with the radial pattern shown in Figure 5.12. As a comparison, the measured radial distribution in a combined analysis of data sets F, G, and H, with a detector-background

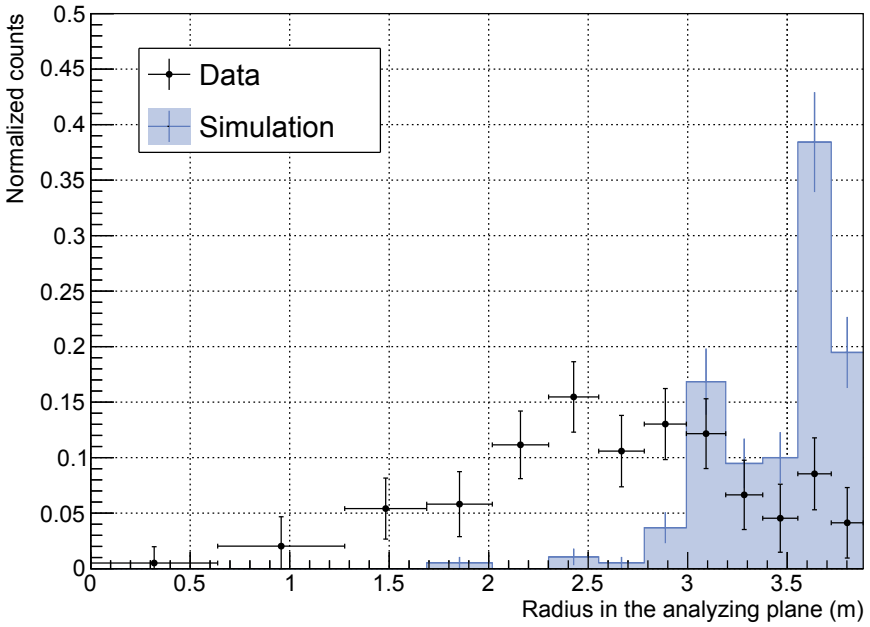


**Figure 5.12: Simulated radial event distribution of 30-keV electrons emitted from the inner surface of the spectrometer.** In the underlying KASSIOPEIA simulation a total of $5 \times 10^7$ electrons with an initial energy of 30 keV was started. Starting points were homogeneously distributed over the inner surface of the spectrometer vessel with the wire electrode not being considered. A total of 190 electrons reached the detector with their radial arrival distribution on the wafer shown in blue. The black data points correspond to the measured radial distribution of the L-shell conversion electrons from $^{210}$Pb in a combined analysis of the data sets F, G and H. Both distributions are scaled to unit area. Note that the detector channels served by preamplifier card 14 are excluded from the analysis of the measured data. The simulated distribution is scaled accordingly.

corrected rate of $R = (2.2 \pm 0.2)$ mcps in the 'lead ROI' is shown in addition. The two distributions not match up as the simulated electrons do not reach far enough into the observed flux tube, appearing only at large radii $> 3$ m, while the measured distribution extends to small radii $< 3$ m as well. Based on the number of detected electrons an arrival probability of $P = (3.8 \pm 0.3) \times 10^{-6}$ is found. Together with the measured rate $R$ and the intensity $\mathcal{I}$ of the L-shell conversion line (Tab. 5.2), the activity of $^{210}$Pb in the spectrometer can be calculated according to

$$A_{210}^{\mathrm{Pb}} = \frac{R}{P \cdot \mathcal{I}} = (998 \pm 117)\,\mathrm{Bq} \quad . \tag{5.5}$$

In a second simulation, another ensemble of $5 \times 10^7$ 30-keV electrons was started, now, however, homogeneously distributed on the inner electrode system only. Figure 5.13 shows the resulting radial pattern of the 220 electrons that reached the detector. A comparison to the measurement shows that the two distributions match quite well at large radii, while the long tail of the measured distribution to smaller radii is not reproduced by the simulation. This tail can possibly be explained by the radial $\nabla\vec{B} \times \vec{B}$-drift of stored conversion electrons from outer flux-tube regions into the center of the spectrometer. This drift is induced by small deviations of the magnetic field from axial symmetry that are not taken into account in the simulation. For a homogeneous distribution of the $^{210}$Pb atoms on the inner electrode system an arrival probability of $P = (4.4 \pm 0.3) \times 10^{-6}$ is found.

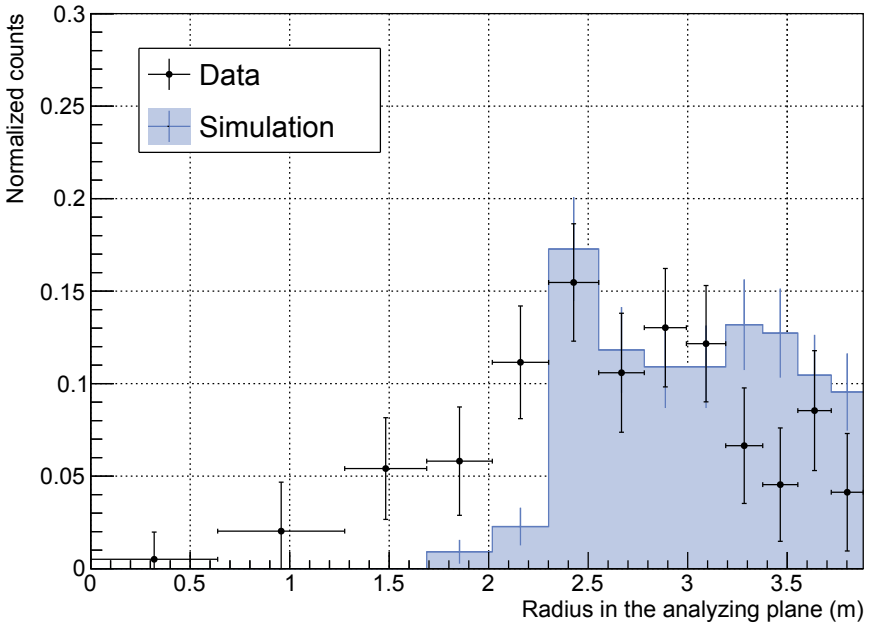


**Figure 5.13: Simulated radial event distribution of 30-keV electrons emitted from the inner wire electrode system.** In the underlying KASSIOPEIA simulation a total of $5 \times 10^7$ electrons with an initial energy of 30 keV was started. The starting points were homogeneously distributed over the inner wire electrode system of the main spectrometer. The radial arrival distribution of the 220 electrons that reached the detector is shown in blue. The black data points correspond to the measured radial distribution of the L-shell conversion electrons from $^{210}$Pb in a combined analysis of the data sets F, G and H. Both distributions are scaled to an area of unity. Note that the detector channels served by preamplifier card 14 are excluded from the analysis of the measured data. The simulated distribution is scaled accordingly.

This results in a total activity in the spectrometer of

$$A_{210}^{\mathrm{Pb}} = \frac{R}{P \cdot \mathcal{I}} = (862 \pm 99)\,\mathrm{Bq} \quad . \tag{5.6}$$

While in both simulations electrons were started homogeneously distributed, the starting points of those electrons which actually reached the detector were localized in distinct regions as can be seen in Figure 5.14. Nearly all of the electrons mapped on the FPD started from the flat-cone regions on both sides of the spectrometer. In these parts of the system the observed magnetic flux tube reaches close to internal structures. Moreover, in these regions the field lines do not run in parallel to the surface of the spectrometer making it easier for electrons to enter the flux tube (see Fig. 2.3). This result clearly shows that the estimated activity in Equation 5.5 (5.6) only holds for the specific case of a homogeneous distribution of $^{210}$Pb on the inner vessel walls (the inner electrode system). The real activity could differ significantly, if the $^{210}$Pb deposition would have had happened localized in specific parts of the spectrometer.

The $^{210}$Pb activities of about 1 kBq given in Equations 5.5 and 5.6 are well below the upper limit for the activity estimated in Equation 5.2.

### 5.3.2 Arrival Probability of Surface-Emitted Electrons on the Detector

In the previous section, the activity of $^{210}$Pb in the main spectrometer has been estimated to be about 1 kBq under the assumption of a homogeneous deposition of the isotope on

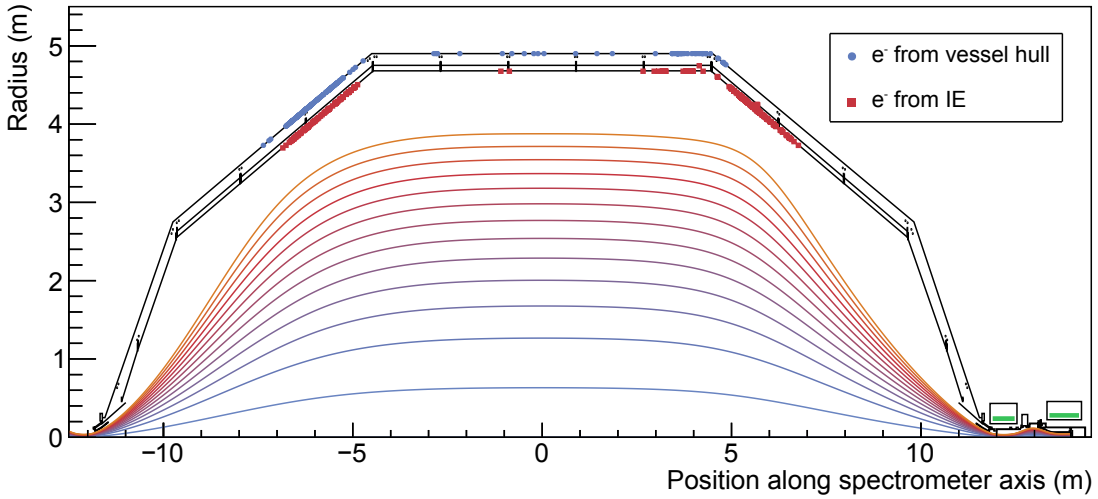


**Figure 5.14: Starting points of simulated $^{210}$Pb conversion electrons that reached the detector.** The MC-starting points of electrons reaching the detector in the simulation shown in Figure 5.12 (Figure 5.13) are indicates by blue dots (red squares). The field lines for the 3.8-G magnetic field setting (Tab. 3.1) are shown in addition. In both simulations, electrons most likely reach the detector when starting close to the region where the cylindrical part and the flat cones of the spectrometer meet. Here, the field lines reach close to the internal structures and also are not aligned parallel to the inner surfaces.

either the inner electrode system or the vessel surface. While conversion electrons appear with energies far outside the standard ROI and will therefore not directly contribute to the spectrometer background, the prominent $\beta$-spectrum of $^{210}$Pb extends also to low energies so that parts of it will reach into this ROI. However, for decreasing primary energies the cyclotron radius of stored electrons decreases as well, so that low-energy electrons have a smaller probability to enter the observed flux tube than high-energy conversion electrons.

In order to determine the energy dependence of the arrival probability $P(E_{\text{initial}}, \vec{x}_{\text{initial}})$ on the detector, five additional KASSIOPEIA simulations were carried out. In each simulation an ensemble of $2 \times 10^7$ electrons was started homogeneously distributed on the inner electrode system while their starting energy was varied from 5 keV to 25 keV. The resulting total arrival probabilities are plotted together with the previous result for 30-keV electrons on the left side of Figure 5.15. As expected, the probability to be mapped onto the detector increases with the energy of the electrons. If the electrons are subdivided into a fraction starting from the upstream side ($z < 0$) of the spectrometer and from the downstream side ($z > 0$), an additional effect is observed: the arrival probability of electrons with $z < 0$ increases with energy while it seems to reach saturation around 30 keV for those which start on the downstream side of the spectrometer. The plot on the right side of Figure 5.15 shows the arrival probabilities per detector ring and electron energy. This distribution underlines the important fact that electrons at smaller energies do not gyrate far into the observed flux tube due to the reduced cyclotron radius and only appear on the outermost detector rings.

Making use of an empirical 2$^{\text{nd}}$-order polynomial fit to $P(E_{\text{initial}})$ in the left plot of Figure 5.15 and of the simulated energy spectrum of electrons from $^{210}$Pb decays in the stainless steel (Fig. 5.10), the spectrum expected for electrons which actually reach the detector can be calculated according to Equation 5.1. This is done under the assumption of a homogeneous deposition of $^{210}$Pb on the inner electrode system. Figure 5.16 shows the corresponding result, where the low-energy part of the spectrum is strongly suppressed

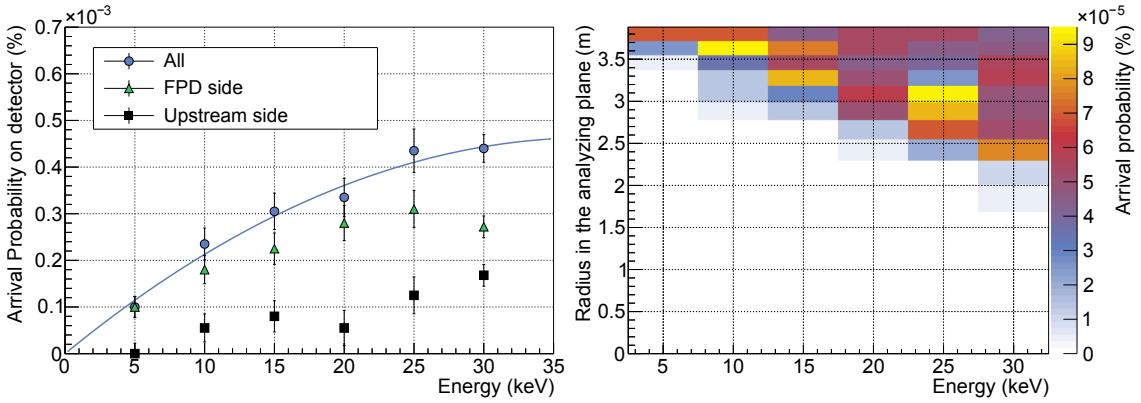


**Figure 5.15: Energy dependence of the detector-arrival probability of electrons homogeneously emitted from the inner electrode system.** Six simulations of electrons with energies ranging from 5 keV to 30 keV were carried out with KASSIOPEIA [FG15]. **Left:** The total arrival probability of the electrons on the detector is shown for all six simulations as blue dots. In order to interpolate between the simulated electron energies, a 2$^{\text{nd}}$-order polynomial fit $P(E) = p_0 \cdot E^2 + p_1 \cdot E$ is applied. The fit gives $p_0 = (-3 \pm 1) \times 10^{-7}\,{}^1/_{\text{keV}^2}$ and $p_1 = (2.5 \pm 0.3) \times 10^{-5}\,{}^1/_{\text{keV}}$. In addition to the total arrival probabilities, the contributions from electrons that started on the FPD (pre-spectrometer) side of the spectrometer are shown as green triangles (black squares). **Right:** The individual arrival probabilities for each detector ring and simulated electron energy are shown. With increasing energy, the electrons reach further into the observed flux tube and will therefore appear on inner detector rings as well.

due to the small arrival probabilities on the detector.

The results obtained here are also of particular importance for source-related backgrounds, as the $\beta$-spectrum of $^{210}$Pb closely matches the tritium $\beta$-spectrum. Thus, the results obtained here demonstrate that any implanted tritium in the spectrometer walls will only enhance the background in the very outer parts of the flux tube.

In order to estimate the expected background contribution due to electrons from $^{210}$Pb decays which directly reach the detector with energies in the standard ROI, the spectrum in Figure 5.16 is scaled to a rate of $R = (2.2 \pm 0.2)$ mcps in the 'lead ROI', similar to the measurements. For the standard HV operation of the spectrometer, the background energy spectrum shown in Figure 5.16 will appear shifted to higher energies by $E_{\text{inc}}$ and only the first 2 keV of the spectrum contribute to the background rate in the standard ROI. From the spectrum in Figure 5.16 the rate in these 2 keV is found to be $R_{\text{ROI}} = (0.17 \pm 0.02)$ mcps. Thus, the direct background contribution of electrons from $^{210}$Pb decays in the standard ROI is found to be negligible. However, as it will be shown in the following sections, $^{210}$Pb decays can contribute indirectly to the background in the standard ROI via storage of the corresponding high-energy electrons or by a decay of its daughter nuclei $^{210}$Bi and $^{210}$Po.

### 5.3.3 Storage Probability of Electrons from $^{210}$Pb Decays

In Chapter 4 of this thesis it was shown that high-energy electrons emitted during radon $\alpha$-decays in the flux tube can be stored in the main spectrometer, causing a substantial correlated background level due to ionization of residual gas. Similarly, a high-energy conversion electron from a $^{210}$Pb decay can also be stored and generate background. However, while radon decays occur homogeneously distributed in the volume, the $^{210}$Pb decays occur close to the inner surfaces of the spectrometer. If at all, high-energy electrons will be stored only in the outermost regions of the observed flux tube. Therefore, their background contribution is expected to show a substantial radial dependence featuring an increase to outer radii on the detector. In the following the possible $^{210}$Pb contribution to radon-like background is investigated.

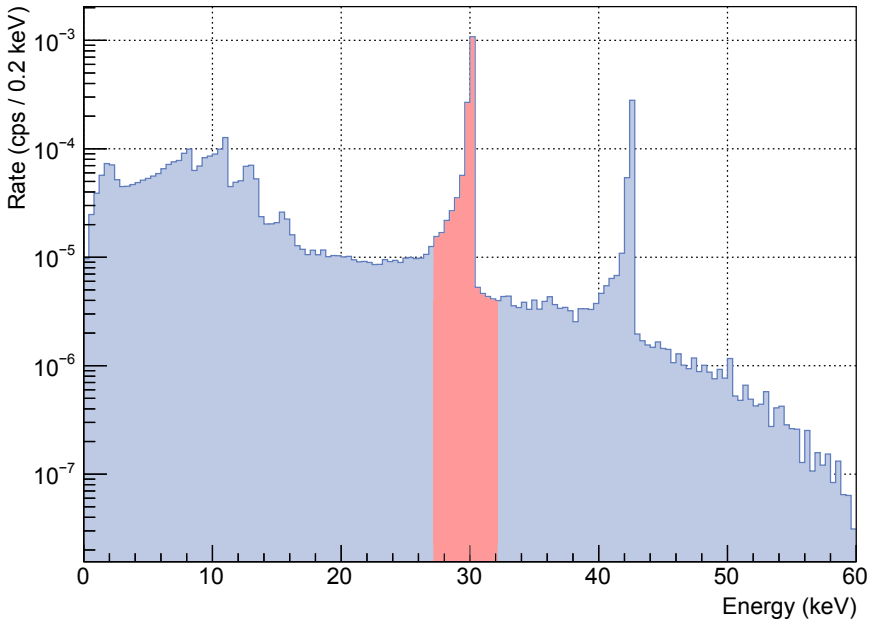


**Figure 5.16: Expected energy spectrum of $^{210}$Pb-decay electrons that reach the detector.** The energy spectrum of electrons from $^{210}$Pb-decays after their passage through a thin layer of stainless steel shown in Figure 5.10 has been weighted by the energy-dependent arrival probability of electrons on the detector, as given by the fit in Figure 5.15. In addition, the spectrum is scaled such that the rate in the lead ROI from 27.15 keV to 32.15 keV (marked in red) fits to the measured rate in the combined data sets F, G and H of $R = (2.2 \pm 0.2)$ mcps.

When defining a large cluster-size threshold of $N_0 \geq 6$, the rate of correlated events in the radon background measurements at elevated pressure and with all baffles cold is found to be small. In particular, no radial increase was observed for clusters of large size in Chapter 4. However, a radially increasing contribution of clusters of small size $2 \leq N < 6$ was observed in the cold baffle measurements where the contribution from the, otherwise dominant, radon background was small. As a high-energy electron being stored in the outermost regions of the active flux tube has a rather high probability to either hit internal structures such as the electrode system, or to leave the observed volume before being fully cooled down, it will (in contrast to radon-induced electrons) only cause clusters of small size. In Section 4.2.2, an excess of clusters of small size in cold baffle measurements was attributed to accidental clusters from the uncorrelated background. However, the accidental-correction algorithm does not fully remove this excess (see Fig. 4.19). Besides potential higher-order effects that are not covered by the correction, this effect could also be explained by a small contribution of correlated backgrounds from stored $^{210}$Pb-induced primary electrons. This hypothesis is supported by the fact that the contribution of small-size clusters has been found to increase with the radius in the analyzing plane (see Fig. 4.19).

In order to investigate a possible background contribution from stored $^{210}$Pb primary electrons, in-depth storage simulations with KASSIOPEIA are required, similar to those in [Wan13a] for the case of radon. In the case of $^{210}$Pb these detailed simulations will be significantly more challenging, as an electromagnetic tracking of stored electrons very close to inner structures of the spectrometer is required. This fact makes the calculation of non-axially symmetric electric fields more challenging, requiring large amounts of computation time even if GPUs are used. For this reason, no detailed storage simulations close to the inner electrodes were performed in this thesis for the standard configuration with the

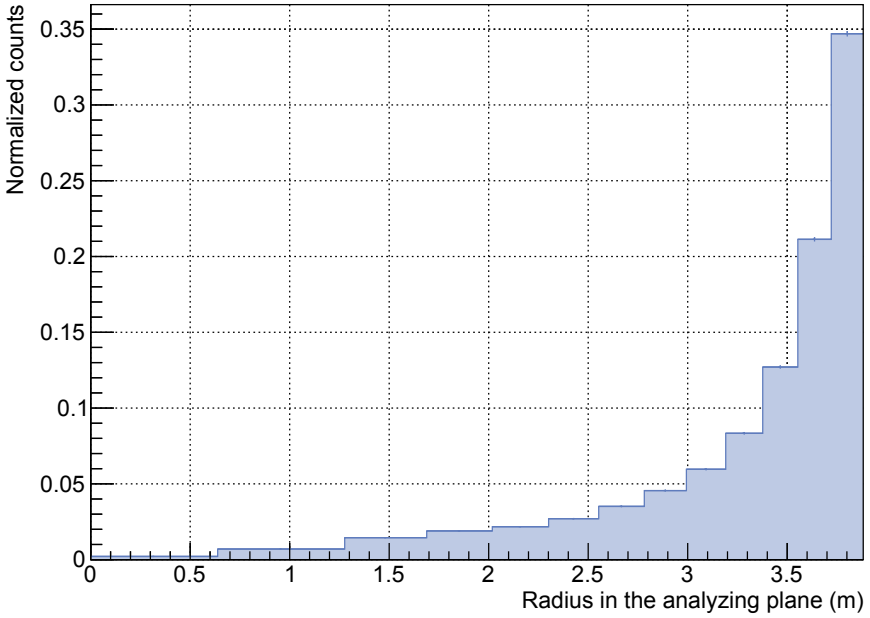


**Figure 5.17: Radial distribution of $^{210}$Pb-induced secondary electrons.** A total of $9.82 \times 10^6$ $^{210}$Pb decays homogeneously distributed on the inner electrode system of the main spectrometer was simulated with the use of KASSIOPEIA [FG15]. The simulation was carried out for a 3.8-G magnetic field in the analyzing plane while electric fields were absent due to the zero-potential configuration. The energy and number of electrons emitted in each decay was calculated from the theoretical $^{210}$Pb spectrum shown in Figure 5.5. Electrons were tracked until they either hit a geometrical boundary, exited the spectrometer on the upstream or downstream side, or reached a minimum energy of 10 eV by multiple scattering processes off residual hydrogen gas (partial pressure of $1 \times 10^{-9}$ mbar). In the latter case, low-energy secondary electrons were created. The radial distribution of the points of creation of all secondary electrons generated within the observed flux tube is shown for a projection to the spectrometer analyzing plane.

spectrometer at elevated potential, due to the limited time available. However, a simplified storage simulation for the zero-potential case was carried out. A total of $9.82 \times 10^6$ $^{210}$Pb decays was simulated, again homogeneously distributed on the inner electrode system of the spectrometer for a 3.8-G magnetic field in the analyzing plane. The energies of the emitted electrons were calculated according to the theoretical $^{210}$Pb spectrum in Figure 5.5 and electrons were tracked until they either hit a geometrical boundary, left the spectrometer on the upstream or downstream side, or reached a minimum energy of 10 eV. Stored primary electrons were interacting with residual gas by scattering off hydrogen molecules at a partial pressure of $1 \times 10^{-9}$ mbar to generate low-energy secondary electrons. Figure 5.17 shows the corresponding radial distribution of the points of creation of all secondary electrons created within the observed flux tube and mapped into the analyzing plane. As expected, the number of generated secondaries does increase to outer radii.

While the storage simulation described at this point only holds for the specific case of a configuration without electric fields, similar results for the HV-case can be expected. In Chapter 6 it will be shown that the spectrometer background rate with cold baffles indeed shows an increase to outer radii comparable to that in Figure 5.17. In the context of discussing the pressure dependence of the remaining spectrometer background, a possible contribution due to stored electrons from $^{210}$Pb decays in the outermost regions of the observed flux tube will be important.

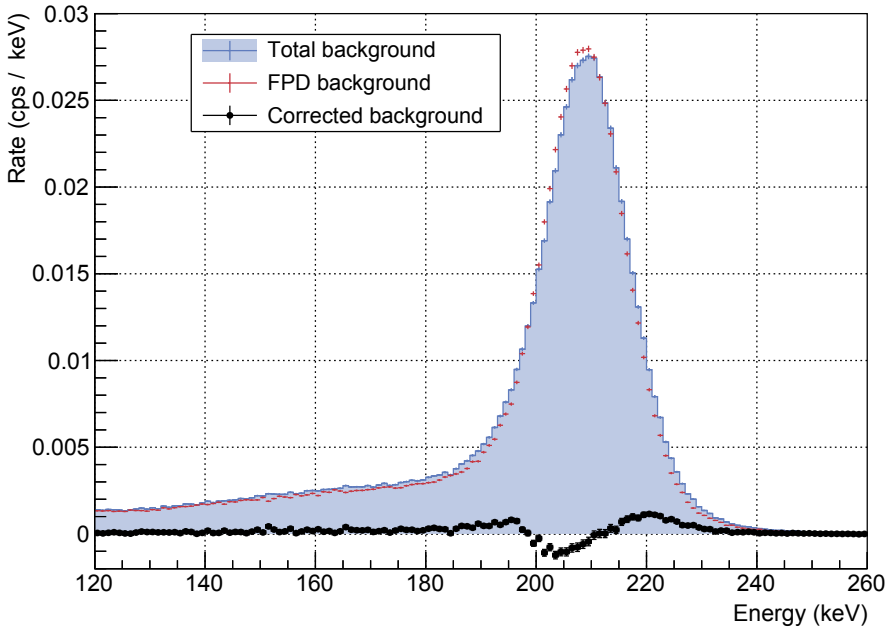


**Figure 5.18: High energy part of the main spectrometer background spectrum** between 120 and 260 keV. If the detector background (red) is subtracted from the total background (blue), the corrected main spectrometer background is retrieved (black points). The distortions of the corrected spectrometer background around 200 keV are due to different shapes of the detector overflow peak in the two measurements. The details are discussed in the text.

### 5.3.4 Impact of the $^{210}$Pb Daughter Nuclei on the Spectrometer Background

With $^{210}$Pb being identified as novel source of electrons in the spectrometer, a possible background contribution by its two radioactive progenies, namely $^{210}$Bi and $^{210}$Po, has to be discussed as well. This is of particular interest as these two isotopes decay with half-lifes being short compared to that of $^{210}$Pb. Thus, they are expected to be in secular equilibrium with the mother isotope $^{210}$Pb.

#### The $\beta$-decay of $^{210}$Bi

$^{210}$Bi undergoes a $\beta$-decay with a short half-life of 5 days and a very high endpoint of 1 162 keV. Electrons with energies in the few hundreds of keV generated close to the analyzing plane in a magnetic field of about 4 G will gyrate with cyclotron radii that are much larger than the spectrometer radius. Thus, these electrons cannot reach the detector on usual cyclotron trajectories. However, the guidance of such high-energy electrons will no longer be adiabatic so that their motion in the spectrometer is chaotic [Wan13a]. If this chaotic movement causes a $^{210}$Bi $\beta$-electron to escape the main spectrometer and reach the detector, its signal will appear in the overflow peak of the detector energy spectrum.

Figure 5.18 shows the high-energy part of the main spectrometer background spectrum (120-260 keV) in data set J. For energies above 130 keV the detector background is dominated by the Landau-distributed energy-losses of cosmic muons that directly pass through the thin detector wafer. Most of these events end up in the Gaussian overflow peak above 180 keV (see Sec. 3.8 for details). The shape of this peak in the FPD background measurement differs from that in data set J, such that the corrected spectrometer background spectrum appears significantly distorted (i.e. negative rates between 200 and 210 keV).

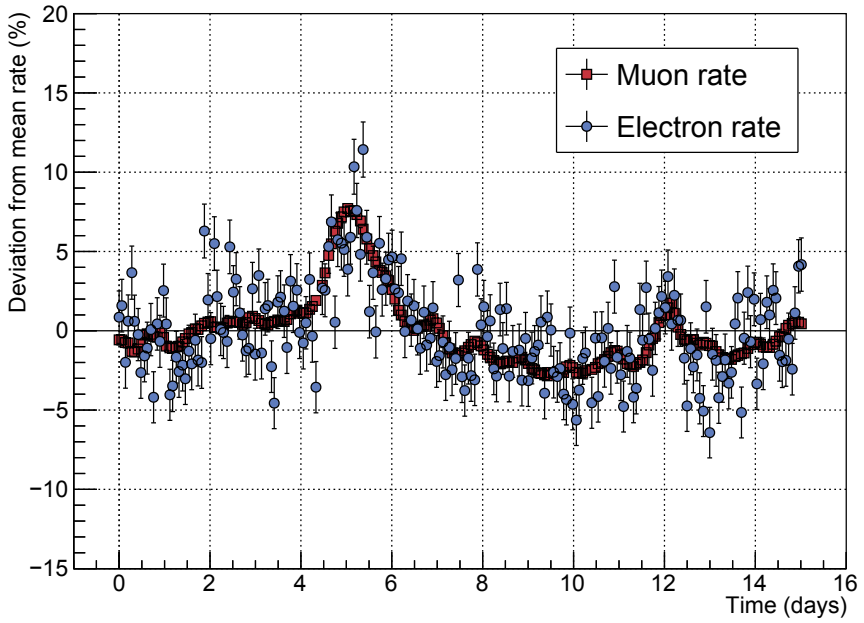


**Figure 5.19: Relative changes in the high-energy FPD event rate and the measured flux of cosmic muons** over the course of 15 days. The FPD events are restricted to those with energies $E \geq 130\,\mathrm{keV}$. Details are given in the text.

Since the FPD background was measured several weeks prior to the measurement J, the different shapes of the overflow peak can be explained by fluctuations and drifts of the baseline voltage of individual detector channels over time [Sch14c]. However, while the shape of the peak depends on detector related time-dependent effects, the total measured rate of high-energy events should, to first approximation, be independent of detector properties and only fluctuate with the flux of cosmic-muons. In Figure 5.19, the high-statistics data set J has been divided into sub-sets of 5 000-s length each, to plot the relative changes of the rate of high-energy FPD events with $E \geq 130\,\mathrm{keV}$ over the course of 15 days. In addition, the muon rate in the KATRIN experimental hall, as measured by the muon-detection system of the main spectrometer (Sec. 3.5) over the same period of time is shown. Both data sets show a similar trend of the event rate with a prominent peak around day 5. In [Lin15] it was shown that the trend in the measured muon rate anti-correlates with the atmospheric pressure at the site of the experiment, as it is well known from theory [All75].

In order to determine the fraction of high-energy detector-correlated background events being induced by cosmic muons, a similar analysis as in [Lin15] is performed: The high-energy event rate measured by the FPD is assumed to consist of two contributions

$$R(t) = \alpha \cdot R_\mu(t) + C \quad , \tag{5.7}$$

with a time-dependent part that is directly proportional to the rate of cosmic muons $R_\mu(t)$ and a time-independent part $C$, which originates from other background processes like for example the $\beta$-decay of $^{210}$Bi. By normalizing Equation 5.7 to the mean rate $\bar{R}$ of high-energy FPD events over the full course of data set J, one obtains

$$\frac{R(t)}{\bar{R}} = \underbrace{\alpha \cdot \frac{\bar{R}_\mu}{\bar{R}}}_{a} \cdot \frac{R_\mu(t)}{\bar{R}_\mu} + \underbrace{\frac{C}{\bar{R}}}_{1-a} \quad . \tag{5.8}$$

Here, $\bar{R}_\mu$ corresponds to the mean rate of cosmic muons over the course of the 15 days

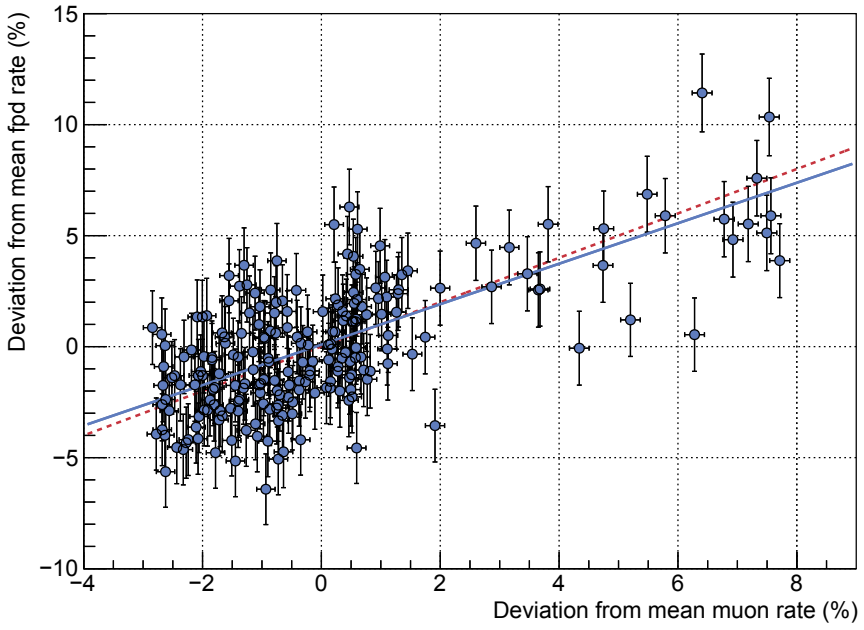


**Figure 5.20: Correlation between the muon rate and the high-energy detector background event rate.** The relative deviations of the FPD event rate and the muon rate over the course of 15 days (data set J) are shown in a scatter-plot representation. A linear fit according to Equation 5.8 that is applied to the data points (blue solid line) gives a ratio of $a = (91 \pm 5)\%$ of the FPD events being muon induced. The theoretical slope for a 100% muon correlation is shown as dashed red line.

and $a$ denotes the high-energy fraction of the detector background which is muon induced. Figure 5.20 shows a scatter plot of the deviations from the mean FPD event rate $R(t)/\bar{R}$ and the deviations from the mean muon rate $R_\mu(t)/\bar{R}_\mu$. A linear fit of the data points according to Equation 5.7 gives

$$a = (91 \pm 5)\% \quad . \tag{5.9}$$

Thus, the large majority of high-energy background events is found to be induced by cosmic muons. This in turn, implies that a smaller fraction of about 10% of the events does not originate from muons and thus can possibly be caused by electrons from $^{210}$Bi decays. In order to test this hypothesis, one could repeat the same analysis for a FPD background measurement like the one presented in Section 3.8 of this thesis. If the fraction of muon-induced background rate is higher in such a measurement, the contribution of non-muon induced background originates from the main spectrometer. This would be a rather strong evidence for an origin due to $^{210}$Bi $\beta$-electrons. However, as the muon-detection system of the main spectrometer was not operated in parallel to standard detector background measurements yet, this analysis cannot be performed at this point. Nevertheless, as no significant contribution from $^{210}$Bi $\beta$-electrons to the background in the standard ROI is expected, this topic is of minor concern at this point.

### The $\alpha$-decay of $^{210}$Po

The second $^{210}$Pb progeny, $^{210}$Po, decays via an $\alpha$-decay into the stable isotope $^{206}$Pb with a half life of $t_{1/2} = 138$ days. The $\alpha$-particles which are emitted isotropically in the decay have an energy of 5.3 MeV [Nat15], so that a fraction of them will pass through the implantation depth of several nm of stainless steel to enter the spectrometer volume. During this passage they will ionize atoms close to the surface. While the electrons generated along the highly ionizing $\alpha$-track are too low in energy to propagate to the vessel surface, their

appearance close to the surface can disturb the surface potential. This disturbance can, according to [Val04], cause the surface shake-off of several low-energy electrons. According to [Feo08], the actual direction of the $\alpha$-particle is of little importance as both incoming and outgoing $\alpha$-particles will generate approximately the same number of secondary electrons (with approximately the same angular distribution). Thus, it is expected that a 5.3-MeV $\alpha$-particle, emitted in a $^{210}$Po decay close to the inner surface of the main spectrometer vessel, will cause the emission of several low-energy electrons when entering the volume of the spectrometer and when hitting the vessel surface again at the opposite side. Due to the excellent magnetic shielding in the standard operation of the spectrometer, the electrons being generated will not reach the detector and will therefore not directly contribute to the spectrometer background. In Appendix B however, the emission of time-correlated electrons from the inner surfaces of the spectrometer is discussed in the context of measurements at 'asymmetric' magnetic-field configurations. In this discussion a possible emission of secondary electrons in the course of the $^{210}$Po $\alpha$-decays is of importance.

## 5.4 Conclusion

In this chapter, the results of several background measurements with the spectrometer in its standard HV-operation and at $U_{\text{vessel}} = 0\,\text{kV}$ during the SDS-IIA commissioning phase have been used to investigate the background characteristics outside of the standard energy window (ROI). In this context a previously unknown background signature resulting from L-shell conversion electrons from the decay of $^{210}$Pb could be clearly identified for the first time. Based on the experience of low-background experiments like BOREXINO or GERDA, a model for the deposition of this lead isotope on the inner surfaces of the spectrometer could be established: During the five-years long installation procedure of the inner electrode system, the progeny of the naturally occurring noble gas $^{222}$Rn is expected to have been plated-out on the inner surfaces of the vessel and its inner electrode system. As part of the $^{238}$U decay chain, $^{210}$Pb has been implanted into sub-surface layers of the stainless steel due to the high recoil energy of 146 keV. Simulations of the remaining energy of keV-electrons from the $^{210}$Pb decay after their passage through a small layer of stainless steel are consistent with the observations made in the background measurements.

To estimate the activity of $^{210}$Pb in the spectrometer, MC-tracking simulations with KASSIOPEIA were performed in order to determine the transport mechanisms of 30-keV electrons from the inner surfaces of the spectrometer to the detector. With a measured $^{210}$Pb L-shell conversion-electron rate of $(2.2 \pm 0.2)\,\text{mcps}$ and by assuming that $^{210}$Pb decays occur homogeneously distributed on the inner surface of the spectrometer vessel [on the inner electrode system], a $^{210}$Pb activity of $(998 \pm 117)\,\text{Bq}$ [$(862 \pm 99)\,\text{Bq}$] in the spectrometer is found. However, the simulation results also indicate that the probability of conversion electrons to be mapped onto the detector strongly depends on their starting position. Thus, the actual activity of $^{210}$Pb in the spectrometer could differ from the above stated results if the lead deposition was localized.

Based on the above described observations and simulations, the implications of the $^{210}$Pb activity for the background in the KATRIN standard ROI are the following:

- A direct contribution by electrons from the $\beta$-decay spectrum of $^{210}$Pb with low energies ($< 2\,\text{keV}$) that directly reside in the standard ROI can be estimated to be less than 0.2 mcps and therefore being negligible.
- An indirect background contribution by the storage of electrons from $^{210}$Pb decays in the outermost regions of the flux tube was evaluated on the basis of MC-storage simulations with KASSIOPEIA. The results show a strong increase of the production rate of secondary electrons to outer detector rings which is consistent with observations made in high-pressure measurements during SDS-IIA. In the context of an

evaluation of the pressure dependence of the main spectrometer background level in Chapter 6 a possible contribution from $^{210}$Pb-induced stored electrons will be further discussed.

- A background contribution from the daughter nuclei of $^{210}$Pb was evaluated: The decay of the direct daughter $^{210}$Bi is expected to have a negligible impact on the background level in the standard ROI as the major part of the $\beta$-electrons from its decay are far too energetic ($E_0 = 1\,162\,\mathrm{keV}$) to be stored in the spectrometer volume. The $\alpha$-decay of the resulting $^{210}$Po is also assumed to not affect the background level in the standard ROI directly. However, it provides a potential explanation for time-correlated electron rates from the inner surfaces of the spectrometer that were observed in SDS-IIA measurements at 'asymmetric' magnetic field configurations. This effect is further discussed in Appendix B.

CHAPTER 6

# A Spectrometer Background Model

In Chapter 4 of this thesis it is shown that the spectrometer background rate is no longer dominated by contributions from radon-induced events once the baffles in front of the NEG-equipped pump ports 2 and 3 are operated close to $LN_2$ temperature. Based on this important fact it is now possible to characterize the remaining background. To do so, a variety of cold-baffle[1] measurements was carried out during the SDS-II campaign. In contrast to previous investigations in which the spectrometer background was investigated over a wide range of energies, this chapter focuses on the background in the standard ROI only.

After briefly discussing basic characteristics of the spectrometer background with cold baffles (Sec. 6.1), the impact of several key operating parameters on the background level and signature is evaluated in detail (Sec. 6.2). In particular, the emission of secondary electrons from inner surfaces of the spectrometer is investigated (Sec. 6.3) and likely sources of the spectrometer background are discussed (Sec. 6.4). In this context, the recently proposed spectrometer background model based on excited Rydberg states of atomic hydrogen is investigated in detail, before final conclusions are drawn (Sec. 6.5).

## 6.1 The Spectrometer Background with Cold Baffles

Over the course of the 15-days-long 2014/15 Christmas break, a high-statistics data set (147 hours) with cold baffles was recorded with the spectrometer in its standard HV-mode (data set N2 in Tab. 6.1). In the following, this data set is used to discuss the remaining, non-radon induced spectrometer background in the standard ROI. The mean pressure in the spectrometer during these measurements was about $6 \times 10^{-10}$ mbar, as measured by Extractor gauge 3110. The magnetic field was set to 3.8 G in the analyzing plane (Tab. 3.1). In order to allow for a parallel investigation of the $^{210}$Pb background (see Chapter 5), the PAE was operated at a reduced potential of +4 kV, while the inner electrode system was set to a moderate electrostatic shielding potential of $U_{\mathrm{IE,common}} = -100$ V.

Figure 6.1 shows the distribution of interarrival times between subsequent events at the detector. As expected for cold-baffle measurements, single background events show no correlation such that the interarrival time spectrum follows an exponential distribution. A fit of the distribution gives a mean background rate

$$R = (691 \pm 1)\,\mathrm{mcps} \quad , \tag{6.1}$$

[1] From now on, all SDS-II measurements with at least baffles 2 and 3 cold will be denoted as 'cold-baffle' measurements.

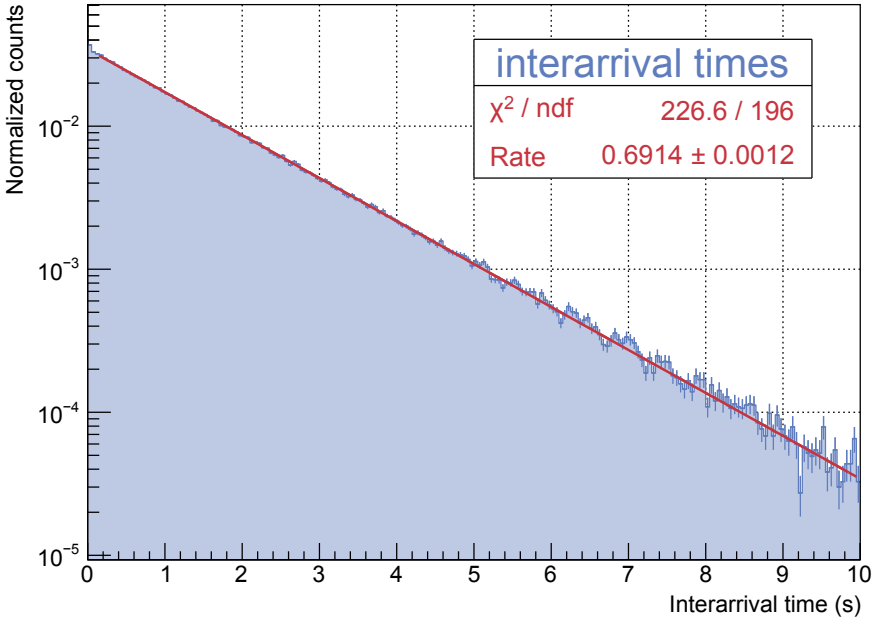


**Figure 6.1: Interarrival time distribution of the spectrometer background in the standard ROI with cold baffles.** The 147-hour-long cold-baffle background data set N2 (see Tab. 6.1) was recorded with the spectrometer in its standard HV-mode and a 3.8-G magnetic field in the analyzing plane. Displayed here are the interarrival times between subsequent detector events. The mean pressure in the spectrometer was about $6 \times 10^{-10}$ mbar (measured by Extractor gauge 3110). The steep cones of the inner electrode system were set to more positive potential with regard to the cylindrical and flat-cone parts with $U_{\mathrm{IE,common}} = -100\,\mathrm{V}$ and $U_{\mathrm{SC,offset}} = +97\,\mathrm{V}$, in order to keep the electromagnetic field (transmission) conditions in the spectrometer as similar as possible to later neutrino-mass measurements (Sec. 6.2.2). The interarrival times clearly follow an exponential distribution, as expected for uncorrelated background events. A corresponding fit gives an absolute background rate for all 148 detector channels of $R = (691 \pm 1)\,\mathrm{mcps}$.

as observed by 148 operational detector pixels. When compared to the result for the non-radon-induced background that is derived in Chapter 4 (Equation 4.7), the background level here appears significantly increased. However, data set N2 was recorded at a different magnetic-field setting, a reduced electrostatic shielding potential on the steep-cone parts of the inner electrode ($U_{\mathrm{SC,offset}} = +97\,\mathrm{V}$), and with a different pressure in the spectrometer vessel than the radon-related measurements. As will be shown in Section 6.2 these parameters have a significant impact on the observed background level, such that the two results do not contradict each other.

Taking advantage of the availability of all 148 detector channels during parts of the SDS-II campaign, the spatial distribution of the background on the detector could be analyzed in great detail. The left-hand side of Figure 6.2 shows the background rate in the standard ROI as measured by the individual detector pixels. A significant increase of the background rate to outer detector rings is clearly visible. This is consistent with observations detailed in Section 4.2.2 in terms of the accidental cluster events during measurements at elevated spectrometer pressure. Apart from a visible increase to outer rings also an azimuthal dependence of the background rate is manifest. In particular, the rate in the lower part of the detector is smaller by a factor of about two in comparison to the pixels in the upper left part of the wafer. In Chapter 3 it is shown that a slight misalignment along the SDS beamline can induce shifts of the observed magnetic flux tube relative to the mechanical axis of the spectrometer (see Fig. 3.24). During the SDS-IIA phase this shift resulted in a

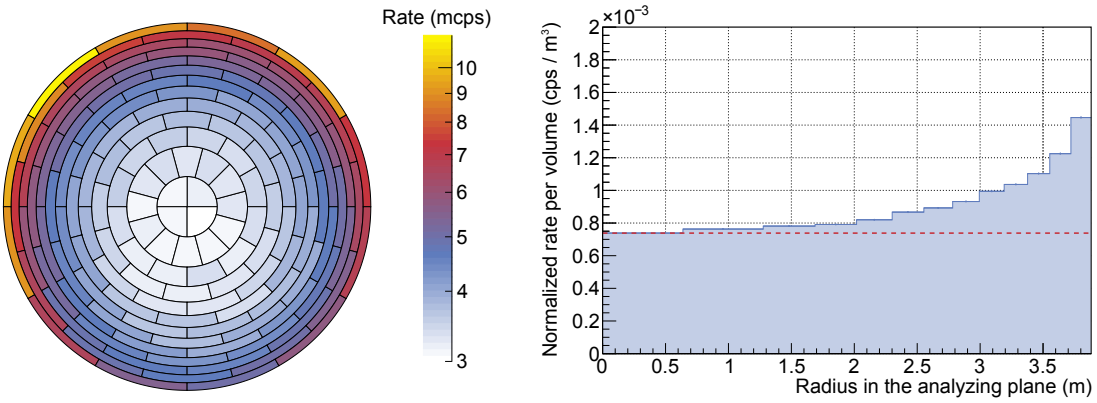


**Figure 6.2: Detector event distribution of the spectrometer background in the standard ROI with cold baffles.** The cold-baffle data set N2 (see Tab. 6.1) is analyzed with regards to the spatial distribution of the spectrometer background. **Left:** The background rates per detector pixel show both a radial and an azimuthal dependence. The latter appears as a region of reduced rate in the lower part of the detector, while the rate in the upper left part is about a factor of 2 larger. **Right:** The radial dependence of the background is shown in a detector ring-wise representation where the rate on a particular ring is normalized to the observed flux tube volume. Furthermore, the radii of the detector rings are scaled to the corresponding radius of the flux tube in the analyzing plane. A dashed red line indicates two potentially different background contributions: a flat part which makes up $\approx 75\%$ of the total background and a radially increasing part that makes up the other $\approx 25\%$.

reduced clearance between the flux tube and the inner electrode system in the upper left part of the spectrometer (looking from the detector side). Thus, the region of elevated rate at about 11 o'clock on the wafer can partly be explained by secondary electrons from the inner structures of the spectrometer, which more easily enter this part of the flux tube. An additional azimuthal dependence of the rate of secondary electrons being emitted from the inner surfaces of the spectrometer will be briefly discussed in Section 6.3.

The right-hand side of Figure 6.2 shows the background rate as measured by each detector ring, normalized to the corresponding volume observed by the ring. The radius of each ring is scaled to the radial extension of the flux tube in the analyzing plane of the spectrometer. A similar representation was already used in Chapter 4 (see Fig. 4.11) in the context of the radial distribution of radon-induced backgrounds. While this representation ignores the azimuthal dependence of the background, it provides two major advantages: Firstly, measurements with different magnetic-field settings now can directly be compared (see Sec. 6.2.4). Secondly, the rather large differences in the observed volumes per detector ring, caused by the characteristic shape of the flux tube in the SDS apparatus, are taken into account. Due to the latter effect, the differences between outer and inner detector rings appear less pronounced in the ring-wise representation on the right-hand side of Figure 6.2, which could indicate two background contributions: A dominant contribution which makes up $\approx 75\%$ of the total background and seems to be homogeneously distributed in the volume appears flat in the ring-wise representation. A smaller contribution which shows an increase to large radii could partly be attributed to the previously described process of secondary electrons drifting into the flux tube volume.

Despite the excellent suppression of radon-induced background by the $LN_2$-cooled baffle system, the spectrometer background is found to exceed the ambitious KATRIN design goal of $R_{\mathrm{bg}} \leq 10\,\mathrm{mcps}$ by almost two orders of magnitude. A further reduction of the background is therefore essential to achieve the targeted neutrino-mass sensitivity of the experiment. To develop efficient background reduction techniques, however, the individual sources of the background need to be identified and characterized first in detail.

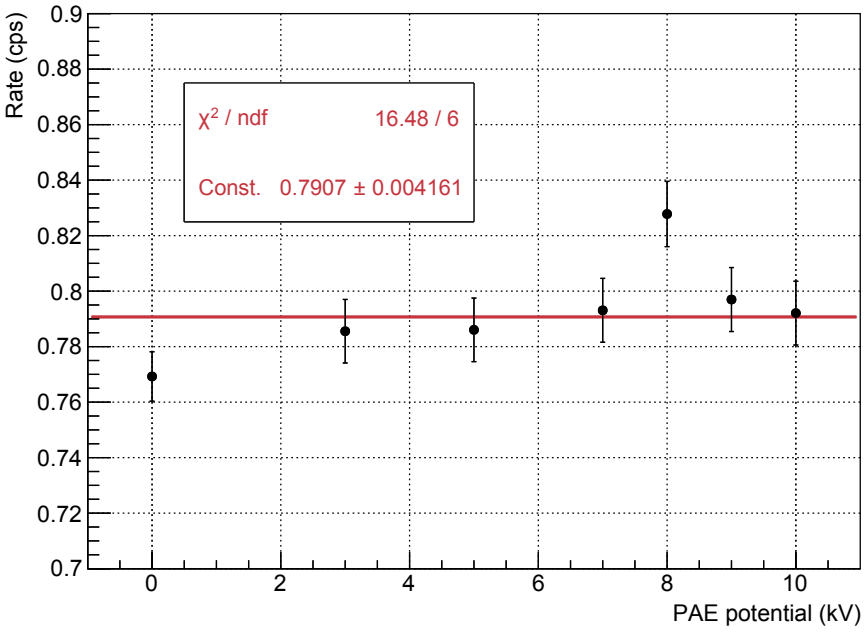


**Figure 6.3: Spectrometer background rate as a function of the post-acceleration potential.** The absolute background rate measured by 122 operational detector channels in a series of SDS-I measurements at a 3.8-G magnetic-field setting is shown as a function of the post-acceleration potential. In the analysis the ROI has been shifted to match the variation of the PAE potential. Note that in these warm-baffle measurements the (Poisson) error bars do not take into account the correlation of the radon-induced events. More details are given in the text.

## 6.2 Background Dependence on Key Operating Parameters

In order to characterize the non-radon-induced background, key operating parameters of the SDS apparatus were varied to investigate their impact on the background rate.

### 6.2.1 Post-Acceleration Potential

To first order, the detector background spectrum is found to be independent from the post-acceleration potential (see Sec. 3.8 and [Sch14c]). Now, when investigating spectrometer-related background, low-energy electrons leaving the spectrometer volume on the detector side are energetically boosted by the positive PAE potential. In order to exclude the existence of additional influences of the post-acceleration potential on the background rate, measurements at different $U_{\mathrm{PAE}}$ were performed already early in the SDS-I campaign (runs #8028 - #8043). Figure 6.3 shows the absolute background rates measured by the 122 detector pixels that were usable during SDS-I as a function of the PAE potential. Again, a 3.8-G magnetic field in the analyzing plane and a standard inner electrode offset potential of $U_{\mathrm{IE,common}} = -100\,\mathrm{V}$ were used. The background does not show any dependence on the PAE potential and the rather large $\chi^2$/ndf value of the constant fit applied to the data points can be explained by the larger fluctuations of radon-induced background events in these warm-baffle measurements, which are not taken into account in the statistical analysis and the error bars.

### 6.2.2 Inner Electrode Offset Potential

As described in detail in Chapter 3 of this thesis, a long-term operation of the inner electrode system in double-layer configuration was not possible during the SDS-I and SDS-II

**Table 6.1: Background measurements at different inner electrode offset potentials.** All listed data sets were recorded with a 3.8-G magnetic field in the analyzing plane, pressures of $p < 1 \times 10^{-9}$ mbar in the spectrometer, and with cold baffles. In all cases the vessel potential was adjusted such that $U_0 = U_{\text{vessel}} + U_{\text{IE,common}} = -18.6\,\text{kV}$. Apart from the steep cones ($U_{\text{SC}}$), the offset power supplies of the individual electrode rings were not used. The given rates correspond to the number of events that were recorded with energies in the corresponding standard ROI by 142 operational detector pixels per unit time.

| Set | $U_{\text{IE,common}}$ (V) | $U_{\text{SC}}$ (V) | $U_{\text{PAE}}$ (kV) | Rate (mcps) | Runs |
|---|---|---|---|---|---|
| L | 0 | 0 | +10 | $890 \pm 5$ | #21832 + $i \cdot 4$ ending with #21900 |
| M | −5 | +2 | +4 | $824 \pm 1$ | #21427 + $i \cdot 3$ ending with #21748 (excluding run #21670) |
| | −10 | +2 | +10 | $789 \pm 5$ | #21387 - #21394 |
| | −15 | +2 | +10 | $755 \pm 6$ | #21395 - #21400 |
| | −20 | +2 | +10 | $729 \pm 7$ | #21407 - #21410 |
| | −35 | +2 | +10 | $701 \pm 12$ | #23961 - #23963 |
| | −50 | +2 | +10 | $643 \pm 5$ | #21411 - #21417 |
| N | −100 | +1 | +10 | $620 \pm 8$ | #23810 - #23812 |
| N2 | −100 | +97 | +4 | $664 \pm 1$ | #21428 + $i \cdot 3$ ending with #21749 (excluding run #21521) |
| | −200 | +1 | +10 | $587 \pm 7$ | #23813 - #23815 |
| | −300 | +1 | +10 | $555 \pm 7$ | #23816 - #23818 |
| | −400 | +1 | +10 | $545 \pm 7$ | #23819 - #23822 |
| | −575 | +2 | +10 | $490 \pm 12$ | #23919 - #23920 |
| | −800 | +2 | +10 | $517 \pm 12$ | #24252 - #24253 |

campaigns. Apart from this restriction, however, the partition of the electrode system into rings and dipole halves did provide a rather high degree of flexibility in adjusting the electric fields inside the main spectrometer. Accordingly, a large variety of measurements at different electric field configurations was carried out during SDS-II. In this thesis, however, only selective topics of the performance of the electrode in terms of background, namely the electrostatic shielding and a fine-shaping of the electric field are investigated. Other background studies focusing on investigations of the electrode system operated in a static or pulsed electric-dipole mode, as well as in a short-term double-layer operation during a temperature cycle of the spectrometer vessel, are discussed in [Hil16] and [Dyb16].

### Electrostatic Shielding

A key task of the inner electrode system is to electrostatically shield low-energy secondary electrons emitted from the spectrometer walls. During the SDS-I phase, several measurements in both 'asymmetric' and 'symmetric' magnetic field configurations were carried out in order to investigate the impact of such a shielding on the rate of electrons emitted from the walls. The resulting background rates for the standard spectrometer operation can be found in [Lei14]. At that time however, the $LN_2$-cooled baffle system could not be operated continuously so that about half of the background originated from radon-induced events. Moreover, the limited number of usable detector channels (122) during SDS-I restricted the spatial resolution significantly.

During SDS-IIA these two drawbacks were no longer impedimental, so that a series of background measurements with a 3.8-G magnetic field in the analyzing plane and various

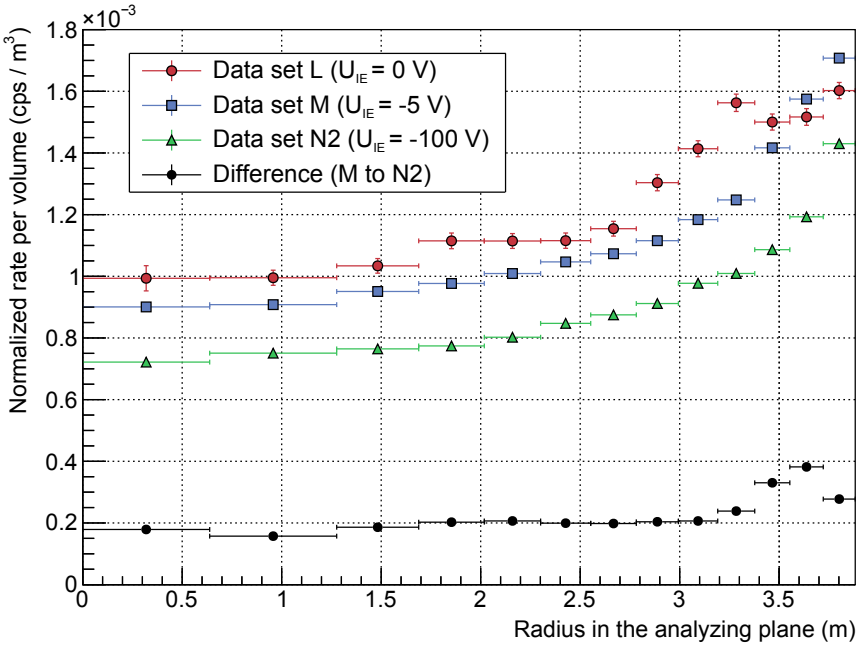


**Figure 6.4: Radial background distribution as a function of the inner electrode offset potential.** The radial dependence of the (volume-normalized) background rate in the standard ROI in data sets L, M and N2 is shown in a ring-wise representation. The difference between the distributions in data sets M and N2 is shown in addition. Apart from small effects on the outermost detector rings, the more negative inner electrode offset potential in data set N2 reduces the spectrometer background in a largely radially independent way. More details are given in the text.

inner electrode offset potentials $U_{\mathrm{IE,common}}$ was carried out. The corresponding data sets are listed in Table 6.1 together with the total background rates in the standard ROI. Interestingly, the background rate moderately decreases with increasing $U_{\mathrm{IE,common}}$, much less however, than expected in case of an electrostatic shielding effect.

Figure 6.4 shows the (volume-normalized) radial distributions of the observed background per detector ring for the high-statistics data sets L, M, and N2. At large radii the distribution of data set L shows a distinct distortion which at this point is attributed to a modified electron transport mechanism in the rather inhomogeneous electric fields in the outer flux tube regions at $U_{\mathrm{IE,common}} = 0\,\mathrm{V}$. A similar effect will be discussed later in this section with regard to the signal electrons fulfilling the transmission conditions. Apart from this distortion in data set L, the three distributions feature a flat behavior with a noticeable increase of the background rate towards outer detector rings. In order to visualize the background suppression effect of a larger inner electrode offset potential, the difference between the distributions of data sets M at $U_{\mathrm{IE,common}} = -5\,\mathrm{V}$ and N2 at $U_{\mathrm{IE,common}} = -100\,\mathrm{V}$ is shown in addition.

Most interestingly, this distribution, which shows the radial-dependent shielding efficiency of the inner electrode system, appears flat for radii smaller than about 3 m, while increasing for the outermost flux tube regions. The latter effect could be explained by a more effective electrostatic shielding of medium-energy electrons ($E < 100\,\mathrm{eV}$). In contrast, the uniform background reduction on the innermost ten detector rings does not fit to the generic expectation for an electrostatic-shielding effect. According to [Lei14], electrons with $E < 100\,\mathrm{eV}$ from the inner surface of the vessel can only enter the inner parts of the spectrometer volume via a two-stage process: The electron needs to be stored in the outer regions of the flux tube to then slowly drift towards the spectrometer axis due to the

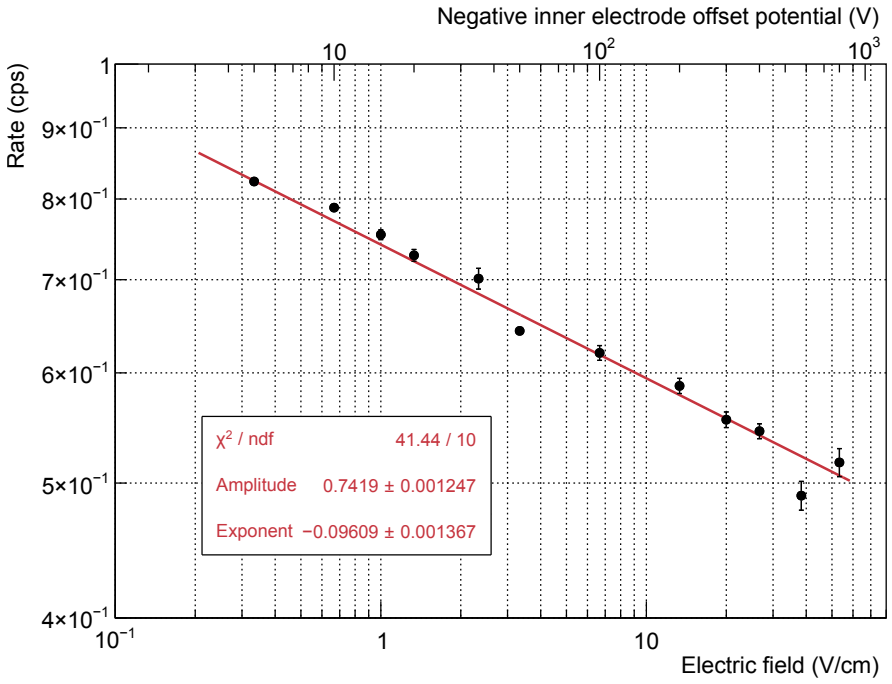


**Figure 6.5: Dependence of the total spectrometer background rate on the inner electrode offset potential.** The total background rate measured by 142 operational detector pixels in all data sets listed in Table 6.1 (excluding L and N2) in the standard ROI, is shown as a function of $U_{\mathrm{IE,common}}$. In addition to the potential on the top axis, the corresponding electric field $\mathcal{E}$ between the spectrometer vessel and the 15-cm distant first wire layer of the electrode system is given at the bottom of the plot. A power-law fit (red line) of the data points gives $R(\mathcal{E}) = 0.742 \cdot \mathcal{E}^{-0.096}$.

presence of non-axially symmetric magnetic and electric fields ($\vec{E}\times\vec{B}$- and $\nabla\vec{B}\times\vec{B}$-drifts). During its drift, the stored electron will ionize residual gas molecules and, thus, generate background electrons. As the drift process will occur on rather long time-scales compared to the relatively short storage times of these electrons [Lei14] it is, however, unlikely that the electrons will propagate to the inner parts of the flux tube before breaking the storage condition. Thus, a background contribution caused by these electrons should mainly appear on outer detector rings and feature a strong decrease towards smaller radii. This entails that a larger electrostatic shielding factor should reduce background predominantly in the outer flux tube regions and not radially independent as visible in Figure 6.4. At this point it can be stated that increasing inner electrode offset potentials only result in a minor background suppression effect. The radial dependence of electrostatic shielding does not manifest in the data, implying a novel, hitherto unexplained effect.

Apart from the three high-statistics data sets L, M and N2, shorter-term measurements at various inner electrode offset potentials were carried out during various phases of SDS-IIA. While the statistics in most of the corresponding data sets are not sufficiently large to investigate radial dependences of spectrometer-related backgrounds decisively, the overall event rates collected by the total of 142 operational detector channels allow to study the total background rate as a function of the parameter $U_{\mathrm{IE,common}}$. Figure 6.5 shows the corresponding analysis for all data sets listed in Table 6.1 (excluding L and N2). Here, the background rate is given as the function of the electric field $\mathcal{E} = {}^{U_{\mathrm{IE,common}}}/_{15\,\mathrm{cm}}$ between the outer wire layer of the electrode and the vessel surface[2] together with the corresponding offset potentials. The background rate decreases with increasing (negative) offset potential even in the regime $U_{\mathrm{IE,common}} < -200\,\mathrm{V}$. This behavior stands in stark contrast to earlier

[2]This particular display will be explained later in Section 6.4.1.

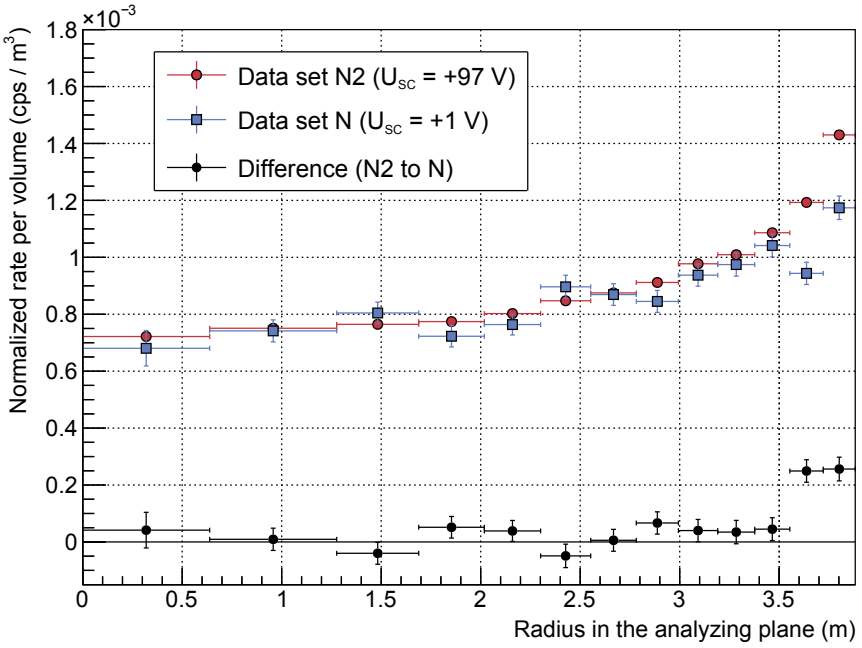


**Figure 6.6: Radial distribution of background events for two different positive steep-cone offset potentials.** The radial dependence of the background rate in the standard ROI is displayed for the two data sets N and N2. The difference between the two distributions is shown as well (black dots). The radial distributions follow a similar shape and feature a difference of about 40 mcps in the total background rate, originating from the outermost two detector rings only.

observations made in SDS-I, where the background rate was found to strongly increase for inner electrode offset potentials of $U_{\mathrm{IE,common}} < -200\,\mathrm{V}$ due to the onset of field-electron emission [Sch14c]. Possible explanations for the absence of the field-electron emission in the SDS-II measurements could be the better axial symmetry of the magnetic field or the different vacuum commissioning during the two long-term campaigns.

### Fulfillment of the Transmission Conditions

The majority of the measurements presented in this thesis were targeted to investigate particular characteristics of the spectrometer-related background and, therefore, were carried out using non-standard configurations of the SDS setup. In the later neutrino-mass measurements, however, a minimized background level has to be achieved while fulfilling the transmission condition for signal electrons. In this context, the distorting effect of early-retardation[3] needs to be avoided by setting the potential on the steep-cone modules of the electrode system more positive than the one on the rings in the cylindrical and flat-cone parts of the spectrometer [Gro15]. For most of the measurements listed in Table 6.1 this condition was not fulfilled. Figure 6.6 compares the two data sets N and N2, both recorded with $U_{\mathrm{IE,common}} = -100\,\mathrm{V}$, now however with different offset potentials applied to the steep-cone rings of the electrode system. A difference in the total background rate of about 40 mcps is observed, which originates mainly from the significantly reduced rate on the outermost two detector rings in data set N.

A reduced rate on outer detector rings has already been observed in the case of data set L at $U_{\mathrm{IE,common}} = 0\,\mathrm{V}$ in Figure 6.4. As the drop in rate appears suddenly, a change in

[3] Early retardation occurs if the collimation of a signal electrons momentum into longitudinal direction by the decreasing magnetic field strength happens too slowly, such that the electron is reflected by the electric field before it reaches the point of minimum magnetic field (usually the analyzing plane).

**Table 6.2: Background measurements at different main spectrometer vessel potentials.** All listed measurements were performed with cold baffles and a 3.8-G magnetic field in the analyzing plane. Note that that some of the data sets were recorded at a modified 3.8-G setting as the PS1 magnet was turned off [Beg14]. In this configuration, parts of the observed flux tube touch the inner electrode system, such that the outermost detector ring had to be excluded from the analysis. The inner electrode offset potential was set to $U_{\mathrm{IE,common}} = -5\,\mathrm{V}$, while the steep cone rings were set to an offset potential of $U_{\mathrm{SC}} = +2\,\mathrm{V}$.

| $U_{\mathrm{vessel}}$ (V) | Runs |
|---|---|
| −18 595 | #21377 - #21384 |
| −5 000 | #23833 - #23834 |
| −1 000 | #23876 - #23877 and #23836 |
| −500 | #23874 - #23875 |
| −200 | #23910 - #23911 |
| −5 | #23824 - #23825 |

the drift processes of secondary electrons into the flux tube seems unreasonable at this point. Instead, the common feature that distinguishes the two data sets L and N from set N2 is the fact that the steep cones are in both cases at the same potential as the central and flat-cone electrode rings. In the outer flux tube regions, small inhomogeneities in the electric field can be expected due to the specific geometry of the inner electrode system [Wan13a]. Low-energy background electrons generated close to the analyzing plane can, thus, be reflected by these inhomogeneities on their way to the detector. In the case of more positive steep cone potentials, however, these electrons will achieve a boost in longitudinal energy when traversing towards the exit sites of the spectrometer, so that they are less susceptible to local disturbances in the potential.

### 6.2.3 Spectrometer Vessel Potential

A series of measurements at different vessel potentials $U_{\mathrm{vessel}}$ was carried out in order to investigate the impact of this crucial parameter on the spectrometer background level. The corresponding data sets are listed in Table 6.2. The plot at the top of Figure 6.7 shows the corresponding radial background distributions as measured by the innermost 12 detector rings. Due to a non-standard 3.8-G setting with the PS1 magnet turned off [Beg14], parts of the inner electrode support structure were mapped onto the outermost detector ring in some of the measurements, so that this ring had to be excluded from this analysis.

At multi-keV potentials ($U_{\mathrm{vessel}} = -18\,595\,\mathrm{V}$ and $U_{\mathrm{vessel}} = -5\,000\,\mathrm{V}$) the rather flat radial distributions show only minor changes at the outer flux tube parts. At lower potentials, however, significant reductions in the background rate are found: When decreasing the potential from $U_{\mathrm{vessel}} = -5\,000\,\mathrm{V}$ to $U_{\mathrm{vessel}} = -500\,\mathrm{V}$, the background level on the outermost detector rings decreases by more than a factor of two. The region covering the inner detector rings, however, features a constant background level comparable to the one at $U_{\mathrm{vessel}} = -18\,595\,\mathrm{V}$. Below $U_{\mathrm{vessel}} = -500\,\mathrm{V}$, the background rate on the central detector rings decreases as well, so that a quasi-flat distribution is found for small potentials ($U_{\mathrm{vessel}} = -5\,\mathrm{V}$). Even in the latter case, where the vessel potential is essentially comparable to zero, the spectrometer background rate remains at a surprisingly large absolute value of about 100 mcps. This result is comparable to earlier ones obtained in measurements at zero vessel potential during SDS-I [Fra13].

Over the course of the SDS-IIB phase additional measurements at various $U_{\mathrm{vessel}}$ were carried out in [Tro16], to further investigate the above described phenomena. The lower

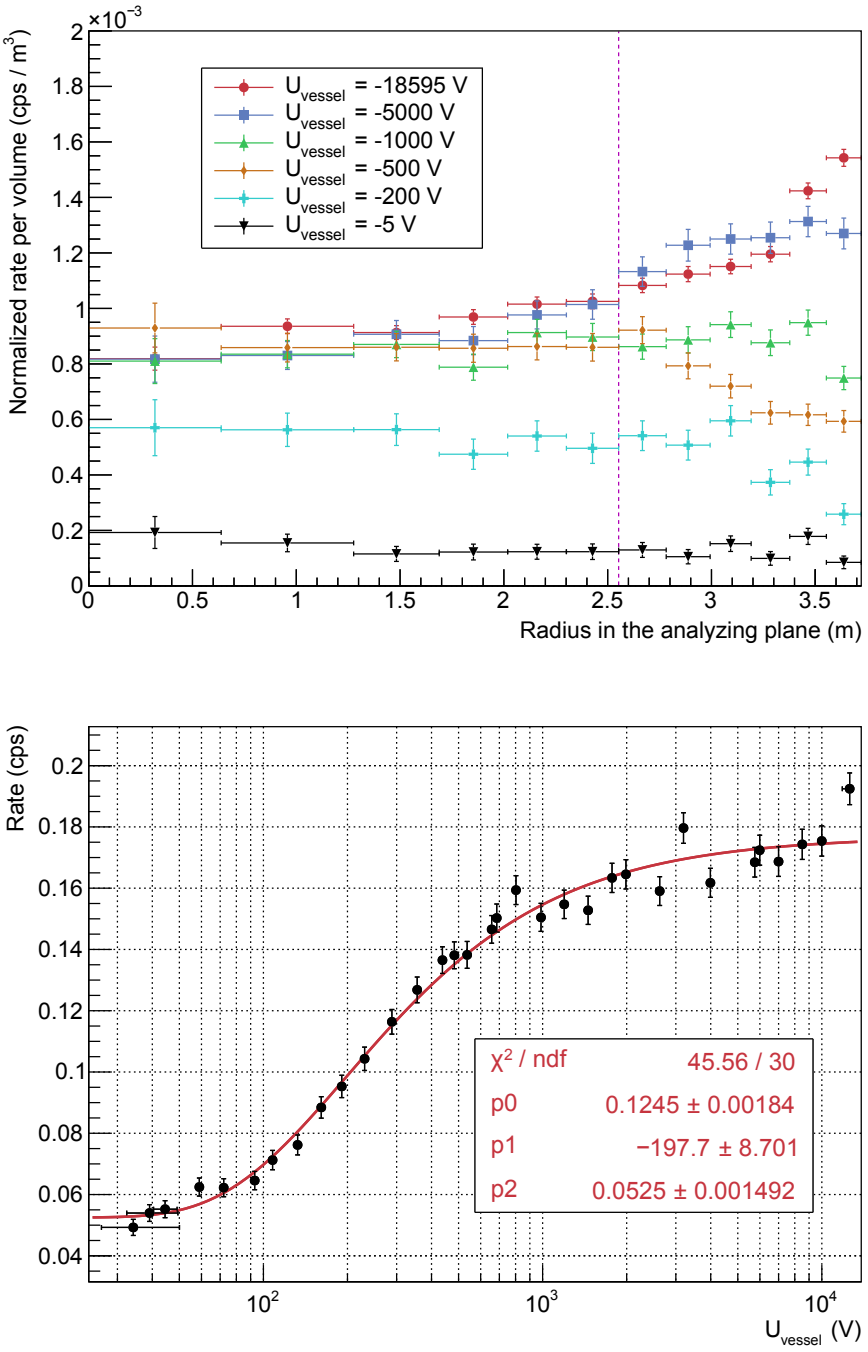


**Figure 6.7: Impact of the spectrometer vessel potential on the background level. Top:** The radial background distributions measured by the innermost 12 detector rings in the six background data sets, recorded at different vessel potentials, listed in Table 6.2, are shown. As the outer detector ring in some of these measurements images internal structures of the inner electrode system onto the detector, this ring is excluded from the analysis. **Bottom:** The spectrometer background rate in the standard ROI as measured by all operating pixels of the innermost six detector rings (see purple dashed line in the upper plot) in the SDS-IIB runs #25992 - #26057 is shown as a function of the vessel potential $U_{\text{vessel}}$. An empirical fit according to Equation 6.2 is applied to the data points.

plot in Figure 6.7 shows the background rate as measured by all operating detector channels of the innermost six detector rings in dependence of $U_{\text{vessel}}$. An empirical fit according to

$$R(U_{\text{Vessel}}) = p_0 \cdot \exp(-\frac{p_1}{U_{\text{Vessel}}}) + p_2 \tag{6.2}$$

is found to best describe the $U_{\text{vessel}}$-dependence of the background rate ($\chi^2/\text{ndf} \approx 1.5$).

In order to better understand the above described findings a series of MC-storage simulations was performed in [Glu15]. These simulations were targeted to investigate whether a possible change in the storage conditions of low-energy background electrons in the spectrometer volume could be the main reason for the reduction of the observed background rate when decreasing the vessel potential. The simulation results, however, show that altered storage conditions as origin of the observed background dependence are rather unlikely. A second possible explanation could be an increase of the number of secondary electrons that are produced per high-energy primary electron released during radon decays. With a remaining radon background under cold-baffles conditions of $\approx$ 25 mcps at $-18.6$ kV (see Eq. 4.8), an increase of the secondary electron yield of about a factor of four at zero vessel potential would be sufficient to explain the 100-mcps background. However, during a series of warm-baffle measurements to corroborate this hypothesis (see Appendix A.3), this could not be verified. There, an artificial radon source was installed at pump port 3 and the spectrometer vessel was operated at different potentials. Indeed, the opposite effect was observed: The secondary electron yield of the radon decays significantly decreases for vessel potentials $U_{\text{vessel}} > -300$ V.

The search for the cause of the peculiar spectrometer-background dependence on the vessel potential $U_{\text{vessel}}$ is ongoing in the context of [Tro16]. At the date of writing this thesis, no conclusive explanation of the observed effects is found, yet.

### 6.2.4 Magnetic-Field and Volume Dependence

Another major parameter to influence the background level is the absolute value of the magnetic field in the analyzing plane of the spectrometer. A change of the magnetic field there will change several properties at once. First of all, secondary electrons emitted from inner spectrometer surfaces are guided back to their origin due to the inherent magnetic shielding of the MAC-E filter (see Sec. 2.1.2). The shielding efficiency, however, depends on several parameters such as the absolute magnetic field strength in the center of the spectrometer, the shape of the magnetic flux tube, and the interplay between the electric and the magnetic field in the volume of the spectrometer. Furthermore, also the storage conditions for electrons depend on the magnetic field strength according to Equation 4.1. Besides influencing background processes, the absolute value of the magnetic field also changes the dimension of the observed magnetic flux tube according to Equation 2.3. Figure 3.3 visualizes the flux tube dimensions for standard magnetic field settings used during the SDS-IIA phase. Of key importance here is the fact that the radial extension of the flux tube changes with the magnetic field in the analyzing plane. This effect has to be accounted for when investigating radially-dependent processes such as drifts of secondary electrons into the flux tube. As previously described, the ring-wise representation of the volume-normalized rates that is used throughout this thesis to illustrate the radial background distribution incorporates both effects, the modified observed volume as well as the corresponding radial extension of the flux tube in the analyzing plane[4]. In this way it allows for a direct comparison of measurements at different 'symmetric' magnetic field settings.

[4]Note that possible azimuthal dependencies of the background rate per unit volume (1 m$^3$) as well as the profile of the flux tube outside the analyzing plane are not accounted for here.

**Table 6.3: Background measurements at different 'symmetric' magnetic field settings** during SDS-IIA. All listed measurements were carried out with cold baffles and the spectrometer in its standard HV-mode. The listed rates correspond to the number of background events per unit time, as measured by 142 operational detector channels. The solenoid and air coil currents (the observed flux tube volumes) for all magnetic field settings are given in Table 3.1 (Table 3.2).

| Set | Magnetic field setting | $U_{\mathrm{IE,common}}$ (V) | Rate (mcps) | Runs |
|---|---|---|---|---|
| L | 3.8 G (*double*) | 0 | $890 \pm 5$ | #21832 + $i \cdot 4$ ending with #21900 |
| N2 | 3.8 G (*double*) | $-100$ | $664 \pm 1$ | #21428 + $i \cdot 3$ ending with #21749 (excluding run #21521) |
| O | 4.3 G (*single*) | $-100$ | $511 \pm 4$ | #22217 + $i \cdot 6$ ending with #22259 |
| P | 5 G (*double*) | 0 | $645 \pm 4$ | #21833 + $i \cdot 4$ ending with #21901 |
| Q | 9 G (*double*) | 0 | $349 \pm 3$ | #21834 + $i \cdot 4$ ending with #21902 |

Table 6.3 lists several background measurements at 'symmetric' magnetic field settings and for different $U_{\mathrm{IE,common}}$ values that were carried out during SDS-II. A comparison of the background rates in the data sets L, P, and Q, all obtained with $U_{\mathrm{IE,common}} = 0\,\mathrm{V}$, shows that the overall background rate decreases when the magnetic field strength in the analyzing plane increases. However, when adjusting for the corresponding flux tube volume changes, a different picture emerges, which is of central importance for understanding non-radon-induced background processes. The top part of Figure 6.8 shows the radial dependence of the background in data sets L, P, and Q in a volume-normalized ring-wise representation. Apart from smaller fluctuations which are most probably caused by slightly changed azimuthal background dependences, the three distributions show a similar radial profile. This remarkable and a priori unexpected observation implies that the non-radon-induced spectrometer background scales with the observed volume.

Another key observation of vital importance for understanding background processes is shown in the lower part of Figure 6.8. Here, a comparison of the radial background profiles in data sets N2 and O is given, with the latter being measured for a single-minimum magnetic field setting (see Sec. 3.1). As can be seen in Figure 3.3, the observed volume in such a setting is strongly decreased compared to the two-minimum case. At the same time, the shape of the flux tube differs such that its clearance to internal structures in the flat-cone regions of the spectrometer is increased. The shapes of the radial background distributions in data sets N2 and O exhibit only slight differences for the innermost detector rings, an effect not yet understood. When looking at the absolute background rates given in Table 6.3, however, the background in the single-minimum case is significantly reduced by about 150 mcps compared to the standard 3.8-G setting. This can be traced back to the smaller observed volume in the single-minimum case. A more detailed discussion of the influence of single- to double-minimum magnetic field settings on the transmission conditions for signal electrons and of a background optimization in terms of an observed-volume minimization is given in [Erh15].

Based on these observations it can be stated that the non-radon-induced background to first order only depends on the observed flux tube volume rather than on the magnetic field strength in the central parts of the spectrometer. This surprising result implies that

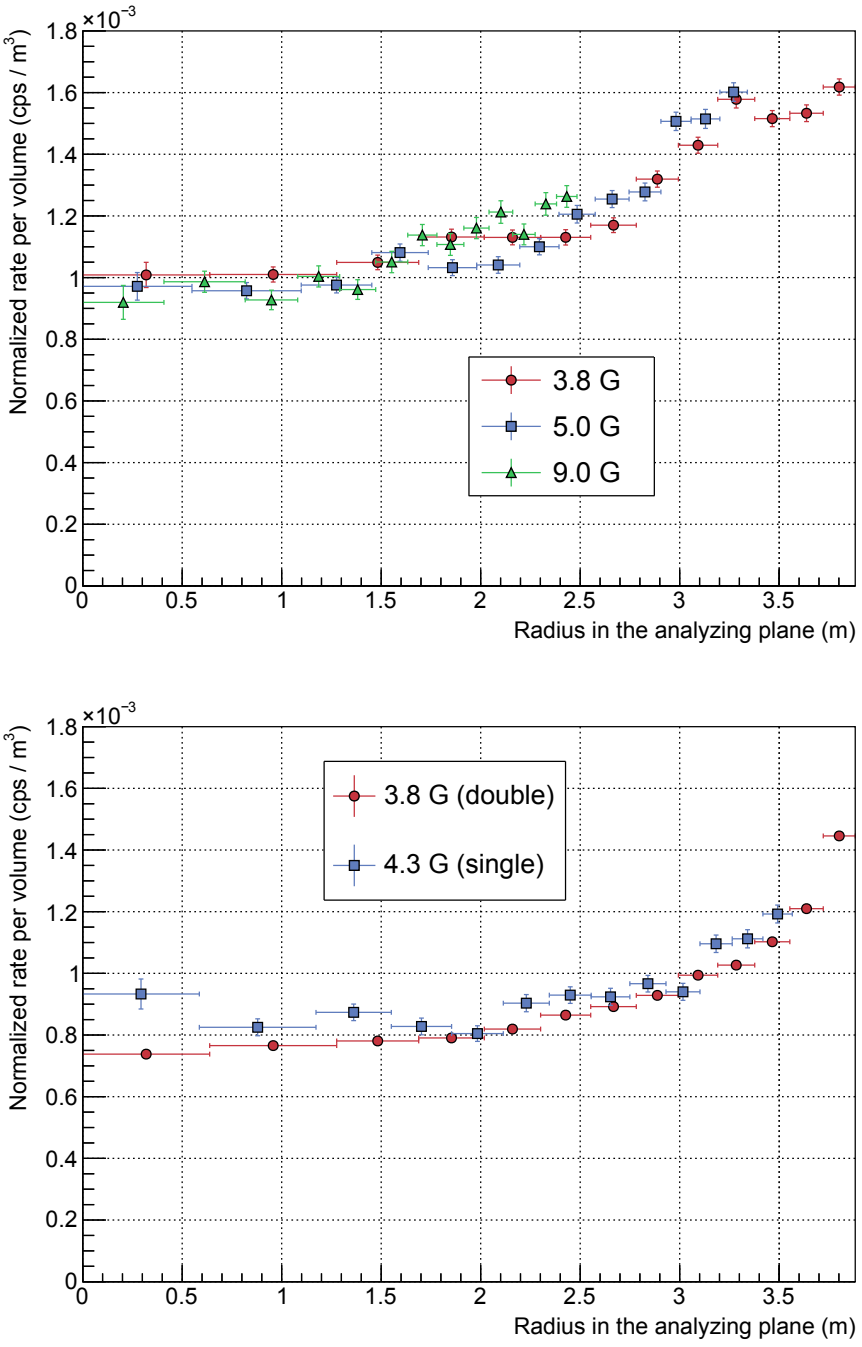


**Figure 6.8: The radial background distribution for different 'symmetric' magnetic field settings.** The radial dependence of the background rate in the standard ROI, as measured by 142 operational detector channels, is shown in a ring-wise representation. **Top:** Comparison of the data sets L, P and Q for the three 'symmetric' double-minimum 3.8-G, 5-G, and 9-G magnetic field settings. Apart from smaller fluctuations, the radial profiles of the background appear similar. Note the different radial extensions of the three profiles. **Bottom:** Comparison of data sets N2 and O taken with almost identical absolute values of the magnetic field in the analyzing plane, but with different minimum conditions of the observed flux tube (see Fig. 3.3). More details are given in the text.

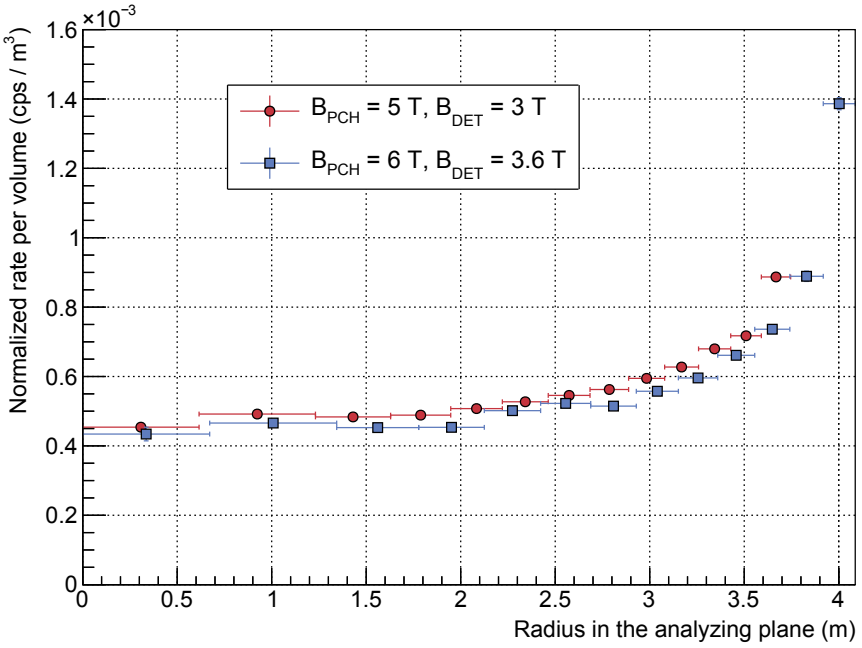


**Figure 6.9: Dependence of the radial background distribution on the magnetic field of the FPD magnets.** The radial distribution of the spectrometer background for a nominal magnetic field of the pinch (detector) magnet of 6 T (3.6 T) is compared to the reduced-field case of 5 T (3 T). The magnetic field in the analyzing plane of the spectrometer is about 3.8 G in both measurements, while the magnetic field strength at the location of the detector wafer differs by about 0.6 T. The latter difference results in a disparity in the radial extension of the two distributions. Moreover, the data points at nominal magnetic-fields appear collectively lower than those in case of reduced fields.

background electrons are being generated in such manner that they are homogeneously distributed over the volume of the spectrometer. This fact stands in contradiction to a conventional background model based on secondary electrons emitted from inner surfaces of the spectrometer as source of the background. However, this finding concurs with the observations made in Section 6.2.2, pointing to a completely novel background generating mechanism.

### Background Level at Nominal Magnetic Fields

The installation of a new pinch magnet after the end of the SDS-IIA phase allowed the joint operation of the pinch and detector magnet at nominal fields of 6 T and 3.6 T. In order to ensure magnetic field strengths in the analyzing plane for the SDS-IIB data comparable to those in SDS-IIA, the LFCS air coil currents had to be adjusted accordingly (see Table C.4 in Appendix C).

Figure 6.9 shows the radial profile of the SDS-IIB background for nominal magnetic fields of the FPD magnets (runs #24700 - #24717) compared to the earlier case with reduced fields of 5 T and 3 T (runs #24627 - #24671). Interestingly, the two distributions are similar in shape, while the observed flux tube in the case of nominal fields extends to larger radii in the analyzing plane, although the magnetic field strength is comparable in both measurements. This effect is explained by the larger magnetic field strength at the position of the detector wafer of $B_{\mathrm{FPD}}^{\mathrm{nominal}} \approx 3.3\,\mathrm{T}$ compared to $B_{\mathrm{FPD}}^{\mathrm{reduced}} \approx 2.7\,\mathrm{T}$. According to Equation 2.4 this effect will increase the diameter of the observed flux tube in the spectrometer by about 0.4 m.

Apart from the radial extension, the background distribution at nominal fields is only marginally lower than in the case of reduced fields. In general, this effect can be explained by the change of the ratio of the pinch magnet field, $B_{\mathrm{PCH}}$, relative to the field of the PS2 magnet, $B_{\mathrm{PS2}}$. When this ratio is being increased from $^{10}/_{9}$ in the reduced-fields case to $^{4}/_{3}$ in the nominal case, stored background electrons generated in the flux tube volume will have a larger chance to be magnetically reflected on the downstream side of the spectrometer and to escape towards the source without being detected. This mirror effect will occur also for signal electrons that are emitted in the source with large polar starting angles as described in Section 2.1.1. A similar observation at the Mainz experiment triggered the design of the KATRIN MAC-E filter such that the maximum magnetic field appears downstream from the analyzing plane [Ang05].

The visible effect in Figure 6.9 is smaller than expected for stored electrons with $E_{\mathrm{kin}} > 1\,\mathrm{eV}$. This, together with the earlier observations points to a novel source of background with extremely low-energy electrons with $E_{\mathrm{kin}} < 1\,\mathrm{eV}$. These electrons are not subject to the magnetic mirror effect.

### 6.2.5 Pressure in the Spectrometer

Further information on the energy spectrum and storage conditions of background electrons can be obtained by variation of the absolute pressure in the spectrometer vessel. While the studies of the radon-induced background in Chapter 4 were carried out at an artificially elevated pressure of about $1 \times 10^{-8}\,\mathrm{mbar}$, the pressure in the SDS setup in nominal operation mode is about one to two orders of magnitude smaller. During the SDS-IIA phase, the mean pressure level in the spectrometer continuously dropped over time due to the vacuum system being unbaked and the number of cold baffles being increased over the course of the campaign (see Sec. 3.2). Thus, knowledge of the pressure dependence of the spectrometer background is essential when studying background characteristics.

The level of radon-induced background events is known to increase in case of elevated pressure in the spectrometer. This results from the effect that the cool-down of the primary electron via inelastic scatterings with residual gas molecules dominates then relative to energy losses via emission of synchrotron radiation [Sch13c]. A possible pressure dependence of the remaining non-radon-induced background, however, was investigated for the first time in the SDS-IIA phase.

Table 6.4 lists four data sets that were recorded with similar inner electrode offset potentials and at different pressure levels in the spectrometer vessel. Due to the restricted number of measurements at comparable settings, measurements at different 'symmetric' magnetic field settings are combined in the following analysis. To do so, the rate in the 3.8-G data set T is obtained from the innermost 9 detector rings only, as the flux tube that is observed by these rings has about the same radial extension as the total 5-G flux tube in the other data sets. The resulting rate is then linearly scaled by the differences in observed volumes ($551\,\mathrm{m}^3$ in the 5-G measurements versus $517\,\mathrm{m}^3$ for the 9 rings in the 3.8-G measurement), a procedure justified by the findings in Section 6.2.4. The background rate in data sets R, S, T and U as a function of the pressure is shown in the top part of Figure 6.10 with an empirical $2^{\mathrm{nd}}$-order polynomial fit applied to the data, yielding $R(p) = 0.478\,\mathrm{cps} + 2 \cdot 10^{15} \cdot p^2\,{}^{\mathrm{cps}}/_{\mathrm{mbar}^2}$. However, due to the limited number of data points this fit result is intended for rough interpolation purposes. At pressure levels above $10^{-9}\,\mathrm{mbar}$ the background rate increases while remaining on a rather constant level below. This behavior allows to directly compare data sets recorded at different times and pressure levels if $p < 10^{-9}\,\mathrm{mbar}$ is maintained.

A key question concerning the understanding of the background-generating processes taking place inside the KATRIN main spectrometer is the cause of the increase of background

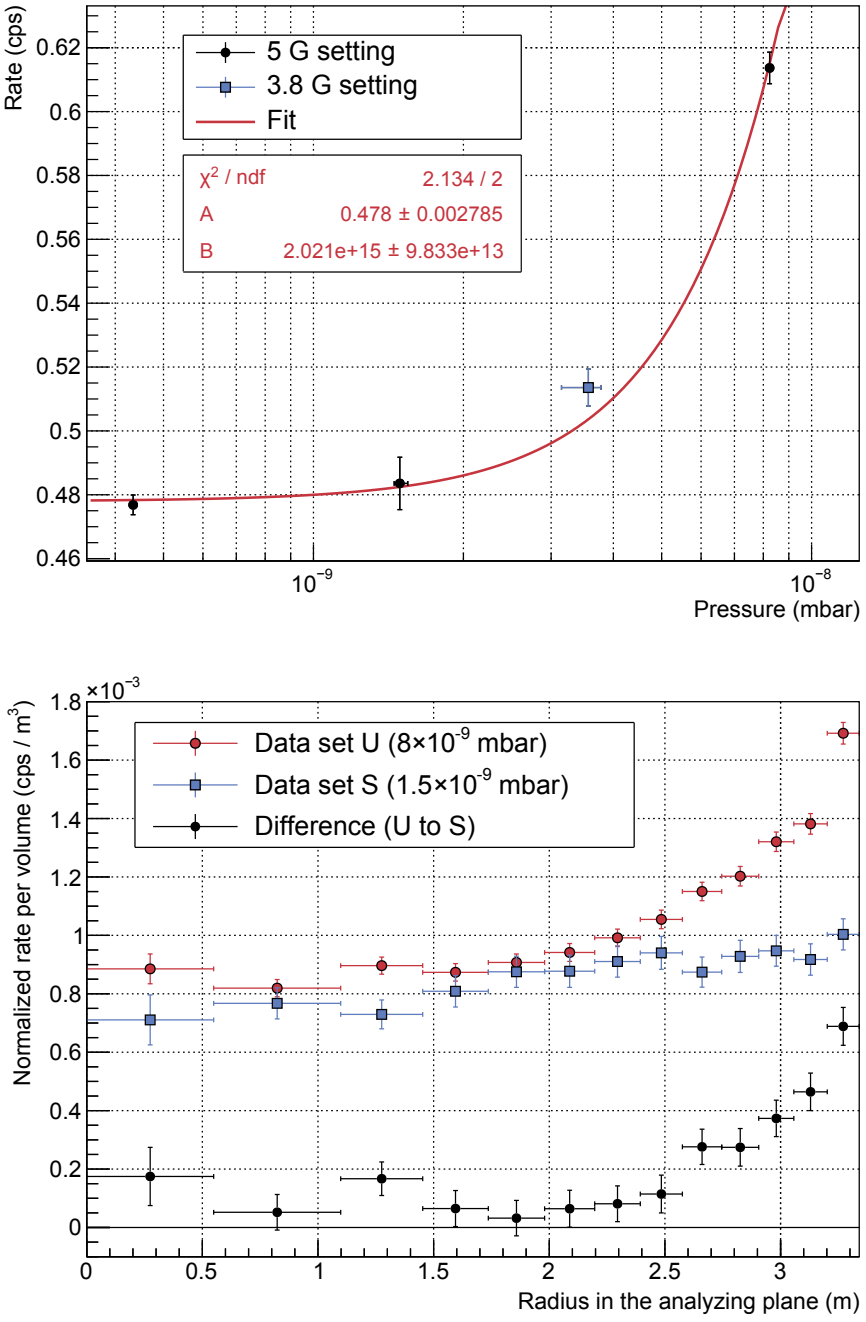


**Figure 6.10: Background levels for various pressure regimes in the spectrometer. Top:** The background rate of the four data sets listed in Table 6.4 is displayed as a function of the corresponding pressures in the spectrometer vessel. A 2$^{\text{nd}}$-order polynomial fit (red line) to the data allows to guide the eye. The result of the renormalized 3.8-G data set T is explicitly highlighted. Details are given in the text. **Bottom:** The radial background distributions in the 5-G data sets U (elevated pressure) and S (medium pressure) are compared. While the rate on the innermost detector channels remains almost constant up to $r = 2.5\,\text{m}$, the background in the outer flux tube regions with $r > 2.5\,\text{m}$ increases when elevating the pressure in the spectrometer.

**Table 6.4: Background measurements at different UHV pressure levels in the spectrometer.** All data sets listed were recorded at similar potential settings ($U_{\mathrm{IE,common}} = -100\,\mathrm{V}$, $U_{\mathrm{SC}} \approx +1\,\mathrm{V}$, $U_{\mathrm{PAE}} = +10\,\mathrm{kV}$) and with at least the baffles 2 and 3 cold. In contrast to the potential settings, the magnetic field settings of the measurements differ (3.8 G and 5 G). The background rates listed correspond to the number of events with energies in the standard ROI that are measured per unit time for 142 operational detector pixels in the 5-G measurements. In the 3.8-G data set T, only the innermost 9 detector rings were used to derive the background rate, which in addition is scaled by the ratio of the observed volumes at 3.8 G and 5 G. The pressures listed are calculated from data of the $N_2$-calibrated Extractor gauge 3110. The uncertainties are given by the maximum deviations of the pressure reading from the mean value over the course of the corresponding measurement.

| Data set | Pressure ($\times 10^{-10}$ mbar) | B-field | Rate (mcps) | Runs |
|---|---|---|---|---|
| R | $4.35^{+0.07}_{-0.06}$ | 5 G | $477 \pm 3$ | #22031 - #22044 |
| S | $14.9^{+0.6}_{-0.4}$ | 5 G | $484 \pm 8$ | #20911 - #20912 |
| T | $36^{+2}_{-4}$ | 3.8 G | $514 \pm 6$ | #22164 - #22168 |
| U | $82.4 \pm 0.1$ | 5 G | $614 \pm 5$ | #22064 - #22070 |

for conditions $p > 10^{-9}$ mbar. To investigate this, the lower part of Figure 6.10 compares the radial background distributions in data set U at elevated and data set S at nominal pressure. The higher absolute background rate at elevated pressure mainly originates from an enhancement of background events in the outer flux tube regions, whereas the contribution on the innermost detector rings appears only slightly increased. This observation points towards a background contribution from electrons that enter the flux tube from the vessel surface. Conventional candidates for these events would be low-energy secondary electrons generated by cosmic muons or environmental radiation. However, as these electrons are confined to small cyclotron radii, they would need to experience a radial drift over their storage time to enter the observed flux tube volume (see Sec. 2.1.2 or Sec. 6.2.2). With an increase of the pressure, however, the probability for these electrons to scatter off residual gas molecules at an early stage of this drift would be increased. Additional background should, thus, appear at the very outer edges of the mapped flux tube. It appears difficult to explain the increased part of the background at elevated pressure which reaches as far as 1 m into the observed flux tube by such low-energy secondaries.

In Section 5.3.3, the background contribution from high-energy electrons from $^{210}$Pb decays was discussed. These keV-scale electrons are stored over short time periods in the outer flux tube regions. In contrast to low-energy secondaries, the L-shell conversion electrons from $^{210}$Pb-decays have much larger cyclotron radii of $\approx 1.2\,\mathrm{m}$ (at a 0.5 mT magnetic field) and can therefore gyrate into the observed flux tube without the need of a fast radial drift. At elevated pressure level in the vessel, the probability of these electrons to generate secondary electrons by inelastic scatterings off residual gas during their short storage time is increased. A comparison of the profile of the pressure dependent background in Figure 6.10 and the radial distribution of the points of creation of secondary electrons that are induced by stored primaries from $^{210}$Pb decays in Figure 5.17, indicates $^{210}$Pb-related electrons to be a likely explanation for the pressure-dependent and radially increasing part of the spectrometer background. At this point however, it should be mentioned that cosmic muons as well as environmental radiation also will generate high-energy electrons in the keV-scale on the spectrometer surfaces, albeit with much smaller probability than low-energy ones [Lei14]. The generation rates of these electrons are expected to be comparable to those of the $^{210}$Pb-induced ones.

It is at this point strongly recommended to perform additional measurements in the future

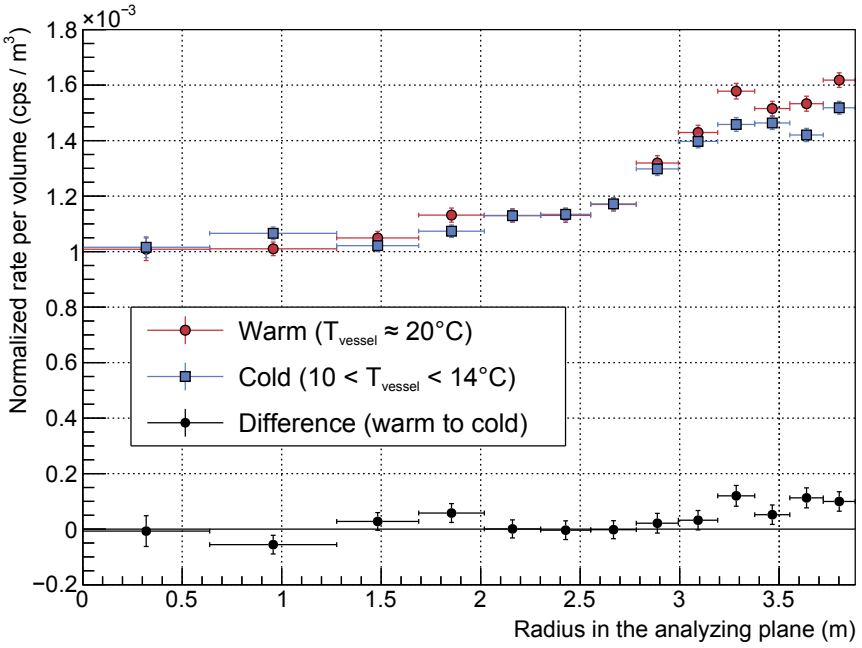


**Figure 6.11: Dependence of the radial background distribution on the vessel temperature.** The radial dependence of the spectrometer background rate in the standard ROI as measured by 142 operational detector channels in runs #23157 - #23168 ($10 < T_{\text{vessel}} < 14\,^{\circ}\text{C}$) is compared to that in the standard background data set N2 ($T_{\text{vessel}} = 20\,^{\circ}\text{C}$). Only in the outermost flux tube regions a reduction in background rate is observed, which can most probably be attributed to a change in the $H_2$ out-gassing rate of the stainless steel and the consequently lower pressure in the spectrometer volume.

to target the pressure dependence of the spectrometer background in the SDS-III phase as the number of usable SDS-II data sets is not large enough to study this important topic with the required degree of accuracy. In this context, a combined scan of the inner-electrode and the pressure dependence of the background would help to identify the origin of the radially increasing part of the background.

### 6.2.6 Temperature of the Spectrometer

In order to investigate a possible background dependence on the temperature of the spectrometer vessel, the 60 kW of cooling power of the *HTT* temperature regulation system (see Sec. 3.2) was used to cool-down the vessel to a temperature of 10 °C during the SDS-IIA phase. Figure 6.11 shows the radial distribution of the background rate during the end phase of the cool-down with $10 < T_{\text{vessel}} < 14\,^{\circ}\text{C}$ (runs #23157 - #23168) compared to the standard background data set N2 ($T_{\text{vessel}} = 20\,^{\circ}\text{C}$). The profiles of the two distributions only feature minor changes in the outer flux tube regions. This in turn could be caused by the reduced absolute pressure in the vessel due to a decreased hydrogen out-gassing from the stainless steel surfaces. A second effect could be due to the better temperature control of the baffles at $T < 14\,^{\circ}\text{C}$, resulting in an increased pumping efficiency of the baffles for $H_2O$ in the spectrometer volume. No direct influence of the spectrometer cool-down on the non-radon-induced background is noticed at this point. A temporary warm-up of the spectrometer during the SDS-IIB phase to about 50 °C will be discussed in [Tro16].

### 6.2.7 Impact of a Spectrometer Vacuum Bake-Out

Between the SDS-IIA and SDS-IIB phases, an extended vacuum bake-out procedure of the main spectrometer was carried out successfully (see Sec. 3.2). This bake-out is being

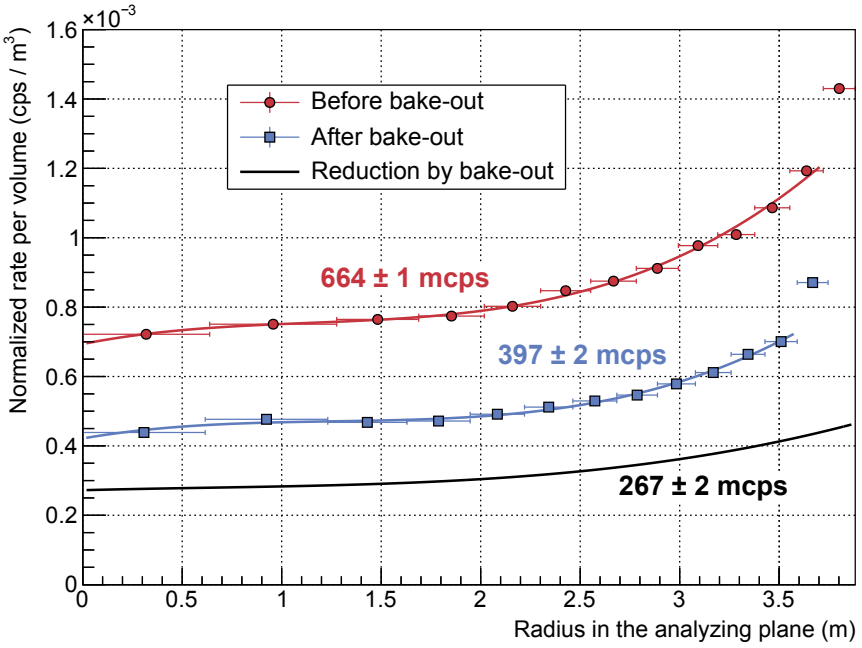


**Figure 6.12: Influence of a vacuum bake-out procedure on the spectrometer background.** The radial background distributions of the SDS-IIA data set N2 (red dots) and the SDS-IIB runs #24627 - #24671 (blue rectangles) are compared. Both data sets were recorded at a 3.8-G magnetic field in the analyzing plane and inner-electrode offset potentials of $U_{\mathrm{IE,common}} = -100\,\mathrm{V}$ and $U_{\mathrm{SC}} = +97\,\mathrm{V}$. The absolute background rates, as measured by 142 operational detector channels, are stated in the plot. Due to the different radial extensions of the flux tube in the two data sets, 3$^{\mathrm{rd}}$-order polynomial fits of the radial distributions are used to obtain the background reduction by the bake out as a function of the radius (black line). Note that the data points of the outermost detector ring are not used for the fits as they feature a significantly increased rate. More details are given in the text.

used to drive off molecules ($H_2O$) that are adsorbed on inner surfaces. Of major interest for a better understanding of background characteristics was, thus, the question if changes in the physical conditions on the surfaces influence the spectrometer background level. In the following this is investigated by comparing SDS-IIA with SDS-IIB measurements.

At the end of the SDS-IIA phase standard pressures in the mid $10^{-10}$-mbar regime were achieved due to the fact that the three cold baffles were acting as additional cryogenic pumps. After the vacuum bake-out procedure, the pressure level dropped to a regime below $1 \times 10^{-10}$ mbar. However, in Section 6.2.5 the spectrometer background was found to be constant already for pressure regimes $p < 10^{-9}$ mbar. Thus, the absolute value of the UHV can be neglected to first order when comparing SDS-IIA and SDS-IIB data sets. In Appendix A, the reduction of the baffle pumping efficiency by an allocation of water on its surfaces is discussed. Due to the reduced desorption rate of $H_2O$ into the volume and better surface conditions of the $LN_2$-cooled copper baffles, an increased radon pumping efficiency is expected for SDS-IIB. However, with baffles 2 and 3 being operated cold, this effect is small as already in SDS-IIA a reduction efficiency of $> 90\%$ was found for that baffle configuration (Chapter 4).

A comparison of the SDS-IIA data set N2 and the SDS-IIB data in runs #24627 - #24671 shows a reduction of the absolute background rate in the standard ROI (142 operational detector channels) from a level of $(664 \pm 1)$ mcps prior to the bake-out to a new reduced value of $(397 \pm 2)$ mcps after the thermal conditioning of the inner spectrometer surfaces. In both measurements the FPD magnets were operated at reduced fields of $B_{\mathrm{PCH}}^{\mathrm{SDS\text{-}IIA}} = 5\,\mathrm{T}$

and $B_{\mathrm{DET}}^{\mathrm{SDS\text{-}IIA}} = 3\,\mathrm{T}$ and the LFCS currents in each case were optimized for a 3.8-G magnetic field in the analyzing plane (see Tables 3.1, C.4, 3.2, and C.5 for details). The inner electrode was also set to similar potentials $U_{\mathrm{IE,common}} = -100\,\mathrm{V}$ and $U_{\mathrm{SC}} = +97\,\mathrm{V}$. Figure 6.12 shows the radial distributions of the background in the two data sets. A background reduction is found which is almost flat for all radii and only slightly increases in the outer regions of the flux tube. The latter effect can only partly be explained by the slightly improved pressure conditions in the spectrometer after the bake-out. The similar shapes of the two radial distributions is a most important finding and strong clue to better understand background processes. For completeness it should be noted that although the flux tube has a smaller extension in the analyzing plane in the SDS-IIB case, the outermost detector ring shows a noticeable increase in rate in both data sets. This effect here is attributed to the fact that the flux tube clearance in the flat-cone parts of the spectrometer is still being similar in the SDS-IIA and SDS-IIB cases.

The finding that the SDS-IIB distribution (blue) shows a similar shape as the SDS-IIA one (red), has the major implication that the background is causally linked to the surface conditioning. Unfortunately, a proper bake-out only partly eliminated this novel background process.

### 6.2.8 Correlation with the Muon Flux

The main spectrometer vessel with its large surface of about $690\,\mathrm{m}^2$ is located above ground and, thus, exposed to a flux of $10^5$ muons passing the stainless steel hull per second [Lei14]. As previously described, these muons can cause the emission of secondary electrons from inner surfaces. Even in case of excellent intrinsic magnetic shielding of a MAC-E filter and electrostatic shielding by the inner electrode system, a significant background contribution from surface-generated secondary electrons from cosmic muons was expected prior to the SDS-II measurement campaign [Sch14c, Lei14]. Therefore, considerable efforts were made to investigate a possible correlation of the electron background level and the flux of cosmic muons in the KATRIN experimental hall. Over the course of the 2014/15 Christmas break, a series of long-term measurements (listed in Table 6.5) was carried out in the context of [Lin15] in which the muon detection system located close to the main spectrometer (Sec. 3.5) recorded the flux of cosmic muons in parallel. In the following the two data sets M and N2 are analyzed in same way as the correlation between the high-energy event rate on the detector and the muon flux in Section 5.3.4. This time, however, the focus lies on the electron background in the standard ROI.

For both data sets M and N2, the correlation factors of the electron background and the muon flux, as given in Table 6.5, are found to be consistent with zero. In contrast to conventional expectations prior to the SDS-II phase, the excellent intrinsic magnetic shielding of the spectrometer together with a careful minimization of stray fields of structural materials, is sufficient to suppress fast radial drifts of low-energy electrons into the inner parts of the flux tube. This observation fits to earlier results in Section 6.2.2, where it was shown that the inner electrode offset potential affects the spectrometer background rate in an unexpected (radially flat) way for $U_{\mathrm{IE,common}} \leq -5\,\mathrm{V}$.

## 6.3 Secondary-Electron Emission from Inner Surfaces

In the last section, the spectrometer background at standard 'symmetric' magnetic field configurations was characterized in detail. In this context it was found that secondary-electron emission from the inner surfaces of the spectrometer does not contribute in a significant manner to the background level. To further investigate secondary-electron emission from inner surfaces, data sets V and W (listed in Table 6.6) that were recorded

**Table 6.5: Measurements targeting a background correlation with the flux of cosmic-muons.** The rate trend of the electron background in the 3.8-G data sets M and N2, measured by 148 detector channels over the course of the 2014/15 Christmas break, is compared to the observed muon flux in runs #4621 - #4751 of the muon detection system. The correlation between the deviations in the muon rate $^{R_\mu(t)}/_{\bar{R}_\mu}$ and the electron rate in the standard ROI $^{R_\mathrm{e}(t)}/_{\bar{R}_\mathrm{e}}$ with time is given by the Pearson product-moment correlation factor [Pea95], while the corresponding uncertainties are calculated via a bootstrap-method in which the data points ($^{R_\mu(t)}/_{\bar{R}_\mu}$, $^{R_\mathrm{e}(t)}/_{\bar{R}_\mathrm{e}}$) are re-sampled $10^5$ times with replacement [Efr79].

| Data set | $U_{\mathrm{IE,common}}$ (V) | Correlation factor | Runs |
|---|---|---|---|
| M | $-5$ | $0.07 \pm 0.10$ | #21427 + $i \cdot 3$ ending with #21748 (excluding run #21670) |
| N2 | $-100$ | $0.13 \pm 0.08$ | #21428 + $i \cdot 3$ ending with #21749 (excluding run #21521) |

**Table 6.6: Measurements at 'asymmetric' magnetic field setting A2.** The magnetic-field lines in the spectrometer for setting A2 are shown in Figure 6.13. Due to their different mapping characteristics, the innermost two detector rings are excluded from all analyses that involve data sets V and W. In data set V, the inner electrode system was short-circuited to the vessel hull.

| Data set | $U_{\mathrm{IE,common}}$ (V) | Rate (cps) | Runs |
|---|---|---|---|
| V | 0 | $790.2 \pm 0.3$ | #21831 + $i \cdot 4$ ending with #21899 |
| W | $-5$ | $247.44 \pm 0.04$ | #21426 + $i \cdot 3$ ending with #21747 (excluding runs #21453 and #21669) |

at the 'asymmetric' magnetic field configuration A2 during SDS-IIA, are analyzed in the following.

Figure 6.13 shows the magnetic field lines in the spectrometer for setting A2. This setting was optimized in [Lin15] to obtain an image of the central part of the spectrometer surface which maps equally sized areas onto individual detector rings. Due to the fact that the PS1 and PS2 magnets were operated at their standard magnetic field, the innermost two detector rings do not fulfill this condition and, thus, are excluded from this analysis. Accordingly, a total surface area of about $250\,\mathrm{m}^2$ is mapped onto the remaining 11 detector rings.

In data set V, a total event rate of $(790.2 \pm 0.3)\,\mathrm{cps}$ is observed from a surface area of about $250\,\mathrm{m}^2$. Figure 6.14 shows the corresponding event distribution on the detector. Surprisingly, the rate of secondary electrons shows a clear azimuthal dependence with a minimum in the lower part of the detector wafer. While a radial dependence could be explained by variations in the surface area mapped onto individual detector rings, a rather strong azimuthal dependence cannot result from geometrical effects, but must originate from azimuthal effects related to the source of secondary electrons on the surface. Cosmic muons as the main source of the secondary electrons can only partly explain these specific observations. Muons as minimum-ionizing particles are not attenuated, thus, causing identical levels of electron emission when entering the vessel (from above) as when

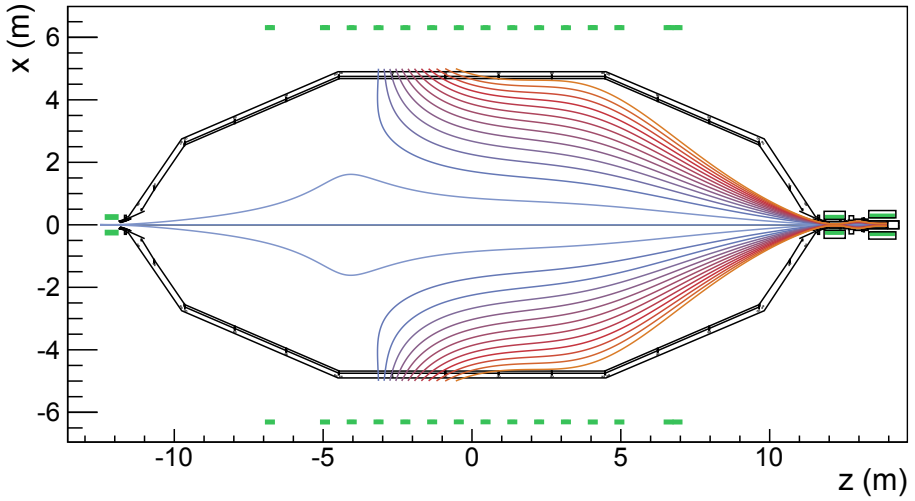


**Figure 6.13: Magnetic field lines in the spectrometer for setting A2** listed in Table 3.1. The flip-box devices on some of the LFCS coils are used to flip the current polarity. In this way, all detector rings (except the bullseye) 'look' onto the inner surface of the main spectrometer. In difference the other detector rings, the second innermost ring sees a significantly larger surface area and is therefore, together with the bullseye, excluded from the analysis of data sets recorded at setting A2. A surface area of about $250\,\mathrm{m}^2$ is mapped onto the remaining 11 detector rings.

leaving the vessel (towards the bottom). A small top-bottom asymmetry for muons can be expected, however, due to the fact that the bottom half of the spectrometer is below ground level, so that low-energy muons pointing to this part of the spectrometer could be shielded by the soil.

Another potential source of secondary electrons is environmental radiation. When the KATRIN experimental hall was built, special low-activity concrete was used for the base plate, while the walls of the building are made of standard concrete with an about a factor of 7-9 higher activity [Dre15b]. Thus, building-material related environmental radiation as the cause of the non-uniformity of the secondary electron emission on the surface is easily conceivable.

A third explanation is related to the $^{210}$Pb signal discussed earlier. At the end of the installation phase of the inner-electrode system, the bottom part of the spectrometer was extensively cleaned to remove possible contaminations from the mechanical works in the vessel. Thus, a reduced contribution from intrinsic radiation in terms of $^{210}$Pb and its progenies on the bottom of the spectrometer could also be thought of as reason for the observed non-uniformities of the secondary electron emission rate. However, as discussed in Chapter 5, the $^{210}$Pb signal likely originates not from the vessel surface itself, but from the inner electrode system, which did not undergo cleaning after its installation.

When comparing the detector event pattern in Figure 6.14 to the event pattern of the standard cold-baffle background at 'symmetric' magnetic fields (Fig. 6.2), the azimuthal dependence on the outer detector rings appears similar. This again points towards electrons emitted from inner surfaces as cause of the main part of the radially increasing background contribution.

Recent measurements with a partial water-shielding of the bottom panel of the KATRIN experimental hall were targeting the question of secondary electron emission by environmental radiation. The data is currently being analyzed in the context of [Mue16, Tro16]

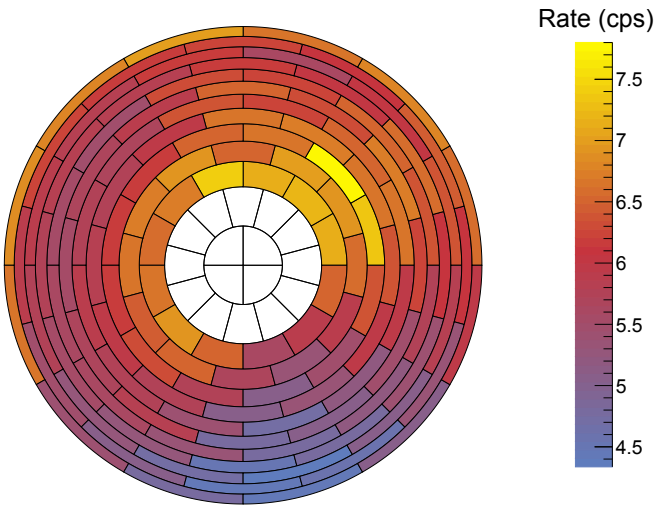


**Figure 6.14: Detector distribution of secondary electrons emitted from the spectrometer surface.** The innermost two detector rings are excluded from the analysis of data set V. A non-uniformity of the rate of emitted secondary electrons with a minimum in the lower part of the wafer can clearly be seen.

and does not corroborate the hypothesis of non-uniform environmental radiation of structural materials being the major source of the secondary electrons.

### Impact of the Magnetic-Mirror Effect

Up to this point an important aspect in measurements at 'asymmetric' magnetic field settings has not yet been discussed. Electrons that are emitted from the surface in a weak magnetic field of $B_{\mathrm{min}} \approx 2.7\,\mathrm{G}$ (setting A2) have to pass through the 5-T pinch-magnet field when being mapped onto the detector. A large fraction of the electrons will therefore be reflected by the magnetic mirror effect (see Sec. 2.1.1), so that the actually detected number of electrons by the detector will be significantly smaller than the number of emitted ones. In the context of the SDS-I measurements, KASSIOPEIA tracking simulations were performed in [Lei14] to deduce the detector-arrival probability of low-energy electrons emitted in an 'asymmetric' magnetic field setting with $B_{\mathrm{min}} = 4.2\,\mathrm{G}$ from the surface of the spectrometer. Assuming the starting angles of the electrons to be cosine-distributed, an arrival probability of the electrons of 6.28% was found. Due to the smaller $B_{\mathrm{min}}$ in the SDS-II case, this value can be used as an upper limit, so that the total detected event rate in data set V corresponds to an overall secondary-electron emission rate of about $R_{\mathrm{em}}(250\,\mathrm{m}^2) \gtrsim 12\,600\,\mathrm{cps}$. If the non-uniformity of the secondary-electron induced detector event pattern in Figure 6.14 is ignored, this rate can be scaled to the full inner surface of the vessel of $690\,\mathrm{m}^2$, resulting in a total electron emission rate of about $R_{\mathrm{em}}(690\,\mathrm{m}^2) \gtrsim 34\,700\,\mathrm{cps}$ from the surface of the spectrometer.

### Correlation with the Flux of Cosmic Muons

In contrast to data set V discussed above, the $U_{\mathrm{IE,common}} = -5$-V data set W was recorded in an alternating way together with data sets M and N2 over the 2014/15 Christmas break (compare run numbers in Tab. 6.1 and 6.6) and can therefore be used to investigate a correlation of the observed emission rate of secondary electrons from the spectrometer walls with the flux of cosmic muons. In this configuration the excellent magnetic shielding no longer holds, so that only a moderate electrostatic shielding by $U_{\mathrm{IE,common}} = -5\,\mathrm{V}$ remains. Accordingly, the correlation between the muon flux and the electron rate significantly increases to $0.66 \pm 0.06$ compared to the data sets M and N2. The top part of Figure 6.15

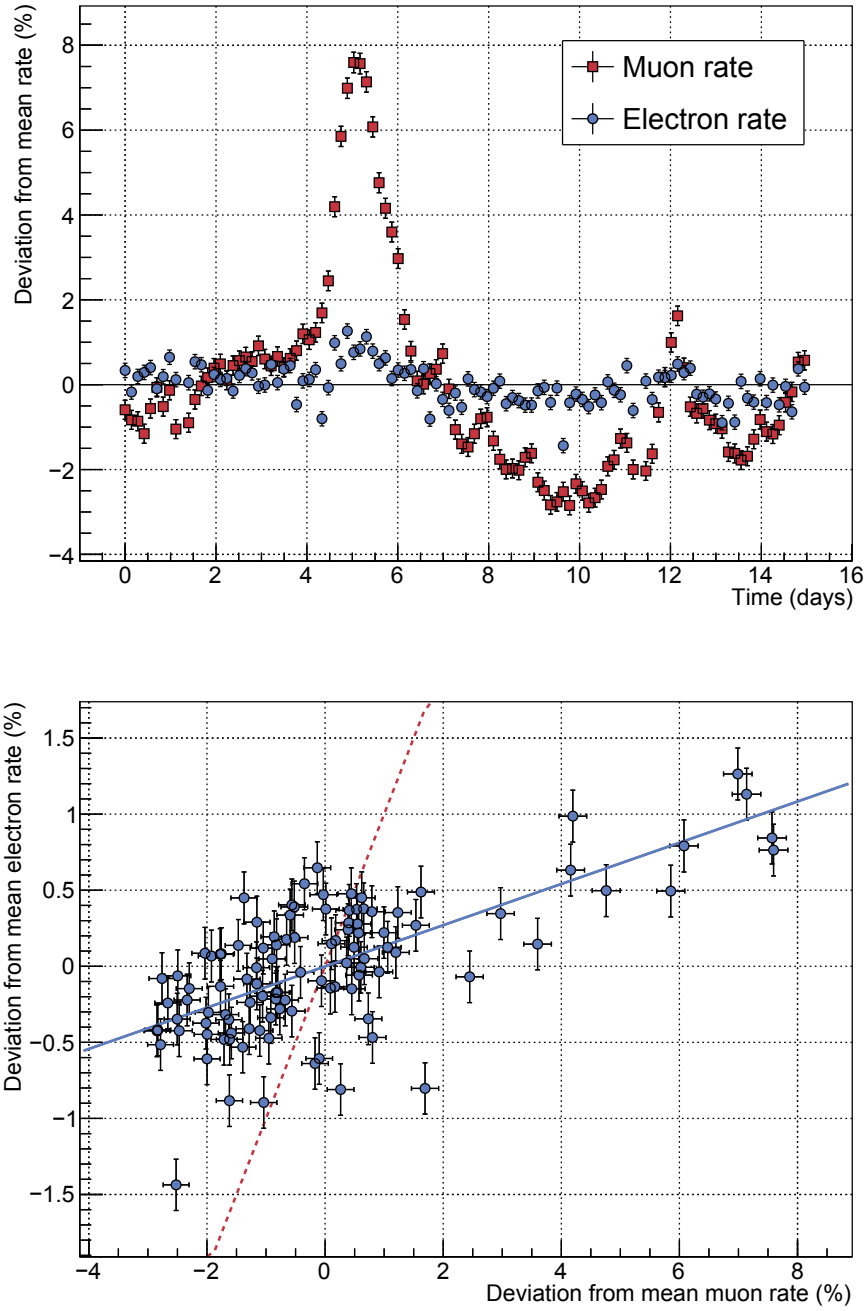


**Figure 6.15: Correlation between the muon flux and the background in the standard ROI at 'asymmetric' magnetic fields. Top:** The relative deviations of the electron and the muon rate over the course of 15 days are shown. The correlation between the two can clearly be seen around day 5 where a low pressure area that passed KIT Campus North caused the muon rate to temporarily increase by about 8%. **Bottom:** The relative deviations of the muon flux and the rate of secondary electrons from the inner spectrometer surface are shown in a scatter-plot representation. A fit according to Equation 5.8 is applied to the data points (blue solid line) and gives a ratio of $a = (13.6 \pm 0.8)\%$ of the secondary electrons being muon induced. The expected slope for 100% muon-induced secondaries is shown as dashed red line.

shows the relative deviations of the muon rate $R_\mu(t)/\bar{R}_\mu$ and the electron rate $R_\mathrm{e}(t)/\bar{R}_\mathrm{e}$ over the course of 15 days. The rate of secondary electrons from the walls follows the trend of the cosmic muon flux, similar to the case of high-energy events in the FPD discussed in Section 5.3.4. In order to derive the contribution of muon-induced electrons to the total secondary-electron rate, an analysis according to Equation 5.8 is carried out. The corresponding scatter plot of the deviations from the mean muon rate $R_\mu(t)/\bar{R}_\mu$ and the mean electron rate $R_\mathrm{e}(t)/\bar{R}_\mathrm{e}$ is shown in the lower part of Figure 6.15. A linear fit of the data points gives a muon-induced fraction of the background of

$$a = (13.6 \pm 0.8)\% \quad . \tag{6.3}$$

This result is intriguing as it in turn implies that a large fraction of about 86% of all electrons that are emitted from the inner surface of the spectrometer (and are neither electrostatically repelled by the −5-V shielding potential or reflected by the magnetic mirror effect) are not muon induced. These electrons must therefore originate from other processes. Surprisingly, this majority of events shows a similar top-bottom asymmetry, as expected from cosmic muons. The impact of the above described magnetic-mirror effect on the ratio of muon-induced to non-muon-induced secondary electrons is difficult to estimate. Assuming identical hemispherical electron emission from the surface in both cases, the magnetic-mirror effect will not influence the result given in Equation 6.3.

**Impact of an Electrostatic shielding**

When comparing the total event rates measured in data sets V and W given in Table 6.6, even a small electrostatic shielding potential of $U_\mathrm{IE,common} = -5\,\mathrm{V}$ already results in a reduction of the observed rate of secondary electrons from the spectrometer walls by about 70%. This implies that surface-generated electrons are characterized by eV-scale energies, as outlined in [Lei14].

In Appendix B of this thesis, secondary electron emission from the inner surfaces of the spectrometer is further investigated in terms of the apparent time-correlations of events registered by the detector. In this context it is shown that muon-induced secondary electrons appear mostly uncorrelated in time, while the remaining part of the secondary electrons shows strong time-correlations that persist even at $U_\mathrm{IE,common} = -5\,\mathrm{V}$. The latter effect and the fact that the correlations are not eliminated by the magnetic mirror effect indicates quite distinct background characteristics, pointing to electrons being emitted with rather high energies of $E > 5\,\mathrm{eV}$ and quite similar starting angles from the surface.

## 6.4 Discussion of Possible Background Sources

Up to this point, the main spectrometer background has been characterized in detail by using specific measurement configurations such as an elevated pressure (Chapter 4) or zero potential (Chapter 5). This has allowed to identify background contributions induced by radioactive decays. Also, the background dependence on other key operating parameters of the SDS apparatus was studied (Sec. 6.2). Furthermore, potential sources of secondary-electron emission from the inner surfaces of the spectrometer have been evaluated (Sec. 6.3). Based on these studies, possible sources of the remaining spectrometer background in the normal operating mode of the SDS apparatus (cold baffles, high voltage, 'symmetric' magnetic fields) will be discussed in the following.

**Stored Electrons in the Volume**

In Chapter 4, the background contribution from stored high-energy electrons emitted in radon $\alpha$-decays in the spectrometer volume was discussed in great detail. As radon decays are homogeneously distributed in the observed flux tube, this constant background level

per unit volume of radon decays could explain the specific volume dependence of the remaining background that is discussed in Section 6.2.4. However, measurements at an elevated spectrometer pressure that were carried-out in the context of this work clearly showed that all time-correlated multi-hit signatures of such stored particles disappear to a small (almost negligible) level when the SDS setup is operated in its standard cold-baffle mode. High-energy electrons from radon decays that are stored in the spectrometer volume can therefore be excluded as main source of the remaining spectrometer background.

During the SDS-IIA phase, measurements with static and pulsed electric-dipole fields showed no significant reduction of the background level for all cold-baffle configurations [Hil15a, Hil15b]. In [Wan13a], however, it was shown on the basis of MC-tracking simulations that such dipole fields should efficiently remove stored low-energy electrons from the observed flux tube volume by an $\vec{E}\times\vec{B}$ drift. The non-observation of this effect in all dipole measurements suggests that the spectrometer background is not due to electrons which are stored. Instead, these results suggest that the background electrons directly leave the spectrometer towards the detector after their creation. An electron that is emitted in the analyzing plane (3.8 G) must (according to Equation 4.1) have a transverse energy of $E_\perp < 1.6\,\mathrm{eV}$ so that it is not stored between the 5-T pinch and the 4.5-T PS2 magnet. This requirement most strongly restricts the energy of background electrons produced in the volume of the spectrometer.

Apart from magnetic storage of electrons, earlier measurements at the KATRIN pre-spectrometer have shown that even small-scale Penning traps can cause severe backgrounds in a MAC-E filter (see Section 2.1.2). However, based on the experience gained during the pre-spectrometer measurements particular care was exercised to prevent Penning traps in the design of the inner electrode system [FGV14]. An indication of a direct background contribution due to Penning traps, materializing as a time dependent, localized, potential-dependent, and in particular pressure dependent increase of the background level could neither be found in SDS-I nor in SDS-IIA.

**Secondary Electrons Emitted from Inner Surfaces**

The conventional background scenario for MAC-E filters was based on secondary electrons emitted from inner surfaces of the spectrometer with rather low energies of several eV. They were assumed to result from various processes such as ionizations of the stainless steel bulk of the vessel by cosmic muons, environmental radiation penetrating the spectrometer hull, or field electron emission. The noticeable reduction that even moderate electrostatic shielding potentials of the inner electrode achieved for the total background rate in SDS-I measurements seemed to support this hypothesis [Bar14, Lei14, Sch14c]. In the SDS-II measurements performed in the context of this thesis, however, the full spatial resolution of the detector together with the elimination of radon allowed to much better investigate the effect of electrostatic shielding. A key element therein were the radial distributions of the background.

As discussed in Section 6.2.2 the inner electrode shielding potential is found to reduce the spectrometer background independently of the radial position of the background event. This new and surprising observation cannot be reconciled with a scenario of low-energy electrons being emitted from the vessel surface. According to [Lei14], the latter would have to drift towards the center axis of the spectrometer with unrealistic fast radial drift velocities to reproduce the radial distributions discussed earlier (see Fig. 2.3). For reasonable assumptions on the radial drift velocities, surface-generated electrons would preferably generate background in the outer flux tube regions rather than in the center of the spectrometer. Even under the (unrealistic) assumption of their storage times being larger than the time needed to drift all the way to the center of the flux tube, tertiary electrons from

ionizations of residual gas should not appear radially independent on the detector. In addition, an increase of the spectrometer pressure in this case should reduce the background in the center of the flux tube as the storage times of the electrons would be decreased while the radial drift times would remain the same. This effect is not observed in the SDS-IIA measurements where the background level in the center of the flux tube is found to be more or less pressure independent (see Fig. 6.10).

Apart from low-energy secondaries, also high-energy electrons with several keV of energy are expected to be generated by cosmic muons or environmental radiation [Lei14]. Furthermore, a previously unknown source of keV-electrons from $^{210}$Pb $\beta$-decays on the spectrometer surface was found in SDS-IIA measurements that were carried out in the context of this thesis. In Chapter 5 the activity of this radiation source on the whole inner spectrometer surface was estimated to be $< 1\,\mathrm{kBq}$. MC-storage simulations confirm that keV-scale electrons preferably ionize residual gas in the outer flux tube regions determined by the gyration radius in the analyzing plane (see Fig. 5.17). A similar effect is expected for high-energy electrons from cosmic muons and environmental radiation. This fits to the observed pressure dependence of the spectrometer background in the outer flux tube regions only, as discussed in Section 6.2.5.

A possible background contribution by field electron emission at this point has not been considered as the inner electrode potential only caused a decrease of background rate in SDS-IIA rather than an increase as happened earlier. The latter effect was observed in the context of SDS-I measurements for high electric shielding potentials of $U_{\mathrm{IE,common}} < -200\,\mathrm{V}$ as reported in [Sch14c].

In conclusion it can be stated that secondary electrons emitted from the inner surfaces of the spectrometer can be excluded as dominant source of remaining background events for configurations with cold baffles. Only in the outer parts of the observed flux tube, where the spectrometer background shows a pressure dependence as well as a slightly increased reduction efficiency of the inner electrodes (see Fig. 6.4), these secondary electrons contribute noticeably to the background. Due to the rather small influence of the electrostatic shielding compared to the effect of a pressure increase, this background contribution here is attributed to high-energy secondary electrons from muons (sub-dominant) and electrons from $^{210}$Pb $\beta$-decays (dominant). In order to make conclusive statements on the different contributions, however, further measurements targeting the pressure dependence and the electrostatic (or magnetic) shielding at the same time must be performed in SDS-III.

### 6.4.1 The Deexcitation of Hydrogen Rydberg States as Source of Background

As the conventional scenarios of surface-related electron background processes fail to explain key characteristics of the non-radon-induced background, it is mandatory to look out for completely novel sources of background. A successful scenario has to generate low-energy electrons ($E < 1.5\,\mathrm{eV}$), which are homogeneously distributed over the entire spectrometer volume to explain the volume dependence of the background (Sec. 6.2.4). Furthermore, a background hypothesis has to depend on the conditions on the inner surfaces of the spectrometer, in particular due to the observation that a proper vacuum bake-out of the spectrometer reduces the background level by about 40% (Sec. 6.2.7). From the experience with the radon-induced background it is known that neutral, excited unstable particles are some kind of the "Achilles heel of MAC-E filters" [Dre15b]. These particles can propagate freely in the spectrometer volume without being affected by the highly efficient magnetic shielding of the MAC-E filter. The impact that the vacuum bake-out procedure between SDS-IIA and SDS-IIB had on the background level could potentially

be explained by a reduction of the number density of adsorbed neutral particles on the inner surfaces.

**The Auto-ionization of Excited Hydrogen Molecules**

Due to the findings in the course of this thesis, a scenario based on excited hydrogen molecules that emit low-energy electrons via an auto-ionization in the spectrometer volume as source of the background was proposed in [Dre15a]. As atomic hydrogen is present in large quantities on the inner surfaces of the spectrometer, desorption processes from the stainless-steel surface will generate a large number of $H_2$ molecules. A small number of these molecules will be desorbed in an excited electron level, thus entering the flux tube volume undisturbed. This scenario requires the subsequent auto-ionization of the molecule to produce electrons in the meV-range. These would fit well with the previously described findings in the dipole measurements.

The radiative lifetime of excited hydrogen molecules is usually rather small ($\ll 1\,\mathrm{ms}$) [Dre15a] and only one specific molecular level (the $c^3\pi_u^2 p\pi$ state) is known to be meta-stable. To auto-ionize, this state would however have to absorb a photon of 3.66 eV energy, which is highly unlikely. Thus, with travel times through the spectrometer volume in the ms-regime it is not possible to explain a homogeneous generation of background electrons by auto-ionization of highly excited $H_2$ molecules. From now on, the discussion will therefore no longer focus on this first scenario, but on a revised model [Dre15a] that involves exited hydrogen Rydberg atoms, which do not ionize spontaneously but under an external radiation field.

**Interactions of Rydberg Atoms with Black-Body Radiation**

Rydberg atoms are highly-excited states close to the ionization threshold that feature a long radiative lifetime in the ms-regime $\propto n^3$ (see [Gal88]), so that they can propagate freely after desorption. Due to the large dipole moments of the transitions between their high $n$-states, Rydberg atoms are extremely sensitive to electromagnetic fields. This also includes the field of the black-body radiation (BBR) [Bet09]. The interaction of the BBR with a Rydberg state can be classified into three different processes: a) stimulated photon-emission due to an induced transition to a lower-lying $n$-state (decay), b) stimulated transition to a higher-lying $n$-state (excitation) after absorption of a BBR photon, and c) the ionization of the Rydberg atom [Glu10]. In the latter case, the electrically neutral atom is split into an $H^+$ ion and a free electron with meV-energy [Gal94]. Due to the rather small ionization rate $R_{\mathrm{np}}^{\mathrm{ion}} < 1\,500\,1/\mathrm{s}$, the probability for ionization of a propagating $H^*$ Rydberg atom is constant per unit time. Electrons from BBR-induced ionizations will therefore appear as homogeneously distributed background-events on the detector. Figure 6.16 shows the interaction rates of hydrogen Rydberg states with the BBR field at room temperature ($T = 300\,\mathrm{K}$) in more detail for the three above described processes.

The temperature dependence of the BBR-induced ionization rate $R(T, n_{\mathrm{eff}}, \ell)$ of a hydrogen Rydberg state can, according to [Leh83], be approximated by

$$R(T, n_{\mathrm{eff}}, \ell) = 5\,400 \cdot \frac{T}{n_{\mathrm{eff}}^2} \cdot \exp\left(-\frac{157\,890}{n_{\mathrm{eff}}^2 \cdot T}\right) \cdot \mathcal{I}(T, n_{\mathrm{eff}}, \ell)\,1/\mathrm{s} \quad , \tag{6.4}$$

where $n_{\mathrm{eff}} = n + \mu_{\mathrm{L}}$ takes into account the quantum defect $\mu_L$ of Rydberg states, $T$ gives the temperature in Kelvin, and $\mathcal{I}(T, n_{\mathrm{eff}}, \ell)$ is a function that only slowly varies with $T$. In Section 6.2.6 the dependence of the spectrometer background on the vessel temperature was investigated on the basis of two background measurements at $T_{\mathrm{vessel}}^{\mathrm{warm}} \approx 293\,\mathrm{K}$ and $T_{\mathrm{vessel}}^{\mathrm{cold}} \approx 283\,\mathrm{K}$. Under the assumption $\mathcal{I}(T, n_{\mathrm{eff}}, \ell) \approx \mathcal{I}(n_{\mathrm{eff}}, \ell)$, the expected reduction factor $\beta(n_{\mathrm{eff}})$ of the BBR-induced ionization rate $R(T)$ for a temperature decrease from

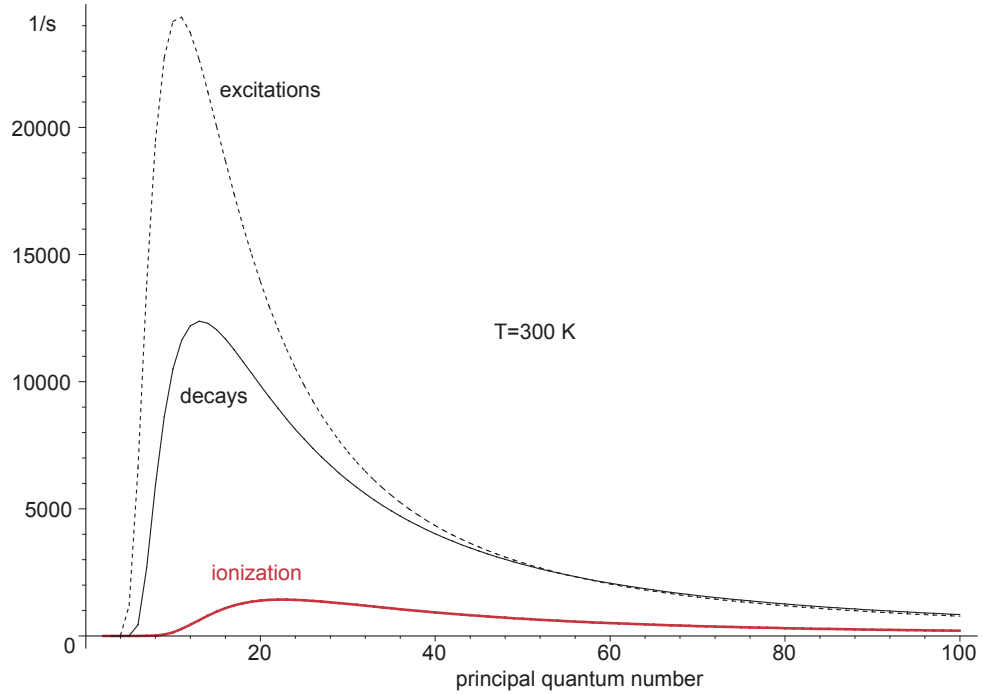


**Figure 6.16: Interaction rates of photons from black-body radiation (BBR) with hydrogen Rydberg states.** The figure is adapted from [Glu10] where the BBR-induced decay (thin solid line), excitation (thin dashed line), and ionization (thick red solid line) rates for the p-orbitals of a hydrogen Rydberg atom at room-temperature ($T = 300\,\mathrm{K}$) are calculated on the basis of numerical data. For the ionization process, the interaction rates are found to be $R^{\mathrm{ion}}_{n\mathrm{P}} < 1\,500\,{}^{1}\!/_{\mathrm{s}}$. This value corresponds to typical ionization time scales of $\tau > 0.7\,\mathrm{ms}$, or typical flight paths of an 1-eV Rydberg atom of $d > 9.7\,\mathrm{m}$ before being ionized by the BBR field.

$T^{\mathrm{warm}}_{\mathrm{vessel}}$ to $T^{\mathrm{cold}}_{\mathrm{vessel}}$ can be approximated to

$$\beta(n_{\mathrm{eff}}) \approx \frac{T^{\mathrm{cold}}_{\mathrm{vessel}}}{T^{\mathrm{warm}}_{\mathrm{vessel}}} \cdot \exp\left[-\frac{157\,890}{n^2_{\mathrm{eff}}} \cdot \left(\frac{1}{T^{\mathrm{cold}}_{\mathrm{vessel}}} - \frac{1}{T^{\mathrm{warm}}_{\mathrm{vessel}}}\right)\right] - 1 \tag{6.5}$$

$$\beta(n_{\mathrm{eff}}) \approx 1.035 \cdot \exp\left[-\frac{19.04}{n^2_{\mathrm{eff}}}\right] - 1 \quad . \tag{6.6}$$

For the highly excited Rydberg states with $n_{\mathrm{eff}} > 30$ that have flight paths long enough to be ionized in the observed flux tube volume, a reduction of the BBR-induced ionization rate of $\beta \leq 5\%$ is expected. In Section 6.2.6, the cool-down of the spectrometer vessel was found to result in a decrease of the total background level by about 3% which fits to the expectations for the background being caused by a BBR-induced ionization of hydrogen Rydberg atoms. However, as the pressure in the spectrometer volume also slightly fell during the cool-down, the decrease in background rate could likewise be attributed to the pressure dependence of the background (see Sec. 6.2.5).

**Selective-Field Ionization of Rydberg Atoms:**

Apart from their important interaction with the electromagnetic field of the BBR, Rydberg atoms will also interact with all electric fields present in the spectrometer volume. While the electric-field strength is small in the central region of the spectrometer (so that the ionization by BBR will be the dominant process), both the entrance and exit sides of the spectrometer, as well as the regions between the inner electrode system and the vessel surface feature high electric fields.

Here, only the impact of the electric field generated by the inner electrode offset potential

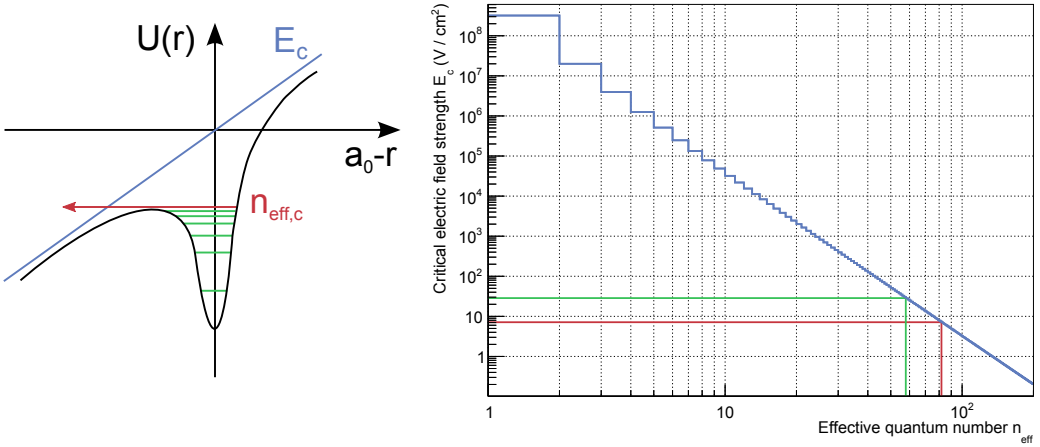


**Figure 6.17: State-selective field ionization of hydrogen Rydberg atoms. Left:** Illustration of the selective field ionization of a Rydberg atom. The presence of a critical electric field $E_\mathrm{c}$ disturbs the Coulomb potential of a Rydberg atom such that all states with principle quantum numbers $n_\mathrm{eff} \geq n_\mathrm{eff,c}$ are ionized. Illustration inspired by [Bet09]. **Right:** Calculated critical electric-field strengths $E_\mathrm{c}$ for effective principle quantum numbers up to $n_\mathrm{eff} = 200$ according to Equation 6.7. The corresponding $n_{eff,c}$-level for an inner electrode offset potential of $U_\mathrm{IE,common} = -100\,\mathrm{V}$ ($U_\mathrm{IE,common} = -400\,\mathrm{V}$) is indicated by a red (green) line.

will be discussed in terms of the so-called selective field ionization (SFI) of Rydberg states. The left side of Figure 6.17 illustrates the principle of this process: With the presence of an electric field $E_\mathrm{c}$, the Coulomb potential of the hydrogen atom is distorted such that all exited Rydberg states above a critical principle quantum number $n_\mathrm{c}$ are ionized. The critical electric-field strength $E_\mathrm{c}$ for state $n = n_\mathrm{c}$ to be ionized is according to [Bet09] given by

$$E_\mathrm{c} \approx n_\mathrm{eff,c}^{-4} \cdot 3.2 \times 10^8 \,\frac{\mathrm{V}}{\mathrm{cm}} \quad . \tag{6.7}$$

The principle of the SFI of Rydberg atoms allows to explain the radially independent background-reduction effect of various inner electrode offset potentials that was discussed in Section 6.2.2. When emitted from the inner surface of the spectrometer, hydrogen Rydberg atoms first have to pass the area between the vessel surface and the 14-cm distant outer wire layer of the inner electrode. For a moderate wire electrode offset potential of $U_\mathrm{IE,common} = -100\,\mathrm{V}$, the corresponding electric field in this region is $\mathcal{E} \approx 7\,\mathrm{V/cm}$, which is sufficient to ionize all exited Rydberg states with $n_\mathrm{eff} \geq n_\mathrm{eff,c} = 82$. Thus, the highly-excited fraction of Rydberg atoms is already ionized close to its point of creation, i.e. far outside the observed flux tube volume, so that these states can no longer contribute to the spectrometer background. This rather straightforward explanation for the unexpected, radially independent background-reduction effect by the inner electrode offset potential represents probably the strongest argument for the 'Rydberg scenario'.

At this point it should be noted that the BBR-induced ionizations of Rydberg atoms in the spectrometer volume not necessarily have to occur homogeneously distributed. Depending on the initial $n$- and $\ell$-distribution of Rydberg atoms being created on the spectrometer surface, they can undergo a fast spontaneous decay, well before an induced ionization would occur. Thus, an interplay of the effects of spontaneous decay, BBR-induced excitation, deexcitation and ionization, as well as the SFI process relevant for high $n$-states modify the generic constant ionization probability per unit volume. Thus, the generation of low-energy background electrons can be modified to occur inhomogeneously in the volume

and therefore to show a radial dependence. At present, efforts are made in the context of [Tro15a, Mer15, Tro16] to establish a realistic model for the initial distribution of $n$- and $\ell$-states that reproduces the experimental radial background dependencies given in Figure 6.12. At the same time this model needs to reproduce the observed dependence of the absolute background rate on the inner electrode potential given in Figure 6.5.

While the Rydberg model provides a straightforward explanation for the inner-electrode dependence, at the point of writing this thesis, the experimentally observed dependence on the vessel potential cannot yet be brought into accordance with the model of deexciting hydrogen Rydberg states.

As the hydrogen Rydberg model can naturally explain all observed effects (scalability with the observed volume, impact of inner electrode offsets, pressure-independence of the background rate, inefficiency of electric dipole fields, absence of magnetic-mirror effects of the pinch magnet when increasing $B_{PCH}$ from 5 T to 6 T, a.s.o.) it is very important to identify the mechanism which results in the desorption of a large number of excited hydrogen atoms per unit time. There are at least three different processes which can potentially cause the desorption of hydrogen Rydberg atoms from inner surfaces of the spectrometer.

### 6.4.2 Possible Generation Mechanisms of Hydrogen Rydberg States

The surfaces of the spectrometer provide a large reservoir of molecular and atomic hydrogen by out-gassing from the bulk stainless steel. Accordingly, several processes are conceivable that can cause an excitation and emission of atomic hydrogen from the surface.

- **Electron-stimulated desorption (ESD):** The impact of electrons with energies of $E > 20\,\text{eV}$ on $H_2$ adsorbed on a stainless steel surface can, according to [Sch75, Sch79, Jan03], cause the emission of hydrogen Rydberg states $H^*$ with a broad range of possible n-states in a dissociative reaction

$$H_2 + e^- \;\rightarrow\; H + H^* + e^- \quad . \tag{6.8}$$

  While $H_2$ is present in large quantities on the surface of the spectrometer, a sufficiently large number of electrons with energies of $E > 20\,\text{eV}$ impacting the spectrometer surface is difficult to sustain. Although the magnetic shielding of the MAC-E filter causes a constant impact of repelled electrons on the surface, their energy is typically below the 20-eV threshold (cosmic-muon or environmental-radiation induced low-energy electrons). For larger electron energies their number is too small to achieve the required number of dissociations (high-energy electrons from cosmic muons, environmental radiation, or from $^{210}$Pb decays).

- **Photon-stimulated desorption (PSD):** In accelerator physics, the impact of synchrotron radiation in the keV-energy regime onto the metal surface of the beam tube is known to cause the effect of PSD: strongly-bound molecules on the surface can be exited by secondary electrons from the impact of the incident photon and may spontaneously desorb from the surface into the volume [Kra99, Piv00]. A possible PSD of hydrogen Rydberg states caused by the environmental radiation in the KATRIN experimental hall or by the presence of UV photons inside the spectrometer was studied in a series of measurements during SDS-IIB [Tro15b, Thu15, Ran15]. At the point of writing this thesis, the ongoing analyses of these measurements yet do not corroborate environmental $\gamma$-photons and x-rays to be the source of hydrogen Rydberg atoms.

- **Ion-induced desorption:** Besides electrons and photons also positive ions that are accelerated by the negative potential of the spectrometer vessel and impact the

stainless steel surface with up to 18.6-keV kinetic energy could cause the emission of hydrogen Rydberg atoms [Jan03]. This generation process of the excited Rydberg states seems rather promising at present as it might provide an explanation for the background dependence on the spectrometer vessel potential described in Section 6.2.3. Furthermore, a series of measurements at the very end of SDS-IIB have given first indications for a possible generation of hydrogen ions in the entrance and exit regions of the spectrometer. However, these results are highly preliminary and on the brink of the current background investigations at KATRIN.

All three above described processes are considered in the ongoing investigations and discussions of excited hydrogen Rydberg states as possible source of the KATRIN main spectrometer background [Dre15b, Tro16]. These investigations are based on the detailed knowledge of the background characteristics that has been gained through the extensive measurements and analyses carried out in the context of this thesis.

## 6.5 Conclusion

In this chapter, the spectrometer background in the standard ROI with the SDS-setup in its nominal operational mode with cold baffles and at low pressures has been analyzed in detail. With a remaining non-radon-induced background rate of $R = (691 \pm 1)$ mcps during SDS-IIA, this background exceeds the KATRIN design goal by a factor of about 70 and efficient countermeasures to further reduce the background are needed. For this purpose, however, the characteristics of the background must be known in detail to determine its origin. Based on the investigations in this chapter, several statements can be made on the characteristics of the cold-baffle background:

- The background events show no significant correlation of interarrival times, thus, is stochastic in nature,
- the event pattern on the detector features two prominent contributions, one which appears radially independent and one that increases to outer radii and shows an azimuthal dependence,
- the total background level is independent from the PAE potential,
- an increasing inner electrode offset potential results in a nearly radially independent background decrease,
- a decrease of the spectrometer vessel potential causes a drop of background rate, first on the outer detector rings, later in the center,
- even at zero vessel potential a background level of about 100 mcps remains,
- the background scales with the observed flux tube volume,
- the background shows no significant dependence on the magnetic-field strength in the analyzing plane,
- an increase of the pressure in the spectrometer increases the background only on the outer detector rings, while the background in the center of the flux tube appears almost constant,
- a cool-down of the spectrometer vessel by a few °C only shows a minor effect in terms of background reduction, which could potentially be pressure-related,
- the vacuum bake-out of the spectrometer vessel reduced the background level by $(40.2 \pm 0.3)\%$ in a nearly radially independent way,

- and, finally, no noticeable correlation of the background with the flux of cosmic muons in the KATRIN experimental hall was found.

As the latter observation does not support the previous paradigm of muon-induced secondary electrons representing the major background contributer, a survey of electron emission processes from inner surfaces of the spectrometer hull is carried out in this chapter. In this context, the total emission rate of low-energy electrons is estimated to $R_{\mathrm{em}}(690\,\mathrm{m}^2) \gtrsim 34\,700\,\mathrm{cps}$. Furthermore, an azimuthal dependence of the emission is found which partly fits to that of the spectrometer background. About 70% of the secondary electron emission is found to be blocked by a small electrostatic shielding potential of $U_{\mathrm{IE,common}} = -5\,\mathrm{V}$. With this blocking applied, a correlation of the secondary electrons emitted from the spectrometer hull and the cosmic-muon flux of $(13.6 \pm 0.8)\%$ is derived.

To conclude it can be said that the cold-baffle background is dominated by two major contributions: A radially increasing part which can be attributed to medium- and high-energy electrons being emitted from the inner surfaces of the spectrometer and which shows a strong dependence on pressure, and a second and dominant part, which appears homogeneously distributed in the spectrometer volume. All previously known sources of background in MAC-E filters fail to explain the characteristics of this second contribution. Thus, a novel model based on excited hydrogen Rydberg atoms being emitted from inner surfaces of the spectrometer was put forward. In this scenario, background in the volume results from interactions of Rydberg atoms with the black-body radiation. This model crucially relies on the detailed characterization of the non-radon-induced background realized in this chapter.

CHAPTER 7

# Summary and Outlook

The thesis in hand reports on an extensive body of work performed targeted to identify, characterize, and finally minimize a variety of novel background sources in the large-volume spectrometer of the Karlsruhe Tritium Neutrino (KATRIN) experiment. The results obtained here are of crucial relevance to assess the absolute mass scale of neutrinos with the targeted $\nu$-mass sensitivity of 200 meV (90% C.L.).

The trailblazing discovery of neutrino flavor oscillations in 1998 has given irrefutable evidence for physics beyond the standard model in terms of massive neutrinos. In the past twenty years various experimental approaches have been exploited in order to assess the absolute mass scale of the 'little neutral' one. The leading experimental method is high-precision spectroscopy of the tritium $\beta$-decay spectrum close to the kinematic endpoint of 18.6 keV. There, a non-zero effective mass of the electron antineutrino $m_{\bar{\nu}_e}$ manifests as a tiny spectral modification. The KATRIN experiment, being the most advanced next-generation tritium-based neutrino-mass experiment, uses the well-established MAC-E filter technique in combination with an ultra-luminous windowless gaseous tritium source to improve the present sensitivity of $m_{\bar{\nu}_e} < 2.0\,\text{eV}$ (95 % C.L.), from the pioneering experiments in Mainz and Troitsk by one order of magnitude. This ambitious goal requires in particular to keep the background level in the 1 240-$m^3$ volume main spectrometer of the experiment in the few mcps regime.

In early 2013, the main spectrometer and the focal-plane detector (FPD) system of the KATRIN experiment were jointly operated for the first time in a 4-months-long data-taking period (SDS-I). These initial measurements were, however, prone to technical challenges due to the parallel commissioning of various subcomponents in this complex apparatus. Apart from a generic understanding of parameters influencing the absolute background level in the spectrometer, limited progress was made to fix the relative contributions from background sources that are well-known from MAC-E filters, such as stored electrons in the spectrometer volume and surface-related secondary electrons.

Based on the findings in the first measurement campaign, the performance of several key hardware components of the spectrometer and detector section (SDS) was substantially improved. This includes the full functionality of all 148 segments of the silicon PIN-diode FPD and a significantly improved alignment of the SDS beamline. Both are key requirements to guarantee full mapping of the sensitive spectrometer volume onto the detector. Furthermore, a long-term and stable operation of liquid $N_2$-cooled copper baffles was achieved for 18.6 kV vessel high-voltage operation. This in turn, led to a substantial background reduction in the spectrometer. As a result, the whole SDS apparatus could

be operated reliably in a second, two-stage data-taking phase (SDS-II) which lasted from October 2014 to September 2015. During this unprecedented long-term operation of the system, previously unknown sources of background could be identified, while established backgrounds were minimized and characterized in detail in the context of this thesis.

## Identification of $^{210}$Pb in the Main Spectrometer

The energy analysis of tritium $\beta$-electrons in the KATRIN experiment is carried out by the integrating MAC-E filter spectrometer, so that the FPD only counts the event rate within a predefined energy region-of-interest (ROI). While previous background investigations were mainly focused on studying the event rate within this ROI, a series of measurements was carried out in the context of the thesis in hand to examine the spectrometer background outside of this rather narrow 5-keV energy window. In this context, a previously unexpected background signature by L-shell conversion electrons from the decay of $^{210}$Pb was clearly identified for the first time. The event rate in this signature was measured to $R = (2.2 \pm 0.2)$ mcps by the FPD.

A scenario for the deposition of $^{210}$Pb inside the spectrometer was established, based on the deposition or implantation of the progenies of the naturally occurring noble gas $^{222}$Rn onto the inner surfaces of the spectrometer over the course of the five-years-long installation period of an inner electrode system. Being part of the $^{238}$U decay chain, the long-lived $^{210}$Pb isotope being implanted into sub-surface layers of the stainless steel with a high recoil energy of 146 keV will generate background electrons at constant rate. Simulations of the implantation profile of this isotope in stainless steel and of the energy-loss of electrons in correspondingly thin subsurface layers have shown that this implantation scenario is compatible with the experimental observation of a small energy smearing of the L-shell conversion electron signature in the spectrometer background.

Monte-Carlo tracking simulations were carried out to derive the probability for an L-shell conversion electron emitted from inner surfaces to reach the FPD. The simulation results indicate a strong dependence of the detector-arrival probability on the deposition pattern of $^{210}$Pb in the spectrometer. A comparison of the experimentally observed radial distribution of the conversion electron signals on the detector with simulations suggests that $^{210}$Pb background mainly stems from the surface of the inner electrode system of the spectrometer. Under the assumption of a homogeneous distribution of $^{210}$Pb on the inner electrode system, a total activity of $(862 \pm 99)$ Bq could be derived, which is non-negligible with respect to other surface-related sources of background.

Further simulations were carried out to estimate the direct contribution of low-energy electrons from $^{210}$Pb $\beta$-decays to the background in the standard ROI of KATRIN. Such a contribution was found to be negligible due to the small detector-arrival probability of surface-related electrons at low energies. However, MC-storage simulations have also shown that high-energy $^{210}$Pb conversion electrons being trapped in the outermost regions of the spectrometer volume will generate low-energy background electrons inside the sensitive volume of the spectrometer. The simulated radial generation profile of this secondary electrons reproduces characteristics of the pressure-dependent component in the spectrometer background observed in the SDS-II measurements.

As the $\beta$-spectrum of the $^{210}$Pb decays closely matches that of tritium, the characteristic impact of the $^{210}$Pb implantation on the spectrometer background found in this thesis allows for a better understanding of possible source-related backgrounds. This includes the implantation of minute amounts of tritium ions from the source (WGTS) into the spectrometer walls in case of non-ideal tritium retention in the intermediate transport section of the experiment.

## The Radon-Induced Background

In previous works, a large background contribution due to electrons from $\alpha$-decays of the two radon isotopes $^{219}$Rn and $^{220}$Rn in the spectrometer volume was identified and characterized. However, due to technical limitations at that time, no conclusive statements could be made on the emanation sites of radon in the spectrometer, on the effectiveness of the liquid $N_2$-cooled copper baffles in terms of radon suppression, and finally on the relative contribution of electrons from radon decays to the absolute background level in the spectrometer. Owing to the full functionality of all SDS subcomponents during the SDS-II campaign, preexisting analysis methods were further refined to allow a more reliable identification of radon-decay signatures, so that radon background now has been fully characterized.

A key question with respect to radon background is related to the relative contributions of specific emanation sites to the overall background level. In order to achieve a stringent ultra-high vacuum (UHV) inside the large-volume spectrometer, each of its three main pump ports will be equipped with 1 km of non-evaporable getter (NEG) strips. While guaranteeing a high pumping speed for hydrogen and tritium, the NEG material also represents a known source of $^{219}$Rn emanation. Together with the emanation of radon from other sources, such as the large stainless steel surface of the spectrometer, or auxiliary vacuum equipment, the total observed radon activity in the sensitive spectrometer volume sums up to $(196 \pm 4)$ mBq. By reducing the amount of NEG material in the spectrometer by one third in SDS-II, the different radon contributions could be disentangled to $A_{\mathrm{NEG}} = (77 \pm 14)$ mBq from a single NEG-equipped pump port and $A_{\mathrm{other}} = (-35 \pm 42)$ mBq from other radon sources. This important result unequivocally has identified the NEG pumps as major (and potentially also single) source of radon emanation in the KATRIN main spectrometer.

Each of the main pump ports of the spectrometer is additionally equipped with a liquid $N_2$-cooled copper baffle which blocks the direct line-of-sight between the NEG strips and the sensitive volume of the spectrometer. Radon atoms impinging on the baffle system will stick to the cold copper surfaces for a prolongated time period to decay well outside of the sensitive spectrometer volume. With the baffle system being fully operational for the first time, its effectiveness in terms of radon suppression could be studied in detail in SDS-II. With all three baffles operated in cold conditions, the number of radon decays in the sensitive volume of the spectrometer was found to be reduced by $(95.1 \pm 0.3)\%$. Furthermore, the experimentally derived radon suppression efficiencies of the baffle system were compared to results of advanced test-particle MC-vacuum simulations. This comparison supports the previous findings of the NEG material being the major source of radon in the spectrometer. Additional measurements with an artificial $^{220}$Rn source installed at different ports of the spectrometer have revealed a significantly reduced radon-suppression efficiency of one baffle, most probably due to a limited reliability in its temperature regulation.

A detailed comparison of several long-term background measurements with different combinations of baffles cooled to liquid $N_2$-temperature allowed to derive the remaining radon-induced background rate for nominal spectrometer operation. For a configuration in which all pump ports are NEG-equipped together with liquid $N_2$-cold baffles, an upper limit of the radon-induced background rate of $R \leq 36^{+18}_{-15}$ mcps was found.

## Characterization of the Non-Radon-Induced Background

Due to the fact that the radon-induced background contribution for nominal cold-baffle operation was reduced to a very small level, the remaining non-radon-induced spectrometer

background could be characterized in detail in this thesis. Prior to a vacuum bake-out of the system a total background level of $R = (691 \pm 1)$ mcps was found. A proper thermal conditioning of the inner spectrometer surfaces reduced the background rate by $(40.2 \pm 0.3)\%$ to $(413 \pm 2)$ mcps. The level of background can be minimized further to the 100-mcps level by increasing the magnetic field in the center of the spectrometer and thereby the sensitive volume observed by the detector. However, this comes with the drawback of a reduced energy resolution of the MAC-E filter. Even in this extreme case the remaining background level remains too high to achieve the KATRIN design sensitivity of 200 meV, which calls for a dedicated investigation of the nature and characteristics of the remaining background.

Prior to the SDS-II campaign, the main contribution of non-radon-induced background was attributed to muon-induced secondary electrons emitted from inner surfaces of the spectrometer. In a study of surface-related electron-emission processes during SDS-II, a total emission rate from the 690-m$^2$ inner spectrometer surface of $R_{\mathrm{em}} \gtrsim 35 \times 10^3$ electrons per second was found. This value can be reduced by about 70% if small electrostatic shielding potentials are applied to the electrode system which covers the inner surfaces of the spectrometer. A correlation analysis of the remaining electron emission rate and the flux of cosmic muons in the KATRIN experimental hall has revealed that a fraction of only $(13.6 \pm 0.8)\%$ of surface electrons are cosmic muon induced, a fact that stands in contradiction to the prevalent, conventional background scenario for MAC-E filters.

In a MAC-E filter, the vast majority of surface-related secondary electrons is shielded by the almost perfect axial-symmetry of the magnetic guiding field. Accordingly, only a small fraction of electrons from the surface can enter the sensitive volume and, thus, contribute to the background via ionization of residual gas. Detailed investigations of the dependence of the non-radon-induced background on key operating parameters of the SDS apparatus have shown that the effectiveness of the magnetic shielding significantly exceeds the expectations. As a result, no noticeable correlation of the background level with the flux of cosmic muons could be observed in SDS-II. Even more importantly, the background per unit volume was found to be independent from the magnetic-field strength in the center of the spectrometer, again in stark contrast to conventional background scenarios. Finally, the impact of various electrostatic shielding potentials of the inner electrode system on the radial distribution of background events could not be reconciled with the now discarded earlier hypothesis of surface-related secondary electrons as major contributor to the background.

Another key finding of the SDS-II campaign was the fact that well-known active methods to expel low and medium energy stored electrons from the sensitive volume (e.g. a pulsed or static electric dipole field) showed no visible effect on the background level. Thus, stored electrons with transverse energies on the eV-scale acting as main contributor to the spectrometer background could be ruled out. This conclusion was further supported by the fact that a strengthening of the magnetic mirror at the exit side of the spectrometer only led to a minor effect in terms of background reduction, an observation incompatible with a scenario based on stored-electron-induced background.

With all conventional background generating mechanisms being unable to explain key characteristics of the non-radon-induced background in the main spectrometer, a completely novel scenario of background processes has to be envisioned. A promising model implying a paradigm change in background scenarios is based on hydrogen Rydberg atoms, which generate meV-scale background electrons due to their ionization by the black-body radiation of the vessel at 300 K. This recently proposed scenario correctly describes all characteristics of the remaining spectrometer background found in the course of this work. Among others, this includes exact scaling of the background level with the sensitive spec-

trometer volume, a radially independent impact of an electrostatic shielding potential on the background, and, in particular, the significant reduction of the background due to a proper vacuum bake-out of the spectrometer.

## Outlook

Coinciding with the completion of this thesis, since September $10^{\text{th}}$, 2015 all major components of the KATRIN beamline are on site at the Tritium Laboratory Karlsruhe (TLK) at the KIT Campus North. Currently, the whole system is being prepared for the start of tritium data-taking in mid-2016. The SDS part of the experiment has proven to function very reliably over the course of an 11-months-long second commissioning measurement campaign, even under aggravated conditions in terms of continuously changing operating parameters. This fact represents an important milestone on the way to a five-years-long continuous operation of the system in neutrino-mass measurements.

Thanks to the high reliability of the SDS apparatus, detailed insights into the background-generating processes in the large-scale spectrometer could be achieved in this thesis. The identification of the NEG pumps as major contributor of radon-induced background in the spectrometer is one of the key findings of this work, implying that a reduction of the number of NEG pumps from the originally foreseen level of three units would directly translate to a reduction of the radon-induced background level at an equal relative level. Evidently, this would come at the expense of an increased final pressure and a reduced tritium pumping speed, it is recommended at this point to restrict the number of NEG pumps in the spectrometer to two or even one unit only. Furthermore, it is recommended to improve the temperature regulation of all baffle systems to achieve the best possible radon suppression. By meeting these prerequisites and by further developing active stored-electron removal techniques such as the electric dipole or the magnetic pulse method, the radon-induced background is expected to be no longer a limiting factor for the neutrino mass sensitivity of KATRIN.

By excluding all background sources that are well-known from MAC-E filters as cause of the non-radon-induced background in the main spectrometer, the detailed background characterization carried out in this thesis has formed the basis for the development of a novel background-generation scenario based on the promising 'hydrogen Rydberg model'. Together with the well-known radon background, the hydrogen Rydberg model has established the pre-eminence of neutral, excited atoms being emanated or desorbed from the inner surfaces to be the dominant source of background. This new paradigm will guide the on-going efforts to eliminate the novel background class to the few mcps level to ensure that the KATRIN experiment can reach its design sensitivity of 200 meV to perform a key measurement in astroparticle physics.

# Appendix

## A Measurements with an Artificial Radon Source

In order to investigate the efficiency of the $LN_2$-cooled baffle system as a function of its operating temperature, several measurements with an artificial $^{220}$Rn source, integrated into the main spectrometer vacuum system, were carried out in the context of this thesis. The radon source consists of an incandescent mantle installed inside a KF40 stainless-steel pipe that can be connected to the main spectrometer via an adapter piece KF40-to-CF40.

### A.1 Baffle Efficiencies in Dependence of the Source Positioning

During the SDS-IIA campaign the artificial $^{220}$Rn source was installed at three different positions in the spectrometer vacuum system (see Fig. 3.4): first, at port A behind the baffle and the NEG pump in pump port 3, secondly in direct view to the spectrometer vessel at port B, and finally located at port C behind the baffle and the NEG pump in pump port 2. For each location of the source, a measurement at elevated spectrometer pressure and with all baffles cold was carried out. The observed radon cluster rates $R_{\mathrm{X}}$ in these measurements are listed in Table A.1.

In this context it should be noted that the gas-inlet system of the main spectrometer that is usually installed at port B (see Fig. 3.4) had to be moved to port C in one of the measurements in order to install the artificial radon source to port B. Furthermore, the artificial radon source is composed of several KF-sealed parts and is therefore not fully UHV compatible. With the source installed to port A, the pressure in pump port 3 was locally elevated compared to the rest of the main spectrometer volume and the reading of the standard Extractor gauge 3110, located directly beside port A, was no longer reliable in these measurements. Thus, the Inverse Magnetron gauge 2320 in pump port 2 had to

**Table A.1: Measurement configurations with an artificial radon source installed to the main spectrometer vacuum system at different locations.** The location of ports A, B, and C are marked in Figure 3.4. In some of the elevated pressure measurements, the gas inlet system of the main spectrometer was moved from port B to port C. The slight variations of the exact pressure inside the spectrometer vessel are taken into account by choosing a moderate time-window length of $\Delta t = 0.3\,\mathrm{s}$ and a large cluster-size threshold of $N_0 = 6$ to derive the accidental-corrected rate of radon-induced clusters $R_{\mathrm{X}}$ in each data set, as measured by 142 detector pixels. To compare to the case with no radon source installed, the background data set D (see Tab. 4.1) is analyzed as well.

| Location of the radon source | $R_{\mathrm{X}}$ (mcps) | Duration (h) | Runs |
|---|---|---|---|
| Port A (PP3) | $6.4 \pm 0.4$ | 9.2 | #22401 - #22410 |
| Port B (Spectrometer) | $166 \pm 6$ | 1.4 | #22172 - #22173 |
| Port C (PP2) | $37 \pm 2$ | 3 | #22126 - #22129 |
| No source (background) | $1.49 \pm 0.08$ | 62 | #22064 - #22125 |

be used to set the pressure in the spectrometer to the desired level of $p \approx 1 \times 10^{-8}$ mbar. Therefore, it is expected that the pressure level inside the vessel slightly varied between each of the measurements listed in Table A.1. In order to take this effect into account, the rates of radon-induced clusters in each data set are derived by employing a slightly increased interarrival time-window length $\Delta t = 0.3$ s, combined with a rather large cluster-size threshold of $N_0 = 6$ (see Sec. 4.2.2).

With the radon source directly installed to the main spectrometer volume (port B), with $R_{\mathrm{B}} = (166 \pm 6)$ mcps by far the largest rate of clusters is derived. This can be explained by the fact that the pumping efficiency of the baffles for radon propagating in the spectrometer volume is significantly smaller than for radon released in the pump ports, as the latter has to pass through the baffle geometry [compare plots a) and b) in Figure 4.21 for the $^{219}$Rn case]. With the artificial source moved to port C at the end of pump port 2, the rate of clusters is reduced by about 78%. However, the rate in this configuration is still 5.8 times larger than the cluster rate with the radon source installed to port A in pump port 3. The latter effect cannot be explained when assuming a similar pumping efficiency of baffles 2 and 3. As the geometries of all three baffle systems are identical, the only explanation for the reduced pumping efficiency of baffle 2 is a higher operating temperature of this baffle compared to baffle 3. This conclusion is reinforced by the fact that the installation of the 'electrified' NEG pump in port 3 was used to replace the temperature sensors on the corresponding baffle and to improve their thermal coupling to the copper blades prior to SDS-II. In this way, the operating temperature of baffle 3 can be regulated much better than that of the other two baffles. An upgrade of the temperature sensors of baffles 1 and 2 after the end of SDS-IIB is strongly recommended at this point.

With the artificial radon source dismounted from port A, the rate of clusters drops by another 77% to the background level in data set D (see Tab. 4.1) of $R_{\mathrm{bg}} = (1.49 \pm 0.08)$ mcps. This implies that a large fraction of the radon atoms that emanate from the artificial source pass through the geometry of the cold baffle to decay inside the spectrometer volume. At first view, this observation contradicts the high radon reduction efficiencies in the background measurements that were derived in Section 4.4. However, in contrast to the NEG pumps, which only emanate short-lived $^{219}$Rn, the artificial source emanates long-lived $^{220}$Rn with a half life of $t_{1/2} = 55.6$ s. This radon isotope, thus, can undergo several adsorption and desorption processes on a cold baffle surface before it actually decays. In this time it can pass through the baffle geometry and enter the spectrometer volume.

Based on these detailed measurements with the artificial $^{220}$Rn source, it can be concluded that individual baffle systems have specific and non-identical pumping efficiencies for radon. A reduced pumping efficiency of a specific baffle in this context is most probably due to a weak thermal coupling of the temperature sensors on the corresponding baffle resulting in a poor regulation of the baffle operating temperature.

## A.2 Baffle Efficiency as a Function of the Operating Temperature

In order to study the temperature dependence of the reduction efficiency of the baffles for radon, the artificial $^{220}$Rn source was permanently installed to port A while the operating temperature of the corresponding baffle 3 was varied between 85 K and room temperature. In parallel, the radon-induced cluster rate R(T) at elevated pressure was recorded in a series of measurements. A detailed analysis of all these measurements is given in [Mue15b], while this work will focus on two data sets only. This includes the runs #23964 - #23967 which were taken during the first 2 hours of the final warm-up of baffle 3 at the end of SDS-IIA, and runs #23992 - #23995, taken after the baffle had reached room temperature ($T = 300$ K). The latter data set is used to derive a reference cluster rate $R(300\ \mathrm{K})$ which is utilized to calculate the radon reduction efficiency $Eff_{exp}(T)$ of the baffle at temperature T

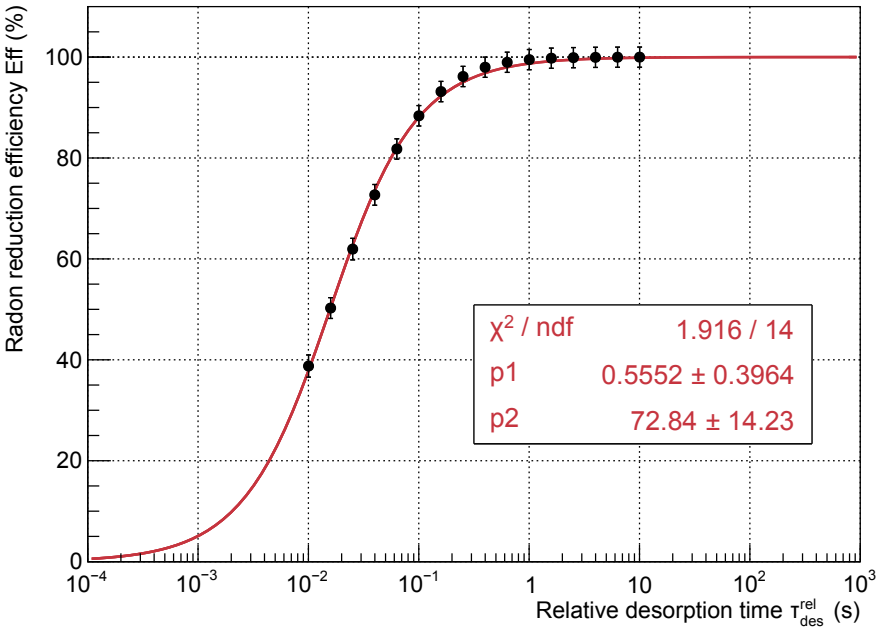


**Figure A.1: Radon-reduction efficiencies derived in a MolFlow+ simulation with a $^{220}$Rn-source installed to pump port 3.** The efficiency *Eff* is shown as a function of the (relative) mean desorption time $\tau_{\text{des}}^{\text{rel}}$ of radon on baffle 3 and is given relative to a simulation with all baffles warm. An arctangent-function according to Equation 4.27 is fitted to the simulated data points with the boundary conditions $Eff\,(0)_{\text{sim}} = 0\%$ and $Eff\,(\infty)_{\text{sim}} = 100\%$. The too small $\chi^2$/ndf-value can probably be traced back to an overestimation of the uncertainty introduced in [Mue15b] to take an inaccuracy in the spectrometer geometry in the MC simulations into account.

according to

$$Eff\,(T)_{\text{exp}} = 100 \cdot \left(1 - \frac{R(T)}{R(300\,\text{K})}\right) \quad . \tag{7.1}$$

Here, a cluster-size threshold of $N_0 = 6$ and a time-window length of $\Delta t = 0.3\,\text{s}$ are used for the cluster identification and the warm-up measurement is split into subsamples of 150-s length. To translate the derived efficiencies into mean desorption times $\tau_{\text{des}}$ of radon atoms from the baffle surface, a Molflow+ simulation similar to those described in Section 4.4.4 was performed, this time, however, with similar conditions as in the measurements with the artificial radon source. Figure A.1 shows the results of the simulation. A fit according to Equation 4.27 is applied to the simulated data where the efficiency varies between $Eff\,(\tau_{\text{des}}^{\text{rel}} = 0)_{\text{sim}} = 0\%$ and $Eff\,(\tau_{\text{des}}^{\text{rel}} = \infty)_{\text{sim}} = 100\%$.

By inserting the experimentally derived efficiency $Eff\,(T)_{\text{exp}}$ for a given baffle temperature

**Table A.2: Literature values for the oscillation period $\tau_0$ and the desorption enthalpy $H_{\text{des}}$ for radon at different surface conditions.** These two parameters define the mean desorption time $\tau_{\text{des}}$ at a given surface temperature according to Equation 4.24.

| Surface | Phonon oscillation period $\tau_0$ (s) | Desorption enthalpy $H_{\text{des}}^{\text{lit}}$ ($^{\text{kJ}}/_{\text{mol}\cdot\text{K}}$) |
|---|---|---|
| Ice | $3 \times 10^{-13}$ [Eic00b] | $-19.2 \pm 1.6$ [Eic00b] |
| CuO | $1.2 \times 10^{-13}$ [Jun89] | $-26.0$ [ES02] |
| Cu | $1.5 \times 10^{-13}$ [ES02] | $-37.0 \pm 2.0$ [ES02] |

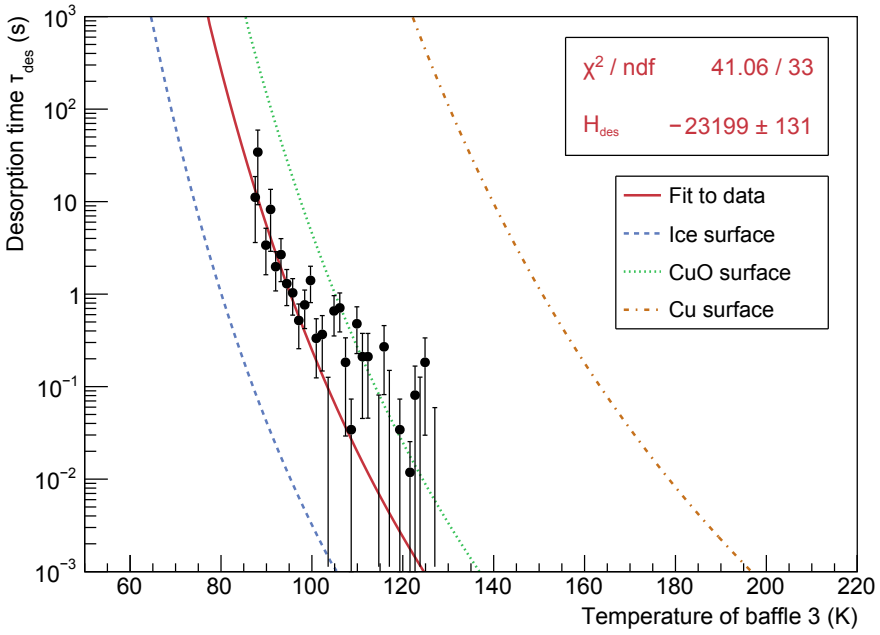


**Figure A.2: The mean desorption time $\tau_{\mathrm{des}}$ as a function of the temperature of baffle 3.** Measurements with an artificial $^{220}$Rn-source installed to port A of the main spectrometer are used to experimentally study the temperature dependence of the mean desorption time of radon from baffle 3. The radon-induced clusters are identified with a time-window length of $\Delta t = 0.3\,\mathrm{s}$ and a cluster-size threshold of $N_0 = 6$. The plot shows data from the first 1.5 hours of a warm-up of baffle 3. The data is subdivided into segments of 150-s length to gain sufficient statistics for each temperature point. A second measurement at $T = 300\,\mathrm{K}$, is used as reference in order to calculate radon reduction efficiencies. These again are translated into mean desorption times $\tau_{\mathrm{des}}$ via the functional relation $\tau_{\mathrm{des}}(\mathit{Eff})$ derived from MC-simulations and shown in Figure A.1. The red solid line represents a fit to the data points according to Equation 4.24 with $\tau_0 = (1.9 \times 10^{-13})\,\mathrm{s}$ fixed to the mean value of the literature values listed in Table A.2. The theoretical expected results for different surface conditions of the baffles (ice-coverage, CuO-surface, and pure copper) are shown in addition.

$T$ into the inverse of the fit function in Figure A.1, value pairs $(\tau_{\mathrm{des}}, T)$ are derived. They are plotted in Figure A.2. The functional relation between the mean desorption time and the surface temperature that is expected from theory is given in Equation 4.24. It depends on the desorption enthalpy $H_{\mathrm{des}}$ and the oscillation period $\tau_0$. Table A.2 lists literature values for these quantities in the case of an allocation of ice on the baffles, an oxidized, and a bare copper surface. The corresponding functions are shown in Figure A.2 in addition to the data points. Furthermore, a fit according to Equation 4.24 is applied to the data points, where the oscillation period is fixed to the mean value of the literature values for the three surface conditions $\tau_0 = (1.9 \times 10^{-13})\,\mathrm{s}$. The fit gives

$$H_{\mathrm{des}} = (23.2 \pm 0.1)\,\frac{\mathrm{kJ}}{\mathrm{mol}\cdot\mathrm{K}} \quad , \tag{7.2}$$

which suites well to the expectation of a partly ice-covered CuO surface of the baffle.

At temperatures $T > 100\,\mathrm{K}$ a rather large spread of the derived desorption times is observed[1]. This discloses the limitation of the analysis performed here. The Molflow+ simulations assume a uniform temperature profile over the whole baffle geometry at all times.

[1]Note that some slightly negative results for $\tau_{\mathrm{des}}$ are not visible in Figure A.2 due to the logarithmic y-axis. However, the applied fit takes these fluctuations into account.

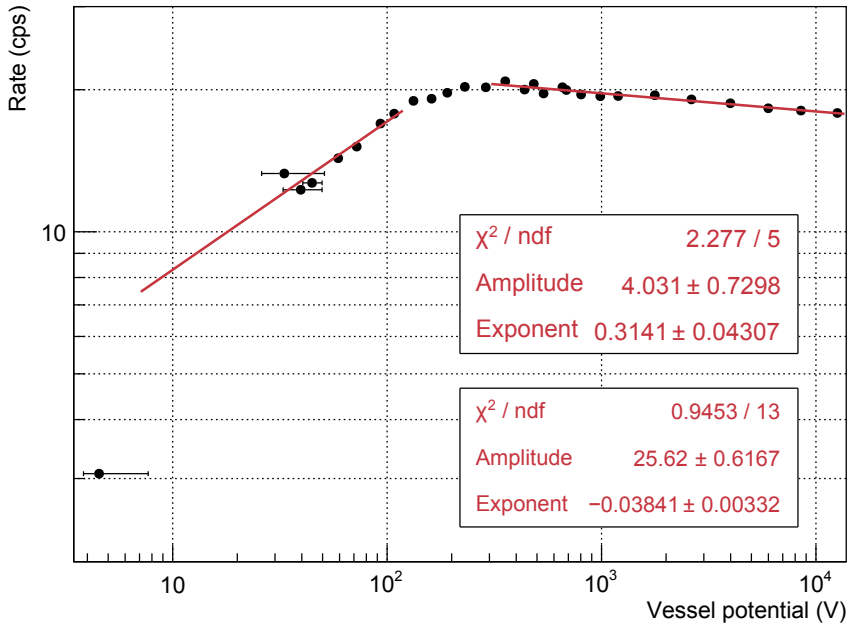


**Figure A.3: Radon-induced electron background rate as function of the vessel potential.** The total warm-baffle background rate with the artificial $^{220}$Rn source installed at port A is shown as a function of the vessel potential $U_{\text{vessel}}$. Two unweighted power-law fits are applied to the data points.

In reality, however, the baffle system is expected to have a high thermal inertia such that different parts of it will warm up at different speeds. The resulting non-uniformity of the warm-up process can cause a systematic shift of the measured temperature of the baffle at the specific position of the corresponding temperature sensor compared to the effective temperature of the whole baffle. It is reasonable that such a shift will increase over the course of the warm-up, which may explain the long tail of the data points in Figure A.2 towards larger temperatures.

## A.3 Dependence of the Radon Background on the Vessel Potential

In Section 6.2.3, a radially independent remaining background of about 100 mcps was found with the vessel operated close to zero potential. One possible explanation for this unexpectedly high background level could be an increase of the secondary electron yield for stored primary electrons from radon-decays with decreasing vessel potential. In order to investigate the impact of the vessel potential $U_{\text{vessel}}$ on the storage conditions of radon-induced electrons in the spectrometer, a series of measurements (runs #26509 - #26564) with the artificial $^{220}$Rn source installed at port A of the spectrometer was carried out during SDS-IIB. In these measurements, all baffles were operated warm and the vessel potential was varied from $\approx -5$ V to about $-12\,600$ V. Figure A.3 shows the results. Due to the high rates induced by the radon source, the non-radon-induced background is negligible at this point. Up to a vessel voltage of $U_{\text{vessel}} = -300$ kV the background rate strongly increases before it reaches its maximum of about 20 cps. At voltages higher than $-300$ V a slow decrease of the background rate is observed.

In order to derive the underlying cause of the background dependence shown in Figure A.3, MC storage simulations with KASSIOPEIA for different vessel potential must to be performed. At this point, however, radon can be excluded as cause of the $\approx$ 100-mcps

background level that was found in Section 6.2.3 for $U_{\text{vessel}} = 0\,\text{V}$. With a radon-induced background contribution of about 25 mcps in the HV-case (see Equation 4.8, this background would have to increase by a factor of about 4. In Figure A.3, the opposite effect is observed.

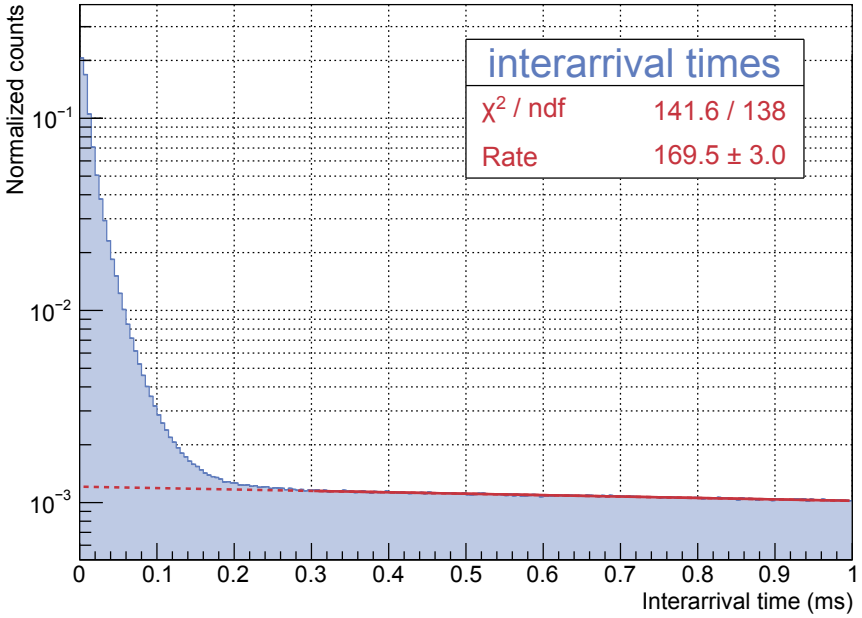


**Figure B.4: Interarrival time spectrum of electrons being emitted from the inner surfaces of the spectrometer.** In data set W (listed in Table 6.5) an 'asymmetric' magnetic field setting guides secondary electrons from the inner surfaces of the spectrometer directly onto the detector. The interarrival-time distribution of these electrons shows a steep increase at times smaller than 0.2 ms which corresponds to events highly correlated in time. An exponential fit (red line) applied to the uncorrelated part of the distribution above 0.3 ms gives a rate of $R = (170 \pm 3)$ cps.

# B Correlated Events from the Inner Spectrometer Surfaces

Figure B.4 shows the interarrival time distribution of the events in data set W for an 'asymmetric' magnetic field configuration (see Tab. 6.6). The visible increase of the distribution for interarrival times smaller than 0.2 ms corresponds to processes which result in the emission of multiple electrons from the inner surfaces of the spectrometer. Based on the analysis techniques that were already successfully used in Chapter 4 in the context of the radon-induced background at elevated pressure, these correlated events in data sets V and W are investigated in more detail in the following.

A cluster search with a time window length $\Delta t = 0.2$ ms and a cluster-size threshold of $N_0 = 2$ (see Sec. 4.2.2 for details) allows to separate correlated from uncorrelated events. Due to the large size of the data files in measurement at 'asymmetric' magnetic fields and the resulting long computation times, an accidental correction is not applied at this point. However, due to the small interarrival timescales on which correlated events appear on the detector, the probability for the formation of accidental clusters is small compared to the case of the radon-induced backgrounds. Table B.3 lists the different event rates obtained with the previously defined search parameters in data sets V and W. The true rate of clusters is expected to be larger than the one stated in the table as the background energy spectrum in both data sets features a large contribution of events in the $2 \cdot E_{\mathrm{inc}}$ and $3 \cdot E_{\mathrm{inc}}$ peaks, which correspond to additional correlated events that appeared on the wafer with time differences too small to be resolved by the detector. At this point this effect is not further investigated but should be taken into account in future analyses.

Figure B.5 shows the cluster-size distribution for data set W. In contrast to the radon-induced background (see Fig. 4.10), the electron multiplicity in a single cluster decreases

**Table B.3: Different event rate contributions from inner surfaces of the spectrometer.** The cluster search algorithm introduced in Section 4.2.2 is used with a time window length of $\Delta t = 0.2\,\mathrm{ms}$ and a cluster-size threshold of $N_0 = 2$ to separate the correlated events from the uncorrelated ones in data sets V and W. An accidental correction is not applied due to the long computation times required at the high event rates in these data sets. The errors for the correlated cluster events (and the total event rate) are derived from MCs by utilizing the distribution of cluster sizes and the rate of clusters. The innermost two detector rings are excluded from the analysis. More details are given in the text.

| Contribution | Rate in data set V (cps) | Rate in data set W (cps) |
|---|---|---|
| Total | $790.2 \pm 0.3$ | $247.44 \pm 0.04$ |
| Single events | $197.0 \pm 0.1$ | $109.88 \pm 0.03$ |
| Clusters | $159.3 \pm 0.1$ | $47.18 \pm 0.02$ |
| Cluster events | $593.2 \pm 0.2$ | $137.56 \pm 0.03$ |

exponentially. Only at small cluster sizes $N < 5$ an excess of events is observed, a part of which can be traced back to uncorrected accidental clusters. The exponential multiplicity distribution points to the stochastic nature of the transport process of an electron from the spectrometer surface to the detector. From this, two conclusions can be drawn: first, the initial electron multiplicity is exceptionally high, taking into account the small probability of a single electron to pass the magnetic mirror at the pinch magnet. Second, electrons which do not pass the mirror will be guided back to their point of origin. A quite different scenario can be envisioned when the electron emission processes at the surface would result in very low-energy electrons with transverse energies $E_\perp < 1\,\mathrm{eV}$. These electrons would pass the magnetic mirror unimpeded, so that the stochastic nature of the electron multiplicity in clusters would be due to the (unknown) emission process at the surface. However, as data set W was recorded with an inner electrode offset potential of $U_{\mathrm{IE,common}} = -5\,\mathrm{V}$, the source of such low-energy electrons would have to be the inner electrode system.

In principle, the clustered events can originate from several different processes like environmental or intrinsic radiation, field electron emission, or cosmic muons. The latter background component, however, is limited to a small fraction of about 14% of the secondary electrons (see Section 6.2.8 of this thesis). A priori it is difficult to judge whether the muon-induced part of the background contributes to uncorrelated or to correlated events. In order to target this question, the analysis successfully used in Section 6.2.8 is repeated in the following, this time for the single events and clustered ones separately.

Figure B.6 shows the correlation between the muon flux and uncorrelated background events in data set W found with the cluster search algorithm for $\Delta t = 0.2\,\mathrm{ms}$ and $N_0 = 2$. Compared to the total background displayed in Figure 6.15, the correlation factor is significantly increased to $0.88 \pm 0.03$ and a fraction of $a = (24 \pm 1)\%$ of the uncorrelated events is found to be muon induced. This is about 10% more in absolute terms than what was found for the total background rate. Consequently, for the clustered events the opposite effect is observed: While for $N_0 = 2$ a non-vanishing contribution by muon-induced events of $(5 \pm 1)\%$ (correlation factor of $0.22 \pm 0.08$) is still found, the results for larger cluster-size thresholds are consistent with zero. Figure B.7 shows the corresponding result for $N_0 = 3$ with a correlation factor of $0.07 \pm 0.05$ and a muon-induced fraction of the clustered events of $a = (0.7 \pm 1.3)\%$. These results suggest that cosmic muons preferably result in the emission of a single secondary electron when passing through the spectrometer hull. The correlated events must thus originate from a different source of background.

However, data set W which is analyzed at this point was recorded with an inner-electrode

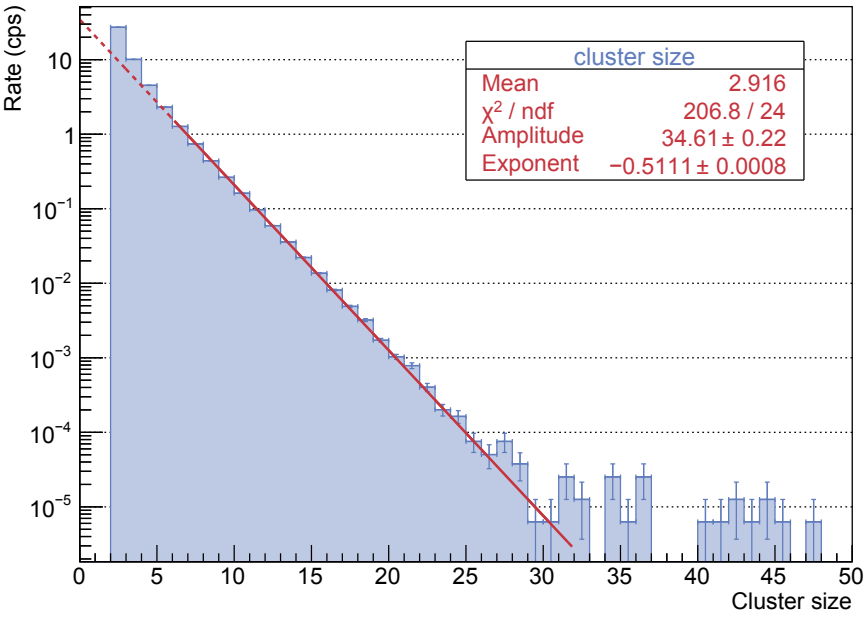


**Figure B.5: Cluster-size distribution of correlated events originating from the inner spectrometer surfaces.** A time window length of $\Delta t = 0.2\,\text{ms}$ and a cluster-size threshold of $N_0 = 2$ are used to identify event clusters in data set W (Tab. 6.5) where secondary electrons are directly guided from the inner surfaces of the spectrometer onto the detector via an 'asymmetric' magnetic field configuration. An exponential fit of the distribution for $5 < N < 32$ gives $R(N) = 34.6 \cdot \exp(-0.511 \cdot N)$. At low cluster sizes ($N \leq 5$) the distribution shows an excess of events which can partly be explained by uncorrected accidental clusters. In general, the obtained value for the exponent is surprisingly small, much smaller than expected for an effect of the magnetic mirror (which gives a $\approx 6\%$ probability for an electron to pass the pinch magnet).

offset potential of $U_{\text{IE,common}} = -5\,\text{V}$ applied. Thus, a large fraction of low-energy electrons is expected to be reflected by the electrostatic shielding in this data set. Data set V which was recorded with $U_{\text{IE,common}} = 0\,\text{V}$, but unfortunately features insufficient statistics to investigate a potential correlation with the muon flux, shows an about 3 times larger background rate. Interestingly, the rate of single (non time-correlated) events is only increased by less than a factor of two, compared to the $U_{\text{IE,common}} = -5$-V case, while the rate of time-correlated cluster events appears significantly increased by more than a factor of four. With the knowledge of muon-induced electrons appearing uncorrelated in time, this indicates that even at $U_{\text{IE,common}} = 0\,\text{V}$, the contribution of muon-induced secondary electrons to the total number of electrons emitted from the inner surfaces of the spectrometer is small.

**Spatial Correlation of the Events:**

It is interesting to investigate whether electron hits in a cluster are also correlated in space. We first recall that radon-induced events in a cluster were forming a distinct ring-like pattern. With this in mind, the time-correlated background events in data set W are checked for additional spatial correlations. The top part of Figure B.8 shows the distribution of distances between subsequent cluster events on the detector in terms of the difference in ring number and in azimuthal angle. The characteristic dartboard pattern of the detector (see Fig. 3.10) leads to the checkered distribution shown here. A large number of events is found to occur close to the previous one on the detector so that the distribution steeply increases to small values of the variables $\Delta\text{ring}$ and $\Delta\phi$. This means

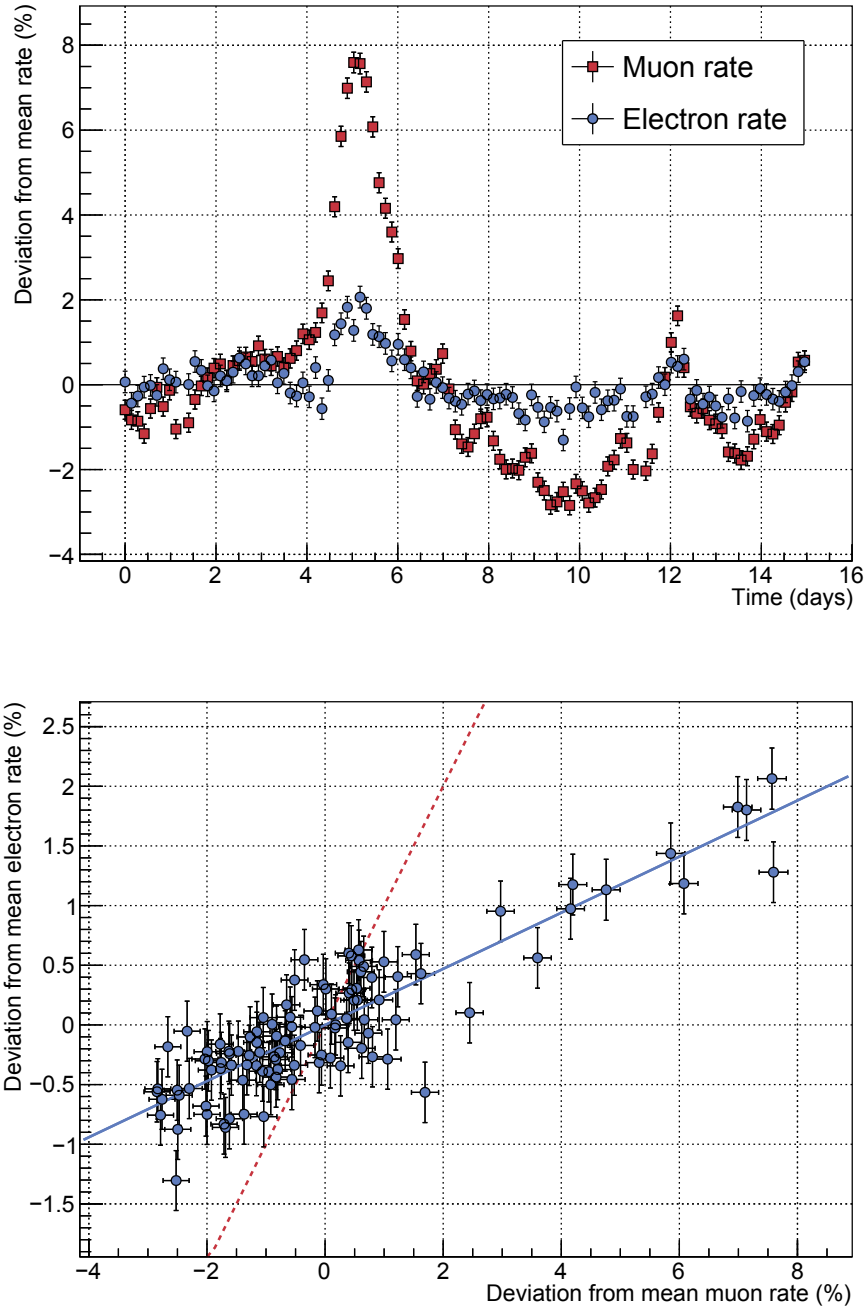


**Figure B.6: Correlation between the muon flux and uncorrelated secondary electrons from the inner spectrometer surfaces.** A cluster size threshold of $N_0 = 2$ and a time window length of $\Delta t = 0.2$ ms are used to separate correlated from uncorrelated events in data set W. **Top:** The relative deviations of the muon flux and the rate of uncorrelated background events observed by the FPD over the course of about 15 days show a similar trend. **Bottom:** The relative deviations are shown in a scatter plot representation and a fit according to Equation 5.8 is applied to the data points (blue solid line). The fit result gives a ratio of $a = (24 \pm 1)\%$ of the uncorrelated electron background being muon induced. The expected slope for 100% muon-induced background is shown as dashed red line.

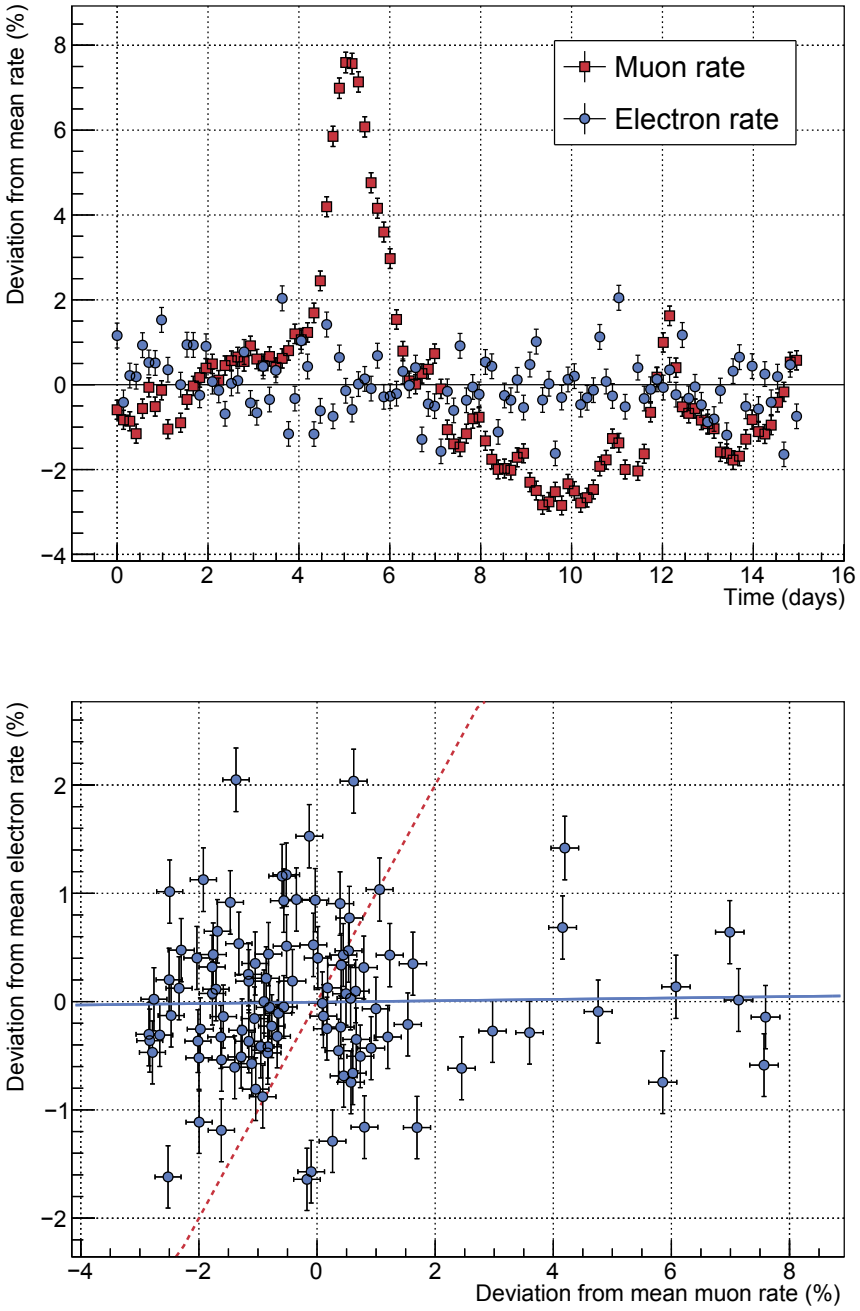


**Figure B.7: Correlation between the muon flux and time-correlated secondary electrons from the inner spectrometer surfaces.** A cluster size threshold of $N_0 = 3$ and a time window length of $\Delta t = 0.2$ ms are used to separate correlated from uncorrelated events in data set W. **Top:** The relative deviations of the muon flux and the rate of correlated background events observed by the FPD over the course of about 15 days show no visible correlation. **Bottom:** The relative deviations are shown in a scatter plot representation and a fit according to Equation 5.8 is applied to the data points (blue solid line). The fit result gives a ratio of $a = (0.7 \pm 1.3)\%$ of the correlated electron background being muon induced. The expected slope for 100% muon-induced background is shown as dashed red line.

that the correlated events not only appear clustered in time but also on the detector pixel map. The lower part of Figure B.8 displays two generic examples of such a pattern. The majority of clusters appears as a single, well-localized area on the detector (left plot), which corresponds to the point of creation on the inner surfaces of the spectrometer. Interestingly, some clusters consist of two clearly separated patterns (right plot). This cluster topology could be interpreted as the start and end point of the trajectory of the background-generating particle in the spectrometer volume. Due to the large spread in the time-of-flight of cluster electrons to the detector (as well as the limited timing resolution of the FPD) the investigation of those double-patterns requires an in-depth analysis which currently is being performed in [Mue16].

With cosmic muons being excluded as source of the observed pattern in data set W, environmental or intrinsic radiation are the most likely candidates to cause such localized bursts of electrons on the inner spectrometer surface. Field electron emission, in contrast, can definitely be excluded at this point due to the minimal inner electrode offset potential of $U_{\mathrm{IE,common}} = -5\,\mathrm{V}$ during the measurement.

In Section 5.3.4 the $\alpha$-decay of the $^{210}$Pb daughter nucleus $^{210}$Po on the inner surfaces of the spectrometer was discussed briefly. In this context, a background scenario with the surface-related emission of several low-energy electrons into the spectrometer volume, caused by the passage of the $\alpha$-particle through a small layer of stainless steel, was postulated. According to [Val04], both the number and the angular distribution of electrons emitted in this process do not depend on the direction of the $\alpha$-particle. The two localized sub-clusters in the plot on right lower part of Figure B.8 could therefore potentially be thought of as the 'fingerprints' of an $\alpha$-particle being emitted from the spectrometer surface at point A and hitting the vessel surface again at a different point B. Due to the 'asymmetric' magnetic field setting, the two points A and B are mapped onto the detector via the large number of secondary electrons that are generated in each case. With its high kinetic energy of several MeV, an $\alpha$-particle will traverse through the spectrometer volume on much faster time-scales than the detector timing resolution. Accordingly, the two observed secondary electron patterns on the detector cannot be separated in terms of their arrival time even on a statistical basis (note again that the travel time of single electrons from the surface to the detector is much longer than the travel time of an $\alpha$-particle). Furthermore, due to its high kinetic energy, the trajectory of the $\alpha$-particle will not noticeably be influenced by the magnetic or electric fields in the spectrometer and will therefore appear as a straight line.

A similar effect can also be envisioned for high-energy $\gamma$-photons from environmental radiation (like $^{40}$K decays in the concrete of the KATRIN experimental hall) that penetrate the spectrometer vessel at point A and strike the inner surface again at point B. Due to ionizations close to the inner surface of the stainless steel vessel, several low-energy secondary electrons are emitted in both cases which would map the entrance and exit point of the $\gamma$-photon onto the detector. This scenario could better explain the extended size of sub-clusters[2], which typically comprise several detector pixels and, thus, would correspond to a quite extended area at the inner spectrometer surface. During the SDS-IIB phase, specific background measurements were carried out with an artificial 53.3-MBq $^{60}$Co $\gamma$-source [Sch15a] placed in the basement of the KATRIN experimental hall. While the measurements at 'symmetric' magnetic field configurations showed no significant changes in the background level, once more proving the effectiveness of the intrinsic magnetic shielding of a MAC-E filter, the location of the $^{60}$Co source was clearly visible in terms of elevated rates in measurements at 'asymmetric' fields. A comparison of measurements with the $^{60}$Co source being screened and those were it is kept unshielded is described in

[2] An $\alpha$-particle is expected to generate a well-localized area of electron emission of small size.

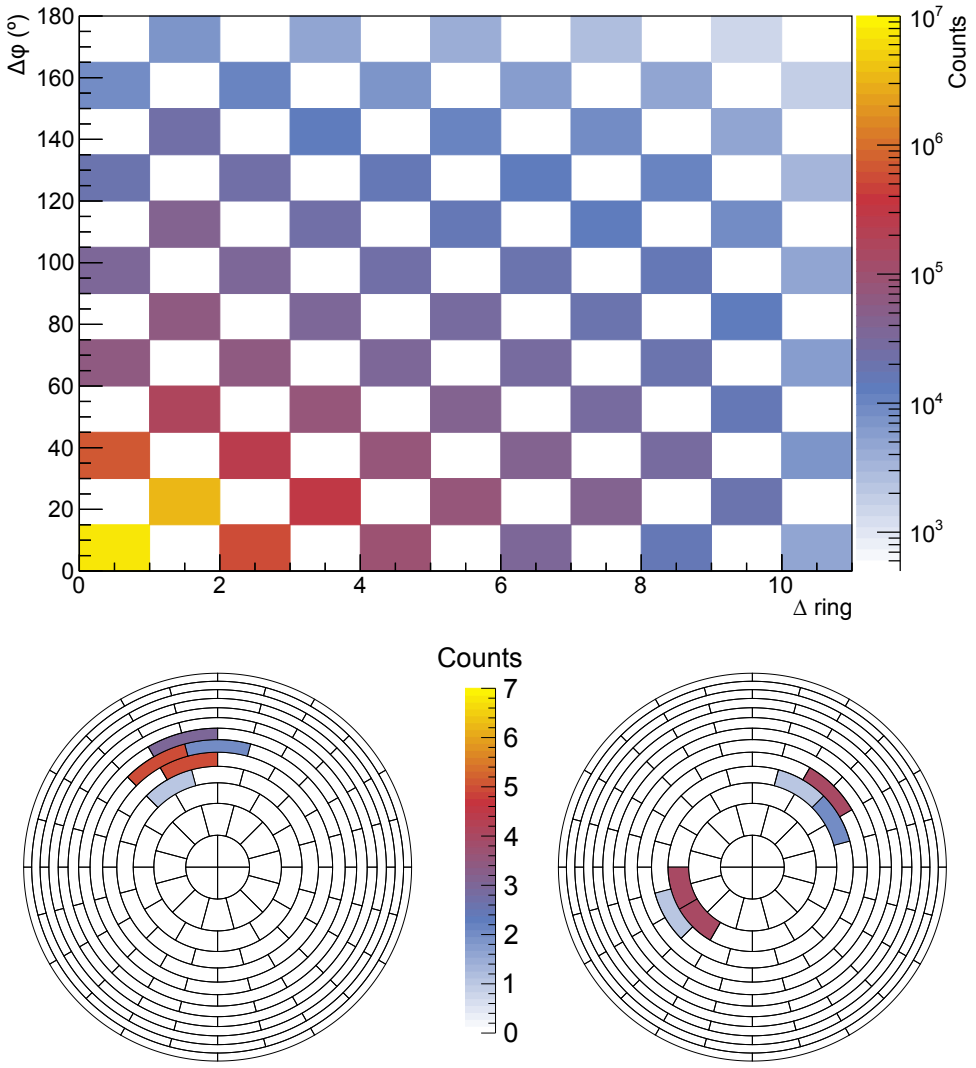


**Figure B.8: Spatial characteristic of the correlated background events from the inner surfaces of the spectrometer.** The time-correlated events in data set W at 'asymmetric' magnetic fields, as listed in Table 6.5, are analyzed with respect to a possible additional spatial correlation. **Top:** The differences in the detector ring and the azimuthal angle of subsequent cluster events are shown in a two-dimensional distribution. A steep increase to small $\Delta$ring and $\Delta\phi$ values corresponds to a localized appearance of the events on the detector wafer. **Bottom:** Exemplary pixel pattern of time-correlated events in data set W. While most of the time-correlated clusters appear as single coherent area on the detector (left plot) some clusters also feature two separated event pattern on the detector (right plot).

[Mue15a]. It indicates that environmental radiation only causes time-correlated cluster of small size but cannot explain the large-scale clusters observed in data set W. However, at the time of writing this thesis the corresponding analysis is still ongoing in the context of [Mue16].

# C Additional Tables

**Table C.4: Magnetic-field configurations commonly used during SDS-IIB** and in the context of this thesis. All listed settings are symmetric field settings optimized for a two-minima solution (see Sec. 3.1). The configurations are split in those where the FPD-magnets are operated at similar fields as in SDS-IIA (*reduced*) and those where these solenoids are operated at their nominal fields (*nominal*). Note that the listed currents refer to the new pinch magnet, in difference to those stated in Table 3.1.

| Magnet | 3.8 G (*reduced*) | 5 G (*reduced*) | 3.8 G (*nominal*) | 5 G (*nominal*) |
|---|---|---|---|---|
| PS1 | 156.0 | 156.0 | 156.0 | 156.0 |
| PS2 | 156.0 | 156.0 | 156.0 | 156.0 |
| LFCS coil 1 | 21.1 | 52.9 | 74.8 | 52.9 |
| LFCS coil 2 | 25.6 | 35.6 | 9.8 | 60.7 |
| LFCS coil 3 | 20.4 | 33.8 | 12.8 | 33.8 |
| LFCS coil 4 | 28.4 | 34.5 | 15.1 | 34.5 |
| LFCS coil 5 | 38.8 | 61.8 | 14.6 | 61.8 |
| LFCS coil 6 | 27.5 | 75.2 | 27.4 | 75.2 |
| LFCS coil 7 | 34.4 | 27.1 | 65.0 | 27.1 |
| LFCS coil 8 | 50.7 | 51.5 | 58.9 | 51.5 |
| LFCS coil 9 | 10.3 | 66.4 | 30.7 | 66.4 |
| LFCS coil 10 | 43.1 | 50.6 | 20.0 | 50.6 |
| LFCS coil 11 | 37.2 | 54.5 | 15.7 | 54.5 |
| LFCS coil 12 | 23.7 | 35.8 | 25.3 | 35.8 |
| LFCS coil 13 | 44.8 | 56.2 | 25.9 | 56.2 |
| LFCS coil 14 | −50.3 | −42.8 | −50.1 | −42.8 |
| vert. EMCS | 50.0 | 50.0 | 50.0 | 50.0 |
| horiz. EMCS | 9.0 | 9.0 | 9.0 | 9.0 |
| Pinch | 72.483 | 72.483 | 86.980 | 86.980 |
| Detector | 46.795 | 46.795 | 56.150 | 56.150 |

**Table C.5: Observed flux tube volumes per detector ring for the standard magnetic-field configurations during SDS-IIB.** The volumes were calculated for $|z| \leq 12\,\mathrm{m}$ with the KATRIN simulation framework KASSIOPEIA [FG15]. Note that the innermost detector ring (bullseye) has only four segments compared to the other rings with 12 pixels. Thus, the volume that is observed by ring 0 is reduced by a factor of about three. All volumes listed are given in $\mathrm{m}^3$.

| Detector ring | 3.8 G (*reduced*) | 3.8 G (*nominal*) |
|---|---|---|
| 0 | 16.5 | 18.8 |
| 1 | 50.0 | 57.1 |
| 2 | 51.0 | 58.5 |
| 3 | 52.1 | 59.9 |
| 4 | 53.2 | 61.3 |
| 5 | 54.2 | 62.8 |
| 6 | 55.4 | 64.4 |
| 7 | 56.5 | 66.0 |
| 8 | 57.8 | 67.7 |
| 9 | 59.0 | 69.5 |
| 10 | 60.4 | 71.5 |
| 11 | 61.8 | 73.5 |
| 12 | 63.3 | 75.8 |
| Total | 691.3 | 806.7 |

# List of Acronyms

| | |
|---|---|
| **ADC** | **A**nalog-to-**d**igital **c**onverter |
| **ADEI** | **A**dvanced **d**ata **e**xtraction **i**nfrastructure |
| **AGS** | **A**lternating **g**radient **s**ynchrotron |
| **ALEPH** | **A**pparatus for **LEP** **p**hysics |
| **APE** | **A**nti-**P**enning **e**lectrode |
| **BBR** | **B**lack-**b**ody **r**adiation |
| **BNL** | **B**rookhaven **N**ational **L**aboratory |
| **BOREXINO** | **Bor**on solar neutrino **ex**periment |
| **CAD** | **C**omputer-**a**ided **d**esign |
| **CC** | **C**harged-**c**urrent |
| **CDM** | **C**old **d**ark **m**atter |
| **CERN** | **C**onseil **E**uropéen pour la **R**echerche **N**ucléaire |
| **cFP** | **c**ompact **F**ield **P**oint |
| **CKM** | **C**abbibo-**K**obayashi-**M**askawa |
| **CNGS** | **C**ERN **n**eutrinos to **G**ran **S**asso |
| **CMB** | **C**osmic **m**icrowave **b**ackground |
| **COBE** | **Co**smic **B**ackground **E**xplorer |
| **CP** | **C**harge and **p**arity |
| **CPS** | **C**ryogenic **p**umping **s**ection |
| **COBRA** | **C**admium Zinc Telluride **0**-Neutrino Double-**B**eta **R**esearch **A**pparatus |
| **DAQ** | **D**ata-**ac**q**u**isition |
| **DET** | **Det**ector |
| **DONUT** | **D**irect **o**bservation of the **nu** **t**au |
| **DPS** | **D**ifferential **p**umping **s**ection |
| **ECHo** | **E**lectron **C**apture $^{163}$**Ho** |
| **ee** | **e**qual-**e**qual |
| **EMCS** | **E**arth **m**agnetic field **c**ompensation **s**ystem |
| **ES** | **E**lastic-**s**cattering |

| | |
|---|---|
| **ESD** | **E**lectron-**s**timulated **d**esorption |
| **EXO** | **E**nriched **X**enon **O**bservatory |
| **FLT** | **F**irst-**l**evel **t**rigger |
| **FPD** | **F**ocal-**p**lane **d**etector |
| **FPGA** | **F**ield-**p**rogrammable **g**ate **a**rray |
| **FT-ICR** | **F**ourier **t**ransform-**i**on **c**yclotron **r**esonance |
| **FWHM** | **F**ull **w**idth at **h**alf **m**aximum |
| **GERDA** | **Ger**manium **D**etector **A**rray |
| **GNO** | **G**allium **N**eutrino **O**bservatory |
| **GPU** | **G**raphics **p**rocessing **u**nit |
| **HEPA** | **H**igh **e**fficiency **p**articulate **a**rrestance filter |
| **HV** | **H**igh **v**oltage |
| **HVac** | **H**igh **vac**uum |
| **IMB** | **I**rvine-**M**ichigan-**B**rookhaven |
| **IPE** | **I**nstitute for Data **P**rocessing and **E**lectronics |
| **JFET** | **J**unction-gate **f**ield-**e**ffect **t**ransistor |
| **K2K** | **K**EK **to** **K**amioka |
| **KATRIN** | **Ka**rlsruhe **Tri**tium **N**eutrino |
| **KaLi** | **Ka**trin **li**brary |
| **KamLAND** | **Kam**ioka **L**iquid Scintillator **An**tineutrino **D**etector |
| **KIT** | **K**arlsruhe **I**nstitute of **T**echnology |
| **LARA** | **La**ser **Ra**man |
| **LEP** | **L**arge **E**lectron-**P**ositron Collider |
| **LFCS** | **L**ow-**f**ield **c**orrection **s**ystem |
| **LHC** | **L**arge **H**adron **C**ollider |
| **$LN_2$** | **L**iquid **n**itrogen |
| **LNGS** | **L**aboratori **N**azionali del **G**ran **S**asso |
| **MC** | **M**onte-**C**arlo |
| **MAC-E** | **M**agnetic-**a**diabatic **c**ollimation combined with an **e**lectrostatic |
| **MACRO** | **M**onopole, **A**strophysics and **C**osmic **R**ay **O**bservatory |
| **MARE** | **M**icrocalorimeter **A**rrays for a **R**henium **E**xperiment |
| **MINOS** | **M**ain **I**njector **N**eutrino **O**scillation **S**earch |
| **MobSU** | **Mob**ile **s**ensor **u**nit |
| **MSW** | **M**ikheyev-**S**mirnov-**W**olfenstein |
| **NC** | **N**eutral-**c**urrent |

| | |
|---|---|
| **NEG** | **N**on-**e**vaporable **g**etter |
| **NMR** | **N**uclear-**m**agnetic **r**esonance |
| **NOvA** | **N**uMI **O**ff-Axis **v** **A**ppearance |
| **oo** | **o**dd-**o**dd |
| **OPERA** | **O**scillation **P**roject with **E**mulsion T**r**acking **A**pparatus |
| **ORCA** | **O**bject-Oriented **R**eal-Time **C**ontrol and **A**cquisition |
| **PAE** | **P**ost-**a**cceleration **e**lectrode |
| **PCH** | **P**in**ch** |
| **PENELOPE** | **Pen**etration and **E**nergy-**Lo**ss of **P**ositrons and **E**lectrons |
| **PIN** | **P**-type, **i**-type, **n**-type semiconductor |
| **PMNS** | **P**ontecorvo-**M**aki-**N**akagawa-**S**akata |
| **PMT** | **P**hoto-**m**ultiplier **t**ube |
| **PS1** | **P**re-**s**pectrometer magnet **1** |
| **PS2** | **P**re-**s**pectrometer magnet **2** |
| **PSD** | **P**hoton-**s**timulated **d**esorption |
| **RENO** | **R**eactor **E**xperiment for **N**eutrino **O**scillations |
| **RGA** | **R**esidual-**g**as **a**nalyzer |
| **RMS** | **R**oot-**m**ean-**s**quare |
| **ROI** | **R**egion **o**f **i**nterest |
| **SAGE** | **S**oviet-**A**merican **G**allium **E**xperiment |
| **SDS** | **S**pectrometer and **d**etector **s**ection |
| **SDS-I** | **1**$^{\text{st}}$ commissioning phase of the **s**pectrometer and **d**etector **s**ection |
| **SDS-II** | **2**$^{\text{nd}}$ commissioning phase of the **s**pectrometer and **d**etector **s**ection |
| **SDS-IIA** | **SDS-II** - part **A** |
| **SDS-IIB** | **SDS-II** - part **B** |
| **SDSS** | **S**loan **D**igital **S**ky **S**urvey |
| **SFI** | **S**elective **f**ield **i**onization |
| **SK** | **S**uper-**K**amiokande |
| **SLC** | **S**tanford-**L**inear **C**ollider |
| **SLT** | **S**econd-**l**evel **t**rigger |
| **SM** | **S**tandard **M**odel |
| **SNLS** | **S**uper**n**ovae **L**egacy **S**urvey |
| **SNO** | **S**udbury **N**eutrino **O**bservatory |
| **SRIM** | The **S**topping and **R**ange of **I**ons in **M**atter |
| **SSM** | **S**tandard **s**olar **m**odel |

| | |
|---|---|
| **T2K** | **T**okai **to** **K**amioka |
| **TLK** | **T**ritium **L**aboratory **K**arlsruhe |
| **TMP** | **T**urbo-**m**olecular **p**ump |
| **UHV** | **U**ltra-**h**igh **v**acuum |
| **UV** | **U**ltra **v**iolet |
| **WGTS** | **W**indowless **g**aseous **t**ritium **s**ource |
| **WMAP** | **W**ilkinson **M**icrowave **A**nisotropy **P**robe |

# List of Figures

# List of Tables

# Bibliography


[Aar15] M. G. Aartsen et al. (The IceCube Collaboration), "Determining neutrino oscillation parameters from atmospheric muon neutrino disappearance with three years of IceCube DeepCore data," *Phys. Rev. D*, vol. 91, p. 072004, 2015, DOI: 10.1103/PhysRevD.91.072004.

[Abe08] S. Abe et al. (The KamLAND Collaboration), "Precision Measurement of Neutrino Oscillation Parameters with KamLAND," *Phys. Rev. Lett.*, vol. 100, p. 221803, 2008, DOI: 10.1103/PhysRevLett.100.221803.

[Abe11] K. Abe et al. (T2K Collaboration), "The T2K Experiment," *Nucl. Inst. Meth. Phys. Res. A*, vol. 659, no. 1, pp. 106 – 135, 2011, DOI: 10.1016/j.nima.2011.06.067.

[Abe12] Y. Abe et al. (Double Chooz Collaboration), "Reactor $\overline{\nu}_e$ disappearance in the Double Chooz experiment," *Phys. Rev. D*, vol. 86, p. 052008, 2012, DOI: 10.1103/PhysRevD.86.052008.

[Abe13] K. Abe et al. (Super-Kamiokande Collaboration), "Evidence for the Appearance of Atmospheric Tau Neutrinos in Super-Kamiokande," *Phys. Rev. Lett.*, vol. 110, p. 181802, 2013, DOI: 10.1103/PhysRevLett.110.181802.

[Abe14] K. Abe et al. (T2K Collaboration), "Precise Measurement of the Neutrino Mixing Parameter $\theta_{23}$ from Muon Neutrino Disappearance in an Off-Axis Beam," *Phys. Rev. Lett.*, vol. 112, p. 181801, 2014, DOI: 10.1103/PhysRevLett.112.181801.

[Abe15] ——, "Measurements of neutrino oscillation in appearance and disappearance channels by the T2K experiment with $6.6 \times 10^{20}$ protons on target," *Phys. Rev.*, vol. 91, p. 072010, 2015, DOI: 10.1103/PhysRevD.91.072010.

[Ack13] K. Ackermann et al. (GERDA Collaboration), "The Gerda experiment for the search of $0\nu\beta\beta$ decay in $^{76}$Ge," *The European Physical Journal C*, vol. 73, p. 2330, 2013, DOI: 10.1140/epjc/s10052-013-2330-0.

[Ada13] P. Adamson et al. (MINOS Collaboration), "Measurement of Neutrino and Antineutrino Oscillations Using Beam and Atmospheric Data in MINOS," *Phys. Rev. Lett.*, vol. 110, p. 251801, 2013, DOI: 10.1103/PhysRevLett.110.251801.

[Ada15] B. Adams, "Untersuchung magnetischer Materialien und Inbetriebnahme der Magnetfeldüberwachung am KATRIN-Hauptspektrometer," *Karlsruhe Institute of Technology*, 2015, master thesis.

[Ade15] P. A. R. Ade et al. (Planck Collaboration), "Planck 2015 results. XIII. Cosmological parameters," *Astr. and Astrophys.*, 2015, arXiv:1502.01589.

[Aga15] N. Agafonova et al. (OPERA Collaboration), "Discovery of tau neutrino appearance in the CNGS neutrino beam with the OPERA experiment," 2015, arXiv:1507.01417v1.

[Ago13] M. Agostini et al. (GERDA Collaboration), "Results on Neutrinoless Double-$\beta$ Decay of $^{776}$Ge from Phase I of the GERDA Experiment," *Physical Review Letters*, vol. 111, p. 122503, 2013, DOI: 10.1103/PhysRevLett.111.122503.

[Aha05] B. Aharmim et al. (SNO Collaboration), "Electron energy spectra, fluxes, and day-night asymmetries of $^{8}$B solar neutrinos from measurements with NaCl dissolved in the heavy-water detector at the Sudbury Neutrino Observatory," *Phys. Rev. C*, vol. 72, p. 055502, 2005, DOI: 10.1103/PhysRevC.72.055502.

[Aha10] ——, "Low-energy threshold analysis of the Phase I and Phase II data sets of the Sudbury Neutrino Observatory," *Phys. Rev. C*, vol. 81, p. 055504, 2010, DOI: 10.1103/PhysRevC.81.055504.

[Aha13] ——, "Combined analysis of all three phases of solar neutrino data from the Sudbury Neutrino Observatory," *Phys. Rev. C*, vol. 88, p. 025501, 2013, DOI: 10.1103/PhysRevC.88.025501.

[Ahn06] M. H. Ahn et al. (K2K Collaboration), "Measurement of neutrino oscillation by the K2K experiment," *Phys. Rev. D*, vol. 74, p. 072003, 2006, DOI: 10.1103/PhysRevD.74.072003.

[Ahn12] J. K. Ahn et al. (RENO Collaboration), "Observation of Reactor Electron Antineutrinos Disappearance in the RENO Experiment," *Phys. Rev. Lett.*, vol. 108, p. 191802, 2012, DOI: 10.1103/PhysRevLett.108.191802.

[AK14] M. Ady and R. Kersevan, "MolFlow+ user guide," 2014, User Manual. [Online]. Available: https://test-molflow.web.cern.ch/sites/test-molflow.web.cern.ch/files/molflow_user_guide.pdf

[Alb14] J. B. Albert et al. (EXO-200 Collaboration), "Search for Majorana neutrinos with the first two years of EXO-200 data," *Nature*, vol. 510, pp. 229 – 234, 2014, DOI: 10.1038/nature13432.

[Ale87] E. N. Alekseev et al., "Possible detection of a neutrino signal on 23 February 1987 at the Baksan underground scintillation telescope of the Institute of Nuclear Research," *JETP Lett.*, vol. 45, no. 10, pp. 589 – 592, 1987, [Pisma Zh. Eksp. Teor. Fiz. 45, 461-464 (1987)].

[Ale88] ——, "Detection of the neutrino signal from SN 1987A in the LMC using the INR Baksan underground scintillation telescope," *Phys. Lett. B*, vol. 205, no. 2 - 3, pp. 209 – 214, 1988, DOI: 10.1016/0370-2693(88)91651-6.

[Ali09] G. Alimonti et al. (Borexino Collaboration), "The Borexino detector at the Laboratori Nazionali del Gran Sasso," *Nucl. Inst. Meth. Phys. Res. A*, vol. 600, no. 3, pp. 568 – 593, 2009, DOI: 10.1016/j.nima.2008.11.076.

[All75] O. C. Allkofer, "Introduction to Cosmic Radiation," *Verlag Karl Thiemig München*, 1975. [Online]. Available: http://physics111.lib.berkeley.edu/Physics111/Reprints/MUO/06-Introduction_to_Cosmic_Radiation.pdf

[All97] W. W. M. Allison et al., "Measurement of the atmospheric neutrino flavor composition in Soudan 2," *Phys. Lett. B*, vol. 391, pp. 491 – 500, 1997, DOI: 10.1016/S0370-2693(96)01609-7.

[All99] ——, "The atmospheric neutrino flavor ratio from a 3.9 fiducial kiloton-year exposure of Soudan 2," *Phys. Lett. B*, vol. 449, pp. 137 – 144, 1999, DOI: 10.1016/S0370-2693(99)00056-8.

[Amb98] M. Ambrosio et al. (MACRO Collaboration), "Measurement of the atmospheric neutrino-induced upgoing muon flux using MACRO," *Phys. Lett. B*, vol. 434, pp. 451 – 457, 1998, DOI: 10.1016/S0370-2693(98)00885-5.

[Ams07] C. Amsler, "Kern- und Teilchenphysik," *vdf Hochschulverlag AG an der ETH Zürich*, 2007, ISBN: 978-3-8252-2885-9 (paperback).

[Ams15] J. F. Amsbaugh et al., "Focal-plane detector system for the KATRIN experiment," *Nucl. Inst. and Meth. in Phys. Res. A*, vol. 778, pp. 40 – 60, 2015.

[An 12] F. P. An et al. (Daya Bay Collaboration), "Observation of Electron-Antineutrino Disappearance at Daya Bay," *Phys. Rev. Lett.*, vol. 108, p. 171803, 2012, DOI: 10.1103/PhysRevLett.108.171803.

[An 15] ——, "New Measurement of Antineutrino Oscillation with the Full Detector Configuration at Daya Bay," *Phys. Rev. Lett.*, vol. 115, p. 111802, 2015, DOI: 10.1103/PhysRevLett.115.111802.

[And07] E. Andreotti et al., "MARE, Microcalorimeter Arrays for a Rhenium Experiment: A detector overview," *Nucl. Inst. Meth. Phys. Res. A*, vol. 572, pp. 208 – 210, 2007, DOI: 10.1016/j.nima.2006.10.198.

[Ang05] J. Angrik et al., "KATRIN Design Report 2004," *FZKA Scientific Report 7090*, 2005.

[AS09] E. K. Akhmedov and A. Y. Smirnov, "Paradoxes of neutrino oscillations," *Phys. Atom. Nucl.*, vol. 72, no. 8, pp. 1363 – 1381, 2009, DOI: 10.1134/S1063778809080122.

[Asa15] K. Asakura et al., "Search for double-beta decay of $^{136}$Xe to excited states of $^{136}$Ba with the KamLAND-Zen experiment," 2015, arXiv: 1509.03724.

[Ase11] V. N. Aseev et al., "Upper limit on electron antineutrino mass from Troitsk experiment," *Phys. Rev. D*, vol. 84, no. 11, p. 112003, 2011, DOI: 10.1103/PhysRevD.84.112003.

[ATL12] ATLAS Collaboration, "Observation of a new particle in the search for the Standard Model Higgs boson with the ATLAS detector at the LHC," *Physics Letters B*, vol. 716, no. 1, pp. 1 – 29, 2012, DOI: 10.1016/j.physletb.2012.08.020.

[Aug23] P. Auger, "Sur les rayons $\beta$ secondaires produits dans un gaz par des rayons X," *C.R.A.S.*, vol. 177, pp. 169 – 171, 1923.

[AVV02] J. N. Abdurashitov, E. P. Veretenkin, and V. M. Vermul et al., "Solar neutrino flux measurements by the Soviet-American gallium experiment (SAGE) for half the 22-year solar cycle," *Journal of Experimental and Theoretical Physics*, vol. 95, no. 2, pp. 181 – 193, 2002, DOI: 10.1134/1.1506424.

[Bab11] M. Babutzka, "Untersuchung eines verfahrbaren Monitordetektors zur Überwachung der Aktivität des $\beta$-Zerfalls in der kryogenen Pumpstrecke bei KATRIN," *Karlsruhe Institute of Technology*, 2011, diploma thesis.

[Bab12] M. Babutzka et al., "Monitoring of the operating parameters of the KATRIN Windowless Gaseous Tritium Source," *New Journal of Physics*, vol. 14, p. 103046, 2012, DOI: 10.1088/1367-2630/14/10/103046.

[Bab14] M. Babutzka, "Design and development for the Rearsection of the KATRIN experiment," *Karlsruhe Institute of Technology*, 2014, doctoral thesis.

[Bah64a] J. N. Bahcall, "Solar Neutrino Cross Sections and Nuclear Beta Decay," *Phys. Rev.*, vol. 135, no. 1B, pp. B137 – B146, 1964, DOI: 10.1103/PhysRev.135.B137.

[Bah64b] ——, "Solar Neutrinos. I. Theoretical," *Phys. Rev. Lett.*, vol. 12, no. 11, pp. 300 – 302, 1964, DOI: 10.1103/PhysRevLett.12.300.

[Bah05] J. N. Bahcall et al., "New Solar Opacities, Abundances, Helioseismology, and Neutrino Fluxes," *The Astrophysical Journal Letters*, vol. 621, no. 1, p. 621, 2005, DOI: 10.1086/428929.

[Ban14] F. Bandenburg, "Inbetriebnahme des Fokalebenendetektor-Systems für eine zweite Messphase am KATRIN-Hauptspektrometer," *Karlsruhe Institute of Technology*, 2014, diploma thesis.

[Bar95] J. Baro, J. Sempau, J.M. Fernandez-Varea, F. Salvat, "PENELOPE: An algorithm for Monte Carlo simulation of the penetration and energy loss of electrons and positrons in matter," *Nucl. Inst. Meth. Phys. Res. B*, vol. 100, no. 1, pp. 31 – 46, 1995, DOI: 10.1016/0168-583X(95)00349-5. [Online]. Available: http://pypenelope.sourceforge.net/

[Bar14] J. Barrett, et al., "Results of the first KATRIN SDS measurement phase," 2014, internal KATRIN document.

[Bau13a] S. Bauer, "Energy calibration and stability monitoring of the KATRIN experiment," *Westfälische Wilhelms-Universität Münster*, 2013, doctoral thesis.

[Bau13b] S. Bauer et al., "Next generation KATRIN high precision voltage divider for voltages up to 65kV," *Journal of Instrumentation*, vol. 8, p. P10026, 2013, DOI: 10.1088/1748-0221/8/10/P10026.

[BD76] J. N. Bahcall and R. Davis Jr., "Solar Neutrinos: A Scientific Puzzle," *Science*, vol. 191, pp. 264 – 267, 1976. [Online]. Available: www.bnl.gov/bnlweb/raydavis/Science-01-23-76.pdf

[Bec01] H. Becquerel, "The Radio-Activity of Matter," *Nature*, vol. 63, no. 1634, pp. 396 – 398, 1901.

[Bec92] R. Becker-Szendy et al., "Electron- and muon-neutrino content of the atmospheric flux," *Phys. Rev. D*, vol. 46, no. 9, pp. 3720 – 3724, 1992, DOI: 10.1103/PhysRevD.46.3720.

[Beg14] A. Beglarian, M. Erhard, F. Glück, F. Harms, J. Schwarz, "Status Quo of Air Coils before SDS2," 2014, internal KATRIN elog. [Online]. Available: https://neutrino.ikp.kit.edu:8080/SDS-Measurements+Phase+2/4

[Beh13] J. D. Behrens, et al., "EMD consequences of electrical shorts at the inner electrode system," 2013, internal KATRIN document. [Online]. Available: http://fuzzy.fzk.de/bscw/bscw.cgi/d775431/EMD%20consequences%20of%20electrical%20shorts%20at%20the%20inner%20electrode%20system.pdf

[Beh14a] J. D. Behrens, "Active Background Removal by Magnetic Pulse," 2014, internal KATRIN talk, 26th collaboration meeting. [Online]. Available: http://fuzzy.fzk.de/bscw/bscw.cgi/d877040/95-TRP-5636-C1-JBEHRENS.odp.pdf

[Beh14b] J. D. Behrens et al., "Reduction of stored-particle background by magnetic pulse in the KATRIN spectrometers," *New Journal of Physics*, 2014, paper in preparation.

[Beh15] J. Behrens, 2015, doctoral thesis in preparation.

[Bel14a] G. Bellini et al. (Borexino Collaboration), "Final results of Borexino Phase-I on low-energy solar neutrino spectroscopy," *Phys. Rev. D*, vol. 89, p. 112007, 2014, DOI: 10.1103/PhysRevD.89.112007.

[Bel14b] ——, "Neutrinos from the primary proton-proton fusion process in the Sun," *Nature*, vol. 512, pp. 383 – 386, 2014, DOI: 10.1038/nature13702.

[Ber12] T. Bergmann et al., "FPGA-based multi-channel DAQ systems with external PCI express link to GPU compute servers," *Real Time Conference (RT), 2012 18th IEEE-NPSS*, pp. 1 – 5, 2012, DOI: 10.1109/RTC.2012.6418197.

[Bes10] B. Beskers, "Messung und Optimierung der Eigenschaften des Monitordetektors für keV-Elektronen in der kryogenen Pumpstrecke des KATRIN Experiments," *Westfälische Wilhelms-Universität Münster*, 2010, diploma thesis.

[Bet09] I. I. Beterov, D. B. Tretyakov, I. I. Ryabtsev, V. M. Entin, A. Ekers, N. N. Bezuglov, "Ionization of Rydberg atoms by blackbody radiation," *New J. Phys.*, vol. 11, p. 013052, 2009, DOI: 10.1088/1367-2630/11/1/013052.

[Bet14a] M. Betoule et al., "Improved cosmological constraints from a joint analysis of the SDSS-II and SNLS supernova samples," *Astr. and Astrophys.*, vol. 568, no. A22, p. 32, 2014, DOI: 10.1051/0004-6361/201423413.

[Bet14b] A. Bettini, "Introduction to Elementary Particle Physics," *Cambridge University Press*, 2014, ISBN: 978-1-107-05040-2 (Hardcopy).

[Beu11] F. Beutler et al., "The 6dF Galaxy Survey: baryon acoustic oscillations and the local Hubble constant," *Monthly Notices of the Royal Astronomical Society*, vol. 416, no. 4, pp. 3017 – 3032, 2011, DOI: 10.1111/j.1365-2966.2011.19250.x.

[BG06] L. Bergström and A. Goobar, "Cosmology and Particle Astrophysics," *Springer*, 2006.

[Bio87] R. M. Bionta et al., "Observation of a Neutrino Burst in Coincidence with Supernova 1987A in the Large Magellanic Cloud," *Phys. Rev. Lett.*, vol. 58, p. 1494, 1987, DOI: 10.1103/PhysRevLett.58.1494.

[Bod11] T. Bode, "Optimierung des 2-Phasen-Kühlkonzepts für den WGTS-Demonstrator von KATRIN," *Karlsruhe Institute of Technology*, 2011, diploma thesis.

[Bot12] R. Bottesch, "Set-up of the motion control and characterization of the ablation laser for the condensed $^{83m}$Kr conversion electron source of the KATRIN experiment," *Westfälische Wilhelms-Universität Münster*, 2012, diploma thesis.

[BP34] H. Bethe and R. Peierls, "The Neutrino," *Nature*, vol. 133, p. 532, 1934, DOI: 10.1038/133532a0.

[BP95] J. Bahcall and M. Pinsonneault, "Solar models with helium and heavy-element diffusion," *Rev. Mod. Phys.*, vol. 67, no. 4, pp. 781 – 808, 1995, DOI: 10.1103/RevModPhys.67.781.

[BPT80] G. Beamson, H. Q. Porter, and D. W. Turner, "The collimating and magnifying properties of a superconducting field photoelectron spectrometer," *Journal of Physics E*, vol. 13, no. 1, p. 64, 1980, DOI: 10.1088/0022-3735/13/1/018.

[BR96] R. Brun and F. Rademakers, "ROOT - An Object Oriented Data Analysis Framework," *Proceedings AIHENP'96 Workshop, Lausanne*, 1996. [Online]. Available: http://root.cern.ch/

[BR97] ——, "ROOT - An Object Oriented Data Analysis Framework," *Nucl. Inst. and Meth. in Phys. Res. A*, vol. 389, pp. 81 – 86, 1997. [Online]. Available: http://root.cern.ch/

[Bra88] C. B. Bratton et al., "Angular distribution of events from SN1987A," *Phys. Rev. D*, vol. 37, p. 3361, 1988, DOI: 10.1103/PhysRevD.37.3361.

[Byr05] J. Byrne, "Experience with high electric and magnetic Penning traps," *FZK Karlsruhe*, 2005, released talk. [Online]. Available: https://neutrino.ikp.kit.edu/owncloud/data/katrin/files/Public/Presentations/Byrne-talk-14Apr2005-FZK.pdf

[CB11] Cryomagnetics Inc. and L. I. Bodine, "User's Manual, 6T Detector and Pinch Superconducting Magnet Pair for University of Washington (KATRIN)," 2011, internal KATRIN document. [Online]. Available: https://fuzzy.fzk.de/bscw/bscw.cgi/d653154/Magnet%20User%27s%20Manual.pdf

[Cha14] J. Chadwick, "Intensitätsverteilung im magnetischen Spektrum der $\beta$-Strahlen von Radium B + C / The Intensity Distribution in Magnetic Spectrum of $\beta$-Rays of Radium B + C," *Verhandl. Dtsch. phys. Ges.*, vol. 16, p. 383, 1914.

[Cha32] ——, "Possible Existence of a Neutron," *Nature*, vol. 129, no. 3252, p. 312, 1932.

[Chi10] S. Chilingaryan, A. Beglarian, A. Kopmann, S. Vöcking, "Advanced data extraction infrastructure: Web based system for management of time series data," *Journal of Physics: Conference Series*, vol. 219, no. 4, p. 042034, 2010, DOI: 10.1088/1742-6596/219/4/042034.

[CK35] D. Coster and R. D. L. Kronig, "New type of auger effect and its influence on the X-ray spectrum," *Physica*, vol. 2, no. 1 - 12, pp. 13 – 24, 1935, DOI: 10.1016/S0031-8914(35)90060-X.

[CMS12] CMS Collaboration, "Observation of a new boson at a mass of 125 GeV with the CMS experiment at the LHC," *Physics Letters B*, vol. 716, no. 1, pp. 30 – 61, 2012, DOI: 10.1016/j.physletb.2012.08.021.

[Cor14] T. Corona, "Methodology and Application of High Performance Electrostatic Field Simulation in the KATRIN Experiment," *University of North Carolina, Chapel Hill*, 2014, doctoral thesis.

[Cow56] C. L. Cowan, F. Reines, F. B. Harrison, H. W. Kruse, A. D. McGuire, "Detection of the Free Neutrino: a Confirmation," *Science*, vol. 124, no. 3212, pp. 103 – 104, 1956, DOI: 10.1126/science.124.3212.103.

[Cry03] Cryogenic Ltd., "4.5 Tesla Cryogen-Free Magnet Systems, Job Number 2054, Temporary manual," 2003, internal KATRIN document. [Online]. Available: http://fuzzy.fzk.de/bscw/bscw.cgi/d966341/BAL_Cryonenics_PS-Magnets.pdf

[Cry15] Cryomagnetics Inc., "Operating Instruction Manual for University of Washington Pinch II Magnet System," 2015, internal KATRIN document. [Online]. Available: https://fuzzy.fzk.de/bscw/bscw.cgi/d956461/9198-C1890M%20UW%20MANUAL.pdf

[Dan62] G. Danby et al., "Observation of High-Energy Neutrino Reactions and the Existence of Two Kinds of Neutrinos," *Phys. Rev. Lett.*, vol. 9, no. 1, pp. 36 – 44, 1962, DOI: 10.1103/PhysRevLett.9.36.

[Dav64] R. Davis Jr., "Solar Neutrinos. II. Experimental," *Phys. Rev. Lett.*, vol. 12, no. 11, pp. 303 – 305, 1964, DOI: 10.1103/PhysRevLett.12.303.

[Dav94] ——, "A review of the homestake solar neutrino experiment," *Progress in Particle and Nuclear Physics*, vol. 32, pp. 13 – 32, 1994, DOI: 10.1016/0146-6410(94)90004-3.

[DEC79] R. Davis Jr., J. C. Evans, and B. T. Cleveland, "The solar neutrino problem," *AIP Conf. Proc.*, vol. 52, no. 17, 1979, DOI: 10.1063/1.31802.

[DeC89] D. DeCamp et al. (ALEPH Collaboration), "Determination of the number of light neutrino species," *Phys. Lett. B*, vol. 231, no. 4, pp. 519 – 529, 1989, DOI: 10.1016/0370-2693(89)90704-1.

[Doe13] P. Doe, F. Harms, H. Robertson, J. Schwarz, M. Steidl, "Quench Report," 2013, internal KATRIN document. [Online]. Available: https://fuzzy.fzk.de/bscw/bscw.cgi/d857193/4th%20pich%20quench%20report.pdf

[DON01] DONUT Collaboration, "Observation of Tau Neutrino Interactions," *Phys. Lett. B*, vol. 504, no. 3, pp. 218 – 224, 2001, DOI: 10.1016/S0370-2693(01)00307-0.

[Dre13] G. Drexlin, V. Hannen, S. Mertens, C. Weinheimer, "Current Direct Neutrino Mass Experiments," *Advances in High Energy Physics*, p. 293986, 2013, DOI: 10.1155/2013/293986.

[Dre15a] G. Drexlin, "Excited Molecules and Atoms as background source," 2015, internal KATRIN talk, 28th collaboration meeting. [Online]. Available: fuzzy.fzk.de/bscw/bscw.cgi/d950495/95-TRP-5833-D1.3-GDrexlin.pptx

[Dre15b] ——, "Rydberg states of hydrogen atoms - a novel source of background," 2015, internal KATRIN talk, SDS2b Workshop, KIT. [Online]. Available: https://indico.scc.kit.edu/indico/event/104/session/1/contribution/4/material/slides/0.pptx

[Dwy15] D. A. Dwyer, "Antineutrinos from nuclear reactors: recent oscillation measurements," *New J. Phys.*, vol. 17, p. 025003, 2015, DOI: 10.1088/1367-2630/17/2/025003.

[Dyb14] S. Dyba, "Repair of electrical short-circuits in wire electrode system - status and perspectives," 2014, internal KATRIN document. [Online]. Available: http://fuzzy.fzk.de/bscw/bscw.cgi/d931902/30-WRP-3506-01-Wire_Electrode_Repair_Report-DRAFT-V2014-07-21.pdf

[Dyb16] ——, 2016, doctoral thesis in preparation.

[Ebe13] J. Ebert et al., "Current Status and Future Perspectives of the COBRA Experiment," *Advances in High Energy Physics*, vol. 2013, p. 703572, 2013, DOI: 10.1155/2013/703572.

[Efr79] B. Efron, "The 1977 Rietz Lecture - Bootstrap Methods: Another Look at the Jackknife," *The Annals of Statistics*, vol. 7, no. 1, pp. 1 – 26, 1979.

[Eic00a] B. Eichler, H. P. Zimmermann, H. W. Gäggeler, "Adsorption of Radon on Ice Surfaces," *J. Phys. Chem. A*, vol. 104, pp. 3126–3131, 2000, DOI: 10.1021/jp9932158.

[Eic00b] R. Eichler, H. P. Zimmermann, H. W. Gäggeler, "Adsorption of Radon on Ice Surfaces," *J. Phys. Chem. A*, vol. 104, pp. 3126 – 3131, 2000, DOI: 10.1021/jp9932158.

[Eic08] F. Eichelhardt et al., "First tritium results of the KATRIN test experiment Trap," *Fusion Science and Technology*, vol. 54, no. 2, pp. 615 – 618, 2008.

[Eli15] S. Eliseev et al., "Direct Measurement of the Mass Difference of $^{163}$Ho and $^{163}$Dy Solves the Q-Value Puzzle for the Neutrino Mass Determination," *Phys. Rev. Lett.*, vol. 115, p. 062501, 2015, DOI: 10.1103/PhysRevLett.115.062501.

[Erh12] M. Erhard, "Untersuchung der Langzeitstabilität des nuklearen Standards für die Energieskala des KATRIN-Experiments," *Karlsruhe Institute of Technology*, 2012, diploma thesis.

[Erh14] M. Erhard et al., "High-voltage monitoring with a solenoid retarding spectrometer at the KATRIN experiment," *Journal of Instrumentation*, vol. 9, p. P06022, 2014, DOI: 10.1088/1748-0221/9/06/P06022.

[Erh15] M. Erhard, 2015, doctoral thesis in preparation.

[ES02] R. Eichler and M. Schädel, "Adsorption of Radon on Metal Surfaces: A Model Study for Chemical Investigations of Elements 112 and 114," *J. Phys. Chem. B*, vol. 106, pp. 5413 – 5420, 2002, DOI: 10.1021/jp015553q.

[EV02] S. R. Elliott and P. Vogel, "Double Beta Decay," *Annual Review of Nuclear and Particle Science*, vol. 52, pp. 115 – 151, 2002, DOI: 10.1146/annurev.nucl.52.050102.090641.

[Far14] Faro, "FaroArm," 2014. [Online]. Available: http://www.faro.com/en-us/products/metrology/measuring-arm-faroarm/overview

[Fel07] G. Feldman, M. Messier, J. Cooper, R. Ray, N. Grossman (The NOvA Collaboration), "NuMI Off-Axis $\nu_e$ Appearance Experiment," 2007. [Online]. Available: http://www-nova.fnal.gov/nova_cd2_review/tdr_oct_23/tdr.htm

[Feo08] A. I. Feoktistov, et al., "Investigation of the $e_0$-electron yield from the surface of thin films under bombardment by $\alpha$ and $\beta$ particles from radioactive sources," *Bull. Rus. Acad. Sci. Phys.*, vol. 72, no. 2, pp. 262 – 265, 2008.

[Fer34] E. Fermi, "Versuch einer Theorie der $\beta$-Strahlen. I," *Zeitschrift für Physik*, vol. 88, no. 3 - 4, pp. 161 – 177, 1934, DOI: 10.1007/BF01351864.

[FG15] D. Furse and S. Groh et al., "Kassiopeia: A Modern, Extensible C++ Particle Tracking Package," 2015, paper in preparation.

[FGV14] F. Fraenkle, F. Glück, and K. Valerius et al., "Penning discharge in the KATRIN pre-spectrometer," *Journal of Instrumentation*, vol. 9, no. 1, p. P07028, 2014, DOI:10.1088/1748-0221/9/07/P07028.

[Fis12] J. Fischer, "Analysen zur Langzeitstabilität und den Betriebsmodi des KATRIN Pinch-Magneten," *Karlsruhe Institute of Technology*, 2012, bachelor thesis.

[Fix96] D. J. Fixsen, et al., "The Cosmic Microwave Background Spectrum from the Full COBE/FIRAS Data Set," *The Astrophysical Journal*, vol. 473, no. 2, 1996, DOI: 10.1086/178173.

[Fix09] D. J. Fixsen, "The Temperature of the Cosmic Microwave Background," *The Astrophysical Journal*, vol. 707, no. 2, 2009, DOI: 10.1088/0004-637X/707/2/916.

[For08] Forschungszentrum Karlsruhe, Hauptabteilung Sicherheit, "Ergebnisse der gammaspektroskopischen Analyse," 2008, internal KATRIN document. [Online]. Available: http://fuzzy.fzk.de/bscw/bscw.cgi/d495586/MPI-0201_1_Getter_Evaluation.pdf

[For12] R. G. Forbes, "Extraction of emission parameters for large-area field emitters, using a technically complete Fowler-Nordheim-type equation," *Nanotechnology*, vol. 23, no. 9, p. 095706, 2012, DOI: 10.1088/0957-4484/23/9/095706.

[Fra10] F. Fraenkle, "Background Investigations of the KATRIN Pre-Spectrometer," *Karlsruhe Institute of Technology*, 2010, doctoral thesis.

[Fra11] F. Fraenkle et al., "Radon induced background processes in the KATRIN pre-spectrometer," *Astroparticle Physics*, vol. 35, no. 3, pp. 128 – 134, 2011, DOI: 10.1016/j.astropartphys.2011.06.009.

[Fra13] F. Fraenkle, "analysis of main spectrometer background at 0V (symmetric magnetic fields)," 2013, internal KATRIN elog. [Online]. Available: https://neutrino.ikp.kit.edu:8080/SDS-Measurements/48

[Fuk94] K. Fukuda et al., "Atmospheric $\nu_\mu/\nu_e$ ratio in the multi-GeV energy range," *Phys. Lett. B*, vol. 335, pp. 237 – 245, 1994, DOI: 10.1016/0370-2693(94)91420-6.

[Fuk96] Y. Fukuda et al. (Kamiokande Collaboration), "Solar Neutrino Data Covering Solar Cycle 22," *Phys. Rev. Lett.*, vol. 77, pp. 1683 – 1686, 1996, DOI: 10.1103/PhysRevLett.77.1683.

[Fuk98] Y. Fukuda et al. (Super-Kamiokande Collaboration), "Evidence for Oscillation of Atmospheric Neutrinos," *Phys. Rev. Lett.*, vol. 81, no. 8, pp. 1562 – 1567, 1998, DOI: 10.1103/PhysRevLett.81.1562.

[Fuk02] S. Fukuda et al. (Super-Kamiokande Collaboration), "Determination of solar neutrino oscillation parameters using 1496 days of Super-Kamiokande-I data," *Phys. Lett. B*, vol. 539, pp. 179 – 187, 2002, DOI: 10.1016/S0370-2693(02)02090-7.

[Fuk03] ——, "The Super-Kamiokande detector," *Nucl. Inst. Meth. Phys. Res. A*, vol. 501, pp. 418 – 462, 2003, DOI: 10.1016/S0168-9002(03)00425-X.

[Fur39] W. H. Furry, "On Transition Probabilities in Double Beta-Disintegration," *Phys. Rev.*, vol. 56, no. 12, pp. 1184 – 1193, 1939, DOI: 10.1103/PhysRev.56.1184.

[Gal88] T. F. Gallagher, "Rydberg atoms," *Rep. Prog. Phys.*, vol. 51, pp. 143 – 188, 1988, DOI: 10.1088/0034-4885/51/2/001.

[Gal94] ——, "Rydberg atoms," *Cambridge University Press*, 1994, ISBN: 978-0-521-02166-1 (Paperback).

[GAL99] GALLEX Collaboration, "GALLEX solar neutrino observations: results for GALLEX IV," *Physics Letters B*, vol. 447, no. 1 - 2, pp. 127 – 133, 1999, DOI: 10.1016/S0370-2693(98)01579-2.

[Gal13] P. T. Gallagher, "Introduction to Plasma Physics," 2013, Lecture of the Astrophysics Research Group, Trinity College Dublin. [Online]. Available: http://www.tcd.ie/Physics/people/Peter.Gallagher/lectures/PlasmaPhysics/

[Gan11] A. Gando et al. (KamLAND Collaboration), "Constraints on $\theta_{13}$ from A Three-Flavor Oscillation Analysis of Reactor Antineutrinos at KamLAND," *Phys. Rev. D*, vol. 83, p. 052002, 2011, DOI: 10.1103/PhysRevD.83.052002.

[Gas14] L. Gastaldo et al., "The Electron Capture $^{163}$Ho Experiment ECHo," *J. Low Temp. Phys.*, vol. 176, no. 5, pp. 876 – 884, 2014, DOI: 10.1007/s10909-014-1187-4.

[GGS58] M. Goldhaber, L. Grodzins, and A. W. Sunyar, "Helicity of Neutrinos," *Phys. Rev.*, vol. 109, no. 3, pp. 1015 – 1017, 1958, DOI: 10.1103/PhysRev.109.1015.

[GH14] T. Gaisser and F. Halzen, "IceCube," *Annu. Rev. Nucl. Part. Sci.*, vol. 64, pp. 101 – 123, 2014, DOI: 10.1146/annurev-nucl-102313-025321.

[Gil10] W. Gil et al., "The Cryogenic Pumping Section of the KATRIN Experiment," *Applied Superconductivity, IEEE Transactions*, vol. 20, no. 3, pp. 316 – 319, 2010, DOI: 10.1109/TASC.2009.2038581.

[Gla61] S. L. Glashow, "Partial Symmetries of Weak Interactions," *Nucl. Phys.*, vol. 22, no. 4, pp. 579 – 588, 1961, DOI: 10.1016/0029-5582(61)90469-2.

[Glu10] I. L. Glukhov, E. A. Nekipelov and V. D. Ovsiannikov, "Blackbody-induced decay, excitation and ionization rates for Rydberg states in hydrogen and helium atoms," *Journal of Physics B*, vol. 43, p. 125002, 2010, DOI: 10.1088/0953-4075/43/12/125002.

[Glu13] F. Glueck et al., "Electromagnetic design of the large-volume air coil system of the KATRIN experiment," *New Journal of Physics*, vol. 15, p. 083025, 2013, DOI: 10.1088/1367-2630/15/8/083025.

[Glu15] F. Glueck, "electron storage simulation at small vessel potential," 2015, internal KATRIN elog. [Online]. Available: https://neutrino.ikp.kit.edu:8080/SDS-Analysis/63

[GNO05] GNO Collaboration, "Complete results for five years of GNO solar neutrino observations," *Physics Letters B*, vol. 616, no. 3 - 4, pp. 174 – 190, 2005, DOI: 10.1016/j.physletb.2005.04.068.

[Goe35] M. Goeppert-Mayer, "Double Beta-Disintegration," *Phys. Rev.*, vol. 48, no. 6, pp. 512 – 516, 1935, DOI: 10.1103/PhysRev.48.512.

[Goe10] S. Goerhardt, "Reduktion der durch Radon induzierten Untergrundprozesse in den KATRIN Spektrometern," *Karlsruhe Institute of Technology*, 2010, diploma thesis.

[Goe14] ——, "Background Reduction Methods and Vacuum Technology at the KATRIN Spectrometers," *Karlsruhe Institute of Technology*, 2014, doctoral thesis.

[Gol61] J. Goldstone, "Field theories with Superconductor solutions," *Il Nuovo Cimento*, vol. 19, no. 1, pp. 154 – 164, 1961, DOI: 10.1007/BF02812722.

[Gou10] J. Goullon, "Installation and commissioning of the monitor spectrometer," *Karlsruhe Institute of Technology*, 2010, diploma thesis.

[GP69] V. Gribov and B. Pontecorvo, "Neutrino Astronomy and Lepton Charge," *Phys. Lett. B*, vol. 28, no. 7, pp. 493 – 496, 1969, DOI: 10.1016/0370-2693(69)90525-5.

[Gro10] S. Groh, "Untersuchung von UV-Laser induziertem Untergrund am KATRIN Vorspektrometer," *Karlsruhe Institute of Technology*, 2010, diploma thesis.

[Gro11] S. Grohmann, T. Bode, H. Schön, M. Süßer, "Precise temperature measurement at 30 K in the KATRIN source cryostat," *Cryogenics*, vol. 51, no. 8, pp. 438 – 445, 2011, DOI: 10.1016/j.cryogenics.2011.05.001.

[Gro13] S. Grohmann, T. Bode, M. Hötzel, H. Schön, M. Süßer, T. Wahl, "The thermal behaviour of the tritium source in KATRIN," *Cryogenics*, vol. 55 - 56, pp. 5 – 11, 2013, DOI: 10.1016/j.cryogenics.2013.01.001.

[Gro15] S. Groh, "Modeling of the Response Function and Measurement of Transmission Properties of the KATRIN Experiment," *Karlsruhe Institute of Technology*, 2015, doctoral thesis.

[Gui10] V. E. Guiseppe, S. R. Elliott, A. Hime, K. Rielage, S. Westerdale, "A Radon Progeny Deposition Model," 2010, arXiv:1101.0126 [nucl-ex].

[Hab09] F. Habermehl, "Electromagnetic measurements with the KATRIN pre-spectrometer," *Universität Karlsruhe*, 2009, doctoral thesis.

[Hac15] M. Hackenjos, "Die Differentielle Pumpstrecke des KATRIN-Experiments - Inbetriebnahme und Charakterisierung des Supraleitenden Magnetsystems," *Karlsruhe Institute of Technology*, 2015, master thesis.

[Han07] V. Hannen, "Production of the wire electrode for the KATRIN main spectrometer," 2007, internal KATRIN talk, 13th collaboration meeting. [Online]. Available: http://fuzzy.fzk.de/bscw/bscw.cgi/d425777/95-TRP-4303-S1-VHannen.pdf

[Han08] ——, "Results of additional test measurements of the main spectrometer electrode modules," 2008, internal KATRIN talk, 15th collaboration meeting. [Online]. Available: http://fuzzy.fzk.de/bscw/bscw.cgi/d477715/95-TRP-4538-C1-VHannen.pdf

[Han13] V. Hannen, H.-W. Ortjohann, M. Zacher, Ch. Weinheimer, "Electrical short circuits in the main spectrometer wire electrode," 2013, internal KATRIN document. [Online]. Available: https://fuzzy.fzk.de/bscw/bscw.cgi/d875473/430-doc-3-9001-shortcircuit_report.pdf

[Har12] F. Harms, "Assembly and First Results of the KATRIN Focal-Plane Detector System at KIT," *Karlsruhe Institute of Technology*, 2012, diploma thesis.

[Hax13] W. C. Haxton, R. G. H. Robertson, A. M. Serenelli, "Solar Neutrinos: Status and Prospects," *Annu. Rev. Astron. Astrophys.*, vol. 51, pp. 21 – 61, 2013, DOI: 10.1146/annurev-astro-081811-125539.

[Hel02] R. L. Helmer et al. (SNO Collaboration), "First Results from the Sudbury Neutrino Observatory," *Nucl. Phys. B (Proc. Suppl.)*, vol. 111, no. 1 - 3, pp. 122 – 127, 2002, DOI: 10.1016/S0920-5632(02)01693-6.

[Hig64] P. W. Higgs, "Broken Symmetries and the Masses of Gauge Bosons," *Phys. Rev. Lett.*, vol. 13, p. 508, 1964, DOI: 10.1103/PhysRevLett.13.508.

[Hil11] B. Hillen, "Untersuchung von Methoden zur Unterdrückung des Spektrometeruntergrunds beim KATRIN Experiment," *Westfälische Wilhelms-Universität Münster*, 2011, doctoral thesis.

[Hil15a] D. Hilk, F. Fränkle, F. Harms, M. Kraus, F. Glück, "Measurements with Static Electric Dipole," 2015, internal KATRIN elog. [Online]. Available: https://neutrino.ikp.kit.edu:8080/SDS-Measurements+Phase+2/73

[Hil15b] D. Hilk, M. Kraus, F. Fränkle, F. Harms, F. Glück, "Measurements with Pulsed Electric Dipole," 2015, internal KATRIN elog. [Online]. Available: https://neutrino.ikp.kit.edu:8080/SDS-Measurements+Phase+2/90

[Hil16] D. Hilk, 2016, doctoral thesis in preparation.

[Hin13] G. Hinshaw et al., "Nine-Year Wilkinson Microwave Anisotropy Probe (WMAP) Observations: Cosmological Parameter Results," *The Astrophysical Journal Supplement Series*, vol. 208, no. 2, p. 19, 2013, DOI: 10.1088/0067-0049/208/2/19.

[Hir87] K. Hirata et al., "Observation of a neutrino burst from the supernova SN1987A," *Phys. Rev. Lett.*, vol. 58, p. 1490, 1987, DOI: 10.1103/PhysRevLett.58.1490.

[Hir88a] ——, "Observation in the Kamiokande-II detector of the neutrino burst from supernova SN1987A," *Phys. Rev. D*, vol. 38, p. 448, 1988, DOI: 10.1103/PhysRevD.38.448.

[Hir88b] K. S. Hirata et al., "Experimental study of the atmospheric neutrino flux," *Phys. Lett. B*, vol. 205, no. 2 - 3, pp. 416 – 420, 1988, DOI: 10.1016/0370-2693(88)91690-5.

[Hoe12] M. Hoetzel, "Simulation and analysis of source-related effects for KATRIN," *Karlsruhe Institute of Technology*, 2012, doctoral thesis.

[How04] M. A. Howe et al., "Sudbury neutrino observatory neutral current detector acquisition software overview," *Nuclear Science, IEEE Transactions*, vol. 51, no. 3, pp. 878 – 883, 2004, DOI: 10.1109/TNS.2004.829527.

[How09] M. A. Howe, et al., "ORCA, An Object-Oriented Real-Time Data-Acquisition System," *TUNL XLVIII PROGRESS REPORT*, vol. 48, pp. 171 – 172, 2009. [Online]. Available: http://www.tunl.duke.edu/documents/public/tunlxlviii.pdf

[How14] ——, "ORCA webpage," 2014. [Online]. Available: http://orca.physics.unc.edu/

[Hug08] K. Hugenberg, "Design of the electrode system of the KATRIN main spectrometer," *Westfälische Wilhelms-Universität Münster*, 2008, diploma thesis.

[Jan03] R. K. Janev, D. Reiter, U. Samm, "Collision Processes in Low-Temperature Hydrogen Plasmas," *Berichte des Forschungszentrums Jülich*, vol. 4105, 2003.

[Jan15] A. Jansen, "The Cryogenic Pumping Section of the KATRIN Experiment - Design Studies and Experiments for the Commissioning," *Karlsruhe Institute of Technology*, 2015, doctoral thesis.

[JK94] V. T. Jordanov and G. F. Knoll, "Digital synthesis of pulse shapes in real time for high resolution radiation spectroscopy," *Nucl. Inst. and Meth. in Phys. Res. A*, vol. 345, no. 2, pp. 337 – 345, 1994, DOI: 10.1016/0168-9002(94)91011-1.

[Jun89] A. Junod, D. Eckert, G. Triscone, J. Müller, W. Reichardt, "A study of the magnetic transitions in CuO: specific heat (1-330 K), magnetic susceptibility and phonon density of states," *J. Phys.: Condens. Matter*, vol. 1, pp. 8021 – 8034, 1989.

[Jur08] M. Juretzko, "Studie zur geometrischen Vermessung der Modul-Befestigungsbolzen des KATRIN Spektrometertanks," 2008, internal KATRIN document.

[Jur09] ——, "Positioning of the Electrode Modules of the KATRIN Experiment by Using a Laser Tracker," *Optical 3-D Measurement Techniques IX*, vol. 2, pp. 91 – 98, 2009.

[Kaj98] T. Kajita for the Super-Kamiokande and Kamiokande collaborators, "Atmospheric neutrino results from Super-Kamiokande and Kamiokande," *Nucl. Phys. B (Proc. Suppl.)*, vol. 77, pp. 123 – 132, 1998, DOI: 10.1016/S0920-5632(99)00407-7.

[Kaj10] T. Kajita, "Atmospheric neutrinos and discovery of neutrino oscillations," *Proc. Jpn. Acad. B*, vol. 86, pp. 303 – 321, 2010, DOI: 10.2183/pjab.86.303.

[KL13] S. F. King and C. Luhn, "Neutrino mass and mixing with discrete symmetry," *Reports on Progress in Physics*, vol. 76, no. 5, p. 056201, 2013, DOI: 10.1088/0034-4885/76/5/056201.

[Kla88] H. V. Klapdor, "Neutrinos," *Springer-Verlag*, 1988, ISBN: 978-3-642-46650-2.

[Kla01] H. V. Klapdor-Kleingrothaus, A. Dietz, H. L. Harney, I.V. Krivosheina, "Evidence for Neutrinoless Double Beta Decay," *Modern Physics Letters A*, vol. 16, no. 37, pp. 2409 – 2420, 2001, DOI: 10.1142/S0217732301005825.

[Kle14] M. Kleesiek, "A Data Analysis and Sensitivity-Optimization Framework for the KATRIN Experiment," *Karlsruhe Institute of Technology*, 2014, doctoral thesis.

[KM69] T. Kirsten and H. W. Müller, "Observation of $^{82}$Se double-beta decay in selenium ores," *Earth and Planetary Science Letters*, vol. 6, no. 4, pp. 271 – 274, 1969, DOI: 10.1016/0012-821X(69)90167-8.

[Kno10] G. F. Knoll, "Radiation Detection and Measurement, 4th Edition," *John Wiley & Sons, Inc.*, 2010, ISBN: 978-0-470-13148-0 (hardback).

[Kop08] A. Kopmann et al., "FPGA-based DAQ system for multi-channel detectors," *Nuclear Science Symposium Conference Record, 2008. NSS 08. IEEE*, pp. 3186 – 3190, 2008, DOI: 10.1109/NSSMIC.2008.4775027.

[Kos12] A. Kosmider, "Tritium Retention Techniques in the KATRIN Transport Section and Commissioning of its DPS2-F Cryostat," *Karlsruhe Institute of Technology*, 2012, doctoral thesis.

[KR83] P. Kruit and F. H. Read, "Magnetic field paralleliser for $2\pi$ electron-spectrometer and electron-image magnifier," *Journal of Physics E*, vol. 16, no. 4, p. 313, 1983, DOI: 10.1088/0022-3735/16/4/016.

[Kra99] D. Kraemer, "Vacuum systems of electron storage rings," *Cern-Open-2000-289*, pp. 307 – 320, 1999, talk at the CERN Accelerator School Course on Vacuum Technology for Particle Accelerators.

[Kra05] C. Kraus et al., "Final results from phase II of the Mainz neutrino mass search in tritium $\beta$ decay," *The European Physical Journal C*, vol. 40, no. 4, pp. 447 – 468, 2005, DOI: 10.1140/epjc/s2005-02139-7.

[Kra15a] M. Kraus, 2015, doctoral thesis in preparation.

[Kra15b] M. Krause, "Molflow+ simulations of radon decays in the main spectrometer," 2015, internal KATRIN talk, 28th collaboration meeting. [Online]. Available: http://fuzzy.fzk.de/bscw/bscw.cgi/d950125/95-TRP-5803-A1.3-MKrause.pdf

[Kuc16] L. Kuckert, 2016, doctoral thesis in preparation.

[Lan44] L. Landau, "On the energy loss of fast particles by ionization," *J.Phys.(USSR)*, vol. 8, pp. 201 – 205, 1944.

[Laz81] G. Lazarides, Q. Shafi, C. Wetterich, "Proton lifetime and fermion masses in an SO(10) model," *Nucl. Phys. B*, vol. 181, pp. 287 – 300, 1981, DOI: 10.1016/0550-3213(81)90354-0.

[Leb10] M. L. Leber, "Monte Carlo Calculations of the Intrinsic Detector Backgrounds for the Karlsruhe Tritium Neutrino Experiment," *University of Washington*, 2010, doctoral thesis.

[Leh83] G. W. Lehman, "Rate of ionisation of H and Na Rydberg atoms by black-body radiation," *J. Phys. B: At. Mol. Phys.*, vol. 16, pp. 2145 – 2156, 1983, DOI: 10.1088/0022-3700/16/12/011.

[Lei14] B. Leiber, "Investigations of background due to secondary electron emission in the KATRIN-experiment," *Karlsruhe Institute of Technology*, 2014, doctoral thesis.

[Leu06] M. Leung, "The Borexino Solar Neutrino Experiment: Scintillator Purification and Surface Contamination," *Princeton University*, 2006, doctoral thesis.

[Lid03] A. Liddle, "An Introduction to Modern Cosmology," *Wiley*, 2003, ISBN: 978-1-118-50214-3.

[Lin15] J. Linek, "Investigation of the muon induced background at the KATRIN main spectrometer," *Karlsruhe Institute of Technology*, 2015, master thesis.

[LL02] T. J. Loredo and D. Q. Lamb, "Bayesian analysis of neutrinos observed from supernova SN 1987A," *Phys. Rev. D*, vol. 65, p. 063002, 2002, DOI: 10.1103/PhysRevD.65.063002.

[Lob85] V. M. Lobashev, "A method for measuring the electron antineutrino rest mass," *Nucl. Inst. and Meth. in Phys. Res. A*, vol. 240, no. 2, pp. 305 – 310, 1985, DOI: 10.1016/0168-9002(85)90640-0.

[LR60] L. Lassen and G. Rau, "Die anlagerung radioaktiver atome an aerosole (schwebstoffe)," *Zeit. für Phys.*, vol. 160, pp. 504 – 519, 1960, german, abstract in english.

[LT14] B. Leiber and N. Trost, "210Pb Simulations," 2014, internal KATRIN elog. [Online]. Available: https://neutrino.ikp.kit.edu:8080/SDS-Analysis/28

[LU00] L. L. Lucas and M. P. Unterweger, "Comprehensive Review and Critical Evaluation of the Half-Life of Tritium," *Journal of Research of the National Institute of Standards and Technology*, vol. 105, no. 4, pp. 541 – 549, 2000, DOI: 10.6028/jres.105.043.

[Luk12] S. Lukic et al., "Measurement of the gas-flow reduction factor of the KATRIN DPS2-F differential pumping section," *Vacuum*, vol. 86, no. 8, pp. 1126 – 1133, 2012, DOI: 10.1016/j.vacuum.2011.10.017.

[Luo06] X. Luo, Chr. Day, V. Hauer, O.B. Malyshev, R.J. Reid, F. Sharipov, "Monte Carlo simulation of gas flow through the KATRIN DPS2-F differential pumping system," *Vacuum*, vol. 80, no. 8, pp. 864 – 869, 2006, DOI: 10.1016/j.vacuum.2005.11.044.

[LY56] T. D. Lee and C. N. Yang, "Question of Partity Conservation in Weak Interactions," *Phys. Rev.*, vol. 104, no. 1, pp. 254 – 258, 1956, DOI: 10.1103/PhysRev.104.254.

[Maj37] E. Majorana, "Teoria symmetrica dell elethrone e del positrone," *Il Nuovo Cimento (1924-1942)*, vol. 14, pp. 171 – 184, 1937, DOI: 10.1007/BF02961314.

[Mar14] E. L. Martin, "FPD Wafer Test Board," 2014, internal KATRIN document. [Online]. Available: http://fuzzy.fzk.de/bscw/bscw.cgi/d875187/FPDWaferTester.pdf

[Mei22] L. Meitner, "Über die Entstehung der $\beta$-Strahl-Spektren radioaktiver Substanzen," *Z. Physik*, vol. 9, no. 1, pp. 131 – 144, 1922, DOI: 10.1007/BF01326962.

[Mer12a] S. Mertens, "Study of Background Processes in the Electrostatic Spectrometers of the KATRIN experiment," *Karlsruhe Institute of Technology*, 2012, doctoral thesis.

[Mer12b] S. Mertens et al., "Stochastic Heating by ECR as a Novel Means of Background Reduction in the KATRIN spectrometers," *Journal of Instrumentation*, vol. 7, p. 08025, 2012, DOI: 10.1088/1748-0221/7/08/P08025.

[Mer13] ——, "Background due to stored electrons following nuclear decays in the KATRIN spectrometers and its impact on the neutrino mass sensitivity," *Astroparticle Physics*, vol. 41, pp. 52 – 62, 2013, DOI: 10.1016/j.astropartphys.2012.10.005.

[Mer15] S. Mertens, "Rydberg Background Simulations," 2015, internal KATRIN talk, SDS2b Workshop, KIT. [Online]. Available: https://indico.scc.kit.edu/indico/event/104/session/1/contribution/5/material/slides/1.pdf

[Mes15] M. Messier, "Exploring Neutrinos via Oscillations in the Atmosphere, at Reactors, and at Accelerators," 2015, talk at the DPF Meeting of the American Physical Society in Ann Arbour, Michigan. [Online]. Available: http://nova-docdb.fnal.gov/cgi-bin/RetrieveFile?docid=13886&filename=DPF2015-Messier.pdf&version=2

[MNS62] Z. Maki, M. Nakagawa, and S. Sakata, "Remarks on the Unified Model of Elementary Particles," *Progress of Theoretical Physics*, vol. 28, no. 5, pp. 870 – 880, 1962, DOI: 10.1143/PTP.28.870.

[Moh81] R. N. Mohapatra and G. Senjanovic, "Neutrino masses and mixings in gauge models with spontaneous parity violation," *Phys. Rev. D*, vol. 23, no. 1, pp. 165 – 180, 1981, DOI: 10.1103/PhysRevD.23.165.

[MP15] B. Monreal and F. Priester, "Rear Section status update," 2015, internal KATRIN talk, 28th collaboration meeting. [Online]. Available: http://fuzzy.fzk.de/bscw/bscw.cgi/d950718/95-TRP-5841-S1-BMonreal.pdf

[MS80] R. N. Mohapatra and G. Senjanovic, "Neutrino Mass and Spontaneous Parity Nonconservation," *Phys. Rev. Lett.*, vol. 44, no. 14, pp. 912 – 915, 1980, DOI: 10.1103/PhysRevLett.44.912.

[MS86] S. P. Mikheyev and A. Y. Smirnov, "Resonant amplification of $\nu$ oscillations in matter and solar-neutrino spectroscopy," *Il Nuovo Cimento C*, vol. 9, no. 1, pp. 17 – 26, 1986, DOI: 10.1007/BF02508049.

[Mue14a] A. Mueller, "Field Alignment Studies at the KATRIN Pinch Magnet," *Karlsruhe Institute of Technology*, 2014, bachelor thesis.

[Mue14b] ——, "High Voltage Simulation of the PAE," 2014, internal KATRIN document. [Online]. Available: fuzzy.fzk.de/bscw/bscw.cgi/d968904/High%20voltage%20simulation%20of%20the%20PAE.pptx

[Mue15a] ——, "Report on the ongoing analysis of correlated events from the spectrometer surface," 2015, internal KATRIN elog. [Online]. Available: https://neutrino.ikp.kit.edu:8080/SDS-Analysis/65

[Mue15b] F. Mueller, "Efficiency Studies of the Background Suppression by a Liquid-Nitrogen Cooled Baffle System in the KATRIN Experiment," *Karlsruhe Institute of Technology*, 2015, master thesis.

[Mue16] A. Mueller, 2016, master thesis in preparation.

[Nat15] National Nuclear Data Center, Brookhaven National Laboratory, "NuDat (Nuclear Structure and Decay Data)," 2015. [Online]. Available: http://www.nndc.bnl.gov/nudat2/

[Nuc02] A. Nucciotti et al., "The Milano neutrino mass experiment with arrays of $AgReO_4$ microcalorimeters," *AIP Conf. Proc.*, vol. 605, p. 453, 2002, DOI: 10.1063/1.1457684.

[Nuc12] ——, "Neutrino mass calorimetric searches in the MARE experiment," *Nuclear Physics B - Proceedings Supplements, Neutrino 2010*, vol. 229 - 232, pp. 155 – 159, 2012, DOI: 10.1016/j.nuclphysbps.2012.09.025.

[Oer07] Oerlikon leybold vacuum, "IONIVAC IM 540 Ionization Gauge Controller - Operating Manual GA 09419_0402," 2007.

[Oer14] J. Oertlin, "Analysis of Radon-Induced Background during First Measurements at the KATRIN Main Spectrometer," *Karlsruhe Institute of Technology*, 2014, master thesis.

[Oli14] K. A. Olive et al. (Particle Data Group), "090001 (2014) Review of Particle Physics," *Chin. Phys. C*, vol. 38, 2014, DOI: 10.1088/1674-1137/38/9/090001.

[Osi12] A. Osipovicz et al., "A mobile Magnetic Sensor Unit for the KATRIN Main Spectrometer," *Journal of Instrumentation*, vol. 7, p. T06002, 2012, DOI: 10.1088/1748-0221/7/06/T06002.

[Ott94] E. Otten, "The Mainz neutrino mass experiment," *Prog. Part. Nucl. Phys.*, vol. 32, pp. 153–171, 1994, DOI: 10.1016/0146-6410(94)90016-7.

[Ott10] ——, "Searching the absolute neutrino mass in tritium $\beta$-decay - interplay between nuclear, atomic and molecular physics," *Hyperfine Interactions*, vol. 196, no. 1, pp. 3 – 23, 2010, DOI: 10.1007/s10751-009-0150-2.

[Pau30] W. Pauli, "Offener Brief an die Gruppe der Radioaktiven bei der Gauvereins-Tagung zu Tübingen," 1930. [Online]. Available: http://www.symmetrymagazine.org/sites/default/files/legacy/pdfs/200703/logbook_letter.pdf

[Pea95] K. Pearson, "Note on Regression and Inheritance in the Case of Two Parents," *Proc. R. Soc. Lond.*, vol. 58, pp. 240 – 242, 1895, DOI: 10.1098/rspl.1895.0041.

[Pen36] F. M. Penning, "Die Glimmentladung bei niedrigem Druck zwischen koaxialen Zylindern in einem axialen Magnetfeld," *Physica*, vol. 3, no. 9, pp. 873 – 894, 1936, DOI: 10.1016/S0031-8914(36)80313-9.

[Per75] M. L. Perl et al., "Evidence for Anomalous Lepton Production in $e^+ - e^-$ Annihilation," *Phys. Rev. Lett.*, vol. 35, no. 22, pp. 1489 – 1492, 1975, DOI: 10.1103/PhysRevLett.35.1489.

[Phi10] D. G. Phillips et al., "Characterization of an FPGA-based DAQ system in the KATRIN experiment," *Nuclear Science Symposium Conference Record (NSS/MIC), 2010 IEEE*, pp. 1399 – 1403, 2010, DOI: 10.1109/NSSMIC.2010.5874002.

[Pic90] A. Picard, "Aufbau und Test eines Solenoid-Retardierungs-Spektrometers zur Bestimmung der Neutrinoruhemasse aus dem Tritium-beta-Zerfall," *Universität Mainz*, 1990, doctoral thesis.

[Pic92] A. Picard et al., "A solenoid retarding spectrometer with high resolution and transmission for keV electrons," *Nucl. Inst. and Meth. in Phys. Res. B*, vol. 63, no. 3, pp. 345 – 358, 1992, DOI: 10.1016/0168-583X(92)95119-C.

[Piv00] M. Pivi, "Vacuum System and Synchrotron Radiation in the Very Large Hadron Collider - VLHC," 2000, talk at the VLHC annual meeting. [Online]. Available: http://www0.bnl.gov/magnets/docs/meetings/VLHC-101600/Mauro_Pivi.pdf

[Pon57a] B. Pontecorvo, "Inverse beta processes and nonconservation of lepton charge," *Zh. Eksp. Teor. Fiz.*, vol. 34, p. 247, 1957.

[Pon57b] ——, "Mesonium and anti-mesonium," *Zh. Eksp. Teor. Fiz.*, vol. 33, pp. 549 – 551, 1957.

[Pon67] ——, "Neutrino Experiments and the Problem of Conservation of Leptonic Charge," *Zh. Eksp. Teor. Fiz.*, vol. 53, pp. 1717 – 1725, 1967.

[Pra11] M. Prall, "Background Reduction of the KATRIN Spectrometers: Transmission Function of the Pre-Spectrometer and Systematic Test of the Main-Spectrometer Wire Electrode," *Westfälische Wilhelms-Universität Münster*, 2011, doctoral thesis.

[PRG12] M. Prall, P. Renschler, and F. Glück et al., "The KATRIN pre-spectrometer at reduced filter energy," *New Journal of Physics*, vol. 14, p. 073054, 2012, DOI: 10.1088/1367-2630/14/7/073054.

[PSW14] A. Poon, A. Smith, and J. Wolf, "Radon Emanation in the KATRIN Main Spectrometer," 2014, internal KATRIN document. [Online]. Available: fuzzy.fzk.de/bscw/bscw.cgi/d898720/LBNL-MainSpec_SST_Avtivity-Report-2013-v0.pdf

[Raa69] O. Raabe, "Concerning interactions that occur between radon decay products and aerosols," *Health Physics*, vol. 17, no. 2, p. 177, 1969.

[Rac37] G. Racah, "Sulla simmetria tra particelle e antiparticelle," *Il Nuovo Cimento*, vol. 14, no. 7, pp. 322 – 328, 1937, DOI: 10.1007/BF02961321.

[Ran15] P. Ranitzsch, K. Schlösser, T. Thümmler, J. Wolf, "Co-60 measurement," 2015, internal KATRIN elog. [Online]. Available: https://neutrino.ikp.kit.edu:8080/SDS-Measurements+Phase+2/157

[RC56] F. Reines and C. L. Cowan, "The Neutrino," *Nature*, vol. 178, pp. 446 – 449, 1956.

[Rei97] F. Reines, C. Cowan, "Celebrating the Neutrino, The Reines-Cowan Experiments - Detecting the Poltergeist," *Los Alamos Science*, vol. 25, pp. 4 – 27, 1997. [Online]. Available: http://www.fas.org/sgp/othergov/doe/lanl/pubs/00326606.pdf

[Rei98] J. Reichenbacher, "Untersuchung der optischen Eigenschaften großflächiger Plastikszintillatoren für den KARMEN-Upgrade," *Technische Universität Karlsruhe (TH)*, 1998, diploma thesis.

[Rei09] S. Reimer, "Ein elektrostatisches Dipolsystem zur Eliminierung von Ionen in der DPS2-F des KATRIN Experimentes," *Karlsruhe Institute of Technology*, 2009, diploma thesis.

[Ren11] P. Renschler, "A new Monte Carlo simulation code for low-energy electron interactions in silicon detectors," *Karlsruhe Institute of Technology*, 2011, doctoral thesis.

[RK88] R. G. H. Robertson and D. A. Knapp, "Direct measurement of neutrino mass," *Annual Review of Nuclear and Particle Science*, vol. 38, pp. 185 – 215, 1988.

[Roe15] M. Roellig, "Tritium analytics by beta induced x-ray spectrometry," *Karlsruhe Institute of Technology*, 2015, doctoral thesis.

[Rov13] P. Rovedo, "Muon induced secondary electrons at the KATRIN experiment - Detector installation and setup & data analysis," *Karlsruhe Institute of Technology*, 2013, diploma thesis.

[RP13] M. Röllig and F. Priester et al., "Activity monitoring of a gaseous tritium source by beta induced X-ray spectrometry," *Fusion Engineering and Design*, vol. 88, no. 6 - 8, pp. 1263 – 1266, 2013, DOI: 10.1016/j.fusengdes.2012.11.001.

[Rut03] E. Rutherford, "The Magnetic and Electric Deviation of the Easily Absorbed Rays from Radium," *Phil. Mag.*, vol. 5, no. 26, pp. 177 – 187, 1903.

[Sal68] A. Salam, "Weak and Electromagnetic Interactions," *Conf. Proc.*, vol. C680519, pp. 367 – 377, 1968.

[Sch75] J. A. Schiavone, K. C. Smyth and R. S. Freund, "Dissociative excitation of $H_2$ by electron impact: Translational spectroscopy of long-lived high Rydberg fragment atoms," *J. Chem. Phys.*, vol. 63, pp. 1043 – 1051, 1975, DOI: 10.1963/1.431445.

[Sch79] J. A. Schiavone, S. M. Tarr and R. S. Freund, "High-Rydberg atomic fragments from electron-impact dissociation of molecules," *J. Chem. Phys.*, vol. 70, pp. 4468 – 4473, 1979, DOI: 10.1063/1.437283.

[Sch84] G. Schiller, "A theoretical convective-transport model of indoor radon decay products," *University of California Berkeley*, 1984, doctoral thesis.

[Sch88] J. Schneps, "Proceedings of the International Conference on Neutrino Physics and Astrophysics. 13. Boston (Medford)," *World Scientific*, p. 574, 1988, ISBN: 978-9-971-50796-1.

[Sch11] M. Schupp, "Inbetriebnahme des Monitorspektrometers und erste Messungen," *Karlsruhe Institute of Technology*, 2011, diploma thesis.

[Sch13a] M. Schlösser, "Accurate calibration of the Raman system for the Karlsruhe Tritium Neutrino Experiment," *Karlsruhe Institute of Technology*, 2013, doctoral thesis.

[Sch13b] M. Schlösser et al., "Accurate calibration of the laser Raman system for the Karlsruhe Tritium Neutrino Experiment," *Journal of Mol. Struct.*, vol. 1044, pp. 61 – 66, 2013, DOI: 10.1016/j.molstruc.2012.11.022.

[Sch13c] J. Schwarz, "Background Investigation at Increased Argon Pressure," 2013, internal KATRIN talk, 25th collaboration meeting. [Online]. Available: http://fuzzy.fzk.de/bscw/bscw.cgi/d858187/95-TRP-5539-D1-JSchwarz.pdf

[Sch14a] S. Schmid, "Performance des Fokalebenendetektors zu Beginn der zweiten gemeinsamen Messphase mit dem KATRIN Hauptspektrometer," *Karlsruhe Institute of Technology*, 2014, bachelor thesis.

[Sch14b] R. W. Schnee et al., "Removal of long-lived $^{222}$Rn daughters by electropolishing thin layers of stainless steel," 2014, arXiv:1404.5843 [physics.ins-det].

[Sch14c] J. Schwarz, "The Detector System of the KATRIN Experiment - Implementation and First Measurements with the Spectrometer," *Karlsruhe Institute of Technology*, 2014, doctoral thesis.

[Sch15a] K. Schloesser, "Erwerb von offenen radioaktiven Stoffen," 2015, internal KATRIN document. [Online]. Available: http://fuzzy.fzk.de/bscw/bscw.cgi/d969922/Monats-meldung-Erwerb-offen-Jul-2015.pdf

[Sch15b] J. Schwarz, "ROI cut," 2015, internal KATRIN elog. [Online]. Available: https://neutrino.ikp.kit.edu:8080/SDS-Analysis/50

[Sco35] F. A. Scott, "Energy Spectrum of the Beta-Rays of Radium E," *Phys. Rev.*, vol. 48, no. 5, pp. 391 – 395, 1935, DOI: 10.1103/PhysRev.48.391.

[Sie14] Siemens AG, "Prozessleitsystem SIMATIC PCS 7," 2014, Catalog. [Online]. Available: https://www.automation.siemens.com/w2/efiles/pcs7/pdf/00/stpcs7_201415_catalog_de_Web.pdf

[Sim03] H. Simgen, C. Buck, G. Heusser, M. Laubenstein, W. Rau, "A new system for the $^{222}$Rn and $^{226}$Ra assay of water and results in the Borexino project," *Nucl. Inst. and Meth. in Phys. Res. A*, vol. 497, no. 2 - 3, pp. 407 – 413, 2003, DOI: 10.1016/S0168-9002(02)01823-5.

[Sim06] H. Simgen, "Ultrapure gases for GERDA," *Progress in Particle and Nuclear Physics*, vol. 57, no. 1, pp. 266 – 268, 2006, DOI: 10.1016/j.ppnp.2005.11.006.

[Sis04] M. Sisti et al., "New limits from the Milano neutrino mass experiment with thermal microcalorimeters," *Nucl. Inst. Meth. Phys. A*, vol. 520, no. 1 - 3, pp. 125 – 131, 2004, DOI: 10.1016/j.nima.2003.11.273.

[Sle11] M. Slezak, "The source of monoenergetic electrons for the monitoring of spectrometer in the KATRIN neutrino experiment," *Charles University in Prague, NPI Rez*, 2011, diploma thesis.

[Sle13] M. Slezak et al., "Electron line shape of the KATRIN monitor spectrometer," *Journal of Instrumentation*, vol. 8, p. T12002, 2013, DOI: 10.1088/1748-0221/8/12/T12002.

[SNO00] SNO Collaboration, "The Sudbury Neutrino Observatory," *Nucl. Inst. and Meth. in Phys. Res. A*, vol. 449, pp. 172 – 207, 2000, DOI: 10.1016/S0168-9002(99)01469-2.

[Sta13] N. Stallkamp, "Optimierung und erste Messung der Transmissionseigenschaften des KATRIN-Hauptspektrometers," *Karlsruhe Institute of Technology*, 2013, diploma thesis.

[Stu10] M. Sturm, "Aufbau und Test des Inner-Loop-Systems der Tritiumquelle von KATRIN," *Karlsruhe Institute of Technology*, 2010, doctoral thesis.

[SW64] A. Salam and J. C. Ward, "Electromagnetic and Weak Interactions," *Phys. Lett.*, vol. 13, no. 2, pp. 168 – 171, 1964, DOI: 10.1016/0031-9163(64)90711-5.

[Thu09] T. Thuemmler, R. Marx, C. Weinheimer, "Precision high voltage divider for the KATRIN experiment," *New Journal of Physics*, vol. 11, p. 103007, 2009, DOI: 10.1088/11367-2630/11/10/103007.

[Thu15] T. Thuemmler, J.Wolf, K.Schlösser, P. Ranitzsch, N.Trost, "Water shielding measurements," 2015, internal KATRIN elog. [Online]. Available: https://neutrino.ikp.kit.edu:8080/SDS-Measurements+Phase+2/158

[Tro15a] N. Trost, "Rydberg simulations," 2015, internal KATRIN talk, SDS2b Workshop, KIT. [Online]. Available: https://indico.scc.kit.edu/indico/event/104/session/1/contribution/5/material/slides/0.pdf

[Tro15b] N. Trost, P. Ranitzsch, K. Schlösser, A. Müller, F. Heizmann, F. Fränkle, J. Schwarz, "UV detection," 2015, internal KATRIN elog. [Online]. Available: https://neutrino.ikp.kit.edu:8080/SDS-Measurements+Phase+2/164

[Tro16] N. Trost, 2016, doctoral thesis in preparation.

[Ubi09] M. Ubieto-Diaz, D. Rodriguez, S. Lukic, Sz. Nagy, S. Stahl, K. Blaum, "A broad-band FT-ICR Penning trap system for KATRIN," *International Journal of Mass Spectrometry*, vol. 288, no. 1 - 3, pp. 1 – 5, 2009, DOI: 10.1016/j.ijms.2009.07.003.

[Ubi11] M. Ubieto-Diaz, "Off-line commissioning of a non-destructive FT-ICR detection system for monitoring the ion concentration in the KATRIN beamline," *Ruprecht-Karls-Universität, Heidelberg, Germany*, 2011, doctoral thesis.

[Uni15] United States Enviromental Protection Agency, "Radiation Protection: Radon," 2015. [Online]. Available: http://www.epa.gov/radiation/radionuclides/radon.html

[Val04] A. O. Valchuk, et al., "Study of the electron emission from the Al foil surface induced by $\alpha$-particles in forward and backward directions," *Ukr. J. Phys.*, vol. 49, no. 12, pp. 1145 – 1149, 2004.

[Val05] K. Valerius, "Simulations on tolarances for the inner electrode of the main spectrometer and check for residual radioactivity in wire materials," 2005, internal KATRIN talk, 9th collaboration meeting. [Online]. Available: http://fuzzy.fzk.de/bscw/bscw.cgi/d172207/95-TRP-1926-A2-KValerius.pdf

[Val06] ——, "Electromagnetic design and inner electrode for the KATRIN main spectrometer," *Progress in Particle and Nuclear Physics*, vol. 57, no. 1, pp. 58 – 60, 2006, DOI: 10.1016/j.ppnp.2005.11.011.

[Val09] ——, "Spectrometer-related background processes and their suppression in the KATRIN experiment," *Westfälische Wilhelms-Universität Münster*, 2009, doctoral thesis.

[Val10] ——, "The wire electrode system for the KATRIN main spectrometer," *Progress in Particle and Nuclear Physics*, vol. 64, no. 2, pp. 291 – 293, 2010, DOI: 10.1016/j.ppnp.2009.12.032.

[Van12] B. VanDevender et al., "Performance of a TiN-coated monolithic silicon pin-diode array under mechanical stress," *Nucl. Inst. and Meth. in Phys. Res. A*, vol. 673, pp. 46 – 50, 2012, DOI: 10.1016/j.nima.2012.01.033.

[vW35] C. F. v. Weizsäcker, "Zur Theorie der Kernmassen," *Zeitschrift für Physik*, vol. 96, no. 7 - 8, pp. 431 – 458, 1935, DOI: 10.1007/BF01337700.

[Wac15] O. Wack, "Automation of high-precision calibrations for the KATRIN high-voltage system," *Karlsruhe Institute of Technology*, 2015, master thesis.

[Wal14] B. L. Wall et al., "Dead layer on silicon p-i-n diode charged-particle detectors," *Nucl. Inst. Meth. Phys. Res. A*, vol. 744, pp. 73 – 79, 2014, DOI: 10.1016/j.nima.2013.12.048.

[Wan09] N. Wandkowsky, "Design and Background Simulations for the KATRIN Main Spectrometer and Air Coil System," *Karlsruhe Institute of Technology*, 2009, diploma thesis.

[Wan13a] ——, "Study of background and transmission properties of the KATRIN spectrometers," *Karlsruhe Institute of Technology*, 2013, doctoral thesis.

[Wan13b] N. Wandkowsky, G. Drexlin, F. M. Fränkle, F. Glück, S. Groh, S. Mertens, "Modeling of electron emission processes accompanying radon-$\alpha$-decays within electrostatic spectrometers," *New Journal of Physics*, vol. 15, p. 083040, 2013, DOI: 10.1088/1367-2630/15/8/083040.

[Wei67] S. Weinberg, "A Model of Leptons," *Phys. Rev. Lett.*, vol. 19, no. 21, pp. 1264 – 1266, 1967, DOI: 10.1103/PhysRevLett.19.1264.

[WH14] J. Wolf and F. Harms, "BG08.03 Calibration of main spec vacuum gauges," 2014, internal KATRIN elog. [Online]. Available: https://neutrino.ikp.kit.edu:8080/SDS-Measurements+Phase+2/10

[Wik15] Wikimedia, "Uranium decay series," 2015. [Online]. Available: http://commons.wikimedia.org/wiki/File:Decay_chain%284n+2,_Uranium_series%29.PNG

[Win11] A. Windberger, "Berechnungen und Simulationen zum Verhalten von Ionen in der differenziellen Pumpstrecke des KATRIN-Experiments," *Karlsruhe Institute of Technology*, 2011, diploma thesis.

[Wol78] L. Wolfenstein, "Neutrino oscillations in matter," *Phys. Rev. D*, vol. 17, p. 2369, 1978, DOI: 10.1103/PhysRevD.17.2369.

[Wol15a] J. Wolf, "Radon Processes in the KATRIN Experiment," 2015, Spring Meeting of the German Physical Society, Berlin. [Online]. Available: fuzzy.fzk.de/bscw/bscw.cgi/d953753/Wolf_Radon_KATRIN_DPG2015.pptx

[Wol15b] J. Wolf et al., "Commissioning of the vacuum system of the KATRIN Main Spectrometer," *Journal of Instrumentation*, 2015, paper in preparation.

[Wu 57] C. S. Wu et al., "Experimental Test of Parity Conservation in Beta Decay," *Phys. Rev.*, vol. 105, no. 4, pp. 1413 – 1415, 1957, DOI: 10.1103/PhysRev.105.1413.

[Wue07] S. Wuestling, "An inexpensive magnetometer system for the KATRIN main spectrometer," 2007, internal KATRIN talk, 12th collaboration meeting. [Online]. Available: http://fuzzy.fzk.de/bscw/bscw.cgi/d358586/95-TRP-4250-C1-SWuestling.pdf

[Wue11] ——, "KATRIN Main Detector (Focal Plane Detector) Electronics Design Description," 2011, internal KATRIN document. [Online]. Available: https://fuzzy.fzk.de/bscw/bscw.cgi/d732369/Description%20of%20FPD%20readout%20electronics.pdf

[WZ13a] M. Wójcik and G. Zuzel, "$^{226}$Ra, $^{210}$Pb, $^{210}$Bi and $^{210}$Po deposition and removal from surfaces and liquids," *J. Radioanal. Nucl. Chem.*, vol. 296, pp. 639 – 645, 2013, DOI: 10.1007/s10967-012-2180-5.

[WZ13b] ——, "Removal of the long-lived $^{222}$Rn daughters from copper and stainless steel surfaces," *Nucl. Inst. Meth. Phys. Res. A*, vol. 676, pp. 140 – 148, 2013, DOI: 10.1016/j.nima.2011.12.043.

[Zac09] M. Zacher, "Electromagnetic design and field emission studies for the inner electrode system of the KATRIN main spectrometer," *Westfälische Wilhelms-Universität Münster*, 2009, diploma thesis.

[Zbo11] M. Zboril, "Solid electron sources for the energy scale monitoring in the KATRIN experiment," *Westfälische Wilhelms-Universität Münster*, 2011, doctoral thesis.

[Zie04] J. F. Ziegler, "SRIM-2003," *Nucl. Inst. and Meth. in Phys. Res. B*, vol. 219 - 220, pp. 1027 – 1036, 2004, DOI: 10.1016/j.nimb.2004.01.208.

[Zie13] ——, "SRIM-2013, SRIM - The Stopping and Range of Ions in Matter," 2013. [Online]. Available: http://www.srim.org/

[Zub11] K. Zuber, "Neutrino Physics," *CRC Press*, vol. 2, 2011, ISBN: 978-1-4200-6471-1.

# Danksagung

Zum Abschluss möchte ich mich ganz herzlich bei all den Menschen bedanken, die mich in den spannenden und intensiven letzten drei Jahren bei meiner Promotion unterstützt und damit zum Gelingen dieser Doktorarbeit beigetragen haben. Mein besonderer Dank gilt hierbei:

- Prof. Dr. Guido Drexlin für die ausgesprochen gute und sehr motivierende Betreuung während der letzten drei Jahre und dafür, dass er mir die Möglichkeit gegeben hat, meine Promotion in einem so spannenden und abwechslungsreichen Umfeld wie dem KATRIN Experiment durchzuführen.
- Prof. Dr. Ulrich Husemann, der sich freundlicherweise zur Übernahme der Koreferenz dieser Arbeit bereiterklärt hat.
- Prof. Dr. Peter Doe, Prof. Dr. Hamish Robertson, Dr. Diana Parno, and all others of the US colleagues for their help and support and the great atmosphere in the detector working group of KATRIN.
- Prof. Dr. Sanshiro Enomoto for answering my many questions concerning data analysis and programming.
- Dr. Johannes Schwarz für die tolle Zusammenarbeit im Büro und am Detektorsystem und den vielen Spaß, den wir dabei hatten!
- Dr. Stefan Groh und Dr. Marco Kleesiek für die schöne Anfangszeit im gemeinsamen Büro und die vielen Hilfestellungen in Sachen Programmierung.
- Dr. Florian Fränkle und Axel Müller dafür, dass sie mir in den letzten Monaten den Rücken freigehalten haben und ich mich so voll auf das Verfassen dieser Arbeit konzentrieren konnte.
- Marcel Krause, Florian Müller, Dr. Klaus Schlösser und Dr. Joachim Wolf für die gute Zusammenarbeit bei den Messungen und den Simulationen zur Bestimmung der Baffle-Effizienz.
- Dr. Ferenc Glück, Rainer Gumbsheimer, Dr. Markus Steidl, Dr. Thomas Thümmler, Dr. Kathrin Valerius und Dr. Sascha Wüstling für ihre Unterstützung und die hilfreichen Diskussionen während der letzten drei Jahre.
- Allen Ingenieuren und Technikern, ohne deren unerbittlichen Einsatz keine der in dieser Arbeit beschriebenen Messungen hätte stattfinden können. Ein besonderer Dank geht hierbei an Armen Beglarian, Bernard Bender, Luisa La Cascio, Holger Frenzel, Martin Jäger, Alan Kumb und Klaus Mehret!
- Moritz Erhard, Daniel Hilk und Marcel Kraus für die tolle Zusammenarbeit während drei gemeinsamen Jahren Promotion.
- Allen KATRIN Young Scientists für die sehr gute Atmosphäre in der Arbeitsgruppe und die vielen lustigen Stammtisch-Abende.

- Meinen Studienkollegen und Freunden Johannes Bellm, Dr. Christian Böser, Dr. Felix Frensch und Ewa Holt, die mich auf meinem Weg durch das Physikstudium und die Promotion begleitet haben.
- Philip Mussgnug und Daniel Unser stellvertretend für all die wichtigen Menschen in meinem Leben, die ich in den letzten Jahren viel zu wenig gesehen habe. Danke für eure Freundschaft!
- Elke Rosswag und Dr. Ulrich Rosswag für ihre Unterstützung, insbesondere während der letzten anstrengenden Monate der Promotion.

Außerdem möchte ich mich bei meinen Eltern Heidrun Harms und Karsten Harms und meiner Schwester Friederike Harms von ganzem Herzen dafür bedanken, dass sie mich während des Studiums und der Promotion in allen Belangen uneingeschränkt unterstützt haben.

Der größte Dank gebührt an dieser Stelle meiner Frau Verena Harms, die mit mir durch alle Höhen und Tiefen der Promotion gegangen ist und mir dabei stets vor Augen geführt hat, was das wirklich Entscheidende und Wichtige in meinem Leben ist!